Relaxation Processes in a System of Two Spins*

I. SOLOMON†
Lyman Laboratory, Harvard University, Cambridge, Massachusetts
(Received March 29, 1955)

Abragam and Pound's method for the calculation of the longitudinal relaxation time T_1 has been extended to the transverse relaxation time T_2. Explicit calculations have been carried out for a pure dipole-dipole interaction, showing that for an interacting pair of like spins, or for nuclei in paramagnetic solution, T_1 is exactly equal to T_2 in the extreme narrow case. For a pair of interacting unlike spins, it is shown that the longitudinal components of the magnetic moments do not have simple exponential decays. This gives rise to a steady and transient Overhauser effect. The transverse components, however, have in all cases, simple exponential decay defined by a single relaxation time T_2. A set of modified Bloch's equations is found, giving the correct equation of motion of the macroscopic magnetic moments of such a system of pairs of unlike spins.

The equality of T_1 and T_2 has been verified in paramagnetic solutions, and a nuclear Overhauser effect has been observed in anhydrous hydrofluoric acid. If one assumes that the extreme narrow case corresponds to the actual motion, the experimental results are not consistent with the picture of a pure dipole-dipole interaction between the hydrogen and fluorine nuclei of a molecule without taking into account the effect of the other molecules.

I. INTRODUCTION

We consider a particle of spin $\mathbf{I}$ interacting with another particle of spin $\mathbf{S}$. The Hamiltonian of such an interacting pair, in a magnetic field H_0 along the z direction is

$$\mathcal{H}=\mathcal{H}_M-\hbar\gamma_I H_0 I_z-\hbar\gamma_S H_0 S_z+\mathcal{H}'. \tag{1}$$

$\mathcal{H}_M$ is the Hamiltonian of the motion of the particles and commutes with the spin operators. The next two terms are the Zeeman energies of the spins in the constant magnetic field H_0. $\mathcal{H}'$ is the spin-spin interaction term considered as a perturbation. All the explicit calculations will be performed in the case of a dipole-dipole type interaction:

$$\mathcal{H}'=-(\hbar^2\gamma_I\gamma_S/b^3)[3(\mathbf{I}\cdot\mathbf{r})(\mathbf{S}\cdot\mathbf{r})-\mathbf{I}\cdot\mathbf{S}], \tag{2}$$

but any other type of interaction, e.g., electron-coupled interaction $A\mathbf{I}\cdot\mathbf{S}$, can be treated in the same way.

We will consider only spins of value $\frac{1}{2}$ so that there is no quadrupole interaction. Larger values for the spins would make computations more complicated without fundamental changes.

II. TRANSITION PROBABILITIES

If $|m_i\rangle$ and $|m_j\rangle$ are two eigenstates of the unperturbed Hamiltonian with the corresponding energies E_i and E_j, the transition probability per unit time between these two states is, in the first order, given by

$$w_{ij}=\frac{1}{t}\frac{1}{\hbar^2}\left|\int_0^t\langle m_j|\mathcal{H}'(t')|m_i\rangle e^{-i\omega_{ij}t'}dt'\right|^2, \tag{3}$$

with

$$\omega_{ij}=(E_j-E_i)/\hbar.$$

In the case of a randomly fluctuating perturbing Hamiltonian $\mathcal{H}'(t)$, this integral has been calculated by Abragam and Pound.[1] When the fluctuations are rapid, as in liquids and gases, the result is a time-independent transition probability per unit time. In the present case of spin $\frac{1}{2}$, we define four eigenstates of the spins by the following relations:

$$\begin{aligned} I_z|+\rangle&=+\tfrac{1}{2}|+\rangle,\\ I_z|-\rangle&=-\tfrac{1}{2}|-\rangle,\\ S_z|+\rangle&=+\tfrac{1}{2}|+\rangle,\\ S_z|-\rangle&=-\tfrac{1}{2}|-\rangle, \end{aligned} \tag{4}$$

so that the four unperturbed eigenstates of a pair are $|+\rangle|+\rangle$, $|+\rangle|-\rangle$, $|-\rangle|+\rangle$, and $|-\rangle|-\rangle$ with the respective occupation numbers N_{++}, N_{+-}, N_{-+}, and N_{--}.

The transition probabilities per unit time w_0, w_1, w_1', and w_2 between these four states, which we are going to use in the discussion of the motion of the longitudinal component of the magnetic moment are indicated in diagram (A) of Fig. 1.

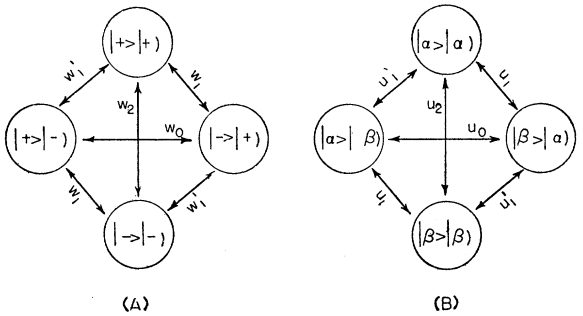


FIG. 1. (A) Transition probabilities between the eigenstates of the longitudinal components of the spin operators. (B) Transition probabilities between the eigenstates of the transverse components of the spin operators.

* This work was supported in part by the joint program of the Office of Naval Research and the U. S. Atomic Energy Commission.

† The author was supported during his residence as Research Fellow at Harvard University by Centre d'Etudes Nucléaires de SACLAY. Present address: C. E. N. de Saclay, GIF-SUR-YVETTE, France.

[1] A. Abragam and R. V. Pound, Phys. Rev. **92**, 953 (1953).

The equations of motion of the transverse components of the magnetic moment involve the operators I_x (or I_y) and S_x (or S_y). So, in similarity to set (4) we define four eigenstates of the spins by

$$\begin{aligned} I_x|\alpha\rangle &= +\tfrac{1}{2}|\alpha\rangle, \\ I_x|\beta\rangle &= -\tfrac{1}{2}|\beta\rangle, \\ S_x|\alpha\rangle &= +\tfrac{1}{2}|\alpha\rangle, \\ S_x|\beta\rangle &= -\tfrac{1}{2}|\beta\rangle. \end{aligned}$$

The four states of a pair $|\alpha\rangle|\alpha\rangle$, $|\alpha\rangle|\beta\rangle$, $|\beta\rangle|\alpha\rangle$, and $|\beta\rangle|\beta\rangle$ are not eigenstates of the energy. However, these four states are orthogonal, so it is still meaningful to speak of the occupation numbers $N_{\alpha\alpha}$, $N_{\alpha\beta}$, $N_{\beta\alpha}$, $N_{\beta\beta}$ and of the transition probabilities per unit time u_0, u_1, u_1', and u_2 between these states as indicated on Fig. 1(B).

To calculate the transition probabilities, we proceed as follows:

Consider two orthogonal states $|a\rangle$ and $|b\rangle$ that are not eigenstates of the energy. They can always be expanded in eigenvectors of the energy.

$$\begin{aligned} |a\rangle &= \textstyle\sum_i a_i|m_i\rangle, \\ |b\rangle &= \textstyle\sum_j b_j|m_j\rangle. \end{aligned} \tag{5}$$

For example, in the present case of spin $\frac{1}{2}$ we have:

$$\begin{aligned} |\alpha\rangle &= (1/\sqrt{2})[|+\rangle+|-\rangle], \\ |\beta\rangle &= (1/\sqrt{2})[|+\rangle-|-\rangle]. \end{aligned} \tag{5'}$$

Using the expansion (5) and the fact that $\langle a|b\rangle=0$, we get a formula generalizing (3). The transition probability per unit time between the states $|a\rangle$ and $|b\rangle$ is

$$u_{ab}=\frac{1}{t}\frac{1}{\hbar^2}\left|\int_0^t \sum_{ij}\langle m_j|\mathcal{H}'(t')|m_i\rangle a_i b_j e^{-i\omega_{ij}t'}dt'\right|^2.$$

This integral can be calculated in the same technique as Abragam and Pound[1] used and will be shown to be time independent in the case of rapid motion.

III. EQUATIONS OF MOTION OF THE MAGNETIC MOMENT

From the definltion of the w's, it follows that

$$\begin{aligned} dN_{++}/dt &= -(w_1+w_1'+w_2)N_{++}+w_1'N_{+-} \\ &\quad +w_1N_{-+}+w_2N_{--}+\text{constant}, \\ dN_{+-}/dt &= w_1'N_{++}-(w_0+w_1+w_1')N_{+-} \\ &\quad +w_0N_{-+}+w_1N_{--}+\text{constant}, \\ dN_{-+}/dt &= w_1N_{++}+w_0N_{+-}-(w_0+w_1+w_1')N_{-+} \\ &\quad +w_1'N_{--}+\text{constant}, \\ dN_{--}/dt &= w_2N_{++}+w_1N_{+-}+w_1'N_{-+} \\ &\quad -(w_1+w_1'+w_2)N_{--}+\text{constant}. \end{aligned} \tag{6}$$

The constants are obtained by considering the system at temperature equilibrium by inserting the proper Boltzman's factor, and are unimportant in the computation of the relaxation times.

The experimentally observable quantities are the macroscopic magnetic moments $\bar{I}_z$ and $\bar{S}_z$, distinguishable by their different Larmor frequencies and proportional to:

$$\begin{aligned} (N_{++}+N_{+-})-(N_{-+}+N_{--}) &= K\bar{I}_z, \\ (N_{++}+N_{-+})-(N_{+-}+N_{--}) &= K\bar{S}_z. \end{aligned} \tag{7}$$

Inserting the values (7) in (6) we get:

$$\begin{aligned} d\bar{I}_z/dt &= -(w_0+2w_1+w_2)\bar{I}_z \\ &\quad -(w_2-w_0)\bar{S}_z+\text{constant} \\ d\bar{S}_z/dt &= -(w_2-w_0)\bar{I}_z \\ &\quad -(w_0+2w_1'+w_2)\bar{S}_z+\text{constant}. \end{aligned} \tag{8}$$

These equations along with the results of identical calculations for the transverse components I_x and S_x lead finally to the following set of equations:

$$\begin{aligned} d\bar{I}_z/dt &= -(w_0+2w_1+w_2)(\bar{I}_z-I_0) \\ &\quad -(w_2-w_0)(\bar{S}_z-S_0), \\ d\bar{S}_z/dt &= -(w_2-w_0)(\bar{I}_z-I_0) \\ &\quad -(w_0+2w_1+w_2)(\bar{S}_z-S_0), \end{aligned} \tag{9}$$

$$\begin{aligned} d\bar{I}_x/dt &= -(u_0+2u_1+u_2)\bar{I}_x-(u_2-u_0)\bar{S}_x, \\ d\bar{S}_x/dt &= -(u_2-u_0)\bar{I}_x-(u_0+2u_1'+u_2)\bar{S}_x. \end{aligned} \tag{10}$$

I_0 and S_0 are the equilibrium values of the magnetic moments of the spins **I** and **S**, and make explicit the values of the constants of Eqs. (8). These equations show that, in general, the decay of the observed quantities is not a simple exponential, but rather a linear combination of two exponentials. There are two cases that can easily be seen to give simple exponential decays:

(a) The two spins **I** and **S** are alike ("alike" meaning that $\gamma_I=\gamma_S$). Then the only observable quantities are $\bar{I}_z+\bar{S}_z$ and $\bar{I}_x+\bar{S}_x$. From the definition it follows that $w_1'=w_1$ and $u_1'=u_1$; thus the equation of motion of the two observable quantities is

$$\begin{aligned} \frac{d}{dt}(\bar{I}_z+\bar{S}_z) &= -2(w_1+w_2)(\bar{I}_z+\bar{S}_z-I_0-S_0), \\ \frac{d}{dt}(\bar{I}_x+\bar{S}_x) &= -2(u_1+u_2)(\bar{I}_x+\bar{S}_x). \end{aligned} \tag{11}$$

These are the usual decays with the relaxation times

$$\begin{aligned} 1/T_1 &= 2(w_1+w_2), \\ 1/T_2 &= 2(u_1+u_2). \end{aligned} \tag{12}$$

(b) Nuclei relaxed in a paramagnetic solution. The relaxation of such a nuclear spin **I** will be almost entirely the result of the dipole-dipole interaction $\mathcal{H}'$, when paired with an electronic spin **S** of a paramagnetic ion. On the other hand, this interaction $\mathcal{H}'$ is a negligible relaxation process for the electronic spin **S**, so that, in the time scale of observation of the nuclear magnetic

moment, we may consider to have $\bar{S}_z=S_0$ and $\bar{S}_x=0$. Then Eqs. (9) and (10) show that the nuclear spins **I** have simple decays with relaxation times:

$$1/T_1=w_0+2w_1+w_2,$$
$$1/T_2=u_0+2u_1+u_2. \tag{13}$$

IV. BLOCH'S EQUATIONS FOR A TWO-SPIN SYSTEM

Equations (9), which we will rewrite for convenience as

$$d\bar{I}_z/dt=-\rho(\bar{I}_z-I_0)-\sigma(\bar{S}_z-S_0),$$
$$d\bar{S}_z/dt=-\rho'(\bar{S}_z-S_0)-\sigma(\bar{I}_z-I_0), \tag{14}$$

with

$$\rho=w_0+2w_1+w_2,$$
$$\rho'=w_0+2w_1'+w_2, \tag{15}$$
$$\sigma=w_2-w_0$$

are the usual macroscopic Bloch equations[2] in which we have added a term representing the spin **I**—spin **S** interaction.

It is less straightforward to compare the equation of motion (10) for the transverse components with Bloch's equations because our Eqs. (10) are the equation of motion of the expectation values of the time independent spin operators, and therefore describe the motion of I_x and S_x in coordinates rotating respectively with angular velocity $\omega_I=\gamma_I H_0$ and $\omega_S=\gamma_S H_0$. Nevertheless, let us try to represent the motion of the transverse components of the macroscopic magnetic moment by a set of Bloch's equations similarly modified by adding a spin-spin interaction term. These equations will be in the laboratory coordinates:

$$dI_+'/dt=-i\omega_I I_+'-\nu I_+'-\mu S_+',$$
$$dS_+'/dt=-i\omega_S S_+'-\nu' S_+'-\mu I_+', \tag{16}$$

with

$$I_+'=I_x'+iI_y',$$
$$S_+'=S_x'+iS_y'.$$

Now to compare with Eqs. (10) we shall write Eqs. (16) in the rotating coordinates ($I_+=I_+'e^{i\omega_I t}$ and $S_+=S_+'e^{i\omega_S t}$):

$$dI_+/dt=-\nu I_+-\mu e^{-i(\omega_S-\omega_I)t}S_+,$$
$$dS_+/dt=-\nu' S_+-\mu e^{-i(\omega_I-\omega_S)t}I_+. \tag{17}$$

(a) In the case of like spins, $\omega_S=\omega_I$ and Eqs. (17) give simply: (ν and ν' are obviously equal by symmetry considerations)

$$\frac{d}{dt}(I_++S_+)=-(\nu+\mu)(I_++S_+).$$

That is exactly the second of Eq. (11) with

$$\nu+\mu=2(u_1+u_2). \tag{18}$$

(b) In the case of unlike spins, "unlike" meaning that

$$|\omega_I-\omega_S|\gg\nu,\quad |\omega_I-\omega_S|\gg\nu',$$

the last term of Eq. (17) will average out so that the transverse components have simple exponential decays:

$$dI_+/dt=-\nu I_+,$$
$$dS_+/dt=-\nu' S_+. \tag{19}$$

So these modified Bloch equations of the transverse components, obtained by analogy with the Eq. (14) for the longitudinal components, predict that, in Eqs. (10), we shall have

$$u_2-u_0=0. \tag{20}$$

This will be proven quantum mechanically in the next section. Then Eqs. (17) represent the correct motion of the transverse components in all the cases with the set of values

$$\nu=u_0+2u_1+u_2,$$
$$\nu'=u_0+2u_1'+u_2, \tag{21}$$
$$\mu=u_2-u_0.$$

To summarize, it has been shown in this section, that the Bloch equations do not hold for a two-spin system. However, by a slight modification of these, one can still find a set of equations [Eqs. (14) and (17)] that represent the motion of the macroscopic magnetic moment. It has been seen, too, that unlike the longitudinal components, the transverse components always have a simple exponential decay.

V. STEADY AND TRANSIENT OVERHAUSER EFFECT

In any steady-state condition, the first of Eqs. (14) will give

$$-\rho(\bar{I}_z-I_0)-\sigma(\bar{S}_z-S_0)=0. \tag{22}$$

If we apply an intense rf field at the resonance frequency of the spins S, for example, so that we equalize the populations in state $|+)$ and $|-)$ ("saturation"), we will have

$$S_z=0. \tag{23}$$

Now, inserting the value (23) in Eq. (22) we get the value of I_z, when S_z is saturated:

$$\bar{I}_z=I_0+(\sigma/\rho)S_0. \tag{24}$$

This is the effect first derived by Overhauser,[3] and extended by Bloch[4] to the case of dipole-dipole interaction. It is to be remarked that in the case of nuclear spins, Eq. (24) could be used to determine the relative signs of the gyromagnetic ratios of the two spins: The effect would be an increase of the static magnetic moment if the two signs are the same, and a decrease if the signs are opposite.

A solution of Eqs. (14) of particular interest is the one corresponding to the initial conditions:

$$(\bar{I}_z-I_0)_{t=0}=0,$$
$$(\bar{S}_z-S_0)_{t=0}=S_i. \tag{25}$$

The solution, in the case $\rho=\rho'$, is, (the case $\rho\neq\rho'$ gives more complicated formulas, without any funda-

[2] F. Bloch, Phys. Rev. **70**, 460 (1946).

[3] A. Overhauser, Phys. Rev. **89**, 689 (1953); **92**, 477 (1953).

[4] F. Bloch, Phys. Rev. **93**, 944 (1954).

mental difference)

$$\bar{I}_z-I_0=\tfrac{1}{2}S_i[e^{-(\rho+\sigma)t}-e^{-(\rho-\sigma)t}],$$
$$\bar{S}_z-S_0=\tfrac{1}{2}S_i[e^{-(\rho+\sigma)t}+e^{-(\rho-\sigma)t}]. \quad (26)$$

These equations show that the relaxation of the spins **S** changes the difference of populations of spins **I** in time. This could be called a "transient" Overhauser effect and has been studied experimentally. The results will be discussed in Sec. VII.

VI. COMPUTATION OF THE TRANSITION PROBABILITIES

As an illustration of the method given in Sec. II we are going to compute the transition probabilities when the perturbing Hamiltonian $\mathcal{H}'$ is the dipole-dipole interaction (2). This perturbing Hamiltonian will be written as in Bloembergen, Purcell, and Pound's paper[5]:

$$\mathcal{H}'=[I_zS_z-\tfrac{1}{4}(I_+S_-+I_-S_+)]F_0+[I_+S_z+I_zS_+]F_1 +[I_-S_z+I_zS_-]F_1^*+I_+S_+F_2+I_-S_-F_2^*, \quad (27)$$

with

$$F_0(t)=k[1-3\cos^2\theta(t)],$$
$$F_1(t)=-\tfrac{3}{2}k\sin\theta(t)\cos\theta(t)e^{i\varphi(t)},$$
$$F_2(t)=-\tfrac{3}{4}k\sin^2\theta(t)e^{2i\varphi(t)}, \quad (28)$$
$$k=\hbar^2\gamma_I\gamma_S/b^3.$$

We shall assume, as usual, that

$$\langle F(t)F^*(t+\tau)\rangle=\langle|F(0)|^2\rangle e^{-|\tau|/\tau_c},$$

the brackets meaning average among all pairs.

It can be seen[5] that

$$\langle F_0^2\rangle=\tfrac{4}{5}k^2,$$
$$\langle|F_1|^2\rangle=\tfrac{3}{10}k^2,$$
$$\langle|F_2|^2\rangle=\tfrac{3}{10}k^2.$$

Now we can calculate the transition probabilities used in the preceding sections. Equation (3) gives

$$w_0=\frac{1}{t\hbar^2}\left|\int_0^t\tfrac{1}{4}F_0(t')e^{-i(\omega_I-\omega_S)t'}dt'\right|^2,$$
$$w_1=\frac{1}{t\hbar^2}\left|\int_0^t\tfrac{1}{2}F_1(t')e^{-i\omega_It'}dt'\right|,$$
$$w_1'=\frac{1}{t\hbar^2}\left|\int_0^t\tfrac{1}{2}F_1(t')e^{-i\omega_St'}dt'\right|^2, \quad (29)$$
$$w_2=\frac{1}{t\hbar^2}\left|\int_0^t\tfrac{1}{2}F_2(t')e^{-i(\omega_I+\omega_S)t'}dt'\right|^2.$$

Equation (6) gives, with the use of the expansion (5′),

$$u_0=\frac{1}{t\hbar^2}\left|\frac{1}{4}\int_0^t\{(1-\tfrac{1}{4}[e^{-i(\omega_I-\omega_S)t'}+e^{i(\omega_I-\omega_S)t'}])F_0(t')-(e^{-i\omega_It'}-e^{-i\omega_St'})F_1(t') +(e^{i\omega_It'}-e^{i\omega_St'})F_1^*(t')-e^{-i(\omega_I+\omega_S)t'}F_2(t')-e^{i(\omega_I+\omega_S)t'}F_2^*(t')\}dt'\right|^2,$$
$$u_1=\frac{1}{t\hbar^2}\left|\frac{1}{4}\int_0^t\{\tfrac{1}{4}(e^{-i(\omega_I-\omega_S)t'}-e^{i(\omega_I-\omega_S)t'})F_0(t')+e^{-i\omega_St'}F_1(t') +e^{i\omega_St'}F_1^*(t')-e^{-i(\omega_I+\omega_S)t'}F_2(t')+e^{i(\omega_I+\omega_S)t'}F_2^*(t')\}dt'\right|^2, \quad (30)$$
$$u_2=\frac{1}{t\hbar^2}\left|\frac{1}{4}\int_0^t\{(1+\tfrac{1}{4}[e^{-i(\omega_I-\omega_S)t'}+e^{i(\omega_I-\omega_S)t'}])F_0(t')+(e^{-i\omega_It'}+e^{-i\omega_St'})F_1(t') -(e^{i\omega_It'}+e^{i\omega_St'})F_1^*(t')+e^{-i(\omega_I+\omega_S)t'}F_2(t')+e^{i(\omega_I+\omega_S)t'}F_2^*(t')\}dt'\right|^2.$$

u_1' is obtained from u_1 by interchanging ω_I and ω_S.

It is seen that, before performing the integration, we must distinguish the cases where $\omega_I=\omega_S$ and $\omega_I\neq\omega_S$. We will assume that the motion is rapid, so that $\tau_cw\ll1$ and $\tau_cu\ll1$.

(a) Pairs of Like Spins: $\omega_I=\omega_S=\omega$

$$w_0=\frac{\tau_c}{8\hbar^2}\langle F_0^2\rangle,$$
$$w_1=w_1'=\frac{\tau_c}{2\hbar^2}\langle|F_1|^2\rangle\frac{1}{1+\omega^2\tau_c^2}, \quad (31)$$
$$w_2=\frac{2\tau_c}{\hbar^2}\langle|F_2|^2\rangle\frac{1}{1+4\omega^2\tau_c^2},$$
$$u_0=\frac{\tau_c}{8\hbar^2}\left[\frac{\langle F_0^2\rangle}{4}+\langle|F_2|^2\rangle\frac{2}{1+4\omega^2\tau_c^2}\right],$$
$$u_1=u_1'=\frac{\tau_c}{8\hbar^2}\left[\langle|F_1|^2\rangle\frac{2}{1+\omega^2\tau_c^2}+\langle|F_2|^2\rangle\frac{2}{1+4\omega^2\tau_c^2}\right], \quad (32)$$
$$u_2=\frac{\tau_c}{8\hbar^2}\left[\frac{9}{4}\langle F_0^2\rangle+\langle|F_1|^2\rangle\frac{8}{1+\omega^2\tau_c^2}+\langle|F_2|^2\rangle\frac{2}{1+4\omega^2\tau_c^2}\right].$$

[5] Bloembergen, Purcell, and Pound, Phys. Rev. **73**, 679 (1948).

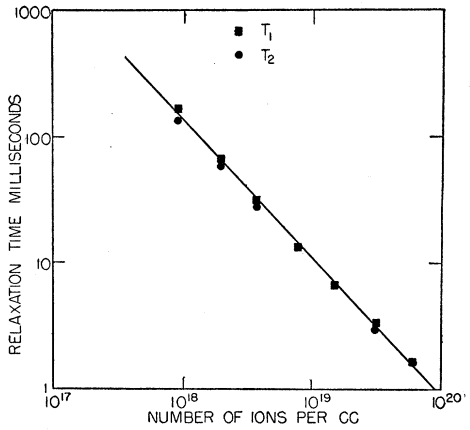


FIG. 2. Longitudinal and transverse relaxation times of protons at room temperature in paramagnetic solutions of ferric ions ($FeNH_4(SO_4)_2+12H_2O$) of different concentrations.

Using these values in Eqs. (12) we get the relaxation times:

$$\frac{1}{T_1}=\frac{6}{20}\frac{\hbar^2\gamma^4}{b^6}\left[\frac{\tau_c}{1+\omega^2\tau_c^2}+\frac{4\tau_c}{1+4\omega^2\tau_c^2}\right],$$
$$\frac{1}{T_2}=\frac{3}{20}\frac{\hbar^2\gamma^4}{b^6}\left[3\tau_c+\frac{5\tau_c}{1+\omega^2\tau_c^2}+\frac{2\tau_c}{1+4\omega^2\tau_c^2}\right]. \tag{33}$$

These results are identical to Kubo and Tomita's.[6] In the extreme narrow case ($\omega^2\tau_c^2\ll1$), we can see that $T_1=T_2$.

$$1/T_1=1/T_2=\tfrac{3}{2}(\hbar^2\gamma^4/b^6)\tau_c. \tag{34}$$

(b) Pairs of Unlike Spins

The w's give the straightforward generalization

$$w_0=\frac{\tau_c}{8\hbar^2}\langle F_0^2\rangle\frac{1}{1+(\omega_I-\omega_S)^2\tau_c^2},$$
$$w_1=\frac{\tau_c}{2\hbar^2}\langle|F_1|^2\rangle\frac{1}{1+\omega_I^2\tau_c^2},$$
$$w_1'=\frac{\tau_c}{2\hbar^2}\langle|F_1|^2\rangle\frac{1}{1+\omega_S^2\tau_c^2}, \tag{35}$$
$$w_2=\frac{2\tau_c}{\hbar^2}\langle|F_2|^2\rangle\frac{1}{1+(\omega_I+\omega_S)^2\tau_c^2}.$$

In computing the u's, if we suppose that $|\omega_I-\omega_S|\gg1/T$, so that any integral of the form:

$$\frac{1}{T}\frac{1}{\hbar^2}\int_0^T\int_0^T F^*(t')e^{-i\omega_I t'}F(t'')e^{i\omega_S t''}dt'dt''$$

averages out for any macroscopic time of observation T ($1/T$ is of order of magnitude of the u's) we get

$$u_0=u_2=\frac{\tau_c}{8\hbar^2}\left\{\left(1+\frac{1}{8}\frac{1}{1+(\omega_I-\omega_S)^2\tau_c^2}\right)\langle F_0^2\rangle+\left(\frac{2}{1+\omega_I^2\tau_c^2}+\frac{2}{1+\omega_S^2\tau_c^2}\right)\langle|F_1|^2\rangle+\frac{2}{1+(\omega_I+\omega_S)^2\tau_c^2}\langle|F_2|^2\rangle\right\},$$
$$u_1=\frac{\tau_c}{8\hbar^2}\left\{\frac{1}{8}\frac{1}{1+(\omega_I-\omega_S)^2\tau_c^2}\langle F_0^2\rangle+\frac{2}{1+\omega_S^2\tau_c^2}\langle|F_1|^2\rangle+\frac{2}{1+(\omega_I+\omega_S)^2\tau_c^2}\langle|F_2|^2\rangle\right\}, \tag{36}$$
$$u_1'=\frac{\tau_c}{8\hbar^2}\left\{\frac{1}{8}\frac{1}{1+(\omega_I-\omega_S)^2\tau_c^2}\langle F_0^2\rangle+\frac{2}{1+\omega_I^2\tau_c^2}\langle|F_1|^2\rangle+\frac{2}{1+(\omega_I+\omega_S)^2\tau_c^2}\langle|F_2|^2\rangle\right\}.$$

In the extreme narrow conditions ($\omega_I^2\tau_c^2\ll1$ and $\omega_S^2\tau_c^2\ll1$), the above formulas are considerably simplified:

$$w_0=\tfrac{1}{10}\delta,$$
$$w_1=w_1'=(3/20)\delta, \tag{37}$$
$$w_2=\tfrac{3}{5}\delta,$$

$$u_0=u_2=27/80,$$
$$u_1=u_1'=13/80, \tag{38}$$

with $\delta=\hbar^2\gamma_I^2\gamma_S^2\tau_c/b^6$.

With these values, the equation of motion (14) and (17) become

$$\frac{d}{dt}(\bar{I}_z-I_0)=-\delta[(\bar{I}_z-I_0)+\tfrac{1}{2}(\bar{S}_z-S_0)],$$
$$\frac{d}{dt}(\bar{S}_z-S_0)=-\delta[\tfrac{1}{2}(\bar{I}_z-I_0)+(\bar{S}_z-S_0)], \tag{39}$$
$$dI_+/dt=-\delta I_+,$$
$$dS_+/dt=-\delta S_+.$$

And the solution (26) for the longitudinal components is,

$$\bar{I}_z-I_0=\tfrac{1}{2}S_i[\exp(-\tfrac{3}{2}\delta t)-\exp(-\tfrac{1}{2}\delta t)],$$
$$\bar{S}_z-S_0=\tfrac{1}{2}S_i[\exp(-\tfrac{3}{2}\delta t)+\exp(-\tfrac{1}{2}\delta t)]. \tag{40}$$

[6] R. Kubo and K. Tomita, J. Phys. Soc. (Japan) 9, 888 (1954).

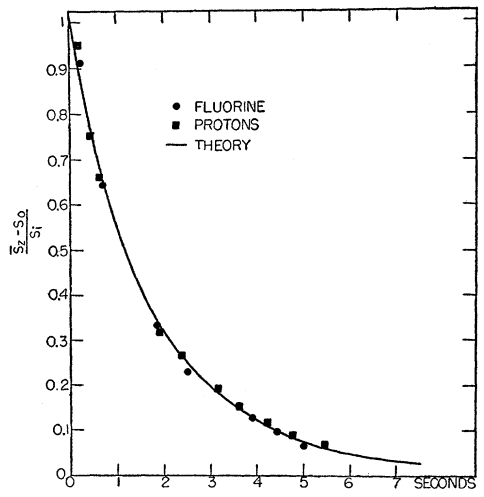


FIG. 3. Motion of the longitudinal component of the magnetic moment of one kind of nuclei toward its equilibrium value in hydrofluoric acid. The equation of the solid curve is

$$(\bar{S}_z-S_0)/S_i=\tfrac{1}{2}[\exp(-t/D_1)+\exp(-t/T_1)],$$

with $T_1=1.27$ sec and $D_1=2.25$ sec.

(c) Relaxation of Nuclei in Paramagnetic Solution

Inserting the values (35) and (36) in the Eqs. (13) one gets:

$$\frac{1}{T_1}=\frac{1}{10}\frac{\hbar^2\gamma_I^2\gamma_S^2}{b^6}\left[\frac{\tau_c}{1+(\omega_I-\omega_S)^2\tau_c^2}+\frac{\tau_c}{1+\omega_I^2\tau_c^2}+\frac{\tau_c}{1+(\omega_I+\omega_S)^2\tau_c^2}\right],$$

$$\frac{1}{T_2}=\frac{\hbar^2\gamma_I^2\gamma_S^2}{20b^6}\left[4\tau_c+\frac{\tau_c}{1+(\omega_I-\omega_S)^2\tau_c^2}+\frac{3\tau_c}{1+\omega_I^2\tau_c^2}+\frac{6\tau_c}{1+\omega_S^2\tau_c^2}+\frac{6\tau_c}{1+(\omega_I+\omega_S)^2\tau_c^2}\right]. \tag{41}$$

In the extreme narrow case, as expected, $T_1=T_2$:

$$1/T_1=1/T_2=(\hbar^2\gamma_I^2\gamma_S^2/b^6)\tau_c. \tag{42}$$

We have measured the relaxation times of protons in paramagnetic solutions containing different concentrations of ferric ions. As it is shown in Fig. 2, the predicted equality between T_1 and T_2 has been verified within about 2.5 percent.

VII. EXPERIMENTAL RESULTS

The most sensitive test of the theory outlined above appears to be the Overhauser effect discussed in Sec. V. This effect has been observed in anhydrous hydrofluoric acid HF at room temperature. The boiling point of the acid, at atmospheric pressure, is 19.4°C. As a result, the commercially obtained acid is stored in steel cylinders, necessitating subsequent distillation. After triple distillation in transparent Kel-F plastic tubes, the acid became colorless. The resonance studies were carried out in small samples of acid sealed in Kel-F tubes.[7]

Free precession techniques[8,9] ("spin echo") were used, permitting a direct measurement of $\bar{S}_z$, $\bar{I}_z$, $\bar{I}_x$, and $\bar{S}_x$.

The initial conditions (25) were obtained by applying at the time $t=0$ a "180° pulse" at the resonance frequency of the spins **S**. Then at $t=0$,

$$(\bar{S}_z)_{t=0}=-S_0.$$

So the initial conditions (25) are in this case:

$$(\bar{I}_z-I_0)_{t=0}=0,\qquad S_i=(\bar{S}_z-S_0)_{t=0}=-2S_0. \tag{43}$$

In the extreme narrow case, we have in Eqs. (14) $\rho=\rho'$. Even if we are not in the extreme narrow case, this equality will hold approximately in hydrofluoric acid, for the Larmor frequencies of hydrogen and fluorine differ by less than 6 percent. In this condition, solution (26) with the initial condition (43) is

$$\bar{I}_z-I_0=S_0[e^{-(\rho-\sigma)t}-e^{-(\rho+\sigma)t}],\qquad \bar{S}_z-S_0=-S_0[e^{-(\rho-\sigma)t}+e^{-(\rho+\sigma)t}]. \tag{44}$$

Figures 3 and 4 show the experimental results, that are, as expected from our simple theory, symmetrical with respect to the hydrogen and fluorine nuclei. The figures show that the experimental points can be fitted very

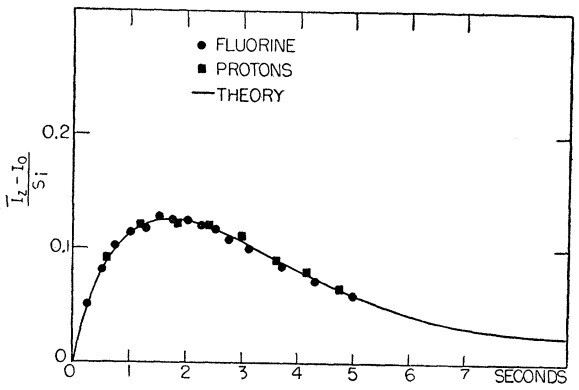


FIG. 4. Motion of the longitudinal component of one kind of spin after having applied a 180° pulse to the other kind of spin in hydrofluoric acid. The equation of the solid curve is

$$(\bar{I}_z-I_0)/S_i=\tfrac{1}{2}[\exp(-t/D_1)-\exp(-t/T_1)],$$

where T_1 and D_1 are the same as in Fig. 3.

[7] The first experiments were performed in Teflon. But after a few days in Teflon, the liquid acid becomes colored and the relaxation times drop considerably, showing that commercial Teflon is not completely inert to hydrofluoric acid.

[8] E. L. Hahn, Phys. Rev. **80**, 580 (1950).

[9] H. Y. Carr and E. M. Purcell, Phys. Rev. **94**, 630 (1954).

well by (44) with the values:

$$T_1=1/(\rho+\sigma)=1.27 \text{ sec},$$

$$D_1=1/(\rho-\sigma)=2.55 \text{ sec}.$$

The estimated error in these times is about 20 percent. These results show a ratio $\sigma/\rho=\frac{1}{3}$. The same ratio is obtained directly from the steady Overhauser effect: Saturation of protons (or fluorine nuclei) increases the magnetization due to fluorine (or to protons if fluorine has been saturated) by a factor of about 30 percent. The static magnetic moments of hydrogen and fluorine being approximately equal, Eq. (24) gives $\sigma/\rho\cong\frac{1}{3}$.

This ratio of $\frac{1}{3}$ is, however, in disagreement with the value $\frac{1}{2}$ calculated for a pure dipole-dipole interaction in the extreme narrow case [Eqs. (39) and (40)].

The decay of the transverse component is, within experimental errors, simply exponential with the same time constant T_2 for protons and fluorine nuclei:

$$T_2=0.43\pm0.015 \text{ sec}.$$

This again is in disagreement with Eq. (39), showing that either the effect of neighboring molecules needs to be taken into account, or that the interaction is not a pure dipole-dipole one, or both. It has been possible to remove the discrepancy by adding to the pure dipole-dipole interaction an electron-coupled exchange interaction $A\mathbf{I}\cdot\mathbf{S}$ of reasonable amplitude. Further experiments on purer hydrofluoric acid are being carried out to investigate this effect.

Figure 5 is an example of the signals obtained: It shows the increase of the magnetization due to fluorine, following a 180° pulse for protons. The magnitude of the longitudinal magnetic moment of fluorine is indicated by the amplitude of the tail following a 90° pulse for fluorine.

On the same photograph are superimposed: (a) the thermal equilibrium value of the magnetic moment of the fluorine obtained by simply applying a 90° pulse for fluorine (tails *a* and *b*). (b) the value of the magnetic moment of the fluorine when the protons are saturated (tail *c*). Similar photographs have been obtained by interchanging the role of hydrogen and fluorine.

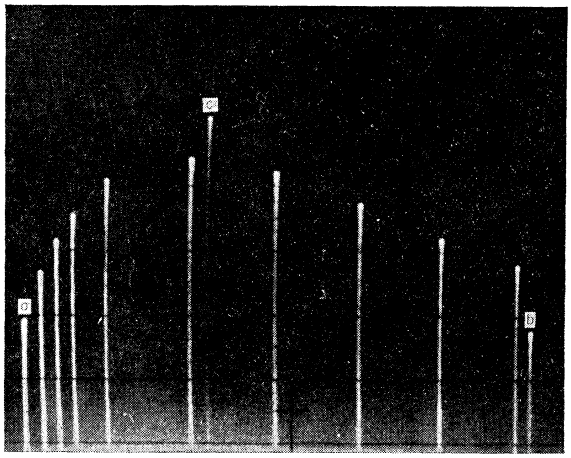


FIG. 5. Amplitude of tails of 90° pulses at fluorine frequency after having applied a 180° pulse at hydrogen frequency in hydrofluoric acid. *a* and *b* represent the amplitude of the tail when no 180° pulse has been applied; *c* represents the amplitude of the tail when the proton resonance has been saturated (steady Overhauser effect).

ACKNOWLEDGMENTS

The experiment was suggested, during a discussion on the subject, by Professor N. Bloembergen. It is a pleasure to thank him for his constant interest in the development of this work and for many valuable suggestions. I wish to thank Dr. K. Tomita and Professor R. V. Pound for many helpful discussions. Professor E. M. Purcell drew my attention to some important theoretical inaccuracies in the early stages of this work. I want to express my gratitude to Dr. G. B. Benedek for having introduced me to the spin echoes techniques and for having kindly revised the manuscript.

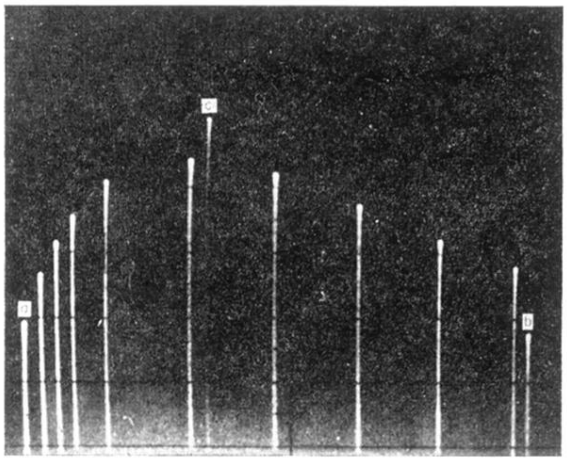


FIG. 5. Amplitude of tails of 90° pulses at fluorine frequency after having applied a 180° pulse at hydrogen frequency in hydrofluoric acid. *a* and *b* represent the amplitude of the tail when no 180° pulse has been applied; *c* represents the amplitude of the tail when the proton resonance has been saturated (steady Overhauser effect).

Invited Review

The Magic Angle Effect: A Source of Artifact, Determinant of Image Contrast, and Technique for Imaging

Mark Bydder, PhD,[1] Andres Rahal, MD,[2] Gary D. Fullerton, PhD,[2] and Graeme M. Bydder, MB, ChB[1]*

This review provides a formalism for understanding magic angle effects in clinical studies. It involves consideration of the fiber-to-field angle for linear structures such as tendons, ligaments, and peripheral nerves, disc-like and circular structures such as menisci and labra, as well as complex three-dimensional structures. There may be one or more fiber types with different orientations within each of these tissues. The orientation of these fibers to B_0 is crucial in determining their magic angle effect. Tissues may show a variety of appearances depending on their baseline T2, as well as the increase in T2 produced by the magic angle effect. The appearances are affected by TE, which affects both the general tissue signal level and the change in signal produced by the magic angle effect, fiber-to-slice orientation, and partial volume effects. Deliberate positioning of structures and tissues at particular orientations to B_0 can be used to increase the signal from tissues such as tendons and ligaments and so allow them to be imaged with conventional sequences. The technique can also be used to produce contrast between tissues with fibers that have different orientations to B_0.

Key Words: magnetic resonance imaging; magic angle effects; artifact; magic angle imaging; contrast
J. Magn. Reson. Imaging 2007;25:290–300.
© 2007 Wiley-Liss, Inc.

IN PULSE SEQUENCES with a moderate or short TE, the signal intensity of tendons and ligaments depends on their orientation to the static magnetic field (B_0) (1–3). These highly ordered, collagen-rich tissues contain water that is bound to collagen. The protons within this water are subject to dipolar interactions whose strength depends on the orientation of the fibers to B_0. These interactions usually result in rapid dephasing of the MR signal after excitation. As a consequence, tendons and ligaments typically produce little or no detectable MR signal and appear dark when imaged with conventional clinical pulse sequences.

The dipolar interactions are modulated by the term $3\cos^2\theta - 1$, where θ is the angle the structures make with the magnetic field B_0. When $3\cos^2\theta - 1 = 0$ ($\theta = 55°$, 125°, etc., approximately, the magic angle), dipolar interactions are minimized with the result that the T2 of these tissues is increased and signal intensity may become evident within them when they are imaged with conventional pulse sequences. The magnitude of the magic angle effect may be quite large. For example, Fullerton et al (1) have described an increase in T2 of Achilles tendon from 0.6 to 22 msec and Henkelman et al (2) have described an increase from 7 to 23 msec when the orientation of the tendon to B_0 was changed from 0° to 55°. With some commonly used pulse sequences this may correspond to the tendon signal intensity increasing from the bottom of the imaging gray scale to the top of it.

In initial studies with clinical MRI the effect was seen principally in tendons that underwent a change of direction along their course such as the supraspinatus tendon near its insertion so that the fibers of one part of the tendon were oriented at or near 55° to B_0. The high signal resulting from the increase in T2 in the part of the tendon at 55° to B_0 simulated an increase in T2 produced by disease, and so the effect was found to be a source of confusion and was regarded as an artifact, which was to be avoided if possible (3,4).

The main method of avoiding magic angle effects was to increase the echo time (TE) of the pulse sequences used to image tendons and ligaments. If the TE of the pulse sequence was increased sufficiently (e.g., to greater than 37 msec for tendons in one study (5), the increase in T2 produced by the magic angle effect did not result in an increase in signal in the tendon or ligament, whereas diseases that increased tissue T2 more than the magic angle effect did, resulting in an increase in signal that could be correctly attributed to disease. While this approach helped with specificity, it could result in a loss of sensitivity for disease that did

[1]Department of Radiology, University of California, San Diego, San Diego, California, USA.
[2]Department of Radiological Sciences, University of Texas Health Sciences Center at San Antonio, San Antonio, Texas.
*Address reprint requests to: G.M.B., Department of Radiology, University of California San Diego, 200 West Arbor Drive, San Diego CA 92103 8226. E-mail: gbydder@ucsd.edu
Received July 3, 2006; Accepted September 28, 2006.
DOI 10.1002/jmri.20850
Published online in Wiley InterScience (www.interscience.wiley.com).

© 2007 Wiley-Liss, Inc.

not increase T2 as much as the magic angle effect did. Since the effect produces a relatively large increase in T2, this could be a common occurrence, as noted by Peterfy et al (6) in imaging tears in the meniscus of the knee.

Another way of avoiding diagnostic confusion due to the magic angle effect is to use T1-weighted approaches, which may be more effective in distinguishing effects due to disease from those due to magic angle effects, providing that effects due to the increase in T2 can be minimized. This is because the T1 of tendons and ligaments is not changed, or only slightly changed, by the magic angle effect and changes in T1 due to disease may be quite large. In distinguishing disease from magic angle effects there is also a role for alternative patient positioning, although this may be limited by physical constraints due to the confined space within most MR systems.

Several recent developments have prompted a reconsideration of the role of magic angle effects in clinical practice and have extended its role to other situations besides that of a source of artifact. The more widespread use of vertical static field magnets now means that different orientations of tendons and ligaments to the static magnetic field are seen, in addition to the well-known patterns found with the typical horizontal bore solenoidal magnets, and so magic angle effects are now seen in a wider range of situations. The use of a vertical field magnet may resolve the problem of distinguishing magic angle artifact from degeneration in the supraspinatus tendon, but create difficulty with the infraspinatus tendon, which may display a high signal because fibers are at the magic angle. Open magnets may allow an even wider range of orientations of tissues to B_0, particularly if dynamic studies are being performed, and this may result in magic effects appearing in even more situations.

There has been interest in reducing pulse sequence TEs to times as short as 8–80 μsec (7,8). With these ultrashort TE (UTE) sequences, signal can be detected from tendons, ligaments, and menisci with their fibers at 0° to B_0. These tissues previously gave no signal with conventional sequences except when their fibers were orientated at 55° to B_0. The signals detectable with UTE sequences may vary with orientation to B_0 and the situation may be complicated by the fact that UTE sequences are frequently used with long T2 suppression methods, which may decrease the signal from tissues when their T2 has been increased by the magic angle effect, rather than increase it (8).

There has also been recognition of magic angle effects in a wider range of tissues including peripheral nerve (9) and tissues with short T2s such as the basal layers of articular cartilage and some forms of fibrocartilage in which MR signal has previously been undetectable with conventional pulse sequences, but can now be seen with UTE sequences (8).

While magic angle effects have been described in the posterior root of the lateral meniscus when this tissue is imaged in a typical solenoidal horizontal bore magnet and not elsewhere in the meniscus (6), far more widespread magic angle effects are seen in the meniscus with vertical field magnets. These may involve circumferential, radial, and superficial fibers of the meniscus, which may all be in different orientations to B_0 and produce a variety of different appearances depending on slice orientation, partial volume effects, and other factors. It may be difficult to understand signal intensity and conspicuity of the meniscus in this situation without including an appreciation of magic angle effects. Similar considerations apply to articular cartilage, although magic angle effects in this tissue have been studied in far more detail.

Although emphasis has been placed on orientations of fibers at 55° to B_0 producing an increase in signal relative to the orientation at 0° a loss of signal may be seen in the fibers at 0° relative to the majority of fibers at angles different from 0°. There are also situations in which fibers are oriented in the same general direction but cover a wider or narrower range of angles. High contrast may result between tissues with different angular dispersions of fibers, with structures orientated at or near angles of 55° or 90° relative to B_0.

It has also been possible to deliberately position tendons and ligaments at or near the magic angle to increase their T2 so that signal from them becomes detectable with conventional pulse sequences (10–13). Changes in this signal due to disease, contrast enhancement, or both can then be detected. The available signal also provides access to other MRI parameters such as magnetization transfer and diffusion. In addition the same general approach of purposefully orientating structures or tissues at particular angles to B_0 can be used to produce conspicuity between tissues or components of tissues with fibers oriented in different directions.

In clinical practice it is no longer possible to regard the magic angle effect just as a source of artifact in certain tendons and ligaments that happen to be at 55° to B_0 when these structures are imaged in typical solenoidal magnets. The broader view of the role of magic angle effects includes localized artifacts as first described, but in a wider range of situations, magic angle effects as a major determinant of contrast in tissues such as the menisci and articular cartilage, as well as an imaging technique in applications where detectable signal can be increased such as in disease in tendons (both with and without contrast enhancement) and a method for exploiting differences in fiber direction to develop conspicuity. In this article we elaborate on this concept and provide examples in clinical and research applications.

THE MAGIC ANGLE EFFECT

The structure of collagen and the physical chemistry underlying the magic angle effect are the subject of another article in this issue and are not dealt with in this article, which is concerned with magic angle effects in clinical imaging.

Tissues or structures that have demonstrable magic angle effects with proton MRI are listed in Table 1. A common feature of most tissues in the list is ordered collagen. This includes peripheral nerve, which has collagen in the epineurium, perineurium, and endoneurium. Ordered collagen of this type is not seen in the central nervous system (CNS). Magic angle effects have

Table 1
Tissues or Structures Demonstrating Magic Angle Effects With Proton MR Imaging

Tendons
Ligaments
Entheses
Peripheral nerve
Labra (glenoid and acetabular)
Intervertebral discs
Other discs
Menisci
Fibrocartilage
Articular cartilage
Fasciae, membranes, capsules, bands (variable)
Muscle (uncertain with proton MR imaging)
Cortical bone (uncertain)

been described in muscle with phosphorous spectroscopy (14) but demonstration of these with proton imaging has proved elusive; if they are present they are quite small. There has been one description of magic angle effects in cortical bone samples (15). Although signal can now be detected from cortical bone with UTE imaging techniques, and bone does contain ordered collagen, to date there has been no convincing demonstration of magic angle effects in vivo with MRI.

The imaging demonstration of articular cartilage now includes the deepest layers (calcified layer and deep radial zones) that can be visualized with UTE sequences, and these tissue components display magic angle effects. Likewise, the fibrocartilage present in entheses can now be detected with UTE sequences, and this tissue also displays magic angle effects (16).

The change in signal intensity produced by differences in fiber-to-field orientation provides the characteristic signature of the magic angle effect. The basic pattern of T2 and signal intensity change is shown in Fig. 1. Both T2 and signal intensity are maximal at 55° (and 125°) to B_0 with minimal at 0° and to a lesser extent, 90° to B_0. The width of the peak varies with dispersion of fiber angles to B_0 within tissue. If the fibers are highly parallel, a narrow peak results, but if the fibers are spread over a range of angles, a broader peak is seen.

While the magic angle effect is commonly manifested as a local increase in signal intensity when fibers are oriented at or close to 55° relative to the signal from adjacent fibers at angles greater or lesser than 55°, the effect may also be manifest as a local area of decreased signal intensity when fibers are at 0° or 90° relative to the signal from adjacent fibers at angles greater or lesser than each of these angles.

Although a small change in T1 has been described in some tissues as a result of magic angle effects (2), this is a much smaller than the change in T2 and is usually not significant in the clinical context.

For consistency, we take the T2 and the signal from a collagen-rich tissue with its dominant fibers oriented at zero degrees to B_0 to be the baseline value, and consider situations in which the T2 (and signal intensity) are increased from this level as a result of magic angle effects. A major determinant of this increase is the fiber-to (static) field orientation and this forms the subject of the next section.

FIBER-TO-FIELD ORIENTATION

The signal intensity of a tissue containing ordered collagen depends on a number of factors, beginning with those that determine fiber-to-static field orientation.

Magnet Type and Static Field (B_0) Orientation

The orientation of the patient to B_0 is largely determined by the magnet type with: 1) the long axis of the patient parallel to B_0 in a typical solenoidal magnet; 2) the long axis of the patient perpendicular to B_0 in a vertical field magnet; and 3) variable orientations of the patient to B_0 with (truly) open magnets. Of particular interest in the third case are orientations not achievable, or not easily achievable; such as, in the first two cases, left-right orientation of B_0 relative to the patient. These consid-

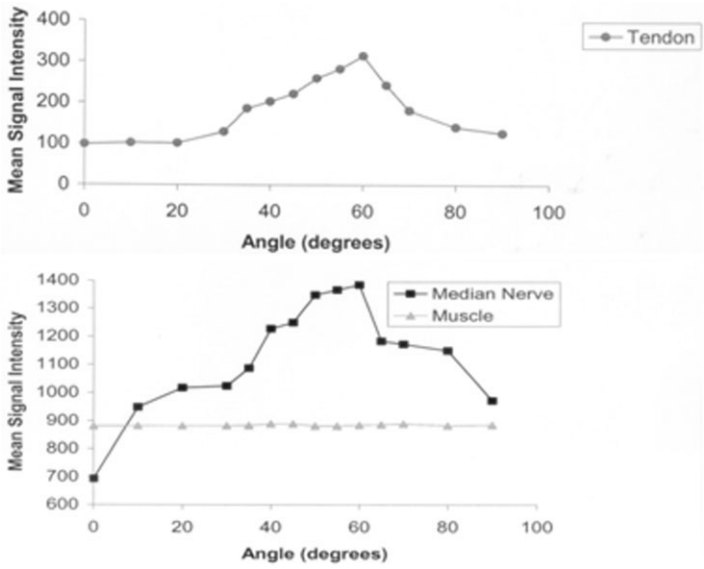


Figure 1. Plot of signal intensity vs. orientation to B_0 for flexor tendons (**a**) and median nerve (**b**). The signal intensity increases up to a maximum at about 55° and decreases toward 90°.

erations generally dictate the macroscopic orientation of structures and tissues, although with the limbs, additional options are available with creative positioning.

It is useful to consider tendons, ligaments, and peripheral nerve, in which the basic orientation of the tissue is essentially linear, as one group of tissues; menisci, labra, intervertebral discs, and some articular cartilage such as the tibial plateau, in which the basic configuration of the tissue is disc-like or circular, as a second group; and articular cartilage in other situations as well as fibrocartilage, in which the tissue geometry is more complex, as a third group. Within these groups tissue fibers may be oriented in a single direction or in multiple directions.

Tissue Structure: Direction and Planes

With tendons, ligaments, and peripheral nerves the macroscopic fiber structure is linear and the orientation of fibers largely follows this pattern. There is some dispersion of fibers at branches as well as at attachments of tendons and ligaments. The direction of tendons may also change at pulleys but the internal fiber orientation follows the direction of the tendon or ligament as a whole.

In the case of knee menisci, which is used to illustrate general principles involved, the following situations are found:

Situation 1. In a typical solenoidal magnet, with the patient horizontal and supine in the bore of the magnet, the plane of the meniscus is perpendicular to B_0.

Situation 2. In a vertical field magnet, with the patient lying horizontal and supine between the pole pieces, the plane of the meniscus is parallel to B_0.

Situation 3. With an open MR system, the plane of the meniscus could be perpendicular to B_0 as in Situation 1, as well as parallel to B_0 with the meniscus oriented anterior to posterior as in Situation 2. However, another possibility is with the patient upright or supine with his or her long axis transverse to the B_0. In this situation, B_0 is parallel to the plane of the meniscus but in a left-right, or medial-lateral, direction rather than the anteroposterior direction.

With articular cartilage, the plane of articular cartilage reflects the underlying bone structure with a disc-like appearance on the tibial plateau, for example, and more complex curved shapes at other sites such as the lower end of the femur.

Fiber Orientation and Type

While collagen fibers vary in size in tendons, they usually have the same general orientation within a predominantly linear structure. In ligaments the orientation is also linear but the fibers may be present in sheets.

Fiber types within the meniscus have been studied for many years, with improved results obtained more recently using scanning electron microscopy (17). This technique shows three distinct layers of organization. 1) A mesh-work of thin fibers of approximately 30 μm in diameter, which covers the surface of the tissue. Beneath this is a superficial, lamella-like layer of collagen fibers to a depth of 150–200 μm, which is predominantly radial in direction. India ink staining shows deviation from the radial orientation at the surface, particularly at the junction of the body and posterior horns of the medial meniscus. 2) The main body of the meniscus, which is composed of predominantly circumferential bundles of collagen fibers with a concentration of these at the roots of the menisci. 3) A smaller proportion of radial fibers (radial ties). In addition, loose connective tissue continuous with the perimeniscal tissue enters the meniscus from its outer margin.

The basic orientation of fibers in articular cartilage is well known, with a calcified layer, deep radial fibers, a transitional layer, and tangential superficial fibers. The radial fibers are generally perpendicular to bone. The radial and tangential fibers are perpendicular, providing a wide range of fiber-to-static field angles.

Fiber-to-Field Orientation

The fiber-to-field orientation is relatively straightforward for tendons, ligaments, and peripheral nerves. For menisci and cartilage, the different planes and fiber orientations result in more complex patterns. In Situation 1 (solenoidal cryomagnet), both the circumferential fibers and the radial ties are generally at 90° to B_0. In Situation 2 (a vertical field magnet), meniscus circumferential fibers are at a range of angles to B_0, including the magic angle. In addition, radial ties are at another set of angles to B_0 some of which include the magic angle (3). With open systems other orientations of fibers to B_0 are possible.

In cartilage the dominant fiber direction is radial with a smaller transitional zone and a thinner superficial zone with tangential fibers. The orientation of the bone provides a guide to the direction of the (perpendicular) radial fibers. At the margins of cartilage, fiber direction may become more parallel to the underlying bone.

BASELINE TISSUE T2 AND OTHER TISSUE PROPERTIES

Baseline Tissue T2

The mean baseline T2 of tendons and ligaments is taken as that with fibers oriented at 0° to B_0 and is in the range of about 2–8 msec, although precise measurements are difficult to obtain and both tissues probably have several short T2 components (8). The majority of these tissues probably show magic angle effects. Peripheral nerve is different in that it has a much longer mean baseline T2 (e.g., 50–60 msec) and only a minority of the tissue is ordered collagen, although this part may produce significant magic angle effects (9).

In tissues with multiple fiber orientations, the baseline T2 is taken as that of the dominant fiber type in a particular region of the tissue. The meniscus as a whole has a T2 or T2* of about 6–8 msec (18). No significant susceptibility effects are thought to be present in the meniscus. With conventional spin-echo sequences with TEs of 10–20 msec, most if not all the signal decays to noise level by the time the receive mode of the MR

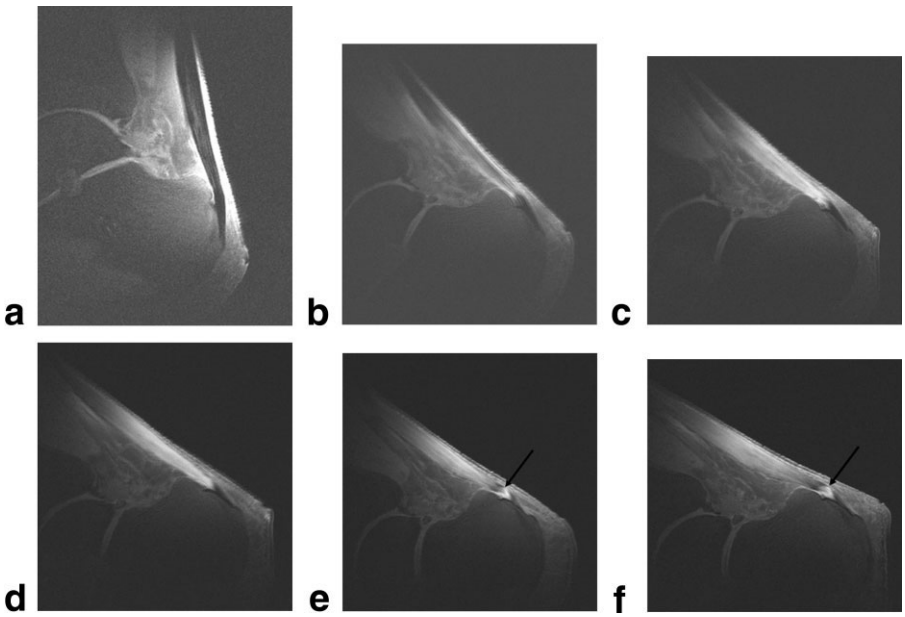


Figure 2. Achilles tendon at 10° (**a**), 30° (**b**), 40° (**c**), 50° (**d**), and 60° (**e**) to B_0. The signal intensity increases with angle in the midtendon region. Contrast is developed around the sesamoid fibrocartilage (arrow).

system is enabled. Loose connective tissue has a longer T2, probably with a value similar to the values of 14–15 msec found for perimeniscal tissue (18). The measured T2 of fibrofatty tissue may be shorter than its T2 because of phase differences between signals from protons in water and those from protons in fat producing signal interference effects. Articular cartilage has a range of baseline T2s of about 1–10 msec for the deep layers up to 30–40 msec for the more superficial layers.

Increase in T2 Due to Magic Angle Effects

Magic angle effects results in an increase in T2 from that seen with fibers oriented to B_0. The dependence of T2 on fiber orientation to magnetic field for highly-ordered, linearly-oriented collagen-rich tissues such as tendon and ligaments is shown in Figs. 1 and 2. T2 has a baseline value at 0°, reaches a maximum at 55°, decreases toward 90° then increases again to a peak at 125°. This peak has the same magnitude as that at 55° and drops down again to the baseline value at 180°. The shape of the curve depends on the fiber type, size, and properties, as well as the detail of fiber orientation within a tissue. Highly parallel fibers showed narrow peaks, while tissue with a wider spread of orientations showed a broader peak. The relative increase in T2 tends to be greater for short T2 than in longer T2 components of tissues, which have a range of T2s similar to articular cartilage. The effect of the increase of T2 on signal intensity depends on the pulse sequence, and in particular, TE (see below).

T1

The values of T1 for tendons and ligaments at 1.5T are in the range of 350–450 msec at 1.5T but because of the low signal available with conventional sequences there is a dearth of clinical data. It is assumed that T1 values of other similar connective tissues are in the same range as tendons and ligaments, and that as with other tissues magic angle effects change T2 but have little effect on T1 (2). The conspicuity of a tissue displaying a magic angle effect may vary depending on the T1 of the tissue and the T1-dependence of the sequence used to examine it.

Other Tissue MR Properties

The mobile proton density of the meniscus is linked to its T2 and is probably less than that of soft tissues. By analogy with articular cartilage, significant magnetization transfer effects would be expected. There are particular difficulties with diffusion-weighted techniques using pulsed gradients for imaging short T2 tissues. The gradient pulses are typically of significant duration and result in TEs of 50–100 msec for b-values in the 500–1000 second/mm^2 range. This is too long to detect signal from short T2 tissues. Diffusion may be limited by the partial binding of water to collagen, which may also make it less easy to detect. On the other hand some anisotropic behavior may be expected as a result of the asymmetric fiber structure of these tissues. Diffusion may be accessible in tissues with longer T2s such as the peripheral nerve and the more superficial layers of articular cartilage. It can also be accessed when the T2s of tissues such as tendons and ligaments are increased by placing them at the magic angle (see below).

TE AND OTHER MACHINE FACTORS

TE

TEs can be grouped in to ultrashort short, moderate, long, and ultralong. The signal intensity detected with tendons and ligaments with their fibers parallel to B_0 is a very low or zero with TEs of 10 msec or longer. These tissues typically showed moderate or high signal with ultrashort UTE sequences even with their fibers at 0° to B_0.

Not only does TE effect the general signal level of the meniscus signal but it also modulates the signal intensity produced by magic angle effects. In general, magic

angle effects are absent at long and ultralong TEs, become more obvious with moderate and short TEs and are reduced with ultrashort TEs. With UTE sequences, subtraction of later echo images from the first image (which is used to reduce the signal from long T2 tissues) may lead to different effects. If as a result of magic angle effects the tissue T2 is prolonged and the TE of the subsequent echo image is not too long, the subtraction image will show low signal. If the TE of the later echo image is prolonged but the signal decays rapidly relative to TE, the signal on the subtraction image may be high.

TR, Flip Angle, and T1

These sequence parameters effect the T1-dependence of the signal. In general, with gradient and spin-echo sequences T1-dependent contrast is maximized when TR is about the same as the T1 of the tissues to be distinguished. Increasing the flip angle within the range of 0–90 degrees generally increases T1 dependence and decreasing the flip angle reduces it. The T1 of short T2 components in tissue may differ from that of long T2 components and if the short T2 components become detectable as a result of magic angle effects, this may produce differences in conspicuity.

In attempting to achieve T1 weighting, inversion pulses may be used. When the length of the inversion pulse is the same order as T2 or longer, the magnetization may not be inverted and the tissue may be saturated. If the T2 of the tissue is prolonged by magic angle effects, then its magnetization may be inverted, producing different T1-dependent contrast.

Other Pulse Sequence Parameters

It is possible that off-resonance fat suppression pulses may partially saturate the short T2 components in the meniscus and reduce their signal. This may produce increased contrast between fibers at the magic angle (longer T2s), which are minimally affected, and fibers at other angles (shorter T2s), which may be more affected.

Other Hardware

Hardware effects such as the nonuniform receiver field associated with surface coils may alter signal intensity in well-recognized ways.

GEOMETRIC FACTORS

Slice Orientation

The position of the slice, whether relative to whole body (sagittal, coronal, or axial) or related to the shape of the tissue of interest, produces characteristic appearances with planar imaging.

Partial Volume Effects

General

Partial volume effects occur when two or more fluids or tissues with different signal intensities partly occupy a voxel and produce in that voxel signal intensity that is intermediate between the two. A boundary between the two tissues or fluids is present within the voxel. The effect may occur in-plane, which is usually the smaller voxel dimension, through-plane (the slice thickness), which is usually a larger voxel dimension with conventional two-dimensional (2D) imaging, or as a combination of these. The partial volume effect may occur within the tissue such as at a boundary between a blood vessel and tissue parenchyma, or at the external margin of a tissue or organ.

Fibers

Partial volume effects involving fibers such as those in the nervous system, tendons, ligaments, and menisci have some more specific features. The tissue fibers may be surrounded by nonfibrous tissue or other fibers at the same or different orientations. The fibers are asymmetric, with long and short axes. The relative dimensions of fibers or groups of fibers are often similar to those of voxels used in MRI. Fibrous tissues may show a characteristic fascicular or punctate pattern when the fibers are oriented at or near 90° to the slice plane, but this pattern is readily lost as the fiber orientation moves away from 90° (19). At the other extreme, through-plane fibers may show high signal intensity if the slice thickness is low and their direction is parallel to the image plane. Loss of these conditions leads to a loss of visualization of the fiber pattern.

Magic Angle Effects

In addition to fiber-to-slice considerations described above, the signal intensity of the fibers may show magic angle effects, i.e., fiber-to-field dependency. This does not occur with nerve fibers within the CNS, but it occurs in the perineurium and endoneurium of peripheral nerves (which contain collagen), and in tendons and ligaments. It may occur more for fibers than endotenon, resulting in a loss of fascicular definition.

In the particular case of meniscus, fiber-to-field dependency occurs in circumferential fibers and radial ties but to a lesser degree in superficial fibers and may be small in the multidirectional small-fiber matrix. The fact that two or more sets of fibers, and in particular, circumferential and radial fibers, produce different signal intensities at different orientations to B_0 has potential for a wide range of different conspicuities between the fibers.

External partial volume effects occur at the boundary between the meniscus and perimeniscal tissue and at the boundary between the external surface of the meniscus and joint fluid. The meniscus is subject to the distinctive features associated with fibers and magic angle effects, but the perimeniscal tissue and joint fluid are not. Joint fluid has a long T1 and T2 and its signal intensity relative to the meniscus varies with T1-weighted sequences (low signal) or proton density–weighted or T2-weighted sequences (higher signal). The perimeniscal tissue has a longer T2 and is of higher signal intensity.

CONTRAST ENHANCEMENT

Contrast enhancement depends on the tissue, the pulse sequence, geometric factors, and the contrast

agent. The patterns vary with the tissue, pulse sequence, and contrast agent. The meniscus is an interesting example because it has a vascular peripheral red zone and an avascular central white zone. It is surrounded by vascular perimeniscal connective tissue. The meniscus has a short T2 and signal has not been detectable with conventional sequences after enhancement. By use of magic angle effects, UTE sequences, or both, signals can be detected in the meniscus and increase can been seen after enhancement. UTE sequences are usefully combined with subtraction since this suppresses the signal from the more vascular perimeniscal tissue (18). In studies with a gadolinium chelate to date, a nonionic agent was used with a high concentration (0.3 mmol/kg) to increase enhancement. This allowed the red zone to be visualized separately from the white zone though increased signal was measured in this zone. This is probably due to diffusion of contrast agent from the red zone or joint fluid.

NORMAL APPEARANCES

These can be seen as an interplay between the following: 1) Fiber-to-field orientation and magic angle effects. 2) T2 (both baseline and increased T2 caused by the magic angle effect) and TE, which determines both the general signal level of the tissue (shorter TE leads to a higher signal level) and modulates the signal produced by the magic angle effect. 3) T1 and TR, flip angle, and inversion time (TI). The T1 of most tissues of interest is moderately short and does not vary with magic angle effect. 4) Other tissue properties and sequence parameters. These have been largely unexplored, but susceptibility effects with gradient echo sequences may be important with calcification. 5) Slice orientation, which determines the basic configuration of the tissue, and partial volume effects. These reflect general principles but the fiber structure is anisotropic and may match the anisotropic shape of voxels. These may show a fascicular type of pattern when fibers are perpendicular to the slice and a linear pattern when fibers are parallel to the slice as well as a nonspecific appearance at intermediate angles. Partial volume effects are modulated by magic angle effects, which effect the signal intensity of the fibers involved. 6) Contrast enhancement, as outline above.

APPEARANCE IN DISEASE

Changes in morphology including size, shape, and position may be diagnostic but this article is primarily concerned with changes in signal intensity. In general, there are two approaches. In the first, the background signal is low or kept low by the use of a sufficiently long TE and abnormalities are recognized as an increase in signal intensity. There is a risk that the TE necessary to keep the background low by suppressing magic angle effects will result in a low signal and that small increases in T2 will not be detectable.

The second approach is to achieve a detectable signal level using a shorter TE with the options to manipulate it by use of sequence parameters and to recognize changes in signal due to differences in relaxation times and other tissue properties. This gives the additional option of recognizing disease processes that reduce signal intensity.

Degenerative changes are typically associated with an increase in T2. If there is overt fluid the T2 may be longer and be best shown with longer TR sequences, which reduce T1 effects. Calcification generally produces a reduction in signal intensity due to low mobile proton density, short T2, and susceptibility effects. It may also be associated with a decrease in T1 (20). Some forms of calcification show an increase in T2 with a decrease in T1, which may lead to an increase in signal intensity with T1-weighted sequences.

Crystal deposition disease is associated with both a low signal and an increase in T2. Fibrosis and scar formation may be associated with a mild increase in T2 in the initial stages, but a reduction in T2 later. Other pathologic processes are also of interest. In the intervertebral discs, desiccation is associated with a reduction in T2 and it is possible that a similar process may occur in other tissues such as tendons and ligaments, but this has not been recognizable using low signal approaches. It may be observable if the tissue is placed at the magic angle.

Loss of order in collagen could result in an increase in T2 and of loss of magic angle effect (i.e., a reduction in the change of signal with shift of orientation from, for example, 0 to 55 degrees.)

MEASURMENTS

Measurements of T2 depend on the range of TEs used to detect signal. Tendons, ligaments, and menisci requires sequences with TEs in the short and ultrashort range for both T2 and T2*. The measurement of T1 is also dependent on the TE of the sequence since this defines what tissues contribute signal. If TE is relatively long, only part of the tissue may contribute signal.

Although there has been some work on diffusion-weighted sequences suitable for short T2 tissues (21,22), these sequences may be difficult to implement on clinical MR systems. If magic angle effects are used to prolong T2, the diffusion weighting is only for fibers with signal in the detectable range.

ARTIFACTS

Artifacts are the most widely recognized manifestation of magic angle effects and are typically recognized on solenoidal magnets as a localized region of signal intensity in a tendon or ligament undergoing a change in direction, as with the supraspinatus tendon and tendons posterior to the medial and lateral malleoli (3,4).

Not so well recognized are areas of increased signal in peripheral nerves due to magic angle effects (9). The roots, cords, and nerves of the brachial plexuses as a whole are generally at about 55° to B_0 when patients are examined in typical horizontal bore cryomagnets. This produces an increase in signal relative to nerves at 0° and also relative to skeletal muscle, which is usually taken as a reference for signal level of peripheral nerve. With typical fat-suppressed T2-weighted or short-tau inversion recovery (STIR) sequences normal nerve sig-

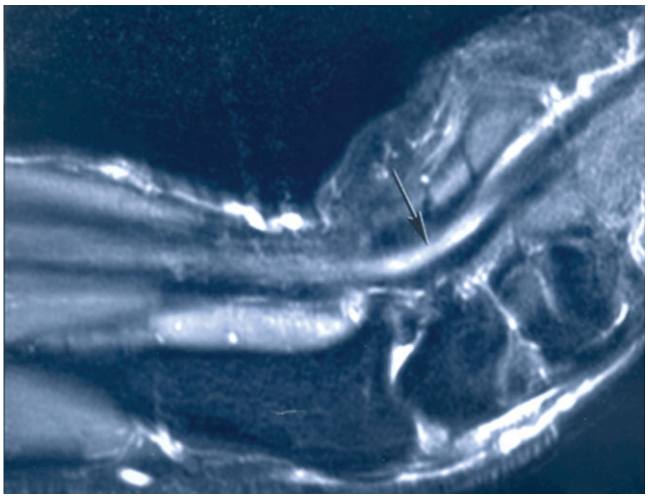


Figure 3. Median nerve. Sagittal T1-weighted spin-echo image. The signal for the nerve is increased at 55° to B_0.

nal is generally less than or equal to muscle signal. If this rule is applied, the whole brachial plexus may appear to have an elevated signal intensity. In addition, the rule of increasing TE (e.g., to greater than 37 msec) to avoid detecting the signal increase due to magic angle effects in tendons does not apply to nerves.

In addition to these difficulties, provocative testing has been recommended for increasing the sensitivity of MR neurography to changes in carpal tunnel syndrome (23,24). This is performed by flexing or extending the wrist but this maneuver may result in a localized increase in signal in the region of the carpal tunnel as a result of magic angle effects (Fig. 3). Likewise, it has been suggested that the elbow should be examined in flexion to detect ulnar nerve entrapment but this can also result in an unwanted increase in signal intensity in the region of clinical suspicion (25).

With typical STIR sequences at the wrist, the median nerve may show visible magic angle effects when the surrounding flexor tendons do not. This is particularly evident with larger TEs. The T1-dependent approaches for distinguishing magic angle effects from disease require the use of short TE or UTE sequences to minimize the T2 dependence of the sequence and may require a short inversion pulse to fully invert the tendon or ligament magnetization. Contrast enhancement may also help if there is a focal area of enhancement.

MAGIC ANGLE EFFECTS AS A DETERMINANT OF IMAGE CONTRAST

This section includes the more complex situations in which the tissue as a whole is at different orientations to B_0 and contains fibers at different orientations to one another. The examples discussed here are the meniscus of the knee, labra, and articular cartilage.

The Meniscus of the Knee

In general, magic angle effects are minimized with the common orientation of the knee in a solenoidal magnet since both circumferential and radial fibers are at 90° to B_0. As a result, magic angle contrast between them is minimized in this situation. The lateral meniscus root fibers may be at 55° and give a high signal. The superficial fibers are at a variety of angles and this may produce a signal with low magic angle dependence.

The patterns with a vertical field are much more variable; circumferential fibers may be at the magic angle, while radial fibers are far from the magic angle and vice versa (Fig. 4). The appearances may vary in a given slice and partial volume effects may result in different appearances when the image slice orientation is changed. The contrast with disease varies. For example chronic calcification has a generally lower signal intensity than either fibers examined with a UTE sequence or fibers at the magic angle.

Labra

The glenoid and acetabular labra show features in common with the menisci, with predominantly circumferential fibers following the bony attachment. These display magic angle effects (26) and produce patterns that vary with B_0, TE, slice orientation, and other factors, as outlined previously.

Articular Cartilage

Magic angle effects are readily seen in articular cartilage and have been the subject of extensive and detailed

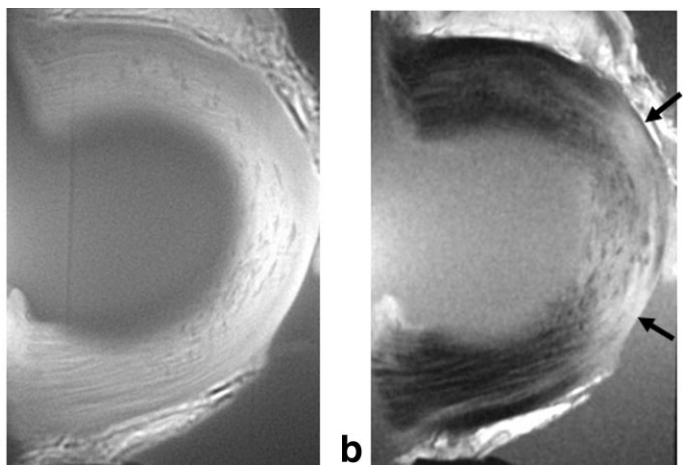


Figure 4. Meniscus. UTE image (**a**) and conventional T1-weighted spin-echo (**b**) with vertical B_0. The UTE image shows high signal (with lower signal from calcification). The conventional spin-echo image shows a marked magic angle effect.

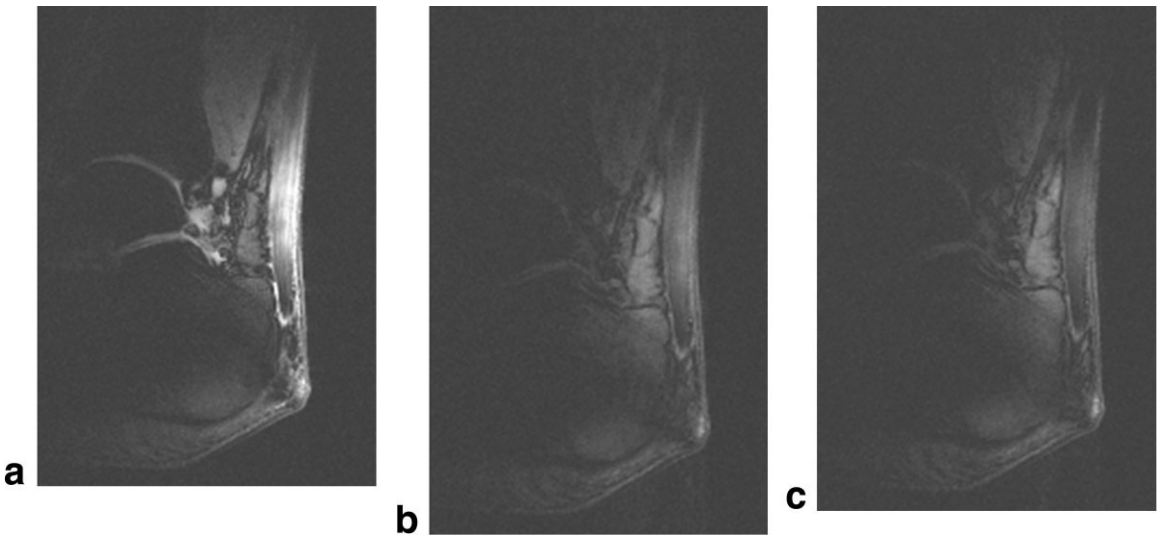


Figure 5. Diffusion-weighted imaging of the Achilles tendon. b = 0 second/mm^2 image (**a**), AP sensitization (b = 500 second/mm^2) image (**b**), and superior-inferior sensitization (b = 500 second/mm^2) image (**c**). There is a similar reduction in signal intensity in the diffusion-weighted images.

study (Figs. 6 and 8) (27–31). The baseline T2 of articular cartilage varies from deep to superficial. In relative terms, greater magic angle effects may be seen with the deep-layer short T2 components. The calcified layer of cartilage has a short T1 and this may lead to high signal from it. Techniques using long T2 reduction to highlight the deep layers of cartilage may reduce its signal intensity when its T2 is increased by magic angle effects.

MAGIC ANGLE IMAGING

By deliberately placing tendons and ligaments at or near the magic angle, increased signal may be seen within them. This provides an opportunity to measure T1 and T2 and to detect effects due to increases or decreases in these parameters that may not otherwise be apparent. It is best suited to linear structures with a single dominant fiber orientation such as tendons, ligaments, and nerves.

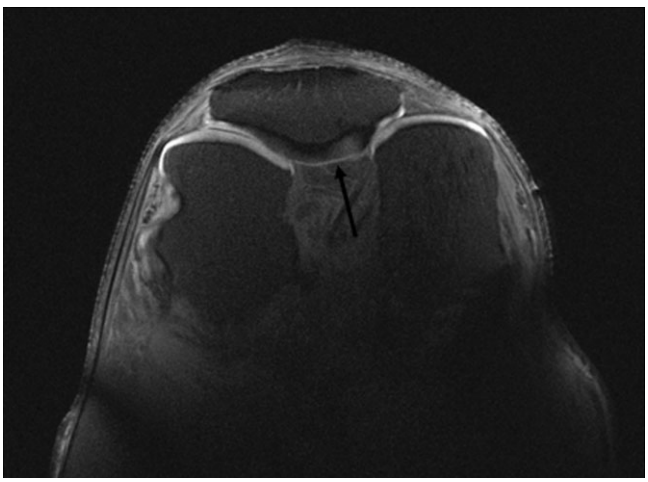


Figure 6. Articular cartilage. The radial fibers are at 0° and the transverse fibers (arrow) are at 90° to B_0.

When signal is detectable it is also possible to assess magnetization transfer effects. The magic angle effects create a free pool that allows indirect access to the shorter T2 components. There is also scope to study other effects such as T1 in the rotating frame. Contrast enhancement is detectable with tendons at the magic angle and more marked and more prolonged enhancement has been identified in Achilles tendinopathy using this technique (11–13). It has also been used to access diffusion. Preliminary studies have shown only a relatively mild degree of anisotropy in spite of the very asymmetric structure of the tendon. This may reflect binding of water to collagen and limited mobility. The appearances are dependent on fiber-to-gradient field orientation (diffusion) as well as fiber-to-static field and fiber-to-slice orientation (Fig. 5).

By placing articular cartilage with the radial fibers at 0° to B_0 contrast may be developed with tangential fibers at 90° to B_0 (Fig. 5). Entheses are a particular application of magic angle imaging in which positioning is used to differentiate tissues with different fiber orientations. To demonstrate sesamoid fibrocartilage it is useful to place tendons near the magic angle so that the signal from the very linear tendon fibers is low but that from the less linear (basket-weave) fibers of fibrocartilage is not reduced to the same degree because the fibers are spread over a much wider range of angles and a significant proportion may be at or close to the magic angle even when the bulk of the tendon fibers are at 10 or more degrees from this angle (Fig. 2). In addition UTE sequences can be used with magic angle imaging to increase signal (Fig. 7) to demonstrate enthesis fibrocartilage exploiting the fact that the fibers of this tissue are largely orientated

perpendicular to the bone to which they are attached. (Fig. 8).

SUMMARY

For a long period, the magic angle effect has been consigned to the dustbin of MR history. It is manifest as an unwanted increase in signal intensity of tendons and ligaments that happen to be at 55° to B_0. It is usually regarded as an artifact and most of the technical effort in relation to it has been spent on avoiding it, or if this was not possible, distinguishing its results from those due to disease.

This review discusses various different tissues in which magic angle effects may be seen and provides a formalism for relating the magic angle effects to the type of magnet the patient is examined in, the macroscopic structure of the tissue under study, and the fiber direction or directions within the tissue. The signal intensity seen in the tissues of interest also depends on the baseline T2 of the tissue and the increase in T2 produced by the magic angle effect. The signal is affected by the TE of the sequence, which sets the general level of signal for the tissue and determines the size of signal change produced by the magic angle effect.

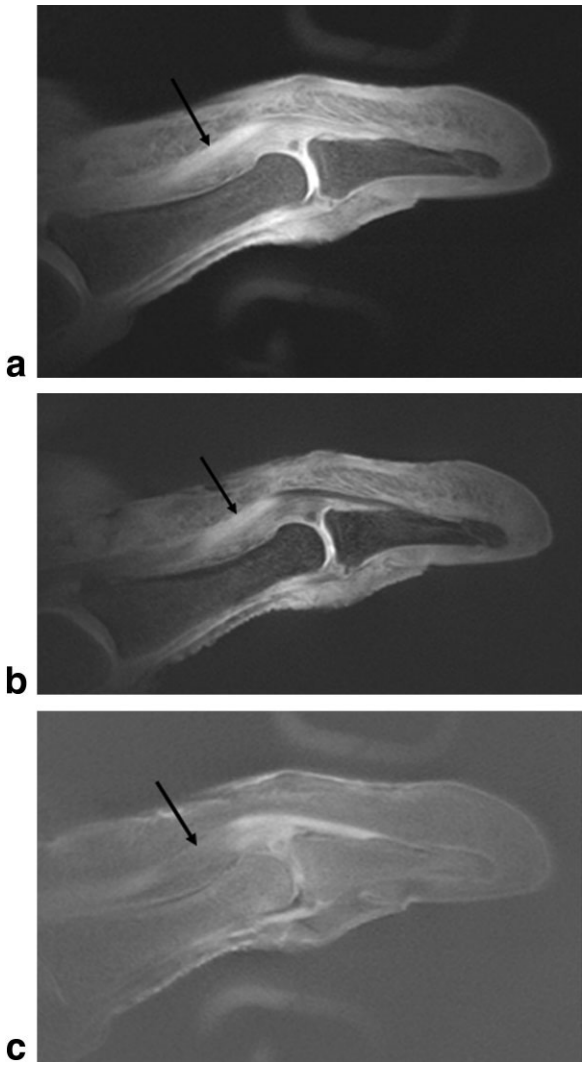


Figure 7. Flexor tendon of the thumb with proximal component at the magic angle. UTE image (**a**), longer echo (**b**), subtraction image (**c**). Higher signal is seen on the UTE image from the part of the tendon at the magic angle (arrow). The signal is also higher on the longer echo image due to its long T2, but it is low on the difference image in (c).

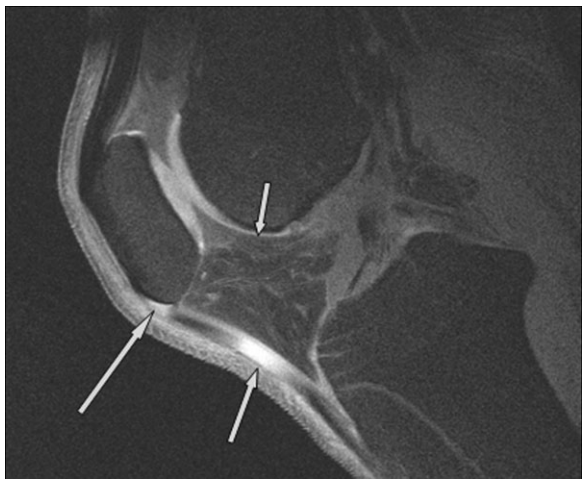


Figure 8. Sagittal signal of lower end of femur and patella tendon. High signal is seen from magic angle effects in the midtendon (medium arrow) and at the enthesis (long arrow). The superficial zone of the articular cartilage is seen (short arrow) but the signal in the radial zone in this region is low and is not seen.

Partial volume effects of fibers may produce fascicular or linear patterns or an indeterminate appearance. These appearances are affected by the magic angle effect as well as the fiber-to-slice orientation.

By deliberately placing tendons and ligaments at or near the magic angle, signal may be generated within them with conventional sequences and this allows study of T1 and T2, contrast enhancement, magnetization transfer, and diffusion. Magic angle imaging may also be used to generate contrast between fibers at different orientations in the same or different tissues.

It is now possible to take a broader view of the magic angle effect and regard it not only as a source of unwanted artifacts, but also as a major determinant of image contrast and an imaging technique.

REFERENCES

1. Fullerton GD, Cameron IL, Ord VA. Orientation of tendons in the magnetic field and its effect on T2 relaxation times. Radiology 1985; 155:433–435.
2. Henkelman RM, Stanisz GJ, Kim JK, Bronskill MJ. Anisotropy of NMR properties of tissues. Magn Reson Med 1994;32:592–601.
3. Erickson SJ, Cox IH, Hyde S, Carrera GF, Strandt JA, Estkowski LD. Effect of tendon orientation on MR imaging signal intensity: a manifestation of the "magic angle" phenomenon. Radiology 1991; 181:389–392.
4. Hayes CW, Parellada JA. The magic angle effect in musculoskeletal MR imaging. Top Magn Reson Imaging 1996;8:51–56.
5. Peh WC, Chan JH. The magic angle phenomenon in tendon: effect varying the MR echo time. Br J Radiol 1998;71:31–36.
6. Peterfy CG, Janzen DC, Tirman PF, Van Dijke CF, Pollack M, Genant HK. "Magic-angle" phenomenon: a cause of increased signal in the normal lateral meniscus on short-TE images of the knee. AJR Am J Roentgenol 1994;163:149–154.

7. Brittain JH, Shankaranarayanan A, Ramanan V, et al. Ultra-short TE imaging with single-digit (8 μs) TE. In: Proceedings of the 12th Annual Meeting of ISMRM, Kyoto, Japan, 2004 (Abstract 629).
8. Robson MD, Gatehouse PD, Bydder M, Bydder GM. Magnetic resonance: an introduction to ultrashort TE (UTE) imaging. J Comput Assist Tomogr 2003;27:825–846.
9. Chappell KE, Robson MD, Stonebridge-Foster A, et al. Magic angle effects in MR neurography AJNR Am J Neuroradiol 2004;25:431–440.
10. Oatridge A, Herlihy AH, Thomas RW, et al. Magnetic resonance: magic angle imaging of the Achilles tendon. Lancet 2000;358:1610–1611.
11. Marshall H, Howarth C, Larkman DJ, Herlihy AH, Oatridge A, Bydder GM. Magnetic resonance: contrast enhanced "magic angle" imaging of the Achilles tendon. AJR Am J Roentgenol 2002;179:187.
12. Gatehouse PD, Bydder GM. Magnetic resonance imaging of short T2 components in tissue. Clin Radiol 2003;58:1–19.
13. Oatridge A, Herlihy AH, Thomas RW, et al. Magic angle imaging of the Achilles tendon in patients with chronic tendinopathy. Clin Radiol 2003;58:384–388.
14. Boesch C, Kreis R. Dipolar coupling and ordering effects observed in magnetic resonance spectra of skeletal muscle. NMR Biomed 2001;14:140–148.
15. Hopkins AL, Kirshner DA, Bratton CB. Proton relaxation time measurements for bone tissue. Magn Reson Med 1984;1:168–169.
16. Benjamin M, Toumi TT, Ralphs JR, Bydder G, Best TM, Milz S. Where tendons and ligaments meet bone: attachment sites (entheses) in relation to exercise and mechanical load. J Anat 2006;208: 471–490.
17. Petersen W, Tillmann B. Collagenous fibril texture of the human knee joint menisci. Anat Embryol 1998;197:317–324.
18. Gatehouse PD, He T, Puri BK, Thomas RD, Resnick D, Bydder GM. Contrast-enhanced MRI of the menisci of the knee using ultrashort echo time (UTE) pulse sequences: imaging of the red and white zones. Br J Radiol 2004;77:641–647.
19. Filer AG, Kliot M, Howe FA, et al. Application of magnetic resonance neurography in the evaluation of patients with peripheral nerve pathology. J Neurosurg 1996;85:299–309.
20. Henkelman RM, Watts JF, Kucharczyk W. High signal intensity in MR images of calcified brain tissue. Radiology 1991;179:199–206.
21. Merboldt KD, Hanicke W, Bruhn H, Gyngell ML, Frahm J. Diffusion imaging of the human brain in vivo using high speed STEAM MRI. Magn Reson Med 1992;23:179–192.
22. Cho H, Chavez L, Sigmund EE, Modio DP, Song YQ. Fast imaging with the MMME sequence. J Magn Reson 2006;180:18–28.
23. Horch RE, Allman JH, Laubenger J, Manger M, Stark GB. Median nerve compression can be detected by magnetic resonance imaging of the carpal tunnel. Neurosurgery 1997;41:76–82.
24. Allman KH, Horch RE, Uhl M, et al. MR imaging of the carpal tunnel. Eur J Radiol 1997;25:141–145.
25. Kim YS, Yeh LR, Trudell D, Resnick D. MR imaging of the major nerves about the elbow: cadaver study examining the effect of the flexion extension of the elbow and pronation and supination of the forearm. Skeletal Radiol 1998;27:419–426.
26. Sasaki T, Yodono H, Prado GL, et al. Increased signal intensity in the normal glenoid labrum in MR imaging: diagnostic pitfalls caused by the magic angle effect. Magn Reson Med Sci 2002;1:149–156.
27. Goodwin DW, Wadghiri YZ, Dunn JF. Micro-imaging of articular cartilage: T2 proton density, and the magic angle effect. Acad Radiol 1998;5:790–798.
28. Goodwin DW, Wadghiri YZ, Zhu H. Vinton CJ, Smith ED, Dunn F. Macroscopic structure of articular cartilage of the tibial plateau; influence of characteristic matrix architecture on MRI appearance. AJR Am J Roentgenol 2004;182:311–318.
29. Xia Y. Relaxation anisotropy in cartilage by NMR microscopy (muMRI) at 14-microm resolution. Magn Reson Med 1998;39:941–949.
30. Xia Y. Magic-angle effect in magnetic resonance imaging of articular cartilage: a review. Invest Radiol 2000;35:602–621.
31. Xia Y, Moody JB, Alhadlaq H. Orientational dependence of T2 relaxation in articular cartilage: a microscopic MRI (microMRI) study. Magn Reson Med 2002;48:460–469.

NMR IN BIOMEDICINE
NMR Biomed. 2001;**14**:57–64
DOI:10.1002/nbm.683

Review Article

Magnetization transfer in MRI: a review

R. M. Henkelman[1,2]*, G. J. Stanisz[1] and S. J. Graham[1]

[1]Department of Medical Biophysics University of Toronto, Toronto, Canada
[2]Department of Medical Imaging, University of Toronto, Toronto, Canada

Received 18 February 2000; revised 13 October 2000; accepted 20 October 2000

ABSTRACT: This review describes magnetization transfer (MT) contrast in magnetic resonance imaging. A qualitative description of how MT works is provided along with experimental evidence that leads to a quantitative model for MT in tissues. The implementation of MT saturation in imaging sequences and the interpretation of the MT-induced signal change in terms of exchange processes and direct effects are presented. Finally, highlights of clinical uses of MT are outlined and future directions for investigation proposed. Copyright © 2001 John Wiley & Sons, Ltd.

KEYWORDS: magnetization transfer; MRI

INTRODUCTION

Magnetization transfer (MT) in a magnetic resonance imaging (MRI) context was first discovered accidentally by Dr Bob Balaban *et al.* (Bob Balaban, private communication).[1] These investigators were attempting to perform a spin transfer experiment by selective saturation of urea looking for small signal suppression in water. Instead, they found a significant loss of image intensity from the proton signal in tissue, which did not depend on the specific offset frequency of the irradiation. This generalized signal suppression, now known as MT, has become accepted as an additional way to generate unique contrast in MRI that can be used to advantage in a variety of clinical applications.[2,3] The detailed underlying biophysics of MT is quantitatively understood, enabling MT to be optimally exploited in MRI.

HOW MT WORKS

Proton MRI detects signal only from mobile protons which have sufficiently long T_2 relaxation times (i.e. greater than 10 ms) so that spatial encoding gradients can be played out between excitation and acquisition before the signal has completely decayed. The T_2 of the less mobile protons associated with macromolecules and membranes in biological tissues are too short (i.e. less than 1 ms) to be detected directly in MRI. However, coupling between the macromolecular protons and the mobile or 'liquid' protons allows the spin state of the macromolecular protons to influence the spin state of the liquid protons through exchange processes. As shown in Fig. 1, it is possible to saturate the macromolecular spins preferentially using an off-resonance radio frequency pulse. The macromolecular spins have a much broader absorption lineshape than the liquid spins, making them as much as 10^6 times more sensitive to an appropriately placed off-resonance irradiation. This preferential saturation of the macromolecular spins can be transferred to the liquid spins, depending on the rate of exchange between the two spin populations, and hence can be detected with MRI.

Figure 2 shows a two-pool model that is simple yet sufficient for quantitative interpretation of MT.[4] Pool A represents the liquid spins. The number of spins in this compartment is by convention normalized to unity ($M_{0A} = 1$). Pool B represents the macromolecular spins. In tissues, the number of macromolecular spins is much less than the liquid spins and the relative fraction is given by M_{0B}. In each pool, and at any instant in time, some of the spins are in the longitudinal orientation represented by the upper unshaded portion of the compartment and some spins are saturated, represented by the lower shaded portion. The partition into longitudinal spins and

**Correspondence to:* R. M. Henkelman, Imaging and Bioengineering Research, Sunnybrook and Women's College Health Sciences Centre, 2075 Bayview Avenue, Toronto, Ontario, Canada M4N 3M5.
E-mail: mark.henkelman@swchsc.on.ca

Abbreviations used: B_{eff}, effective magnetic field; CRMG, Carr–Purcell–Meiboom–Gill; CW, continuous wave; FAIR, flow sensitive alternating inversion recovery; Gd-DTPA, gadolinium diethylene-triminepentaacetic acid; MRA, magnetic resonance angiography; MRI, magnetic resonance imaging; MS, multiple sclerosis; MT, magnetization transfer; MTR, magnetization transfer ratio; RF, radio frequency; SAR, specific absorption rate.

Copyright © 2001 John Wiley & Sons, Ltd.

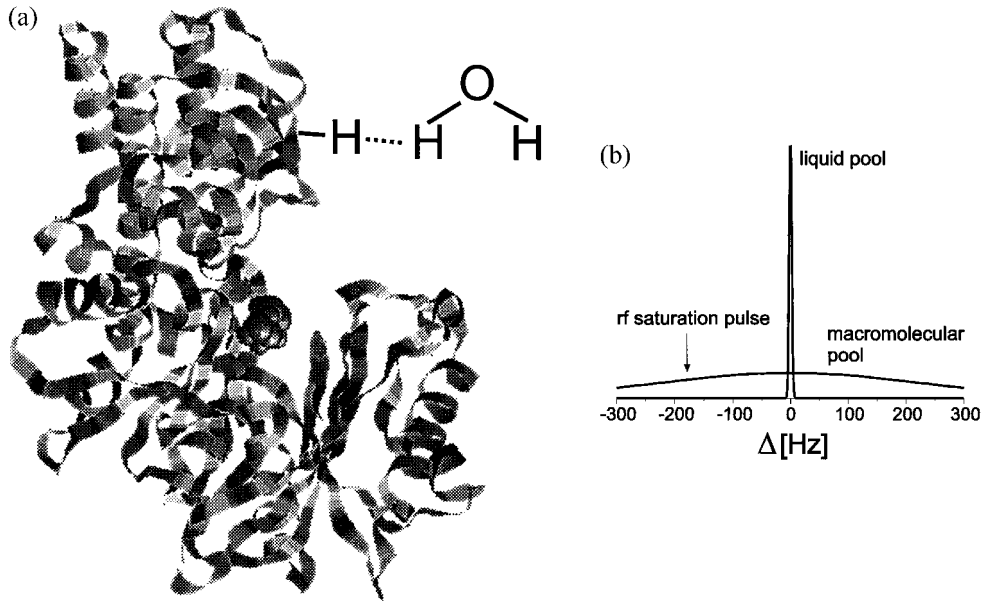


Figure 1. (a) Magnetization transfer exchange between macromolecular and water protons. (b) The macromolecular spins, exhibiting much broader absorption lineshape than the liquid protons, can be preferentially saturated using an off-resonance RF pulse

saturated spins depends on the prior irradiation history. When the irradiation is turned off, the time-dependent changes in the model are represented by three rate constants: R_A and R_B are the longitudinal relaxation rates of pools A and B respectively and R is the exchange rate between pools A and B. Because M_{0A} is set to 1, k_{AB} is a pseudo-first-order rate constant and the rate of transfer of spins from A to B is RM_{0B}. The rate from B to A is therefore R to conserve compartment sizes. The simple model pictured in Fig. 2 can be readily expressed by a set of coupled differential equations.[4]

The effect of off-resonance irradiation on this system is different for the two pools. For pool B, the protons in the macromolecules are strongly coupled to each other resulting in a homogeneously broadened absorption lineshape as is shown in Fig. 1(b). Thus, off-resonance irradiation results in progressive saturation of the ensemble of spins, with the effective saturation rate being given by the probability of absorption at the corresponding offset frequency times the average radio frequency (RF) power at the offset frequency.[5]

In MT experiments, the intent is to manipulate the liquid pool indirectly by saturating the macromolecular pool. However, some direct saturation of the liquid pool is inevitable in this process and must be included in any quantitative analysis of MT effects. Because spins in the liquid pool are only weakly coupled due to motional narrowing, the effect of an off-resonance irradiation is governed by the Bloch equations. In the case of continuous wave (CW) irradiation at a single frequency off-resonance, liquid pool magnetization dynamics are most easily considered in the rf rotating reference frame, as shown in Fig. 3. In this frame, the effective field B_{eff} consists of the vector sum of the transverse B_1 field and a residual longitudinal field equal to Δ/γ where Δ is the

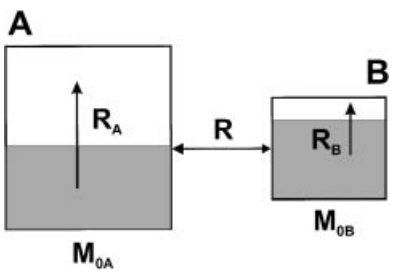


Figure 2. A two-pool model of magnetization transfer exchange. The shaded region in each pool represents saturated spins. R_A and R_B represent longitudinal relaxation rates in liquid and macromolecular pools respectively. R denotes magnetization transfer exchange between the pools

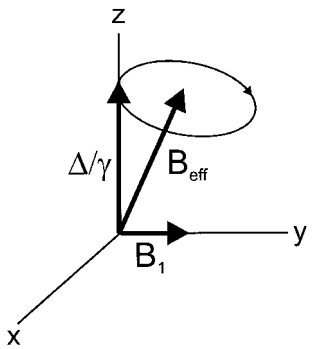


Figure 3. Excitation of the liquid pool magnetization with a saturation pulse of amplitude B_1 and offset-frequency Δ, results in precession about an effective field B_{eff}

Copyright © 2001 John Wiley & Sons, Ltd.

difference between the resonant Larmor frequency (ω_o) and the rotating frequency of the RF (ω_{RF}), as shown in Fig. 3. In MT imaging experiments, the offset frequency $\Delta = \omega_{RF} - \omega_O$ is typically in the order of 2 kHz and the B_1 field seldom exceeds a rotational frequency of 0.5 kHz due to specific absorption rate (SAR) limitations and hardware limits, ensuring that B_{eff} does not deviate from B_0 by more than 15°. Nonetheless, CW off-resonance irradiation initially results in a precession of the liquid spins about the effective field and leads to transient oscillations of transverse magnetization known as Rabi oscillations which decay with a time constant of $T_{2\rho}$. The resultant magnetization along B_{eff} relaxes with a time constant of $T_{1\rho}$. To bring this picture into agreement with the simple longitudinal and saturated compartment represented in Fig. 2, it is necessary to suppress the transverse magnetization by spoiler gradients or by phase cycling. This is usually not an issue in MT imaging experiments because saturation pulses (see below) are sufficiently smooth that they are adiabatic or they are repeated sufficiently frequently that the transverse components are incoherently dephased. Irrespective of these technical issues, off-resonance irradiation inevitably produces some saturation of the longitudinal magnetization in the liquid pool.

Off-resonance irradiation in MRI can be applied in a CW mode or in a pulsed mode.[6] CW experiments are best for characterizing the mechanisms of the MT process because they provide the cleanest separation between the amount of saturation in the two pools. For practical imaging experiments, however, repetitive pulsed off-resonance irradiation of shorter duration is necessary to allow time for the interleaved imaging experiment, to keep the SAR within reasonable limits, and because imaging RF transmitters are designed for pulsed RF and not CW operation. Off-resonance RF pulses are usually delivered with an amplitude modulation that varies smoothly in time, such as a Gaussian envelope. The exact shape is not important provided that the Fourier transform of the off-resonance pulse does not have any amplitude in the vicinity of the Larmor frequency of the liquid pool. Alternatively, on resonance composite pulses (e.g. $1\ \bar{2}\ 2\ \bar{1}$) can be used that saturate the macromolecular pool but flip liquid pool magnetization back to its longitudinal orientation.[7] Although this is an interesting concept, these pulses can produce a large amount of direct saturation of the liquid spins, depending on their T_2 value, which masks the intended MT effect.[8] Finally, it should be noted that any off-resonance RF pulses in an imaging sequence saturate the macromolecular pool to some degree. Thus, unintended MT effects are observed in multi slice imaging when many slice selection refocusing pulses are used particularly in fast spin echo or turbo spin echo imaging[9–11] and in perfusion imaging with FAIR.[12]

The most important process in MT is the exchange between the macromolecular pool and the liquid pool. It is this exchange that transfers macromolecular saturation to the liquid pool, resulting in decreased longitudinal magnetization being available for imaging. This spin exchange can occur via dipolar coupling or via direct chemical exchange. The model and the algebra cannot distinguish these two options, nor can the MT experiment. Experiments using isotopically substituted protons showed in a few model systems that the exchange was not chemical.[13] Other experiments in tissue and tissue models have shown a significant pH effect, suggesting chemical exchange, but the pH effect is too small and too broad for the whole MT exchange to be chemical.[14,15] Whether the exchange is dipolar or chemical, the nature of the interaction sites has yet to be determined. Are there only a few 'docking' sites per macromolecule that facilitate very effective exchange, or are there many possible locations for exchange that are less efficient? What are the chemical characteristics of these interaction sites? Is there any possibility of increasing the specificity of MT from a knowledge of the interaction chemistry? These are all questions related to the molecular basis of MT that require further investigation.

EXPERIMENTAL DEMONSTRATIONS

The theoretical understanding described above has been validated in a large number of experiments by a variety of groups in tissue models and tissues, *in vivo* and *in vitro*.[16–18] Agreement between calculations and measured data to within 1–3% has allowed quantitative parameterization of biophysical models of MT in tissues. Agar was the first model system to be studied in detail.[4]

Figure 4 shows representative MT measurements for an aqueous gel sample containing 4% agar by weight.

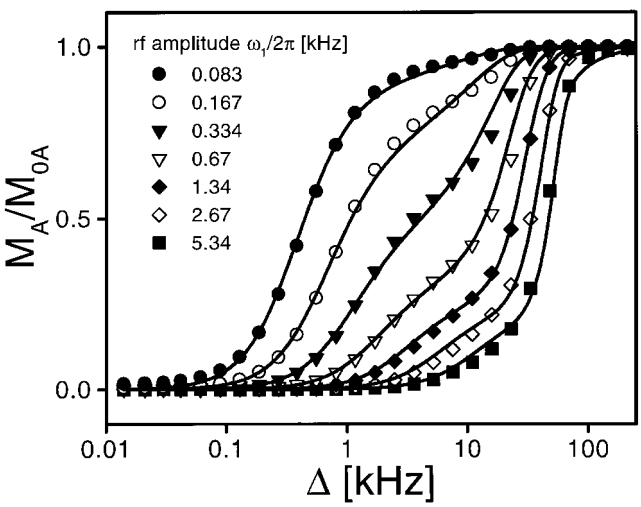


Figure 4. Magnetization transfer data for 4% agar. Data are plotted for seven different RF amplitudes as a function of 26 offset frequencies Δ. Solid lines result from a two-pool model fit

Copyright © 2001 John Wiley & Sons, Ltd.

The data show the fraction of longitudinal magnetization remaining after CW irradiation to a steady-state condition (7 s) as a function of the frequency offset (Δ) for seven different irradiation amplitudes (expressed as the nutational frequency of B_1, $\omega_1/2\pi$). The details of the experiment are given in Graham and Henkelman.[6] These spectra have been named *Z*-spectra by Dr Bob Bryant.[19] The solid lines in Fig. 4 are a fit to a two-pool model with exchange as described above. In the case of agar, the macromolecular absorption lineshape is assumed to be Gaussian—an appropriate assumption for the 'solid-like' agar matrix.[20] Over the whole data set, the average residual deviation is 1.5%. From the fitted parameters, it is learned that the effective T_2 of the macromolecular spins is very short with a time constant of only 13 μs, attesting to the immobility of the gel molecules. The fraction of macromolecular spins M_{0B} is 0.011 ± 0.002, which amounts to 60% of the stoichiometric inventory of gel protons in the sample and indicates that spin diffusion extends to most of the molecule. The fitting of the model is weakly dependent on the parameter R_B, suggesting that this parameter cannot be determined from such MT experiments.

With a quantitative model of the underlying biophysics, it is possible to ask what would happen in this MT experiment if the exchange between the two compartments did not occur. Figure 5 shows the same MT data as Fig. 4 for 4% agar at a single B_1 amplitude frequency of 0.67 kHz. The upper curve shows the relative magnetization that would have been obtained if there had been no exchange between the water proton spins and those of agar. There is still saturation of the water as the offset frequency falls below 10 kHz but this is the direct effect of the irradiation on the water and is not due to MT. The sigmoidal shape is the irradiation profile of a Lorentzian lineshape expected for liquids plotted *vs* the logarithm of the frequency offset (Δ). The shaded region shows the amount of saturation coming from saturated agar spins exchanging with the water spins. For completeness, the dashed line shows the fraction of unsaturated agar spins without exchange if they were detected directly. The fact that they are saturated out to 35 kHz is indicative of their broad lineshape. If we consider an irradiation frequency of 8 kHz and a nutation frequency of 0.67 kHz (these would constitute an appropriate set of experimental parameters for MT imaging of agar), we can see the reduced signal M_{SAT} obtained following the saturating RF compared with the unperturbed signal M_0. It is customary in MT imaging to calculate the magnetization transfer ratio (MTR) which can be seen from Fig. 5 to consist of two contributions: M_{dir}, the direct effect contribution, and M_{MT}, the true MT contribution,

$$\mathrm{MTR} = \frac{M_0 - M_{SAT}}{M_0} = 1 - \left(\frac{M_{dir}}{M_0} + \frac{M_{MT}}{M_0}\right) \quad (1)$$

Depending on the choice of imaging pulse sequence, this equation is slightly modified to substitute equilibrium magnetization for the effect of incomplete longitudinal recovery produced by short repetition times. Although it is important to distinguish both contributions (M_{dir} and M_{MT}) in studies that are attempting to quantitate MT, in qualitative imaging it can be quite appropriate to have contrast generated by both MT *and* the direct effect. The direct effect does become more pronounced as T_1/T_2 of the sample increases. Thus, some studies, which have claimed correlations of MT with either T_1 or T_2, are probably influenced primarily by direct effects.

Other investigators have attempted to quantify MT images by calculating a rate constant,

$$k_{SAT} = \frac{1}{T_{1SAT}}\left[1 - \frac{M_{SAT}}{M_0}\right] \quad (2)$$

where T_{1SAT} is the time constant for the two pools to come to equilibrium during irradiation. As shown by Edzes and Samulski,[21] k_{SAT} would be the first-order rate constant for the exchange provided the macromolecular spins were kept fully saturated and provided there was no direct effect on the liquid spins. Although the algebra in eqn (2) can always be performed, the rate constant k_{SAT} has no physical meaning unless these two necessary conditions are satisfied. Originally shown by Yeung,[22] k_{SAT} varies from 9 to 0.7 over the offset frequency range of 1–20 kHz when calculated for the data in Fig. 5. Thus for quantitation of MT effects in imaging, MTR is a valid and useful phenomenological measure even though it

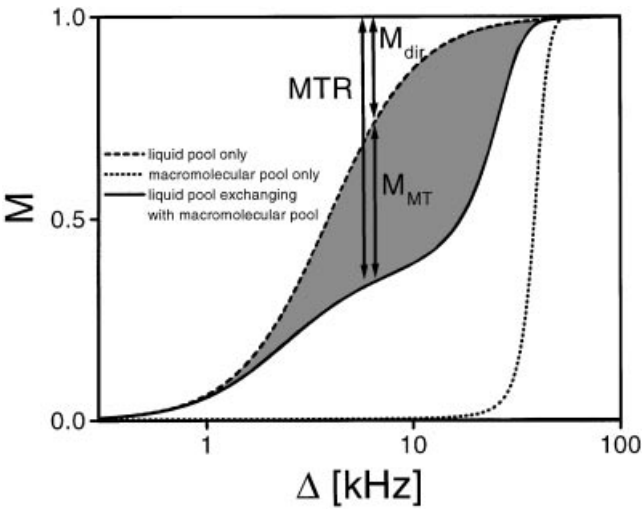


Figure 5. Longitudinal magnetization of the liquid and macromolecular pool for 4% agar and the amplitude of the RF saturation pulse B_1 of 0.67 kHz. The shaded region between the curves illustrates the saturation due to magnetization transfer (M_{MT}). M_{dir} indicates saturation due to the direct effect

Copyright © 2001 John Wiley & Sons, Ltd.

depends on tissue type and pulse sequence. In contrast, k_{SAT} purports to be a constant of the NMR dynamics, but is misleading and is bad science, because it is not a constant in tissue MT imaging.

Similar experiments to those described for agar have been performed for various biological tissues. The results are qualitatively similar and analysis with the same two-pool model can be successfully undertaken. Not surprisingly, the macromolecular absorption lineshape for tissues is not Gaussian as it is in agar, but is 'softer'. Reasonable fits can be obtained using a super-Lorentzian lineshape[17] as is done for liquid crystals. However, given the variety of macromolecular protons in tissue, it seems better not to use some *a priori* lineshape, but instead to let the data 'speak for itself' and to extract a parameterized absorption lineshape from the measured MT experiments.[23] Figure 6 shows the results of such an exercise for four different tissues. The logarithm of the absorption is plotted on the vertical axis to allow comparison of the low absorption probabilities in the tails of the distributions. The experimental lineshapes are shown only over the range of offset frequencies where they are determined to a precision of $\pm 10\%$. For comparison, a Gaussian distribution is shown as a dashed line and a super-Lorentzian distribution is shown as a dotted line. The super-Lorentzian is a better approximation to the experimentally derived absorption lineshapes for tissue than the Gaussian lineshape which is unacceptable. For numerical model fitting, the super-Lorentzian is more practical to use than are the experimentally derived lineshapes.

Somewhat surprisingly, the macromolecular absorption lineshape is relatively independent of tissue type even for tissues that have markedly different MTRs. The data in Fig. 6 suggest that within the complex molecular environments in tissues, the MT exchange sites are not very different in different tissues. Given such similarity in the absorption lineshapes, why then do tissues have such different MTRs?

The amount of magnetization transfer in a tissue depends upon a competition between two processes. Longitudinal spins in the liquid pool become saturated by exchanging with macromolecular spins that have been saturated by off-resonance irradiation. The greater the exchange rate, (RM_{0B}), the greater the MTR, but saturated spins can recover equilibrium magnetization by longitudinal relaxation mechanisms governed by R_A. The larger the R_A, the less the MTR. Thus, an appropriate indicator for the amount of MT is the ratio of the two competing rates (RM_{0B}/R_A). Figure 7 shows the MTR for a typical MT irradiation of average amplitude 0.67 kHz and offset frequency of 8 kHz. The data point shows an MTR of 66% for white matter for this irradiation and it can be seen to be made up of 14% direct effect and 52% actual MT. If the ratio of rates that govern magnetization transfer decrease, the MTR decreases. The MTR curve is almost single valued and is shown as a single line for both the exchange decreasing with R_A fixed and R_A increasing with the exchange held constant. In either case, a drop in the ratio of rates causes a drop in the MTR. It is the ratio of rates between the two competing processes that is the primary determinate of the amount of MT for a particular irradiation experiment for different tissues. Figure 7 also explains the effect of contrast agents such as Gd-DTPA on MT imaging. Such agents increase the rate of longitudinal recovery and hence decrease the amount of MT, which must be recognized when MT imaging is performed as part of a larger examination protocol that involves prior contrast agent administration. This can be

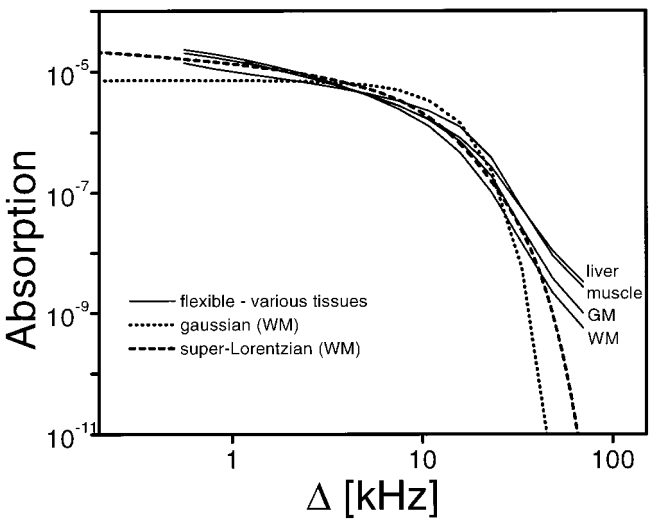


Figure 6. Flexible lineshapes derived from MT data for liver, skeletal muscle, gray matter (GM) and white matter (WM) in comparison to analytical Gaussian and super-Lorentzian lineshapes

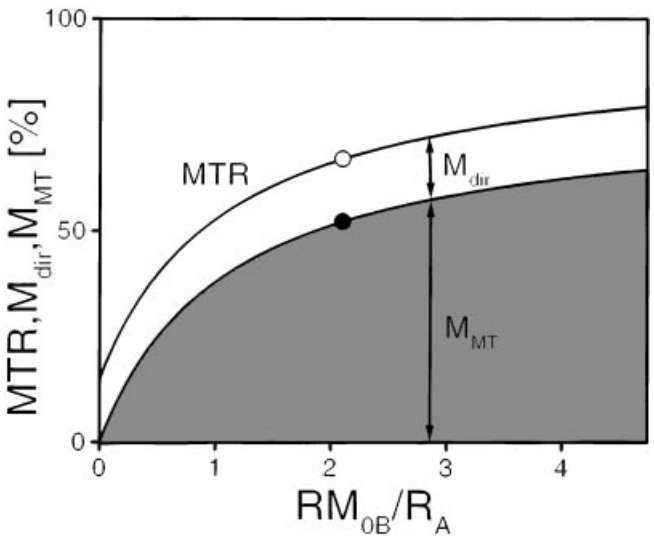


Figure 7. Calculated values of MTR, M_{dir}, M_{MT} as a function of parameter RM_{0B}/R_A for $\omega_1/2\pi = 0.67$ and $\Delta = 8$ kHz. Experimental values of MTR and MT effect for white matter are shown as data points

Copyright © 2001 John Wiley & Sons, Ltd.

used to advantage to obtain high SNR with MT contrast.[24] It can also be seen from Fig. 7 that the MTR for a tissue would be expected to increase as field strength increases. This is not a result of the exchange rate, which has been shown to be independent of field strength,[4] but is due to diminished competition from recovery of longitudinal magnetization at higher fields.

Although the discussion so far has focused on CW off-resonance irradiation for the production of magnetization transfer, the same theoretical analysis can be applied to generation of MT by pulsed irradiation.[11] For the effect of pulsed irradiation on the semisolid pool, the frequency content of the saturation pulse needs to be multiplied by the absorption lineshape and integrated over all frequencies.[25] For the liquid component, the effect of a time varying saturating pulse is best calculated from the Bloch equations. Between pulses, the two-pool system is propagated according to the model in Fig. 2. The most complete experimental verification of this model for pulsed MT in tissues is given by Sled and Pike[26] who have shown a similar 1–2% residual error between calculation and experiment. It can also be seen from this discussion that, holding all other experimental parameters constant, to a first approximation it is the average power of the off-resonance irradiation that determines the degree of macromolecular saturation and hence MT.

More complex models of MT have been explored. Using more than two pools is a natural extension but it has not been shown to provide a statistically better agreement to the MT data except for particularly complex tissues, such as lens of the eye.[27] Extending the model to include a dipolar reservoir with its own relaxation time has also been shown not to be of advantage.[25,28]

However, when some other NMR experiment is used to compartmentalize spins in tissue in combination with a MT experiment, it is possible to identify additional different MT compartments.[29,30] For example, MT combined with the Carr–Purrell–Meiboom–Gill (CPMG) sequence for measurement of T_2 relaxation allows the MT properties of slowly relaxing and rapidly relaxing spins to be evaluated independently.[31] The analysis of such hybrid data becomes much more difficult and successful data analysis poses stringent SNR requirements that are difficult to achieve in MR imaging. Nevertheless, such multi-compartment experiments with MT have been performed on excised muscle,[30] nerve[31] and white matter.[30,31,33] It is quite likely that more insight about MRI of tissue water will be obtained from hybrid experiments of this type.

APPLICATIONS IN IMAGING

Magnetization transfer is more than just a probe into the proton spin interactions within tissues. It can be used to provide additional advantageous contrast in MR images. One universally agreed upon MT application is in magnetic resonance angiography (MRA). MRA uses specific imaging sequences to suppress the signal from static tissues while enhancing signal from blood by means of inflow or phase effects. The signal contrast between the blood and other tissue can always be enhanced by using MT (which need not affect blood) to further suppress the background tissue signal.[34] Better contrast between blood and tissue leads to better angiograms. The improvement produced by MT in MRA is predicted to become even greater at higher fields because of the larger MT effect. Figure 8 is kindly provided by Dr Matt Bernstein of the Mayo Clinic, Rochester, and shows superb cerebral MR angiograms acquired at 3 T with the application of MT.

The second major application of MT is characterization of white matter disease in the brain, principally multiple sclerosis (MS). MS is a diffuse, progressive disease, grossly characterized by the presence of lesions in brain white matter tissue with pathological characteristics that vary as the lesions evolve. The evolution and history of specific MS lesions is difficult to resolve with conventional T_1-weighted or T_2-weighted MRI, and some lesions are unobservable. Using MT imaging for region-of-interest analyses, however, MS lesions are more conspicuous and MTR values provide information on lesion evolution.[35,36] More recently, the diffuse characteristics of MS have been characterized by plotting the MTR histogram of the whole brain (Fig. 9). This process indicates that there are significant differences between the MTR ratio of the so-called 'normal-appearing white matter' in MS patients and the white matter of healthy individuals. Histogram-based measures of MTR show strong correlation with cognitive decline in MS patients and may provide a useful method to study the natural course of MS or to evaluate the effect of drug treatments.[37]

Other areas of application for MT that are less well established include breast,[38] knee[39] and cartilage.[40] Within cartilage, it may be possible using Gd-DTPA to separate the effect of proteoglycan degradation, from the effect of collagen disruption, which is the major contributor to MT in this tissue (Deb. Burstein, MIT, private communication).

The first application for MT was envisaged approximately 10 years ago and involved the detection of specific metabolites. Only very recently has MT from metabolites been demonstrated.[41–43] MT-MRS is discussed further in the article by D. Leibfritz and W. Dreher in this issue.[44] It is still possible that this effect will have significant application in understanding tissue metabolism in the future.

CONCLUSIONS

Magnetization transfer is a unique contrast mechanism in MRI that has been known for the past decade. Over this

Copyright © 2001 John Wiley & Sons, Ltd.



Figure 8. MR angiogram taken with a 3 Tesla imager with MT suppression of brain tissue of 7–16% across the image. The high Signal to Noise and MT combined to give exceptionally high quality MRAs. Image is kindly provided by Dr Matt Bernstein, Mayo Clinic, Rochester, Minnesota

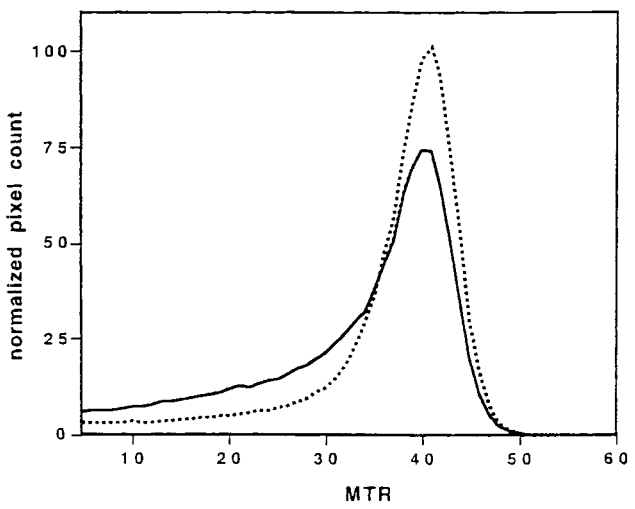


Figure 9. Normalized histogram of magnetization transfer ratio (MTR) for the whole brain of a healthy individual (dotted line) and a patient with multiple sclerosis (MS, solid line). The MS patient exhibits reduced peak MTR value and a larger proportion of brain pixels with low MTR values, reflecting micro- and macroscopic lesion lead in the whole brain. Reproduced from Van Buchem *et al.*[37] with permission

period, researchers have characterized the underlying NMR physics, exchange and relaxation rates that govern MT, although detailed understanding of the chemistry and molecular interactions is still needed. Full models of MT have allowed for confident optimization of MRI pulse sequences for MT. MT has shown its value in MRA and white matter disease and holds continuing promise for use in imaging other tissues and diseases. May MT in MRI have an equally exciting second decade!

REFERENCES

1. Wolff SD, Balaban RS. Magnetization transfer contrast (MTC) and tissue water proton relaxation in vivo. *Magn. Reson. Med.* 1989; **10**: 135–144.
2. Grossman R, Gomori JM, Ramer KN, Lexa FJ, Schnall MD. Magnetization transfer: theory and clinical applications in neuroradiology. *RadioGraphics* 1994; **14**: 279–290.
3. Wolff SD, Balaban RS. Magnetization transfer imaging: practical aspects and clinical applications. *Radiology* 1994; **192**: 593–599.
4. Henkelman RM, Huang X, Xiang Q-S, Stanisz GJ, Swanson SD. Quantitative interpretation of magnetization transfer. *Magn. Reson. Med.* 1993; **29**: 759–766.

Copyright © 2001 John Wiley & Sons, Ltd.

5. Hua J, Hurst GC. Analysis of on- and off-resonance magnetization transfer techniques. *J. Magn. Reson. Imag.* 1995; **5**: 113–120.
6. Graham SJ, Henkelman RM. Pulsed magnetization transfer imaging: evaluation of technique. *Radiology* 1999; **212**: 903–910.
7. Hu BS, Conolly SM, Wright GA, Nishimura DG, Macovski A. Pulsed saturation transfer contrast. *Magn. Reson. Med.* 1992; **26**: 231–240.
8. Graham SJ, Henkelman RM. Understanding pulsed magnetized transfer. *J. Magn. Reson. Imag.* 1997; **7**: 903–912.
9. Constable RT, Anderson AW, Zhong J, Gore JC. Factors influencing contrast in fast spin-echo MR imaging. *Magn. Reson. Med.* 1992; **10**: 497–511.
10. Dixon WT, Engels H, Castillo M, Sardashti M. Incidental magnetization transfer contrast in standard multislice imaging. *Magn. Reson. Med.* 1990; **8**: 417–422.
11. Santyr GE. Magnetization transfer effects in multislice MR imaging. *Magn. Reson. Med.* 1993; **11**: 521–532.
12. Wong EC, Buxton RB, Frank LR. Implementation of quantitative perfusion imaging techniques for functional brain mapping using pulsed arterial spin labeling. *NMR Biomed.* 1997; **10**: 237–249.
13. Ceckler TL, Balaban RS. Tritium-proton magnetization transfer as a probe of cross-relaxation in aqueous lipid bilayer suspensions. *J. Magn. Reson.* 1991; **93**: 572–588.
14. Kucharczyk W, Macdonald PM, Stanisz GJ, Henkelman RM. Relaxivity and magnetization transfer of white matter lipids at MR imaging: Importance of cerebrosides and pH[1]. *Radiology* 1994; **192**: 521–529.
15. Hills BP, Favret FA. A comparative multinuclear relaxation study of protein–DSMO and protein–water interaction. *J. Magn. Reson. B* 1994; **103**: 142–151.
16. Quesson B, Thiaudière E, Delalande C, Dousset V, Chateil J-F, Canioni P. Magnetization transfer imaging *in vivo* of the rat brain at 4.7 T: interpretation using a binary spin-bath model with a super-Lorentzian lineshape. *Magn. Reson. Med.* 1997; **38**: 974–980.
17. Kruiskamp MJ, de Graaf RA, van Vliet G, Nicolay K. Magnetic coupling of creatine/phosphocreatine protons in rat skeletal muscle, as studied by ^{1}H-magnetization transfer MRS. *Magn. Reson. Med.* 1999; **42**: 665–672.
18. Morrison C, Henkelman RM. A model for magnetization transfer in tissues. *Magn. Reson. Med.* 1995; **33**: 475–482. [See also Erratum. *Magn. Reson. Med.* 1996; **35**: 277.]
19. Grad J, Bryant RG. Nuclear magnetic cross-relaxation spectroscopy. *J. Magn. Reson.* 1990; **90**: 1–8.
20. Abragam A. The Principles of Nuclear Magnetism. Oxford University Press: London, 1961.
21. Edzes HT, Samulski ET. Cross relaxation and spin diffusion in the proton NMR of hydrated collagen. *Nature* 1977; **265**: 521–523.
22. Yeung HN. On the treatment of the transient response of a heterogeneous spin system to selective RF saturation. *Magn. Reson. Med.* 1993; **30**: 146–147.
23. Li JG, Graham SJ, Henkelman RM. A flexible magnetization transfer lineshape derived from tissue experimental data. *Magn. Reson. Med.* 1997; **37**: 866–871.
24. Jones RA, Haraldseth O, Schjøtt J, Brurok H, Jynge P, Øksendal AN, Rinck PA. Effect of Gd-DTPA-BMA on magnetization transfer: Application to rapid imaging of cardiac ischemia. *J. Magn. Reson. Imag.* 1993; **3**: 31–39.
25. Graham SJ, Henkelman RM. Quantifying the magnetization transfer produced by RF irradiation with multiple frequency components. *Proc. Int. Soc. Magn. Reson. Med.* 1996; **1**: 469.
26. Sled JG, Pike GB. Quantitative interpretation of magnetization transfer in spoiled gradient echo MRI sequences. *J. Magn. Reson.* 2000; **145**: 24–36.
27. Yeung HN, Tzou D-L, Lee SM, Huang F-Y, Hur Y. Indirect estimation of lens protein dynamics via magnetization transfer. *J. Magn. Reson.* B 1996; **113**: 167–171.
28. Morrison C, Stanizs G, Henkelman RM. Modeling magnetization transfer for biological-like systems using a semi-solid pool with a super-Lorentzian lineshape and dipolar reservoir. *J. Magn. Reson. B* 1995; **108**: 103–113.
29. Yang H, Schleich T. T_1 discrimination contributions to proton magnetization transfer in heterogeneous biological systems. *Magn. Reson. Med.* 1994; **32**: 16–22.
30. Harrison R, Bronskill MJ, Henkelman RM. Magnetization transfer and T_2 relaxation components in tissue. *Magn. Reson. Med.* 1995; **33**: 490–496.
31. Stanisz GJ, Kecojevic A, Bronskill MJ, Henkelman RM. Characterizing white matter with magnetization transfer and T_2. *Magn. Reson. Med.* 1999; **42**: 1128–1136.
32. Does MD, Beaulieu C, Allen PS, Snyder RE. Multi-component T_1 relaxation and magnetization transfer in peripheral nerve. *Magn. Reson. Med.* 1998; **16**: 1033–1041.
33. Vavasour IM, MacKay AL et al., Differential magnetization transfer effects for the short and long T_2 components in white matter. *Proc. Int. Soc. Magn. Reson. Med.* 1999; **7**: 648.
34. Parker DL, Buswell HR, Goodrich KG, Alexander AL, Keck N, Tsuruda JS. The application of magnetization transfer in MR angiography with reduced total power. *Magn. Reson. Med.* 1995; **34**: 283–286.
35. Petrella JR, Grossman RI, McGowan JC, Campbell G, Cohen JA. Multiple sclerosis lesions: Relationship between MR enhancement pattern and magnetization transfer effect. *American Journal of Neuroradiology* 1996; **17**: 1041–1049.
36. Silver NC, Lai M, Symms MR, Barker GJ, McDonald WI, Miller DH. Serial magnetization transfer evolution of new MS lesions. *Neurology* 1998; **51**: 758–764.
37. Van Buchem MA, Grossman RI, Armstrong C, Polansky M, Miki Y, Heyning FH, Boncoeur-Martel MP, Wei L, Udupa JK, Grossman M, Kolson DL, McGowan JC. Correlation of volumetric magnetization transfer imaging with clinical data in MS. *Neurology* 1998; **50**: 1609–1617.
38. Santyr GE, Kelcz F, Schneider E. Pulsed magnetization transfer contrast with MR imaging with application to breast. *J. Magn. Reson. Imag.* 1996; **1**: 203–212.
39. Wolff SD, Chesnick S, Frank JA, Lim KO, Balaban RS. Magnetization transfer contrast: MR imaging of the knee. *Radiology* 1991; **179**: 623–628.
40. Kim DK, Ceckler TL, Hascall VC, Calabro A, Balaban RS. Analysis of water–macromolecule proton magnetization transfer in articular cartilage. *Magn. Reson. Med.* 1993; **29**: 211–215.
41. Dagher AP, Aletra AH, Choyke R, Balaban RS. Detection of human kidney metabolites using saturation transfer at 1.5 Tesla. *Proc. Int. Soc. Magn. Reson. Med.* 1999; **7**: 1919.
42. Meyerhoff DJ. Proton magnetization transfer of metabolites in human brain. *Magn. Reson. Med.* 1999; **42**: 417–420.
43. Roell SA, Dreher W, Leibfritz D. Combining CW and pulsed saturation allows in vivo quantitation of magnetization transfer observed for total creatine by ^{1}H-NMR-spectroscopy of rat brain. *Magn. Reson. Med.* 1999; **42**: 222–227.
44. Leibfritz D, Dreher W. Magnetization Transfer MRS. *NMR Biomed.* 2001; **14**: 65–76.

Copyright © 2001 John Wiley & Sons, Ltd.

Prog. Biophys. molec. Biol., Vol. 35, pp. 103–134.
© Pergamon Press Ltd., 1979. Printed in Great Britain
0079–6107/79/0301–0103$05.00/0

THE NMR STUDIES OF WATER IN BIOLOGICAL SYSTEMS

R. MATHUR-DE VRÉ

Université Libre de Bruxelles, Laboratoire de Radiobiologie Moléculaire, rue des Chevaux 67, 1640 *Rhode St. Genèse, Belgium and*
Institut d'Hygiène et d'Epidémiologie, Département de l'Environnement, rue Juliette Wytsman 14, 1050 *Bruxelles, Belgium*

CONTENTS

I. INTRODUCTION 103

II. HYDRATION WATER 104

III. NMR AND ITS APPLICATION TO WATER STUDIES 106
1. *Basic Concepts* 106
2. *The Relaxation Rates* 108
3. *Diffusion Constant* 110
4. *A Comparison of Different Water Nuclei* 110

IV. THE NMR STUDIES OF WATER IN DIFFERENT BIOLOGICAL SYSTEMS 111
1. *Randomly Oriented Systems* 112
(a) *Biopolymer solutions and hydrated proteins* 112
(b) *Effects of γ-irradiation on hydration water* 114
(c) *Muscles and tissues* 115
(d) *Membranes and cell water* 121
(e) *Tumours and cancerous cells* 124
(f) *NMR imaging by zeugmatography* 126
2. *Oriented Fibres* 127
(a) *Collagen* 127
(b) *DNA Fibres* 128

V. SUMMARY AND CONCLUSIONS 129

ACKNOWLEDGEMENTS 130

REFERENCES 130

I. INTRODUCTION

The state of water in the body constituents of living organisms and in the vicinity of biological macromolecules differs significantly from the state of water in solutions of simple molecules and in pure water. Nuclear magnetic resonance (NMR) spectroscopy is a powerful technique for studying in detail the structure, mobility, and extent of ordering of water molecules in various biological systems. The NMR spectra of water present in a sample can be obtained either from the total water content, or specifically from the hydration water or intracellular water depending on the nature of the sample. In order to fully appreciate the unique contribution of NMR spectroscopy in the domain of hydration studies, it is important to note that the behaviour of a water molecule  can be investigated by looking at the nuclear magnetic resonance of four different nuclei; these are the three isotopes of hydrogen: proton (^{1}H), deuterium (^{2}H), tritium (^{3}H), and oxygen ^{17}O. Of these, the most widely and extensively studied nucleus is ^{1}H; the applications of ^{2}H and ^{17}O NMR of water have been limited to the study of relatively few systems. The NMR studies of tritiated water in biological systems apparently have been neglected so far, but in the course of time they are likely to become a centre of intensive and growing research as a result of the recent progress in the development of tritium NMR spectroscopy. The importance of the NMR studies of tritiated water lies in the fact that such investigations are expected to offer a new and promising method for exploring the biological hazards of tritium (the radioactive isotope of hydrogen) present in the environment. The widespread risks

arise because tritium released from nuclear reactors inevitably pervades the environment as tritiated water: a form in which tritium can be readily absorbed by plants and animals.

The NMR parameters most useful in the study of water are the relaxation times, T_1, T_2 and $T_{1\rho}$. The diffusion constant and the distribution of correlation times for water can generally be evaluated from relaxation times measured under specific conditions. It is well known that the relaxation processes for protons, deuterons, and ^{17}O, are influenced by different factors. Therefore, for a comprehensive study of the state of water in any system, using NMR, it is important to compare the relaxation time data for more than one nucleus.

The present article comprises: a brief discussion of the characteristics of hydration water, an outline of the theory of NMR relaxation times with emphasis on the factors relevant to the study of water, and finally an extensive review covering the NMR studies of the different water nuclei in various biological systems and in the damage induced by γ-irradiation in the aqueous medium. Different theories related to either the structure of water in general, or to cell water in particular, have not been described at any length in this review. Several monographs have covered these subjects in considerable detail (Ling, 1962, 1969; Cope, 1970; Kavanau, 1964; Eisenberg and Kauzmann, 1969; Franks, 1972–1975). A variety of physical techniques other than NMR spectroscopy are also highly suitable for the study of the hydration of biological macromolecules. A number of methods which have been applied to nucleic acids are discussed explicitly in a recent article by Texter (1978).

II. HYDRATION WATER

Biological macromolecules induce a characteristic water structure in their close vicinity due to weak macromolecular–water interactions. The solvent water molecules interact with the solute species by electrostatic forces (dispersion and induction forces) because of the high dipole moment of water, as well as through extensive hydrogen bonding by virtue of the potentially available proton donor and proton accepting sites. Consequently, macromolecules form a well-defined hydration layer in solution, in hydrated fibres (DNA, collagen) and in all biological samples such as intracellular water, tissues, muscle, and membrane. The water molecules contributing to the hydration layer are dynamically oriented, and exhibit restricted motion due to a significant decrease in the translational and rotational modes of motion caused by macromolecular–water interactions. As a result, the mobility and the extent of ordering of hydration water molecules are distinctly different from those characterizing the fast and random motion of the bulk water. Furthermore, the overall behaviour of water molecules in the hydration layer is influenced by factors other than simple molecular interactions. Berendsen (1975) has distinguished three aspects of hydration water: thermodynamic aspects, dynamic aspects, and structural aspects. A complete description of hydration should necessarily comprise all three aspects.

The NMR studies of water illustrate that certain coherent and cumulative processes come into effect when biological macromolecules interact with water, either in solution or in biological systems. These processes (outlined below) are favoured by the extended, ordered, and complex structure of macromolecules (such as proteins and nucleic acids), and they govern different dynamic states of the hydration water molecules. (1) The restricted motion of water in different fractions of the hydration layer is not uniform, and all the dynamic modes of these water molecules cannot be described completely by a single correlation time but require a distribution of correlation times. (2) The diffusion of water molecules in the hydration layer occurs in an anisotropic manner. (3) The hydrogen bonded interactions between water molecules and several proton donor and proton accepting groups of macromolecules give rise to a continuous hydrogen bonded path in the hydration layer. This process promotes enhanced proton transfer along the

macromolecular chain in a continuous and an extensive path having a well-defined structure.

From the temperature-dependent changes in the relaxation times of water protons, the activation energy values of the order of 10.0 and 5.0 kcal/mole were calculated for the processes of proton transfer and diffusion, respectively (Berendsen and Migchelsen, 1966; Migchelsen and Berendsen, 1973; Mathur-De Vré *et al.*, 1976). These processes involve the breaking of two hydrogen bonds for the proton transfer and one hydrogen bond for the diffusion process. In general, the hydrogen bonds are very sensitive to the nature and orientation of groups interacting with water, and to small changes in the temperature. Therefore, the relaxation processes that are influenced predominantly by proton transfer in the hydrogen bonded path are also expected to exhibit a characteristic dependence on the above mentioned factors. When macromolecules are present in a medium containing ^2H_2O and ^3H_2O, the exchangeable or labile protons undergo isotopic substitution by exchange. This leads to incorporation of ^2H and ^3H throughout the system in preferential sites on the macromolecular chain. Furthermore, there is evidence suggesting that the isotopic distribution in the hydration layer is not random.

At temperatures well below the freezing point of solvent, the hydration water molecules remain unfrozen or mobile on the NMR time scale. This phenomenon is distinctly different from the physical processes such as freezing point depression and formation of eutectic mixtures. For the macromolecular solutions and all biological samples, the NMR spectra of water observed between -5 and $\sim -60°C$ arise from only a fraction of the total water content, i.e. the hydration water. From the temperature-dependent changes in these spectra, activation energy values for the relaxation processes have been calculated. In frozen samples, the extra-hydration layer water freezes to form a rigid ice-like structure (as in free water) giving rise to a very broad signal. The area under the water proton signals obtained from frozen solutions was shown to vary linearly with the concentration of macromolecules (Kuntz *et al.*, 1969; Mathur-De Vré *et al.*, 1976). This indicates that the water NMR signals observed in frozen samples arise from water associated with macromolecules. Kuntz and Kauzmann (1974) defined hydration water as the unfrozen water. The potential of this phenomenon for detailed studies of the properties of water in biological systems was soon recognized. This is evident from the numerous examples cited in Section IV.

Franks (1977) has described water–protein interactions in solutions as illustrated diagrammatically in Fig. 1. The A shell includes solvent molecules which are in the neighbourhood of the protein side chains or the backbone. The motion of water molecules in the primary hydration sphere (A shell) is determined by the motion of protein molecules or their localized groups. The region C represents the water molecules that are unperturbed by macromolecules. Finally, "incompatibility of the hydrogen

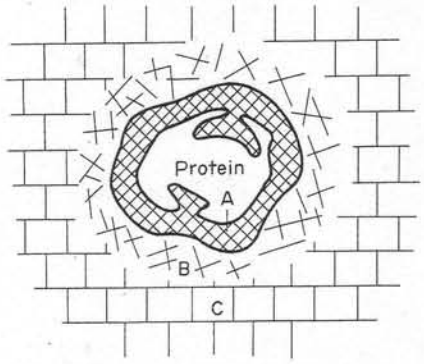


FIG. 1. (Franks, 1977) Diagrammatic representation of the protein environment in solution. The protein can be regarded as a hydrodynamic sphere with a primary hydration shell A in which the molecular motions are largely determined by those of the polar protein sites. C is the unperturbed water "structure" and region B arises from the spatial and orientational mismatch between regions A and C.

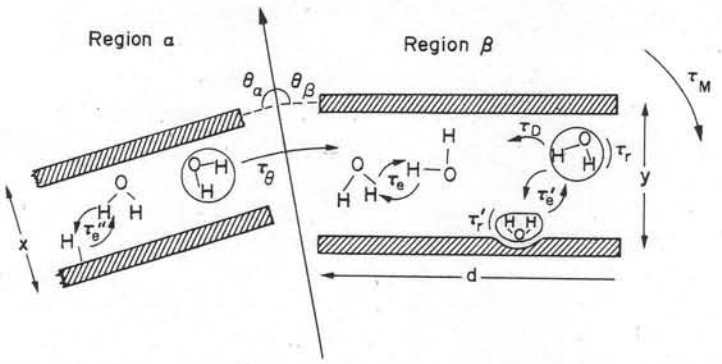


FIG. 2. (Packer, 1977) A schematic illustration of small-scale heterogeneity and various dynamic processes which may be experienced by water molecules in such a system. The shaded regions represent macromolecular structures characterized by dimensions d, x, y, etc., orientations θ_α, θ_β etc. with respect to an external fixed axis, and correlation times for tumbling, τ_m. Water molecules free of the influence of the macromolecules diffuse and rotate and exchange protons with characteristic times τ_D, τ_r and τ_e, respectively. Water molecules interacting with the macromolecule tumble anisotropically, this process being represented by a collective correlation time τ_r' and have a lifetime in this state designated by τ_e'. Water molecules may diffuse from one region to another, their lifetime in a given region being $\tau_\theta (\sim d^2/2D_s)$ whilst they exchange protons with macromolecules with a lifetime τ_e''.

bonding in regions A and C" gives rise to the region B. Franks indicated that water in regions A and B markedly influences the NMR spectra and contributes to the unfrozen fraction. In other words, regions A and B represent the hydration layer, and region C represents the extra-hydration water or the frozen fraction.

Berendsen (1975) defined the hydration of macromolecules in terms of specific and nonspecific hydration. The interactions between water and specific binding sites on the macromolecular chains result in specific hydration. Nonspecific hydration is the amount of water affected by the macromolecules in such a manner that it exhibits slightly lower rate of rotation than molecules in the bulk liquid state, and it also contributes to the unfrozen fraction of water. The regions of specific and nonspecific hydration may be compared with regions A and B in Fig. 1.

Packer (1977) has represented diagrammatically (see Fig. 2) different modes of motion of dynamically oriented water near a macromolecular surface. Distribution of correlation times for water protons arise because water molecules are subjected to largely diverse dynamic processes as a result of their interactions with a variety of sites and groups constrained in different environments on the macromolecular chain. In Fig. 2, α and β represent two components of a heterogeneous macromolecular surface, oriented by θ_α and θ_β with respect to an external reference axis. Packer proposed that water molecules near the macromolecular surface move in an anisotropic potential whose spatial properties remain unchanged during the reorientation of a water molecule; as a result the anisotropic potential experienced by each water molecule is not averaged out during its reorientation time. On the other hand, in liquid and bulk water the potential experienced by a molecule at any instant is also anisotropic but its axis undergoes a rapid change during the reorientation of water molecules, consequently the effects due to anisotropic potential are averaged out

III. NMR AND ITS APPLICATION TO WATER STUDIES

Several authors have discussed in detail the theory and techniques of NMR spectroscopy (Emsley *et al.*, 1965; Carrington and McLachlan, 1969; Ferrar and Becker, 1971; Shaw, 1976). Therefore, in this section only the basic principles of the NMR phenomenon will be described briefly and concisely, with special emphasis on the relaxation processes.

1. *Basic Concepts*

A nucleus with spin I is characterized by a spin angular momentum and possesses a magnetic moment (μ). In addition, a nucleus also has an electric quadrupole moment Q

if $I > 1/2$. For the NMR studies of water, the nuclei of interest are: proton ($I = 1/2$), deuteron ($I = 1$), tritium ($I = 1/2$), and oxygen ^{17}O ($I = 5/2$). In the presence of a large magnetic field H_0, the nuclear energy levels split into $2I + 1$ states. The distribution of spins between these energy levels attains thermal equilibrium with the lattice in such a manner that the lower energy level has a slight excess of spins. At equilibrium there is no net transfer of spins. However, in the presence of a second oscillating radiofrequency field $H_1(W)$ (RF field) whose magnetic component is perpendicular to H, the absorption of energy occurs and induces spin transfer from the lower to the upper energy level, provided the frequency (ν) of oscillating field satisfies the resonance condition: $h\nu = g_N\beta_N H_0$; where g_N is the nuclear g factor and β_N is nuclear magneton. This phenomenon gives rise to the nuclear resonance absorption signals. It is clear that the process of spin transfer would eventually lead to a state of saturation if there were no relaxation processes to re-establish the excess spin population in the lower level. However, spins in the higher energy level can relax to the lower level by means of relaxation processes that are induced by: (i) coupling interactions between the nuclear spin and the local fluctuating fields arising from thermal motion of the lattice, (ii) molecular motion, (iii) proton exchange processes and (iv) paramagnetic centres. The ultimate effects of the interactions (i)–(iii) on different nuclear magnetic relaxation processes are a function of the time scale and the nature of fluctuations in motion. Herein lies the basis of the application of the NMR relaxation times as a sensitive tool to monitor dynamic processes.

The process of energy exchange between the magnetic nuclei and the lattice is known as spin–lattice relaxation, designated by the time constant T_1. In addition, the magnetic nuclei also interact with each other, therefore each nuclear magnet experiences an additional small local field H_{loc} produced by the neighbouring nuclear magnets. Only the nearest neighbours exert an important influence because H_{loc} falls off rapidly with increasing distance. The spread of the steady magnetic field experienced by each nucleus results in dipolar broadening. The spin–spin interaction time constant T_2 represents the lifetime (or phase memory time) of a nuclear spin state. T_1 and T_2 are also defined as longitudinal and transverse relaxation times, respectively. This follows from the fact that when the RF field applied initially to a system of nuclear spins is removed, the magnetization aligned along H_0 (M_z component) returns exponentially to the equilibrium value with a time constant T_1, whereas the M_{xy} component decays with the time constant T_2. A third relaxation time constant $T_{1\rho}$ known as spin–lattice relaxation in rotating frame corresponds to the decay of magnetization aligned along $H_{(1\rho)}$ at right angles to H_0, rather than along H_0. Due to fast rotational and translational motions persisting in the liquid state, the local fluctuating fields of the surrounding lattice molecules are averaged thereby reducing the T_1 relaxation rates, while the averaging of the dipolar coupling interactions between nuclei decreases the T_2 relaxation rates.

In liquid samples very sharp water NMR signals are observed because magnetic interactions are averaged to zero. However, due to restricted motion in more rigid states (e.g. frozen samples, macromolecular–water interface) the fluctuating fields and dipolar interactions are not totally averaged, their residual effects on the NMR spectra constitute a valuable source of information concerning the mechanisms of relaxation rates and molecular interactions. At low temperatures, the averaging of dipolar and quadrupolar interactions is less effective because of reduced thermal motion, orientation, and ordering of water molecules. Ferrar and Becker (1971), and Frey *et al.* (1972) showed that the relaxation time T_1, T_2 and $T_{1\rho}$ are sensitive to dynamic processes occurring at different frequencies. For instance, T_1 is most sensitive to motions corresponding to the Larmor frequency $\omega_0 = \gamma H_0$, $T_{1\rho}$ detects motions corresponding to RF frequency $\omega_1 = \gamma H_{(1\rho)}$, and T_2 exhibits sensitivity to motions characterized by frequency $\omega_2 = \gamma H_{loc}$. For protons, $T_1, T_{1\rho}$, and T_2 were shown to be sensitive to motions occurring with frequencies of the order of 30 MHz, 50 kHz and 10 Hz, respectively (Frey *et al.*, 1972). Generally, proton exchange processes contribute to T_2 and $T_{1\rho}$. High

frequency processes affect both T_1 and T_2, but the low frequency processes (such as chemical exchange and slow diffusion) influence mainly the T_2 relaxation, causing T_2 to be much shorter than T_1 provided $\omega_0\tau_c \gg 1$.

The line broadening is an approximate measure of spin–spin relaxation time; T_2 may be obtained from the half-linewidth ($\Delta 1/2$) of the signals observed in the steady state, $\Delta 1/2 = 1/\pi T_2$. The relaxation times are measured accurately by the pulse techniques; for a detailed discussion of the theory and experimental pulse techniques one may refer to Ferrar and Becker (1971) and Shaw (1976). In this method a strong RF field is applied for short durations, i.e. in pulses. The effects of pulses depend on their magnitude and duration. The principle of the pulse method is that by applying either an initial 90° RF pulse M_z is reduced to zero, or it is reversed by a 180° pulse. A second pulse is used to tip M_z into the xy plane where the exponential regrowth of magnetization can be detected, and the relaxation time constants T_1 and T_2 measured. T_2 is generally obtained by the "spin echo" experiment (Carr–Purcell method), i.e. by applying a 90° pulse followed by a succession of 180° pulses. T_1 can be measured by applying a series of pulse sequences of the type 180°–τ–90° or by monitoring the amplitude of the induction decay signal M_z following a 90° pulse. The advent of the pulsed Fourier transform technique has greatly facilitated precise measurements of the relaxation times, particularly of nuclei present in low quantities.

2. *The Relaxation Rates*

The relaxation rates of the water molecules are governed by two important factors: (i) the strength of local magnetic interactions between water nuclei; (ii) the molecular motion and proton exchange rates.

(i) The important interactions between water nuclei are: nuclear magnetic dipole–dipole coupling (inter- and intramolecular), and nuclear quadrupole coupling for deuterium and ^{17}O. Quadrupole interactions result because the electric moment Q interacts with the neighbouring electric field gradient. Within the hydration layer, the magnetic interactions are partially averaged by specific processes depending on the interactions of water with macromolecules such as proton transfer, dynamic orientation and diffusion of water molecules through regions of different orientations. Whereas, in free or bulk water, motional averaging of magnetic interactions dominate the relaxation behaviour.

(ii) The effects of molecular motion are generally incorporated into the theory of nuclear magnetic relaxation in terms of the correlation time, (τ_c). τ_c is considered as the time taken by a molecule to translate through a molecular distance, or the average time between molecular collisions for a molecule in its actual state of motion. For fast motion, i.e. when $1/\tau_c \gg \omega_0$, T_1 and T_2 are equal. For slow and restricted motion, both T_1 and T_2 decrease and may not necessarily be identical as already mentioned in the previous section. The nuclear spin relaxation times are sensitive to molecular motions of 10^{-8}–10^{-12} sec. Water molecules tumble in liquid solutions at a rate of about 10^{-12} sec; this motion is considerably slowed down when water molecules interact with biological macromolecules in solution, in muscle, or in cells, but still falls within the limits of NMR sensitivity. For example, the rotational motion of water molecules associated by hydrogen bonds with polar groups on the macromolecular chains are reduced so that their correlation time is of the order of 10^{-6} sec instead of $\sim 10^{-12}$ sec for the remaining water (Fung, 1977a). Under the conditions of rapid exchange between the hydration and bulk water in liquid solutions of macromolecules, the observed relaxation rate $(1/T_1)_{obs}$ is given by:

$$(1/T_1)_{obs} = X_f(1/T_1)_f + X_h(1/T_1)_h. \tag{1}$$

Even though the fraction of free water X_f is much greater than the fraction of hydration water X_h, the term $X_h(1/T_1)_h$ can still make an important contribution to $(1/T_1)_{obs}$, since $(1/T_1)_h > (1/T_1)_f$ because of the restricted motion of water molecules in the hydration layer. If the rates of exchange of water between different regions in a

sample is fast compared with the regional relaxation rates, then an average water resonance signal is observed (fast-exchange condition); on the other hand, if the exchange rate is slow compared with relaxation rates in each site, then a resonance signal characteristic of water in each site may be observed (slow-exchange condition).

Assuming the motions involved in intramolecular relaxation, the following expressions were reported for $1/T_1$, $1/T_2$ and $1/T_{1\rho}$ in terms of the correlation time τ (Finch and Homer, 1974; Knispel *et al.*, 1974; Belton *et al.*, 1973; Fung and McGaughy, 1974).

$$1/T_1 = C\left(\frac{2\tau}{1+\omega_0^2\tau^2} + \frac{8\tau}{1+4\omega_0^2\tau^2}\right) \tag{2}$$

$$1/T_2 = C\left(3\tau + \frac{5\tau}{1+\omega_0^2\tau^2} + \frac{2\tau}{1+4\omega_0^2\tau^2}\right) \tag{3}$$

$$1/T_{1\rho} = C\left(\frac{3\tau}{1+4\omega_1^2\tau^2} + \frac{5\tau}{1+\omega_0^2\tau^2} + \frac{2\tau}{1+4\omega_0^2\tau^2}\right), \tag{4}$$

where ω_0 is the Larmor angular frequency in the constant magnetic field H_0 and is related to the resonance frequency ν_0 by the relation $\omega_0 = 2\pi\nu_0$, ω_1 is the Larmor frequency in the rotating frame in the presence of a RF field ($H_{1\rho}$), and C is a constant having the form $k'\gamma^4\hbar I(I+1)r_{jk}^{-6}$ for protons. A similar expression for deuteron $1/T_1$ was given where the constant C is equal to $k''\pi^2(1+\eta^2/3)(e^2qQ/h)^2$ (Fung *et al.*, 1975a); γ is the gyromagnetic ratio, $\hbar$ = Planck constant, $h/2\pi$, r_{jk} is the internuclear distance, e^2qQ/h is the nuclear quadrupolar coupling constant, η is the asymmetry parameter, and finally k' and k'' are the numerical values. Both ω_0 nd ω_1 are variable parameters. It can be seen from eqns (2)–(4) that when $\omega_0\tau > 1$, information about τ (and motion) can be obtained by studying the ω_0 dependence of relaxation times. In pure water, τ is very small ($<10^{-11}$ sec) and $\omega_0\tau \ll 1$ even at very high ω_0 values, therefore T_1 and T_2 values are independent of the ω_0 values.

Berendsen has shown that in the hydration layer of biopolymers, T_2 can be related to the diffusion of water molecules and the exchange lifetime of protons in the following manner (Berendsen, 1975; Mathur-De Vré *et al.*, 1976):

$$1/T_2 = (\gamma^2/20)(\Delta H)^2\tau_c, \tag{5}$$

where γ is the proton gyromagnetic ratio; ΔH is the maximum splitting of the proton resonance in the event that the biopolymer is completely aligned with the magnetic field, and $\tau_c = (6D/a^2) + \tau_{exch}^{-1}$; D is the diffusion constant; a is the measure for the length over which the macromolecules are oriented; and τ_{exch} is the exchange lifetime of a proton on the water molecule. It was shown that in frozen DNA solutions the diffusion process determines the behaviour of T_2 or $(\Delta 1/2)$ at low temperatures, while at higher temperatures the exchange rate dominates the relaxation process: where $(\Delta 1/2) = 1/\pi T_2$.

In free or bulk water, the rotational and translational motions of water molecules are strongly coupled, as a result the motion of water molecules can be defined by a single correlation time (Eisenberg and Kauzmann, 1969). Whereas, in the hydration layer the translational and rotational motions are no longer appreciably coupled due to molecular interactions, restricted motion and ordering of water molecules. Under the influence of the decoupling effect, the motion of the entire mass of water cannot be expressed by a single correlation time but requires a distribution function. At temperatures below the freezing point of the solvent, the molecules of unfrozen water in biological samples have been treated as spherical molecules undergoing translational and rotational motion, governed by a distribution of correlation times (Fung and McGaughy, 1974). The normalized log-Gaussian distribution function is given by the relation:

$$g(\tau) = \frac{\alpha}{\sqrt{\pi\tau}} \times \exp\left[-(\alpha \ln \tau/\tau_0)^2\right]. \tag{6}$$

The parameters τ_0 and α are temperature-dependent, τ_0 is the median of distribution and α is a parameter that determines the width of the distribution. The distribution of correlation times leads to different frequency dependence of T_1, $T_{1\rho}$ and T_2 from that given by eqns (2)–(4).

At temperatures above the freezing point of water, the following distribution function was suggested:

$$g'(\tau) = X \times g(\tau_1) + (1 - X)\delta(\tau_2), \tag{7}$$

where X = fraction of molecules at any instant having a log-Gaussian distribution of the correlation times. Equation (7) signifies that above the freezing temperatures, each water molecule spends part of its time behaving as isotropic water with a single correlation time.

The correlation between the motion of protons from the water molecules and from macromolecules gives rise to the process of cross-relaxation or spin diffusion. The observed relaxation rates of water protons can be influenced significantly by the cross-relaxation rates. Spin diffusion occurs by way of mutual exchange of spin magnetization between water protons of the hydration layer and protons on the macromolecular chain. The contribution of cross-relaxation becomes very important under the conditions of slow molecular diffusion and when $T_2 \ll T_1$ (such as in many biological systems). Under these conditions, the energy exchanges much more rapidly within the system of spins than between the surrounding lattice and the spin system (Berendsen, 1975).

3. *Diffusion Constant*

The self-diffusion coefficient is a measure of the interchange of identical molecules by way of thermal movements. The diffusion constant (D) of water can be evaluated from the spin-echo decay of the NMR signals by applying a known magnetic field gradient. Several authors have discussed in detail the NMR methods of calculating the self-diffusion constant of water in biological systems (Andrasko, 1976; Packer, 1973; Chang *et al.*, 1972; Hazlewood *et al.*, 1974b; Cleveland *et al.*, 1976). Theoretically, the contribution of diffusion to the spin-echo decay is given by the expression:

$$A(\tau, G) = \exp\left[-2/3\gamma^2 G^2 D_s \tau^3\right], \tag{9}$$

where $A(\tau, G)$ is the echo amplitude for a 90°–180° pulse separation τ in the presence of an applied field gradient G, γ is the gyromagnetic ratio (Cleveland *et al.*, 1976).

The interest in the theory and measurements of the diffusion constant of water in muscle and cell water has centred mainly on the following two objectives: (i) to study the extent of ordering of water molecules by comparing the self-diffusion constant of water (H_2O, ^2H_2O) in various biological samples and in free water; (ii) to investigate any possible effects of diffusion of water molecules through the internal field gradients (generated by the heterogeneity of the magnetic susceptibility in biological samples) on the relaxation processes of water nuclei (Packer, 1973; Hazlewood *et al.*, 1971; Chang *et al.*, 1972). Diffusion of water in the hydration layer is an activation process in which a molecule must attain sufficient energy to cross over a potential barrier; the values of (D) depend on molecular interactions in the system under consideration.

4. *A Comparison of Different Water Nuclei*

Certain characteristic nuclear properties of proton, deuteron, tritium and ^{17}O are given in Table 1 (Emsley *et al.*, 1965, p. 589). The relaxation of protons is influenced by inter- and intramolecular dipolar interactions; whereas, the relaxation behaviour of deuterium and ^{17}O is dominated by the quadrupolar interactions. Glasel (1967) has reported the following equations for relaxation rates of ^1H, ^2H and ^{17}O.

TABLE 1. NUCLEAR PROPERTIES OF ^1H, ^2H, ^3H, ^{17}O (EMSLEY *et al.*, 1965)

Isotope	NMR frequency in Mc/sec for a 10 kG field	Natural abundance (%)	Relative sensitivity for equal number of nuclei: At constant field	At constant frequency	Magnetic moment μ, in multiples of the nuclear magneton ($eh/4\pi$ Mc)	Spin I, in multiples of $h/2\pi$	Electric quadrupole moment Q, in multiples of $e \times 10^{-24}$ cm^2
^1H	42.577	99.9844	1.000	1.000	2.7927	1/2	—
^2H	6.536	1.56×10^{-2}	9.64×10^{-3}	0.409	0.85738	1	2.77×10^{-3}
^3H	45.414	—	1.21	1.07	2.9788	1/2	—
^{17}O	5.772	3.7×10^{-2}	2.91×10^{-2}	1.58	−1.8930	5/2	-4×10^{-3}

Protons:

$$(1/T_1)_{D,\text{intra}} = \frac{3\gamma^4\hbar^2}{2r^6}\tau_c$$

$$(1/T_1)_{D,\text{inter}} = \frac{\pi N\gamma^4\hbar^2}{5aD} \tag{10}$$

Deuterons:

$$(1/T_1)_Q = \frac{3}{8}\left(\frac{e^2qQ}{\hbar}\right)^2_{^2H}\tau_c \tag{11}$$

^{17}O:

$$(1/T_1)_Q = \frac{3}{125}\left(\frac{e^2qQ}{\hbar}\right)^2_{^{17}O}\tau_c, \tag{12}$$

where τ_c is correlation time; a = radius of a molecule; D = microscope diffusion coefficient; and N = number density of molecules.

In water, deuterons relax about 10-times faster than protons, and ^{17}O nuclei relax about 100-times faster than deuterons. Such fast relaxation rates of ^{17}O satisfy the slow-exchange condition in the studies of cell water. Whereas, in general the relaxation behaviour of protons and deuterons is governed by the fast-exchange condition. The spin-lattice relaxation time T_1 for deuterons in ^2H_2O is governed completely by rotational time of the individual ^2H_2O molecules; as a result the ^2H NMR easily detects the anisotropic motion of water. The dipolar interactions of water protons are sensitive to rotational and translational motion, proton exchange, and the presence of paramagnetic centres in a given sample. The quadrupolar interactions are higher in magnitude than the magnetic dipolar interactions; therefore, for small changes in the nuclear environment the deuteron relaxation times exhibit much greater sensitivity than the proton relaxation times. However, the "NMR" sensitivity for the detection of deuteron resonance signal is much lower than for the proton signal (see Table 1). The NMR studies of tritiated water in biological systems should be favoured by high sensitivity to detect tritium resonance (Table 1); eventually such measurements face a great drawback because low quantities of ^3H are required to be present in samples due to its radioactivity. The NMR spectroscopy of tritium has been developed and applied successfully during the past few years mainly by the research group of Professor Elvidge (Bloxsidge *et al.*, 1971; Al-Rawi *et al.*, 1974; Al-Rawi *et al.*, 1975).

IV. THE NMR STUDIES OF WATER IN DIFFERENT BIOLOGICAL SYSTEMS

A large variety of biological systems whose hydration properties have been investigated by NMR spectroscopy may be classified broadly into two groups on the basis of the NMR spectra of water.

1. Randomly oriented systems such as macromolecular solutions, cell suspensions, muscle, tissues and membranes give rise to water proton and deuteron resonance signals consisting of a single peak even at low temperatures in frozen samples.
2. Oriented samples: the water spectra from oriented fibres of DNA and collagen appear either as a single broad resonance line or a signal split into two lines. The characteristic feature of these spectra, which distinguishes them from the group (1) spectra, is that the linewidth or the splitting of proton and deuteron resonance signals are a function of the orientation of samples with respect to the magnetic field.

1. *Randomly Oriented Systems*

(a) *Biopolymer solutions and hydrated proteins*

The initial efforts to study water by NMR had shown that the water signal from DNA solutions was much broader than the signal from pure water. In order to explain these results, Jacobsen *et al.* (1954) proposed that line-broadening was due to increased ordering in the water structure and the formation of hydration shells near DNA. This early concept of hydration water in terms of a static model describing shells of water molecules near macromolecules proved inadequate. The current theories and the proposed models for water in macromolecular solutions or in different biological systems consider hydration water in terms of dynamic processes. Several examples of dynamic models of water in hydrated biological systems are discussed in different sections of this article. Lubas and Wilczok (1966, 1967, 1971) studied the hydration of DNA in solutions by measuring the relaxation times, using the spin-echo technique. They also interpreted the results in terms of firmly bound hydration shells (non-rotational binding), and rotationally bound water (freedom of movement as in free water). Lower ionic strength was found to favour an increase in the hydration of DNA (Lubas and Wilczok, 1970).

Further studies revealed that the relaxation behaviour of water was characterized by the conformation and structure of different biopolymers in solution. Glasel (1970) investigated the role of water in conformational changes of several biological macromolecules by studying the deuteron magnetic relaxation of water at 31°C. The following polymers were studied: poly(L-glutamic acid), poly(L-lysine), poly(adenylic acid), poly(uridylic acid), poly(methacrylic acid), poly(vinyloxazolidinone methyl), and poly(vinylpyrrolidone). He gave the following equation for the observed relaxation rate under the fast-exchange condition:

$$(1/T_1)_{\text{obs}} = (1/T_1)_{\text{free}} + C\omega K\tau_a, \tag{13}$$

where: $(1/T_1)_{\text{obs}}$ is the measured relaxation rate for solutions; $(1/T_1)_{\text{free}}$ is the relaxation rate for pure solvent; C is the concentration of the polymer; ω is the time-independent weight of water associated per gram of polymer; K is the quadrupole coupling term; and τ_a is the rotational reorientation time of water molecules associated with the polymer. Straight line plots of $(1/T_1)_{\text{obs}} - (1/T_1)_{\text{free}}$ vs C were observed.

In this work, the importance of polymer–water interactions by hydrogen bonding was pointed out; for example, poly(U) did not show any interaction, whereas strong interaction was recorded for poly(A) and poly(L-glutamic acid). It was observed that strong water interactions were favoured by the stable topology of polymers.

The magnetic field dependence of the relaxation rates of protons, deuterons, and ^{17}O nuclei of water (termed as relaxation dispersion) was investigated in detail for a variety of proteins in liquid solutions (Hallenga and Koenig, 1976; Koenig and Schillinger, 1969; Koenig *et al.*, 1975: Koenig *et al.*, 1978; Grösch and Noack, 1976). Koenig *et al.* (1975) showed that for lysozyme and haemocyanin solutions, the relaxation dispersion for ^1H, ^2H and ^{17}O nuclei of water were essentially the same. In general, these authors observed that the plots of $1/T_1$ vs H_0 for ^1H, ^2H and ^{17}O show an inflexion at a value of H_0 that corresponds to the Larmor frequency ν_c given by the relation $\nu_c = \sqrt{3}/(2\pi\tau_R)$; where τ_R is the rotational relaxation time of the protein molecule. It was proposed that the correlation time for orientation of water molecules in the neighbourhood of

protein macromolecules was determined by the Brownian motion (tumbling rate) of macromolecules. A hydrodynamic mechanism describing a small transfer of the protein τ_c to the solvent molecules was considered to be the common cause for the observed dispersion in T_1 for all three nuclei. By studying the dispersion behaviour of protein solutions in partially deuterated water, Koenig *et al.* (1978) were led to conclude that cross-relaxation between solvent and solute protons makes an important contribution to the proton relaxation rates, but not to the deuteron relaxation rates of water. The rate of cross-relaxation between protein and solvent protons shows a similar dispersion behaviour as the T_1 relaxation rates. Proton transfer between water protons and the titrable groups on the protein surface was suggested as a possible mechanism for the cross-relaxation, and the cross-relaxation term was shown to be proportional to the protein–solvent interface. A detailed description of the cross-relaxation effects within proteins is given by Kalk and Berendsen (1976), Sykes *et al.* (1978). The exchange of spin-magnetization was considered to occur at a rate faster than the rate of spin-lattice relaxation of protons.

Finally, Grösch and Noack (1976) interpreted the frequency-dependent changes of the proton relaxation rates (T_1, T_2) of BSA solutions in terms of a three-state model for water in protein solutions.

The original work of Kuntz *et al.* (1969) showed that when solutions of proteins or nucleic acids were frozen, a relatively sharp and distinct signal was observed from hydration water at temperatures as low as -35°C. The area under this signal gave a measure of the unfrozen water. The activation energy values of the processes influencing the relaxation rates were calculated from the temperature-dependent changes in the linewidth of water signal. These interesting observations reported by Kuntz *et al.* were immediately elaborated and applied by several groups of workers for studying extensively the hydration water characteristics in different biological systems. Using the same procedure, Kuntz (1971a,b) investigated the hydration of several polypeptides. He demonstrated that the linewidth of water signals observed in frozen solutions was very sensitive to the polypeptide conformation. All those systems known to be in random coils at room temperature exhibited sharper lines than the corresponding systems in the helical conformation. Kuntz indicated that the hydration of globular proteins could be estimated from the hydration of appropriate polypeptides, but the linewidth of water signal could not be calculated from the amino acid composition. The results of Mathur-De Vré *et al.* (1975) have shown clearly that the nature and structure of polynucleotides: poly(A), poly(U), poly(C) and their complexes: poly(A + U), poly(A + 2U) and poly(AH^+) exert a marked influence on the linewidth of water proton signals in frozen solutions $(\Delta 1/2)_{-5°}$. The formation of double-stranded helical complexes from single-stranded polynucleotides is accompanied by a large increase in the $(\Delta 1/2)_{-5°}$ values. This observation was explained by considering that proton transfer in the hydration layer of polynucleotides decreases due to the formation of inter-chain links in the complexes. The increase in the rigidity of the macromolecular structure accompanying the formation of complexes is expected to influence the water spectra when measurements are performed in the liquid state. The NMR studies of frozen macromolecular solutions show clearly that the diffusion motion, proton transfer, and macromolecular–water interactions are important factors influencing the relaxation behaviour of hydration water protons.

The wide-line proton magnetic resonance spectra of ribonuclease and BSA were studied in the hydrated and vacuum dried states over the temperature range of -140 to -180°C (Blears and Danyluk, 1968). Considerable translational and rotational motion of water was shown to persist at such low temperatures by comparing the second moment of ice with that of water in proteins. The hydration of ribonuclease and total ribosomal RNA, as studied from the water spectra at -35°C, was found to increase steadily as a 70S particle was successively broken into smaller and more expanded fragments (White *et al.*, 1972). Fuller and Brey (1968) reported the NMR spectra of water sorbed on serum albumin as a function of temperature and water content. They explained that sorbed water could exist in different states depending on the water

content: water up to 75 mg/g protein represented water strongly bonded to polar groups of the protein, the "primary water". The NMR signal from the primary layer was strongly influenced by the protein–water interactions, further addition resulted in strongly hydrogen bonded water to the primary layer which is much less influenced by the protein; these two states may be compared with regions A and B in Fig. 1. The amount of water strongly bound to a solid protein is less than that for protein in solution. The water deuteron relaxation studies of the protein elastin (ligamentum nuchae of mature beef) soaked in excess ^2H_2O showed that the deuteron relaxation exhibited a multi-component behaviour, thereby suggesting the existence of distinct regions of water in the sample. These are: water contained within the bulk elastin and water surrounding the bulk elastin. The hydration of elastin is particularly important in rendering it rubber-like properties (Ellis and Packer, 1976). Hilton and Bryant (1977) studied the relaxation times of hydrated lysozyme powder as a function of temperature and water content. A model based on cross-relaxation was found to account satisfactorily the behaviour of proton relaxation rates.

(b) *Effects of γ-irradiation on hydration water*

When biological systems are subjected to γ-irradiation, the induced radiation damage is known to localize on the DNA molecule (Blok and Loman, 1973; Latarjet, 1972). For a full understanding of the radiation effects on DNA in an aqueous medium and the role of water at molecular level in mediating the overall damage, it is essential to study the effects of irradiation on the characteristics of hydration water, e.g. on macromolecular–water interactions, on water mobility and proton transfer along the hydration layer. A detailed investigation of the effects of γ-irradiation on the hydration water of DNA and polynucleotides in H_2O, ^2H_2O, $X\%H_2O/Y\%^2H_2O$ solvents was undertaken by Mathur-De Vré *et al.* (1976), Mathur-De Vré and Bertinchamps (1977a,b). The solutions were irradiated at 0, −80, and −196°C, and the linewidth of the water proton NMR signals was measured from −5 to −45°C. It is known that when aqueous solutions are subjected to γ-irradiation, free radicals are generated that are stable at low temperatures but decay rapidly at about 0°C. The solutions irradiated at −80 and −196°C were thawed at 0 to +5°C and refrozen before the NMR measurements. This process curtailed the possible line-broadening effects of paramagnetic free radicals trapped in the frozen irradiated solutions, on the linewidth of water signals observed from the irradiated solutions below −5°C.

It was shown by comparing linewidths at −5°C, that the irradiation of DNA solutions at 0 and −80°C resulted in a decrease in linewidth of water proton signal as compared with that of the corresponding non-irradiated solution; furthermore, the observed decrease was greater when irradiation was performed at −80°C. No significant change in linewidth was recorded after irradiating the solutions at −196°C, by irradiating the dry solid (at −196°C) before dissolution, or by sonication of the DNA solutions. An interesting observation was that irradiation at 0°C of poly(A + U) and poly(A + 2U) complexes resulted in a large broadening, whereas much sharper signals were observed by irradiating the same solution at −80°C. Above 0°C, the bulk water is liquid and highly mobile, and the segments of macromolecular chains possess considerable flexibility. In frozen samples at −80°C, the hydration water remains unfrozen and mobile but the bulk water is frozen and the segmental mobility of the macromolecular chains is restricted. Consequently, when the solutions of macromolecules are irradiated at different temperatures, the process of either radiation-induced cross-linking or separation of the chains (causing the linewidth of water proton signals to increase or decrease) predominates depending on the dynamic states of the hydration and bulk water molecules, and on the flexibility of the segments of the macromolecular chains, favoured under the conditions of irradiation. It was suggested that the striking differences observed in the hydration water proton spectra after γ-irradiation were largely due to important changes in the proton transfer along the hydration layer resulting from the modifications induced in the structure of macromolecules.

TABLE 2. RELAXATION TIMES FOR A FEW SELECTED SYSTEMS

Sample	Temp (°C)	Frequency (MHz)	Nucleus	Relaxation times (msec) T_1	$T_{1\rho}$	T_2	Reference
Pure water	25	4	^1H	2300		2300	Cope (1969)
				2830		2830	James and Gillen (1972)
			^2H	470		450	Cope (1969)
			^{17}O		3.7	6.5	Swift and Barr (1973)
Ice			^1H			6 (μsec)	Foster *et al.* (1976)
Muscle	25	4	^2H	92		9	Cope (1969)
Brain				131		22	
Frog skeletal muscle	30		^{17}O			1.22	Swift and Barr (1973)
	10					1.18	
Frog gastrocnemius muscle	22.7		^1H	700	180	44	Finch and Homer (1974)
Plasma	25	25	^{17}O	3.9			Fabry and Eisenstadt (1975)
Red cell inertia				1.7			
Membrane bound water phase	30	23.3	^1H	91.9	22.2		Finch and Schneider (1975)
Random population of HeLa cells	25		^1H	667			Beall *et al.* (1976)
Cell pellets				1.0–1.10			Shporer and Civan (1975)
Cell suspension in the presence of Mn^{2+}	22–24	8.13	^{17}O	1.0–1.05			
Partially hydrated muscle fibres 1 g H_2O/g protein	25	51.6	^1H	200		42	Cooke and Wien (1971)
Normal cells Oxy	22	44.4	^1H	560		88	Zipp *et al.* (1976)
Deoxy				550		84	
Sickle cells Oxy				530		56	
Deoxy				550		26	
Liver Normal	26	100	^1H	570			Damadian *et al.* (1974)
Tumorous				832			
Lung Normal				788			
Tumorous				1110			
Breast Normal				367			
Tumorous				1080			
Healthy C3H mice Liver		30	^1H	386	47	25	Frey *et al.* (1972)
Lung				641	117	47	
Mice with large MC-1 Tumour ($8–37\ cm^2$) Liver				461	56	33	
Lung				665	124	49	
Tumour				853	208	47	

The NMR studies of water in frozen samples proved to be a very informative method in revealing that hydration water molecules make a distinct contribution in mediating the overall radiation-induced damage to the structure of DNA and polynucleotides in solution.

(c) *Muscles and tissues*

Considerable evidence has accumulated leading to the general conclusion that water in muscles and tissues exists in more than one fraction, and that fast exchange of water molecules occurs between different regions. One of the fractions has been assigned to a well-defined and ordered water phase. In addition, it was affirmed that the motion of all the water molecules cannot be described satisfactorily by a single correlation time.

In general, the relaxation times and the diffusion constant for muscle water were found to be reduced with respect to the values for pure water. The values for a few selected systems are included in Table 2.

Bratton *et al.* (1965) postulated a two-state model for water in muscle. Hazlewood *et al.* (1969) concluded that at least two ordered phases of water (major and minor) exist in muscle; water molecules in the major phase were considered to exhibit greater motional freedom than in the minor phase and exchange rapidly with free water. Cooke and Wien (1971) fitted their data of T_1 and T_2 measurements (33°C) on live muscle fibres with a model in which 4–5% of the total water was associated with proteins and represented the fraction with fast relaxation rate, while the bulk of the water inside a muscle was considered to be free. It was suggested that fast exchange of water protons could occur between these two phases. Three-state models for water in muscle were proposed by Hazlewood *et al.* (1974b) and by Belton *et al.* (1972).

Deuteron magnetic resonance studies of Cope (1969) also indicated the existence of two distinct fractions of tissue water in muscle and brain of adult rats. He suggested that each fraction may be composed of multiple subfractions. The ^{17}O spectra of $H_2{}^{17}O$ in frog skeletal muscle has further provided evidence in favour of the restricted motion in muscle water as compared with pure water (Swift and Barr, 1973). In both these studies, the reported T_2 and T_1 values were found to be much smaller than the values for pure water ($T_1 = T_2$), see Table 2.

In an attempt to describe the relaxation behaviour of water in muscles, tissues and cells, most authors explained the observed shortening of relaxation times by considering the existence of an ordered phase of water. In this phase, the motional freedom of individual water molecules is restricted by their interactions with cellular macromolecules reducing the relaxation time (Hazlewood *et al.*, 1969; Hazlewood *et al.*, 1971; Hazlewood *et al.*, 1974b). Hansen and Lawson (1970) and Hansen (1971) pointed out that the line-broadening was induced, at least partially, by diffusion of water molecules through microscopic magnetic field inhomogeneities present in the heterogeneous samples. Cooke and Wien (1971) measured T_1 and T_2 for solutions of F-actin and G-actin. These authors reported a decrease in the T_2 values when actin solutions were polymerized, and they emphasized that diffusion through increased magnetic field heterogeneity contributes significantly to the relaxation behaviour of water. Chang *et al.* (1972) have contested the discussion of Hansen and Lawson; Chang *et al.* (1972) argued that unusually large values of the local field inhomogeneity must be assumed in order that the proposed mechanism be effective. On the basis of the detailed calculations, Packer (1973) concluded that the effects of diffusion of water through inhomogeneous internal field gradients in striated muscle were negligible. He pointed out analogies between the effects of restricted diffusion, the motional narrowing of resonance lines, and diffusion through periodically heterogeneous and structured systems. Yet another mechanism describing the water relaxation rates was proposed based on the effects of cross-relaxation between the water protons and macromolecular protons of muscle (Edzes and Samulski, 1978).

Ratković and Sinadinović (1977) investigated the relaxation times for water protons in tissues of the thyroid glands of rats. They obtained evidence indicating that the relaxation times decrease (as compared with free water) by long-range interactions of water with macromolecules and the effects of compartmentalization, rather than due to diffusion of water through the microscopic magnetic field inhomogeneity inside the sample. It may be important to differentiate between the physical compartmentalization of water in macroscopic regions of complex biological samples and the distinguishable fractions of water structured at the molecular level. Both these phenomena may produce similar effects on the relaxation rates of water nuclei.

Hazlewood *et al.* (1974b) demonstrated, by decomposing the spin-echo decay curves at 24°C, that at least three distinguishable fractions of water protons were required to fit the data for skeletal muscle: water associated with macromolecules represents approximately 8% of the total tissue water and it does not exchange rapidly with

the remaining intracellular water (T_2 less than 5 msec), myoplasm fraction 82% ($T_2 = 45$ msec), extracellular space ~10% ($T_2 = 196$ msec), T_2 of pure water or Ringer's solution = 1.6 sec. These authors showed that water in different fractions did not exchange rapidly and considered the possibility that each fraction may be composed of fast-exchanging sub-fractions. Hazlewood *et al.* (1974b), and Belton *et al.* (1972) attributed the fastest relaxing fraction to the closely bound water: three fractions detected by Belton *et al.* correspond to T_2 values of 250, 40 and 9 msec, respectively. This interpretation has since been contested by Foster *et al.* (1976) and Fung (1977b); both these groups of workers have postulated that the fastest relaxing fraction (4–9 msec) of protons arises from the nonrigid protons of macromolecules rather than from "bound" water.

The relaxation studies performed at a single frequency furnished ample evidence to show that water in muscles and tissues is not homogeneous but exists in more than one fraction. Further new and revealing details about the dynamic states of water, e.g. distribution of correlation times and dispersion of proton relaxation rates, were brought into evidence by careful measurements of the relaxation times over a wide range of frequency and at varied temperatures. Outhred and George (1973a,b) described a method for analysing the frequency-dependent behaviour of relaxation rates. They analysed the distribution of correlation times for toad muscle water from measurements at three frequencies: 2.3, 8.9 and 30 MHz (1973b). A very clear and detailed treatment of the dispersion of water proton spin–lattice relaxation times T_1 and $T_{1\rho}$ at 25°C for selected mouse tissues was given by Knispel *et al.* (1974). The dispersion (frequency dependence of relaxation times) of $T_{1\rho}$ was attributed to proton exchange between water molecules, whereas the major contribution to T_1 came from processes such as molecular rotational and translational diffusion. The correlation times for exchange, molecular rotation and fast diffusion processes were given as 7×10^{-6}, 2×10^{-8} and $\sim 10^{-10}$ sec. Figure 3 shows the dispersion of the total relaxation for muscle water. In a subsequent paper, Diegel and Pintar (1975b) recognized the exchange process as arising from the slow-exchange diffusion of water molecules between the hydration layer and free water and not from the exchange of protons as discussed earlier (Knispel *et al.*, 1974; Thompson *et al.*, 1973). Figure 4 illustrates different relaxation processes discussed by Diegel and Pintar (1975b). One may compare the dynamic states of H_2O molecules participating in the slow-exchange diffusion and undergoing slow reorientation as defined by Diegel and Pintar, with the water molecules designated by the lifetime τ'_e and τ'_r, respectively, in Packer's diagram (see Fig. 2).

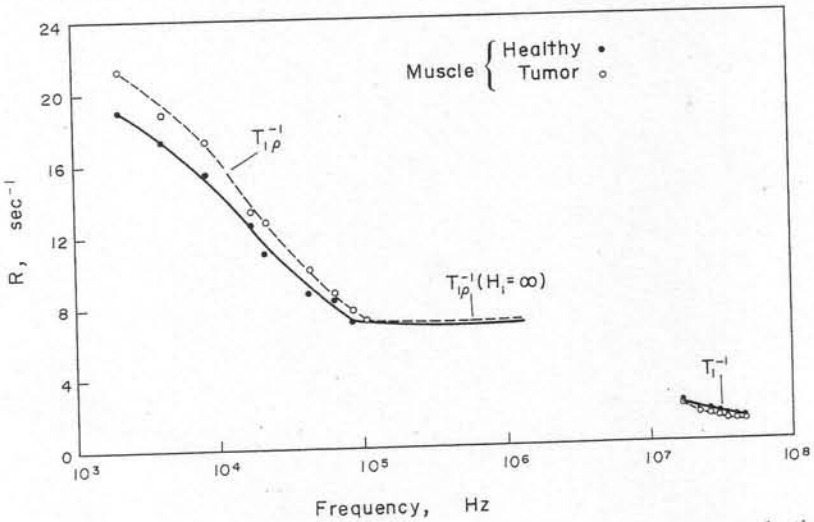


FIG. 3. (Knispel *et al.*, 1974) Dispersion of T_1 and $T_{1\rho}$ in samples of mouse muscle tissue. R = relaxation rate.

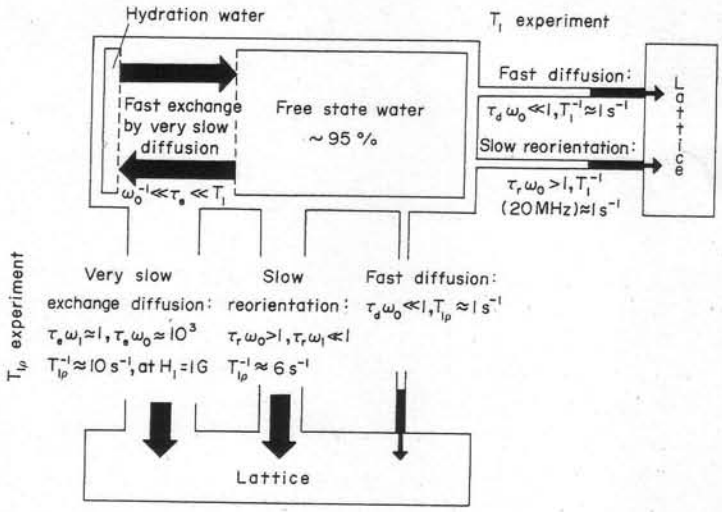


FIG. 4. (Diegel and Pintar, 1975b) The three relaxation processes and their contribution to the high field and the rotating field Zeeman relaxation. The numerical values shown for the relaxation rates are approximative.

Finch and Homer (1974) reported the values of T_1, T_2 and $T_{1\rho}$ for frog muscle water protons at different temperatures above 0°C and over a wide range of frequency. They obtained a distribution of correlation times for muscle water, ranging from $\sim 10^{-5}$ to $\sim 10^{-11}$ sec. The results were interpreted in terms of exchange of water molecules between two fractions: one with a distribution of different degrees of restricted motion, and the other with unrestricted motion like ordinary water (97%). Fung (1977a) measured T_1 of water protons in mouse muscle in the frequency range from 10^4 to 10^8 Hz, and the deuteron T_1 from 2.0×10^3 to 1.54×10^7 Hz. He proposed relaxation mechanisms for hydration water protons and deuterons based on the observed frequency and temperature-dependent behaviour of relaxation times above 0°C, and the isotope substitution effects (discussed in a subsequent section).

The NMR studies of muscle water performed on frozen samples have revealed that the unfrozen fraction of water is characterized by the frequency-dependent variations of relaxation times. From the pulsed NMR measurements of the transverse relaxation times of water protons in striated frog muscle, Belton *et al.* (1972) showed that the bound water did not freeze; as a result, below -7 to -10°C about 20% of the signal was observed. In another paper, Belton *et al.* (1973) investigated in detail the spin-lattice relaxation times and the dynamics of the unfrozen fraction of water in muscle at two frequencies (30 and 60 MHz) and over a wide range of temperature ($+10$ to -75°C). A distribution of correlation times was indicated for the unfrozen water. Fung and McGaughy (1974) measured the relaxation times of water in rat gastrocnemius muscle at frequencies ranging from 4.5 to 60 MHz at $+37$ to -70°C. The T_1 values of H_2O and ^2H_2O for muscle and liver were also reported at different frequencies and in the temperature range $+37$ to -70°C (Fung *et al.*, 1975a). In samples at sub-freezing temperatures, the unfrozen fraction of water was shown to exhibit a distribution of correlation times; while, above -8°C a single correlation time was observed which was short enough to render T_1 independent of frequency. Based on these results, Fung and McGaughy (1974) and Fung *et al.* (1975a) supported a two-phase model: one phase exhibiting a distribution of correlation times (the unfrozen fraction) and the other with a single correlation time (the frozen fraction). It may be noted that a similar model was also proposed by Finch and Homer (1974) from the results obtained above 0°C (discussed in the previous section). Of the various models suggested to describe the state of water in muscle (and other biological systems), this model accounts in the most satisfactory manner the behaviour of water. Contrary to Cope (1969), Fung *et al.* concluded that all the ^2H_2O was "NMR" visible. Duff and Derbyshire (1974) also reported a complex

behaviour of relaxation times (T_1, T_2, $T_{1\rho}$) of the bound or unfrozen fraction of water in frozen porcine muscle.

Several authors have demonstrated that the water content of muscles and tissues exerts a determining role on the relaxation behaviour of water nuclei observed in a variety of samples. Cooke and Wien (1971) measured T_1 and T_2 of partially hydrated various muscle proteins by the pulsed spin-echo technique. The relaxation times decreased as the ratio of water to protein decreased, and $1/T_1$ was found to be directly proportional to the protein concentration. Fung (1977c) measured T_1 of water protons for dehydrated mouse muscle at three frequencies (5, 30, 100 MHz) down to very low water contents. At all three frequencies, a decrease in T_1 values with decreasing water content (X) was observed, followed by an increase in T_1 at very low contents ($X \leqq 0.07$). This phenomenon may have arisen because of a change in the structure of hydration layer at low water contents.

Belton and Packer (1974) undertook a detailed study of the effects of water content on the water proton relaxation times T_1 and T_2. The stepwise dehydration of a muscle was found to correlate with changes in the transverse relaxation times in a manner shown in Fig. 5. Dehydration of the muscle followed by rehydration was also investigated. A very important contribution of this experiment was to show that the amount of "unfrozen" water for fresh and rehydrated muscles is the same, but the relaxation behaviour at low temperatures is quite different in these two cases. The fact that the amount of unfrozen water is similar in the two cases reflects that it depends on the concentration rather than on the state of macromolecules in muscle. However, the difference in the relaxation behaviour arises from marked changes in the distribution of water in different fractions.

An interesting study making use of the correlation between the water content and relaxation times was conducted to investigate the action of cholera toxin (Udall *et al.*, 1975). These authors measured the water content and T_1 and T_2 values from the control and cholera-infected small intestinal tissues of rats. It was found that the relaxation times of water in cholera-infected tissues were longer and the tissue hydration was greater than in control tissue samples:

	Control	Cholera
Percentage of tissue water	79.49%	84.52%
T_1 (msec)	521.22	667.96
	±69.5	±119.25
T_2 (msec)	62.34	80.35
	±9.59	±21.46

The abovementioned results suggest that cholera-treated tissues exhibit greater motional freedom of water than the control samples. This observation was considered to support the general view that cholera enterotoxin acts by influencing the intracellular protein–water interactions, giving rise to increased hydration. As a result, the permeability of cells to water is increased, leading to enhanced secretory activity of small intestines.

The importance of the relationship between water content of muscles and different tissues, and the relaxation times for explaining the increase in T_1 when tumours develop will be discussed in a subsequent section.

A very important contribution of the NMR studies of water in tissues and muscles has been to reveal that the relaxation rates of water nuclei can be correlated with the actual state of muscle caused by strain and death. Bratton *et al.* (1965) reported that T_2 of muscle water protons increased with contraction and exhaustion, whereas T_1 remained insensitive to changes in the state. They explained that T_2 increased because the change in tension released 20% of water; part of the bound water was released reversibly during isometric contraction and irreversibly in death. Chang *et al.* (1976) studied the relaxation time of water protons in skeletal muscle (gastrocnemius) at different time intervals after taking the sample from the animal. They obtained two

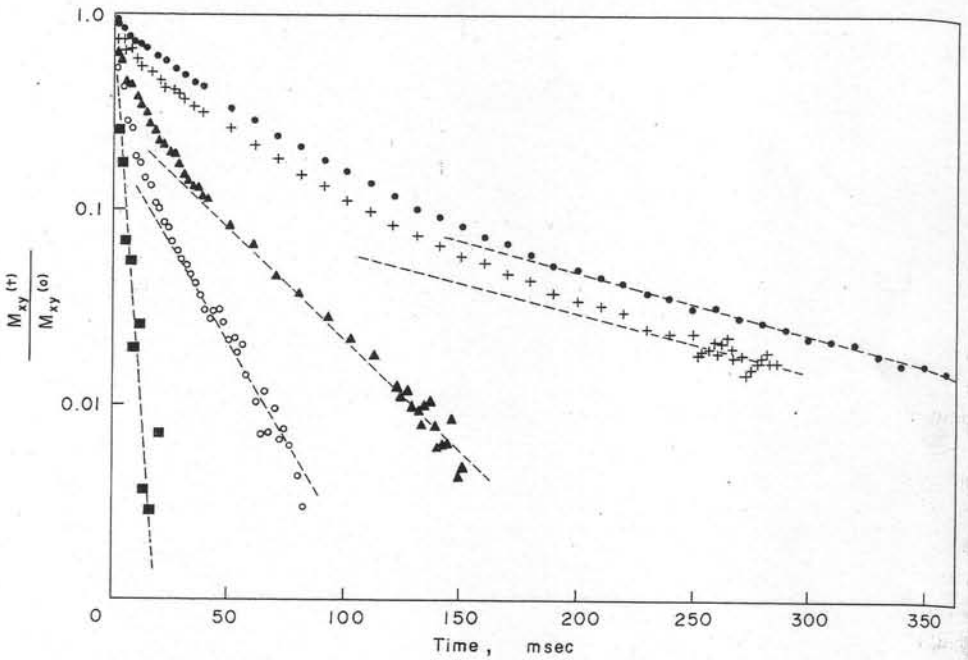


FIG. 5. (Belton and Packer, 1974) The variation of the transverse relaxation behaviour of the water protons in frog gastrocnemius muscle as a function of water content at ~300 K. The measurements were made using a Carr–Purcell/Gill–Meiboon pulse sequence and the symbols correspond to different water contents which, relative to that of fresh muscle taken as 100%, are: ● 100%, + 54%, △ 18%, ○ 10%, ■ 6%. Not all the measured points are shown for clarity.

relaxation times: T_{1B} and T_{1A}. T_{1B} (characterized by the slow relaxation rate) was influenced by the early post-mortem changes, and its value increased with time after the removal of tissues from the muscle. T_{1A} (representing the weighted average of all water protons) remained practically unchanged with the lapse of time. These authors stated that cellular water molecules "recognize" a change of environment as the physiological state of cells undergoes a change. Furthermore, post-mortem changes were observed to be relatively slow, taking about 4 hr for completion. Hazlewood *et al.* (1971) classified T_1 and T_2 of water (28°C) as a function of age. The muscles from animals less than 10 days old were defined as immature muscles, and those from animals greater than 40 days old were considered as mature muscles. The following relaxation times were reported:

	T_1 (sec)	T_2 (sec)
Immature muscle	1.206 ± 0.055	0.127 ± 0.009
Mature muscle	0.723 ± 0.049	0.047 ± 0.004

It was proposed that the fraction of ordered water increased in the post-natal development of muscle. They also suggested that the extent of ordering of muscle water tends to increase with maturation of muscles.

By plotting the amplitude of the spin-echo train of water protons of mouse muscle (at 37°C) as a function of time, Fung (1977b) observed that the decay curve was exponential soon after the dissection, but with time it changed into a non-exponential curve during the first 40 min as illustrated in Fig. 6. On the contrary, for brain tissues very little change in the spin-echo decay curves at 37°C was observed during the first hour after death. He concluded that changes in the relaxation times of hydration water protons observed after death were caused by changes in the conformation of muscle proteins, rather than by a rapid redistribution of water in different parts of the tissue. Shporer *et al.* (1976) showed that the relaxation of ^{17}O from $H_2{}^{17}O$ in rat lymphocytes was non-exponential in the fresh state but became exponential after cell death. Contrary to the opinion of Fung, Shporer *et al.* suggested that necrosis could

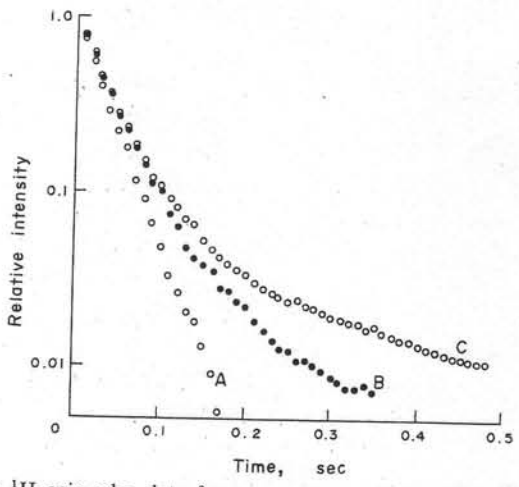


FIG. 6. (Fung, 1977b) ^1H spin-echo data for mouse water at 37°C. The initial intensities are not included because the contribution from organic protons is not negligible. (A) 5 min, (B) 10 min, (C) 30 min.

lead to mixing of water in different compartments of water in tissues, or between nuclear and cytoplasmic water.

The magnetic moment of deuteron is much smaller than the magnetic moment of protons (Table 1), this causes reduced dipolar coupling interactions between protons and deuterons as compared with proton and proton. Therefore, it is expected that partial substitution of H_2O by ^2H_2O in a system should result in sharper water proton signals. Such a behaviour is observed in free water. For water in striated muscle of frog; Civan and Shporer (1975) reported that T_1 of water protons was unaffected after partial substitution of H_2O by ^2H_2O. Resing *et al.* (1977) and Fung (1977a) also reported that deuterium substitution had very little effect on the relaxation times of muscle water. Fung explained this isotope substitution effect by considering that the major relaxation mechanism is the intermolecular dipole–dipole coupling interactions between water protons in the hydration layer and protons in the relatively immobile macromolecules, assisted by the slow water diffusion of the type defined by Knispel *et al.* (1974), and Diegel and Pintar (1975b). The importance of cross-relaxation in explaining the relaxation behaviour of water protons in protein solutions and in collagen has been discussed elsewhere (see Sections IV.1(a) and IV.2(a). In addition, it was observed that for DNA and polynucleotide solutions in $H_2O/^2H_2O$ solvents of various compositions, unlike at +5°C, in each case the linewidth at −5°C was independent of the $H_2O/^2H_2O$ composition but dependent on the nature of macromolecules. Furthermore, for DNA solutions between −5 and −35°C, the temperature-dependence of the linewidth of water proton signal decreased with increasing ^2H_2O content (Mathur-De Vré and Bertinchamps, 1977a,b). These results could be better explained by taking into account the influence of cross-relaxation and indicate that dipolar interactions between macromolecular protons and water protons dominate the T_2 process of unfrozen water. Furthermore, Civan and Shporer (1975), and Civan *et al.* (1978) have reported the following important results from a comparative study of the three nuclei (^1H, ^2H, ^{17}O) in muscle water. (i) The T_1 relaxation rates of ^{17}O, ^2H and ^1H nuclei of muscle water exhibit identical frequency dependence. (ii) The ratio $(T_1)_{^2H}/(T_1)_{^{17}O}$ of muscle water and pure water are closely similar while the ratio $(T_1)_{^1H}/(T_1)_{^{17}O}$ in pure water is 2.1-times greater than for muscle water. (iii) The ratio $(T_1)/(T_2)$ for ^2H and ^1H was found to be in the range of 9–11, whereas this ratio for ^{17}O was approximately 1.5–2.0. Rapid exchange motion between a small immobilized fraction and a large fraction of free water was proposed.

(d) *Membranes and cell water*

The erythrocyte membrane is highly permeable to water, this results in a fast exchange between water in cells and plasma (exchange time of the order of 10 msec).

The NMR technique is particularly fitting for studying such fast-exchange processes. Water molecules present in these two compartments are constrained in widely different environments. Consequently, each type of water exhibits a characteristic and distinct relaxation behaviour. The use of Mn^{2+} in these systems has proved to be of particular value for the following two reasons: (i) in the presence of Mn^{2+}, the relaxation rates of water nuclei can be enhanced by the paramagnetic contribution to such an extent that their NMR signals become unobservable; (ii) the cell membrane is known to be effectively impermeable to Mn^{2+}. Consequently, the addition of Mn^{2+} to a cell suspension results in an enhancement of the relaxation rates of water nuclei in the extracellular region. Therefore, it is possible to selectively resolve the contribution of the intracellular water to the observed spectra. A similar effect can equally well be obtained by freezing samples below 0°C; in this case, only the intracellular water remains unfrozen and therefore contributes to the resulting spectra. It is surprising to note that applications of the freezing technique in this domain is very limited. The only example is that of water in haemoglobin solutions reported by Zipp *et al.* (1976). Certain groups of workers have used the pellets of cells to eliminate the contribution of extracellular water.

Andrasko (1976) measured the water diffusion permeability of human erythrocytes by using pulsed magnetic field gradient techniques. The following values were reported for the diffusion constant (D_1) and the lifetime (τ_B) of water within red blood cells.

	D_1 (cm^2/sec)	τ_B (sec)
blood	1.16×10^{-5}	0.017
blood + *p-Cl. $HgBzO^-$	7.75×10^{-6}	0.048

*p-Chloromercuribenzoate: known to drastically reduce the osmotic water permeability of human red cells.

It was shown that deoxygenation of normal and sickle erythrocyte results in a considerable decrease in the T_2 values but causes no change in the T_1 values of water (Cottam *et al.*, 1974; Thompson *et al.*, 1975; Zipp *et al.*, 1976). A three-state model was proposed to explain the relaxation data, each state exhibiting a characteristic correlation time: bulk water $\cong 10^{-11}$ sec, water hydrated to macromolecule ($10^{-7} > \tau_c > 10^{-11}$ sec), finally the third region of water which is tightly bound exhibits a correlation time similar to that of protein ($\tau_c \geqq 10^{-7}$ sec) (Thompson *et al.*, 1975; Zipp *et al.*, 1976). Zipp *et al.* reported that upon deoxygenation of sickle cells and haemoglobin S solutions the T_2 values at room temperature decreased by a factor of 2; whereas after deoxygenation of normal cells and haemoglobin A solutions, no change in T_2 was observed. The low temperature studies of linewidth at (−15 to −36°C), and T_1 at −20 to −80°C, for oxy- and deoxy-haemoglobin A and haemoglobin S solutions suggested that the characteristics of bound water were similar for all four species. On the basis of the three-state model, Zipp *et al.* proposed that the sickling process altered the irrotationally bound water. Lindstrom and Koenig (1974) and Lindstrom *et al.* (1976) investigated the effects of oxygenation, and aggregation of haemoglobin (HbA) and sickle haemoglobin (HbS) solutions by studying the frequency dependence of water proton relaxation rate ($1/T_1$) (dispersion curves). They calculated τ_c, the correlation times for the rotational motion, of haemoglobin molecule from the inflexion frequency ν_c (see Section IV.1(a), p. 112). It was shown that under the conditions of complete oxygenation, HbS molecules interact with each other more strongly than do the HbA molecules. The orientation time of oxy-HbS molecules was shown to be larger than that of HbA molecules. The T_1 values of water obtained at low frequency gave much more information about the state of aggregation and rotational motion of the haemoglobin macromolecule as compared with the T_1 values obtained at a single high frequency.

A simple NMR technique for measuring the water exchange between erythrocytes

and plasma labelled with Mn^{2+} was described by Conlon and Outhred (1972). The use of paramagnetic ions as a tool for distinguishing the proton NMR signal of intracellular water from that of extracellular water was initially described by Fritz and Swift (1967). These authors successfully applied this method to investigate the state of water in polarized and depolarized frog nerves. The nerves were depolarized by the chemical and electrical stimulation. It was apparent from the results that depolarization of nerves is accompanied by marked changes in the state of intracellular water.

Shporer *et al.* (1976) reported the relaxation behaviour (at 26.5°C) of ^{17}O from $H_2{}^{17}O$ in rat lymphocytes using samples in the form of packed cells (pellets) and supernatant In the fresh state, the non-exponential behaviour of the relaxation data of pellets reflected the presence of two (or more) distinct types of water. The slowly relaxing fraction of water was ascribed to nucleus ($T_1 = 5.1$ msec), and the more rapidly relaxing population to cytoplasm ($T_1 = 3.1$ msec). The T_1 of ^{17}O in supernatant was appreciably longer ($T_1 = 7.5$ msec). The results of temperature effects on the relaxation times led these authors to conclude that the exchange rate of water between these two phases is slower than the relaxation rate of ^{17}O (slow-exchange condition). Two different methods were used to study the NMR of ^{17}O in $H_2{}^{17}O$ enriched human erythrocytes (Shporer and Civan, 1975): (1) direct comparison of relaxation rates of ^{17}O in isolated pellets and supernatant, (2) relaxation rates measured in the presence of Mn^{2+}. It was noted that T_1 for intracellular water ws 4–5-times shorter than for the supernatant. The values of rate constants (k_x) at 25 and 37°C were found to be 60 and 107 sec^{-1}, and the activation energy for k_x as equal to 8.7 ± 1.0 kcal/mole. The authors emphasized the importance of the interaction between water and membrane during the transport of water. Fabry and Eisenstadt (1975) investigated the exchange of water between human red blood cells and the plasma phase by studying water proton NMR in the presence of Mn^{2+}, and by measuring ^{17}O relaxation times of $H_2{}^{17}O$ in the absence of added Mn^{2+} The half-life for cell water at 25°C was found to be 15 msec ± 2 msec; and the exchange time equal to 0.046 msec. The relaxation time values are reported in Table 2. The results were analysed in terms of the classical two-compartment exchange model.

Finch and Schneider (1975) measured T_1 and $T_{1\rho}$ for water protons from 0 to 30°C, and the ω_1 dependence of $T_{1\rho}$ for aqueous dispersion of red cell membrane (see Table 2). From the available data these authors could not specify whether the water detected by NMR was associated with erythrocyte membrane, lipids or polysaccharides, or all three. Nevertheless, they pointed out the importance of the membrane-bound water in defining the structure and functions of membranes. Simple lecithin systems have been used as models for the biological membranes. Klose and Stelzner (1974) reported on the NMR study of specific amounts of water in lecithin–benzene systems. They postulated that water–membrane interactions are limited to three regions: (1) the interaction of water with the phosphate groups, (2) water interacting by additional weak interactions, and (3) water molecules beyond both these regions.

With a view to studying the effects of different cellular materials on the state of water, James and Gillen (1972) measured T_1, T_2 and self-diffusion constant (D) values of water from the unfertilized chicken egg. Only one resonance signal was observed from the mobile and immobile water. The values of relaxation times and diffusion constant are given below:

	Egg yolk	Egg white	Egg albumin (10% solution sealed in vacuum)	Distilled H_2O
Diffusion constant with respect to pure water	0.25	0.80	0.88	
T_1 (msec)	67.0	1180	1270	2830
T_2 (msec)	27.0	—	340	2830

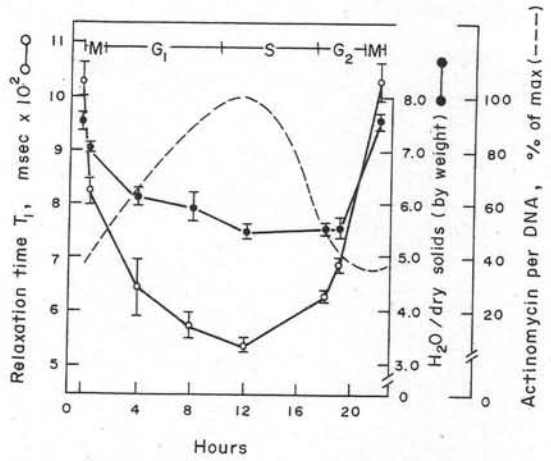


FIG. 7. (Beall *et al.*, 1976) T_1 and water content as a function of HeLa cell cycle. (○——○) T_1 during the cell cycle (mean of eight–ten experiments). Bars denote standard error of the mean. (●——●) Water content during the cell cycle. (----) Actinomycin-D binding ability of the chromatin. Data for the dashed line are from Pederson and Robbins.

Copyright 1978 (25 May) by the American Association for the Advancement of Science.

Significant portions of cellular water are known to exhibit reduced mobility, which can be attributed to the obstruction or hydration effects. On the basis of T_1 measurements, these authors proposed that probably the hydration effects are more important. Fung *et al.* (1975a) also reported that the T_1 values for egg yolk were considerably shorter than for egg white.

Some authors have given evidence showing that the changes in T_1 of cell water are due to alterations in the configuration of macromolecules. T_1 in mammalian cells and tissues was measured as a function of the external ion concentration and total cell water content (Raaphorst *et al.*, 1975). The changes in the fraction of bound and unbound water were shown to be associated with changes induced in the macromolecular configuration by varying the salt concentration and the amount of water. Beall *et al.* (1976) investigated T_1 of water protons (at 25°C) and the total water content as a function of HeLa cell cycle (Fig. 7). They demonstrated the effects of biological and physiological alterations during the growth and division of cells on the T_1 of water. It was proposed that the relation between T_1 and the cyclic pattern of cell growth and division was influenced probably by the conformational changes of macromolecules (associated with the morphological changes during cell division), and by the water content.

(e) *Tumours and cancerous cells*

An important development in the NMR studies of water in biological systems has been to show that the measurements of T_1, T_2 and $T_{1\rho}$ of water in tissues and organs have a potential use in the cancer research. The relaxation times are closely related to the structure, mobility and the content of water in normal and cancerous tissues and cells. As a result, the effects of the presence and growth of tumours on the behaviour of water can be investigated by the NMR technique. Nevertheless, the eventual use of this method for the diagnostic purpose remains a highly controversial issue. The basic problem arises because, even though it is now fairly well established that there is a marked difference between the relaxation behaviour of water protons in the normal and cancerous states, there is no certitude that such a behaviour is strictly specific for the cancerous state.

In his pioneer paper, Damadian (1971) reported that the water proton relaxation times T_1 and T_2 for malignant and normal tissues were distinctly different. Water in malignant tissues exhibited longer relaxation times or a higher motional freedom. These observations were interpreted in terms of the postulate of Szent-Györgyi (1957): it states that the degree of organization of water in the cancerous tissues is much lower than in normal

tissues. The results reported by Damadian were soon confirmed by several groups of workers and initiated extensive research in this field.

Frey *et al.* (1972) showed that many nonmalignant tissues from spleen, kidney, liver, heart, muscle, intestines, stomach, skin and lung for mice with a tumour on hindleg had significantly longer relaxation times (T_1 and $T_{1\rho}$) as compared with the corresponding tissues from healthy mice (see Table 2). They did not observe any systematic variations in the T_2 values. It was proposed that water was more ordered in tissues with tumours. Inch *et al.* (1974) measured the water content and T_1 for neoplastic and non-neoplastic tissues from mice and humans. The T_1 values for tissues of liver, spleen and kidney from animals with large, rapidly growing tumours were longer than T_1 for similar tissues from healthy animals. Whereas, for slowly growing tumours this difference was negligible, i.e. T_1 was found to be related to the rate of growth rather than to malignancy. These authors emphasized that the T_1 values were related directly with the water content. Hollis *et al.* (1975) also observed that the slowly growing and well-differentiated tumours gave shorter T_1 values as compared with more rapidly growing tumours. Schara *et al.* (1974) concluded that proton spin-lattice relaxation (at room temperature) can be a valuable tool for the characterization of the pathological changes in the thyroid gland tissue in case of thyroid gland cancer.

Hazlewood *et al.* (1974a) studied in great detail the relationship between hydration and the relaxation times of water protons in tissues from mice with and without tumour. It was shown that T_1 and T_2 of water protons, and diffusion constant (D), increased monotonically and distinguishably from the normal, to nodule and finally to tumour cells in the development of mammary tumours in mice. These results indicated that macromolecular–water interactions were altered by the presence of a tumour or onum in the host. The changes in T_1 and T_2 were independent of changes in organ hydration. A comparison of the T_1 and T_2 of neoplasms from the breast of normal and diseased tissues showed that the values of relaxation times were correlated with, but not strictly dependent on the hydration of tissues (Medina *et al.*, 1975; Hazlewood *et al.*, 1974a). The tissues could be classified as fibrocystic or neoplastic depending on the values of the pair of T_1, T_2. If $T_1 \leqq 792$ and $T_2 \leqq 58.1$, then the tissue was classified as fibrocystic; if $T_1 > 792$, $T_2 > 58.1$, then the tissue was classified as neoplastic. The T_2 values were considered to be more discriminating than T_1 in certain diseased states. Hazlewood *et al.* (1974a) and Medina *et al.* (1975) pointed out that NMR spectroscopy could be employed as a useful tool for the detection of cancer, and in cancer research. Saryan *et al.* (1974), and Bovée *et al.* (1974) indicated that the increase in NMR relaxation time T_1 (at $\sim$25°C) is determined, in part, by the increased water content of cancerous tissues.

Block and Maxwell (1974) studied the behaviour of water proton T_1 for normal and tumorous tissues of rats. These authors considered a model in which tumorous tissues had lesser amount of water with restricted mobility than the normal tissues. Three mouse cell populations (EL 4 ascitis tumour cells, normal spleen leukocytes, and normal erythrocytes) were studied at 13.56 and 100 MHz by Block *et al.* (1977). At each frequency, the T_1 values for tumour cells were found to be greater than the values for either of the normal cell type (see Table 2). Qualitatively, they attributed this effect to the binding of a fraction of water (exhibiting restricted mobility) to slowly moving macromolecules. The $1/T_1$ values were found to vary approximately linearly with the total water content over the range investigated.

It has been demonstrated by several authors that T_1 of water protons in tumours is considerably longer than in healthy tissues. Furthermore, Damadian *et al.* (1973) have pointed out that the discrimination between the relaxation times of water in normal and cancerous tissues appears to improve at lower frequency, i.e. the overlapping is reduced at low frequencies. Diegel and Pintar (1975a) defined the resolution "r" as:

$$\text{"}r\text{"} = \frac{T_1\,(\text{tumorous}) - T_1\,(\text{healthy})}{T_1\,(\text{tumorous})} = \left(\frac{1/T_1 - R_f}{1/T_1}\right)\frac{\delta_b}{b}$$

3×10^{-4} sec with an activation energy of 4.8 kcal/mole, and the proton exchange time was calculated to be 1.3×10^{-4} sec with an activation energy of 10.0 kcal/mole. The addition of NH_4Cl enhanced the proton exchange rate. It may be remarked that the value of correlation time noted above for collagen is much longer than the value of 2×10^{-8} sec that was reported earlier for the correlation time of molecular rotation of water in muscles (Knispel *et al.*, 1974). The rate of proton exchange that greatly influences the water proton signal from collagen was found to depend on the temperature, pH, and buffer salts (Migchelsen and Berendsen, 1973; Bieńkiewicz *et al.*, 1977).

In order to explain the non-averaging of dipolar and quadrupolar interactions which are responsible for the splitting of ^1H and ^2H signals, respectively, Dehl and Hoeve (1969) assumed a model in which certain preferential hydrogen bonded structures of water were formed. The water molecules could diffuse rapidly between the highly oriented strands of collagen fibres, but their motion was anisotropic. Chapman and McLauchlan (1969) also proposed a continuous chain model for water in collagen. Fung and Trautmann (1971) proposed that the observed dipolar or quadrupolar splittings for water in collagen were the average of two types of water: (1) water molecules adsorbed or bound to the collagen triple helix (the oriented water), and (2) the remaining free water molecules, that undergo rapid reorientation. These authors reported the effects of ions on collagen hydration by studying the ion effects on the deuteron quadrupole splitting. Migchelsen and Berendsen (1973) were led to the conclusion that the chain model was not sufficient to account completely for the hydration of collagen; their results also favoured the specific binding model. Field-dependent splitting of the water signal was also reported for sciatic nerves of rabbits (Chapman and McLauchlan, 1967). The maximum splitting was observed when the nerve axis was parallel to the applied field.

Dehl (1970) described a method for estimating the amount of unfrozen water in frozen fibres of collagen. The method is based on the fact that line separation is given by $K\ (\cos^2\theta - 1)$, where the splitting constant K decreases with increasing ^2H_2O content, and θ is the angle between the fibre axis and the magnetic field axis. Fung and Wei (1973) applied this method to study in detail the effects of water content and salts on quadrupolar splitting of ^2H_2O in hydrated collagen for the maximum splitting ($\theta = 0°$). The amount of "unfrozen water" decreased in the presence of salts. They pointed out that hydrated ions block the binding sites for water in collagen. Only the water molecules bound directly to collagen were oriented and resulted in the dipolar or quadrupolar splitting for H_2O and ^2H_2O, respectively.

The NMR studies of collagen water discussed so far were performed by the continuous wave technique at a single frequency. Fung *et al.* (1974) applied the pulse technique to measure the T_1 values for water in hydrated collagen at different frequencies and over a wide temperature range (25 to $-80°C$). They observed that T_1 was strongly dependent on the temperature and frequency. The correlation times could be described by a distribution function in a manner similar to that for water in muscles, discussed earlier in Section IV.1(c). Edzes and Samulski (1977) used the FT pulse technique to study the proton spin-lattice relaxation decay of hydrated collagen under the conditions when the dipolar splitting is zero (fibre axis perpendicular to magnetic field). By studying the effects of partial substitution of H_2O by ^2H_2O, these authors proposed that dipolar coupling between water protons and collagen protons, i.e. cross-relaxation and spin diffusion make an important contribution to the water proton relaxation mechanism. Edzes and Samulski (1978) further confirmed, by using the method of selective inversion of water proton magnetization with longer 180° pulses, that cross-relaxation contributes to the relaxation of water protons in hydrated collagen.

(b) *DNA fibres*

A study of water from the hydrated DNA (salmon sperm) in the form of oriented fibres was initially reported by Berendsen and Migchelsen (1965). They observed that the second moment of the water proton signal varied qualitatively with the angle between the fibre direction and magnetic field. In the case of oriented DNA, the anisotropy of

water molecules in a direction perpendicular to the fibre axis was proposed in contrast to the model which was put forth for collagen water. Rupprecht (1966) prepared samples of calf thymus DNA (NaDNA) by the wet spinning method. He plotted peak-to-peak amplitude of the derivative signal recorded as a function of the angle between the direction of molecular orientation and the magnetic field. From these results, Rupprecht was led to conclude that the hydration structure in DNA is similar to the structure present in hydrated collagen.

Finally, Migchelsen *et al.* (1968) investigated the proton NMR spectra of water in oriented NaDNA in the A form, and LiDNA in B and C forms. Similar to the results reported by Rupprecht (1966), Migchelsen *et al.* (1968) also observed a single proton signal at room temperature for NaDNA whose linewidth depended on the angle between the fibre direction and the field. However, for LiDNA in the B and C forms, angular dependent splitting was recorded at room temperatures. The proton exchange process was considered to be an important factor influencing the water spectra of NaDNA.

V. SUMMARY AND CONCLUSIONS

This article presents a general perspective of the multifold NMR studies of water performed in various biological systems. A considerable effort has been devoted to investigate the relaxation times of water nuclei (^1H, ^2H, ^{17}O) for a variety of biological samples as a function of temperature and frequency. One common and striking feature observed in nearly all cases studied is that the relaxation times of water nuclei and the diffusion constants of water molecules are much lower than the values observed for free water. Generally, these results can be interpreted in terms of: (1) the restricted and anisotropic motion of water molecules and enhanced proton transfer in the hydration layer; (2) the preferential and dynamic orientations of water molecules in the vicinity of biological macromolecules. The characteristics (1) and (2) arise because a fraction of the total water content (in solution or in biological samples) is associated with proteins and nucleic acids, forming a hydration layer in their close vicinity. In other words, water molecules in the hydration layer exhibit distinctly different properties from those observed for free or extra-hydration layer water. Furthermore, the behaviour of the hydration water molecules was found to depend strongly on the nature of the hydrated species. Two-state and three-state models were proposed to account for the relaxation behaviour of water nuclei.

An important characteristic of hydration water is that it remains unfrozen or mobile (on the NMR time scale) at temperatures much lower than the freezing point of free solvent. This phenomenon proved to be very valuable for investigating the state of water in systems such as muscle, collagen, tissues, membranes; as well as for studying the changes in macromolecular–water interactions induced by external factors (γ-irradiation), and the changes in water structure which result during natural, biological and physical processes such as growth and division of cells, muscle strain, cancerous growth. The proton NMR spectra obtained from hydration water in frozen samples furnish unprecedented information concerning the macromolecular–water interactions and the state of water in biological systems.

There is a vast scope for the application of the NMR studies of hydration water to explore and study in detail the effects produced by certain toxins, drugs, carcinogens and radiations: to investigate the sensitivity and specificity of different organs to these and other related perturbing factors.

There is increasing evidence showing that cross-relaxation between the protons of water molecules and of the macromolecular chain contributes to the relaxation rates of water protons. Eventually, it may become necessary to revise and reconsider the interpretation of certain previously published results in the light of cross-relaxation.

Water constitutes the major component of all living systems, for example it represents about 70–80% of the total cell constituent. There is conclusive evidence showing that water does not simply serve as an inert medium, but it participates at the molecular

level in basic biological interactions and in fundamental biological processes. In fact, the hydration water molecules constitute an integral part of any macromolecular or cellular system under consideration. The importance of water in maintaining the structural integrity of proteins is well-established. Nevertheless, investigators in different domains have not fully recognized the important and crucial role that hydration water molecules may play in various biophysical and radiobiological processes. While postulating ingenious theories and mechanisms to explain such processes, many authors have either totally neglected the participation of water or considered it simply in terms of the overall medium effects. Hopefully, the NMR studies of water carried out very extensively in different laboratories would largely contribute to unravel the vital functional and structural roles played by water at the molecular level in many biological interactions and biophysical processes.

ACKNOWLEDGEMENTS

The author expresses her gratitude to Dr A. J. Bertinchamps (Euratom-ULB) for help and encouragement that made it possible to accomplish this article. Thanks are acknowledged to Dr P. Lejeune (Institut d'Hygiène et d'Epidémiologie) for many useful discussions and his keen interest in this work. Finally, grateful thanks are offered to Dr W. Stone (Université de Louvain) and Dr K. Hallenga (Vrije Universiteit Brussel) for reading the manuscript with interest, and giving several invaluable suggestions.

REFERENCES

AL-RAWI, J. M. A., BLOXSIDGE, J. P., O'BRIEN, C., CADDY, D. E., ELVIDGE, J. A., JONES, J. R. and EVANS, E. A. (1974) Tritium nuclear magnetic resonance spectroscopy. II. Chemical shifts, referencing, and an application. *J. Chem. Soc. Perkin Trans* **2,** 1635–1638.

AL-RAWI, J. M. A., ELVIDGE, J. A., JONES, J. R. and EVANS, E. A. (1975) Tritium nuclear magnetic resonance spectroscopy. III. Coupling constants and isotope effects. *J. Chem. Soc. Perkin Trans* **2,** 449–452.

ANDRASKO, J. (1976) Water diffusion permeability of human erythrocytes studied by a pulsed gradient NMR technique. *Biochim. biophys. Acta* **428,** 304–311.

BEALL, P. T., HAZLEWOOD, C. F. and RAO, P. N. (1976) NMR patterns of intracellular water as a function of HeLa cell cycle. *Science, N.Y.* **192,** 904–907.

BELTON, P. S., JACKSON, R. R. and PACKER, K. J. (1972) Pulsed NMR studies of water in striated muscle. I. Transverse nuclear spin relaxation times and freezing effects. *Biochim. biophys. Acta* **286,** 16–25.

BELTON, P. S., PACKER, K. J. and SELLWOOD, T. C. (1973) Pulsed NMR studies of water in striated muscle. II. Spin-lattice relaxation times and the dynamics of the non-freezing fraction of water. *Biochim. biophys. Acta* **304,** 56–64

BELTON, P. S. and PACKER, K. J. (1974) Pulsed NMR studies of water in striated muscle. III. The effects of water content. *Biochim. biophys. Acta* **354,** 305–314.

BERENDSEN, H. J. C. (1962) Nuclear magnetic resonance study of collagen hydration. *J. chem. Phys.* **36,** 3297–3305.

BERENDSEN, H. J. C. and MIGCHELSEN, C. (1965) Hydration structure of fibrous macromolecules. *Ann. N. Y. Acad. Sci.* **125,** 365–379.

BERENDSEN, H. J. C. and MIGCHELSEN, C. (1966) Hydration structure of collagen and influence of salts. *Fedn Proc.* **25,** 998–1002.

BERENDSEN, H. J. C. (1975) Specific interactions of water with biopolymers. In *Water: A Comprehensive Treatise.* (ed. F. FRANKS), Vol. 5, pp. 293–349. Plenum Press, New York.

BIEŃKIEWICZ, K. J., BERENDSEN, H. J. C. and ANDREE, P. J. (1977) Properties of water in native and modified collagen. *Ann. Soc. Chim. Polonorum.* **51,** 149–158.

BLEARS, D. J. and DANYLUK, S. S. (1968) Proton wide-line nuclear magnetic resonance spectra of hydrated proteins. *Biochim. biophys. Acta* **154,** 17–27.

BLOCK, R. E. and MAXWELL, G. P. (1974) Proton magnetic resonance studies of water in normal and tumor rat tissues. *J. magn. Reson.* **14,** 329–334.

BLOCK, R. E., MAXWELL, G. P., PRUDHOMME, D. L. and HUDSON, J. L. (1977) High resolution proton magnetic resonance spectral characteristic of water, lipid and protein signals from three mouse cell populations. *J. natn. Cancer Inst.* **58,** 151–156.

BLOK, J. and LOMAN, H. (1973) The effects of γ-irradiation in DNA. *Curr. Top. Radiat. Res. Q.* **9,** 165–245.

BOVÉE, W., HUISMAN, P. and SMIDT, J. (1974) Tumor detection and nuclear magnetic resonance. *J. natn. Cancer. Inst.* **52,** 595–597.

BLOXSIDGE, J., ELVIDGE, J. A., JONES, J. R. and EVANS, E. A. (1971) Tritium NMR spectroscopy. I. Technique, internal referencing and some preliminary results. *Org. magn. Reson.* **3,** 127–138.

BRATTON, C. B., HOPKINS, A. L. and WEINBERG, J. W. (1965) Nuclear magnetic resonance studies of living muscle. *Science, N. Y.* **147,** 738–739.

CARRINGTON, A. and MCLACHLAN, A. D. (1967) *Introduction to Magnetic Resonance.* Harper and Row, New York, and John Weatherhill, Tokyo.

CHANG, D. C., HAZLEWOOD, C. F., NICHOLS, B. L. and RORSCHACH, H. E. (1972) Spin echo studies on cellular water. *Nature, Lond.* **235,** 170–171.

CHANG, D. C., RORSCHACH, H. E., NICHOLS, B. L. and HAZLEWOOD, C. F. (1973) Implications of diffusion coefficient measurements for the structure of cellular water. *Ann. N. Y. Acad. Sci.* **204,** 434–443.

CHANG, D. C., HAZLEWOOD, C. F. and WOESSNER, D. E. (1976) The spin-lattice relaxation times of water associated with early post mortem changes in skeletal muscle. *Biochim. biophys. Acta* **437,** 253–258.

CHAPMAN, G. and MCLAUCHLAN, K. A. (1967) Oriented water in the sciatic nerve of rabbit. *Nature, Lond.* **215,** 391–392.

CHAPMAN, G. and MCLAUCHLAN, K. A. (1969) The hydration structure of collagen. *Proc. R. Soc.* B. **173,** 223–234.

CIVAN, M. M. and SHPORER, M. (1975) Pulsed nuclear magnetic resonance study of ^{17}O, ^{2}D and ^{1}H of water in frog striated muscle. *Biophys. J.* **15,** 299–306.

CIVAN, M. M., ACHLAMA, A. M. and SHPORER, M. (1978) The relationship between the transverse and longitudinal nuclear magnetic resonance relaxation rates of muscle water. *Biophys. J.* **21,** 127–136.

CLEVELAND, G. G., CHANG, D. C., HAZLEWOOD, C. F. and RORSCHACH, H. E. (1976) Nuclear magnetic resonance measurement of skeletal muscle. *Biophys. J.* **16,** 1043–1053.

CONLON, T. and OUTHRED, R. (1972) Water diffusion permeability of erythrocytes using an NMR technique. *Biochim. biophys. Acta* **288,** 354–361.

COOKE, R. and WIEN, R. (1971) The state of water in muscle tissue as determined by proton nuclear magnetic resonance. *Biophys. J.* **11,** 1002–1017.

COPE, F. W. (1969) Nuclear magnetic resonance evidence using D_2O for structured water in muscle and brain. *Biophys. J.* **9,** 303–319.

COPE, F. W. (1970) The solid state physics of electron and ion transport in biology. *Adv. biol. med. Phys.* **13,** 1–35.

COTTAM, G. L., VALENTINE, K. M., YAMAOKA, K. and WATERMAN, M. R. (1974) The gelation of deoxyhemoglobin S in erythrocytes as detected by transverse water proton relaxation measurements. *Archs Biochem. Biophys.* **162,** 487–492.

DAMADIAN, R. (1971) Tumor detection by nuclear magnetic resonance. *Science, N. Y.* **171,** 1151–1153.

DAMADIAN, R., ZANER, K., HOR, D., DIMAIO, T., MINKOFF, L. and GOLDSMITH, M. (1973) Nuclear magnetic resonance as a new tool in cancer research: human tumors by NMR. *Ann. N. Y. Acad. Sci.* **222,** 1048–1076.

DAMADIAN, R., ZANER, K., HOR, D. and DIMAID, T. (1974) Human tumors detected by nuclear magnetic resonance. *Proc. natn. Acad. Sci. U.S.A.* **71,** 1471–1473.

DAMADIAN, R., MINKOFF, L., GOLDSMITH, M., STANFORD, M. and KOUTCHER, J. (1976) Field focussing nuclear magnetic resonance (FONAR): visualization of a tumor in a live animal. *Science, N. Y.* **194,** 1430–1432.

DAMADIAN, R., GOLDSMITH, M. and MINKOFF, L. (1977) NMR in cancer: XVI FONAR image of the live human body. *Physiol. Chem. Phys.* **9,** 97–100.

DEHL, R. E. and HOEVE, C. A. J. (1969) Broad-line NMR study of H_2O and D_2O in collagen fibers. *J. chem. Phys.* **50,** 3245–3251.

DEHL, R. E. (1970) Collagen: mobile water content of frozen fibers. *Science, N. Y.* **170,** 738–739.

DIEGEL, J. G. and PINTAR, M. M. (1975a) A possible improvement in the resolution of proton spin relaxation for the study of cancer at low frequency. *J. natn. Cancer Inst.* **55,** 725–726.

DIEGEL, J. G. and PINTAR, M. M. (1975b) Origin of the non exponentiality of the water proton spin relaxation in tissues. *Biophys. J.* **15,** 855–860.

DUFF, I. D. and DERBYSHIRE, W. (1974) NMR investigations of frozen porcine muscle. *J. magn. Reson.* **15,** 310–316.

EDZES, H. T. and SAMULSKI, E. T. (1977) Cross relaxation and spin diffusion in the proton NMR of hydrated collagen. *Nature, Lond.* **265,** 521–523.

EDZES, H. T. and SAMULSKI, E. T. (1978) The measurement of cross-relaxation effects in the proton NMR spin-lattice relaxation of water in biological systems: hydrated collagen and muscle. *J. magn. Reson.* **31,** 207–229.

EGGLESTON, J. C., SARYAN, L. A. and HOLLIS, D. P. (1975) Nuclear magnetic resonance investigations of human neoplastic and abnormal non neoplastic tissues. *Cancer Res.* **35,** 1326–1332.

EISENBERG, D. and KAUZMANN, W. (1969) *The Structure and Properties of Water.* Clarendon Press, Oxford.

ELLIS, G. E. and PACKER, K. J. (1976) Nuclear spin-relaxation studies of hydrated elastin. *Biopolymers* **15,** 813–832.

EMSLEY, J. W., FEENEY, J. and SUTCLIFFE, L. (1965) *High Resolution Nuclear Magnetic Resonance Spectroscopy.* Vols I and II. Pergamon Press, London.

FABRY, M. E. and EISENSTADT, M. (1975) Water exchange between red cells and plasma. Measurements by nuclear magnetic relaxation. *Biophys. J.* **15,** 1101–1110.

FERRAR, T. C. and BECKER, E. D. (1971) *Pulse and Fourier Transform NMR.* Academic Press, New York.

FINCH, E. D. and HOMER, L. D. (1974) Proton nuclear magnetic resonance relaxation measurements in frog muscle. *Biophys. J.* **14,** 907–921.

FINCH, E. D. and SCHNEIDER, A. S. (1975) Mobility of water bound to biological membranes. A proton NMR relaxation study. *Biochim. biophys. Acta* **406,** 146–154.

FOSTER, K. F., RESING, H. A. and GARROWAY, A. N. (1976) Bounds on "bound water": transverse nuclear magnetic resonance relaxation in barnacle muscle. *Science, N. Y.* **194,** 324–326.

FRANKS, F. (1972–1975) *Water: A Comprehensive Treatise,* Vols 1–5. Plenum Press, New York.

FRANKS, F. (1977) Solvation interactions of proteins in solution. *Phil. Trans. R. Soc.* B. **278,** 89–96.

FREY, H. E., KNISPEL, R. R., KRUUV, J., SHARP, A. R., THOMPSON, R. T. and PINTAR, M. M. (1972) Proton spin-lattice relaxation studies of non malignant tissues of tumorous mice. *J. natn. Cancer Inst.* **49,** 903–906.

FRITZ, O. G. JR and SWIFT, T. J. (1967) The state of water in polarized and depolarized frog nerves. A proton magnetic resonance study. *Biophys. J.* **7,** 675–686.

FULLER, M. E. and BREY, W. S. JR (1968) Nuclear magnetic resonance study of water sorbed on serum albumin. *J. biol. Chem.* **243,** 274–280.

FUNG, B. M. and TRAUTMANN, P. (1971) Deuterium NMR and EPR of hydrated collagen fibers in the presence of salts. *Biopolymers* **10,** 391–397.
FUNG, B. M. and WEI, S. C. (1973) The effects of alkali and alkaline earth salts on the structure of hydrated collagen fibers as studied by deuterium NMR. *Biopolymers* **12,** 1053–1062.
FUNG, B. M. (1974) Non-freezable water and spin-lattice relaxation time in muscle containing a growing tumor. *Biochim. biophys. Acta* **362,** 209–214.
FUNG, B. M., WITSCHEL, J. JR and MCAMIS, L. L. (1974) The state of water on hydrated collagen as studied by pulsed NMR. *Biopolymers.* **13,** 1767–1776.
FUNG, B. M. and MCGAUGHY, T. W. (1974) The state of water in muscle as studied by pulsed NMR. *Biochim. biophys. Acta* **343,** 663–673.
FUNG, B. M., DURHAM, D. L. and WASSIL, D. A. (1975a) The state of water in biological systems as studied by proton and deuterium relaxation. *Biochim. biophys. Acta* **399,** 191–202.
FUNG, B. M., WASSIL, D. A., DURHAM, D. L., CHESNUT, R. W., DURHAM, N. N. and BERLIN, K. D. (1975b) Water in normal muscle and muscle with tumor. *Biochim. biophys. Acta* **385,** 180–187.
FUNG, B. M. (1977a) Proton and deuteron relaxation of muscle water over wide ranges of resonance frequencies. *Biophys. J.* **18,** 235–239.
FUNG, B. M. (1977b) Carbon-13 and proton magnetic resonance of mouse muscle. *Biophys. J.* **19,** 315–319.
FUNG, B. M. (1977c) Correlation of relaxation time with water content in muscle and brain tissues. *Biochim. biophys. Acta* **497,** 317–322.
GLASEL, J. A. (1967) A study of water in biological systems by ^{17}O magnetic resonance spectroscopy. II. Relaxation phenomena in pure water. *Proc. natn. Acad. Sci., U.S.A.* **58,** 27–33.
GLASEL, J. A. (1970) Participation of water in conformational changes of biopolymers as studied by deuteron magnetic resonance. *J. Am. Chem. Soc.* **92,** 375–381.
GOLDSMITH, M., KOUTCHER, J. and DAMADIAN, R. (1978) NMR in cancer XI. Application of the NMR malignancy index to human gastro-intestinal tumors. *Cancer* **41,** 183–191.
GRÖSCH, L. and NOACK, F. (1976) NMR relaxation investigation of water mobility in aqueous bovine serum albumin solutions. *Biochim. biophys. Acta* **453,** 218–232.
HALLENGA, K. and KOENIG, S. H. (1976) Protein rotational relaxation as studied by solvent ^{1}H and ^{2}H magnetic relaxation. *Biochemistry* **15,** 4255–4263.
HANSEN, J. R. and LAWSON, K. D. (1970) Magnetic relaxation in ordered systems. *Nature, Lond.* **225,** 542–543.
HANSEN, J. R. (1971) Pulsed NMR study of water mobility in muscle and brain tissue. *Nature, Lond.* **230,** 482–486.
HAZLEWOOD, C. F., NICHOLS, B. L. and CHAMBERLAIN, N. F. (1969) Evidence for the existence of a minimum of two phases of ordered water in skeletal muscle. *Nature, Lond.* **222,** 747–750.
HAZLEWOOD, C. F., NICHOLS, B. L., CHANG, D. C. and BROWN, B. (1971) On the state of water in developing muscle: a study of the major phase of ordered water in skeletal muscle and its relationship to sodium concentration. *Johns Hopkins Med. J.* **128,** 117–131.
HAZLEWOOD, C. F., CLEVELAND, G. and MEDINA, D. (1974a) Relationship between hydration and proton nuclear magnetic resonance relaxation times in tissues of tumor-bearing and non tumor-bearing mice: implications for cancer detection. *J. natn. Cancer Inst.* **52,** 1849–1853.
HAZLEWOOD, C. F., CHANG, D. C., NICHOLS, B. L. and WOESSNER, D. E. (1974b) Nuclear magnetic resonance transverse relaxation times of water protons in skeletal muscle. *Biophys. J.* **14,** 583–606.
HILTON, B. D., HSI, E. and BRYANT, R. G. (1977) ^{1}H nuclear magnetic resonance relaxation of water on lysozyme powders. *J. Am. Chem. Soc.* **99,** 8483–8490.
HOLLIS, D. P., SARYAN, L. A., EGGLESTON, D. and MORRIS, H. P. (1975) Nuclear magnetic resonance studies of cancer. VI. Relationship among spin-lattice relaxation times, growth rate and water content of Morris hepatomas. *J. natn. Cancer Inst.* **54,** 1469–1472.
HOULT, D. I. (1977) Zeugmatography: a criticism of the concepts of a selective pulse in the presence of a field gradient. *J. magn. Reson.* **26,** 165–167.
HUTCHINSON, J. M. S., SUTHERLAND, R., MALLARD, J. R. and FOSTER, M. A. (1977) In *NMR in Biology* (eds R. A. DWEK, I. D. CAMPBELL, R. E. RICHARDS and R. J. P. WILLIAMS), pp. 368–369. Academic Press, London.
INCH, W. R., MCCREDIE, J. A., KNISPEL, R. R., THOMPSON, R. T. and PINTAR, M. M. (1974) Water content and proton spin relaxation time for neoplastic and non-neoplastic tissues from mice and humans. *J. natn. Cancer Inst.* **52,** 353–356.
JACOBSEN, B., ANDERSON, W. A. and ARNOLD, T. (1954) A proton magnetic resonance study of the hydration of deoxyribonucleic acid. *Nature, Lond.* **173,** 772–773.
JAMES, T. L. and GILLEN, K. T. (1972) NMR relaxation time and self-diffusion constant of water in hen egg white and yolk. *Biochim. biophys. Acta* **286,** 10–15.
KALK, A. and BERENDSEN, H. J. C. (1976) Proton magnetic relaxation and spin diffusion in proteins. *J. magn. Reson.* **24,** 343–366.
KAVANAU, J. L. (1964) *Water and Solute–Water Interactions.* Holden-Day, London.
KLOSE, G. and STELZNER, F. (1974) NMR investigations of the interaction of water with lecithin in benzene solutions. *Biochim. biophys. Acta* **363,** 1–8.
KNISPEL, R. R., THOMPSON, R. T. and PINTAR, M. M. (1974) Dispersion of proton spin-lattice relaxation in tissues. *J. magn. Reson.* **14,** 44–51.
KOENIG, S. H. and SCHILLINGER, W. E. (1969) Nuclear magnetic relaxation dispersion in protein solutions. *J. biol. Chem.* **244,** 3283–3289.
KOENIG, S. H., HALLENGA, K. and SHPORER, M. (1975) Protein–water interaction studied by solvent ^{1}H, ^{2}H and ^{17}O magnetic relaxation. *Proc. natn. Acad. Sci. U.S.A.* **72,** 2667–2671.
KOENIG, S. H., BRYANT, R. G., HALLENGA, K. and JACOB, G. S. (1978) Magnetic cross-relaxation among protons in protein solutions. *Biochemistry* **17,** 4348–4358.

KOUTCHER, J. A., GOLDSMITH, M. and DAMADIAN, R. (1978) NMR in cancer X. A malignancy index to discriminate normal and cancerous tissue. *Cancer* **41,** 174–182.

KUMAR, A., WELTI, D. and ERNST, R. R. (1975) NMR Fourier zeugmatography. *J. magn. Reson.* **18,** 69–83.

KUNTZ, I. D., BRASSFIELD, T. S., LAW, G. D. and PURCELL, G. V. (1969) Hydration of macromolecules. *Science, N. Y.* **163,** 1329–1331.

KUNTZ, I. D. (1971a) Hydration of macromolecules. III. Hydration of polypeptides. *J. Am. Chem. Soc.* **93,** 514–516.

KUNTZ, I. D. (1971b) Hydration of macromolecules. IV. Polypeptide conformation in frozen solution. *J. Am. Chem. Soc.* **93,** 516–518.

KUNTZ, I. D. and KAUZMANN, W. (1974) Hydration of proteins and polypeptides. *Adv. Protein Chem.* **28,** 239–345.

LATARJET, R. (1972) Interaction of radiation energy with nucleic acids. *Curr. Top. Radiat. Res. Q.* **8,** 1–38.

LAUTERBUR, P. C. (1973) Image formation by induced local interactions: examples employing NMR. *Nature, Lond.* **242,** 190–191.

LAUTERBUR, P. C. (1974) Magnetic resonance zeugmatography. *Pure Appl. Chem.* **40,** 149–157.

LAUTERBUR, P. C. (1977) Spatially-resolved studies of whole tissue, organs and organisms by NMR zeugmatography. In *NMR in Biology* (eds. R. A. DWEK, I. D. CAMPBELL, R. E. RICHARDS and R. J. P. WILLIAMS), pp. 323–335. Academic Press, London.

LINDSTROM, T. R. and KOENIG, S. H. (1974) Magnetic-field dependent water proton spin-lattice relaxation rates of hemoglobin solutions and whole blood. *J. magn. Reson.* **15,** 344–353.

LINDSTROM, T. R., KOENIG, S. H., BOUSSIOS, T. and BERTLES, J. F. (1976) Intermolecular interactions of oxygenated sickle hemoglobin molecules in cells and cell-free solutions. *Biophys. J.* **16,** 679–689.

LING, G. N. (1962) In *A Physical Theory of the Living State: The Association-Induction Hypothesis.* Blaisdell, New York.

LING, G. N. (1969) A new model for the living cell: a summary of the theory and recent experimental evidence in its support. *Int. Rev. Cytol.* **26,** 1–61.

LUBAS, B. and WILCZOK, T. (1966) Spin-echo technique study of the non-rotational hydration of deoxyribonucleic acid. *Biochim. biophys. Acta* **120,** 427–433.

LUBAS, B. and WILCZOK, T. (1967) Thermal transition of DNA measured by NMR spin-echo technique. *Biopolymers* **5,** 967–974.

LUBAS, B. and WILCZOK, T. (1971) NMR study on molecular mobility of DNA molecules in solution. *Biopolymers* **10,** 1267–1276.

MANSFIELD, P., MAUDSLEY, A. A. and BAINES, T. (1976) Fast scan proton density imaging by NMR. *J. Phys. E.* **9,** 271–278.

MATHUR-DE VRÉ, R., BERTINCHAMPS, A. J. and BERENDSEN, H. J. C. (1976) The effect of γ-irradiation on the hydration characteristics of DNA and polynucleotides. I. An NMR study of frozen H_2O and D_2O solutions. *Radiat. Res.* **68,** 197–214.

MATHUR-DE VRÉ, R. and BERTINCHAMPS, A. J. (1977a) The effects of γ-irradiation on the hydration characteristics of DNA and polynucleotides. II. An NMR study of mixed H_2O/D_2O frozen solutions. *Radiat. Res.* **72,** 181–189.

MATHUR-DE VRÉ, R. and BERTINCHAMPS, A. J. (1977b) The effects of γ-irradiation on the hydration characteristics of DNA and polynucleotides. III. A comparative NMR study of frozen and liquid solutions. *Radiat. Environ. Biophys.* **14,** 311–315.

MEDINA, D., HAZLEWOOD, C. F., CLEVELAND, G. G., CHANG, D. C., SPJUT, H. J. and MOYERS, R. (1975) Nuclear magnetic resonance studies on human breast dysplasias and neoplasms. *J. natn. Cancer Inst.* **54,** 813–818.

MIGCHELSEN, C. and BERENDSEN, H. J. C. (1967) Deuteron magnetic resonance on hydrated collagen. In *Magnetic Resonance and Relaxation* (ed. R. BLINC), pp. 761–766. North-Holland, Amsterdam.

MIGCHELSEN, C., BERENDSEN, H. J. C. and RUPPRECHT, A. (1968) Hydration of DNA. Comparison of nuclear magnetic resonance results for oriented DNA in the A, B and C form. *J. molec. Biol.* **37,** 235–237.

MIGCHELSEN, C. and BERENDSEN, H. J. C. (1973) Proton exchange and molecular orientation of water in hydrated collagen fibers. An NMR study of H_2O and D_2O. *J. chem. Phys.* **59,** 296–305.

OUTHRED, R. K. and GEORGE, E. P. (1973a) A nuclear magnetic resonance study of hydrated systems using the frequency dependence of the relaxation processes. *Biophys. J.* **13,** 83–96.

OUTHRED, R. K. and GEORGE, E. P. (1973b) Water and ions in muscles and model systems. *Biophys. J.* **13,** 97–103.

PACKER, K. J. (1973) The effects of diffusion through locally inhomogeneous magnetic fields on transverse nuclear spin relaxation in heterogeneous systems. Proton transverse relaxation in striated muscle tissue. *J. magn. Reson.* **9,** 438–443.

PACKER, K. J. (1977) The dynamics of water in heterogeneous systems. *Phil. Trans. R. Soc.* B. **278,** 59–87.

RAAPHORST, G. P., KRUUV, J. and PINTAR, M. M. (1975) Nuclear magnetic resonance study of mammalian cell water. *Biophys. J.* **15,** 391–402.

RANADE, S. S., CHAUGHULE, S. R., KASTURI, S. R., NADKARNI, J. S., TALWALKAR, G. V., WAGH, U. V., KORGAONKAR, K. S. and VIJAYARAGHAVAN, R. (1975) Pulsed nuclear magnetic resonance studies on human malignant tissues and cells *in vitro*. *Indian J. Biochem. Biophys.* **12,** 229–232.

RATKOVIĆ, S. and SINADINOVIĆ, J. (1977) Nuclear magnetic resonance studies on the thyroid gland. II. On the state of tissue water in normal thyroid gland. *Studia Biophys.* **63,** 25–39.

RESING, H. A., FOSTER, K. R. and GARROWAY, A. N. (1977) "Bound water" in barnacle muscle as indicated in nuclear magnetic resonance studies. *Science, N. Y.* **198,** 1180–1182.

RUPPRECHT, A. (1966) Hydration of DNA, a wide line NMR study of oriented DNA. *Acta Chem. scand.* **20,** 582–585.

SARYAN, L. A., HOLLIS, D. P., ECONOMOU, J. S. and EGGLESTON, J. C. (1974) Nuclear magnetic resonance studies of cancer. IV. Correlation of water content with tissue relaxation times. *J. natn. Cancer Inst.* **52,** 599–602.

SCHARA, M., SENTJURC, M., AUERSPERG, M. and GOLOUH, R. (1974) Characterization of malignant thyroid gland tissue by magnetic resonance methods. *Br. J. Cancer* **29,** 483–486.

SHAW, D. (1976) *Fourier Transform NMR Spectroscopy*. Elsevier, Amsterdam.

SHPORER, M. and CIVAN, M. M. (1975) NMR study of ^{17}O form $H_2{}^{17}O$ in human erythrocytes. *Biochim. biophys. Acta* **385,** 81–87.

SHPORER, M., HAAS, M. and CIVAN, M. M. (1976) Pulsed nuclear magnetic resonance study of ^{17}O from $H_2{}^{17}O$ in rat lymphocytes. *Biophys. J.* **16,** 601–610.

SINADINOVIĆ, J., RATKOVIĆ, S. KRAINČANIC. M. and JOVANIĆ, M. (1977) Relationship of biochemical and morphological changes in rat-thyroid and proton spin-relaxation of the tissue water. *Endokrinologie* **69,** 55–66.

SWIFT, T. J. and BARR, E. M. (1973) An oxygen magnetic resonance study of water in frog skeletal muscle. *Ann. N. Y. Acad. Sci.* **204,** 191–196.

SYKES, B. D., HULL, W. E. and SNYDER, G. H. (1978) Experimental evidence for the role of cross-relaxation in proton nuclear magnetic resonance spin lattice relaxation time measurements in proteins. *Biophys. J.* **21,** 137–146.

SZENT-GYÖRGYI, A. (1957) *Bioenergetics*. Academic Press, New York.

TEXTER, J. (1978) Nucleic acid–water interactions. *Prog. Biophys. molec. Biol.* **33,** 83–97.

THOMPSON, R. T., KNISPEL, R. R. and PINTAR, M. M. (1973) A study of the proton exchange in tissue water by spin relaxation in the rotating frame. *Chem. Phys. Lett.* **22,** 335–337.

THOMPSON, B. C., WATERMAN, M. R. and COTTAM, G. L. (1975) Evaluation of the water environments in deoxygenated sickle cells by longitudinal and transverse water proton relaxation rates. *Archs Biochem. biophys.* **166,** 193–200.

UDALL, J. N., ALVAREZ, L. A., NICHOLS, B. L. and HAZLEWOOD, C. F. (1975) The effects of cholera enterotoxin on intestinal tissue water as measured by nuclear magnetic resonance spectroscopy. *Physiol. Chem. Phys.* **7,** 533–539.

WALMSLEY, R. H. and SHPORER, M. (1978) Surface induced NMR line splittings and augmented relaxation rates in water. *J. chem. Phys.* **68,** 2584–2590.

WHITE, J. P., KUNTZ, I. D. and CANTOR, C. R. (1972) Studies on the hydration of *Escherichia coli* ribosomes by nuclear magnetic resonance. *J. molec. Biol.* **64,** 511–514.

ZIPP, A., JAMES, T. L., KUNTZ, I. D. and SHOHET, S. B. (1976) Water proton magnetic resonance studies of normal and sickle erythrocytes. Temperature and volume dependence. *Biochim. biophys. Acta* **428,** 291–303.

METHODOLOGY – Review Article

Chemical Exchange Saturation Transfer (CEST): What is in a Name and What Isn't?

Peter C. M. van Zijl,[1,2]* and Nirbhay N. Yadav[1,2]

Chemical exchange saturation transfer (CEST) imaging is a relatively new magnetic resonance imaging contrast approach in which exogenous or endogenous compounds containing either exchangeable protons or exchangeable molecules are selectively saturated and after transfer of this saturation, detected indirectly through the water signal with enhanced sensitivity. The focus of this review is on basic magnetic resonance principles underlying CEST and similarities to and differences with conventional magnetization transfer contrast. In CEST magnetic resonance imaging, transfer of magnetization is studied in mobile compounds instead of semisolids. Similar to magnetization transfer contrast, CEST has contributions of both chemical exchange and dipolar cross-relaxation, but the latter can often be neglected if exchange is fast. Contrary to magnetization transfer contrast, CEST imaging requires sufficiently slow exchange on the magnetic resonance time scale to allow selective irradiation of the protons of interest. As a consequence, magnetic labeling is not limited to radio-frequency saturation but can be expanded with slower frequency-selective approaches such as inversion, gradient dephasing and frequency labeling. The basic theory, design criteria, and experimental issues for exchange transfer imaging are discussed. A new classification for CEST agents based on exchange type is proposed. The potential of this young field is discussed, especially with respect to in vivo application and translation to humans. Magn Reson Med 65:927–948, 2011. © 2011 Wiley-Liss, Inc.

Key words: MRI; chemical exchange; magnetization transfer; contrast agent; dipolar transfer

INTRODUCTION

When using contrast agents in magnetic resonance imaging (MRI), the requirements are pretty much the same as for any other imaging modality, namely generating the desired contrast while using the lowest possible concentration of agent to avoid perturbing the physiological environment and to minimize toxicity. Due to inherent limitations in sensitivity, MRI has a great disadvantage compared to optical and radioactive methods in that high concentrations of contrast agent are required. To make matters worse, most of the (super)paramagnetic metals used to enhance relaxation are toxic when not chelated or coated. This limitation of exogenous MRI contrast to relaxation agents was the status quo until 2000, when Ward and Balaban (1) suggested using exchangeable protons for MRI contrast, which extended the range of possible MR agents to include diamagnetic compounds. They demonstrated the possibility to turn this contrast on and off by using selective radiofrequency (RF) saturation of the protons of interest and named this approach "chemical exchange saturation transfer" or "CEST." Recently, many outstanding reviews (2–11) have been published summarizing the CEST literature with respect to theory and application. To avoid too much repetition, we focus on the basic MR principles underlying CEST (what's in the name) and its similarities to and differences with conventional magnetization transfer contrast [MTC, (12)] used in the clinic, which is based on irradiation of protons in immobile semisolid macromolecules (such as bound proteins, membranes, and myelin). We also critically review many experimental pitfalls underlying the current CEST approach, the interference of competing MT mechanisms (what's not in the name), and some promising approaches that allow the study of exchange transfer without the need for RF saturation.

CEST Mechanism

The underlying principles of CEST imaging are very simple (Fig. 1a): exchangeable solute protons (s) that resonate at a frequency different from the bulk water protons (w) are selectively saturated using RF irradiation.[1] This saturation is subsequently transferred to bulk water when solute protons exchange with water protons (exchange rate k_{sw}) and the water signal becomes slightly attenuated. In view of the low concentration of solute protons (μM to mM range), a single transfer of saturation would be insufficient to show any discernable effect on water protons, the concentration of which is about 110 M. However, because the water pool is much larger than the saturated solute proton pool, each exchanging saturated solute proton is replaced by a nonsaturated water proton, which is then again saturated. If the solute protons have a sufficiently fast exchange rate (residence time in millisecond range) and the saturation time (t_{sat}) is sufficiently long (second range), prolonged irradiation leads to substantial enhancement of this saturation effect, which eventually becomes visible on the water

[1]The Russell H. Morgan Department of Radiology and Radiological Science, Division of MR Research, The Johns Hopkins University School of Medicine, Baltimore, Maryland, USA.

[2]F.M. Kirby Research Center for Functional Brain Imaging, Kennedy Krieger Institute, Baltimore, Maryland, USA.

Grant sponsor: NIH-NCRR; Grant number: P41-RR15241.

*Correspondence to: Peter C. M. van Zijl, Ph.D., Johns Hopkins University School of Medicine, Dept. of Radiology, 217 Traylor Bldg, 720 Rutland Ave., Baltimore, MD 21205. E-mail: pvanzijl@mri.jhu.edu

Received 22 September 2010; revised 1 November 2010; accepted 24 November 2010.

DOI 10.1002/mrm.22761
Published online 17 February 2011 in Wiley Online Library (wileyonlinelibrary.com).

© 2011 Wiley-Liss, Inc.

[1]RF saturation refers to equilibrating the populations of the proton energy levels, which is difficult to achieve fully for times $< 5T_1$. Often, only partial saturation can be achieved, especially when exchange rates are fast (see theory section for saturation efficiency).

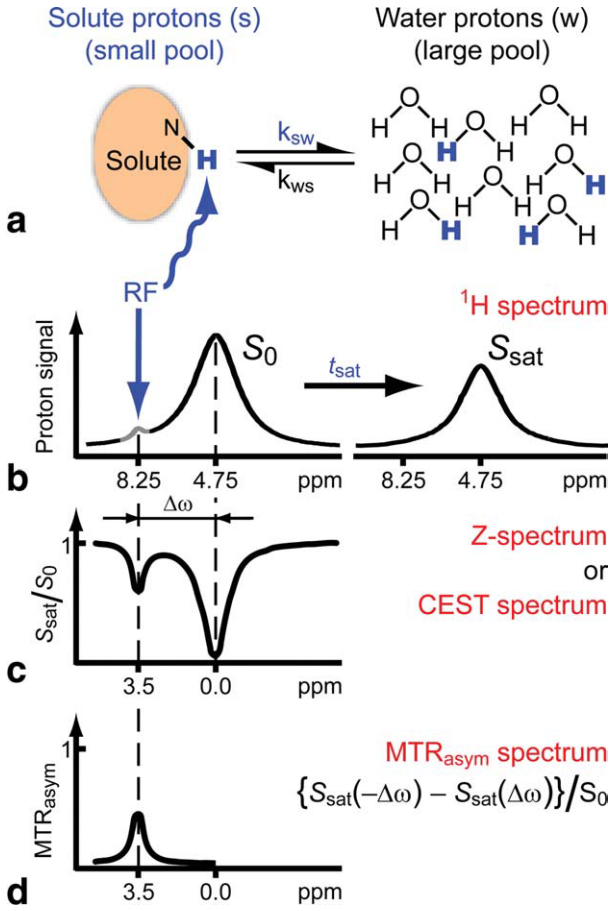


FIG. 1. Chemical exchange saturation transfer (CEST): principles and measurement approach for pure exchange effects. **a, b:** Solute protons (blue) are saturated at their specific resonance frequency in the proton spectrum (here 8.25 ppm for amide protons). This saturation is transferred to water (4.75 ppm) at exchange rate k_{sw} and nonsaturated protons (black) return. After a period (t_{sat}), this effect becomes visible on the water signal (b, right). **c:** Measurement of normalized water saturation (S_{sat}/S_0) as a function of irradiation frequency, generating a so-called Z-spectrum (or CEST spectrum or MT spectrum). When irradiating the water protons at 4.75 ppm, the signal disappears due to direct (water) saturation (DS). This frequency is assigned to 0 ppm in Z-spectra. At short saturation times, only this direct saturation is apparent. At longer t_{sat} the CEST effect becomes visible at the frequency of the low-concentration exchangeable solute protons, now assigned to 8.25 − 4.75 = 3.5 ppm in the Z-spectrum. **d:** result of magnetization transfer ratio (MTR = 1 – S_{sat}/S_0) asymmetry analysis of the Z-spectrum with respect to the water frequency to remove the effect of direct saturation. In the remainder of this article we will use the standard NMR chemical shift assignment for water at 4.75 ppm in ^{1}H spectra, while the 0 ppm assignment will be used in Z-spectra. [Color figure can be viewed in the online issue, which is available at wileyonlinelibrary.com.]

signal (Fig. 1b), allowing the presence of low-concentration solutes to be imaged indirectly. These frequency-dependent saturation effects are visualized similar to conventional MT spectra by plotting the water saturation (S_{sat}) normalized by the signal without saturation (S_0) as a function of saturation frequency (Fig. 1c). This gives what has been dubbed a Z-spectrum (13) or CEST spectrum. Such a spectrum is characterized by the symmetric direct saturation (DS) around the water frequency, which has led to assignment of 0 ppm to the water frequency, a feature confusing for basic NMR spectroscopists. This DS may interfere with detection of CEST effects, which is addressed by employing the symmetry of the DS through a so-called MT ratio (MTR) asymmetry analysis (14) with respect to the water frequency (Fig. 1d). Such an analysis inherently assumes independent contributions of solute and water protons, which need not be the case, but it works well as a first approximation. Using the literature definition of MT ratio (MTR = 1 − S_{sat}/S_0), this process is characterized by subtracting right (−Δω) and left (Δω) signal intensity ratios through (14):

$$\begin{aligned} \mathrm{MTR}_{asym}(\Delta\omega) &= \mathrm{MTR}(\Delta\omega) - \mathrm{MTR}(-\Delta\omega) \\ &= S_{sat}(-\Delta\omega)/S_0 - S_{sat}(\Delta\omega)/S_0, \end{aligned} \quad [1]$$

in which Δω is the frequency difference with water. Similar to MT imaging, it has to be realized that this type of quantification is often difficult to reproduce between laboratories because, unless saturation efficiency is 100%, the effect depends on strength of the applied RF field (B_1), generally referred to as power in MR jargon. This can be somewhat ameliorated by taking left/right ratios of the signal attenuation, but doing this complicates quantification in terms of exchange rates and concentrations. Asymmetry analysis also is based on an inherent assumption of symmetry of non-CEST contributions around the water signal, which often is incorrect, especially in vivo but also in vitro.

Theoretical Description and Spectral Features

The CEST effect is generally expressed in terms of a signal reduction (S_{sat}/S_0 or M_s/M_0 for magnetization), which is then converted to MTR$_{asym}$. However, these are experimentally measured quantities that may have multiple effects contributing (see "Signal and Parameter Quantification" section). As most CEST work relates to protons, we will describe the pure exchange transfer effect in a manner normalized per proton using a so-called proton transfer ratio (PTR), which can be compared for all different mechanisms. Thus, if the measured MTR$_{asym}$ would be caused purely by exchange, it would equal PTR. For a complete description of the exchange process that would be valid at any exchange rate, it is necessary to use the Bloch equations (15–23). Using a two-pool exchange model (small solute pool and large water pool, no back exchange of saturated protons) a simple analytical solution providing PTR in the steady state can be derived under the assumption that RF irradiation of the solute pool does not perturb the water pool [i.e., no spillover (18,23)]:

$$\mathrm{PTR} = x_s \cdot \alpha \cdot k_{sw} \cdot T_{1w}\left(1 - e^{-t_{sat}/T_{1w}}\right), \quad [2]$$

in which

$$x_s = \frac{[\text{exchangeable proton}]}{[\text{water proton}]} = \frac{k_{ws}}{k_{sw}}. \quad [3]$$

Square brackets indicate concentration. Thus, the measured CEST effect increases with the fractional concentration of the solute protons x_s, the saturation efficiency α, and the exchange rate k_{sw}, while being counteracted by the longitudinal relaxation rate ($1/T_{1w}$) of water. It

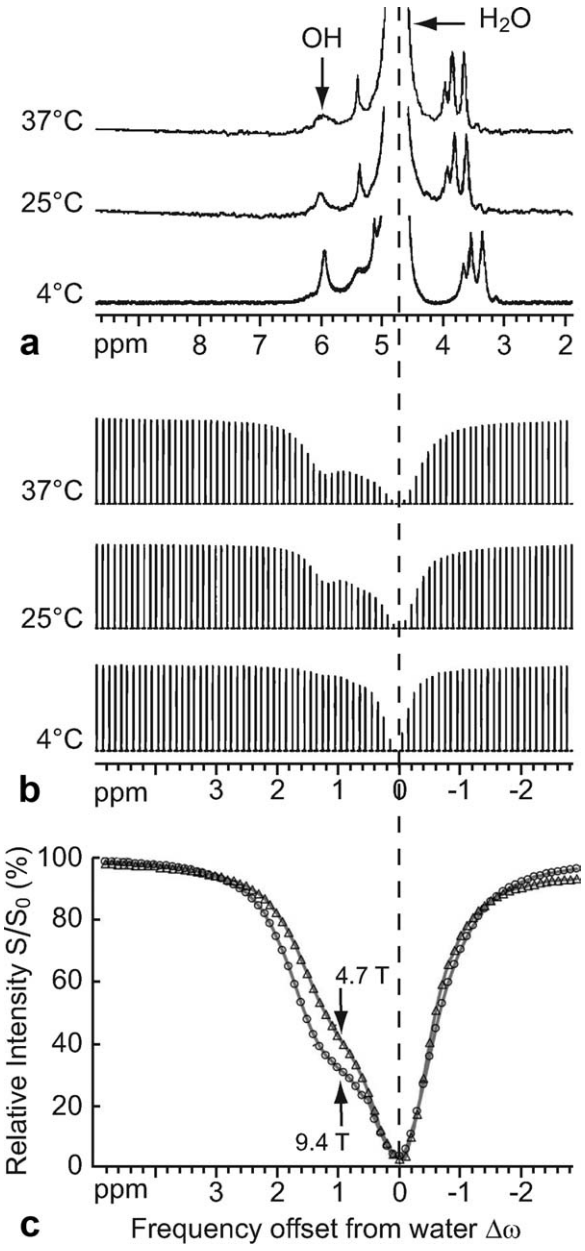


FIG. 2. Effect of exchange regime on proton spectra versus CEST spectra for a solution of 200 mM glycogen. **a:** ^{1}H NMR spectra acquired at 9.4 T in unbuffered H_2O (pH = 7) as a function of temperature. The OH resonances at 1.2 ppm and 0.7 ppm (2:1 ratio) from water broaden at higher temperature, where exchange is faster. **b:** The corresponding CEST-spectra show increased glycogen detectability at higher temperature. **c:** CEST-spectra in PBS buffer (37°C, pH = 7.4) acquired at 9.4 T and 4.7 T using t_{sat} = 10 s, B_1 = 1.9 μT. Notice the better definition of the CEST effect at higher field due to the increased chemical shift difference with water. Reproduced with permission from van Zijl et al., Proc Natl Acad Sci USA 2007;104:4359–4364.

should be pointed out that T_{1w} is the T_1 of water measured without saturation, because, similar to most MR relaxation parameters, measurement of T_1 may depend on the pulse sequence used. For instance, when tissue T_1 is determined using saturation ($T_{1w,sat}$) it will appear different from T_{1w} because there are contributions from exchange. The CEST effect is expected to increase at higher field, because T_{1w} increases with field strength, allowing prolonged storage of saturation in the water pool. However, the two T_{1w} terms counteract each other and, for constant t_{sat}, the expected increase is only about 8% from 1.5 to 3 T and 9% from 3 to 7 T, which may not be worth the trouble in view of the large increases in power deposition with the square of the field. The main advantage at high field is the frequency separation in terms of better adherence to the slow-exchange condition and reduced interference of direct water saturation, which will be discussed later.

For mobile solutes, neglecting transverse relaxation, the saturation efficiency can be approximated by (18,23,24):

$$\alpha \approx \frac{(\gamma B_1)^2}{(\gamma B_1)^2 + (k_{sw})^2}. \quad [4]$$

Therefore, rapidly exchangeable protons can only be saturated efficiently by applying more RF power, which is disadvantageous in vivo due to specific absorption rate (SAR) requirements. This situation is still favorable when studying the amide protons in the peptide bonds of small tissue proteins and peptides, as they exchange with a rate of about 29 Hz (23,25), for which a typical irradiation field (B_1) of 1 μT (γB_1 = 267.5 rad s^{-1}) on a human scanner leads to α = 0.99. However, for contrast agents studied at low concentration, where high exchange rates are needed to visualize any effect, or for the rapidly exchanging water molecules in paramagnetic (paraCEST) agents, power deposition may become a problem when using continuous saturation.

The need to selectively saturate the solute protons appears to require the condition of slow exchange ($\Delta\omega >> k_{sw}$) on the MR time scale to be fulfilled. CEST technology definitely becomes more applicable at higher magnetic fields as the shift difference in Hz increases proportional to field strength. Compared to conventional NMR, however, the CEST approach has a great advantage in that it is not a requirement for the exchangeable proton resonance of interest to be clearly visible in the NMR spectrum to allow detection via saturation transfer. This principle is illustrated in Fig. 2 for glycogen at a field of 9.4 T. Glycogen is a glucose polymer that is highly abundant in liver and muscle, and contains multiple OH groups resonating in the range of 0.5–1.5 ppm ($\Delta\omega$ = 630–1890 rad s^{-1}) from water. Exchange is intermediate on the MR time scale at this field strength and, due to excessive broadening, the hydroxyl protons are not visible in a standard proton spectrum under buffered physiological conditions (pH ~ 7.1–7.3; temperature ~ 37°C). However, in water without buffer, NMR detection is possible. Figure 2a shows high-resolution ^{1}H NMR spectra of glycogen (200 mM concentration per glucose unit) in water as a function of temperature with resonances at 0.7 and 1.2 ppm downfield from water, assigned to the two OH ring protons (C2, C3) and the CH_2OH sidegroup (C6), respectively (26). The linewidth of the —OH resonance at 1.2 ppm gradually broadens when increasing the temperature from 4 to 37 °C, characteristic of —OH protons in relatively slow exchange with free water protons. Interestingly, while the temperature-based increase in —OH exchange rate reduces

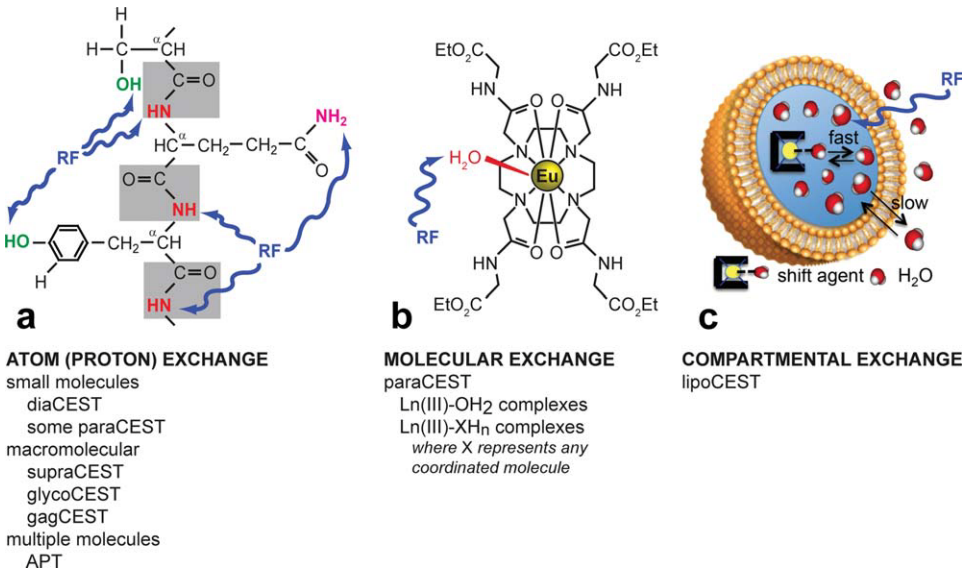


FIG. 3. Classification of CEST contrast based on exchange type. **a:** Proton exchange: magnetic labeling of exchangeable protons, which is the case for most diamagnetic CEST (DIACEST) compounds reported until now and several paramagnetic (PARACEST) agents. As an example, hydroxyl, amide and amine protons in a peptide are shown. SupraCEST relates to paramagnetic agents that are coordinated to macromolecular units in which the exchangeable side group protons are studied (113). **b:** Molecular exchange: magnetic labeling of exchangeable molecules, in this case a water molecule coordinated to Europium in a PARACEST agent. For these agents, the molecular exchange rate is generally faster than the proton–proton exchange rate (Courtesy of Dr. Mark Woods, Portland State University, Portland). **c:** Compartmental exchange: Magnetic labeling of compartmentalized water molecules in a fast-exchange environment resulting in a single average resonance frequency for compartmental water that is different from bulk water. This shift can be induced by either a paramagnetic or diamagnetic agent locked into the compartment or by changing the shape of the compartment to induce a bulk magnetic susceptibility (BMS) anisotropy. The shift difference allows selective irradiation of the compartmental pool. Due to the large size of the irradiated water pool and the fact that the effect spreads beyond the liposome, giga-size enhancements can be induced (Table 1). [Color figure can be viewed in the online issue, which is available at wileyonlinelibrary.com.]

visibility in the proton NMR spectra (Fig. 2a), the detection sensitivity is enhanced in the CEST-spectra (Fig. 2b) due to the dependency of the CEST effect on the proton exchange rate (Eq. 2). When using a glycogen solution in PBS buffer at physiological pH, the exchange rate increases dramatically, but CEST effects are still visible in the Z-spectra (Fig. 2c), indicating that sufficient saturation can be achieved within the brief lifetime of the hydroxyl protons on the glycogen. As expected, the detectability reduces at lower magnetic field (Fig. 2c).

CEST Classifications and Proton Transfer Efficiencies

CEST constitutes a powerful sensitivity enhancement mechanism in which low concentration solutes can be visualized through the water signal. The enhancement depends on the agent proton concentration (Eq. 2) and the rate of exchange (Eqs. 2 and 3), allowing the specific design of agents, constructs, and MRI pulse sequences to optimize the contrast based on these two parameters. CEST is therefore inherently suitable as a molecular and cellular imaging approach and can employ both paramagnetic (2,27–30) and diamagnetic species (1,24,25,31–33), which has led to the nomenclature of paraCEST (2) and diaCEST (4), respectively. This useful classification relates mostly to the size of the chemical shift difference with water, which can be enlarged tremendously when using paramagnetic shift agents, thereby allowing much higher exchange rates to be used while still adhering to the slow-intermediate MR exchange regime. For diaCEST compounds the range is generally 0–7 ppm from water (hydroxy, amine, amide, and imino groups), but this can be extended to 18 or 19 ppm through hydrogen bonding. With respect to nomenclature, early classifications have been made in terms of molecular size, endogenous occurrence and type of molecular construct (10,11). In addition, many approaches have been named specifically for the proton, molecule, or mechanism involved by adding CEST to the name, e.g., glycoCEST for glycogen (26), gagCEST for glycosaminoglycans (34), lipoCEST for liposomes (35). However, there is overlap between the classes as both macromolecular and liposome applications exist for paraCEST and diaCEST agents and many of the same approaches can be applied to either group. An additional issue is that saturation transfer is only one of many possible magnetic label-transfer approaches [see below, (36)] and that the "CEST" nomenclature for the agents is technically incorrect. Here we propose a classification based on the exchange mechanism (Fig. 3), namely atom (proton) exchange, molecular exchange, and compartmental exchange. This is valid for multiple nuclei [e.g., including Xe in hyperCEST (37)], but we will use proton terminology as this dominates the field (>99%). The proton transfer enhancements (PTE) attainable for these classes can be found from the product of the number of contributing exchangeable protons (N_E) per contrast agent (CA), the exchange rate that determines the effect (slowest if there are more than one), and

Table 1
Approximate Ranges for Exchange Rate, Proton Transfer Efficiency (PTE, Eq. 5) and Proton Transfer Ratio (PTR, Eq. 9) of Selected CEST Contrast Agents at Specified Solute Concentrations

	k_{sw}-range (s^{-1})	Functional group	Molecular unit	N_E	PTE/100[a]	[solute] μM	PTR (%)[a]
Proton exchange	10–30[b]	NH (APT)	Multiple unknown amino acids	5.5[c]	0.348–1.04	72,000	2.25–6.75
	20–1200[d]	NH	L-Lysine	7.8[e]	0.988–14.8	100	0.01–0.65[e]
	500–10,000[f]	NH_2	L-Arginine	23.0[e]	72.7–1453	100	0.65–13.1[e]
	500–10,000[f]	OH	Glucose	33.3[e]	105–2107	100	0.95–18.9[e]
	2000–8000[g]	Imino proton	Polyuridylic acid	3.1[e]	3.93–58.9	100	0.04–0.53[e]
Molecular exchange	2000–10,000[h,i]	Bound water	Eu-DOTA-4AmCE	4.0[j]	50.6–12,642	100	0.45–2.27[j]
Compartmental exchange	10–250[k]	Liposomal water	H_2O in 100 nm liposome; R(inner) = 95 nm[k]	240,000[l]	15,147–378,665	0.25	0.34–8.51[l]

[a]For $\alpha = 1$, $T_{1w} = 1$ s, $t_{sat} = 1$ s.
[b]Ref. 25.
[c]Average effect based on in vivo effect size for composite resonance at 3.5 ppm from water (23,25).
[l]Ref. 18.
[e]Per kDa (Eq. 6)
[f]Ref. 39.
[g]Ref. 24.
[h]Maximum rate is really 500,000, but only up to 10,000 included here because of saturation efficiency limits.
[i]Ref. 40.
[j]Per kDa (Eq. 7).
[k]Ref. 38.
[l]Per compartment (Eq. 8).

the attainable saturation efficiency at a power level reasonable for in vivo human and animal experiments. Thus, one has

$$\mathrm{PTE} = N_E \cdot \alpha \cdot k_{sw} \cdot T_{1w}\left(1 - e^{-t_{sat}/T_{1w}}\right), \quad [5]$$

in which

$$N_E = N_{CA} \cdot M_{CA} \quad \text{for proton exchange,} \quad [6]$$

$$N_E = C_m \cdot N_m \cdot M_{CA} \quad \text{for molecular exchange,} \quad [7]$$

$$N_E = 2 \cdot N_A \cdot [H_2O] \cdot V_{comp} \quad \text{for compartmental exchange.} \quad [8]$$

N_{CA} is the number of exchangeable nuclei (generally protons) per kiloDalton (kDa), M_{CA} the molecular weight in kDa of the contrast agent, C_m is the number of molecules coordinated per kDa, and N_m the number of protons in the coordinated molecule; N_A is Avogadro's number (6.0×10^{23} molecules $mole^{-1}$), $[H_2O]$ the water concentration (55.6 M) and V_{comp} the compartmental volume in liters. For a spherical liposome with internal radius R, V_{comp} would be $4\pi R^3/3$. The exchange rate for a liposome depends on the permeability, size, and membrane constituents of the particle (6,7,38). With respect to the classification, it may at first seem as if proton and molecular exchange are the same. But this is not true. In proton exchange, the protons are labeled and the individual exchange rate of the protons determines the PTE. For molecular exchange, contrast depends first on the lifetime of the coordinating molecule on the agent and subsequently on the exchange rate of the proton on the coordinated molecule. If the coordinated molecule is water, this cannot be distinguished from proton exchange, but it can be if it is any other molecule (e.g., a bound alcohol) containing its own exchangeable protons. In that case, the slowest of the two exchange steps towards water protons needs to be used for k_{sw} in Eq. 5, while the rate for the faster step determines the labeling efficiency in Eq. 4. The recent hyperCEST approach (37), employing exchange between nonlabeled and hyperpolarized Xe molecules can fall in either of the classes and a XTE (Xenon Transfer enhancement) can be calculated. For this review we focus only on protons.

Each of the three classes has distinctive advantages and disadvantages. Efficiency seems to depend predominantly on the exchange rate and the number of exchangeable protons per molecule or particle, but this can be misleading. With respect to the exchange rate, it should clear from Eq. 4 that an increased exchange rate will reduce saturation efficiency unless high B_1 can be used, which may not be the case in humans due to SAR restrictions and amplifier duty cycle limitations. In general, it is fair to say that for a contemporary high-end clinical field strength of 3 T, RF irradiation for a period of a second will be limited to powers less than 10–20 μT for the head coil and about 2–3 μT for the body coil. At 7 T these limitations will be more severe because the power deposition increases with the square of the field strength. In Fig. 4a, we evaluate α for the range of exchange rates covering all contrast mechanisms and a power range from 0.1 to 10 μT. It can be seen that the molecular exchange agents as well as rapidly exchanging OH, imino and amino groups for proton exchange compounds (Table 1) have low saturation efficiencies, while amide protons and compartmental exchange particles seem to be in the perfect k_{sw} range of 10–250 Hz. A more balanced view of the competition between saturation efficiency and the exchange rate can be obtained by plotting

the product $\alpha \cdot k_{sw}$ (Fig. 4b) versus k_{sw}, showing very acceptable performance of the high-rate compounds at 2 μT and already an order of magnitude higher effect at the still reasonable power level of 5 μT. Thus, it should be possible to study some of the slower exchanging paraCEST agents in humans. In addition, future developments in chemistry may allow reductions in the exchange rate (5,41). The parameter N_E should be optimized in terms of the number of exchangeable protons per molecule or compartment (denoted "solute" for convenience), because this will lower the concentration needed to see a measurable effect. For pure exchange, the PTE is related to the measured signal change and the PTR through:

$$1 - S_{sat}(\Delta\omega)/S_0 = \mathrm{PTR} = \frac{[\mathrm{solute}] \cdot \mathrm{PTE}}{2[H_2O]}. \quad [9]$$

One type of comparison between different agents can be made by calculating the solute concentration needed to achieve a 5% effect under typical in vivo conditions in humans. This is shown in Table 1 and plotted on a log scale in Fig. 4c. It can be seen that lipoCEST has by far the best return per unit and requires little power. APT requires little power and has the benefit of a high concentration of total amide protons, allowing detection in vivo in animals and humans. For the other compounds, higher power is needed, but all of them can be detected at concentrations that should be achievable in vivo. Again, Fig. 4 and Table 1 should be seen as providing only rough guidelines as it is difficult to compare the different groups directly, because there is no normalization to the same solute volume. Also, different compounds vary in toxicity and some may allow only very low concentrations. So each approach and solute has to be evaluated on an individual basis. Toxicity studies will have to point out which ones will be most suitable as contrast agents, with natural compounds such as sugars and proteins probably having the edge in humans. On the other hand, paramagnetic agents may allow the detection of smaller and/or more specific effects in animal models, leading to new discoveries.

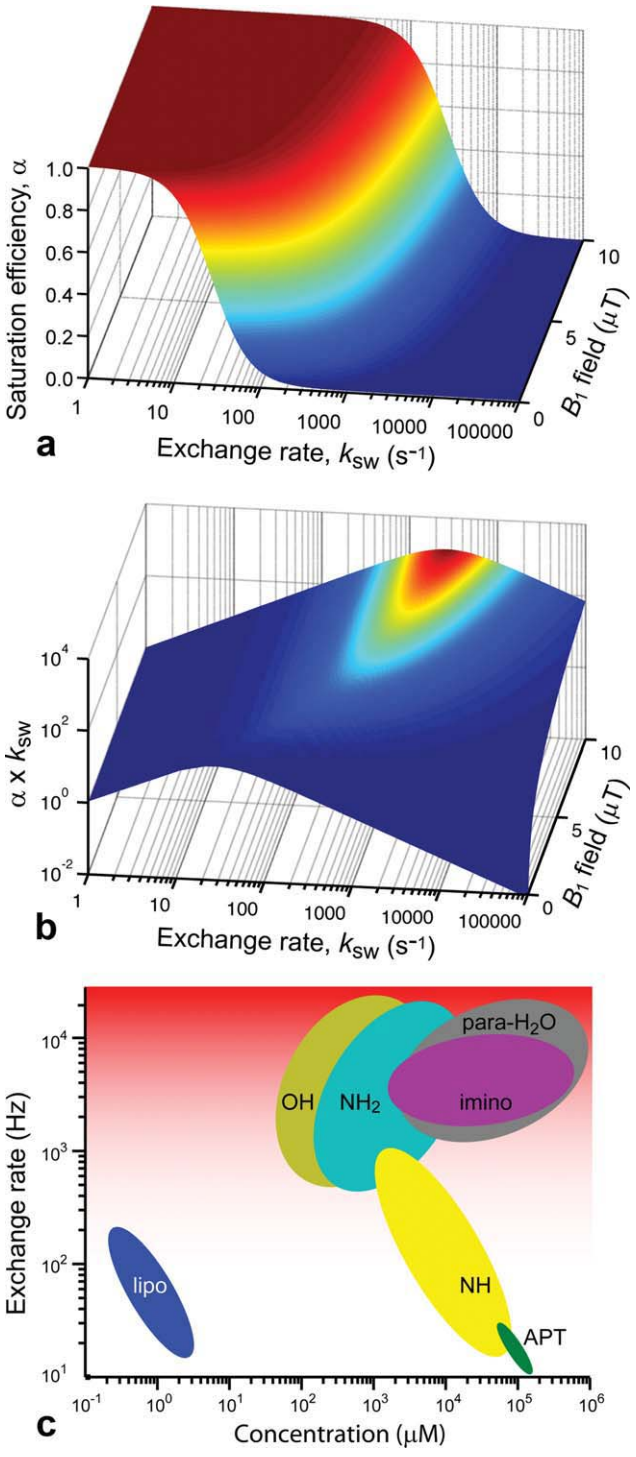


FIG. 4. Factors affecting detectability for the main classes of CEST agents. **a:** Effects of exchange rate (log plot) and RF field B_1 on the saturation efficiency (Eq. 4) for the B_1 range typically used on clinical scanners for SAR-compatible saturation experiments. Saturation transfer efficiency reduces with increased exchange rate, which can only be overcome by increasing B_1. **b:** Dependence of the product of saturation transfer efficiency and exchange rate on k_{sw} and B_1, showing that the increase in rate sufficiently compensates for the lost efficiency at clinically reasonable power levels. **c:** Log-plot of concentrations needed to achieve a 5% CEST effect for the different groups of agents. Notice that the curves for proton exchange and molecular exchange agents are affected by molecular size, while the compartmental exchange curve depends on particle radius, affecting both exchange rate and number of protons. Also, it is important to realize that paraCEST agents can be found in all three classes and water is normally the solvent, which is why we used para-H_2O to indicate molecular exchange. Graph is only approximate and meant to provide rough guideline. [Color figure can be viewed in the online issue, which is available at wileyonlinelibrary.com.]

Exchange and Cross-Relaxation in Liquids and Semisolids

The previous sections discussed the pure CEST mechanism (what's in the name). However, exchange is only one of several possible types of MT pathways that may contribute to saturation transfer experiments. It is well known from basic NMR (42–44) that chemical exchange and dipolar cross-relaxation pathways are active together in most MT experiments and difficult to separate completely. The relative contributions of these pathways may

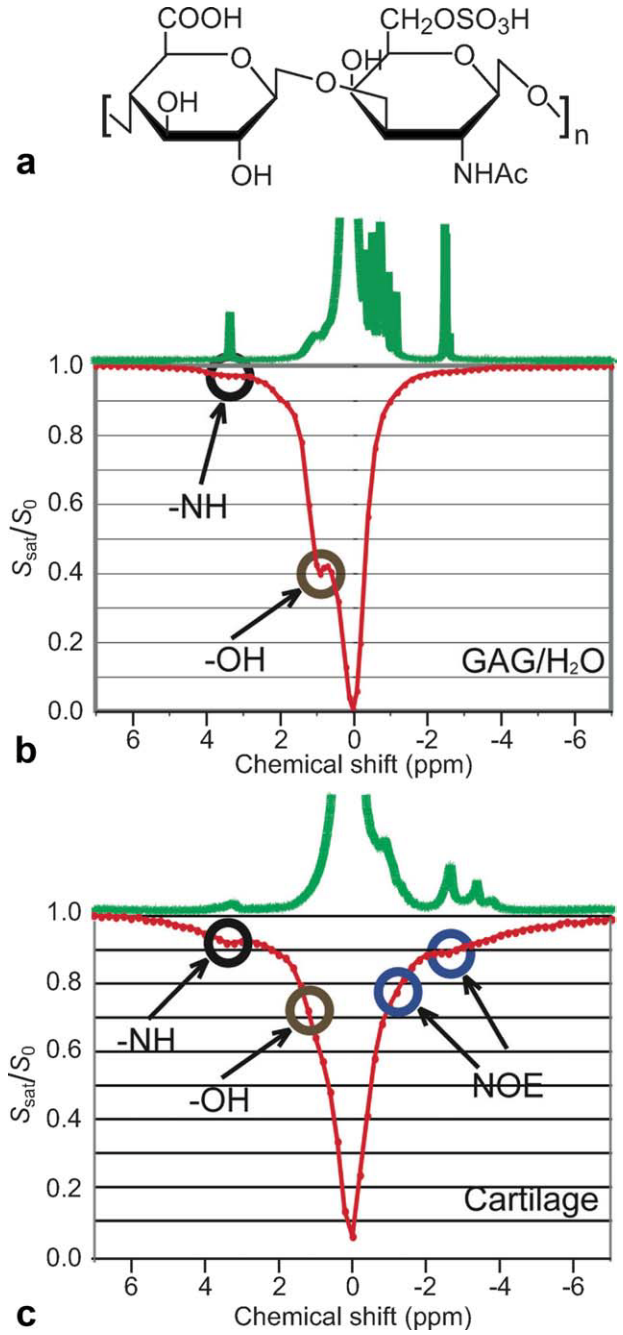


FIG. 5. Z-spectra for glycosaminoglycans (gags) in solution and in cartilage showing CEST and cross-relaxation effects (PBS, 11.7 T, t_{sat} = 4 s, 2.35 μT, 37°C). **a:** structure of gag-unit, showing three OH groups, an amide proton and several aliphatic protons in the ring (CH) and the *N*-Acetyl side chain. **b:** Z-spectra of 125 mM gag units in solution, showing predominantly NH and OH exchange saturation transfer effects. **c:** Z-spectra of cartilage from bovine patella in PBS buffer showing exchange and much increased cross-relaxation [nuclear Overhauser enhancement (NOE)] effects. Reproduced with permission from Ling et al., Proc Natl Acad Sci USA 2008;105:2266–2270. [Color figure can be viewed in the online issue, which is available at wileyonlinelibrary.com.]

vary with the type of excitation scheme used and depend on the molecular mobility and conformation, which will affect dipolar transfer efficiency and water accessibility, respectively. A beautiful example of the simultaneous occurrence of these effects is present in the work by Ling et al. (34,45), who studied glycosaminoglycan (gag) molecular units (Fig. 5a) in solution and in tissue. In solution, the exchangeable OH and NH groups show clear CEST effects at the hydroxyl and amide proton frequencies (Fig. 5b), while only a small saturation effect is visible upfield (i.e., at lower frequency) from water. In tissue, this upfield effect increases dramatically, even showing somewhat distinct effects at −1.0 and −2.6 ppm, corresponding to the CH and *N*-acetyl residues in gag. The origin of these effects was somewhat uncertain and the occurrence of nuclear Overhauser enhancement (NOE) effects, a type of cross-relaxation, between the side groups and water was suggested as a possible source.

The discovery of upfield saturation phenomena is important, both as a possible new source of MRI contrast as well as a possible nuisance with respect to performing the MTR asymmetry analysis used commonly in CEST experiments (Fig. 1, Eq. 1). To get a better understanding of the competing MT processes in medium sized macromolecules, it is possible to study the inverse effect through direct magnetic labeling of water molecules using saturation or inversion and to measure the effect on the proton spectrum as a function of time. This so-called Water-EXchange filter (WEX) experiment has been done for macromolecules in solution (46–48) as well as on perfused cancer cells and in vivo in the brain (49,50). Figure 6a shows the transfer mechanisms that are active after inversion labeling of water. In addition to direct proton exchange, there are exchange-relayed intramolecular NOEs, in which inversion is transferred from water to the molecule through rapidly exchangeable groups (mainly OH and NH_2, but also NH) and subsequently to the backbone aliphatic protons. In this particular experiment, a second cross-relaxation effect (direct intramolecular NOE) occurs because of simultaneous inversion of the C(α)-H protons that resonate close to the water frequency. The exchange-relayed NOEs and intramolecular NOEs build up slower than the proton exchange, which is illustrated for perfused cancer cells in Fig. 6b, where the NH proton intensities at 8.3 ppm (corresponding to about +3.5 ppm in a CEST spectrum) increase rapidly with time, followed by a slower rise of the aliphatic signals. The sign of the NOE effects is the same as for the exchange effects (in-phase), which is typical for intramolecular NOE effects in larger macromolecules in the slow rotational correlation time limit of the extreme narrowing regime. A similar effect can be demonstrated in brain (Fig. 6c), reflecting the presence of mobile macromolecules for which the proton transverse relaxation times are sufficiently long to allow observation in the NMR spectrum. In MTC and CEST experiments, where saturation is transferred to water, the opposite processes are involved. For mobile macromolecules this would lead to exchange-relayed transfer of saturation from the aliphatic protons to water. Notice that, in principle, intermolecular NOEs between bound water molecules and the solutes could also occur, but, for mobile macromolecules, these generally occur on a time scale much slower than exchange-relayed NOEs (46,51). For MTC studies, on the contrary, the motional limit is sufficiently slow for efficient intermolecular NOE transfer with bound water,

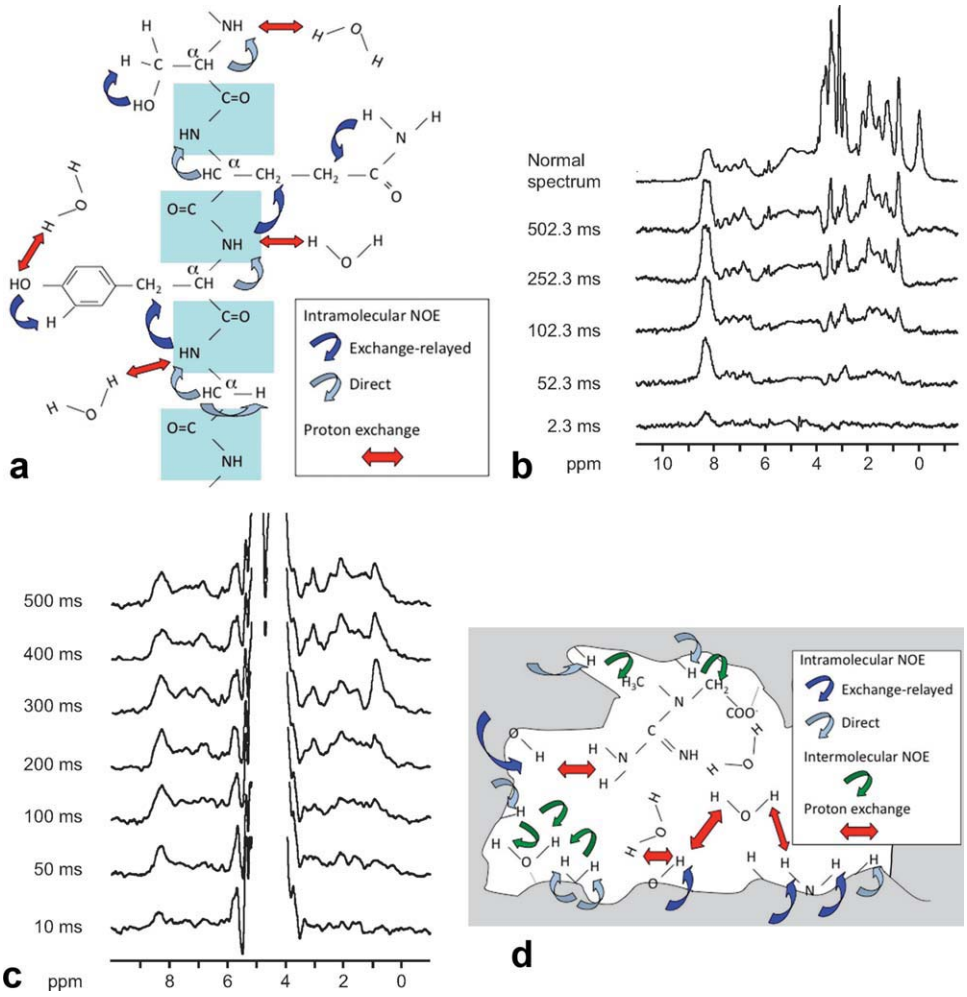


FIG. 6. Illustration of magnetization transfer pathways in proteins. **a:** Possible pathways in a mobile protein during a water exchange (WEX) experiment consisting of selective magnetic labeling (inversion) of bulk water (inverse of CEST/MT approaches) followed by a waiting period. Chemical exchange (red) and cross relaxation (blue) occur, the latter either exchange-relayed or through direct excitation of C(α) protons. These pathways are seen in cancer cells (**b**) as well as rat brain (**c**), showing fast buildup of exchangeable proton signals (especially amide protons at 8.25 ppm) as a function of time after inversion followed by gradual transfer to aliphatic protons through intramolecular NOEs. **d:** Transfer processes occurring during an MTC experiment. The semisolid matrix, where fast intramolecular dipolar transfer occurs, is indicated in grey. Contrary to mobile proteins, the effects of both exchange and intermolecular NOEs with bound water can be substantial. Reproduced with permission from van Zijl et al., Magn Reson Med 2003;49:440–449. [Color figure can be viewed in the online issue, which is available at wileyonlinelibrary.com.]

which occurs together with exchange-relayed transfer (Fig. 6d). Here, the exact proportions of these contributions are still under debate. Within the semisolid lattice itself, all saturation is efficiently transferred through spin diffusion (fast through-space dipolar transfer), which can subsequently be transferred to water though the mentioned processes.

In the presence of multiple molecular systems, such as in cells and tissue, all of the above phenomena take place, complicating the data interpretation. In addition, the simultaneous occurrence of multiple transfer effects invalidates the two-compartment assumption for CEST quantification. In Fig. 7a, the in vivo Z-spectra of several brain regions are shown for a rat with an implanted brain tumor. For the multipulse sequence used there are large MTC effects on which the smaller CEST effects should be superimposed. When trying to extract the CEST effects using MTR asymmetry analysis (Fig. 7b), a clear residual asymmetry is found that has been attributed to MTC effects that are not centered around the water frequency (52–54). Fortunately, most of this MTC asymmetry can be removed through comparison with normal tissue (Fig. 7c), which is assumed to display only the inherent asymmetry reflecting the CEST PTR. Interestingly, this remaining PTR difference shows several percent increase for the tumor while a negligible change is found for edematous areas, indicating the possible separation of these two regions for clinical application. Similar competition between MTC and CEST effects can be seen in a rat model of cerebral ischemia (Figs. 7d–f). Contrary to brain tumors though, a comparison with normal tissue shows a reduction in PTR.

Based on the likely origin of this effect in the exchangeable amide protons of mobile tissue proteins and peptides ((25,49,50), Fig. 6c), this contrast was dubbed Amide Proton Transfer (APT) MRI. In addition

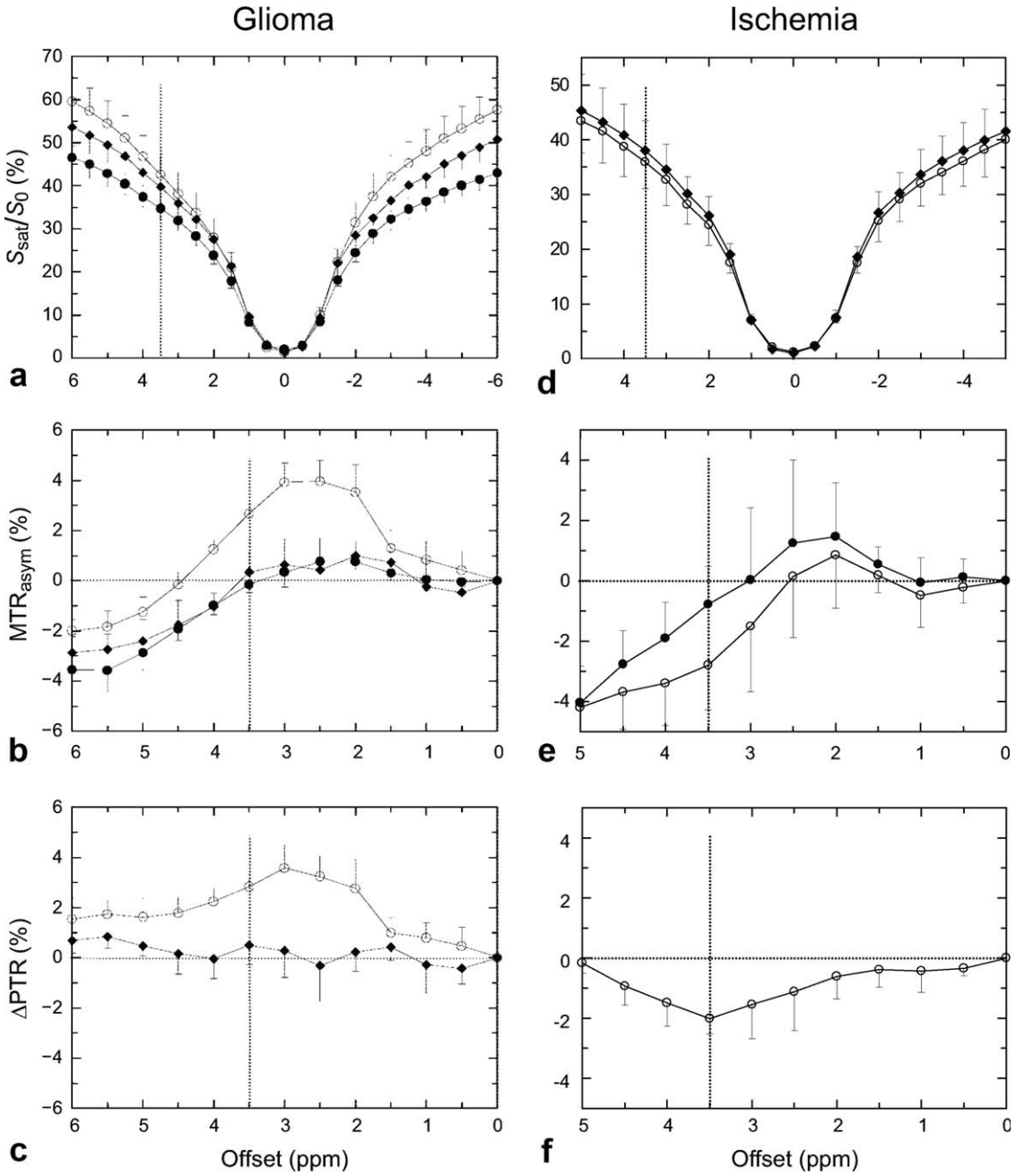


FIG. 7. Effect of MTC on Z-spectra and CEST data analysis for 9L glioma (**a–c**) and ischemia (**d–f**) in rat brain (Multipulse saturation: 400 gaussian 180° pulses, 4.7 T, $t_{sat} = 4$ s, $B_1 = 1.2$ μT). Solid circle: contralateral brain; diamond: peritumoral tissue (a–c); open circle: tumor (a–c) or ischemic lesion (d–f). Signal attenuation in Z-spectra (a, d) is due mainly to direct water saturation close to the water frequency and a large MTC effect (40 to 60%) over the whole spectral range. The MTC contribution is reduced for edema and tumor (a), indicating a higher water content for these tissues. The Z-spectra are slightly asymmetric, which becomes visible when performing asymmetry analysis (b, e). Both exchange effects and asymmetry in the MTC contribute to the residual curve, with the latter reflected in a relatively constant negative MTR_{asym} (2–3%) at offsets above 5 ppm. The PTR for tissue changes can be estimated by comparing lesion with normal brain, removing most of the MTC effects (c, f). This shows that edematous regions can be separated from tumor (c) and ischemia from normal brain (f). The positive (c) and negative (f) PTR differences were attributed to increases in protein content and reduced pH, respectively. Reproduced with permission from Zhou et al., Magn Reson Med 2003;50:1120–1126 (a–c) and Nat Med 2003;9:1085–1090 (d–f).

to the maximum APT effect at around 3.5 ppm from water, it seems likely that multiple exchangeable groups contribute as the effect ranges over offsets from about 1–6 ppm from water. The APT in tumors is positive (Fig. 7c), while an opposite effect is found in acute ischemia (Fig. 7f). The explanation for the difference follows from the contributions in Eq. 2. During acute ischemia brain pH reduces, thereby reducing the amide proton exchange rate (44,55), while amide proton content remains approximately constant, which could be shown with WEX

spectroscopy (25). The tumor, on the other hand, has increased cellular amide proton content (see Fig. 6b as illustrative example for another tumor type) compared to normal brain, while intracellular pH (not extracellular) is known to remain approximately constant (56,57). In the acute ischemia study (25), ΔPTR was also calculated over a range from 0 to 15 ppm from water by comparing ischemic brain with normal. The result showed removal of the asymmetry in MTC, leaving only a negative effect over the range from about 1–6 ppm downfield from water, in line with the expected exchangeable amide proton range in the NMR spectrum.

In summary, saturation transfer studies in vivo are affected by exchange, exchange-relayed NOEs, and intermolecular NOEs (semisolid components). Depending on the materials studied or the pulse sequence parameters used, the relative contributions of each of these mechanisms may vary. For instance, paraCEST agents and other compounds with very rapidly exchanging protons will predominantly show CEST-based MTR asymmetries, while macromolecular proton exchange species may show NOE effects. Increasing the power of the saturation field will increase the MTC contribution, which may negate the slower mobile protein NOE effects and vice versa. This sensitivity to multiple mechanisms and to pulse sequence parameters complicates comparison of MTC and CEST studies between laboratories. It has been a bottleneck for clinical trials studying the use of MTC as a biomarker and will no doubt affect such efforts for CEST studies. However, this multifaceted character also opens up opportunities to assess different cellular components and different transfer processes by varying MRI parameters, which is the topic of the next section.

Pulse Sequences for Studying Exchange Effects

CEST labeling is very similar to MTC labeling in that a pulse sequence is applied to measure the presence of a small pool indirectly via the solvent, which can be done by saturating the small pool and allowing magnetization to transfer between the pools. For MTC, this has led to a range of approaches [for some reviews, (58–64)] employing both on-resonance and off-resonance saturation. In the classical continuous saturation, long (several seconds) low power off-resonance RF irradiation is used with the goal of equilibrating the populations of the two quantum states of the semisolid protons. While doing so, partial saturation is transferred continuously to bulk water. Alternatively, one can apply a series of frequency-selective off-resonance pulses for saturation using higher-power pulses of medium length (millisecond to tens of milliseconds) spaced by ms-length time intervals. This is repeated continuously to build up and maintain a saturation steady state (62–67), which can be done in a multistep preparation as well as in single steps between different k-space acquisitions, for instance when using 3D imaging. The most sensitive approach to reduce the water signal through MT is using multistep on-resonance "saturation" (64). The quotation marks are added to stress that this is not saturation in the classical sense of population equilibration, but rather randomization of magnetization through dephasing. In these experiments the bulk water pool is quickly excited and returned to equilibrium, thereby not really affecting free water, which has a long T_2^*. The semisolid pool, however, has a T_2^* (and T_2) on the order of microseconds and rapidly loses coherence due to random dephasing. As a consequence, longitudinal coherence is lost after each excitation flip-back step. Notice the inherent beauty of this powerful scheme is that it has high "saturation" efficiency for the immobile macromolecules since all excited spins are dephased within microseconds. It should be noted that the pulsed off-resonance scheme is a hybrid approach as it has both classical saturation and dephasing contributions. A third type of MTC scheme (68) is to monitor the recovery of the bulk water pool after a nonselective single inversion pulse, which shows bi-exponential behavior due to the interaction with the semisolid pool.

Intuition indicates that CEST effects should be detectable in a manner similar to MTC, and most CEST studies have employed either continuous (Fig. 8a) or pulsed (25,33,69,70) selective off-resonance saturation of the exchangeable protons. Recently, Vinogradov et al. (71,72) have shown that the presence of micromolar concentrations of paraCEST a gents can be detected using an on-resonance pulse scheme in which water signal is continuously undergoing 360° rotations in a WALTZ multipulse scheme compensated for B_1-inhomogeneity. Notice that this on-resonance paramagnetic exchange effects (OPARACHEE) approach differs from the on-resonance MTC schemes in that the small pool is not excited and that, therefore, its frequency does not need to be known. After a series of such pulses, water signal is reduced due to magnetization exchanging from bulk water to the contrast agent, leading to part of the magnetization not experiencing full 360° pulses. This technique, employing a low-power RF train, is suitable for detecting rapidly exchanging units, such as the water molecules in molecular exchange agents and OH and NH_2 groups in proton exchange agents (if their excitation can be avoided). Similar to standard CEST, however, DS of water reduces the sensitivity and complicates quantification. A disadvantage of OPARACHEE is that it cannot distinguish between different agents or chemically different protons, but it may be the most suitable approach for detecting single agents.

Another interesting phenomenon reported recently is that MT effects are enhanced (73) when using intermolecular multiple quantum [iMQC, (74)] excitation schemes. The double quantum (DQ) analogue of this was recently demonstrated for CEST MRI (45,75). Unfortunately, even after enhancement, the iDQC signal to noise ratio (SNR) is still only about 25% of the standard CEST effect, which reduces its applicability in the clinic (75).

When thinking about alternative CEST technology, it is fundamental to realize that saturation is just one type of magnetic labeling and that many other approaches have not yet been explored. Importantly, CEST compounds differ from the semisolid MTC protons in transverse relaxation properties ($T_{2\text{mobile}}^* \gg T_{2\text{solid}}^*$) and average exchange rate [$k_{\text{CEST}} \gg \langle k_{\text{solid}} \rangle$, which is only 4–8 Hz in the brain (76–78)], which opens up a new range of labeling approaches that cannot be applied to MTC. Such methods may inherently provide new opportunities

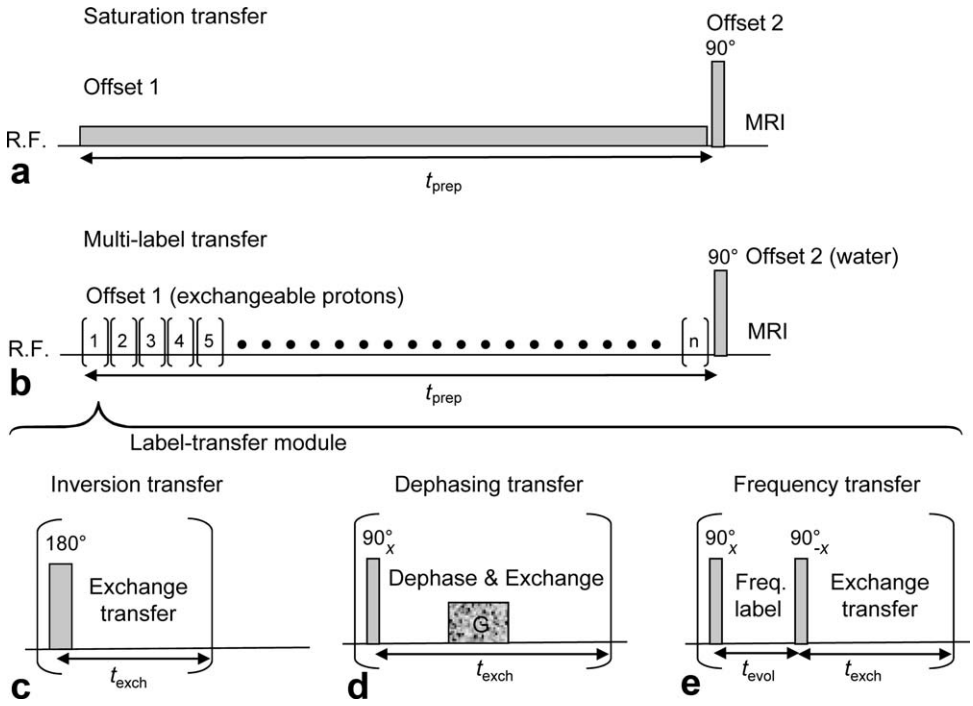


FIG. 8. Possible schemes for exchange transfer MRI. **a:** Standard CEST: protons are labeled through continuous saturation and transferred continuously during labeling. **b:** Exchange transfer using label-transfer modules (LTMs): protons are rapidly labeled through either selective inversion (**c**) or selective excitation followed by a magnetic manipulation (**d, e**). This can be gradient dephasing (**d**) or frequency labeling during an evolution time t_{evol} followed by selective flipback to the *z*-axis (e). After labeling, exchange transfer to water protons occurs during t_{exch}. The label transfer modules, (*n* total), are repeated continuously during preparation period t_{prep} to enhance the effect on bulk water. The water labeling efficiency depends on the exchange rate, which, together with the power deposition limits, determines the number of modules that can be used.

for separating MTC and CEST effects. At first it seems impossible to enhance sensitivity without the continuous saturation labeling that is at the foundation of CEST imaging and even imbedded in its nomenclature. However, building up saturation is actually quite inefficient compared to RF excitation, which can label spins almost instantaneously. Of course, this label exchanges to water, and the process has to be repeated for excitation processes to be able to accomplish enhancements similar to continuous saturation. Recently (36), it was shown that this can be achieved by using a series of so-called label-transfer modules (LTMs), in which exchangeable solute protons are selectively labeled, and subsequently transferred to water (Fig. 8b). Signal amplification occurs because fresh *z*-magnetization is present for the solute protons at the start of each LTM, allowing serial transfer of labeled protons to water when applying multiple (*n*) modules during the preparation time, t_{prep}. This novel principle allows several labeling types to be used, including inversion (Fig. 8c), dephasing (Fig. 8d) and frequency encoding (Fig. 8e). The first two are "saturation-like" approaches in that they reduce the water signal intensity. In the inversion approach, the *z*-magnetization transferred is of sign opposite to the equilibrium water magnetization, and, as such, twice as efficient as continuous saturation, where zero longitudinal magnetization is transferred. The dephasing approach differs from the MTC dephasing approach (employing the short T_2^* of solids) in that protons of interest are excited selectively and that dephasing of transverse magnetization need not be relaxation-based, but can be induced coherently by a pulsed gradient. For very rapid exchange, the dephasing gradient may not be needed as all spins will be transferred to water quickly where they dephase slowly with T_{2w}^*. Frequency labeling (Fig. 8e) has never been used for MTC. It has the potential to extend in vivo MT measurements with high-resolution NMR type multidimensional experiments and high-resolution experiments with the advantage of exchange based sensitivity enhancement through the water signal. The principles of this approach, dubbed frequency-labeled exchange transfer [FLEX, (36)], are explained in Fig. 9 using the example of a mixture of protons of different concentrations and exchange rates.

To get a first impression of the contributions to LTM-based exchange transfer, appropriate two-pool equations can be derived under the assumptions that (i) the length of the labeling module is much shorter than T_1s of water and the exchangeable protons, (ii) the exchange rate is much faster than $1/T_1$ of the exchangeable protons, (iii) there is negligible back exchange from water to agent protons (36):

$$\mathrm{PTR} = x_s \cdot \lambda \cdot A \cdot \left(1 - e^{-k_{sw} \cdot t_{exch}}\right) \cdot \sum_{i=1}^{n} e^{\{-1+(i-1)/n\} t_{prep}/T_{1w}}. \quad [10]$$

Similar to the CEST theory (Eqs. 2 and 3), the expression contains terms for proton fraction, labeling efficiency ($\lambda \cdot A$), exchange transfer efficiency ($1 - e^{-k_{sw} \cdot t_{exch}}$), and water relaxation. The parameter λ describes the LTM excitation efficiency, while $A = 2$ for inversion and $A = 1$ for the

dephasing and FLEX approaches. Notice that exchange transfer efficiency will depend on k_{sw} for inversion and FLEX experiments, but not for dephasing, where the exchange time (t_{exch}) equals t_{prep} for the first LTM and becomes shorter as a function of LTM number. This efficiency term provides capability for exchange filtering. For instance, for rapidly exchanging protons (e.g., $k_{sw} > 2000\ s^{-1}$) one would have 86% efficiency of transfer when using exchange time of 1 ms and 98% for 2 ms. For slower protons (e.g., $k_{sw} \approx 20\ s^{-1}$), these efficiencies would be 2.0% and 3.9%, respectively, and t_{exch} has to be made longer. The summation term reflects that magnetization transferred in the first LTM will experience T_{1w} decay over the full t_{prep}, while that transferred in the nth module will hardly relax.

While CEST, inversion transfer, and dephasing transfer all lead to a signal decrease in the water signal, FLEX detection is different in that the water signal is modulated as a function of evolution time [Fig. 9c, (36)] in a manner depending on the frequency difference between the offset (o1) of the 90_x excitation pulse and the solute resonances ($\Delta\omega_{so1}$). This can be described by a free induction decay (FID):

$$I_{w,tot} = \sum_s PTR_s \cdot e^{-\left(k_{sw}+1/T_{2s}^*\right)\cdot t_{evol}} \cdot \cos(\Delta\omega_{sol} \cdot t_{evol}). \quad [11]$$

Notice that the exponential signal decay term provides the opportunity to remove rapidly decaying components, such as semisolids (short T_2^*), or select different components based on exchange rate. The FLEX approach illustrates the power and beauty of MR where the transfer effect of multiple magnetic species, even though detected through one species (water protons) can still be separated out (Fig. 9). The complete arsenal of techniques for FID analysis is applicable (42,43), including deconvolution techniques such as exponential line-broadening, Lorentzian-Gaussian deconvolution, deconvolution-difference to remove broad components, and especially time domain analysis. The latter is extremely suitable because, when using contrast agents, the presence of only a limited number of components with known frequencies in the FID should allow straightforward interpretation.

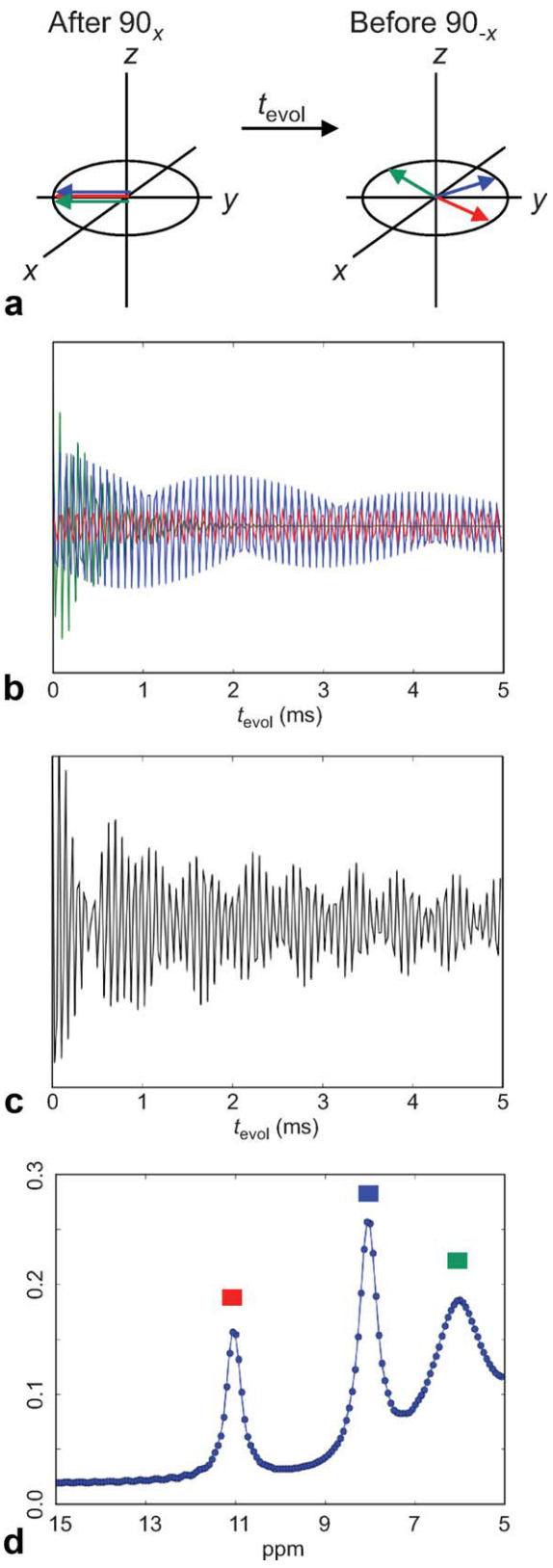


FIG. 9. Principle of frequency labeled exchange transfer (FLEX). A range of frequencies including multiple exchangeable protons is selectively excited (90_x pulse, Fig. 8e), after which chemical shift evolution separates the different frequency components (red, blue, green). Depending on t_{evol}, a different size of magnetization component is flipped back to the z-axis by the 90_{-x} pulse (**a**) and transferred to water protons. When performing a series of acquisitions at different evolution times, a free induction decay (FID) containing the multiple frequency components is obtained (**b**). These components are all part of a single water signal and nondistinguishable (**c**). However, Fourier transform of the convoluted decay can recover a frequency spectrum (**d**), allowing separation of the three different components based on frequency (chemical shift) and exchange rate (peak width). The normal ^{1}H NMR spectral frequencies were used with water assigned to 4.75 ppm. Parameters used in b–d: field of 14.1 T (600 MHz); offset frequency of RF pulse 25 ppm from water; dwell time 25 μs. Signals were green: 20 mM, 6 ppm, $k = 2000$ Hz; blue: 10 mM, 8 ppm, $k = 200$ Hz; red: 5 mM, 11 ppm, $k = 20$ Hz. FID processed using 20 Hz exponential line broadening and zero filling by a factor of four. Courtesy of Josh Friedman, Johns Hopkins University. [Color figure can be viewed in the online issue, which is available at wileyonlinelibrary.com.]

A disadvantage of pulsed approaches is the danger of high power deposition, but this can be avoided by using a sufficiently low average power over the total scan repetition time (TR), which can easily be optimized for each type of coil used. Similar to CEST, inversion and dephasing transfer may require acquisition as a function of frequency and correction for asymmetry with respect to the water signal. FLEX, on the other hand, may be performed without asymmetry analysis, but, similarly to multidimensional experiments, the length of the scan time will depend on the number of points sampled for the FID. The latter can probably be optimized by using sparse sampling schemes in the time domain (79–81), which is the topic of future research.

Signal and Parameter Quantification

Proper quantification requires careful measurement of the CEST effects (uncontaminated and with sufficient SNR), which is far from trivial in view of the many contributions outlined in the previous sections. One universal requirement is to selectively label the protons of interest, which is complicated by "spillover" due to proximity in chemical shift of the solute and water protons for many diaCEST and lipoCEST agents or due to broadening of the DS contribution when using the higher B_1 fields needed for paramagnetic molecular exchange agents and rapidly exchanging proton exchange compounds. In vivo, the effects of MTC, contrast agent (CA) CEST and endogenous (endo) CEST compete and have to be separated out, which cannot be modeled by a two-pool compartment. The theories for three-pool and four-pool systems have been described (16,19,22), but most investigators tend to use a zero-order approach of additive effects:

$$\mathrm{MTR}^{\mathrm{total}} = \mathrm{PTR}^{\mathrm{CA}} + \mathrm{PTR}^{\mathrm{endo}} + \mathrm{MTR}^{\mathrm{MTC}} + \mathrm{DS}, \qquad [12a]$$

and

$$\mathrm{MTR}_{\mathrm{asym}} = \mathrm{PTR}^{\mathrm{CA}} + \mathrm{PTR}^{\mathrm{endo}} + \mathrm{MTR}^{\mathrm{MTC}}_{\mathrm{asym}}. \qquad [12b]$$

The reason that this is acceptable is that the multipool approaches require solving for multiple parameters, which may not improve accuracy due to the limited number of observables available and the already large number of MT contributions. Notice that Eqs. 12a and 12b neglect interference from NOE effects, which may have to be added in for certain agents as well as for the endogenous proteins. The FLEX method has a major advantage for quantification, because competing MTC and direct water excitation effects contribute differently to the time domain signal. The short-T_2^* components (Eq. 11) contribute only to the initial points during which they are incoherently dephased, while water modulation due to direct excitation occurs at a well-known offset frequency. As a consequence, both can be filtered out from the signals of interest (36) and the FLEX spectrum should be able to provide direct determination of PTR for the specific spectral lines without need for asymmetry analysis.

In CEST experiments, experimental determination of $\mathrm{MTR}_{\mathrm{asym}}$ is complicated by variation of the B_0 field over the sample or subject. Good asymmetry analysis requires exact knowledge of the water frequency in each voxel, which can generally be obtained by acquiring a full Z-spectrum and determining the center of the DS line shape. In clinical studies, however, this may be too time-consuming due to limited SNR and the concomitant need to acquire multiple scans. Therefore it has been suggested to acquire CEST data (multiple scans) for only a limited number of essential frequencies around $\pm\Delta\omega$, which is combined with the water frequency determined from a single Z-spectrum (82) or from a rapidly acquired gradient-echo-based field map (69). However, a Z-spectrum is still slow, while field maps are often complicated by the need for phase unwrapping, the presence of image distortions (especially at higher fields), and limited accuracy (several Hz) of the frequency differences. The latter is not an issue for shim optimization, but may be problematic for asymmetry determinations due to the steep shape of the DS contribution to the CEST spectrum. In an alternative referencing scheme, called WASSR [WAter Saturation Shift Referencing, (83)] a water frequency map is acquired using a saturation sequence with low B_1 and short t_{sat} (e.g., 0.5 μT, 50-100 ms), leading to a Z-spectrum dominated by DS (negligible interference from MTC and CEST). Because the shape of the DS line is symmetric (84) the water center frequency can be determined in each voxel with subhertz accuracy (83), of course depending on the field strength (WASSR-bandwidth) and number of points acquired. Similar to field mapping, the WASSR-scan can be acquired rapidly due to lower power deposition, and, if needed, with reduced spatial resolution (e.g., $4 \times 4 \times 4$ or even $8 \times 8 \times 8$ mm^3 in humans), and interpolated to high resolution for data processing. WASSR will be especially useful when there is overlap in the Z-spectrum between the CEST agent line shape and the saturated water signal shape, which causes an asymmetric broadening of the DS curve that prohibits accurate assessment of the exact water frequency.

Inhomogeneity in the B_1 field may also pose problems, because it leads to spatial variation in saturation efficiency. This will especially be a concern for solutes with fast exchange rates (Eq. 4), but not for endogenous APT, where complete spin saturation ($\alpha \approx 1$) is pretty much achieved for a B_1 range of 1–3 μT. For the LTM methods, the amount of signal may differ per voxel, but the signal modulation in FLEX should not. Inhomogeneity in B_1 is not expected to be a major issue in the near future in view of new multichannel transmit hardware becoming available for imaging (85,86).

A final issue complicating asymmetry analysis is the occurrence of image artifacts when studying amide protons. These protons have the same chemical shift difference with water (3.5 ppm) as lipid resonances but on opposite sides of water. When acquiring the amide saturation image, lipid signals are not suppressed. However, they are when saturation is applied at −3.5 ppm. In brain images, this can lead to dark rings close to the skull, especially when using phased-array coil reception for which skull lipid signals are picked up with very high SNR [Fig. 10, (87)]. To obtain an appropriate $\mathrm{MTR}_{\mathrm{asym}}$ image, the lipid signals should be suppressed equally when saturating at both offsets, which has been successfully demonstrated in multislice (88–90) and whole-brain

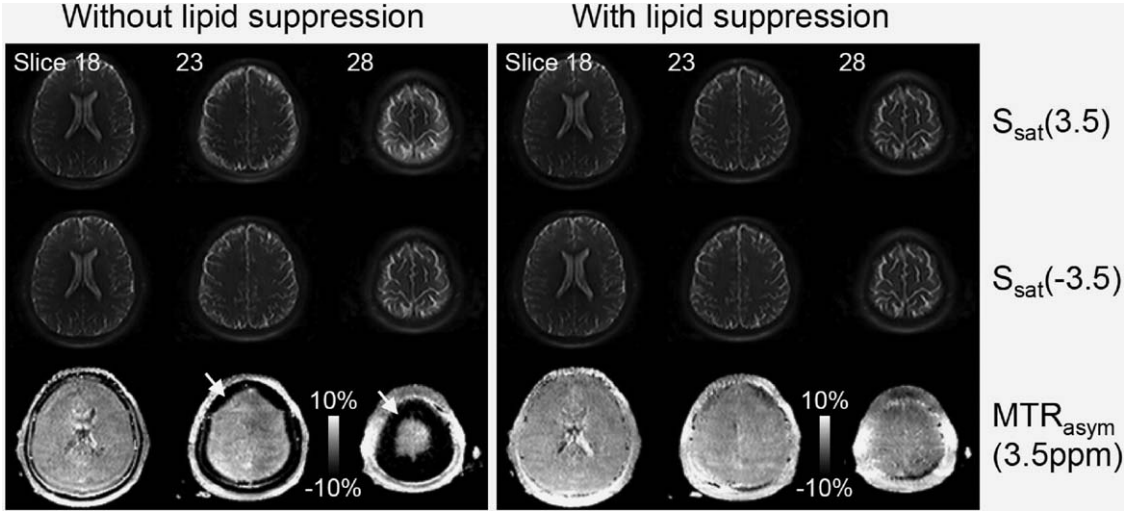


FIG. 10. Illustration of lipid interference and suppression in 3D amide proton transfer (APT) scanning in the human brain. 3D Gradient and spin echo (GRASE) acquisition with multipulse saturation preparation showing saturated images at ±3.5 ppm as well as the calculated MTR_{asym} (3.5 ppm) images for three slices (in three columns) without and with lipid suppression. Without lipid suppression, ring-like hypointensities (white arrows) appear in the MTR_{asym} (3.5 ppm) images, which are removed when applying a frequency-modulated selective lipid suppression pulse in both image acquisitions (±3.5 ppm). Reproduced with permission from Zhu et al., Magn Reson Med 2010;64:638–644.

3D APT imaging [Fig. 10, (87)]. When using EPI methods, ghosting artifacts from lipid signals in the scalp occur in the MTR_{asym} image, which can be removed similarly or through the use of frequency-selective refocusing pulses during spin echo acquisition (91).

Assuming that an appropriate PTR can be measured (uncontaminated and reproducible) the absolute quantification of a parameter requires availability of a theory to describe the effects (Bloch equations or its analytical solutions) and of the other parameters in the equations. For instance, when the solute concentration is to be determined, T_{1w} and k_{sw} need to be known and a concentration reference is needed. Measurement of T_{1w} can be done using conventional MRI techniques, while k_{sw} can be measured using either the WEX approach (Fig. 6) or through measurement of the CEST intensity as a function of saturation time or power (18,92). Exchange transfer measurements have the powerful property that water (111.2 M proton concentration) can be used as an internal reference standard (Eq. 9). Notice that this quantification in actual mM concentration units is possible because MRI measures the free water signal in which the agent is dissolved. If the concentration per voxel volume or per gram tissue would need to be known, a water density correction would have to be applied, but for most applications concentration in mM is what is needed. Using measured WEX exchange rates and APT intensities in the rat brain, it was possible to determine the in vivo amide proton concentration (8.3 ppm) to be about 72 mM (23,25), reflecting the total concentration for a large group of contributing proteins and peptides. The FLEX method seems very suitable for quantification, which was recently demonstrated for a DNA dimer in solution (Fig. 11) as a function of the number of LTMs used. The results show excellent correspondence of the experimental curves to Eq. 10 and gave a DNA concentration of 0.60–0.65 mM per duplex, comparing well to the experimentally estimated concentration based on nucleoside analysis (0.8 mM) and providing further validation of the FLEX method.

Depending on the type of exchangeable proton and the mechanism of exchange catalysis (base, acid or water catalyzed, buffer catalyzed), exchange rates may show pH dependence over a certain pH range. If this dependence can be calibrated under the appropriate in vivo conditions, e.g., using phosphorus spectroscopy as a reference (23,25), exchange transfer allows determination of absolute pH. A very elegant and more straightforward approach was suggested by Ward and Balaban (32), who used a ratiomeric approach for the PTR of two distinguishable protons with different pH dependence in the same molecule. This allows the effect of concentration to be removed according to:

$$\frac{PTR_1}{PTR_2} = \frac{N_{E1} \cdot \alpha_1 \cdot k_1}{N_{E2} \cdot \alpha_2 \cdot k_2}. \quad [13]$$

This principle may allow calibration in a buffered phantom and application in vivo, under the condition that the exchange mechanisms for the protons being compared would be negligibly affected between the conditions. Aime and coworkers (93,94) applied similar principles for assessing pH in a concentration-independent manner using paraCEST agents containing multiple groups in which the molecular exchange was pH independent and the exchange of amide protons contained in the complex pH dependent. Analogously, one could use two molecules with different protons (32), which was applied by Aime et al. for paraCEST agents (27). This latter approach of course requires the concentrations to be added back into Eq. 13, which may complicate in vivo application unless the relative concentration can be kept stable, which may be the case in a protected environment such as a liposome (6,95).

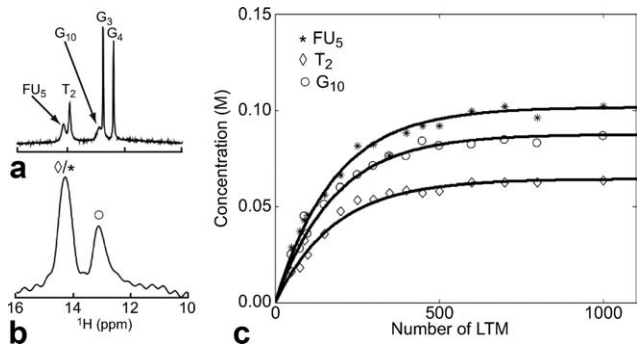


FIG. 11. Illustration of quantitative concentration determination using the FLEX method for the DNA duplex 5′-$C_1T_2G_3G_4FU_5A_6C_7$-$C_8A_9G_{10}$-3′ (T = 10°C; pH = 9.0; C = Cytosine; T = Thymidine; G = Guanosine; FU = Fluorouracil; A = Adenosine). **a:** Conventional jump-return spectrum in which all imino protons are observable. **b:** FLEX spectra in which G3 and G4 do not appear due to slow exchange. **c:** Absolute concentration of labeled protons generated by FLEX as a function of the number of applied LTMs. Data based on time domain fitting using prior knowledge of the chemical shift and decay rate. Black lines are best fits of data to Eq. 10 (concentration = PTR · 2 · [H_2O]). Reproduced with permission from Friedman et al., J Am Chem Soc 2010;132:1813–1815.

In Vivo CEST Imaging and Translation to Humans

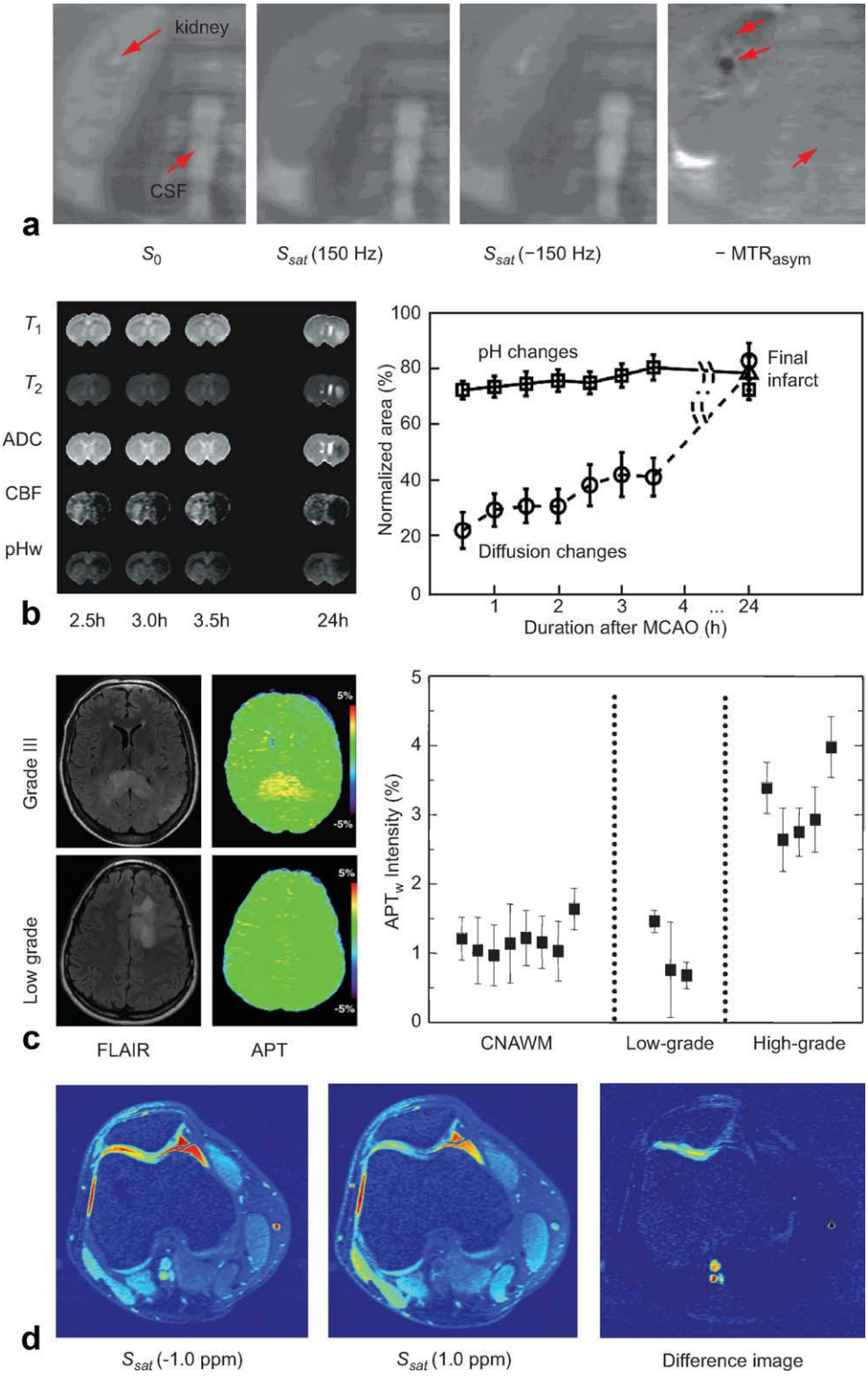
CEST agents provide a powerful source for potential contrast (4,5,7,10,11), including pH imaging (18,25,27,32,56,70,93,94,96–103), metabolite detection (29,104–106), imaging of mobile proteins or peptides in tissue (25,33,82,107,108), metal ion detection (109,110), liposome labeling (6,7,35,111–114), nanoparticle/polymer labeling (31,101,115–117), protein-binding (118), RNA-protein binding (24), DNA-protein binding (119), temperature imaging (32,96,120–122), detecting enzyme activity (123–127), CEST reporter genes (128), and imaging of OH groups (26,34,99), polyamines (129,130), and nucleic acids (24). Similar to many other molecular imaging approaches, most CEST studies have been in vitro, and for a detailed overview of all contrast agent in vitro work to date, we refer the reader to several comprehensive recent reviews (3–5,9–11,131). Here we briefly discuss current progress in vivo and the potential translation to the clinic.

Clinical application requires the investigators to address several issues, including toxicity of the agents (when using exogenous contrast), limited scan time, the need to scan whole organs, and the danger of too much RF power deposition when performing MT experiments. Power deposition increases quadratically with field strength and transmit coil size. This restricts the use of certain MRI pulse sequences, as safety requires the average power over the scan repetition time (TR) to be within FDA-guided SAR requirements on human scanners. Staying within recommended SAR is not straightforward when using multislice or 3D acquisitions with continuous or pulsed saturation combined with band-selective lipid suppression pulses and spin echo acquisitions. This will be equally challenging for the repeated LTMs in the new exchange transfer approaches, which also employ series of high-B_1 pulses. However, history shows that a similar fear has not limited MTC studies, which smoothly moved from 1.5 to 3 T, even for whole organ studies. Recent support for this point of view comes from data showing the possibility to perform multislice (88,90) and 3D (87) CEST at 1.5 T, 3 T and even at 7 T on human scanners (89).

When it comes to clinical translation, the most powerful aspect of CEST MRI is the availability of endogenous agents in the proton exchange family. Already in 2000, shortly after the initial CEST article, Dagher et al. (132) were able to image urea in the kidney at a field of 1.5 T (Fig. 12a). A few years later, Zhou et al. (25) showed that the amide protons of mobile proteins and peptides previously characterized in vivo using WEX spectroscopy [Fig. 6b,c, (49,50)] could also be detected indirectly through the water signal using CEST. This amide proton transfer (APT) MRI was subsequently used to image early ischemia in anesthetized rats [Fig. 12b, (25,70)], where a pH reduction slows the exchange between the amide and water protons, leading to a reduction in CEST contrast (Fig. 7e–f). Such pH contrast seems particularly useful during the very early stages of ischemia where T_1, T_2, or diffusion weighted images may not yet show contrast, but where a pH penumbra may indicate risk for infarction due to impaired oxidative metabolism (Fig. 12b). Contrary to ^{31}P spectroscopy or WEX spectroscopy, APT has sufficient sensitivity to allow imaging and can be used under the standard clinical proton set up. APT-MRI is also showing potential for imaging cancer through an increase in cellular protein/peptide content of malignant cells with respect to normal tissue [Fig. 7a–c, (33)]. Cancer studies in animals indicate the ability to separate edema from tumor in animal (Fig. 7c), which has been confirmed in humans (82,107,108). These studies showed that APT can also detect non-enhancing high grade tumors. Recent human studies show preliminary suitability of APT for tumor grading [Fig. 12c, (82,108)], while animal studies on radiation necrosis models indicate the possibility to separate treatment effects from tumor progression (133). Another impressive example of endogenous CEST is the imaging of the OH group of glucosaminoglycans (gagCEST) in the human knee, which allowed detection of a lesion in the patella [Fig. 12d, (34)]. Measurements of gag concentration could be applied to diagnose gag-deficiency in tissue, such as expected to be the case in osteoarthritis. Another promising approach is the detection of OH-containing endogenous glycogen and glucose (26). These studies are somewhat complicated due to the chemical shift proximity of the OH resonances to the water protons, which hinders asymmetry analysis due to the artificial broadening of the bottom of the DS contribution to the Z-spectrum. This problem can be addressed with the aid of the WASSR approach (83), which allows such detection even at 3 T. GlycoCEST is expected to become more practical with the advent of human 7 T scanning (89,134–136), where the convolved CEST effects in the 0–5 ppm range downfield of water will be spread out more. In addition to the amide proton resonances of proteins and peptides, this region contains the effects of all exchangeable protons of in vivo metabolites and macromolecules resonating there, in a contribution depending

on their exchange rate (at physiological and other pH) and proton concentration. At higher field it may be possible to assign some of these, but due to the bandwidth of saturation, the linewidth of the resonances and the convolution of multiple contributing compounds, this will not be straightforward.

The availability of proton exchange as a contrast mechanism also offers the unique opportunity for using biodegradable natural compounds, such as sugars and proteins (26,29,130) as contrast agents. This seems to come close to the ideal of a totally noninvasive agent. Proteins may still have unknown toxicity though, and will have to be tested in careful trials. Their use currently has also been limited to animal studies (129,137). A nice example is the use of exchangeable protons in cationic polypeptides to both stabilize immunoprotective alginate microcapsules and



produce CEST contrast, allowing the monitoring of viability and functionality of encapsulated cells (138) as well as the distribution of cells and capsules in real-time (139). In addition to natural compounds, there is probably a large group of currently approved pharmaceuticals and contrast agents that contain exchangeable protons and can be employed immediately for CEST detection. A first example of this is discussed in a recent abstract by Liu et al. (124), who monitored cytosine deaminase activity for the conversion of the prodrug 5-Fluorocytosine (5-FC) into the active anti-tumor agent 5-fluorouracil (5-FU) through the difference in Z-spectra between 5-FC and 5-FU. Another example was presented by Longo et al. (103), who showed that the X-ray contrast agent iopamidol can be used to measure pH in vivo using the ratiomeric approach described earlier. Finally, the use of proton exchange instead of molecular exchange as the prime contrast in paramagnetic compounds is growing. A recent in vivo example of this is the monitoring of uptake of two different shift agents conjugated to fifth (G5) and second (G2) generation polyamidoamine (PAMAM) dendrimers in a mouse model of mammary carcinoma [MCF-7, (117)]. The results show a gradual increase of CEST contrast with time after injection, indicating an accumulation of the agent in the tumor.

With respect to paramagnetic exogenous agents, there is always the fear of toxicity, especially for metals becoming unbound and releasing into the tissue. However, chemistry is making rapid progress in the design of agents with both high thermodynamic and kinetic stability (140,141), the importance of the latter often being underestimated. Currently, there are exciting developments towards use of molecular exchange agents, both in vivo and ex vivo (perfused organs or cells). To the best of our knowledge, the first in vivo applications of paraCEST agents have been for the study of dynamic perfusion using the OPARACHEE approach of Vinogradov et al. (71). Figure 13a shows the uptake and clearance of a Tm-DOTAM-Gly compound in the mouse kidney, while Fig. 13b shows the uptake and retaining of a similar agent in a mouse Glioblastoma Multiforme tumor model (142). A limiting factor in the use of several paramagnetic molecular exchange compounds has been that T_1 and T_2 contrast is induced in addition to CEST contrast (143), although this can also be used to ones advantage (144). The 1–3% CEST contrast in the brain tumor model in Fig. 13b was corrected for the effects of relaxation. A very beautiful study highlighting the power of paraCEST agents for molecular sensing was recently performed by Ren et al. (145), who used the compound Europium(III)-1,4,7,10-tetraazacyclododecane-1,7-di-*N*-methylacetamide-4-10-di-*N*(m-phenylborate)acetamide (Eu-D2MA-2PB), which preferably binds glucose over coordinating water (106). Mouse livers containing the glucose sensor showed a 17% increase in CEST contrast when comparing perfusion with glucose to perfusion without glucose at a field of 4.7 T (Fig. 13c). Overall, the paraCEST approach is very promising because of the clean excitation of resonances without much direct water saturation. The disadvantage of the need for high power deposition (inducing strong MTC) may perhaps be overcome with the new FLEX method. The combination proton exchange and molecular exchange paramagnetic compounds offers an order of magnitude increase in sensitivity as well as the use of two sensors with different chemical shift in a single molecule (146).

Based on the potential of high payload, the development of compartmental exchange agents for use in vivo is very important. Recently, the first studies demonstrating the use of paraCEST-based and diaCEST-based liposomes in vivo were reported. In a study employing multiple types of paramagnetic contrast in two types of liposomes (mixed paraCEST/T_2 liposome and mixed T_1/T_2 liposome), Delli Castelli et al. (95) were able to use the CEST contrast to monitor endocytosis of the CEST liposomes in the cells, which reduced the CEST contrast (Fig. 14a). This study combined the CEST images with T_1 and T_2 maps to build a kinetic model for the fate of the paramagnetic complexes loaded into the liposomes. In another study Liu et al. (129) demonstrated the use of

FIG. 12. In vivo CEST studies exploiting the presence of endogenous proton exchange agents. **a:** Imaging of urea in kidney. Comparison of coronal images through the kidney of a normal volunteer kidney without saturation (S_0), and with saturation (S_{sat}) applied symmetrically about the water frequency for the resonance frequency difference (+150 Hz at 1.5 T) of urea protons. The red arrows in the S_0 image indicate the calyx in the kidney (urea collecting system) and CSF in the spinal cord, which is used as a reference. The asymmetry image on the right is inverse of current definition and therefore labeled as $-MTR_{asym}$. This image is darker in the calyx (middle red arrow) and renal papillae (top arrow) while no differences are visible in CSF (bottom arrow). Reproduced with permission from Dagher et al., J Magn Reson Imaging 2000;12:745-748. **b:** Imaging of ischemia using pH dependence of APT MRI. Multiparametric MRI of rat brain as a function of time after permanent middle cerebral artery occlusion (MCAO). Early ischemia (as confirmed by cerebral blood flow weighted MRI) shows negligible changes in T_1, T_2, and ADC (apparent diffusion coefficient) images. However, a reduction in pH could be detected using APT-MRI (dubbed pHw), which predicted well evolution to stroke at 24 hrs, as confirmed by T_2-hyperintensity. In a series of 28 rats studied at 4.7 T, pH-weighted MRI predicted areas of infarction more accurately and earlier than diffusion MRI (graph). Reproduced with permission from Sun et al., J Cereb Blood Flow Metab 2007;27:1129-1136. **c:** Imaging of increased protein content in tumors using APT. FLAIR and APT images at 3 T for patients with a grade III (top) and a low grade (bottom) tumor. Contrast in FLAIR images appears similar for high and low grade. APT contrast, however, while increased by about 3% in the grade III tumor is virtually indistinguishable from contralateral normal-appearing white matter (CNAWM) in the low grade case, which was attributed to increased protein content with grade. This pilot study showed potential to separate high and low grade tumors for a small group (graph). Reproduced with permission from Zhou et al., Magn Reson Med 2008;60:842-849. **d:** GagCEST images at 1.5 T of cartilage lesion on the medial facet of the patellofemoral human knee joint. Left: patella with irradiation at −1.0 ppm and 1 ppm (corresponding to OH protons, see Fig. 5). The MTR_{asym} image shows CEST contrast from the femur and the lateral and medial sides of the patella. A loss of gagCEST is clear. The bright circular sections highlight the location of blood vessels, was attributed to the CEST effect from oligosaccharides and proteins in blood. Reproduced with permission from Ling et al., Proc Natl Acad Sci USA 2008;105:2266–2270. Color image provided by Alexej Jerschow. [Color figure can be viewed in the online issue, which is available at wileyonlinelibrary.com.]

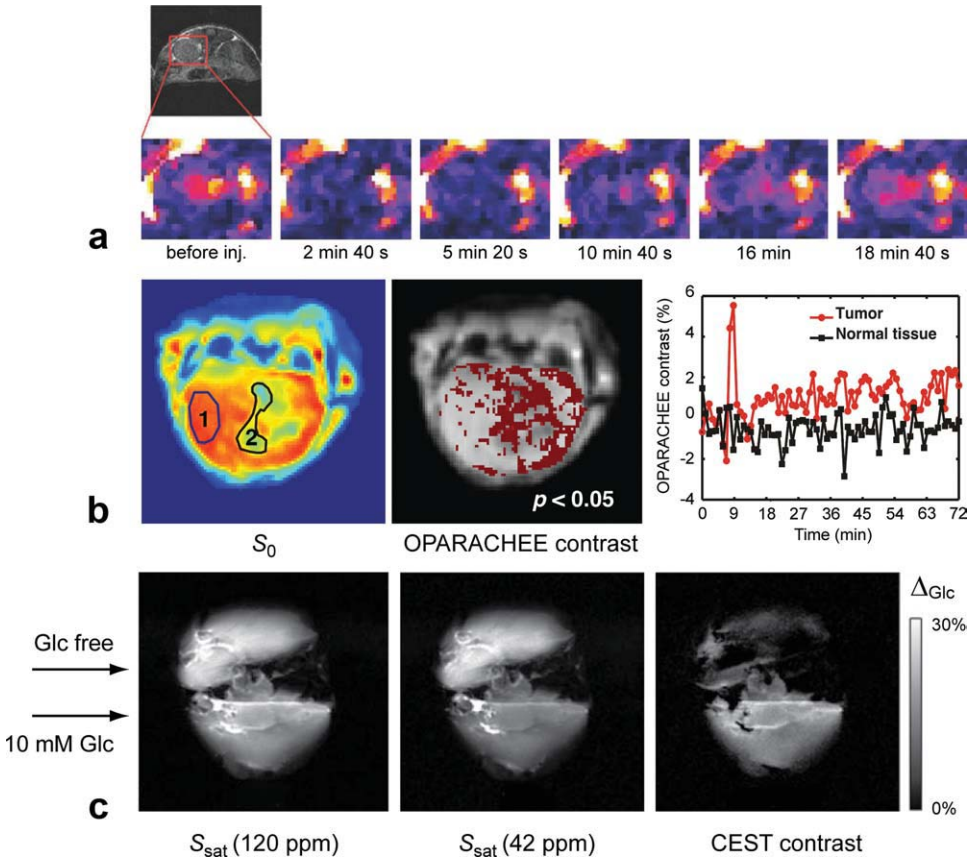


FIG. 13. In vivo and ex vivo CEST studies of molecular exchange compounds. **a, b:** paraCEST perfusion imaging in vivo. a: Kidney perfusion study by Vinogradov, showing CEST images before, during and after injection of Tm-DOTAM-Gly, with hypointensity when the agent reaches the kidney. Reproduced with permission from Vinogradev et al., Magn Reson Med 2007;58:650-655. b: Brain and glioblastoma perfusion study using Tm-DOTAM-Gly-Lys. Left: Flash image for region assignment of healthy tissue (1) and tumor (2). Right: Dynamic signal changes before, during and after perfusion, showing that some agent is retained in the leaky tumors, but not in brain. Middle: significantly changed CEST contrast in regions roughly corresponding to tumor. Reproduced with permission from Li et al., Proceedings of the 18th Annual Meeting of ISMRM, Stockholm, Sweden, 2010. p 3752. **c:** Glucose sensing ex vivo using paraCEST agents. MRI images of two mouse livers, one perfused with Eu-D2MA-2PB solution containing glucose (Bottom) and another without glucose (Top). CEST contrast is clear in the liver perfused with glucose only. Reproduced with permission from Ren et al., Magn Reson Med 2008;60:1047–1055.

"multicolor" mixtures of liposomes loaded with proton exchange agents such as glycogen (Glyc), poly-L-lysine (PLL), and L-arginine (Larg), in which the different chemical shifts of the exchangeable protons (OH, NH and NH_2, respectively) were assigned different colors (130) in analogy to optical imaging. Each liposome type displayed a characteristic MTR_{asym} plot in vitro (Fig. 14b, LEFT). Depending on the diaCEST agent used, the intraparticle exchange rate is not as fast as for paraCEST liposomes and the contrast is probably a mixture of proton exchange and compartmental exchange. When injecting PLL and Larg in the two footpads of mice, signal was found in the ipsilateral regional lymph nodes, showing that transport of these liposomes can be monitored in vivo. In addition, the in vivo MTR_{asym} -spectra (Fig. 14b, RIGHT) resembled the in vitro reference data. From a mechanistic point of view, this diamagnetic approach should be less sensitive than paramagnetic lipoCEST because exchange is slower and protons have to be transferred from the agent to the water inside the liposome (smaller pool) in an additional exchange step that is on the order of magnitude of the compartmental exchange rate (10–200 Hz). If this rate were to be increased, the labeling efficiency would go down or the power demands up, which is not the case for paramagnetic lipoCEST. On the other hand, the original chemical shift of the agent can be used, allowing good separation from the water signal. However, the small shift in paramagnetic liposomes can be increased tremendously by increasing the bulk magnetic susceptibility contributions to the shift through making the particles magnetically anisotropic (113). Both approaches have great possibilities though, and the multifrequency and multicontrast approaches employed in these two studies show only a preliminary glimpse into the promising world of lipoCEST imaging.

CONCLUSION

The discovery of the CEST effect has added a new dimension to the design and detection of MRI contrast agents both with respect to the chemistry involved and

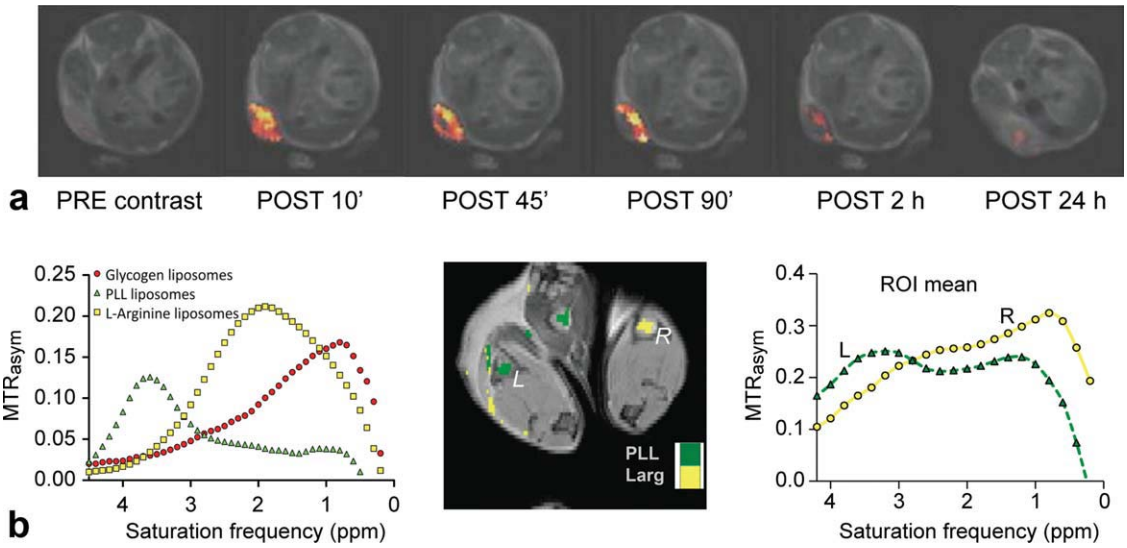


FIG. 14. In vivo CEST studies using compartmental exchange agents. **a:** Paramagnetic lipoCEST MRI. Temporal evolution of CEST contrast after injecting a compartmental exchange agent loaded with Tm-DOTA into the tumor of a murine melanoma model. CEST contrast is lost about 2 hours after administering the compartmental exchange agent, indicating uptake by the cell and removal of the liposome membrane. Reproduced with permission from Delli Castelli et al., J Controlled Release 2010;144:271-279. **b:** Diamagnetic lipoCEST MRI. Left: MTR_{asym} plot showing the water signal intensity reduction as a function of frequency for three diamagnetic liposomes (DLs) at about 30 nM concentration in vitro (pH = 7.3 and 37°C), with red assigned to OH in Glyc DL, yellow assigned to NH_2 in Larg DL, and green assigned to NH in PLL DL. Middle: MRI images of regional lymph nodes in mice showing two-color CEST contrast after being injected with liposomes containing PLL and Larg in left (L) and right (R) footpads, respectively, 24 hours before MRI. Right: mean MTR_{asym} plots of the left (*L*) and right (*R*) lymph nodes. Courtesy of Guanshu Liu and Michael McMahon, Kennedy Krieger Institute and Johns Hopkins University School of Medicine. [Color figure can be viewed in the online issue, which is available at wileyonlinelibrary.com.]

the new MRI technology that can be employed. From a chemistry point of view, the exchange transfer principle has allowed the design of whole new groups of contrast agents. These range from powerful paramagnetic shift agents with multiple functions to simple biodegradable compounds such as peptides and sugars, which have great potential as truly noninvasive contrast agents. Contrary to relaxation agents, exchange transfer contrast can be turned on and off, and compounds can be designed to contain protons that resonate at multiple frequencies, expanding the MRI field to a multicolor type of imaging in analogy to optical imaging. In addition to exogenous agents, many endogenous compounds show CEST contrast, which can be exploited as inherent biomarkers for detection of disease and monitoring of the effects of treatment. In this brief review, we have highlighted mainly the MR-methodological aspects of exchange transfer, which indicate that we are only scratching the surface of possible approaches. Current MR methods have focused mainly on saturation transfer, while a whole new field of multidimensional MR approaches to detect exchange-transfer and cross-relaxation aspects of the contrast remains to be explored. In addition to many chemical advances, we therefore foresee that much new MRI technology will be developed in the coming years, which will rapidly expand this exciting field of research.

ACKNOWLEDGMENTS

The authors are grateful to Dr. Alexej Jerschow (New York University), Dr. Robert Bartha (Robarts Research Institute, London, Ontario), Dr. Mark Woods (Portland State University, Portland), Dr. Dean Sherry (University of Texas, Southwestern Medical Center, Dallas), Dr. Guanshu Liu, Dr. Mike McMahon, and Dr. Josh Friedman for providing some of the figures and Dr. Mike McMahon and Dr. Manus Donahue for carefully reading the paper. The National Center for Research Resources (NCRR) is a component of the National Institutes of Health (NIH). The contents of the paper are solely the responsibility of the authors and do not necessarily represent the official view of NCRR or NIH.

REFERENCES

1. Ward KM, Aletras AH, Balaban RS. A new class of contrast agents for MRI based on proton chemical exchange dependent saturation transfer (CEST). J Magn Reson 2000;143:79–87.
2. Zhang S, Merritt M, Woessner DE, Lenkinski RE, Sherry AD. PARACEST agents: modulating MRI contrast via water proton exchange. Acc Chem Res 2003; 36:783–790.
3. Woods M, Woessner DE, Sherry AD. Paramagnetic lanthanide complexes as PARACEST agents for medical imaging. Chem Soc Rev 2006;35:500–511.
4. Zhou J, van Zijl P. Chemical exchange saturation transfer imaging and spectroscopy. Prog Nucl Magn Reson Spectrosc 2006;48:109–136.
5. Sherry AD, Woods M. Chemical exchange saturation transfer contrast agents for magnetic resonance imaging. Annu Rev Biomed Eng 2008;10:391–411.
6. Terreno E, Delli Castelli D, Cabella C, Dastru W, Sanino A, Stancanello J, Tei L, Aime S. Paramagnetic liposomes as innovative contrast agents for magnetic resonance (MR) molecular imaging applications. Chem Biodivers 2008;5:1901–1912.
7. Aime S, Castelli DD, Terreno E. Chapter 10—lanthanide-loaded paramagnetic liposomes as switchable magnetically oriented nanovesicles. Methods Enzymol 2009;464:193–210.

8. Terreno E, Stancanello J, Longo D, Castelli DD, Milone L, Sanders HM, Kok MB, Uggeri F, Aime S. Methods for an improved detection of the MRI-CEST effect. Contrast Media Mol Imaging 2009;4:237–247.
9. Hancu I, Dixon WT, Woods M, Vinogradov E, Sherry AD, Lenkinski RE. CEST and PARACEST MR contrast agents. Acta Radiol 2010;51: 910–923.
10. Terreno E, Castelli DD, Aime S. Encoding the frequency dependence in MRI contrast media: the emerging class of CEST agents. Contrast Media Mol Imaging 2010;5:78–98.
11. Terreno E, Castelli DD, Viale A, Aime S. Challenges for molecular magnetic resonance imaging. Chem Rev 2010;110:3019–3042.
12. Wolff SD, Balaban RS. Magnetization transfer contrast (MTC) and tissue water proton relaxation in vivo. Magn Reson Med 1989;10: 135–144.
13. Bryant RG. The dynamics of water-protein interactions. Annu Rev Biophys Biomol Struct 1996;25:29–53.
14. Guivel-Scharen V, Sinnwell T, Wolff SD, Balaban RS. Detection of proton chemical exchange between metabolites and water in biological tissues. J Magn Reson 1998;133:36–45.
15. Forsen S, Hoffman RA. Study of moderately rapid chemical exchange reactions by means of nuclear magnetic double resonance. J Chem Phys 1963;39:2892–2901.
16. Li AX, Hudson RH, Barrett JW, Jones CK, Pasternak SH, Bartha R. Four-pool modeling of proton exchange processes in biological systems in the presence of MRI-paramagnetic chemical exchange saturation transfer (PARACEST) agents. Magn Reson Med 2008;60: 1197–1206.
17. McConnell HM. Reaction rates by nuclear magnetic resonance. J Chem Phys 1958;28:430–431.
18. McMahon MT, Gilad AA, Zhou J, Sun PZ, Bulte JW, van Zijl PC. Quantifying exchange rates in chemical exchange saturation transfer agents using the saturation time and saturation power dependencies of the magnetization transfer effect on the magnetic resonance imaging signal (QUEST and QUESP): pH calibration for poly-L-lysine and a starburst dendrimer. Magn Reson Med 2006;55:836–847.
19. Sun PZ. Simplified and scalable numerical solution for describing multi-pool chemical exchange saturation transfer (CEST) MRI contrast. J Magn Reson 2010;205:235–241.
20. Sun PZ, Zhou J, Huang J, van Zijl P. Simplified quantitative description of amide proton transfer (APT) imaging during acute ischemia. Magn Reson Med 2007;57:405–410.
21. Woessner DE. Nuclear transfer effects in nuclear magnetic resonance pulse experiments. J Chem Phys 1961;35:41–48.
22. Woessner DE, Zhang S, Merritt ME, Sherry AD. Numerical solution of the Bloch equations provides insights into the optimum design of PARACEST agents for MRI. Magn Reson Med 2005;53:790–799.
23. Zhou J, Wilson DA, Sun PZ, Klaus JA, Van Zijl PC. Quantitative description of proton exchange processes between water and endogenous and exogenous agents for WEX, CEST, and APT experiments. Magn Reson Med 2004;51:945–952.
24. Snoussi K, Bulte JW, Gueron M, van Zijl PC. Sensitive CEST agents based on nucleic acid imino proton exchange: detection of poly(rU) and of a dendrimer-poly(rU) model for nucleic acid delivery and pharmacology. Magn Reson Med 2003;49:998–1005.
25. Zhou J, Payen JF, Wilson DA, Traystman RJ, van Zijl PC. Using the amide proton signals of intracellular proteins and peptides to detect pH effects in MRI. Nat Med 2003;9:1085–1090.
26. van Zijl PC, Jones CK, Ren J, Malloy CR, Sherry AD. MRI detection of glycogen in vivo by using chemical exchange saturation transfer imaging (glycoCEST). Proc Natl Acad Sci USA 2007;104:4359–4364.
27. Aime S, Barge A, Delli Castelli D, Fedeli F, Mortillaro A, Nielsen FU, Terreno E. Paramagnetic lanthanide(III) complexes as pH-sensitive chemical exchange saturation transfer (CEST) contrast agents for MRI applications. Magn Reson Med 2002;47:639–648.
28. Aime S, Delli Castelli D, Fedeli F, Terreno E. A paramagnetic MRI-CEST agent responsive to lactate concentration. J Am Chem Soc 2002;124:9364–9365.
29. Zhang S, Trokowski R, Sherry AD. A paramagnetic CEST agent for imaging glucose by MRI. J Am Chem Soc 2003;125:15288–15289.
30. Zhang S, Winter P, Wu K, Sherry AD. A novel europium(III)-based MRI contrast agent. J Am Chem Soc 2001;123:1517–1518.
31. Goffeney N, Bulte JW, Duyn J, Bryant LH, Jr, van Zijl PC. Sensitive NMR detection of cationic-polymer-based gene delivery systems using saturation transfer via proton exchange. J Am Chem Soc 2001; 123:8628–8629.
32. Ward KM, Balaban RS. Determination of pH using water protons and chemical exchange dependent saturation transfer (CEST). Magn Reson Med 2000;44:799–802.
33. Zhou J, Lal B, Wilson DA, Laterra J, van Zijl PC. Amide proton transfer (APT) contrast for imaging of brain tumors. Magn Reson Med 2003;50:1120–1126.
34. Ling W, Regatte RR, Navon G, Jerschow A. Assessment of glycosaminoglycan concentration in vivo by chemical exchange-dependent saturation transfer (gagCEST). Proc Natl Acad Sci USA 2008; 105:2266–2270.
35. Aime S, Delli Castelli D, Terreno E. Highly sensitive MRI chemical exchange saturation transfer agents using liposomes. Angew Chem Int Ed 2005;44:5513–5515.
36. Friedman JI, McMahon MT, Stivers JT, van Zijl PC. Indirect detection of labile solute proton spectra via the water signal using frequency-labeled exchange (FLEX) transfer. J Am Chem Soc 2010;132: 1813–1815.
37. Schroder L, Lowery TJ, Hilty C, Wemmer DE, Pines A. Molecular imaging using a targeted magnetic resonance hyperpolarized biosensor. Science 2006;314:446–449.
38. Zhao JM, Har-el YE, McMahon MT, Zhou J, Sherry AD, Sgouros G, Bulte JW, van Zijl PC. Size-induced enhancement of chemical exchange saturation transfer (CEST) contrast in liposomes. J Am Chem Soc 2008;130:5178–5184.
39. Liepinsh E, Otting G. Proton exchange rates from amino acid side chains—implications for image contrast. Magn Reson Med 1996;35:30–42.
40. Viswanathan S, Kovacs Z, Green KN, Ratnakar SJ, Sherry AD. Alternatives to gadolinium-based metal chelates for magnetic resonance imaging. Chem Rev 2010;110:2960–3018.
41. Ratnakar SJ, Woods M, Lubag AJ, Kovacs Z, Sherry AD. Modulation of water exchange in europium(III) DOTA-tetraamide complexes via electronic substituent effects. J Am Chem Soc 2008;130:6–7.
42. Cavanagh J, Fairbrother WJ, Palmer III AF, Skelton NJ. Protein NMR spectroscopy: principles and practice. San Diego: Academic Press; 1996.
43. Ernst RR, Bodenhausen G, Wokaun A. Principles of nuclear magnetic resonance in one and two dimensions. Oxford: Oxford University Press; 1988.
44. Wüthrich K. NMR of proteins and nucleic acids. New York: Wiley; 1986.
45. Ling W, Eliav U, Navon G, Jerschow A. Chemical exchange saturation transfer by intermolecular double-quantum coherence. J Magn Reson 2008;194:29–32.
46. Hwang TL, van Zijl PC, Mori S. Accurate quantitation of water-amide proton exchange rates using the phase-modulated CLEAN chemical EXchange (CLEANEX-PM) approach with a Fast-HSQC (FHSQC) detection scheme. J Biomol NMR 1998;11:221–226.
47. Mori S, Abeygunawardana C, van Zijl PC, Berg JM. Water exchange filter with improved sensitivity (WEX II) to study solvent-exchangeable protons. Application to the consensus zinc finger peptide CP-1. J Magn Reson B 1996;110:96–101.
48. Mori S, O'Neil Johnson M, Berg JM, van Zijl PC. A water exchange filter (WEX-filter) for NMR studies of macromolecules. J Am Chem Soc 1994;116:11982–11984.
49. Mori S, Eleff SM, Pilatus U, Mori N, van Zijl PC. Proton NMR spectroscopy of solvent-saturable resonances: a new approach to study pH effects in situ. Magn Reson Med 1998;40:36–42.
50. van Zijl PC, Zhou J, Mori N, Payen JF, Wilson D, Mori S. Mechanism of magnetization transfer during on-resonance water saturation. A new approach to detect mobile proteins, peptides, and lipids. Magn Reson Med 2003;49:440–449.
51. Otting G, Liepinsh E, Wuthrich K. Protein hydration in aqueous solution. Science 1991;254:974–980.
52. Hua J, Jones CK, Blakeley J, Smith SA, van Zijl PC, Zhou J. Quantitative description of the asymmetry in magnetization transfer effects around the water resonance in the human brain. Magn Reson Med 2007;58:786–793.
53. Pekar J, Jezzard P, Roberts DA, Leigh JS, Jr., Frank JA, McLaughlin AC. Perfusion imaging with compensation for asymmetric magnetization transfer effects. Magn Reson Med 1996;35:70–79.
54. Swanson S, Pang Y. MT is symmetric but shifted with respect to water. In: Proceedings of the 11th Annual Meeting of ISMRM, Ontario, Canada 2003. p 660.
55. Englander SW, Kallenbach NR. Hydrogen exchange and structural dynamics of proteins and nucleic acids. Q Rev Biophys 1984;16: 521–655.

56. Gillies RJ, Raghunand N, Garcia-Martin ML, Gatenby RA. pH imaging. A review of pH measurement methods and applications in cancers. IEEE Eng Med Biol Mag 2004;23:57–64.
57. Griffiths JR. Are cancer cells acidic? Br J Cancer 1991;64:425–427.
58. Balaban RS, Ceckler TL. Magnetization transfer contrast in magnetic resonance imaging. Magn Reson Q 1992;8:116–137.
59. Henkelman RM, Huang X, Xiang QS, Stanisz GJ, Swanson SD, Bronskill MJ. Quantitative interpretation of magnetization transfer. Magn Reson Med 1993;29:759–766.
60. Henkelman RM, Stanisz GJ, Graham SJ. Magnetization transfer in MRI: a review. NMR Biomed 2001;14:57–64.
61. Leibfritz D, Dreher W. Magnetization transfer MRS. NMR Biomed 2001;14:65–76.
62. McGowan JC, III, Schnall MD, Leigh JS. Magnetization transfer imaging with pulsed off-resonance saturation: variation in contrast with saturation duty cycle. J Magn Reson Imaging 1994;4:79–82.
63. Pike GB. Pulsed magnetization transfer contrast in gradient echo imaging: a two-pool analytic description of signal response. Magn Reson Med 1996;36:95–103.
64. Pike GB, Glover GH, Hu BS, Enzmann DR. Pulsed magnetization transfer spin-echo MR imaging. J Magn Reson Imaging 1993;3:531–539.
65. Graham SJ, Henkelman RM. Understanding pulsed magnetization transfer. J Magn Reson Imaging 1997;7:903–912.
66. Hu BS, Conolly SM, Wright GA, Nishimura DG, Macovski A. Pulsed saturation transfer contrast. Magn Reson Med 1992;26:231–240.
67. Yeung HN, Aisen AM. Magnetization transfer contrast with periodic pulsed saturation. Radiology 1992;183:209–214.
68. Gochberg DF, Gore JC. Quantitative imaging of magnetization transfer using an inversion recovery sequence. Magn Reson Med 2003; 49:501–505.
69. Sun PZ, Benner T, Kumar A, Sorensen AG. Investigation of optimizing and translating pH-sensitive pulsed-chemical exchange saturation transfer (CEST) imaging to a 3T clinical scanner. Magn Reson Med 2008;60:834–841.
70. Sun PZ, Zhou J, Sun W, Huang J, van Zijl PC. Detection of the ischemic penumbra using pH-weighted MRI. J Cereb Blood Flow Metab 2007;27:1129–1136.
71. Vinogradov E, He H, Lubag A, Balschi JA, Sherry AD, Lenkinski RE. MRI detection of paramagnetic chemical exchange effects in mice kidneys in vivo. Magn Reson Med 2007;58:650–655.
72. Vinogradov E, Zhang S, Lubag A, Balschi JA, Sherry AD, Lenkinski RE. On-resonance low B_1 pulses for imaging of the effects of PARACEST agents. J Magn Reson 2005;176:54–63.
73. Eliav U, Navon G. Enhancement of magnetization transfer effects by inter-molecular multiple quantum filtered NMR. J Magn Reson 2008;190:149–153.
74. Warren WS, Richter W, Andreotti AH, Farmer BT, II. Generation of impossible cross-peaks between bulk water and biomolecules in solution NMR. Science 1993;262:2005–2009.
75. Zhang S, Zhu X, Chen Z, Cai C, Lin T, Zhong J. Improvement in the contrast of CEST MRI via intermolecular double quantum coherences. Phys Med Biol 2008;53:N287–296.
76. Ropele S, Stollberger R, Hartung HP, Fazekas F. Estimation of magnetization transfer rates from PACE experiments with pulsed RF saturation. J Magn Reson Imaging 2000;12:749–756.
77. Sled JG, Pike GB. Quantitative imaging of magnetization transfer exchange and relaxation properties in vivo using MRI. Magn Reson Med 2001;46:923–931.
78. Yarnykh VL. Pulsed Z-spectroscopic imaging of cross-relaxation parameters in tissues for human MRI: theory and clinical applications. Magn Reson Med 2002;47:929–939.
79. Atreya HS, Szyperski T. Rapid NMR data collection. Methods Enzymol 2005;394:78–108.
80. Frydman L, Scherf T, Lupulescu A. The acquisition of multidimensional NMR spectra within a single scan. Proc Natl Acad Sci USA 2002;99:15858–15862.
81. Mobli M, Stern AS, Hoch JC. Spectral reconstruction methods in fast NMR: reduced dimensionality, random sampling and maximum entropy. J Magn Reson 2006;182:96–105.
82. Zhou J, Blakeley JO, Hua J, Kim M, Laterra J, Pomper MG, van Zijl PC. Practical data acquisition method for human brain tumor amide proton transfer (APT) imaging. Magn Reson Med 2008;60:842–849.
83. Kim M, Gillen J, Landman BA, Zhou J, van Zijl PC. Water saturation shift referencing (WASSR) for chemical exchange saturation transfer (CEST) experiments. Magn Reson Med 2009;61:1441–1450.
84. Mulkern RV, Williams ML. The general solution to the Bloch equation with constant rf and relaxation terms: application to saturation and slice selection. Med Phys 1993;20:5–13.
85. Metzger GJ, Snyder C, Akgun C, Vaughan T, Ugurbil K, Van de Moortele PF. Local B_1^+ shimming for prostate imaging with transceiver arrays at 7T based on subject-dependent transmit phase measurements. Magn Reson Med 2008;59:396–409.
86. Setsompop K, Alagappan V, Zelinski AC, Potthast A, Fontius U, Hebrank F, Schmitt F, Wald LL, Adalsteinsson E. High-flip-angle slice-selective parallel RF transmission with 8 channels at 7 T. J Magn Reson 2008;195:76–84.
87. Zhu H, Jones CK, van Zijl PC, Barker PB, Zhou J. Fast 3D chemical exchange saturation transfer (CEST) imaging of the human brain. Magn Reson Med 2010;64:638–644.
88. Dixon WT, Hancu I, Ratnakar SJ, Sherry AD, Lenkinski RE, Alsop DC. A multislice gradient echo pulse sequence for CEST imaging. Magn Reson Med 2010;63:253–256.
89. Mougin OE, Coxon RC, Pitiot A, Gowland PA. Magnetization transfer phenomenon in the human brain at 7 T. NeuroImage 2010;49: 272–281.
90. Sun PZ, Murata Y, Lu J, Wang X, Lo EH, Sorensen AG. Relaxation-compensated fast multislice amide proton transfer (APT) imaging of acute ischemic stroke. Magn Reson Med 2008;59:1175–1182.
91. Sun PZ, Zhou J, Sun W, Huang J, van Zijl PC. Suppression of lipid artifacts in amide proton transfer imaging. Magn Reson Med 2005; 54:222–225.
92. Dixon WT, Ren J, Lubag AJ, Ratnakar J, Vinogradov E, Hancu I, Lenkinski RE, Sherry AD. A concentration-independent method to measure exchange rates in PARACEST agents. Magn Reson Med 2010; 63:625–632.
93. Aime S, Delli Castelli D, Terreno E. Novel pH-reporter MRI contrast agents. Angew Chem Int Ed 2002;41:4334–4336.
94. Terreno E, Delli Castelli D, Cravotto G, Milone L, Aime S. Ln(III)-DOTAMGly complexes: a versatile series to assess the determinants of the efficacy of paramagnetic chemical exchange saturation transfer agents for magnetic resonance imaging applications. Invest Radiol 2004;39:235–243.
95. Delli Castelli D, Dastru W, Terreno E, Cittadino E, Mainini F, Torres E, Spadaro M, Aime S. In vivo MRI multicontrast kinetic analysis of the uptake and intracellular trafficking of paramagnetically labeled liposomes. J Controlled Release 2010;144:271–279.
96. Burdinski D, Pikkemaat JA, Lub J, de Peinder P, Nieto Garrido L, Weyhermuller T. Lanthanide complexes of triethylenetetramine tetra-, penta-, and hexaacetamide ligands as paramagnetic chemical exchange-dependent saturation transfer contrast agents for magnetic resonance imaging: nona- versus decadentate coordination. Inorg Chem 2009;48:6692–6712.
97. Huang CH, Hammell J, Ratnakar SJ, Sherry AD, Morrow JR. Activation of a PARACEST agent for MRI through selective outersphere interactions with phosphate diesters. Inorg Chem 2010;49: 5963–5970.
98. Huang CH, Morrow JR. A PARACEST agent responsive to inner- and outer-sphere phosphate ester interactions for MRI applications. J Am Chem Soc 2009;131:4206–4207.
99. Huang CH, Morrow JR. Cerium(III), europium(III), and ytterbium(III) complexes with alcohol donor groups as chemical exchange saturation transfer agents for MRI. Inorg Chem 2009;48:7237–7243.
100. Perez-Mayoral E, Negri V, Soler-Padros J, Cerdan S, Ballesteros P. Chemistry of paramagnetic and diamagnetic contrast agents for magnetic resonance imaging and spectroscopy pH responsive contrast agents. Eur J Radiol 2008;67:453–458.
101. Pikkemaat JA, Wegh RT, Lamerichs R, van de Molengraaf RA, Langereis S, Burdinski D, Raymond AY, Janssen HM, de Waal BF, Willard NP, Meijer EW, Grull H. Dendritic PARACEST contrast agents for magnetic resonance imaging. Contrast Media Mol Imaging 2007; 2:229–239.
102. Sun PZ, Sorensen AG. Imaging pH using the chemical exchange saturation transfer (CEST) MRI: correction of concomitant RF irradiation effects to quantify CEST MRI for chemical exchange rate and pH. Magn Reson Med 2008;60:390–397.
103. Longo DL, Dastru W, Digilio G, Keupp J, Langereis S, Lanzardo S, Prestigio S, Steinbach O, Terreno E, Uggeri F, Aime S. Iopamidol as a responsive MRI-chemical exchange saturation transfer contrast agent for pH mapping of kidneys: in vivo studies in mice at 7T. Magn Reson Med 2011;65:202–211.

104. Aime S, Barge A, Cabella C, Crich SG, Gianolio E. Targeting cells with MR imaging probes based on paramagnetic Gd(III) chelates. Curr Pharm Biotechnol 2004;5:509–518.
105. Liu G, Li Y, Pagel MD. Design and characterization of a new irreversible responsive PARACEST MRI contrast agent that detects nitric oxide. Magn Reson Med 2007;58:1249–1256.
106. Trokowski R, Zhang S, Sherry AD. Cyclen-based phenylboronate ligands and their Eu^{3+} complexes for sensing glucose by MRI. Bioconjug Chem 2004;15:1431–1440.
107. Jones CK, Schlosser MJ, van Zijl PC, Pomper MG, Golay X, Zhou J. Amide proton transfer imaging of human brain tumors at 3T. Magn Reson Med 2006;56:585–592.
108. Wen Z, Hu S, Huang F, Wang X, Guo L, Quan X, Wang S, Zhou J. MR imaging of high-grade brain tumors using endogenous protein and peptide-based contrast. NeuroImage 2010;51:616–622.
109. Angelovski G, Chauvin T, Pohmann R, Logothetis NK, Toth E. Calcium-responsive paramagnetic CEST agents. Bioorg Med Chem 2010; doi: 10.1016/j.bmc.2010.07.023.
110. Trokowski R, Ren J, Kalman FK, Sherry AD. Selective sensing of zinc ions with a PARACEST contrast agent. Angew Chem Int Ed 2005;44:6920–6923.
111. Aime S, Delli Castelli D, Lawson D, Terreno E. Gd-loaded liposomes as T_1, susceptibility, and CEST agents, all in one. J Am Chem Soc 2007;129:2430–2431.
112. Terreno E, Castelli DD, Milone L, Rollet S, Stancanello J, Violante E, Aime S. First ex-vivo MRI co-localization of two LIPOCEST agents. Contrast Media Mol Imaging 2008;3:38–43.
113. Terreno E, Delli Castelli D, Violante E, Sanders HM, Sommerdijk NA, Aime S. Osmotically shrunken LIPOCEST agents: an innovative class of magnetic resonance imaging contrast media based on chemical exchange saturation transfer. Chemistry 2009;15:1440–1448.
114. Vasalatiy O, Gerard RD, Zhao P, Sun X, Sherry AD. Labeling of adenovirus particles with PARACEST agents. Bioconjug Chem 2008;19: 598–606.
115. Aime S, Delli Castelli D, Terreno E. Supramolecular adducts between poly-L-arginine and [TmIIIdotp]: a route to sensitivity-enhanced magnetic resonance imaging-chemical exchange saturation transfer agents. Angew Chem Int Ed 2003;42:4527–4529.
116. Ali MM, Liu G, Shah T, Flask CA, Pagel MD. Using two chemical exchange saturation transfer magnetic resonance imaging contrast agents for molecular imaging studies. Acc Chem Res 2009;42: 915–924.
117. Ali MM, Yoo B, Pagel MD. Tracking the relative in vivo pharmacokinetics of nanoparticles with PARACEST MRI. Mol Pharmaceutics 2009;6:1409–1416.
118. Ali MM, Woods M, Suh EH, Kovacs Z, Tircso G, Zhao P, Kodibagkar VD, Sherry AD. Albumin-binding PARACEST agents. J Biol Inorg Chem 2007;12:855–865.
119. Nwe K, Andolina CM, Huang CH, Morrow JR. PARACEST properties of a dinuclear neodymium(III) complex bound to DNA or carbonate. Bioconjug Chem 2009;20:1375–1382.
120. Langereis S, Keupp J, van Velthoven JL, de Roos IH, Burdinski D, Pikkemaat JA, Grull H. A temperature-sensitive liposomal ^{1}H CEST and ^{19}F contrast agent for MR image-guided drug delivery. J Am Chem Soc 2009;131:1380–1381.
121. Li AX, Wojciechowski F, Suchy M, Jones CK, Hudson RH, Menon RS, Bartha R. A sensitive PARACEST contrast agent for temperature MRI: Eu^{3+}-DOTAM-glycine (Gly)-phenylalanine (Phe). Magn Reson Med 2008;59:374–381.
122. Zhang S, Malloy CR, Sherry AD. MRI thermometry based on PARACEST agents. J Am Chem Soc 2005;127:17572–17573.
123. Chauvin T, Durand P, Bernier M, Meudal H, Doan BT, Noury F, Badet B, Beloeil JC, Toth E. Detection of enzymatic activity by PARACEST MRI: a general approach to target a large variety of enzymes. Angew Chem Int Ed 2008;47:4370–4372.
124. Liu G, Bernard SM, Tse T, Walczak P, McMahon MT, Bulte JW, van Zijl PCM, Gilad AA. Direct detection of cytosine deaminase enzymatic activity using CEST MRI. In: Proceedings of the 18th Annual Meeting of ISMRM, Stockholm, Sweden 2010. p 36.
125. Yoo B, Pagel MD. A PARACEST MRI contrast agent to detect enzyme activity. J Am Chem Soc 2006;128:14032–14033.
126. Yoo B, Pagel MD. An overview of responsive MRI contrast agents for molecular imaging. Front Biosci 2008;13:1733–1752.
127. Yoo B, Raam MS, Rosenblum RM, Pagel MD. Enzyme-responsive PARACEST MRI contrast agents: a new biomedical imaging approach for studies of the proteasome. Contrast Media Mol Imaging 2007;2:189–198.
128. Gilad AA, McMahon MT, Walczak P, Winnard PT, Jr, Raman V, van Laarhoven HW, Skoglund CM, Bulte JW, van Zijl PC. Artificial reporter gene providing MRI contrast based on proton exchange. Nat Biotechnol 2007;25:217–219.
129. Liu G, Moake MM, Gilad AA, Jamil M, Har-el Y-E, Long C, Walczak P, Zhang J, Cardona A, DeLiso MA, Sgouros G, Bulte JW, van Zijl PC, McMahon MT. Multi-color in vivo MR imaging of lymph nodes usng DIACEST liposomes. In: Proceedings of the 18th Annual Meeting of ISMRM, Stockholm, Sweden 2010. p 454.
130. McMahon MT, Gilad AA, DeLiso MA, Berman SM, Bulte JW, van Zijl PC. New "multicolor" polypeptide diamagnetic chemical exchange saturation transfer (DIACEST) contrast agents for MRI. Magn Reson Med 2008;60:803–812.
131. Aime S, Castelli DD, Crich SG, Gianolio E, Terreno E. Pushing the sensitivity envelope of lanthanide-based magnetic resonance imaging (MRI) contrast agents for molecular imaging applications. Acc Chem Res 2009;42:822–831.
132. Dagher AP, Aletras A, Choyke P, Balaban RS. Imaging of urea using chemical exchange-dependent saturation transfer at 1.5T. J Magn Reson Imaging 2000;12:745–748.
133. Zhou J, Tryggestad E, Wen Z, Lal B, Zhou T, Grossman R, Wang S, Yan K, Fu D-X, Ford E, Tyler B, Blakeley J, Laterra J, van Zijl PC. Differentiation between glioma and radiation necrosis using molecular magnetic resonance imaging of endogenous proteins and peptides. Nature Med 2011;17:130–134.
134. Dula AN, Dortch RD, Landman BA, Pawate S, Lavin PJ, Welch EB, Gore JC, Smith SA. Application of CEST imaging to study amide proton transfer (APT) in healthy controls and multiple sclerosis pathology at 7 Tesla. In: Proceedings of the 18th Annual Meeting of ISMRM, Stockholm, Sweden 2010. p 4311.
135. Cai K, Haris M, Singh A, Gaddam S, Daye D, Grasley K, II GZ, Hariharan H, Reddy R. Assessment of chemical exchange saturation transfer effects in liver tissue at 7T. In: Proceedings of the 18th Annual Meeting of ISMRM, Stockholm, Sweden 2010. p 2588.
136. Al-Radaideh A, Mougin O, Lim S-Y, Tench C, Constantinescu C, Gowland P. Magnetization transfer (MT) and endogenous chemical exchange saturation transfer (CEST) effects in patients with clinically isolated syndrome. In: Proceedings of the 18th Annual Meeting of ISMRM, Stockholm, Sweden 2010. p 4310.
137. Gilad AA, Winnard PT, Jr, van Zijl PC, Bulte JW. Developing MR reporter genes: promises and pitfalls. NMR Biomed 2007;20:275–290.
136. Chan KW, Liu G, Arifin DR, Bulte JW, McMahon MT. Remote MR sensing of pH and cell viability using LipoCEST-filled microcapsules. In: Proceedings of the 18th Annual Meeting of ISMRM, Stockholm, Sweden 2010. p 1889.
139. Arifin DR, Chan KW, Liu G, Cardona A, Jamil M, Bulte JW, McMahon MT. Remote MRI sensing of pH and cell viability using immunoprotective microcapsules crosslinked with polycationic DIACEST peptides. In: Proceedings of the 18th Annual Meeting of ISMRM, Stockholm, Sweden 2010. p 42.
140. Pasha A, Tircso G, Benyo ET, Brucher E, Sherry AD. Synthesis and characterization of DOTA-(amide)(4) derivatives: equilibrium and kinetic behavior of their lanthanide(III) complexes. Eur J Inorg Chem 2007:4340–4349.
141. Sherry AD, Caravan P, Lenkinski RE. Primer on gadolinium chemistry. J Magn Reson Imaging 2009;30:1240–1248.
142. Li AX, Suchy M, Li C, Poppe C, Gati J, Meakin S, Hudson RH, Menon RS, Bartha M. In vivo detection of a PARACEST agent in mouse brain tumors. In: Proceedings of the 18th Annual Meeting of ISMRM, Stockholm, Sweden 2010. p 3752.
143. Jones CK, Li AX, Suchy M, Hudson RH, Menon RS, Bartha R. In vivo detection of PARACEST agents with relaxation correction. Magn Reson Med 2010;63:1184–1192.
144. Soesbe TC, Rojas-Quijano FA, Merritt ME, Sherry AD. Eu^{3+}-based PARACEST agents with intermediate water exchange rates also act as T_2 exchange (T_{2exch}) contrast agents. In: Proceedings of the 18th Annual Meeting of ISMRM, Stockholm, Sweden 2010. p 39.
145. Ren J, Trokowski R, Zhang S, Malloy CR, Sherry AD. Imaging the tissue distribution of glucose in livers using a PARACEST sensor. Magn Reson Med 2008;60:1047–1055.
146. Wu Y, Zhou Y, Ouari O, Woods M, Zhao P, Soesbe TC, Kiefer GE, Sherry AD. Polymeric PARACEST agents for enhancing MRI contrast sensitivity. J Am Chem Soc 2008;130:13854–13855.

Research article

NMR IN BIOMEDICINE

Received: 28 September 2012, Revised: 25 January 2013, Accepted: 14 February 2013, Published online in Wiley Online Library: 2 April 2013

(wileyonlinelibrary.com) DOI: 10.1002/nbm.2942

A calibration-based approach to real-time *in vivo* monitoring of pyruvate C_1 and C_2 polarization using the J_{CC} spectral asymmetry

Justin Y. C. Lau[a,b], Albert P. Chen[c], Yi-Ping Gu[b] and Charles H. Cunningham[a,b]*

A calibration-based technique for real-time measurement of pyruvate polarization by partial integral analysis of the doublet from the neighbouring *J*-coupled carbon is presented. *In vitro* calibration data relating the C_2 and C_1 asymmetries to the instantaneous C_1 and C_2 polarizations, respectively, were acquired in blood. The feasibility of using the *in vitro* calibration data to determine the instantaneous *in vivo* C_1 and C_2 polarizations was demonstrated in the analysis of rat kidney and pig heart spectral data. An approach for incorporating this technique into *in vivo* protocols is proposed. Copyright © 2013 John Wiley & Sons, Ltd.

Keywords: hyperpolarized; pyruvate; DNP; carbon-13; polarization measurement; asymmetry

INTRODUCTION

Dynamic nuclear polarization (DNP) is a non-equilibrium spin population technique that can provide a temporary, liquid-state ^{13}C NMR signal enhancement of more than four orders of magnitude (1). This signal enhancement facilitates rapid MR observation of ^{13}C *in vivo* (2). One application of particular interest is the *in vivo* monitoring of pyruvate metabolism, which has been shown to change with the onset of numerous disease conditions, including cancer (3) and cardiovascular diseases (4). Quantitative analysis of metabolism requires knowledge of the DNP signal enhancement at all time points such that the spectral intensity can be normalized to concentration, allowing for comparison within a series of measurements. Signal enhancement, or equivalently spin polarization, is conventionally determined by comparison with the corresponding thermal equilibrium signal intensity. Acquisition of a thermal equilibrium carbon spectrum *in vivo* is difficult due to the prohibitively long scan times required to obtain an adequate signal-to-noise ratio (SNR). An alternative approach to polarization measurement is needed for *in vivo* applications.

In measuring the polarization of [^{13}C] urea, Ardenkjaer-Larsen *et al*. examined the normalized difference of partial integrals for the two spectral lines in the ^{15}N doublet, which arise from *J*-coupling with the adjacent ^{13}C nucleus (1). This approach was extended to pyruvate using an analogous partial integrals analysis of the homonuclear *J*-coupled C_2 doublet to estimate the C_1 polarization of [1,2-$^{13}C_2$] pyruvate and [1-^{13}C] pyruvate (from 1% natural abundance of [1,2-$^{13}C_2$] pyruvate) in solution (5). Hurd *et al*. reported that, in solution at 3 T, the T_1 of the C_1 carbon in [1,2-$^{13}C_2$] pyruvate (56 s) was only slightly shorter than that in [1-^{13}C] pyruvate (60 s). The feasibility of measuring the C_1 polarization of [1-^{13}C] pyruvate using the relative spectral intensities of the C_2 doublet (1% natural abundance) has been demonstrated *in vitro* and *in vivo* (6). Although accurate for initial polarization measurement, the C_2 doublet was found to evolve beyond the second-order spectral pattern of a strongly *J*-coupled AB spin system at thermal equilibrium soon after injection of the pre-polarized solution into an animal. The physical mechanisms responsible for the evolution of C_2 doublet asymmetry in the [1,2-$^{13}C_2$] pyruvate system have not been fully understood.

The objective of this research is to extend the work of Hurd *et al*. and Chen *et al*. to enable the measurement of instantaneous C_1 polarization regardless of the time elapsed post-injection. After a brief examination of the theoretical framework underlying polarization measurements based on doublet partial integrals, we pursue an empirical approach. We use calibration data in blood that are consistent with our animal protocols to determine the instantaneous *in vivo* polarization in rat kidney and pig heart metabolic experiments.

* *Correspondence to: C. H. Cunningham, Imaging Research (M7-613), Sunnybrook Health Sciences Centre, 2075 Bayview Ave., Toronto, Ontario, Canada, M4N 3M5.*
E-mail chuck@sri.utoronto.ca

a *J. Y. C. Lau, C. H. Cunningham*
Department of Medical Biophysics, University of Toronto, Toronto, Ontario, Canada

b *J. Y. C. Lau, Y.-P. Gu, C. H. Cunningham*
Imaging Research, Sunnybrook Research Institute, Toronto, Ontario, Canada

c *A. P. Chen*
GE Healthcare, Toronto, Ontario, Canada

Abbreviations used: *DNP, dynamic nuclear polarization; SNR, signal-to-noise ratio; RF, radiofrequency; FA, flip angle; Gd-HP-DO3A, gadolinium (III) 2-[4-(2-hydroxypropyl)-7,10-bis(2-oxido-2-oxoethyl)-1,4,7,10-tetrazacyclododec-1-yl]acetate (gadoteridol); Tris, tris(hydroxymethyl)aminomethane; EDTA, ethylenediaminetetraacetic acid; Gd-DTPA, gadolinium (III) diethylenetriaminepentaacetic acid; RNU, Rowett nude; GEVPDF, generalized extreme value probability density function; Pyr, pyruvate (keto form); Pyh, pyruvate hydrate (gem-diol form); MCT1, monocarboxylate transporter 1.*

 Copyright © 2013 John Wiley & Sons, Ltd.

THEORY

The Hamiltonian operator representing a system of two *J*-coupled ^{13}C nuclei is given in Equation [1]. In the case of negligible *J*-coupling, $J_{CC} \approx 0$ Hz, there are four stationary states: $|\alpha\alpha\rangle$, $|\alpha\beta\rangle$, $|\beta\alpha\rangle$, and $|\beta\beta\rangle$, where the notation $|\psi_1\psi_2\rangle$ represents an ordered tensor product of the two nuclear spin wavefunctions $|\psi_1\rangle_{C_1} \otimes |\psi_2\rangle_{C_2}$. For non-zero J_{CC}, $|\alpha\alpha\rangle$ and $|\beta\beta\rangle$ remain eigenstates, but two new eigenstates arise from mixtures of $|\alpha\beta\rangle$ and $|\beta\alpha\rangle$, as summarized in Figure 1.

$$\hat{\mathcal{H}}_0 = \omega_1 \hat{I}_{z_1} + \omega_2 \hat{I}_{z_2} + 2\pi J_{CC} \hat{\mathbf{I}}_1 \cdot \hat{\mathbf{I}}_2 \qquad [1]$$

The C_1 polarization is the fractional occupation of levels where $|\psi_1\rangle_{C_1} = |\alpha\rangle$ less the fractional occupation of levels where $|\psi_1\rangle_{C_1} = |\beta\rangle$. From Figure 1, the desired C_1 polarization as a function of time $P_{C_1}(t)$ can be written as

$$P_{C_1}(t) = \frac{\left[N_1(t) + |c_2|^2 N_2(t) + |c_1|^2 N_3(t)\right] - \left[|c_1|^2 N_2(t) + |c_2|^2 N_3(t) + N_4(t)\right]}{N_1(t) + N_2(t) + N_3(t) + N_4(t)} \qquad [2]$$

For a single nucleus, the transition probability W_{ij} between two spin states $|\psi_i\rangle$ and $|\psi_j\rangle$ is given by Fermi's golden rule, Equation [3], where $\hat{\mathcal{H}}_1$ is the perturbative Hamiltonian operator, ρ is the density of final states, and the integration is performed over the solid angle Ω. The probability of transition in either direction is the same, $W_{i\to j} = W_{j\to i} = W_{ij}$.

$$W_{ij} = \frac{2\pi}{\hbar^2} \int \left|\left\langle \psi_i \middle| \hat{\mathcal{H}}_1 \middle| \psi_j \right\rangle\right|^2 \rho d\Omega \qquad [3]$$

After stimulation of an ensemble of nuclei with an appropriate $\hat{\mathcal{H}}_1$ by applying a resonant magnetic field $\mathbf{B}_1$ in the form of a radiofrequency (RF) pulse, the measurable signal is the sum of all signals originating from every nucleus in the ensemble. The intensity of the measured signal S_{ij}, corresponding to a transition between energy levels *i* and *j*, is proportional to the combined number of spins N_{ij} in states *i* and *j*, the polarization $P_{ij} = (N_i - N_j)/N_{ij}$ just before the excitation, and the single-nucleus transition probability W_{ij} from Fermi's golden rule, as shown in Equation [4]. The single-nucleus transition probability is proportional to the modulus squared of the matrix element of the perturbative Hamiltonian, $W_{ij} \propto |\langle\psi_i|\hat{\mathcal{H}}_1|\psi_j\rangle|^2$. The signal dependence on the flip angle (FA) arises from this matrix element.

$$S_{ij} \propto N_{ij} P_{ij} W_{ij} \propto (N_i - N_j) \left|\left\langle \psi_i \middle| \hat{\mathcal{H}}_1 \middle| \psi_j \right\rangle\right|^2 \qquad [4]$$

The transition probability formalism suggests that the instantaneous polarization can be obtained directly from measured spectral line intensities. Accurate determination of the proportionality constant can be experimentally difficult, but not necessary if only relative intensities are considered.

Ardenkjaer-Larsen *et al.*, Hurd *et al.*, and Chen *et al.* calculated a spectral parameter known as the C_2 asymmetry, a_{C_2}, defined as the difference of integrals between the lower frequency (upfield, inner) peak and the higher frequency (downfield, outer) peak of the C_2 doublet, all divided by the total C_2 doublet integral, as in Equation [5].

$$a_{C_2} = \frac{S_{C_2}^{(\text{inner})} - S_{C_2}^{(\text{outer})}}{S_{C_2}^{(\text{inner})} + S_{C_2}^{(\text{outer})}} \qquad [5]$$

At thermal equilibrium, $a_{eq} = 0.056$ at 3 T. In literature, the C_1 polarization has been interpreted as $P_{C_1} = a_{C_2} - a_{eq}$. In terms of spin populations, the C_2 asymmetry a_{C_2} can be written as Equation [6] using Equation [4]. It can be seen that the asymmetry $a_{C_2}(t)$ does not correspond directly to the C_1 polarization $P_{C_1}(t)$.

$$a_{C_2}(t) = \frac{[N_1(t) - N_2(t)]\left|\langle\psi_2|\hat{\mathcal{H}}_1|\psi_1\rangle\right|^2 - [N_3(t) - N_4(t)]\left|\langle\psi_4|\hat{\mathcal{H}}_1|\psi_3\rangle\right|^2}{[N_1(t) - N_2(t)]\left|\langle\psi_2|\hat{\mathcal{H}}_1|\psi_1\rangle\right|^2 + [N_3(t) - N_4(t)]\left|\langle\psi_4|\hat{\mathcal{H}}_1|\psi_3\rangle\right|^2} \qquad [6]$$

The theoretical framework supports the correlation between C_1 polarization and C_2 asymmetry, but the relationship is not as simple as $P_{C_1} = a_{C_2} - a_{eq}$. However, we will demonstrate that the C_2 asymmetry, a_{C_2}, correlates strongly with C_1 polarization.

Analogously, the C_1 asymmetry, a_{C_1}, can be defined. In this work, we shall also explore the empirical correlation between C_2 polarization and C_1 asymmetry, a relationship that has not been investigated previously.

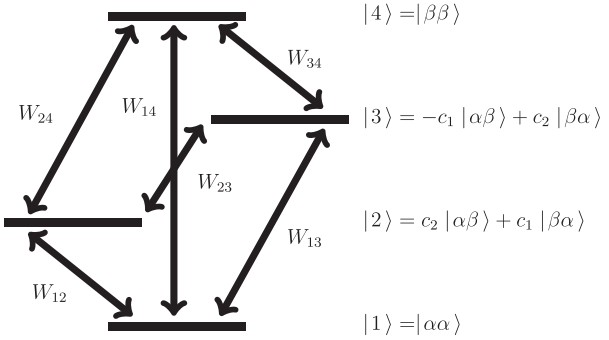


Figure 1. An energy level diagram of a non-weakly *J*-coupled spin-$\frac{1}{2}$ pair. The coefficients c_1 and c_2 represent the degree of superposition of the two mixed uncoupled eigenstates $|\alpha\beta\rangle$ and $|\beta\alpha\rangle$ in the coupled eigenstates $|2\rangle$ and $|3\rangle$. The modulus square of these coefficients represents the probability of measuring a particular eigenvalue in the uncoupled eigenstate basis. The uncoupled eigenstates $|\alpha\alpha\rangle$ and $|\beta\beta\rangle$ remain unchanged as the coupled eigenstates $|1\rangle$ and $|4\rangle$.

METHODS

All experiments were performed using a GE MR750 3 T scanner equipped with 50 mT/m gradients (200 mT/m/ms slew rate) and an 8 kW broadband RF amplifier (GE Healthcare, Waukesha, WI, USA). Animal experiments were approved by the institutional research ethics board and performed in accordance with institutional animal care protocols.

Polarization procedure

Approximately 25 μL of [1,2-$^{13}C_2$] pyruvic acid (99%, Isotec, Miamisburg, OH, USA) doped with 15 mM OX63 trityl radicals (Oxford Instruments, Abingdon, UK) and 1 mM ProHance (Gd-HP-DO3A, Bracco Diagnostics Inc., Princeton, NJ, USA) was polarized to steady state using a HyperSense DNP polarizer (Oxford Instruments). A heated 80 mM NaOH solution with 40 mM NaCl, 40 mM

Copyright © 2013 John Wiley & Sons, Ltd.

Tris buffer, and 100 mg/L EDTA was injected in sufficient volume to rapidly dissolve and neutralize the frozen acid. The collection flask was swirled throughout the dissolution process to ensure thorough mixing.

Experiments in blood

Whole blood was extracted from either the femoral or carotid artery of 20 kg pigs into sodium heparin vacuum tubes (BD, Franklin Lakes, NJ, USA) and stored at 4 °C until use. Before the scan, 18 mL of blood was warmed to 37 °C and placed into a 60 mL syringe.

In one experiment, approximately 7 mL of whole blood was extracted from the ear vein of each of three male New Zealand white rabbits and stored in sodium heparin vacuum tubes. Blood type compatibility was verified by mixing 200 μL of blood from each rabbit. The mixture was left for 15 min at room temperature. No clumping was observed after 15 min under ×200 magnification in an optical microscope. To maintain an experimental volume of 18 mL, 6 mL of blood from each rabbit were combined immediately before the experiment. The blood was warmed to 37 °C and placed in a 60 mL syringe.

[1,2-$^{13}C_2$] pyruvic acid was polarized as described above. The hyperpolarized pyruvate solution was transported to the 3 T scanner within 10 s and 2 mL injected through a 92 cm microbore Luer lock-extension set (Codan US Corporation, Santa Ana, CA, USA) into the blood syringe within 20 s. Care was taken to maintain consistent transfer times between repetitions because the evolution of C_2 asymmetry has been observed to depend on the time spent at low field (Keshari K, Wilson D, VanCriekinge M, private communication 2011). A pulse-acquire sequence with 10° FA 200 μs pulses (TR = 3 s, 4096 points/10 kHz readout, 96 transients) was started immediately after injection. A spoiler gradient was played at the end of each TR. Data were acquired with a linear dual-tuned microstrip $^{1}H/^{13}C$ volume rat coil (Magvale, San Francisco, CA, USA).

At thermal equilibrium polarization, 384 transients at 20°C were acquired with 90° FA 200 μs pulses (4096 points/10 kHz readout) after adding 100 μmol Gd-DTPA (200 μL Magnevist, 0.5 mol/L Gd-DTPA, Bayer HealthCare Pharmaceuticals Inc., Wayne, NJ, USA) to shorten the T_1, allowing full magnetization recovery within TR = 10 s. Data from all 384 transients were combined and a 10 Hz Gaussian apodization filter was applied in the time domain. The blood syringe was weighed before and after injection of pyruvate to determine the total amount of [1,2-$^{13}C_2$] pyruvate added to the syringe. Single-transient spectra from a 20 mL [^{13}C] urea phantom (1.0 M ^{13}C with 100 μmol Gd-DTPA) were acquired with 10° and 90° FAs at the end of each experiment. The urea signal intensity and injected weight of pyruvate solution provided an independent quantification of total ^{13}C content in the syringe.

In vivo experiments

A Rowett nude (RNU) rat (Harlan Laboratories, Indianapolis, IN, USA) was anesthetized in an induction chamber under 5% isoflurane with 1 L/min O_2 supply under a protocol approved by the local animal care committee. The rat was transported to the scanner, placed prone into the previously described rat coil, and maintained at 2% isoflurane with 2–3 L/min O_2 supply via a nose cone. Body temperature was maintained at 37.5 °C with a circulating water blanket. A 24 gauge intravenous catheter was inserted into the tail vein. The rat was administered 3 mL of 80 mM pyruvate over 10 s via tail vein injection. A slice-selective pulse with 10° nominal FA was applied every TR = 3 s (4096 points/10 kHz readout, 96 transients) to obtain *in vivo* spectra integrated over a 2 cm slice centred over the rat kidneys.

Data from cardiac metabolic experiments in three pigs were analysed retrospectively in this work. Preparation and handling procedures for pigs have been described previously (7). *In vivo* ^{13}C spectra from pig hearts (integrated over the entire heart) were acquired using a ^{13}C transmit–receive surface coil and a cardiac-gated sequence with nominal 10° hard pulses every 4 R-R beginning simultaneously with intravenous infusion of 15 mL of 83 mM [1,2-$^{13}C_2$] pyruvate over approximately 15 s, as described in (8). The heart rate of each animal was monitored throughout the study and recorded to provide an estimate of TR.

Spectral analysis

Spectral apodization, Fourier transformation, and phasing were performed using SAGE (GE Healthcare). In some experiments, overlap between the two spectral lines of the doublet complicated the partial integral analysis required to obtain $a_{C_2}(t)$ and $a_{C_1}(t)$. Spectral fitting was required to separate the integral contribution from each spectral line. The general shape of each spectral line was approximated using a generalized extreme value probability density function (GEVPDF), which can be written as a function of frequency f in the form of Equation [7]. The GEVPDF was selected because it encompassed a wide range of skewed peak shapes and was easily implementable in MATLAB (MathWorks, Natick, MA, USA). An initial value of $\xi = 0.5$ for the shape parameter and reasonable values for the chemical shift δ_n and width σ_n of each of the n spectral lines were used as initial parameters for the fit.

$$\begin{aligned} y_n(f) &= \frac{1}{\sigma_n} q_n(f)^{\xi+1} e^{-q_n(f)}, \text{where} \\ q_n(f) &= \begin{cases} [1+\xi(f-\delta_n)/\sigma_n)]^{-1/\xi} & \text{if } \xi \neq 0 \\ e^{-(f-\delta_n)/\sigma_n} & \text{if } \xi = 0 \end{cases} \end{aligned} \quad [7]$$

For each of the four pyruvate spectral lines in the phased spectrum, a GEVPDF $y_n(f)$ and a sinc function centred about the chemical shift δ_n were included in the full spectral fitting function $y(f)$, given in Equation [8]. Amplitudes A_n and B_n are positive and w_n denotes the width of the sinc function. The pyruvate hydrate spectral lines were not included in this fit.

$$y(f) = \sum_{n=1}^{4} A_n . y_n(f) - B_n . \text{sinc}[(f-\delta_n)/w_n] \quad [8]$$

In addition to resolving the problem of spectral overlap, this fitting procedure is able to approximate the baseline resulting from the delay between the end of RF excitation and the beginning of data acquisition. This is particularly beneficial in the analysis of spatially localized spectra where the severely rolling baseline is not easily approximated by a polynomial. Better agreement between calculated and experimental baselines was obtained using the fitted baseline as compared with the cubic spline approximation.

Copyright © 2013 John Wiley & Sons, Ltd.

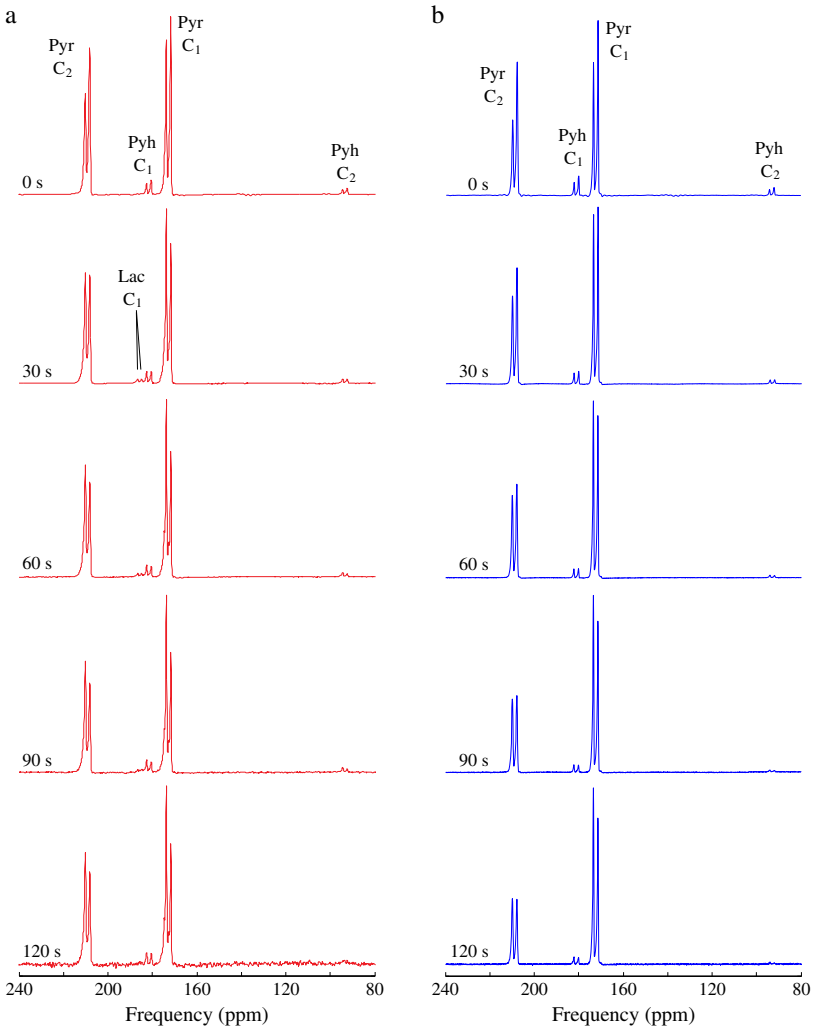


Figure 2. Representative carbon spectra of 80 mM pre-polarized [1,2-$^{13}C_2$] pyruvate (a) injected into 18 mL of 37 °C rabbit blood and (b) in solution at 20 °C. All spectra have been normalized to the same height. Doublets arising from lactate (Lac), the keto form of pyruvate (Pyr), and the gem-diol form of pyruvate (Pyh, pyruvate hydrate) are labelled as shown.

RESULTS

Experiments in blood

Representative *in vitro* carbon spectra of [1,2-$^{13}C_2$] pyruvate injected into rabbit blood are shown in Figure 2(a). Carbon spectra of [1,2-$^{13}C_2$] pyruvate in solution are shown in Figure 2(b) for comparison. The corresponding thermal equilibrium carbon spectra are shown in Figure 3.

Conventionally, the C_1 polarization $P_{C_1}(t)$ for each transient was determined by comparing the C_1 doublet integral to that of the thermal equilibrium spectrum after adjustments for differences in the FA and the number of acquisitions. The analogous analysis was not possible for blood data because a broad resonance centred at 177 ppm, presumably the natural abundance ^{13}C signals of macromolecules in the blood, overlapped with the C_1 doublet and interfered with integration in the thermal equilibrium spectra. As an independent quantification of ^{13}C content in the blood, we prepared a [^{13}C] urea phantom of the same geometry as the blood syringe. The urea signal provides a conversion factor between MR signal intensity and the known amount of ^{13}C in the urea phantom. From the measured mass of injected solution, assuming 80 mM pyruvate concentration in solution, the thermal equilibrium C_1 signal intensity could be estimated using the urea conversion factor for the same gain settings after accounting for FA. For consistency, we report the urea-derived C_1 and C_2 polarizations for all blood experiments.

The asymmetry parameters, a_{C_2} and a_{C_1}, were computed from the fitted spectral line intensities. The correlations between C_1 polarization and C_2 asymmetry for 8 mM [1,2-$^{13}C_2$] pyruvate in whole blood are shown in Figure 4(a) for experiments with 5° FAs ($N = 2$, both pig blood) and in Figure 4(b) for experiments with 10° FAs ($N = 3$, two pig blood and one rabbit blood). The corresponding plots relating C_2 polarization and C_1 asymmetry are shown in Figures 4(c) and 4(d) for experiments with 5° and 10° FAs, respectively.

A linear function with slope m and intercept a_0 was fit to the data; the fitted parameters are summarized in Table 1 according to the data markers in Figure 4. Points with measured polarizations below 1% were not included in the fit because the signal intensity was comparable to the noise levels at these low polarizations. These parameters characterize the mathematical

Copyright © 2013 John Wiley & Sons, Ltd.

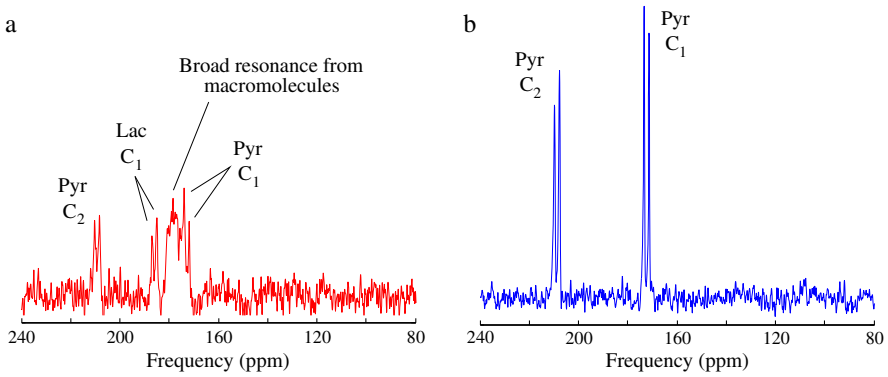


Figure 3. Thermal equilibrium carbon spectra of 80 mM [1,2-$^{13}C_2$] pyruvate (a) in 18 mL of 20 °C rabbit blood doped with 5 mM Gd-DTPA and (b) in solution at 20 °C doped with 4 mM Gd-DTPA. These spectra were formed by combining 384 transients acquired with FA = 90°. Total scan times were (a) 32 min with TR = 5 s and (b) 64 min with TR = 10 s. A 10 Hz Gaussian apodization filter was applied in the time domain before Fourier transform.

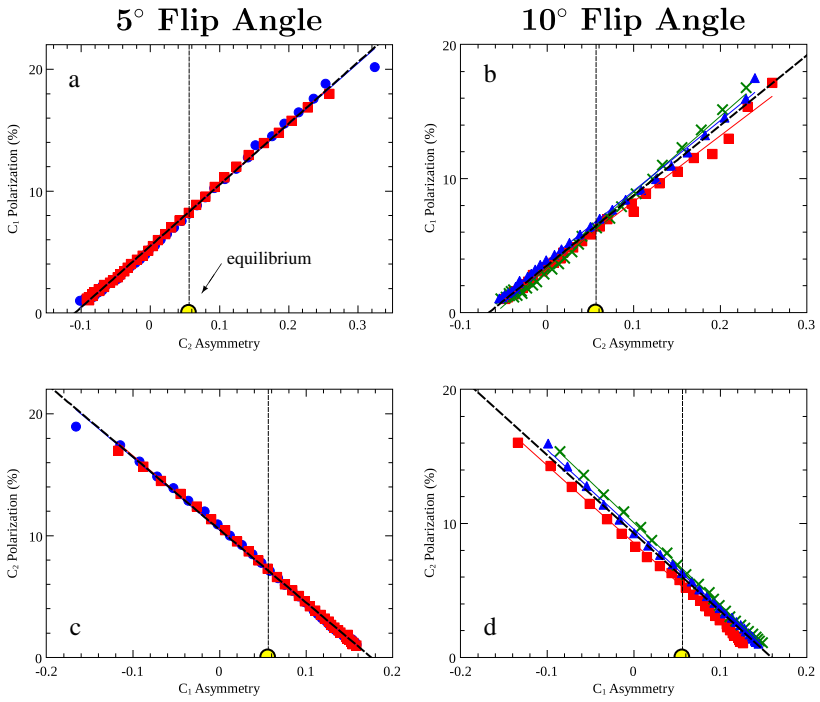


Figure 4. Empirical relationships between doublet asymmetry and polarization in 18 mL of 37°C blood injected with 2 mL of 80 mM pre-polarized pyruvate solution. Panels (a) and (c) show two sets of pig blood data acquired with 5° FAs. Panels (b) and (d) show two sets of pig blood data and one set of rabbit blood data (×) acquired with 10° FAs. A line of best fit is shown for each individual data set. The dashed line shows the best fit to the combined data with computed R^2 values of (a) 0.997, (b) 0.988, (c) 0.997, and (d) 0.981. A highlighted semicircle marks the thermal equilibrium polarization with the thermal equilibrium asymmetry indicated by the connecting dashed vertical line.

models that approximate the experimental data. The curves derived from the average parameters will be considered as calibration curves relating measurable asymmetry to the instantaneous polarization.

A mono-exponential function, with correction for longitudinal magnetization consumption by successive small FA excitations, was fit to the partial integral of each spectral line and to the integral of each doublet, plotted as functions of time, to obtain longitudinal relaxation time constants. These values are summarized in Table 2 according to the data markers in Figure 4. Although the mono-exponential fit modelled the general behaviour of all spectral lines, there was poorer agreement between the downfield partial integrals and the mono-exponential fit ($R^2 < 0.999$), suggesting that the decay may be multi-exponential or non-exponential. Therefore, the values reported in Table 2 may not fully describe the longitudinal relaxation behaviour of some spectral lines. Based on the fit results, the rabbit blood data (×) exhibited shorter longitudinal relaxation time constants compared with the two pig blood data sets with FA = 10°.

In vivo experiments

The average FA = 10° blood calibration curves were used to calculate polarizations from measured doublet asymmetries.

Copyright © 2013 John Wiley & Sons, Ltd.

Table 1. Summary of parameters fitted to blood calibration data. Parameters m (%) and a_0 (%) represent the slope and intercept from linear regression. The identifying symbols correspond to the data markers used in Figure 4

		C_2 asymmetry		C_1 asymmetry	
FA	Marker	m (%)	a_0 (%)	m (%)	a_0 (%)
5°	●	50.1	5.49	−59.6	10.45
	■	50.0	5.54	−60.2	10.54
	Average	50.1	5.52	−59.9	10.50
	Std dev.	0.1	0.03	0.4	0.07
10°	×	56.4	3.37	−61.3	10.06
	▲	52.4	3.86	−59.2	9.57
	■	49.0	3.40	−58.0	8.54
	Average	52.6	3.54	−59.5	9.39
	Std dev.	3.7	0.28	1.7	0.78
Average		51.6	4.33	−59.6	9.83
Std dev.		3.0	1.10	1.2	0.82

Table 2. Summary of longitudinal relaxation time constants for spectral lines of 8 mM [1,2-$^{13}C_2$] pyruvate in blood at 37°C. The identifying symbols correspond to the data markers used in Figure 4. All values are given in seconds

		Upfield		Downfield		Doublet	
FA		C_1	C_2	C_1	C_2	C_1	C_2
5°	●	35.6	31.5	48.9	45.8	43.5	37.6
	■	36.2	31.3	47.9	43.5	41.9	35.9
10°	×	27.4	26.6	35.8	36.1	31.7	30.3
	▲	33.0	29.2	44.0	40.9	38.1	33.7
	■	35.4	30.1	47.6	42.1	40.7	34.5
Average		33.5	29.8	45.0	41.8	38.9	34.7
Std dev.		3.7	2.0	5.5	3.7	5.2	2.3

The calculated C_1 and C_2 polarizations are shown in Figure 5(a) as functions of time after the start of injection. Two data points toward the beginning of the acquisition were not included in the analysis because of low SNR.

Estimated *in vivo* T_1 values of 18.6 s (C_1) and 18.8 s (C_2) were obtained by fitting the calculated polarization data to mono-exponential functions, with correction for successive small FA excitations. It is important to note that the relaxation may not be mono-exponential. However, the monotonic decrease in polarization is markedly different from the *in vivo* signal intensity profile shown in Figure 5(b).

Data from a previous study on porcine whole-heart metabolism (8) were reanalysed in this work to investigate the possibility of determining instantaneous polarization from cardiac spectra. The average FA = 10° blood calibration curves were used to analyse these data. The calculated C_1 and C_2 polarizations for three animals are shown in Figure 6(a) as functions of time. It can be seen that a mono-exponential model is not consistent with these data. However, the decreasing trend of the calculated polarization is markedly different from the corresponding signal intensity profile shown in Figure 6(b).

DISCUSSION

A linear function was found to adequately model the calibration data relating instantaneous polarization to doublet asymmetry. The intercept parameter a_0 represents the polarization at which the two spectral lines of the doublet become of equal intensity. Inversion of asymmetry, visually the flipping over of the doublet, occurs for positive values of a_0. It is interesting to observe that $a_{eq} \neq -a_0/m$, which suggests that this model does not completely describe the relaxation back to thermal equilibrium. The spectral behaviour in the latter stages of relaxation back to thermal equilibrium remains a mystery because the signal intensity at polarizations below 1% becomes comparable to the level of noise under the described experimental conditions. However, we have shown that the linear model provides an adequate estimation of calibration data over the range of usable SNR, approximately 1 min *in vivo*.

[1-^{13}C] pyruvate is expected to have a slightly longer T_1 than [1,2-$^{13}C_2$] pyruvate *in vivo*. However, the low C_2 SNR from the 1% natural abundance of [1,2-$^{13}C_2$] pyruvate in [1-^{13}C] pyruvate limits polarization measurement to a small number of time points. To increase the C_2 SNR, we propose the co-polarization of [1-^{13}C] pyruvic acid with a small amount, e.g. 5%, of [1,2-$^{13}C_2$] pyruvic acid. The longer T_1 of the predominantly singly

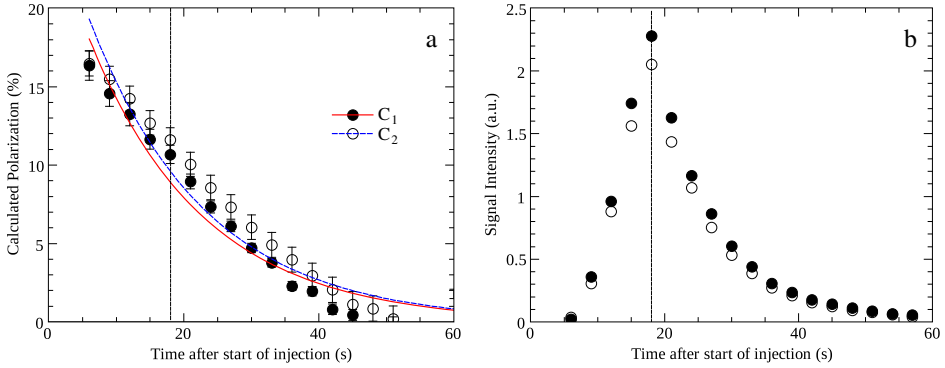


Figure 5. (a) The decay of *in vivo* C_1 (closed symbols) and C_2 (open symbols) polarization observed in the rat kidneys calculated using the average FA = 10° blood calibration curves. The error bars show the propagated errors representing the statistical uncertainties in the calibration curve parameters. Exponential curves of best fit, with FA correction, are shown for the decay of C_1 (solid curve) and C_2 (dashed curve) polarization. (b) The corresponding signal intensity profiles for C_1 (closed symbols) and C_2 (open symbols) doublets, in arbitrary units, as functions of time. The dashed vertical line marks the time of maximal signal intensity on both panels.

Copyright © 2013 John Wiley & Sons, Ltd.

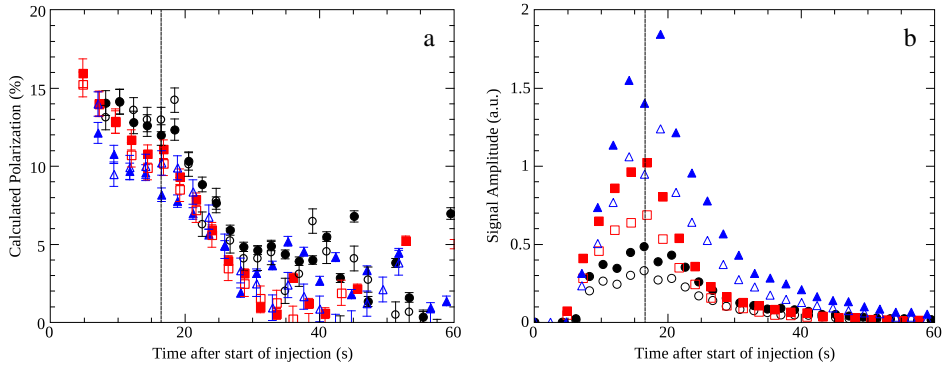


Figure 6. (a) Estimated *in vivo* C_1 (closed symbols) and C2 (open symbols) polarization decay in three experiments observing the whole pig heart. The error bars show the corresponding propagated errors representing the statistical uncertainties in the calibration curve parameters. (b) The corresponding signal intensity profiles for C_1 (closed symbols) and C_2 (open symbols) doublets as functions of time. The dashed vertical line marks the time of maximal signal intensity on both panels.

labelled pyruvate may prolong the available imaging time using the C_1 signal, while the enhanced C_2 signal in the spiked mixture may facilitate the monitoring of C_1 polarization at a greater number of time points throughout the imaging, assuming similar polarizations are achieved for [1-^{13}C] pyruvic acid and [1,2-$^{13}C_2$] pyruvic acid.

Unequal relaxation rates of the two lines within a doublet is a common observation in the presence of cross-correlations in a strongly coupled two-spin system, a phenomenon known as "the multiplet effect" (9). In addition to auto-correlated dipolar relaxation between C_1 and C_2, contributions from cross-correlated relaxation mechanisms (10) may result in non-exponential relaxation, which may further influence the evolution of the doublet asymmetries in [1,2-$^{13}C_2$] pyruvate. The values in Table 2 are reported as longitudinal relaxation time constants (τ) because T_1 may not be defined in cases of non-exponential relaxation.

Although density matrix simulation provided accurate predictions of C_2 asymmetry over a short period after placement in the scanner, agreement between simulation and measurement gradually worsened as the two-spin system was allowed to evolve at field (6). Inclusion of cross-relaxation effects in the simulation may improve its predictive accuracy. However, even for the simple system of [^{13}C] formate, monitoring of ^{13}C polarization using the ^{1}H doublet asymmetry required careful modelling of the $^1H - {}^{13}C$ dipolar cross-relaxation in solution (11). In blood, endogenous molecules may introduce additional relaxation pathways that could further complicate the modelling. Whereas a separate theoretical model would be required for each medium of interest (e.g. serum, normal saline, gels), the protocol described in this work can be applied with little modification to obtain calibration data in arbitrary media.

We have demonstrated that the relationship between C_1 polarization and C_2 asymmetry is much richer than $P_{C_1} = a_{C_2} - a_{eq}$, as previously reported in literature. In particular, we have shown that $m < 100\%$ and $a_0 \neq -a_{eq}$ for the conditions that we examined. The empirical interpretation of asymmetry ensures that unphysical negative polarizations of the coupled carbon are not predicted when the doublet evolves beyond the asymmetry at thermal equilibrium. Furthermore, relating asymmetry to polarization of the coupled carbon via empirical calibration is relatively straightforward and potentially more robust compared with some theoretical approaches. For example, longitudinal relaxation is known to be field dependent. Slower longitudinal relaxation at low field (< 0.1 T) has been exploited to reduce the loss of polarization of [1-^{13}C] pyruvate before placement into the high field of the scanner (12). The effects of slower relaxation at low field on the evolution of pyruvate doublet asymmetries are not well understood, but the calibration-based approach naturally takes into account any evolution that occurs at low field (assuming consistent transfer times between calibration and *in vivo* experiments) without the need to actively correct for the complex spin dynamics that occur during transport from polarizer to scanner.

From density matrix simulations, the asymmetry in the spectral intensities of the C_2 doublet was identified as originating from the two-spin order term of the density matrix (13). We have demonstrated, in blood, an FA dependence in the calibration parameters, which was consistent with simulation and theoretically expected because the line intensities of an AB system depend on the FA if the spin system is not in thermal equilibrium immediately prior to RF pulse application (14). The FA dependence in the calibration parameters may pose some limitations on the choice of pulse sequences. One important case that Tropp considered was the disappearance of spectral asymmetry after the application of a 90° pulse due to complete conversion of two-spin order into double and zero quantum coherences. Pulse sequences with spectrally non-selective 90° pulses may not be compatible with this polarization quantification technique. However, the use of spectrally selective pulses, which excite only one of the two nuclei at a time, may allow interleaved imaging and polarization measurement.

One potential concern regarding the usefulness of this calibration-based technique may be the inter-patient applicability of calibration data. For FA = 5°, calibration data obtained using blood from two different animals are shown in Figures 4 (a) and 4(c). Agreement between the two data sets was better than 1%, which suggests good tolerance for blood chemistry variability between patients. The large deviation of the first data point in each series from the fitted trend may be attributed to incomplete mixing immediately after the injection. Factors such as haematocrit and blood oxygenation were not examined in detail in this study. Further investigation is required to determine the limits of inter-patient variability.

Copyright © 2013 John Wiley & Sons, Ltd.

Another concern may be the validity of using non-human blood results to suggest the potential suitability of this calibration technique for human use. A comparison between the two pig blood calibration curves (■ and ▲) and the rabbit blood calibration curve (×) in Figures 4(b) and 4(d) shows that any one of the curves predicts polarization values within ±1% of the other curves over the range of asymmetries observed. Furthermore, there was close agreement among the three curves even though the longitudinal relaxation time constants in rabbit blood were shorter than those in pig blood, which may be consistent with signal transfer from pyruvate to its downstream metabolites due to higher erythrocyte metabolic activity in rabbit blood. One advantage of using doublet asymmetries instead of signal intensities for polarization measurement is the concentration-insensitivity of the asymmetry parameters, a_{C_1} and a_{C_2}, which are normalized for signal intensity by definition. Polarizations that are derived from doublet asymmetry are largely unaffected by metabolic activity unless the rate of label exchange in both directions may become comparable, as in the case of pyruvate–lactate co-injections with both substrates labelled (15).

In vivo C_1 and C_2 longitudinal relaxation time constants of 19 s were estimated by fitting the rat kidney polarization decay curves to mono-exponential functions. Although the relaxation may not be truly mono-exponential, we observe that a mono-exponential fit approximately models the dominant relaxation behaviour. Both C_1 and C_2 polarizations decreased monotonically with time, which differ markedly from the time profiles of signal intensity. The calculated C_2 polarizations were slightly higher than the calculated C_1 polarizations, but there was no significant difference within statistical uncertainty. However, the agreement (within uncertainty) between the C_1 and C_2 longitudinal relaxation time constants is consistent with the *in vitro* longitudinal relaxation behaviour in blood.

Unlike the rat kidney data, the calculated C_1 and C_2 polarization decay curves in pig hearts are evidently non-exponential. An overall monotonically decreasing trend can be seen with increasing fluctuation in the data. Blood in the different chambers of the heart may have experienced different relaxation histories such that the doublet asymmetries are different in the various compartments. By integrating the signal over the whole heart, only the averaged doublet asymmetry was observed. However, the average doublet asymmetry may not reflect the relaxation behaviour of any compartment. The blood calibration data may not be valid under such circumstances, resulting in a nonsensical analysis. It may be worthwhile to investigate the feasibility of polarization measurement in localized cardiac spectral data that distinguish between the different compartments of the heart.

It is important to recognize that relaxation conditions in tissue may differ from those in blood. Although it can be argued that blood calibration data provide a good model for examining experimental data in the vasculature, the validity of using blood calibration data to analyse spectra localized to regions where tissue content dominates may be less convincing. To ensure validity of the calibration data, it is suggested that localized spectra intended for polarization measurement be acquired in the vasculature immediately upstream of the tissue of interest. The measured polarization should provide a good estimate for the initial polarization in the tissue of interest. Further investigation is required to characterize the errors that could arise from using blood calibration data to analyse spectra localized to tissue-dominated volumes.

CONCLUSIONS

In this work, we have presented a calibration-based method for real-time measurement of pyruvate polarization that can be used for *in vivo* applications. The calibration data offered some new insights into the framework of J_{CC} spectral asymmetry previously established in literature. One important observation in blood is that the C_2 asymmetry is linearly related to the C_1 polarization with a slope that is less than unity. The empirical interpretation of C_2 asymmetry ensures that unphysical negative C_1 polarizations are not predicted when the C_2 doublet evolves beyond the asymmetry at thermal equilibrium. Furthermore, we have demonstrated the feasibility of measuring *in vivo* C_2 polarization using the C_1 doublet asymmetry.

The approach we have presented offers great flexibility and is suitable for a variety of experimental protocols. The collection of empirical calibration data naturally accounts for differences in the medium of interest and transfer times between polarizer and scanner, which may be difficult to model theoretically. Preliminary data suggest good inter-patient applicability. This novel interpretation of spectral asymmetry extends its predictive value to the full range of usable SNR. The *in vivo* polarization decay curves obtained using this technique allow us to report, for the first time, the *in vivo* T_1 of pyruvate C_1 and C_2.

Despite the robustness of this method, care must be taken in acquiring calibration data such that all environmental conditions are similar to those used in experimental protocols. *In vivo* polarizations extracted from asymmetry in the vasculature, immediately upstream of the tissue of interest, are expected to be much closer estimates of the polarization in tissue compared with polarization measurements from previously established techniques.

Acknowledgements

The authors thank Jennifer Barry, Michelle Ladouceur-Wodzak, and Carrie Purcell for their assistance with animal experiments. Funding support was provided by the Ontario Institute for Cancer Research, the Natural Sciences and Engineering Research Council of Canada, and the Ontario Graduate Scholarships program.

REFERENCES

1. Ardenkjaer-Larsen JH, Fridlund B, Gram A, Hansson G, Hansson L, Lerche MH, Servin R, Thaning M, Golman K. Increase in signal-to-noise ratio of >10,000 times in liquid-state NMR. Proc. Natl. Acad. Sci. 2003; 100(18): 10158–10163.
2. Kohler SJ, Yen Y, Wolber J, Chen AP, Albers MJ, Bok R, Zhang V, Tropp J, Nelson S, Vigneron DB, Kurhanewicz J, Hurd RE. *In vivo* ^{13}carbon metabolic imaging at 3T with hyperpolarized ^{13}C-1-pyruvate. Magn. Reson. Med. 2007; 58(1): 65–69.
3. Golman K, in't Zandt R, Lerche M, Pehrson R, Ardenkjaer-Larsen JH. Metabolic imaging by hyperpolarized ^{13}C magnetic resonance imaging for *in vivo* tumor diagnosis. Cancer Res. 2006; 66(22): 10855–10860.
4. Schroeder MA, Clarke K, Neubauer S, Tyler DJ. Hyperpolarized magnetic resonance: a novel technique for the *in vivo* assessment of cardiovascular disease. Circulation 2011; 124(14): 1580–1594.
5. Hurd RE, Chen A, Cunningham CH, Tropp J. Scalar coupling patterns in hyperpolarized spin systems: J_{CC} spectral pattern in hyperpolarized 1,2-[^{13}C]-pyruvate. A potential indirect measure of polarization. *Proceedings of the 50th Experimental Nuclear Magnetic Resonance Conference*. Pacific Grove, CA, 2009, p. 438.
6. Chen AP, Cunningham CH, Tropp J, Keshari K, VanCriekinge M, Kurhanewicz J, Hurd RE. Potential for polarization measurement of

Copyright © 2013 John Wiley & Sons, Ltd.

pre-polarized [1-^{13}C] pyruvate *in vivo* using Jcc spectral pattern. *Proceedings of the International Society of Magnetic Resonance in Medicine*, volume 18. Stockholm, 2010, p. 3261.
7. Lau AZ, Chen AP, Hurd RE, Cunningham CH. Spectral–spatial excitation for rapid imaging of DNP compounds. NMR Biomed. 2011; 24(8): 988–996.
8. Chen AP, Hurd RE, Schroeder MA, Lau AZ, Gu Y-P, Lam WW, Barry J, Tropp J, Cunningham CH. Simultaneous investigation of cardiac pyruvate dehydrogenase flux, Krebs cycle metabolism and pH, using hyperpolarized [1,2-$^{13}C_2$]pyruvate *in vivo*. NMR Biomed. 2012; 25(2): 305–311.
9. Campbell ID, Freeman R. Influence of cross-relaxation on NMR spin-lattice relaxation times. J. Magn. Reson. 1973; 11(2):143–162.
10. Kumar A, Grace RCR, Madhu PK. Cross-correlations in NMR. Prog. Nucl. Magn. Reson. Spectrosc. 2000; 37(3): 191–319.
11. Merritt ME, Harrison C, Mander W, Malloy CR, Sherry AD. Dipolar cross-relaxation modulates signal amplitudes in the ^{1}H NMR spectrum of hyperpolarized [^{13}C]formate. J. Magn. Reson. 2007; 189(2): 280–285.
12. Van Criekinge M, Keshari K, Wilson DM, Vigneron DB, Kurhanewicz J. Retaining polarization by exploiting slower T_1 relaxation of hyperpolarized spins at low field in solution. *Proceedings of the 53rd Experimental Nuclear Magnetic Resonance Conference*. Miami, FL, 2012, p. 139.
13. Tropp J. Multiplet asymmetry and multi-spin order in liquid-state NMR spectra of hyperpolarized compounds. *Proceedings of the International Society of Magnetic Resonance in Medicine*, volume 18. Stockholm, 2010, p. 1026.
14. Bain AD, Martin JS. FT NMR of nonequilibrium states of complex spin systems. I. A Lionville space description. J. Magn. Reson. 1978; 29(1): 125–135.
15. Park JM, Hurd RE, Josan S, Yen Y-F, Pfefferbaum A, Mayer D, Spielman DM. Differentiation of flux and isotopic exchange using co-administration of hyperpolarized [2-13C]Pyr and [1-13C]Lac. *Proceedings of the International Society of Magnetic Resonance in Medicine*, volume 20. Melbourne, 2012, p. 4298.

Copyright © 2013 John Wiley & Sons, Ltd.

NOTE

Magnetic Resonance in Medicine 00:00–00 (2015)

Handheld Electromagnet Carrier for Transfer of Hyperpolarized Carbon-13 Samples

Hong Shang,[1,2] Timothy Skloss,[3] Cornelius von Morze,[1] Lucas Carvajal,[1] Mark Van Criekinge,[1] Eugene Milshteyn,[1,2] Peder E. Z. Larson,[1,2] Ralph E. Hurd,[3] and Daniel B. Vigneron[1,2]*

Purpose: Hyperpolarization of carbon-13 (^{13}C) nuclei by dissolution dynamic nuclear polarization increases signal-to-noise ratio (SNR) by >10,000-fold for metabolic imaging, but care must be taken when transferring hyperpolarized (HP) samples from polarizer to MR scanner. Some ^{13}C substrates relax rapidly in low ambient magnetic fields. A handheld electromagnet carrier was designed and constructed to preserve polarization by maintaining a sufficient field during sample transfer.
Methods: The device was constructed with a solenoidal electromagnet, powered by a nonmagnetic battery, holding the HP sample during transfer. A specially designed switch automated deactivation of the field once transfer was complete. Phantom and rat experiments were performed to compare MR signal enhancement with or without the device for HP [^{13}C]urea and [1-^{13}C]pyruvate.
Results: The magnetic field generated by this device was tested to be >50 G over a 6-cm central section. In phantom and rat experiments, [^{13}C]urea transported via the device showed SNR improvement by a factor of 1.8–1.9 over samples transferred through the background field.
Conclusion: A device was designed and built to provide a suitably high yet safe magnetic field to preserve hyperpolarization during sample transfer. Comparative testing demonstrated SNR improvements of approximately two-fold for [^{13}C]urea while maintaining SNR for [1-^{13}C]pyruvate. **Magn Reson Med 000:000–000, 2015.** © **2015 Wiley Periodicals, Inc.**

Key words: hyperpolarized carbon-13 MRI/MRSI; dynamic nuclear polarization; low magnetic field; T1 relaxation; scalar coupling; urea

INTRODUCTION

Hyperpolarized carbon-13 (HP ^{13}C) MRI with dissolution dynamic nuclear polarization (DNP) (1) has recently been shown to provide biologic information on previously inaccessible aspects of metabolic processes by detecting endogenous, nontoxic ^{13}C-labeled probes to monitor enzymatic conversions through key biochemical pathways (2–4). Because both spatial and chemical information are encoded, this new molecular imaging modality allows simultaneous detection of multiple biologic compounds and metabolic products with sensitivity enhancements of >10,000-fold (1). The recently completed phase 1 clinical trial conducted at the University of California, San Francisco, demonstrated the safety and feasibility of HP ^{13}C-pyruvate MRI in prostate cancer patients without any dose-limiting or other notable toxicities (5).

Some HP ^{13}C substrates can lose polarization extremely quickly in low magnetic field when they are transferred between the polarizer and the MR scanner, reducing the SNR. For example, scalar coupling between fast-relaxing quadrupolar ^{14}N and ^{13}C results in rapid loss of polarization of [^{13}C]urea (6). Although most in vivo HP ^{13}C MRI studies have focused on probing metabolism using metabolically active substrates (7), several studies have shown that metabolically inactive agents such as [^{13}C]urea can be applied to angiography or perfusion imaging (8,9). HP [^{13}C]urea for perfusion MRI has advantages over conventional gadolinium-containing (paramagnetic) contrast agents, including direct proportionality of signal to concentration, inherently high contrast-to-noise ratio due to the absence of background signal, and an excellent safety profile potentially benefitting studies in patients who are currently excluded from contrast imaging studies. In addition, [^{13}C]urea can be copolarized with [1-^{13}C]pyruvate for combined perfusion and metabolic imaging (10,11). Urea is a safe, endogenous compound with normally high concentrations in vivo (typically 1–10 mM, and much higher in the renal medullary interstitium), low toxicity, and neutral pH, as well as the key MR properties of long T_1 relaxation time and high polarization by DNP. Recent studies have also demonstrated the ability of HP [^{13}C]urea to identify changes in urea transport and concentration in the kidney (12).

In previous studies, this loss of polarization of [^{13}C]urea during sample transfer has been addressed by carrying a permanent magnet next to the HP sample, or at the molecular level by secondary labeling with ^{15}N (6,13). However, the cost of [^{13}C,^{15}N$_2$]urea is about five times higher than [^{13}C]urea. Furthermore, J-coupling in [^{13}C,^{15}N$_2$]urea splits the ^{13}C NMR resonance peak into a triplet, thus lowering the signal amplitude and potentially confounding quantitation. The permanent magnet method raises safety concerns, because the magnet could cause harm by flying into the scanner. In addition, permanent magnets provide

[1]Department of Radiology and Biomedical Imaging, University of California, San Francisco, San Francisco, California, USA.
[2] The UC Berkeley - UCSF Graduate Program in Bioengineering, California, USA.
[3]GE Healthcare, USA.

Grant sponsor: University of California, San Francisco Hyperpolarized MRI Technology Resource Center; Grant sponsor: National Institutes of Health; Grant numbers: P41-EB013598, R01-EB013427, K01-DK099451; Grant sponsor: GE Healthcare; Grant number: R01-EB017449.

*Correspondence to: Daniel B. Vigneron, 1700 4th Street, Byers Hall Suite 102F, MC 2512, San Francisco, CA 94158-2330.
E-mail: dan.vigneron@ucsf.edu

Received 5 December 2014; revised 18 January 2015; accepted 24 January 2015
DOI 10.1002/mrm.25657
Published online 00 Month 2015 in Wiley Online Library (wileyonlinelibrary.com).

© 2015 Wiley Periodicals, Inc.

nonuniform fields and are impractical for large samples. To address these limitations, we constructed and tested a new electromagnet carrier device to provide a suitable and relatively uniform magnetic field for the safe transfer of HP samples for ^{13}C MR studies.

THEORY

Spin-lattice relaxation depends on several independent mechanisms, including interactions with paramagnetic centers and scalar coupling between fast-relaxing quadrupolar nuclei, which cause faster relaxation when the magnetic field decreases. Quadrupolar nuclei with spin >1/2 (eg, ^{14}N) have very short T_1 values. The scalar coupling of ^{13}C to ^{14}N provides a relaxation mechanism for ^{13}C as ^{14}N is undergoing very rapid T_1 relaxation. The scalar coupling relaxation rate can be calculated by

$$R_{SC} = \frac{8\pi^2 J^2}{3} I(I+1) \frac{T_1}{1 + (\Delta\omega)^2 T_1^2}, \quad [1]$$

where R_{sc} is the scalar coupling relaxation rate, J is the scalar coupling constant in Hertz, I is the spin quantum number of the coupled nucleus ($I_{14N} = 1$), T_1 is the spin-lattice relaxation time of the quadrupolar nucleus (^{14}N), and $\Delta\omega = \omega_{13c} - \omega_{14N}$ is the difference in Larmor frequencies of coupled nuclei ^{13}C and ^{14}N. For this mechanism to be effective, the Larmor frequencies of these two nuclei must be very close. This condition is met at low magnetic fields (eg, during HP sample transfer), although it may also occur at high fields (eg, for ^{13}C [15.087 MHz] and ^{79}Br [15.023 MHz] at 1.41 T) (14). One approach to reduce the scalar coupling relaxation mechanism is to increase the external magnetic field.

METHODS

Simulation and Background Field Measurements

The ambient magnetic field through which the HP samples were transferred was measured with a three-axis Hall effect magnetometer (THM 7025; Metrolab Technology SA, Geneva, Switzerland), as shown in Figure 1A. R_{sc} was estimated as a function of magnetic field based on Equation 1 according to the parameters described in Chiavazza et al. (6), including $T_1 = 1.0 \pm 0.1$ ms and $J = 14.5 \pm 0.1$ Hz (Fig. 1B). Assuming a piece-wise constant relaxation rate along the path and constant transfer velocity over a 6s transfer, the signal decay curve can be estimated along this path (Fig. 1C).

By adding a magnetic field offset of 50 G (in the vertical direction) in simulation, this scalar coupling relaxation mechanism can be significantly reduced as shown in Figure 1B, resulting in a 1.83-fold signal improvement at the end of the path as shown in Fig. 1C. This field strength specification was used for the design of this device to provide an adequate magnetic field to maintain a long T_1 for HP samples during transfer.

Hardware

The electromagnet carrier device was designed to provide a suitable magnetic field for the safe transfer of HP samples. The key part of the device is a solenoid with a current of 0.5 A powered by a nonmagnetic battery to generate a relatively uniform magnetic field of >50 G over a 6-cm longitudinal section. The size of the solenoid was customized for the specific 3-mL and 5-mL syringes (BD, Franklin Lakes, New Jersey, USA) commonly used for preclinical HP ^{13}C studies. The inner diameter and the length were designed to be 1.65 cm and 7.9 cm, respectively. The gauge of the wire (22 AWG) and number of layers (six) were chosen based on the desired field of 50 G, resulting in a total of 727 turns.

The circuit is shown in Figure 2A. A single-cell (3.7 V), 500-mAH lithium-ion polymer battery (E-flite; Horizon Hobby, Champaign, Illinois, USA) composed of nonmagnetic materials powered the magnetic field. The device can be safely carried into the 3 T MRI scanner room and turned off there. The current was activated by depressing the default-open, push-button momentary switch. When the button was released, the current was turned off automatically. The design of the switch ensures that the device can be safely operated in the scanner room, covering the entire sample transfer path and thus minimizing the loss of polarization. An LED was installed to indicate when the device was activated. The battery can provide stable current for at least 1 hour of continuous use. The sample transfer duration is <10 s, so one battery charge can last for hundreds of hyperpolarization experiments.

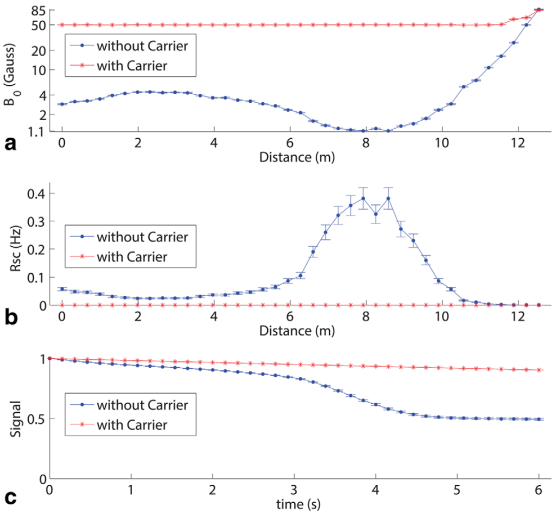


FIG. 1. **A:** Measured ambient magnetic field magnitudes along the sample transfer path (without carrier, blue lines) and simulated field magnitude with 50 G added along the vertical direction (with carrier, red lines). The *y* axis (B_0) is displayed with a log scale. The distance of 15.4 m corresponds to the center of the MR scanner and 0 m corresponds to the location of the DNP polarizer. The range of distance (0–13.4 m) corresponds to the part of the sample transfer path where the device was used. **B:** Estimated scalar coupling relaxation rate of HP [^{13}C]urea along the path corresponding to the two different fields. **C:** Estimated signal decay curve along the path assuming piece-wise constant relaxation rate and constant transfer speed within 6 s.

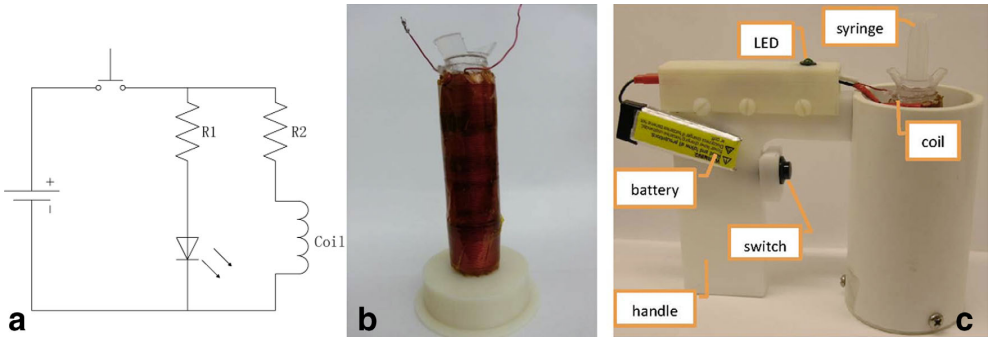


FIG. 2. Hardware design of electromagnet carrier device. **A:** Circuit diagram. Resistance of the coil = 2.9 Ω, R1 = 833 Ω, R2 = 4.4 Ω. A nonmagnetic, 500-mAH lithium-ion polymer battery supplies 3.7 V and a current of 0.5 A in the coil (current in the LED = 2.1 mA). The switch is a default-open, push-button momentary switch. **B:** Photograph of the solenoid inside. **C:** Photograph of the entire device.

The device (Fig. 2C) was constructed using a combination of custom three-dimensional (3D)-printed parts and commercially available parts meeting the design criteria for performance, nonmagnetic materials, and durability. The housing was built with strength to withstand drops to the floor, and the shape was designed for ease of carrying and standing upright. The switch was trigger-mounted to enable easy depression, holding and releasing of the button. The battery was attached on the surface of the device in a manner allowing easy replacement or charging. The inner diameter of the solenoid-encompassed sample chamber closely fits the syringes, which are quickly guided through a conical opening on top of the coil, as shown in Figure 2B.

Magnetic Field Measurements

The strength, stability, and uniformity of the device magnetic field were simulated and measured. The magnetic field strength along the central axis was first simulated based on the Biot-Savart Law. Assuming the magnetic field in the solenoid is uniform, the field strength along the central axis approximates the field inside the solenoid. The same magnetometer described above was used to measure the field inside the solenoid. The solenoid for the actual device had a smaller inner diameter, which was customized for the sample size. This smaller size was too narrow for the probe of the magnetometer. Therefore, a prototype solenoid of larger size was constructed to test the accuracy of the field simulation in comparison with the measured results.

HP MR Phantom Experiments

Experiments were performed to test the effect of the device on HP [^{13}C]urea and copolarization of [^{13}C]urea and [1-^{13}C]pyruvate. Dissolution DNP was performed with a HyperSense polarizer (Oxford Instruments, Oxford, UK) operating at 1.3 K and 3.35 T, using previously described methods, generating 4.5 mL of the 100 mM HP solution (11). MR experiments were performed on a 3 T clinical MRI scanner (GE Healthcare, Waukesha, Wisconsin, USA) with a broadband radiofrequency amplifier. Custom built, dual-tuned mouse birdcage coils (l = 8 cm, d = 5 cm) were used for radiofrequency transmission and signal reception. The radiofrequency transmit gain was calibrated with a ^{13}C-enriched urea phantom with similar size and similar location as the HP phantom.

After dissolution, the HP sample was divided into two equally apportioned syringes, and both were carried to the scanner at the same speed along the same path. One was transferred in the ambient field, while the other was transferred with this device. The device was turned on during DNP dissolution and kept activated throughout the transfer from DNP polarizer to MR scanner. It was deactivated approximately 2 m away from the center of the MR scanner, where the fringe field is already sufficiently large. The device was held vertically during transfer such that the magnetic field from this device was added to the fringe field instead of potentially cancelling each other. The sample transfer took approximately 6 s.

The solutions were then injected into two fixed syringe reservoirs already lying inside the coil, oriented along the longitudinal direction. The signal of these two samples was then acquired together with one pulse sequence and approximately the same local B_0 and B_1 fields. In this manner, the differences in signal between the samples transferred with and without the device were calculated from the same experiment, while controlling for any variations in initial polarization, total amount of sample, and transfer duration. Another control group experiment was performed with the same imaging methods, but both samples were transferred without the device. The urea-only experiment and control group experiment were each repeated four times, and the copolarization experiment was repeated five times.

For the urea-only tests, the axial images were acquired with single-shot echo planar imaging (EPI) readout, with no localization along the longitudinal direction, using the following parameters: flip angle = 90°; echo time (TE) = 100 ms; repetition time (TR) = 250 ms; matrix size = 20 × 20; field of view = 10 × 10 cm. For urea and pyruvate copolarization tests, a dynamic one-dimensional MR spectroscopic imaging sequence was used with hard pulse excitation (0.5 ms duration),

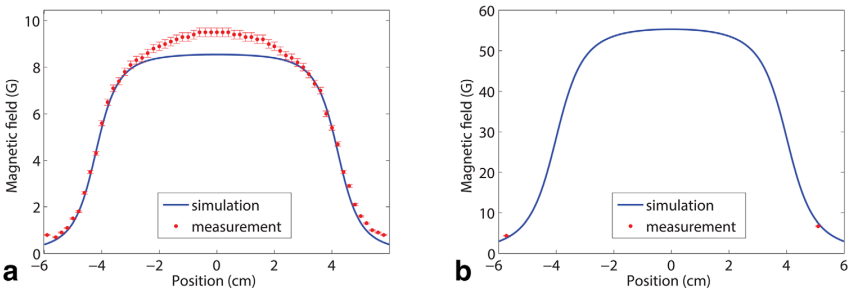


FIG. 3. Simulated (blue line) and measured (red dots) magnetic field distribution in the prototype solenoid with larger diameter (A) and the solenoid used in the device (B). Error of measurement (shown as red error bars) were determined from the accuracy of the magnetometer. The measured field distribution was not available for the solenoid in the device because its size is smaller than the probe of the magnetometer, but the calculation demonstrated a field of greater than 50 G over the central 6 cm.

double spin echo refocusing, and symmetric EPI readout (15). Spatial encoding was only applied along the x direction (right/left) with projections along the y and z directions. Localization along this direction enabled separation of the samples transferred with and without the device. The readout gradient duration was 100 ms, giving a spectral resolution of 10 Hz, with a spectral bandwidth of 543 Hz to include the resonances of both pyruvate and urea. For image reconstruction, the even and odd EPI lobe data were combined by the sum-of-squares method. The data were acquired using the following parameters: flip angle = 10°; TE = 140 ms; TR = 2 s. Although the amounts of HP material in each syringe were approximately equal, the signal at thermal equilibrium was also measured to compensate for any potential residual differences in the amount of HP sample in each syringe.

HP MR In Vivo Experiments

HP [^{13}C]urea in vivo rat experiments were performed using a balanced steady state free precession (bSSFP) sequence (13) to acquire a coronal image (projection along the anterior–posterior direction) following a protocol approved by our Institutional Animal Care and Use Committee. The experiments were repeated twice on the same animal, one with HP sample transferred in ambient field, the other transferred with this device, while keeping all the other parameters the same. [^{13}C]urea was polarized for 88 ± 1 min and transferred to the scanner within 7 s. A 2.5 mL of the 100 mM solution was injected into a rat through tail vein catheter over 12 s with image acquisition starting at 20 s after the beginning of the injection. The imaging parameters were as follows: flip angle = 60°; TR = 15 ms; matrix size = 140 × 70; field of view = 20 × 10 cm; sequential phase encoding.

RESULTS

Magnetic Field Tests

The simulated and measured magnetic field distributions within the solenoid are shown in Figure 3. Figure 3A corresponds to the larger prototype solenoid, while Figure 3B corresponds to the actual solenoid used in this device. The measured results were close to the simulated results, but slightly higher in the center, as shown in Figure 3A. Using the same simulation method, we calculated the magnetic field of the device to be > 50 G over a 6-cm central section, as shown in Figure 3B. Even though the magnetic field drops quickly at both ends, the field is relatively uniform in the 3-cm central section where HP media is usually placed. When holding the switch and keeping the electric current on for about 30 s (the sample transfer usually takes <10 s), the measured magnetic field remained constant, thereby demonstrating the stability of the device.

HP MR Tests

In the HP [^{13}C]urea phantom experiments, the [^{13}C]urea signal in both syringes is shown in one axial image (Fig. 4A). The SNR increase achieved by using this device was demonstrated by the ratio of image intensity. The results showed a significantly ($P = 0.012$) higher (1.9 ± 0.2) [^{13}C]urea signal using the device. The result of the control group demonstrated a small effect between syringe locations (+4%). However, this effect was much smaller than the experimental signal ratio (~1.9) and therefore does not alter the conclusion that SNR increased by about two-fold. Furthermore, this small effect in the control group failed to reach statistical significance ($P = 0.098$).

For the HP copolarization phantom experiments, spectroscopic imaging was acquired to distinguish the different compounds based on frequency, and the different samples transferred with and without the device based on spatial location. The spectra were analyzed for each resonance and each transfer approach (Fig. 4B). The data showed a significantly ($P = 0.002$) higher (1.9 ± 0.3) [^{13}C]urea signal intensity in the sample transferred with the device. [1-^{13}C]pyruvate signal intensity was slightly higher (1.1 ± 0.1); however, it failed to reach statistical significance ($P = 0.550$).

The results of the HP [^{13}C]urea in vivo experiment are shown in Figure 5, along with the corresponding image from a 3D bSSFP ^{1}H scan. The coronal ^{13}C image with

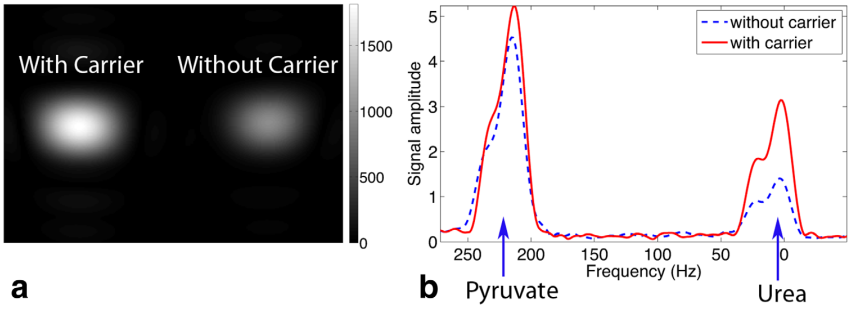


FIG. 4. Example of experimental comparisons between two HP samples scanned in one acquisition. One sample was transported with this device (with carrier), the other was transported in an ambient field (without carrier). The just urea experiment was performed using axial ^{13}C MRI (A), while the copolarization of urea and pyruvate MR spectroscopic imaging experiment resulted in two spectral peaks corresponding to the two HP compounds acquired from the samples transported with (solid red line) and without (dotted blue line) the carrier device (B). For copolarization results, the left peak corresponds to pyruvate and the right peak corresponds to urea. The center frequency was set close to the urea frequency.

sample transferred with the device has improved SNR. Quantitatively measuring the SNR at the center of the right kidney showed an SNR improvement of 1.8-fold with this device.

DISCUSSION

This device enabled a nearly 1.9-fold SNR improvement of HP urea signal compared with samples carried in the ambient field in HP [^{13}C]urea experiments, HP urea and pyruvate copolarization experiments, and one in vivo experiment. The observed 1.8- to 1.9-fold SNR improvement from experiments is close to the expected 1.83-fold increase predicted by simulation, which indicates that the hypothesis of fast signal decay due to scalar coupling relaxation is correct and that the model we use (Eq. 1) is accurate. Therefore, this model can be used for further study with other HP molecules. The SNR improvement may be even more significant in cases where the ambient field along transfer path is lower than in our facility.

Although [1-^{13}C]pyruvate is not affected by scalar coupling relaxation, other relaxation mechanisms could affect it at low fields, such as relaxation via paramagnetic centers (radical and gadolinium in solution). However, in our copolarization experiments, the [1-^{13}C]pyruvate signal was not significantly different with or without the device. Theoretically, the effect of relaxation via paramagnetic centers is small due to very low concentration of radical or gadolinium in the liquid state (16,17). Furthermore, this possible mechanism would likely have a small effect considering the transfer time is just 6 s, as a small fraction of expected T1 value (18). However, use of this device would prevent pyruvate relaxation effects that could occur at very low fields at some locations.

While the initial testing was focused on HP [^{13}C]urea and [1-^{13}C]pyruvate, it could also benefit other compounds. For example, HP [5-^{13}C]glutamine is being developed as a noninvasive imaging marker for

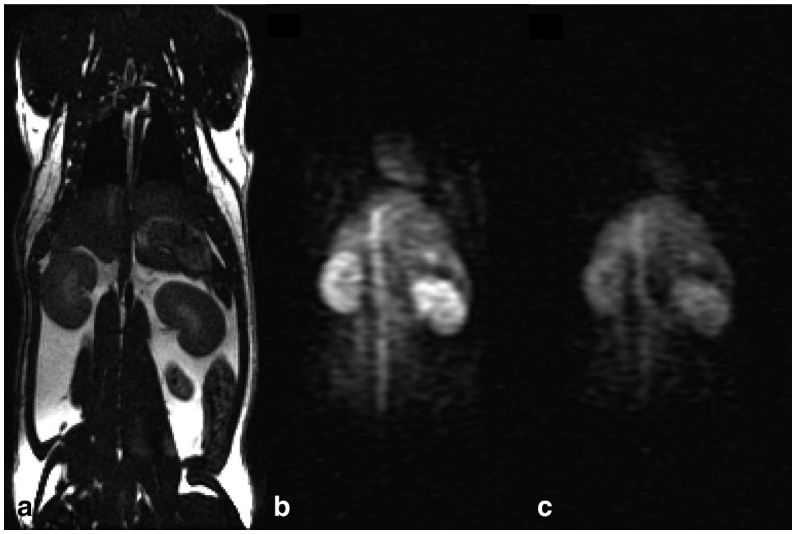


FIG. 5. In vivo rat experiment results. **A:** Coronal slice of a 3D bSSFP ^{1}H sequence. **B:** HP [^{13}C]urea image using a two-dimensional (coronal) bSSFP sequence (projection along the anterior–posterior direction) with sample transferred with the device. **C:** The same acquisition repeated on the same animal and position, but with the sample transferred in an ambient field. Images B and C were acquired with the same imaging parameters and experimental setup and differed only in the transfer method. Images B and C are displayed with the same window. The SNR (measured at right kidney center) in image B was 1.8 times higher using the device than without (image C).

glutaminolysis, allowing improved diagnosis and monitoring of glutamine-dependent tumors (19–21). Similar to urea, this substrate is also affected by coupling between ^{13}C and ^{14}N.

CONCLUSION

An electromagnet carrier device was designed and built to supply a suitable and safe magnetic field (>50 G) to preserve polarization during HP sample transfer, especially for compounds with scalar coupling between fast-relaxing quadrupolar ^{14}N and ^{13}C, such as in HP [^{13}C]urea. In comparative testing, this device demonstrated SNR improvements of approximately two-fold for [^{13}C]urea while maintaining the signal of HP [1-^{13}C]pyruvate.

ACKNOWLEDGMENTS

We thank Jeremy Bancroft Brown for assistance with 3D printing. We also thank Hsin-Yu Chen and Zihan Zhu for assistance with experiments.

REFERENCES

1. Ardenkjær-Larsen JH, Fridlund B, Gram A, Hansson G, Hansson L, Lerche MH, Servin R, Thaning M, Golman K. Increase in signal-to-noise ratio of >10,000 times in liquid-state NMR. Proc Natl Acad Sci U S A 2003;100:10158–10163.
2. Golman K, Ardenkjær-Larsen JH, Petersson JS, Månsson S, Leunbach I. Molecular imaging with endogenous substances. Proc Natl Acad Sci U S A 2003;100:10435–10439.
3. .Golman K, Thaning M. Real-time metabolic imaging. Proc Natl Acad Sci U S A 2006;103:11270–11275.
4. Chen AP, Albers MJ, Cunningham CH, et al. Hyperpolarized C-13 spectroscopic imaging of the TRAMP mouse at 3T-initial experience. Magn Reson Med 2007;58:1099–1106.
5. Nelson SJ, Kurhanewicz J, Vigneron DB, et al. Metabolic imaging of patients with prostate cancer using hyperpolarized [1-^{13}C] pyruvate. Sci Transl Med 2013;5:198ra108.
6. Chiavazza E, Kubala E, Gringeri CV, Düwel S, Durst M, Schulte RF, Menzel MI. Earth's magnetic field enabled scalar coupling relaxation of ^{13}C nuclei bound to fast-relaxing quadrupolar ^{14}N in amide groups. J Magn Reson 2013;227:35–38.
7. Kurhanewicz J, Vigneron DB, Brindle K, Chekmenev EY, Comment A, Cunningham CH, DeBerardinis RJ, Green GG, Leach MO, Rajan SS. Analysis of cancer metabolism by imaging hyperpolarized nuclei: prospects for translation to clinical research. Neoplasia 2011;13:81–97.
8. Johansson E, Månsson S, Wirestam R, Svensson J, Petersson J, Golman K, Ståhlberg F. Cerebral perfusion assessment by bolus tracking using hyperpolarized ^{13}C. Magn Reson Med 2004;51:464–472.
9. Svensson J, Månsson S, Johansson E, Petersson JS, Olsson LE. Hyperpolarized ^{13}C MR angiography using trueFISP. Magn Reson Med 2003;50:256–262.
10. Wilson DM, Keshari KR, Larson PEZ, Chen AP, Hu S, Criekinge MV, Bok R, Nelson SJ, Macdonald JM, Vigneron DB. Multi-compound polarization by DNP allows simultaneous assessment of multiple enzymatic activities *in vivo*. J Magn Reson 2010;205:141–147.
11. von Morze C, Larson PEZ, Hu S, Yoshihara HA, Bok RA, Goga A, Ardenkjaer-Larsen JH, Vigneron DB. Investigating tumor perfusion and metabolism using multiple hyperpolarized ^{13}C compounds: HP001, pyruvate and urea. Magn Reson Imaging 2012;30:305–311.
12. von Morze C, Bok RA, Sands JM, Kurhanewicz J, Vigneron DB. Monitoring urea transport in rat kidney in vivo using hyperpolarized ^{13}C magnetic resonance imaging. Am J Physiol Renal Physiol 2012;302:F1658–F1662.
13. Reed GD, von Morze C, Bok R, Koelsch BL, Van Criekinge M, Smith KJ, Shang H, Larson PEZ, Kurhanewicz J, Vigneron DB. High resolution C-13 MRI with hyperpolarized urea: in vivo T2 mapping and N-15 labeling effects. IEEE T Med Imaging 2014;33:362–371.
14. Lyerla JR Jr, Grant DM, Bertrand RD. Field-dependent contributions to carbon-13 nuclear relaxation. J Phys Chem 1971;75:3967–3971.
15. Cunningham CH, Chen AP, Albers MJ, Kurhanewicz J, Hurd RE, Yen Y-F, Pauly JM, Nelson SJ, Vigneron DB. Double spin-echo sequence for rapid spectroscopic imaging of hyperpolarized ^{13}C. J Magn Reson 2007;187:357–362.
16. Caravan P, Ellison JJ, McMurry TJ, Lauffer RB. Gadolinium(III) chelates as MRI contrast agents: structure, dynamics, and applications. Chem Rev 1999;99:2293–2352.
17. Gordon JW, Fain SB, Rowland IJ. Effect of lanthanide ions on dynamic nuclear polarization enhancement and liquid-state T1 relaxation. Magn Reson Med 2012;68:1949–1954.
18. Chattergoon N, Martinez-Santiesteban F, Handler WB, Ardenkjaer-Larsen JH, Scholl TJ. Field dependence of T_1 for hyperpolarized [1-^{13}C]pyruvate. Contrast Media Mol Imaging 2013;8:57–62.
19. Gallagher FA, Kettunen MI, Day SE, Lerche M, Brindle KM. ^{13}C MR spectroscopy measurements of glutaminase activity in human hepatocellular carcinoma cells using hyperpolarized ^{13}C-labeled glutamine. Magn Reson Med 2008;60:253–257.
20. Keshari KR, Wilson DM. Chemistry and biochemistry of ^{13}C hyperpolarized magnetic resonance using dynamic nuclear polarization. Chem Soc Rev 2014;43:1627–1659.
21. Daye D, Wellen KE. Metabolic reprogramming in cancer: unraveling the role of glutamine in tumorigenesis. Semin Cell Dev Biol 2012;23:362–369.

NMR IN BIOMEDICINE
NMR Biomed. 2006; **19**: 781–821
Published online in Wiley InterScience
(www.interscience.wiley.com) DOI:10.1002/nbm.1102

Sodium and $T_{1\rho}$ MRI for molecular and diagnostic imaging of articular cartilage†

Arijitt Borthakur, Eric Mellon, Sampreet Niyogi, Walter Witschey, J. Bruce Kneeland and Ravinder Reddy*

MMRRCC, Department of Radiology, University of Pennsylvania, Philadelphia, PA 19104-6100, USA

Received 9 March 2006; Revised 9 August 2006; Accepted 10 August 2006

ABSTRACT: In this article, both sodium magnetic resonance (MR) and $T_{1\rho}$ relaxation mapping aimed at measuring molecular changes in cartilage for the diagnostic imaging of osteoarthritis are reviewed. First, an introduction to structure of cartilage, its degeneration in osteoarthritis (OA) and an outline of diagnostic imaging methods in quantifying molecular changes and early diagnostic aspects of cartilage degeneration are described. The sodium MRI section begins with a brief overview of the theory of sodium NMR of biological tissues and is followed by a section on multiple quantum filters that can be used to quantify both bi-exponential relaxation and residual quadrupolar interaction. Specifically, (i) the rationale behind the use of sodium MRI in quantifying proteoglycan (PG) changes, (ii) validation studies using biochemical assays, (iii) studies on human OA specimens, (iv) results on animal models and (v) clinical imaging protocols are reviewed. Results demonstrating the feasibility of quantifying PG in OA patients and comparison with that in healthy subjects are also presented. The section concludes with the discussion of advantages and potential issues with sodium MRI and the impact of new technological advancements (e.g. ultra-high field scanners and parallel imaging methods). In the theory section on $T_{1\rho}$, a brief description of (i) principles of measuring $T_{1\rho}$ relaxation, (ii) pulse sequences for computing $T_{1\rho}$ relaxation maps, (iii) issues regarding radio frequency power deposition, (iv) mechanisms that contribute to $T_{1\rho}$ in biological tissues and (v) effects of exchange and dipolar interaction on $T_{1\rho}$ dispersion are discussed. Correlation of $T_{1\rho}$ relaxation rate with macromolecular content and biomechanical properties in cartilage specimens subjected to trypsin and cytokine-induced glycosaminoglycan depletion and validation against biochemical assay and histopathology are presented. Experimental $T_{1\rho}$ data from osteoarthritic specimens, animal models, healthy human subjects and as well from osteoarthritic patients are provided. The current status of $T_{1\rho}$ relaxation mapping of cartilage and future directions is also discussed.
Copyright © 2006 John Wiley & Sons, Ltd.

KEYWORDS: cartilage; arthritis; spin-lock; T1rho; sodium; MRI

OSTEOARTHRITIS

Osteoarthritis (OA) affects more than half of the population above the age of 65 (1,2) and has a significant negative impact on the quality of life of elderly individuals (3). The economic costs in the USA from OA have been estimated to be more than 1% of the gross domestic product (4). OA is now increasingly viewed as a metabolically active joint disorder of diverse etiologies. The biochemistry of the disease is characterized by the following changes in cartilage: reduced proteoglycan (PG) concentration, possible changes in the size of collagen fibril and aggregation of PG, increased water content and increased rate of synthesis and degradation of matrix macromolecules. The earliest changes in the cartilage due to OA result in a partial breakdown in the proteoglycan matrix with a decrease in total content. The total concentration of collagen remains unaltered in the earliest stages, although there are generally changes in the size and arrangement of the fibers. There is also a small increase in the total water content. All of these changes in the macromolecular matrix lead to an alteration in the mechanical properties of cartilage with the result that it can no longer serve as an effective load-bearing material. Current therapies of the disease have

**Correspondence to:* R. Reddy, MMRRCC, Department of Radiology, University of Pennsylvania, B1 Stellar-Chance Labs, 422 Curie Blvd, Philadelphia, PA 19104-6100, USA.
E-mail: ravi@mail.mmrrcc.upenn.edu
Contract/grant sponsor: NIH, NIAMS; *contract/grant numbers:* R01AR45242, R01AR45404, R01AR051041.
Contract/grant sponsor: NCRR; *contract/grant number:* RR23053.
Contract/grant sponsor: NIH; *contract/grant number:* T32-EB000814.

Abbreviations used: DQF, double quantum filtered; DQFMA, double quantum filtered magic-angle; ECM, extracellular matrix; EFG, electric field gradient; FCD, fixed charge density; GAG, glycosaminoglycans; Gd-DTPA, gadolinium diethylenetriaminepentaacetic acid; MQF, multiple quantum filtered; MRI, magnetic resonance imaging; NMR, nuclear magnetic resonance; NQR, nuclear quadrupolar resonance; OA, osteoarthritis; PBS, phosphate buffered saline; PG, proteoglycan; RA, rheumatoid arthritis; RQI, residual quadrupolar interaction; SNR, signal-to-noise ratio; TQF, triple quantum filtered.

†This paper is published as part of a Special Issue entitled ''NMR of the Musculoskeletal System''.

Copyright © 2006 John Wiley & Sons, Ltd.

been ineffective at halting or reversing its course and have largely been directed toward symptomatic relief. As the disease progresses to its late stages, joint surface replacement (arthroplasty) is the only effective treatment.

More recently, there have been efforts in developing novel techniques for the treatment of OA such as chondroprotective drugs and re-population of the cartilage defects by chondrocyte precursor cells with subsequent regeneration of the cartilage. Further, recent research has led to the development of drugs in animals that have shown the potential of protecting the macromolecules in cartilage from breakdown, effectively halting the progression of OA. Because of the long natural history of OA (10–20 years in humans), validating the efficacy of these drugs requires a noninvasive technique that can directly assess their effect on molecular changes associated with early stages of cartilage degeneration that precede morphological changes.

The current lack of adequate methods for quantifying these changes has hampered research directed towards the development of potential disease-modifying agents. An integrated, and noninvasive measurement of molecular (PG, collagen and water) and morphological (tissue volume) changes in cartilage will enable the detection of OA in its early stages. These measurements will help monitor disease progression, evaluate potential strategies for disease management and verify the efficacy of disease modifying drugs. Current diagnostic methods include radiography, arthrography, computed tomography (CT) and magnetic resonance imaging (MRI).

Joint space narrowing determined from conventional radiographs is widely accepted as an indication for early diagnosis of OA. However, it does not yield accurate and quantifiable results on molecular changes that precede morphological changes. Arthrography, which has these attributes, is an invasive technique that causes pain and discomfort to the subjects and is, therefore, not ideal for routine clinical use. CT, while quantitative, has the drawback of not providing biochemical information. MRI, on the other hand, provides excellent soft tissue contrast and superior delineation of intra-articular structures. From a morphological point of view, there has been substantial progress in improving our ability to study cartilage, using MRI. MRI can assess cartilage lesions and provide morphologic information about the cartilage damage. More specifically, changes such as fissuring, partial or full thickness cartilage loss and signal change within the residual cartilage can be detected. Several approaches have been developed and validated to use three-dimensional volumetric data to quantify articular cartilage in joints. Although MRI is one of the best noninvasive tools, conventional MRI (T_1-, T_2-, density-weighted and magnetization transfer imaging) has proven to be inadequate in quantifying early-stage molecular changes.

Very recently, studies on transgenic animal models have shown that ADAMTS5, an aggrecanase that cleaves the aggrecan at specific site, is responsible for the breakdown of PG and disease initiation (5,6). Although human studies are needed to confirm these studies from transgenic (tg) mice, they indicate that early molecular changes are reflected in a decrease of PG.

Several MR imaging methods have been advanced to detect and quantify such early molecular changes. Prominent in these are: proton–based methods such as T_2 relaxation mapping (7–20), delayed gadolinium-enhanced magnetic resonance imaging contrast (dGEMRIC) (21,22), $T_{1\rho}$ relaxation mapping (23–26) and the direct MRI of sodium (27–30). T_2 is predominantly affected by changes in collagen content and to a smaller extent in PG in the tissue. Since the dominant contribution to T_2 relaxation is the dipolar interaction of protons of water associated with collagen, it is primarily useful in quantifying changes associated with collagen component of the ECM. dGEMRIC has been shown to be useful in quantifying changes in PG and this method and T_2 mapping have been extensively reviewed in recent review articles (31–34). A complete review of MRI of cartilage is beyond the scope of this article. Recent advances in MRI of cartilage have been reviewed extensively (32–43).

In the following sections, we provide: (i) a brief discussion on the structure of normal cartilage, (ii) theoretical aspects of sodium NMR and sodium multiple quantum NMR and MRI studies of cartilage and (iii) theoretical aspects of $T_{1\rho}$ weighted MRI, pulse sequences for relaxation mapping and review of $T_{1\rho}$ relaxation studies of cartilage.

The structure of normal articular cartilage (44)

Articular cartilage is a remarkable type of connective tissue that provides the synovial joints with lubrication and makes normal motion possible. It also serves to absorb mechanical shock and to distribute load over the underlying bone. Although articular cartilage will function over the lifetime of the joint under ideal circumstances, it can be damaged by trauma, osteoarthritis and inflammatory arthritis.

Articular cartilage consists of a small population of specialized cells called chondrocytes within a large extracellular matrix (ECM). The primary components of the ECM are water, collagen (15–20%) and PG (3–10%), which the chondrocytes serve to remodel continuously (Figure 1). The structure of the cartilage varies throughout its depth and consists of four histologic zones or layers. The structure and concentration of collagen and PG vary in these zones. Water is the most abundant component of articular cartilage with concentrations ranging from 80% of the volume on the surface to 65% in the deep zone. However, only a small fraction of the water is bound to collagen molecules. The affinity of cartilage for water arises primarily from the presence of the proteoglycans

Copyright © 2006 John Wiley & Sons, Ltd.

DOI: 10.1002/nbm

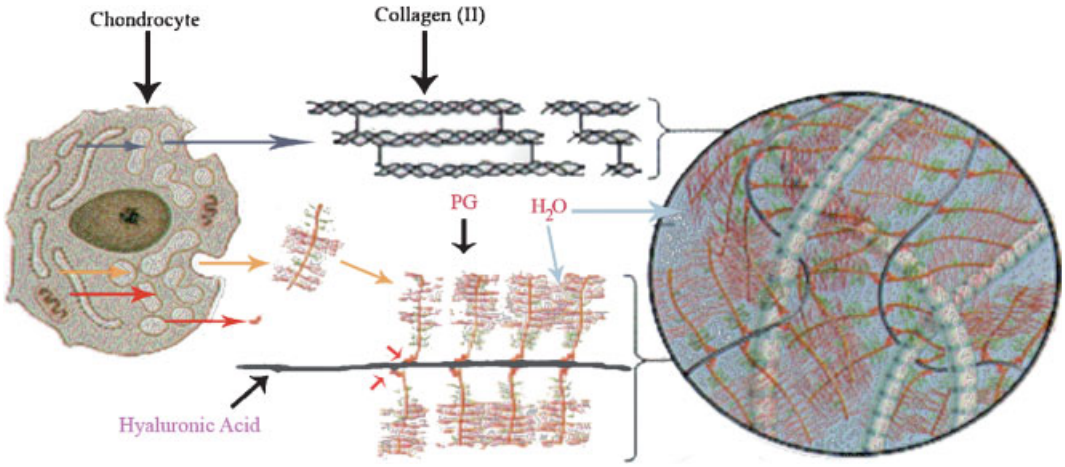


Figure 1. The extracellular matrix (ECM) of cartilage.

whose negative charges serve to attract free-floating positive ions in solution such as Na^+, which in turn attract water molecules through osmotic pressure (an example of the Donnan equilibrium).

Proteoglycans are complex macromolecules that consist of protein and polysaccharides. The most common of proteoglycans, making up 80–90% of the total, is called aggrecan [Figure 2(A)]. It consists of a protein core with a long extended domain to which many glycosaminoglycan (GAG) side chains are attached. Although both chondroitin sulfate (CS) and keratan sulfate (KS) are present in ECM, CS is the predominant GAG molecule found in cartilage [Figure 2(B)]. Several aggrecan molecules are in turn attached to hyaluronate, a long, linear polysaccharide. The resulting structure is described as having a 'lamp-brush' type of appearance. A large number of carboxyl and sulfate residues, present on the glycosaminoglycan side chains, are ionized under physiological conditions to give COO^- and SO_3^-. The negative charge density imparted by these groups is referred to as fixed charge density (FCD). These negative ions attract positive counter-ions and water molecules and provide a strong electrostatic repulsive force between the proteoglycans. These osmotic and electrostatic forces are responsible for the swelling pressure of cartilage. The configuration of the PG macromolecules also contributes to the resistance of the matrix to the passage of water molecules and hence affects the mechanics of the cartilage in this fashion.

Collagens are proteins with a characteristic triple-helical structure. Although many different types of collagen are found in cartilage, the most common is collagen type II (90–95% of the overall mass of collagen in cartilage). The collagen molecules aggregate into fibers that are 10–100 nm in diameter. The major role of the collagen II fibers is to provide a tensile force opposing the tendency of the proteoglycans to expand the cartilage and

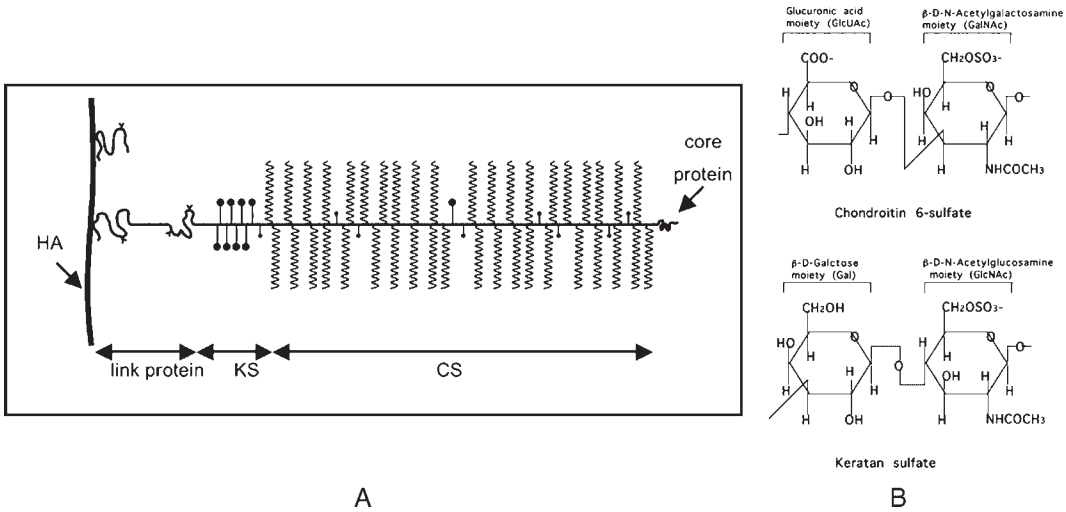


Figure 2. The aggrecan proteoglycan macromolecule (A) comprising hyaluronic acid (HA), keratan sulfate (KS) and chondroitin sulfate (CS). The molecular structures of chondroitin 6-sulfate and keratan sulfate moieties are shown in (B).

Copyright © 2006 John Wiley & Sons, Ltd.

DOI: 10.1002/nbm

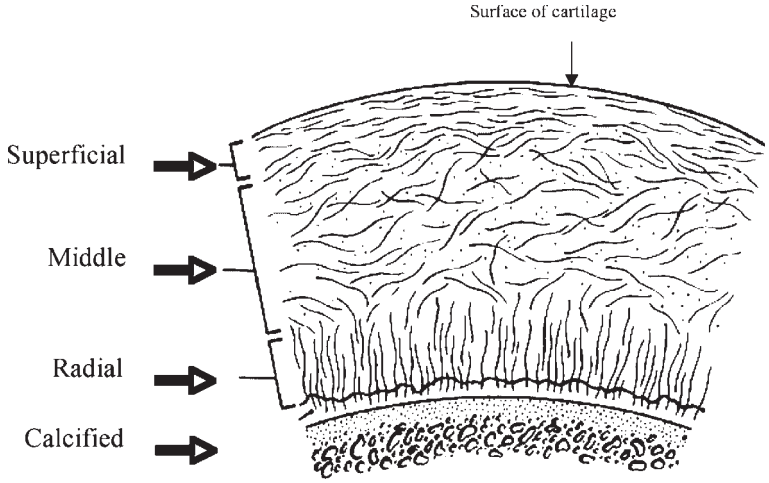


Figure 3. Arrangement of collagen fibers across different layers of the cartilage.

also serve to immobilize the proteoglycans. Since there are no net charges on collagen it does not impart any FCD to the ECM. Collagen fibers have different arrangement across the tissue (Figure 3). In the radial zone collagen arrangement is perpendicular to the surface of the tissue while in the superficial zone it is parallel to the surface. However, in the middle zone the arrangement is almost random. This characteristic arrangement leads to the so called 'magic angle effect' and laminar appearance in the proton MR images. Many other molecules are present in the ECM in low concentrations, most of whose functions are not clearly understood.

Features of articular cartilage during osteoarthritis

Osteoarthritis can affect virtually any joint that contains cartilage; however it is most commonly seen in the hands, knee, hip and spine, either isolated as localized OA or as generalized OA when it affects three or more joints (45). While specific conditions, such as trauma to the joint and congenital disease, may lead to secondary OA, most cases of OA are classified as idiopathic.

The affected joint is victim to a striking breakdown of the cartilage matrix and eventually a total loss of joint cartilage. The OARSI cartilage OA pathology assessment system provides six grades of OA involvement (46). In grade 1, the cartilage matrix undergoes swelling, abrasion and changes in the structure of the cartilage such as patchy condensation of collagen and gain or loss of chondrocytes. Stains such as Safranin O or Toluidene Blue, which are used semi-quantitatively in many studies as markers for proteoglycan, can be indicative of proteoglycan loss at this early point. While structural MRI is sometimes able to see synovial thickening at this early stage (47), only imaging techniques sensitive to molecular changes such as sodium imaging, $T_{1\rho}$-weighted imaging and dGEMRIC MRI can hope to regularly detect and track OA at this stage.

Grade 2 OA begins to see exfoliation of ECM from the surface of the joint and in grade 3 fissuring from the surface into the mid zone of the cartilage is observed. It is not until grade 4 that large-scale structural changes begin to occur. Increased fissuring and delamination of the surface leads to erosion and loss of the superficial zone. Chondrocyte death and metaplasia begin at stage 3, but are prominent at this point. It is at this time that larger structural changes can be regularly seen on T_2-weighted imaging, CT, and after joint space narrowing with loss of cartilage, X-Ray. Grades 5 and 6 OA exhibit almost a total loss of articular cartilage, and changes to the underlying bone structure such as osteophytes and microfracturing are evident.

The etiology of OA is thought to be a complex interplay of mechanical joint trauma and molecular factors where chondrocytes are unable to repair joint damage, leading to progressive cartilage loss (48). The classification of joint disease as OA is often meant to separate the disease process from other types of arthritis, such as rheumatoid arthritis (RA), that have better elucidated inflammatory components. Nevertheless, it is increasingly recognized that inflammatory or other molecular mediators may have a central role in the progression of OA. While it is beyond the scope of this article to discuss the myriad proteins implicated as markers or factors in OA pathogenesis, certain models of OA deserve attention for later discussion.

Models of osteoarthritis in articular cartilage

Early studies determined that a certain factor isolated from synovial fluid and produced by lymphocytes, later discovered to be interleukin-1 (IL-1), stimulates release of GAG from the ECM and suppresses new GAG synthesis in explant cultures (49). It was not long before IL-1β was being used frequently with *in vivo* and *ex vivo* cartilage as a model of arthritis for the testing of

Copyright © 2006 John Wiley & Sons, Ltd.

DOI: 10.1002/nbm

pharmacotherapeutics and investigations of arthritis signaling (50). Genetic evidence for a role of IL-1β in OA came much more recently with the discovery of polymorphisms in the IL-1 gene cluster that act as risk factors for OA (51–53). In arthritis imaging research, IL-1β is now used to simulate osteoarthritis in animal models in order to track progression of mild disease by emerging techniques (54).

The interleukin-1 super-family includes the agonists IL-1α/IL-1F and IL-1β/IL-1F2 (55). IL-1α and IL-1β are produced as approximately 31 kDa precursor forms and are cleaved by IL-1β converting enzyme (ICE), also known as caspase-1, to forms weighing about 17.5 kDa. However, only IL-1β requires cleavage to have activity, while both the pro-form and the mature form of IL-1α are active (56). Activity is often conserved across higher mammals, as evidenced by homologous biological activity of recombinant human IL-1α and IL-1β on many other species, including cow (57), pig (58) and mouse (59).

Interleukin-1 is thought to stimulate breakdown of the ECM by causing the upregulation of two families of metalloproteinases. Messenger RNA of numerous members of the matrix metalloproteinase (MMP) family, including the collagenases MMP-1, MMP-8 and MMP-13, as well as MMP-14, MMP-3 and MMP-9, have been shown to be upregulated by IL-1 in human chondrocytes *in vitro* (60). The same study also showed upregulation of the aggrecanases ADAMTS-4 (aggrecanase-1) and ADAMTS-5 (aggrecanase-2) by IL-1. These proteins belong to the disintegrin and metalloprotease with thrombospondin motifs family (61), and are the only enzymes that have been shown to cleave aggrecan at a site that generates the Glu373-Ala374 fragments (62,63) seen in interleukin-1 stimulated bovine explant cultures (64) and human synovial fluid of OA patients (65).

Very recent studies of transgenic animal models suggest that ADAMTS5 may in fact be necessary for the induction or progression of symptomatic OA (5,6). Two groups working independently found that ADAMTS5 knockout mice were protected from experimentally induced arthritis by IL-1β, foreign antigen stimulation and joint instability. This provides an exciting target for development of medications targeting early mediators of arthritis that will slow or arrest the progression of OA. Testing of these new therapies may benefit from confirmation by noninvasive molecular imaging techniques that show a corresponding halt in ECM loss in tissue.

An alternative model of osteoarthritis is the use of trypsin to induce the degeneration of proteoglycan (66–68). Trypsin is a 24 kDa endopeptidase commonly produced in the pancreas for the digestion of dietary amino acids (69). It cleaves a wide range of proteins at the C-terminus of lysine or arginine except when followed by a proline residue. While collagen, due to its large number of prolines, is not susceptible to trypsin digestion under all but very harsh conditions (70), application of trypsin to explant cartilage cultures readily causes the degradation of PG and other extracellular molecules (71). It is unlikely that trypsin itself plays a major role in the pathogenesis of OA; however imaging techniques are frequently tested by their ability to detect trypsin-induced degeneration of cartilage (72,73).

Sodium NMR

Sodium is one of the most 'NMR-visible' nuclei in living systems. The NMR relaxation properties of a nucleus depend on its immediate environment and its interactions that perturb the dominant Zeeman Hamiltonian in a significant manner. The most important interaction experienced by sodium nuclei is that between the nonspherically symmetric nucleus and surrounding electric field gradients. This is called the quadrupolar interaction. In general, sodium in solids experience most of these interactions while in liquids, the static quadrupolar interaction is averaged to zero. In the intermediate regimes, e.g. in biological tissues, the quadrupolar interaction results in biexponential relaxation rates. Multiple quantum filtered ^{23}Na NMR can be used to analyze spectra from such systems. The following sections describe quadrupolar interaction and its effect on the ^{23}Na NMR spectrum and relaxation rates in greater detail.

The quadrupolar interaction. Sodium is a spin 3/2 nucleus and possesses quadrupole moment (Q), which interacts with electric field gradient (EFG) generated by the electronic distribution around the nucleus. In the absence of external magnetic field, this interaction establishes degenerate energy states in solid state. Transitions induced by appropriate RF pulses (with a frequency that is resonant with the frequency separation of the states) are responsible for the pure nuclear quadrupole resonance (NQR). This has been reviewed extensively in several original articles and books (74–76) and will not be discussed here.

When Zeeman interaction is greater than the quadrupolar interaction, the degeneracy of the energy levels is lifted and the spin dynamics are dictated by the physical status of the material. The theory of NMR of quadrupolar nuclei (74,75,77–80), relaxation-induced sodium single and multiple quantum coherences (MQC) and their applications in the studies of biological systems has been extensively discussed in several original and review articles (81–91). Here a brief overview of steps involved in the calculation of spin dynamics using the density matrix approach is presented.

The nuclear quadrupole interaction is determined by the orientation, magnitude and temporal duration of EFG generated by the surrounding lattice and the electronic configuration around the nucleus and can be described by a tensor. In a system of rapid motion, e.g. fluid, all orientations of the EFG are equally probable. In this 'isotropic' system, the quadrupolar interaction is aver-

Copyright © 2006 John Wiley & Sons, Ltd.

DOI: 10.1002/nbm

aged to zero on the time scale of $1/\omega_0$ (Figure 4). However, in an anisotropically oriented system, such as liquid crystals or oriented macromolecules, the sodium nuclei experience a nonzero average EFG. This static quadrupole coupling induces a shift in the energy levels of the spin system and consequently the spectrum shows multiple lines. The frequency separation between these lines provides indirect information about the magnitude of macroscopic ordering in the system.

In the Redfield regime, where the relaxation of spin 3/2 is described by second-order perturbation theory, the spin dynamics can be solved analytically. It is well known that longitudinal relaxation gives information about relatively fast motions (in MHz) and its dispersion can be studied by measuring relaxation rates at different field strengths. Slow dynamics (frequencies in the range of 0 to a few kHz) can be probed by transverse relaxation (T_2) or relaxation under the influence of a spin-locking pulse ($T_{1\rho}$) known as the 'spin-lattice relaxation in the rotating frame'. Here, we closely follow the treatment by van der Marrel (83,84,92). It is convenient to describe the dynamics of spin $I > 1$, the effects of RF pulses and the evolution under the action of static and fluctuating quadrupolar interactions using the irreducible tensor operator (T_p^l) representation. Where l represents the rank and p represents the order of the tensor. We use the orthonormal unit tensor operators as defined in van der Marrel (83,84). We define symmetric and anti-symmetric combinations as:

$$T_p^l(s) = (1/\sqrt{2})(T_{-p}^l + T_p^l)$$
$$T_p^l(a) = (1/\sqrt{2})(T_{-p}^l - T_p^l) \quad (1)$$

for spin 3/2, the density operator is expanded in terms of 16 orthonormal basis operators, which are shown in Table 1.

In the principal axis system of the spin 3/2 nucleus and for an axially symmetric electric field gradient, the static quadrupolar Hamiltonian is given by:

$$H_{QS} = \omega_Q T_0^2 \quad (2)$$

where ω_Q and represents the static residual quadrupolar interaction (RQI), only the part of the interaction that persists after motional averaging and not the r.m.s. average of the fluctuating part.

Several models have been explored to describe the role of static quadrupolar interaction in biological systems. If this nonaveraged interaction is uniform, as in the case of liquid crystals, then clear quadrupolar splitting is observed in the spectra provided the splitting exceeds the linewidths of the individual peaks. The interaction can be heterogeneous across the sample, as in the case of nonuniformly aligned systems. In this situation, the sample may be modeled as made from individual domains, each characterized by a local director but all possessing the same dynamic properties. The exchange among the domains usually is slow on a time scale of the inverse of the linewidths and the splitting, so that the observed spectrum represents a static average over all domains. Each domain is characterized by a residual quadrupolar coupling (RQC) given by:

$$\omega_Q = \overline{\omega_Q}\left(\frac{3\cos^2\theta - 1}{2}\right) \quad (3)$$

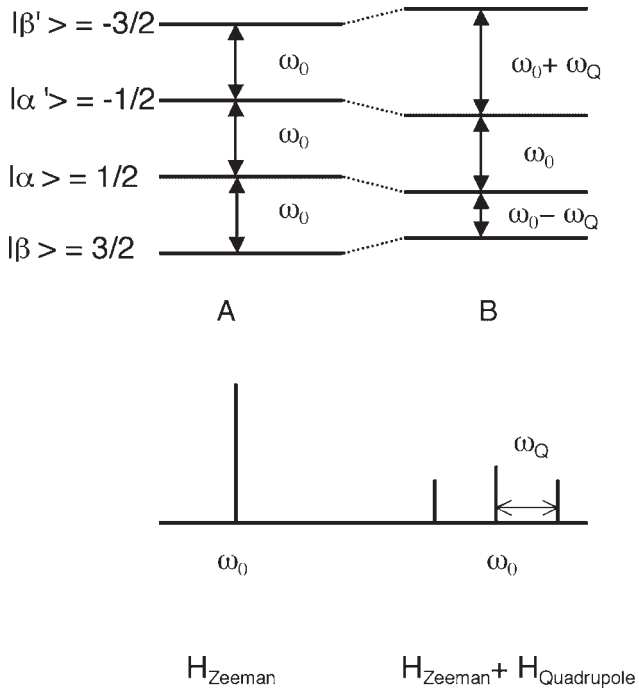


Figure 4. Energy level diagram of spin 3/2 nucleus. The frequency difference between adjacent energy levels is the same, ω_0 (A). It represents the isotropic solution state, where quadrupolar interaction is averaged to zero. (B) Nonzero static quadrupolar interaction shifts the energy levels, producing three spectral peaks. This represents the situation in solids, liquid crystals and oriented macromolecules. The frequency separation between adjacent energy level are given by: $(\omega_0 - \omega_Q)$, ω_0 and $(\omega_0 + \omega_Q)$.

Table 1. The 16 orthonormal basis operators of a spin-3/2 system

Operator	Definition
T_0^0	Identity
$T_0^1 = (1/\sqrt{5})I_z$	Longitudinal magnetization
$T_1^1(a) = (1/\sqrt{5})I_x$, and $T_1^1(s) = (-i/\sqrt{5})I_y$	Proportional to x- and y-magnetization, respectively
T_0^2	Quadrupolar spin polarization
$T_1^2(s)$ and $T_1^2(a)$	Rank 2 single quantum coherences
$T_2^2(s)$ and $T_2^2(a)$	Rank 2 double quantum coherences
T_0^3	Octopolar spin polarization
$T_1^3(s)$ and $T_1^3(a)$	Rank 3 single quantum coherences
$T_2^3(s)$ and $T_2^3(a)$	Rank 3 double quantum coherences
$T_3^3(s)$ and $T_3^3(a)$	Rank 3 triple quantum coherences

Copyright © 2006 John Wiley & Sons, Ltd.

DOI: 10.1002/nbm

where θ is the angle between the local director and the direction of the main magnetic field B_0 and $(\overline{\omega_Q}) = \omega_Q^{loc}$ denotes the maximum splitting measured (in the local director frame) for $\theta = 0^\circ$.

The frequency of the central transition is unaffected in the first order approximation of this interaction, but the satellite transitions are spread out over a large frequency range depending on the distribution in values of θ. The broadening of satellites due to an inhomogeneous static quadrupolar coupling makes it difficult to measure the position of the satellite transitions using conventional methods. Several pulse sequences have been developed to extract this information based on the detection of the formation of the even rank double quantum coherence (86). The spin system evolves under the influence of Zeeman, radiofrequency, static quadrupolar and fluctuating quadrupolar Hamiltonians.

In NMR, the detected signals are equivalent to those obtained by performing the calculations in the rotating frame or interaction representation given by:

$$U = e^{-iH_Z t} \tag{4}$$

$$H_Z = -\omega_0 T_0^1 \tag{5}$$

$$\omega_0 = -\gamma B_0 \tag{6}$$

in which the Zeeman Hamiltonian vanishes.

The total interaction Hamiltonian for spin 3/2 in the interaction representation (represented with '*') is:

$$H_T^* = H_{RF}^* + H_{QS}^* + H_{QF}^* \tag{7}$$

where H^*_{RF} represents the RF field applied in the transverse plane with a phase ϕ.

$$H_{RF}^* = -\omega_{RF}[\sqrt{5}\{-T_1^1(a)\sin\phi + iT_1^1(s)\cos\phi\}] \tag{8}$$

$$H_{QS}^* = \omega_Q T_0^2 \tag{9}$$

Since H_Q commutes with H_z, it remains unaffected in the interaction representation:

$$H_{QF}^*(t) = C_Q \sum_{m=-2}^{2} (-1)^m T_m^2 e^{im\omega_0 t}\left[F_{-m}^2(t) - < F_{-m}^2 >\right] \tag{10}$$

where $C_Q = eQ/(\hbar\sqrt{6})$and Q is the quadrupole moment of the nucleus and EFG components are given by:

$$\begin{aligned} F_2^0 &= (1/2)V_{zz} \\ F_{\pm1}^2 &= \mp(1/\sqrt{6})(V_{xz} \pm iV_{yz}) \\ F_{\pm2}^2 &= (1/2\sqrt{6})(V_{xx} - V_{yy} \pm 2iV_{xy}) \end{aligned} \tag{11}$$

and $\langle F_m^2\rangle$represents their average values.

Macromolecular motions impart fluctuations and hence a time dependence in the EFG components. Having established the Hamiltonians in the interaction representation, we are ready to discuss the spin dynamics. Spin dynamics of quadrupolar nuclei can be described by solving the Liouville equation over a range of motional regimes and following the time evolution of density operator (ρ) in response to RF pulses and in the presence of quadrupolar relaxation and static quadrupolar interaction (75,81–84,93–97). The time evolution of density operator under a static Hamiltonian, such as the static quadrupolar Hamiltonian is given by (74):

$$\frac{d\rho^*}{dt} = -i[H_{QS}^*, \rho^*] \tag{12}$$

The time evolution of the fluctuating quadrupolar Hamiltonian $H_{QF}^*(t)$ can be treated according to the Redfield relaxation theory (98,99). Changes in the density operator are small on the time scale τ_c of the lattice motions i.e. $< H_{QF}^{*2} > \tau_c \ll 1$. Therefore we can justify the use of second-order perturbation theory for our calculations. In most of the biological systems this condition is satisfied because of the rather long correlation times associated with macromolecular motions and relatively small values of corresponding coupling constants. We can also include the contribution from relaxation:

$$\frac{d\rho^*}{dt} = -i[H_{QS}^*, \rho^*] + \Gamma(\rho^*) \tag{13}$$

where the relaxation superoperator is given by:

$$\begin{aligned} \Gamma(\rho^*) = \int_0^\infty < [H_{QF}^*(t), [\exp(-iH_{QF}^*\tau)H_{QF}^*(t-\tau) \\ \times \exp(iH_{QF}^*\tau), \rho^*(t)]] > \delta\tau \end{aligned} \tag{14}$$

Since the static quadrupolar Hamiltonian commutes with $H_{QF}^*(t)$, it vanishes in the relaxation superoperator. If the EFG is completely averaged to zero by molecular motion, then $H_{QS}^* = 0$ and the spin dynamics are governed exclusively by relaxation. This equation can be recast into a more familiar master equation in terms of the Redfield relaxation matrix **R** as:

$$\frac{d\rho_{\alpha\alpha'}^*}{dt} = -i[H_{QS}^*, \rho_{\alpha\alpha'}^*] + \sum_\alpha \sum_{\alpha'} R_{\alpha\alpha'\beta\beta'}\rho_{\alpha\alpha'}^* \tag{15}$$

where $|\alpha>$ and $|\beta>$ are the eigenfunctions of unperturbed Hamiltonian (in the presence of nonaveraged static quadrupolar interaction), identifies the phase coherence between states α and α' which is the $\alpha - \alpha'$th element of spin density operator, and is defined as:

$$\langle\alpha|\rho(t)|\alpha'\rangle = \rho_{\alpha\alpha'}(t) \tag{16}$$

Several authors have solved this equation and described the spin evolution in response to RF pulses, under pure quadrupolar relaxation and in the presence of both quadrupolar relaxation and nonaveraged static quadrupolar interaction. Expressions for single, double and triple quantum-filtered signals have been derived under different limiting conditions. Following an RF pulse, the density matrix evolves in the presence of quadrupolar relaxation and static quadrupolar interaction and can be solved using the solutions to eqns (13) and (15).

Copyright © 2006 John Wiley & Sons, Ltd.

DOI: 10.1002/nbm

Energy levels of sodium nuclei

The energy level diagram shown in Figure 4 depicts the energy level pattern of a spin 3/2 nucleus in different motional regimes. The following three motional regimes are possible.

Case 1: Isotropic motion with motional narrowing ($\omega_0\tau_c \ll 1$). Figure 4(A) illustrates the spectrum from sodium in an isotropic solution state (τ_c is the rotational correlation time). The rapid tumbling of molecules containing sodium lead to a fluctuation of the EFG more rapidly than the Larmor period ($2\pi/\omega_0$), hence the quadrupole interaction is 'motion-narrowed' to zero. Consequently, the Zeeman interaction alone will result in four energy levels with equal frequency separation ω_0. Transitions induced by RF pulses at this frequency lead to a single resonance line at ω_0. Both transverse and longitudinal relaxations are simple exponential decays (100).

Case 2: isotropic motion without motional narrowing ($\omega_0\tau_c \approx 1$). In biological tissues where the macromolecular motion associated with the nucleus is isotropic but $\omega_0\tau_c \approx 1$, the quadrupolar interaction dominates the relaxation. In this case, the satellite and central transitions will have different relaxation rates $R_1^{(\pm 1)}$ and $R_2^{(\pm 1)}$, respectively, with $R_1^{(\pm 1)} > R_2^{(\pm 1)}$. These fast and slow decaying components are dynamically shifted from the Larmor frequency with shifts K_1 and $K_2 - K_1$, respectively. However, these shifts are much smaller than the line-widths and very difficult to detect. Hence, in the subsequent discussion we will ignore these dynamic shifts. This situation is still described by Figure 4(A) with the difference that the relaxation is now bi-exponential.

$$\begin{aligned} R_1^{(\pm 1)} &= J_0 + J_1 \pm iK_1 \\ R_2^{(\pm 1)} &= J_1 + J_2 \mp i(K_1 - K_2) \end{aligned} \tag{17}$$

where

$$\begin{aligned} J_m(m\omega) &= \frac{(2\pi)^2}{20}\left(\frac{\chi^2\tau_c}{1+(m\omega)^2\tau_c^2}\right) \\ K_m(m\omega) &= \omega\tau_c J_m(m\omega) \end{aligned} \tag{18}$$

where the spectral densities J_m and K_m are the real and imaginary parts of the Fourier transform of the EFG correlation function (83). χ_2 is the root mean square coupling constant.

Even in the absence of any quadrupolar splitting, biexponential relaxation can create multiple quantum coherences (MQC), which can be detected (82,101,102). In this case, the observed double quantum coherence is solely due to odd rank, $T_{\pm 2}^3$, and the even-rank double quantum state ($T_{\pm 2}^2$) is never created. Owing to its higher sensitivity, triple quantum filtered (TQF) sodium spectroscopy is well suited for measuring bi-exponential transverse relaxation rates (96).

Case 3: anisotropic motion ($\omega_0\tau_c > 1$). In this case, the single quantum relaxation eigenvalues are given by

$$\begin{aligned} R_1^{(1)} &= J_0 + J_1 + J_2 - \sqrt{(J_2^2 - \omega_Q^2)} \\ R_2^{(1)} &= J_1 + J_2 \\ R_3^{(1)} &= J_0 + J_1 + J_2 + \sqrt{(J_2^2 - \omega_Q^2)} \end{aligned} \tag{19}$$

$R_3^{(1)}$ is present due to the formation of even rank two-quantum coherence, T_2^2.

The following three situations can be identified based on the magnitude of J_2:

(1) If $\omega_Q < J_2$, the relaxation eigenvalues are real and line splitting is absent, despite the presence of a nonzero EFG. The single quantum spectrum is a sum of three Lorentzians and ω_Q influences the line-widths and amplitudes of these components but it is difficult to fit these lines to determine individual line-widths.

In ordered biological tissues where the molecular motion is slow ($\omega_0\tau_c > 1$), there is an RQI that arises as a result of the ions interacting with structural proteins such as collagen fibers in connective tissues and proteins that are part of cell membranes. This results in a very small splitting in the spectrum of sodium, which is masked by the larger single quantum line-widths. Further, the dominant presence of sodium in surrounding fluids in isotropic motion complicates the detection of RQC. Thus, measuring the relatively small RQC from motion-restricted sodium in biological tissues using conventional single quantum NMR is difficult and alternative approaches are required. However, if the residual ω_Q is comparable to line-widths, then it does not lead to line splitting but it still creates double quantum coherence due to the even-rank coherence ($T_{\pm 2}^2$). In this case, the double quantum filtered (DQF) signal due to even rank coherence ($T_{\pm 2}^2$) can be used to detect and measure the RQC (103–105).

(2) If $\omega_Q > J_2$, the satellite signals do not overlap with the central transition and the relaxation eigenvalues $R_1^{(1)}$ and $R_3^{(1)}$ corresponding to outer transitions are complex and the satellite transitions are shifted by $\pm(\omega_Q^2 - J_2^2)^{1/2}$ from the central line. The satellite signals in the single quantum spectrum will have complete amplitudes and are phase twisted with respect to the central line. In this case too, the DQF signal from $T_{\pm 2}^2$ can be used to measure ω_Q.

(3) If $\omega_Q \gg J_2$, the energy levels are all shifted by ω_Q resulting in three distinct frequency separations between the energy levels [see Figure 4(B)]. The transitions between these energy levels are governed by the allowed selection rule ($\Delta m = \pm 1$) and lead to three distinct resonance lines: a central transition and two satellite transitions separated by ω_Q. The nuclear spin relaxation rates of the central line and the

Copyright © 2006 John Wiley & Sons, Ltd.

DOI: 10.1002/nbm

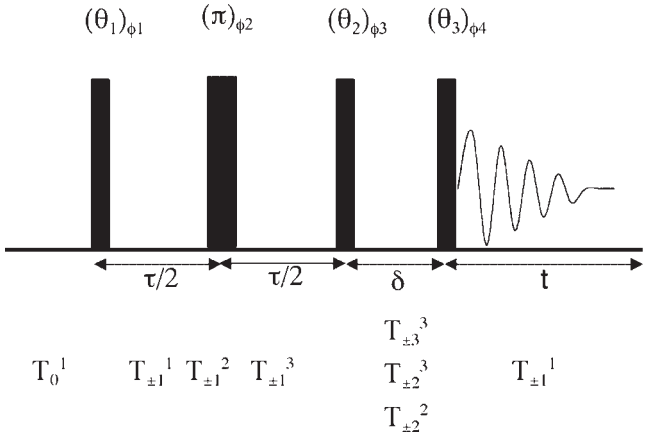


Figure 5. Pulse sequence for multiple quantum filtering. τ, δ and t are preparation, evolution and detection times, respectively. Tensor components during each time period represent the possible coherences. Appropriate phase cycling of the RF pulses is used to select either double or triple quantum coherences.

satellite lines are given by:

$$\begin{aligned} R_s^{(1)} &= J_0 + J_1 + J_2 \\ R_c^{(1)} &= J_1 + J_2 \end{aligned} \tag{20}$$

It should be noted that in the presence of a static quadrupolar interaction, the relaxation rate of satellite lines ($R_s^{(1)} = J_0 + J_1 + J_2$) are different from the corresponding ones in the isotropic situation $R_1^{(1)} = J_0 + J_1$.

Multiple quantum filtered (MQF) NMR

An example of a multiple quantum filter pulse sequence is shown in Figure 5. There is a preparation period (τ) during which time the longitudinal magnetization (T_0^1) magnetization is flipped by an RF pulse of angle θ_1 and phase ϕ_1 into the transverse plane. The new transverse magnetization ($T_{\pm 1}^1$) evolves in the presence of relaxation and/or RQC, creating single quantum coherences (SQC) with different rank ($T_{\pm 1}^1$, $T_{\pm 1}^2$, $T_{\pm 1}^3$) but with the same order, and a second θ_2 and phase ϕ_3 pulse will convert them into multiple quantum coherences ($T_{\pm 1}^1$, $T_{\pm 2}^2$, $T_{\pm 2}^3$, $T_{\pm 3}^3$). The second RF pulse changes the order of the coherences while keeping the same rank. The π-pulse applied at $\tau/2$ does not affect coherences and is used to refocus any resonance offsets and field inhomogeneities. During the evolution period (δ), the MQCs will evolve with a characteristic relaxation time depending upon the order of the coherence. Generally, the evolution time is kept very short to avoid their decay. Since the MQCs cannot be detected directly, the final $(\theta_3)_{\phi 4}$ pulse converts the MQCs into SQCs ($T_{\pm 1}^1$, $T_{\pm 1}^2$, $T_{\pm 1}^3$) which then evolve under relaxation and RQC to detectable SQC ($T_{\pm 1}^1$) during the acquisition time. One may choose to detect the desired order of coherence using appropriate choice of flip angles and phases of the RF pulses (86,106).

Single quantum signal expression. Consider a spin 3/2 nucleus in biological tissues with bi-exponential relaxation and nonzero RQC in a magnetic field. Immediately following the application of a nonselective 90° pulse, the longitudinal magnetization is flipped into transverse plane and then evolves under the influence of biexponential relaxation rates and RQC during the acquisition period, t. Dropping the factors representing temperature, the signal expression following a 90° pulse is given by (83,84,92),

$$S(t) \sim M_0 \frac{1}{5}\left(\frac{3}{2}e^{-(R_s^{(1)} - i\omega_Q)t} + 2e^{-R_c^{(1)}t} + \frac{3}{2}e^{-(R_s^{(1)} + i\omega_Q)t}\right) \tag{21}$$

where M_0 is the thermal equilibrium magnetization, $R_s^{(1)}$ and $R_c^{(1)}$ are relaxation rates of satellite and central transitions respectively and are given above. Here, for the ease of illustration, it is assumed that the nonzero quadrupole interaction is large enough to create line splittings.

Triple quantum filtered signal expression. The triple quantum filtered signal is detected by setting $\theta_1 = \theta_2 = \theta_3 = \pi/2$, and $\phi_1 = \phi_2 = \phi$; $\phi_3 = \phi + \pi/2$, $\phi_4 = 0°$ where ϕ is cycled through 30, 90, 150, 210, 270 and 330° while alternating the receiver phase between 0 and 180°. The addition of all six acquisitions produces the TQF signal:

$$\begin{aligned} S(\tau, t) \sim M_0 \frac{9}{80}\Big[&(e^{-(R_s^{(1)} - i\omega_Q)\tau} - 2e^{-R_c^{(1)}\tau} \\ &+ e^{-(R_s^{(1)} + i\omega_Q)\tau}) \\ &\times (e^{-(R_s^{(1)} - i\omega_Q)t} - 2e^{-R_c^{(1)}t} + e^{-(R_s^{(1)} + i\omega_Q)t})\Big] \end{aligned} \tag{22}$$

A series of TQF spectra are collected (for a fixed δ, usually in few μs) as a function of preparation time, τ, and the resulting spectral amplitudes are fitted to the signal expression to compute the relaxation rates (an example is shown in the case of *in vivo* data). The triple quantum filtered signal has 50% higher sensitivity than the DQF signal and is preferred for measuring biexponential relaxation. It does not have complications of mixing of odd and even rank coherences associated with the DQF signal. Furthermore, it can be used with surface coils, which have inhomogeneous B_1 fields, to study relaxation in biological tissues (106,107).

Double quantum filtered signal expression. A double quantum filtered magic angle (DQF-MA) signal is detected by setting $\theta_1 = \pi/2$, $\theta_2 = \theta_3 = 54.7°$ and $\phi_1 = \phi_2 = \phi_3 = \phi$ and $\phi_4 = 0°$ where ϕ is cycled through 0, 90, 180 and 270° while the receiver phase is alternated between 0 and 180°. This sequence exclusively detects T_2^2 and is important for studying ordered structures.

Copyright © 2006 John Wiley & Sons, Ltd.

DOI: 10.1002/nbm

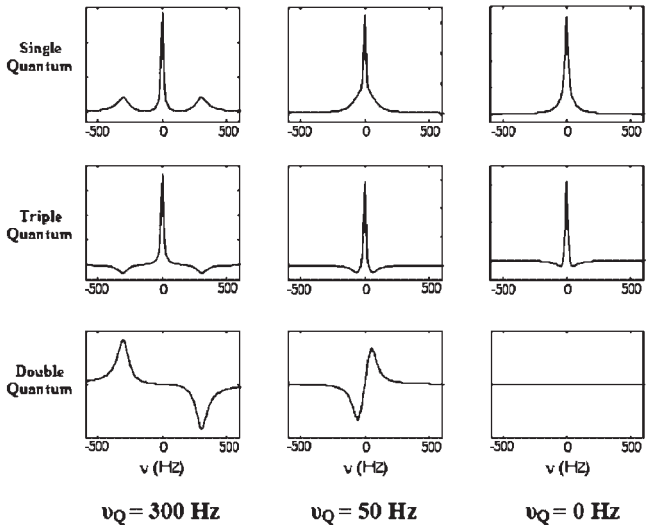


Figure 6. Simulated SQ, TQF and DQF-MA spectra [from eqns (21)–(23)] for different quadrupolar splitting frequencies ($\nu_Q = \omega_Q/2\pi$). The evolution time $\tau = 2$ ms, $T_{2fast} = 1$ ms, $T_{2slow} = 15$ ms. At low ω_Q values greater than 0, clear splittings are absent and experimental DQF-MA spectra can be fitted to extract ω_Q directly.

However, if the flip angles of the last two pulses are set to 90° then the detected DQF signal will be a combination of both T_2^2 and T_2^3. Addition of all four acquisitions produces the DQF-MA signal:

$$S(\tau,t) \sim M_0 \frac{1}{10}\left[\left(e^{-(R_s^{(1)}-i\omega_Q)\tau} - e^{-(R_s^{(1)}+i\omega_Q)\tau}\right) \times \left(e^{-(R_s^{(1)}-i\omega_Q)t} - e^{-(R_s^{(1)}+i\omega_Q)t}\right)\right] \quad (23)$$

Situations corresponding to different motional regimes can be arrived at by choosing appropriate values for ω_Q and spectral densities and the above signal expressions. The DQF-MA sequence has been used to study ordered structures in cartilage, and cytoskeleton (93,103,105, 108,109). Typical simulated spectra using the above signal expressions are shown in Figure 6, and Fig. 7 shows typical SQ, DQF and TQF sodium spectra from articular cartilage. The pronounced negative lobes of DQF spectra are due to the presence of ($T_{\pm 2}^2$) contribution in addition to $T_{\pm 2}^3$.

Other pulse sequences that are useful in studying ordered structures are based on the Jeener-Broekaert (108,110) and spin-locking sequences (84,111). In both these sequences, the signal is detected by filtering through the quadrupolar order T_0^2. The efficiency of both DQF-MA and JB sequences in detecting ordered sodium depends on the precision of the flip angles and hence these methods are very susceptible to B_1 inhomogeneities. The spin-locking method is independent of flip angle precision and is more tolerant to B_1 inhomogeneities. Recently, newer methods have been introduced to study sodium in ordered systems based on suppression of the central transition by applying soft pulses and employing double frequency sweep pulses. These sequences suppress signal from sodium in the isotropic regime and detect only the satellite signals (112) or convert them to a central transition signal (113,114). These methods are robust in spite of B_1 inhomogeneities. Other methods that are promising in detection of ordered sodium ions include quadrupolar filter by nutation (QFN) (115). QFN exploits the dependence of quadrupolar interaction on nutation frequencies to suppress isotropic sodium and detect the central transition of ordered sodium.

Single and multiple quantum sodium NMR has been used extensively to study various biological tissues such as brain (89,90,104,116–120), breast (121) heart (122–128), muscle (129,130), tumors (131–133), blood (122) and cartilage (27,93,134–136) and reviewed in several articles (86,87,91,108,119,137–141). In this review, however, we restrict our discussion to sodium NMR of cartilage.

Sodium NMR of cartilage

Owing to the sparse cellular content (~2% by volume) and highly ordered nature of cartilage, most of the sodium in ECM of cartilage is in a slow motion regime and exhibits multiple quantum coherences. The sodium NMR

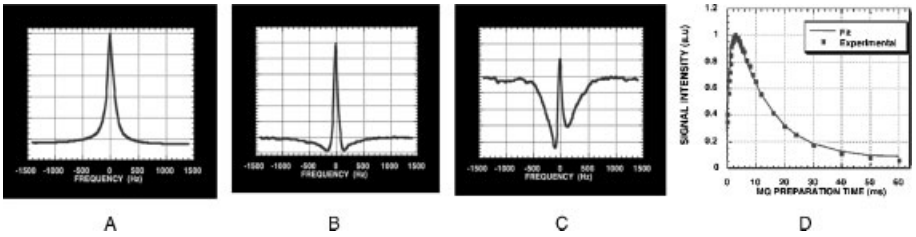


Figure 7. Sodium multiple quantum coherences from articular cartilage: (A) single quantum, (B) double quantum coherence ($T_2^2 + T_2^3$) and (C) triple quantum coherence (T_3^3). Pronounced negative lobes in double quantum coherence ($T_2^2 + T_2^3$) compared with triple quantum coherence is due to the nonaveraged quadrupolar interaction. (D) Normalized triple quantum spectral intensity from human articular cartilage *in vivo* plotted as a function of preparation time. The solid line is the fitted to the TQF signal expression (142).

Copyright © 2006 John Wiley & Sons, Ltd.

DOI: 10.1002/nbm

signal from biological tissues is governed by the relevant values of M_0, R_s, R_c and ω_Q of the system. It should be noted here that 40% of total sodium is observed directly through the central transition, which decays with a longer time constant (T2 slow = T2 fall = $1/R_c^{(1)}$) compared with the 60% of sodium that contributes to the satellite transitions, which decay with a faster relaxation time (T2fast = T2rise = $1/R_s^{(1)}$). Therefore, in order to quantify the absolute sodium concentration from biological tissues, one has to use ultra-short RF pulses and fast acquisition schemes. Otherwise, significant amount of the fast-decaying signal will be lost before detection and this will lead to an underestimation of the total [Na].

Sodium MQF NMR of cartilage

MQ spectroscopy. As stated above, anisotropic motion due to an averaged quadrupolar interaction in biological tissues can be detected via the even-ranked double quantum coherence T_2^2. In the presence of anisotropic motion, transverse relaxation times of the satellite and central transitions measured via TQF sequence are referred to as T_{2rise} and T_{2fall}. The RQC constant can serve as the local order parameter for a given tissue. Although the SQC signal is sum of exponentials and influenced by RQC, it is difficult to determine the relaxation times accurately from this signal. However, as described above, MQ spectroscopy with ultrashort duration RF pulses enables the measurement of all the parameters that govern sodium spin dynamics in tissues. To this end, TQF spectroscopy has been used to measure biexponential relaxation rates of cartilage both *in vitro* (142) and *in vivo* (143). In this study, a flip-angle independent TQF pulse sequence was employed that permitted the use of a surface coil to transmit and receive. Transverse relaxation times of sodium obtained from asymptomatic volunteers were found to be: $T_{2rise} = 1 \pm 0.12$ ms, $T_{2fall} = 12.0 \pm 0.75$ ms (mean $\pm$ SD).

Anisotropic motion of sodium ions was also detected via $T_{\pm 2}^2$ in cartilage and in collagen fibers. DQF spectroscopy was used to measure the RQC constant in nasal cartilage (93). Analytical expressions for the DQF spectra were obtained by calculating the evolution of the second and third rank tensors by solving a modified Redfield equation. It was shown that anisotropy was due to local rather than macroscopic order. The observed spectra were fitted to DQF signal expressions from several models by assuming an isotropic distribution of the local directors of the locally ordered sites. They showed that a model that assumes a Gaussian-weighted distribution of ω_Q values provided the best fit for the MQF-NMR spectra from fresh bovine nasal cartilage. In this analysis, the local RQC was found to be 550 Hz in nasal cartilage. Using isolated models of cartilage, it was shown that the contribution to RQC in cartilage was due to the ordering of collagen bundles and that PG did not contribute to the RQC. A similar model provided the best fit for Jeener–Broekaert spectra obtained from bovine articular cartilage (144).

The effect of interleukin-1β (IL-1β), a cytokine known to induce matrix degradation, was studied in bovine cartilage explants using TQF and double quantum filtered magic angle (DQF-MA) methods (109). Changes on relaxation times and RQC are measured in bovine cartilage specimens. T_{2rise} ranged between 2.26 and 3.5 ms, decreasing with increased PG loss. T_{2fall} increased from 12.3 to 14.9 ms and T_1 increased from 16 to 21 ms while σ (RMS ω_Q) decreased from 180 to 120 Hz over the range of PG depletion investigated. These results indicate that the IL-1β-induced macromolecular depletion has resulted in changes in the local ordering of the tissue. The effect of mechanical compression of cartilage on the MQF sodium spectral line shapes was also analyzed (135). A nonmagnetic compression cell, which enables the NMR experiments while the tissue is compressed, is employed in this study. Bovine cartilage plugs were subjected to single and MQF sodium NMR spectroscopy during a uni-axial compression at 0.7 MPa for 1 h. Compression, although affected the signal amplitude, did not influence the lineshapes of the SQ and TQF spectra significantly. The DQF spectra showed marked line shape changes in the compressed samples, which were attributed to the reduced RQC in compressed samples.

MQ imaging. Feasibility of performing TQF sodium imaging of articular cartilage was first demonstrated on bovine cartilage samples (142) then TQF imaging of the human knee was performed *in vivo* (143). In the *in vivo* study, a twisted projection imaging (TPI) sequence with an ultra-short 400 μs echo time was employed. Unlike SQ, TQF signal reaches a maximum at a preparation time of $\tau \approx 3$ ms. Images were acquired with a voxel size of 0.5 cm. The total imaging time for a three-dimensional data set of 16 slices was $\sim$20 min and provided images with a SNR of 8:1. Single quantum images were also acquired with a voxel size of 0.06 cm. Total SQ imaging time for a three-dimensional data set with SNR of 16:1 was $\sim$10 min. The TQF signal obtained a particular τ value was fitted to the TQF signal expression to calculate the transverse relaxation times. T_{2rise}^* and T_{2fall}^* (the asterisk indicates a measurement of T_2 in the presence of static B_0 inhomogeneities) measured from these studies are 0.84 and 9.6 ms, respectively. These studies clearly demonstrate the importance of a short-echo imaging sequence like TPI in imaging SQ as well as TQF signal from sodium. It also shows that it takes almost three times the total imaging time to acquire TQF images with the same SNR (but 10 times larger voxels) than SQ images, i.e. the TQF signal is an order of magnitude weaker than the SQ signal. In spite of this, MQF sodium NMR studies are indispensable in the quantification of critical parameters (such as relaxation rates and RQC) that characterize sodium dynamics in biological tissues (137).

Copyright © 2006 John Wiley & Sons, Ltd.

DOI: 10.1002/nbm

Sodium MRI of cartilage fixed charge density (FCD)

As discussed in the Introduction, loss of PG is the initiating event in the OA. The ability to quantify these molecular changes will provide a handle for the early diagnosis and treatment monitoring. Based on the fact that Donnan equilibrium holds for cartilage equilibrated in very dilute solutions, Maroudas *et al.* have shown that FCD of cartilage is correlated to the GAG content of cartilage (145). Since the FCD is counter-balanced by the Na^+ ions, loss of PG (hence GAG and FCD) due to cartilage degeneration results in the loss of sodium ions from the tissue. The loss of the negatively charged PG lowers the FCD in the tissue, thereby releasing positively charged sodium ions. Using ideal Donnan equilibrium conditions, FCD can be related to tissue sodium concentration according to the following equation:

$$\mathrm{FCD\ (mM)} = \frac{[\mathrm{Na}^+_{\mathrm{SF}}]^2}{[\mathrm{Na}^+_{\mathrm{tissue}}]} - [\mathrm{Na}^+_{\mathrm{tissue}}] \qquad (24)$$

where $[\mathrm{Na}^+_{\mathrm{SF}}]$ is the sodium concentration in the synovial fluid and $[\mathrm{Na}^+_{\mathrm{tissue}}]$ is the sodium concentration in the tissue. $[\mathrm{Na}^+_{\mathrm{SF}}]$ is typically in the range 140–150 mM, while in phosphate-buffered saline (PBS) it is 154 mM.

Healthy human cartilage FCD ranges from −50 to −250 mM, depending on the age and location in the tissue (136). The FCD from [GAG] can be calculated by the following equation by assuming 2 mol of negative charge per mole of chondroitin sulfate (one from sulfate and one from carboxylate) and a molecular weight of chondroitin sulfate of 502.5 g/mol (136):

$$\mathrm{FCD\ (mM)} = -2 \times \frac{[\mathrm{GAG\ (mg/L)}]}{502.5\ \mathrm{(mg/mM)}} \qquad (25)$$

Because of very short relaxation time of outer (satellite) transitions, one has to perform spectroscopic and imaging experiments with ultrashort echo times. Since invariably NMR and MRI experiments involve finite pulse lengths, some of the fast decaying components are lost and the signal detected following an RF pulse underestimates the true sodium content. In spite of this, as long as the observed signal is calibrated with appropriate relaxation matched reference sodium phantoms, it is possible to measure absolute sodium content of the tissue.

In an early work, sodium NMR spectroscopy was used to study changes in sodium content and relaxation rates in cartilage. In preliminary studies on cartilage, it was found that loss of PG can cause a decrease in FCD and mobility of sodium ions in the ECM. Paul *et al*. (146) and Jelick *et al*.'s (147) measured sodium relaxation rates using single-quantum NMR in nasal cartilage subjected to proteolytic enzymes, trypsin or papain to degrade PG. In this study, it was observed that both T_1 and T_2 relaxation rates were increased following the trypsin or papain treatment. Sodium NMR visibility in cartilage was determined by measuring sodium content using NMR and comparing it with that measured from inductively coupled plasma emission spectroscopy and it was found that sodium in cartilage was 100% NMR visible (136). Sodium content measured using NMR was then used with ideal Donnan theory to estimate FCD and for calf articular cartilage, near physiological conditions, calculated FCD was found to be -280 ± 30 mM. In the epiphyseal cartilage, FCD varied with the position of origin of the tissue within the joint, ranging from −190 to −350 mM in a manner that correlated with tissue GAG content. Similar variations of sodium concentration were also found in a low-resolution sodium image of intact ulnar epiphyseal cartilage.

Changes in sodium content and relaxation times using single quantum sodium MRI and TQF spectroscopy were investigated (148). Over a 50% PG depletion induced by trypsin from bovine cartilage, sodium content changed almost linearly and T_1 increased from 18 to 26 ms, T_{2s} increased from 7.5 to 12 ms and T_{2f} decreased from 2 to 1 ms. These results indicate that care must be taken to account for these changes in the relaxation times with PG depletion/degeneration of the tissue when sodium MRI is used to quantify tissue [Na]. Also in this study, sodium images of bovine cartilage plugs were presented that displayed reduced sodium intensity with increased PG depletion. However, no attempts were made to calculate the FCD of the tissue.

Low-resolution sodium MRI was acquired from human knee *in vivo* (149) at 1.5 T. Reddy *et al.* (27) were the first to demonstrate the feasibility of acquiring a high-resolution (voxel size of 6.25 μl) three-dimensional data set of sodium images of the knee of healthy human volunteers with excellent SNR (16:1) at 4 T (Figure 8). Sodium images were also compared with corresponding proton images to demonstrate the differences in tissue contrast. It was further demonstrated that high-resolution images obtained on bovine patellar cartilage, half of which was subjected to trypsin-induced PG depletion, clearly demarcated the intact tissue (with high sodium content) from PG-depleted tissue (which had lower sodium content). However, in these studies neither sodium nor FCD measurements were performed.

The effect of mechanical compression on sodium and proton NMR relaxation times of bovine articular cartilage specimens was measured as a function of PG depletion. Uni-axial mechanical compressions were performed with an MR-compatible pressure cell and evaluated dynamically via interleaved one-dimensional proton and sodium MR projection imaging (150). Upon full compression, in normal cartilage, sodium T_1 and T_2 relaxation times were decreased by 38 and 37%, respectively, whereas in PG depleted tissue, following full compression, sodium T_1 and T_2 were decreased by 20 and 39%, respectively.

The sensitivity of sodium and proton MRI in detecting trypsin-induced PG changes in bovine articular cartilage

Copyright © 2006 John Wiley & Sons, Ltd.

DOI: 10.1002/nbm

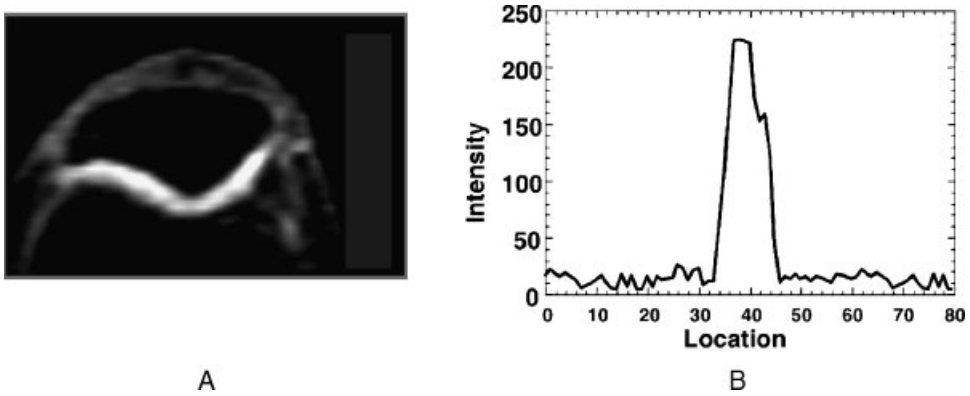


Figure 8. (A) Axial slice of sodium image of a healthy human knee. The high sodium content in articular cartilage is clearly visible. The signal profile across the cartilage is shown in (B) (27).

specimens was investigated at 4 T (151). Over a ~20% PG depletion, sodium image signal change correlated well with the observed PG loss ($r^2 = 0.85, p < 0.01$) while proton density-weighted image intensity change did not exhibit a definite trend ($r^2 = 0.10, p < 0.8$). The change in proton T_1 and T_2 between depleted and nondepleted tissue regions also did not correlate with PG loss ($r^2 = 0.07$ and $r^2 = 0.06$ respectively). Results from this study indicate that sodium MRI is both sensitive and specific in detecting small changes in PG content, whereas proton density and relaxation properties are not sensitive to small changes in cartilage PG.

Shapiro *et al.* described a method to quantify sodium concentration in cartilage (29). Sodium concentration in bovine patellar cartilage was measured by three different methods: NMR spectroscopy of whole cartilage, NMR spectroscopy of liquefied cartilage in concentrated HCL and inductively coupled plasma emission spectroscopy. Using a three-dimensional fast gradient-echo (FGRE) pulse sequence, intact bovine patellae were imaged along with relaxation normalized calibration phantoms to map sodium concentration in cartilage (Figure 9). It was found that sodium concentrations in intact articular cartilage ranged from ~200 mM on the articular and sub-chondral bone surfaces to 390 mM in the middle with an average of 320 mM in several patellae studied. Average measurements from these sodium maps correlated well with those obtained from the spectroscopic methods and sodium was found to be 100% NMR visible in cartilage plugs. In another study, macromolecular depletion was induced in bovine cartilage plugs using trypsin, and the change in [Na] was measured via sodium MRI using the same approach. Following the imaging experiments, the tissue and PG depletion media were subjected to standard dimethylmethylene blue PG assay. A high correlation (slope = 0.89 and $r^2 = 0.81$) between the FCD measure-

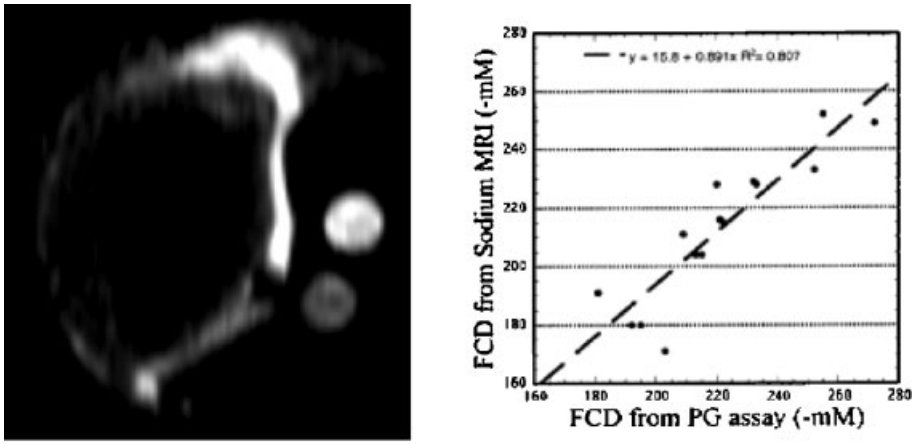


Figure 9. Quantitation and calibration of sodium concentration in articular cartilage. Sodium image of bovine cartilage (A). Trypsin-treated region has low [Na] due to reduced GAG. Circular sodium agarose phantoms that were used to quantify [Na] are also seen in this figure. A plot of FCD measured from sodium MR and that obtained from DMMB assay (B) shows a strong linear correlation between these measurements (29).

Copyright © 2006 John Wiley & Sons, Ltd.

DOI: 10.1002/nbm

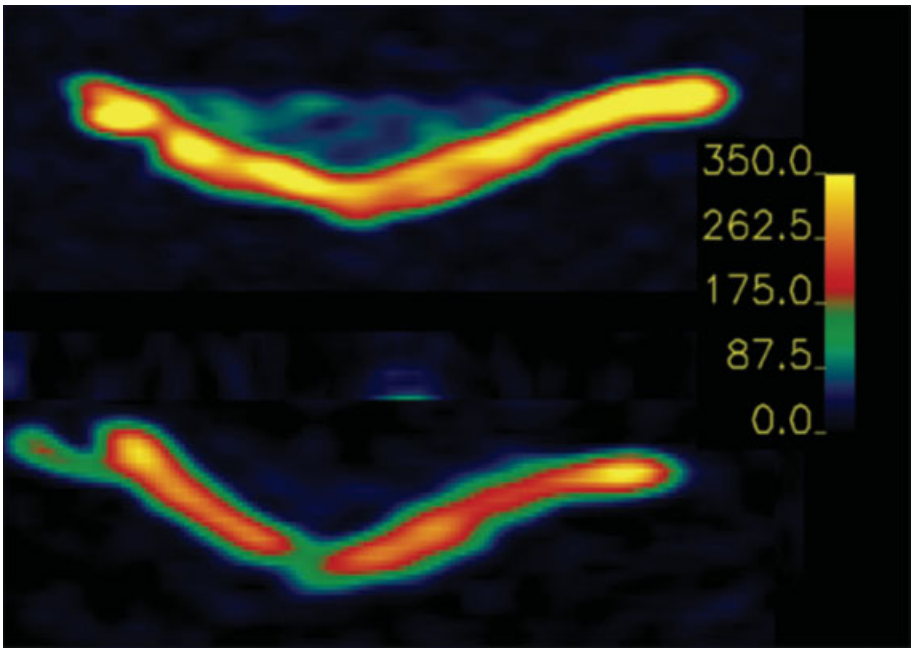


Figure 10. Sodium concentration maps of human patellar cartilage specimens obtained following knee replacement surgery. The top image is from a healthy cartilage while the bottom image is that from an osteoarthritic patient. The scale bar indicates sodium concentration in mM.

ments obtained by ^{23}Na MRI and those obtained by the PG assay (Figure 9) was found. Using the above-described approach involving calibration phantoms, sodium concentration was measured from human cartilage specimens obtained from knee replacement surgery. Clear differences in sodium concentrations in healthy and osteoarthritic specimens were noted (Figure 10).

The same group measured FCD from articular cartilage in the knee of healthy volunteers using two different RF coils, a birdcage coil and a transmit/receive surface coil. High-resolution sodium imaging data (voxel size = 14.6 μL, SNR ≈ 12:1 and a total imaging time of 30 min) obtained with both methods gave similar results, with an average FCD of −158 to −182 mM(152). This variation in FCD has been interpreted as being due to differences in PG content across the tissue. The calibration studies from this work form the basis for computing FCD using sodium MRI. In surface coil experiments, phantom positions were adjusted to match the distance of cartilage from the plane of the surface coil (141).

Although this approach avoids the necessity of compensating for signal drop-off from the inhomogeneous B_1 of a surface coil, any mismatch would lead to erroneous results, a problem that was corrected in a subsequent study by Wheaton *et al.* (30). In this method, the signal intensity of each sodium MR image was corrected for B_1 inhomogeneity, as well as for T_1 and T_2^* weighting, on a pixel-by-pixel basis using a factor derived from the following equation:

$$S_{\mathrm{cor}}(x,y) = \frac{S_{\mathrm{ori}}(x,y)}{B_{1\mathrm{map}}(x,y)\mathrm{e}^{-TE/T_2^*}(1-\mathrm{e}^{-TR/T_1})} \qquad (26)$$

where $S_{\mathrm{cor}}(x,y)$ and $S_{\mathrm{ori}}(x,y)$ are the corrected and original signal intensities, respectively, and $B_{1\mathrm{map}}$ is the value of the B_1 sensitivity map.

The T_1 and T_2^* values of the phantoms measured in progressive saturation experiments were 22 and 8 ms, respectively. The T_1 and T_2^* values used for the human patellar cartilage were 23 and 4.5 ms, respectively, as estimated from data obtained in progressive saturation experiments performed in *ex vivo* bovine patellae. Using this approach, sodium MRI experiments were performed on the knee cartilage of healthy as well as early stage OA patients at 4 T and demonstrated the feasibility of sodium MRI in computing PG loss in early stage OA. The sodium three-dimensional image data set was acquired with a voxel size of 5.3 μL with an SNR of 12:1 in about 20 min. In comparison, it took 30 min to obtain a three-dimensional data set using a volume coil with the same SNR but an increased voxel size of 14.6 μL. With the effects of B_1 inhomogeneity and voxel size accounted for, the surface coil provides an improvement in SNR by a factor of 2. Alternately, an image can be obtained with a surface coil in 25% of the time that it takes to acquire one with a volume coil image with an identical SNR and voxel size. Results from this study revealed that cartilage of healthy subjects had a mean FCD of -182 ± 9 mM

Copyright © 2006 John Wiley & Sons, Ltd.

DOI: 10.1002/nbm

Table 2. Sodium concentration and FCD of healthy human subjects measured from sodium MRI (30)

Sodium concentration (mmol/l)	FCD (mmol/l)
248 ± 39	−175 ± 50
248 ± 29	−175 ± 35
259 ± 24	−187 ± 68
262 ± 60	−192 ± 69
245 ± 48	−171 ± 80
249 ± 49	−176 ± 64
254 ± 36	−182 ± 45
260 ± 60	−190 ± 75
265 ± 56	−196 ± 74

Table 3. FCD measured from sodium MRI of symptomatic osteoarthritic subjects. Percentage change is measured w.r.t the values obtained from healthy subjects (30)

Subject	FCD (mmol/l)[a]	Percentage change[b]
1	−108 ± 56	−41
2	−114 ± 30	−38
2	−144 ± 43	−22

[a]Mean FCDs ± SDs.
[b]Percentage change in mean FCD from normal value—that is, relative to mean FCD of patellae of the healthy subjects (−182 mmol/l).

(Table 3). Data from the symptomatic subjects shown focal regions of decreased FCD ranging from −108 to −144 mM (Table 3), indicating PG loss. Comparisons of axial sodium images of healthy and symptomatic subjects are also shown in Figure 11. Table 3 and 4.

Borthakur and co-workers demonstrated the feasibility of quantifying sodium in the human wrist joint *in vivo* on a 4 T whole-body scanner (153). Employing a fast gradient echo sequence, a three-dimensional data set of 16 slices with 16 averages was obtained in 22 min. The pixel size was 6 μL and it was found that, in healthy human wrist, sodium concentration ranged from 115 to 150 mM in noncartilaginous regions and from 200 to 210 mM in cartilaginous regions. Wheaton *et al*. (154) also demonstrated the

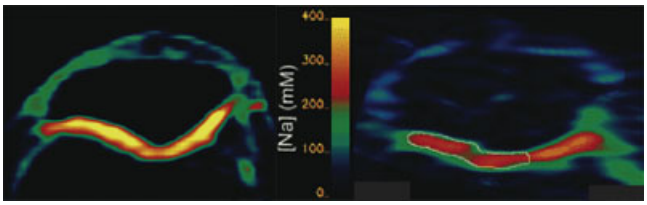


Figure 11. Sodium images of the human knee joint *in vivo* acquired in the axial plane. Cartilage in the patellar–femoral joint is visible in yellow in the image on the left. The scale bar indicates sodium concentration in mM. The image on the left was obtained on a healthy volunteer where uniform high sodium content was observed. The right image is from a symptomatic osteoarthritic subject, demonstrating heterogeneous and low [Na] that reflects a loss of GAG in this subject (30).

Table 4. $T_{1\rho}$ relaxation data from osteoarthritic subjects (239)

Subjects	$T_{1\rho}$ (ms), mean ± SD	$T_{1\rho}$ elevation (%)
1	63 ± 4	26
2	64 ± 3	28
3	65 ± 5	30
4	72 ± 4	44
5	75 ± 6	50
6	95 ± 12	90

feasibility of detecting cytokine-induced arthritic changes in an animal model using sodium MRI. In this study, a biochemical condition similar to OA was created by an intra-articular injection of recombinant porcine interleukin-1β (IL-1β) into the knee joint of Yorkshire pigs. The contralateral knee joint was given a saline injection to serve as the control. Sodium MRI data was acquired at 4 T after 6 h following the injection of IL-1β. Following *in vivo* imaging, the tissue and joint fluid were harvested and subjected to *in vitro* sodium MRI and histologic and immunohistochemical analyses as independent measurements of the cytokine activity and PG loss. Sodium images obtained from treated and untreated joints of pigs are shown in Figure 12. Sodium image data was used to generate FCD maps. On average, the FCD of cytokine-treated cartilage was 49% lower than that of saline-treated cartilage, reflecting a loss of PG content. These results were supported by histologic and immunochemical findings, most notably a reduction in staining for PG and an increase in matrix metalloproteinases in the synovial fluid.

Summary

The sodium spectroscopy work described above was performed at varying field strengths ranging from 2 to 9.4 T. MQF spectroscopy is ideally suited for measuring all the parameters that govern sodium dynamics in cartilage. These are indispensable in obtaining accurate quantification of relaxation rates and RQC, and hence information about ordered tissue. However, the order of magnitude lower SNR of MQF signals restricts them to spectroscopy mode. Most MQF spectroscopy to date has been carried out at magnetic fields greater than 4 T.

The majority of sodium MRI experiments, however, have been performed at 3 and 4 T. In these studies, three-dimensional sodium MRI of 16 slices in the knee joint was performed with volume RF coils in less than half an hour with a voxel size of 6 μL with an SNR of 12:1. The echo times employed in these experiments was a little over 2 ms. However, by exploiting the increased sensitivity of surface coils, it was possible to improve the SNR to 16:1 and the imaging time was reduced to less than 20 min. Sodium imaging at 4 T clearly demonstrated the feasibility of measuring cartilage FCD *in vivo* in

Copyright © 2006 John Wiley & Sons, Ltd.

DOI: 10.1002/nbm

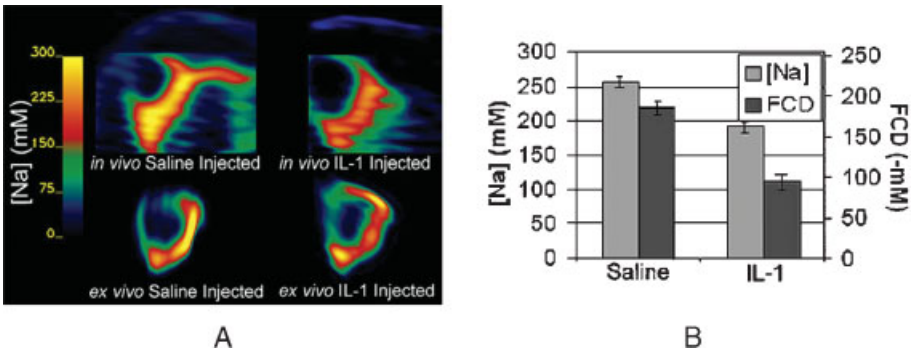


Figure 12. Sodium concentration maps of saline and IL-1β-treated knee joints in swine. The maps shown were acquired from a single specimen, but are representative of the data acquired from all six animals. The resolution of the *in vivo* and *ex vivo* maps were kept identical to allow direct comparison (154). [Na] and FCD from cartilage of saline-treated and IL-1β-treated joints of all six animals (B) demonstrates a significant reduction in FCD from treated cartilage.

healthy as well as osteoarthritic patients. Further, its utility in measuring FCD changes in an animal model of OA has been described. The major advantage of sodium MRI, especially of cartilage, is that it is highly specific to PG content and, since the sodium from surrounding structures in the joint is low (<50 mM), cartilage can be visualized with very high contrast without the requirement for any exogenous contrast agent such as that in dGEMRIC (155). It can be used to quantify early molecular changes in osteoarthritis.

The disadvantages of sodium MRI are that it requires field strengths of $\geq$3 T to obtain quality sodium images that enable accurate quantification of cartilage FCD. Furthermore, due to the limitations of gradient strengths and other hardware requirements, most of the sodium imaging experiments reviewed here employed echo times of $\geq$2 ms. Since the T_{2f} of cartilage lies in the range 1–2 ms, substantial signal is lost before the acquisition. This is a major contributor to the low SNR of sodium compared with conventional proton MRI. Additionally, the sodium gyromagnetic ratio, γ, is one-quarter that of protons, hence sodium MRI requires four times stronger gradients to obtain images with identical resolution to that of proton MRI. With the exception of MQF-prepared TPI imaging, sodium MQF imaging is currently not clinically feasible due to the low sensitivity of the technique and has therefore been relegated to spectroscopic methods to quantify structures of materials and specimens.

However, recent advances in the gradient technology (with a gradient strength of >4 G/cm) may enable one to achieve ultrashort *TE* (<200 μs) that can significantly improve resolution and SNR. Radiofrequency coil technology (multiple channel capability) and parallel imaging approaches such as SENSE (156) and SMASH (157) and tuned pre-amplifiers would further contribute to high SNR. These advances may potentially make clinical sodium MRI feasible on 3 T scanners. Further, the recent proliferation of 7 T whole-body MRI scanners in clinical research centers could have a significant impact on sodium MRI and its potential for clinical use. Since SNR scales as $B_0^{7/2}$(158–161) and the lack of B_1 penetration and B_0 susceptibility are issues that plague proton imaging, sodium MRI can be particularly advantageous at higher fields. Further, unlike proton T_1, which increases with field, as the T_1 of sodium is predominantly due to quadrupolar interaction, it may not change appreciably at higher field. This retains the rapid averaging capability of sodium MRI even at high fields. The low γ of sodium will also mean significantly lower power deposition compared with proton imaging. It is therefore very likely that, with the improved SNR, sodium MRI at 7 T and higher fields would emerge as a robust tool for quantitative imaging of cartilage integrity.

$T_{1\rho}$ MRI

In $T_{1\rho}$ MRI, a long-duration, low-power RF pulse referred to as the 'spin-lock' (SL) pulse is applied to the magnetization in the transverse plane. The magnetization undergoes relaxation in the presence of the applied B_1 field in the rotating frame, a situation similar to that of the longitudinal magnetization in the B_0 field. This spin-locked magnetization will relax with a time constant $T_{1\rho}$, the spin-lattice relaxation in the rotating frame, during the time of the spin-lock pulse (TSL). The B_1 field attenuates the effect of dipolar relaxation, static dipolar coupling, chemical exchange and background gradients on the signal. $T_{1\rho}$ is always greater than T_2. In a typical $T_{1\rho}$ MRI experiment, the TSL time is incremented while the amplitude of SL pulse ($\gamma B_1 \approx 0.1$ to a few kHz) is fixed. Alternatively, the measurement of $T_{1\rho}$ as a function of the B_1 amplitude, for a fixed spin-lock length, is also possible. The '$T_{1\rho}$-dispersion' curve obtained in this case is

Copyright © 2006 John Wiley & Sons, Ltd.

DOI: 10.1002/nbm

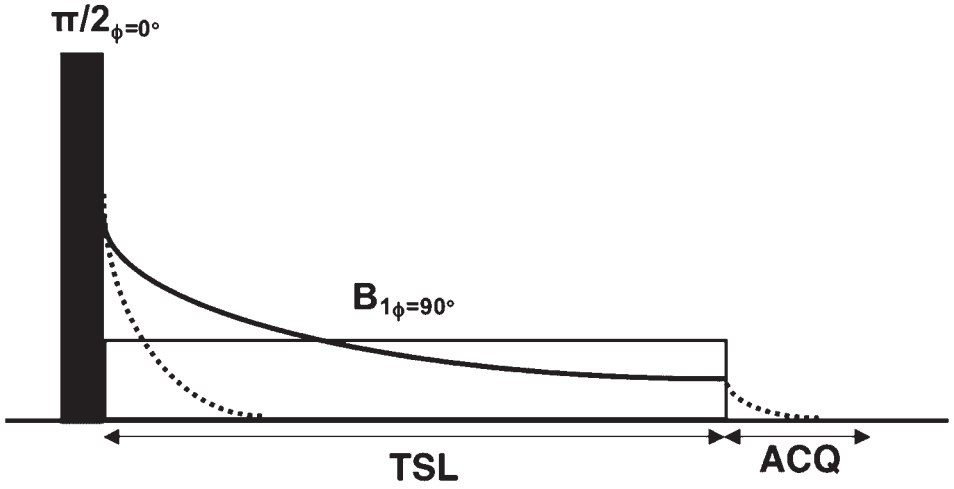


Figure 13. Pulse sequence for spin-locking magnetization in the transverse plane. Initially, a $\pi/2$ pulse flips the longitudinal magnetization into the transverse plane. The open rectangle pulse represents the spin lock (SL) pulse and TSL and B_1 are its duration and amplitude, respectively. The dotted line represents the decay of the magnetization in the absence of spin-locking and is governed by time constant, T_2^*. However, if the magnetization is spin-locked, it decays according to $T_{1\rho}$ (solid line) for the duration of time TSL. But after the SL pulse the decay is again T_2^*, during which time the signal may be acquired.

governed by the spectral density components of the sample that are in the neighborhood of γB_1.

Measurement of the MR signal following the SL pulse (Figure 13) is ideal for spectroscopic measurement of $T_{1\rho}$ of a sample. However for imaging applications, it is often more convenient to prepare the magnetization using a pulse cluster shown in Figure 14. The thermal equilibrium magnetization vector (M_0), initially along the z-axis (panel a), is nutated by the first hard 90° pulse which is applied along the x-axis in the rotating frame of reference, into the transverse plane (panel b). The magnetization, now along the y-axis, is immediately spin-locked by the SL pulse (panel c). For the duration of the TSL period, the magnetization decays with a time constant $T_{1\rho}$ (panel d). The magnetization thereby becomes '$T_{1\rho}$-prepared' and results in a $T_{1\rho}$-weighted signal as a function TSL. This $T_{1\rho}$-prepared magnetization is then restored to the longitudinal axis by the second hard 90° applied along the negative x-axis (panel e) and can be spatially encoded by appending any imaging pulse sequence to this $T_{1\rho}$ pulse cluster. A pixel-by-pixel fit of the spin-locked signal to an appropriate expression provides $T_{1\rho}$. In the above description, on-resonance condition is assumed. The $T_{1\rho}$ experiment can also be performed in off-resonance condition to quantify $T_{1\rho}^{\text{off}}$, where the magnetization is spin-locked at an effective field given by:

$$\omega_{\text{eff}} = \sqrt{\omega_1 + \Delta\omega} \tag{27}$$

where $\Delta\omega$ is the resonance offset.

In biological tissues, off-resonance RF pulse, in addition to spin-locking, also leads to 'magnetization transfer' effect (162) which may complicate the analysis of $T_{1\rho}^{\text{off}}$. The details of off-resonance experiments can be found in the literature (163–165). However, for the rest of the sections we restrict ourselves to describing $T_{1\rho}$ in the on-resonance condition. $T_{1\rho}$ studies in solution-state NMR have been reviewed extensively (166–168). There has been a considerable amount of work on biological tissues using $T_{1\rho}$-spectroscopy and imaging dealing with tumors, muscle, myocardium, blood flow and cartilage (26,165,169–179).

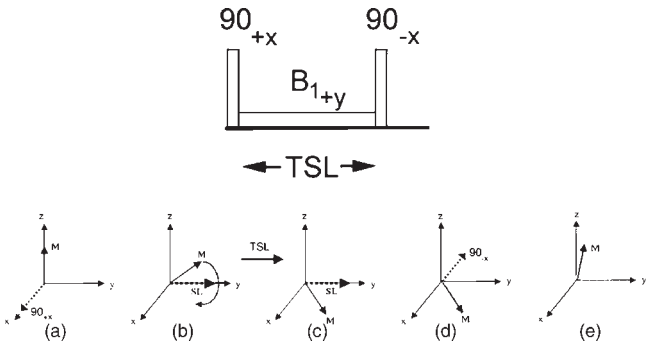


Figure 14. Radiofrequency pulse cluster for $T_{1\rho}$ pre-encoding (left). TSL and B_1 are the length and amplitude of the spin-lock (SL) pulse, respectively. Vector diagram (below) of the evolution of the magnetization during the spin-lock pulse cluster.

Imaging pulse sequences

Two-dimensional $T_{1\rho}$ MRI. Initial $T_{1\rho}$ imaging experiments were performed on articular cartilage using a $T_{1\rho}$

Copyright © 2006 John Wiley & Sons, Ltd.

DOI: 10.1002/nbm

sequence based on a spin-echo, or SE (24), and fast spin echo, or FSE (26). Both these sequences have been implemented on multiple clinical MRI systems and field strengths to produce a single-slice $T_{1\rho}$-weighted image. A typical image data set containing four or five images acquired at different TSL times can be fitted to the following expression to generate a pixel-by-pixel $T_{1\rho}$map:

$$S_y(\mathrm{TSL}) = S_0 \exp\left(\frac{-\mathrm{TSL}}{T_{1\rho}}\right) + C \qquad (28)$$

Three-dimensional $T_{1\rho}$ MRI. Recently, a $T_{1\rho}$-prepared three-dimensional gradient-echo (GRE) based pulse sequence was developed and implemented using either adiabatic pulses (131) or hard pulses (180) in the $T_{1\rho}$ preparation period. In the three-dimensional sequence, the magnetization is $T_{1\rho}$-prepared just as in the case of the two-dimensional sequences. However, in place of the 90° slice-selective pulse of the SE or FSE sequence, a small angle α pulse is used instead to excite a slab; this is followed by a conventional three-dimensional GE readout.

Signal intensities from three-dimensional data sets obtained at varying spin-lock lengths are fitted to the following signal expression:

$$S(TSL) \propto \frac{e^{\frac{-TSL}{T_{1\rho}}}\left(1 - e^{\frac{-(TR-TSL)}{T_1}}\right)}{1 - e^{\frac{-TSL}{T_{1\rho}}} e^{\frac{-(TR-TSL)}{T_1}} \cos\alpha} \sin\alpha \qquad (29)$$

where $S(TSL)$, TSL, TR, T_1 and α represent signal intensity at a given spin-lock duration and frequency, spin-lock length, pulse repetition time, longitudinal relaxation time and flip angle of the slice selective pulse, respectively.

Like most three-dimensional GE-based sequences, the three-dimensional $T_{1\rho}$ sequence enables rapid data collection but produces images with a reduced SNR compared with SE-based images. Further, to accelerate the acquisition, a short TR is typically employed, which introduces significant T_1 weighting in the resultant image and may obscure $T_{1\rho}$-based contrast.

Advantages of this sequence are that it provides volumetric $T_{1\rho}$ maps and that one of the early data set can be used to compute cartilage volume.

Multi-slice $T_{1\rho}$ MRI with spin-echo readout. To overcome the limitations, such as low SNR and poor $T_{1\rho}$ contrast, associated with volumetric data acquisition with a three-dimensional $T_{1\rho}$ prepared sequence, a two-dimensional multi-slice spin-lock (MS-SL) pulse sequence was developed (181). One of the challenges in implementing the $T_{1\rho}$ sequence in multi-slice mode is due to the nonselective nature of the spin-lock pulse, which saturates the longitudinal magnetization from nonexcited regions. In this sequence, saturation of longitudinal magnetization by the application of non-selective SL pulses is experimentally measured and theoretically modeled as $T_{2\rho}$ decay. The saturation data was used to correct the image data as a function of the SL pulse duration to make quantitative measurements of $T_{1\rho}$. It was found that $T_{1\rho}$ measured using saturation corrected MS-SL data is identical to that measured using SS-SL sequence (182). $T_{1\rho}$ relaxation maps are computed for each slice by fitting the image data pixel-by-pixel to eqn (28). During the period between each SL pulse, $\tau = TR/N$, where N is the total number of slices acquired, the longitudinal magnetization recovers according to T_1. After each τ delay, the magnetization becomes saturated by a factor of M^{sat}. Therefore, at the end of the Nth re-growth delay period, the longitudinal magnetization, $M_{z,n}$, is given by:

$$M_{z,n} = M^{\mathrm{sat}}(TSL) \times \left[M_{z,n-1}\exp\left(\frac{-\tau}{T_1}\right) + M_0\left(1 - \exp\left(\frac{-\tau}{T_1}\right)\right)\right] \qquad (30)$$

where

$$M^{\mathrm{sat}}(TSL) = \exp\left(\frac{-TSL}{T_{2\rho}}\right) \qquad (31)$$

and

$$\frac{1}{T_{2\rho}} = \frac{1}{2}\left[\frac{1}{T_1} + \frac{1}{T_2}\right] \qquad (32)$$

Multi-slice $T_{1\rho}$ MRI with spiral readout. Recently a multi-slice $T_{1\rho}$ mapping with spiral readout was implemented at 3 T (183,238). In this sequence, $T_{1\rho}$-prepared magnetization was read by a multi-slice spiral readout. Acquiring a second image that has an inverted longitudinal magnetization compensated for T_1-weighting. The total imaging time for collecting a three-dimensional data set of 14–16 slices was ~13 min. Representative data obtained with this sequence is shown in Figure 34 and was limited to an axial orientation because spiral acquisition does not allow the use of an anti-aliasing filter that is necessary for sagittal or coronal plane acquisition with a knee coil.

Rapid volumetric $T_{1\rho}$ MRI with SSFP readout. In order to implement any research sequence in a clinical setting for quantitative imaging, it should provide three-dimensional coverage and have high precision and high temporal efficiency without exceeding SAR limits. Since $T_{1\rho}$ mapping involves the collection of at least four three-dimensional data sets at varying SL times, it is inherently inefficient. Although the three-dimensional FGRE and multi-slice sequences described above have been implemented on clinical scanners, they typically require 20–25 min to gather a single $T_{1\rho}$ map. Further, three-dimensional $T_{1\rho}$ maps are typically collected with 2–4 mm slice thickness as it is too time-consuming to

Copyright © 2006 John Wiley & Sons, Ltd.

DOI: 10.1002/nbm

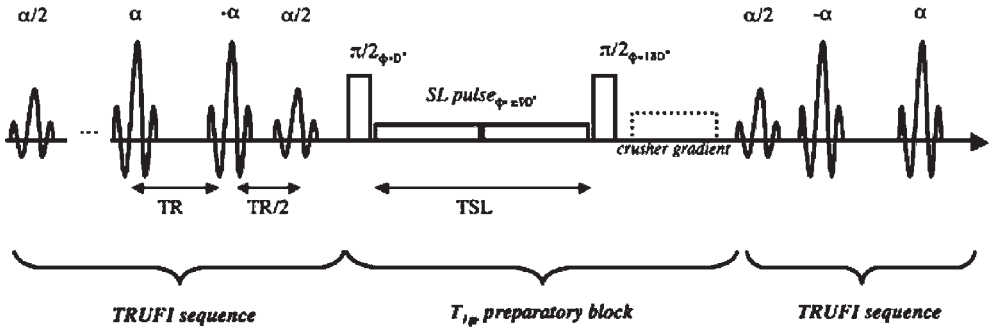


Figure 15. The pulse sequence for acquiring $T_{1\rho}$-weighted true FISP (or TRUFI) images. The steady-state magnetization is stored in the *z*-direction by the last $\alpha/2$ pulse of the TRUFI sequence and then recalled by the $T_{1\rho}$ preparatory cluster and returned to the *z*-axis by the second hard $\pi/2$ pulse. A string crusher gradient (indicated by the dotted box) in then applied at that point to destroy any residual magnetization in the transverse plane.

collect three-dimensional maps with isotropic voxel sizes. Therefore, at least two views, e.g. sagittal and axial, are required to properly visualize anatomical structures in three-dimensional $T_{1\rho}$ maps.

To accomplish this, we recently incorporated $T_{1\rho}$ imaging with a balanced steady-state true precession (SSFP or true FISP or TRUFI) pulse sequence (192). The performance of this sequence (Figure 15) was verified by comparing the $T_{1\rho}$ relaxation maps obtained with this sequence with that of a standard single slice $T_{1\rho}$-TSE sequence. The error in computing $T_{1\rho}$ with $T_{1\rho}$-TRUFI was ~5%. At the same time, the total imaging time for collecting three-dimensional $T_{1\rho}$ maps in both axial and sagittal views was ~20 min. The average $T_{1\rho}$ of cartilage was insignificantly different between the $T_{1\rho}$-TRUFI (39.4 ms) and $T_{1\rho}$-TSE (38.4 ms) readout methods (Figure 16). Integrating this sequence with parallel imaging techniques is expected to further reduce imaging time.

SAR considerations

During MRI, the power of the applied RF pulses has to be monitored at all times to ensure that the energy deposited in the patient remains below Food and Drug Administration (FDA) mandated safety levels for the specific absorption rate. As a safety precaution, invariably all the clinical scanners have built in mechanism to stop the scan if the FDA-mandated power level is exceeded at any point. While the most accurate method would be to measure the power output to the RF coil in real time, *a priori* knowledge of the specific absorption rate (SAR) of a pulse sequence can provide additional safety and save valuable experiment time. A method to calculate SAR has been proposed by Collins *et al.* (193), in which the SAR was calculated from the electric field generated by a typical quadrature coil on a simulated head of known tissue electrical properties and material density. Using this method, the maximum SAR for a 3 ms long

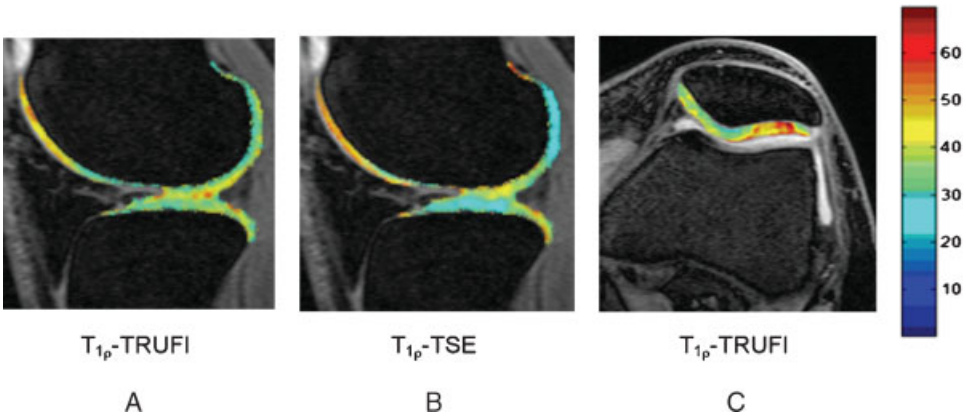


Figure 16. Sagittal $T_{1\rho}$-TRUFI (A) and $T_{1\rho}$-TSE (B) maps (in color) are overlaid on a gray-scale image of the femor–tibial cartilage of a 22-year-old healthy volunteer. Also shown is an axial $T_{1\rho}$-TRUFI map from another healthy volunteer's patellar–femoral cartilage (C). The color bar on the right indicates $T_{1\rho}$ values in milliseconds. Although reduced values are observed in parts of the $T_{1\rho}$-TSE map, the average $T_{1\rho}$ is not significantly different between the $T_{1\rho}$–TRUFI (39.4 ms) and $T_{1\rho}$–TSE (38.4 ms) maps. A region of elevated $T_{1\rho}$ is evident on the lateral facet of the patellar cartilage in (C) and could be an indication of early-stage cartilage degeneration.

Copyright © 2006 John Wiley & Sons, Ltd.

DOI: 10.1002/nbm

rectangular pulse that achieves a flip angle of 90°, or SAR(90°,3), in a simulated quadrature head coil was determined to be 1.46 W/kg in 1 g of tissue. The value was actually smaller (0.708 W/kg in 1 g of tissue) if a sphere containing only muscle tissue was used in the simulation instead. The SAR, of a single pulse of flip angle α and duration τ (in ms), may be calculated using the eqn (193):

$$\mathrm{SAR}(\alpha,\tau) = f\left(\frac{3}{\tau}\right)^2\left(\frac{\alpha}{90^\circ}\right)^2\mathrm{SAR}(90^\circ,3) \qquad (33)$$

where f is a shape factor and equals 1 for a hard pulse or equals the width of the central lobe at the zero crossing point for a sinc pulse.

The minimum *TR* for the pulse sequence was determined from the equation:

$$TR_{\min} = \frac{\sum_{n=1}^{N}\mathrm{SAR}(\alpha_n,\tau_n)\times\tau_n}{\mathrm{SAR}_{\mathrm{FDA}}} \qquad (34)$$

where $\mathrm{SAR}(\alpha_n,\tau_n)$ was calculated from eqn (33) for all $N=4$ pulses in the sequence and SAR_{FDA} is the FDA-suggested maximum *SAR* level and equals 12 W/kg in 1 g of tissue in the extremities (193).

SAR measurements for three-dimensional $T_{1\rho}$-weighted MRI at 1.5 T are described. The signal expression required to fit the data is introduced and critical analysis of energy deposition of the RF pulses in the sequence was performed and validated with experimental data on a known phantom. The temperature increase in the phantom resulting from the sequence was 0.015°C, which is well below the established safety guidelines. Performance of the three-dimensional $T_{1\rho}$ pulse sequence was shown by computing $T_{1\rho}$ maps of bovine patellar cartilage and comparing the data with that obtained with two-dimensional $T_{1\rho}$ mapping sequence. The calculated $T_{1\rho}$ of articular cartilage in the specimen was similar for both three-dimensional and two-dimensional methods (84 ± 2 and 80 ± 3 ms, respectively). Three-dimensional $T_{1\rho}$-weighted images obtained from human knee joint *in vivo* demonstrate an improved contrast between cartilage and surrounding structures.

A low SAR $T_{1\rho}$ pulse sequence

Recently, a reduced SAR version of a $T_{1\rho}$ mapping sequence was developed (194). This method exploits a partial *k*-space acquisition approach in which a full power spin-lock pulse is applied only to the central phase-encode lines of *k*-space, while the remaining phase encode lines receive a low-power (50% amplitude of the maximum) spin-lock pulse. Acquisitions of high- and low-power phase-encode lines are interleaved temporally to minimize average power deposition. This strategy ensures that the majority of signal energy in the central portion of the *k*-space was fully $T_{1\rho}$-weighted, while at the same time the overall SAR of the acquisition was lower, and consequently, total imaging time was reduced. It was demonstrated that, using this approach in the human brain, the SAR could be reduced by 40% while the measurements of $T_{1\rho}$ changed by only 2%. Similarly, a 'keyhole' acquisition approach was exploited in reducing the overall imaging time by 40% for $T_{1\rho}$ mapping (195). These approaches can be combined with any of the acquisition sequences described above to reduce SAR and/or improve temporal resolution.

Mechanism of $T_{1\rho}$ relaxation in cartilage

The spin interactions with different internal Hamiltonians (*J*-coupling, chemical shift, dipole–dipole interaction, chemical exchange, etc.) will take place in the presence of continuous RF fields of SL pulse, thereby imparting time dependence to the interaction Hamiltonians. Thus the RF field not only introduces time dependence into the Hamiltonian, but also changes the axis of quantization of the spins and modifies other characteristics that determine the relaxation behavior. Redfield first demonstrated the spin-lock phenomenon in solid materials and presented relaxation theory in the presence of a time-dependent Hamiltonian (196,197). Later, several investigators developed the theory for applications in liquid state in different conditions (167).

The interactions that are studied using this methodology can be broadly categorized into (i) scalar-coupling, (ii) dipole–dipole and (iii) chemical exchange processes. In NMR, the spin-lattice relaxation in the laboratory frame or rotating frame, the dynamical information is contained in spectral density functions. Depending upon the method used, the experiment may be simultaneously sensitive to more than one time scale. One method of probing relaxation mechanisms is to use the so-called NMR 'dispersion', which measures relaxation times at different field strengths using a field cycling approach (198). Although this method has provided insights into relaxation phenomena of tissues, it is limited to measuring T_1 at different field strengths. With this method, study of slow motions on the order of kHz is difficult as they suffer from poor SNR. On the other hand, $T_{1\rho}$ experiments can be performed at high fields and have the potential to provide information about the low frequency motions (~few kHz) in biological systems with high SNR. Although there is abundant literature on studies of T_1 and T_2 relaxation times in biological systems, there are relatively few studies on $T_{1\rho}$ mechanisms in biological tissues at high static fields.

In biological tissues, the $T_{1\rho}$ relaxation may have contributions from several interactions. Depending upon the tissue type, more than one mechanism may be operative simultaneously but with different relative contributions. In what follows, a brief description of individual relaxation mechanism that may be operative in biological tissues is provided.

Copyright © 2006 John Wiley & Sons, Ltd.

DOI: 10.1002/nbm

Dipolar relaxation. Since the first introduction by Redfield, spin-lattice relaxation in the rotating frame has been studied extensively under different limiting conditions. Using the density matrix approach assuming stochastic time dependence for the lattice variables, a general equation representing the contribution of nuclear spin relaxation due to fluctuating magnetic dipoles to $T_{1\rho}$, in weak collision limit was obtained by Kelly and Sholl (199):

$$\frac{1}{T_{1\rho}} = \frac{3}{8}\gamma^4\hbar^2 I(I+1) \times \left[\frac{\tau_r}{1+4\omega_1^2\tau_r^2} + 10\frac{\tau_r}{1+\omega_0^2\tau_r^2} + \frac{\tau_r}{1+4\omega_0^2\tau_r^2}\right] \quad (35)$$

and

$$\frac{1}{T_1} = \frac{3}{2}\gamma^4\hbar^2 I(I+1)\left[\frac{\tau_r}{1+\omega_0^2\tau_r^2} + \frac{\tau_r}{1+4\omega_0^2\tau_r^2}\right] \quad (36)$$

where I is the nuclear spin number, $\omega_1 = \gamma B_1$, and $\omega_0 = \gamma B_0$, γ is the gyromagnetic ratio of the nuclei, B_0 the Zeeman static magnetic field and τ_r is the molecular rotational correlation time.

From the $T_{1\rho}$ equation, it is clear that it is sensitive to two different time scales, ω_1 and ω_0. Therefore, if the experiment is carried out at constant Zeeman field, the last two terms of the equation will be constant. The last two terms, representing the spectral densities at ω_0 and $2\omega_0$ (J_1 and J_2) can be determined from combination of T_1 and T_{1D} (Jeener–Broekaert) experiments at the same Zeeman field. Then $J(2\omega_1)$ can be determined by measuring $1/T_{1\rho}$ at different B_1 fields. In general, dipolar relaxation is mostly governed by molecular rotational motion with rotational correlation time τ_r. In biological tissues, frequency dependence on relaxation rates, relaxation-dispersion, may arise from (i) rotational motion of a fraction of water bound to proteins, (ii) exchange of protons on macromolecules with bulk water and (iii) the nonaveraged residual dipolar interaction (RDI) of spin associated with oriented macromolecules in the tissue.

Effect of diffusion. It has been shown that, in biological tissues, diffusion (rotational and translational) contributions to all relaxation rates are constant and independent of frequency (200).

Effect of chemical exchange. In proteins and biological tissues, exchange between protons in different environments is expected to contribute to $T_{1\rho}$ relaxation. Prominent exchange mechanisms may be classified as exchange between (i) water molecules in bulk and hydration water on proteins, (ii) hydration water and -OH and -NH protons on proteins (exchange between two sites) and (iii) $H_2{}^{17}O$ and $H_2{}^{16}O$ molecules (scalar relaxation).

Simple exchange of protons between water molecules causes $T_{1\rho}$ dispersion provided the exchange times (τ_e) satisfy the condition that $\omega_1^2\tau_e^2 \approx 1$. When this is valid, $\omega_0^2\tau_e^2 \gg 1$. This type of exchange contribution to the T_1 relaxation rate is zero, it contributes a constant to the T_2 relaxation rate [$1/T_1 \approx 0$: $1/T_2 \approx A\tau_e$] and the $T_{1\rho}$ relaxation rate has a frequency dependence form as shown below:

$$\frac{1}{T_{1\rho}} \approx A\frac{\tau_e}{1+\omega_1^2\tau_e^2} \quad (37)$$

Several groups have investigated exchange mechanisms in a variety of cases using $T_{1\rho}$ and Carr–Purcell–Meiboom–Gill (CPMG) pulse sequences (201–206). Hills and Virta *et al*. (207–213) performed $T_{1\rho}$ studies on proteins, carbohydrates, gelatin, glucose and dextran solutions and demonstrated that the primary mechanism operative in these systems is the exchange between protons in -OH groups on carbohydrates and -OH groups on water molecules. Starting with the Bloch–McConnell equations, Trott *et al*. have derived new expressions for the spin-lattice relaxation rate constant in the rotating frame ($1/T_{1\rho}$), $R_{1\rho}$, for chemical exchange between two sites, A and B, that have distinct magnetic environments and Larmor frequencies (214,215).

$$R_{1\rho} = R_1\cos^2\theta + R_2\sin^2\theta + \frac{\sin^2\theta p_a p_b \delta^2 k}{\omega_{aeff}^2\omega_{beff}^2/\omega_{eff}^2 + k^2} \quad (38)$$

$$\begin{aligned}\delta &= \delta_b - \delta_a = \Omega_b - \Omega_a \\ \omega_{aeff}^2 &= \delta_a^2 + \omega_1^2 \\ \omega_{beff}^2 &= \delta_b^2 + \omega_1^2\end{aligned} \quad (39)$$

$$\begin{aligned}\omega_{eff}^2 &= \Delta\Omega^2 + \omega_1^2 \\ \theta &= \arctan\left(\frac{\omega_1}{\Delta\Omega}\right)\end{aligned} \quad (40)$$

$$\begin{aligned}\overline{\Omega} &= p_a\Omega_a + p_b\Omega_b \\ \Delta\Omega &= \overline{\Omega} - \omega_{rf}\end{aligned} \quad (41)$$

where R_1 and R_2 are the intrinsic longitudinal and transverse relaxation rates respectively, resulting from processes other than chemical exchange.

If R_1 and R_2 are assumed to be population averages, then the effect of difference between the intrinsic relaxation rates for species in sites A and B on $R_{1\rho}$ is negligible. Ω_a and Ω_b are the Larmor precession frequencies of sites A and B, respectively, and $k = k_a + k_b$ is the exchange rate and site populations are $p_a = k_b/k$ and $p_b = k_a/k$.

This equation is simplified if one of the sites is much more populated than the other. In this asymmetric populations limit, $p_a \gg p_b$; $\delta_a \approx \Delta\Omega$ and $\omega_{eff} \approx \omega_{aeff}$:

$$R_{1\rho} = R_1\cos^2\theta + R_2\sin^2\theta + \frac{\sin^2\theta p_a p_b \delta^2 k}{\omega_{beff}^2 + k^2} \quad (42)$$

This equation generalizes the expression previously reported for the special case $R_1 = R_2$ and $\overline{\Omega} = \omega_{rf}$. When

Copyright © 2006 John Wiley & Sons, Ltd.

DOI: 10.1002/nbm

'θ' is 90°, which is the on-resonance condition, then it simplifies to more familiar expression with R_2 representing 'exchange free' transverse relaxation rate:

$$R_{1\rho} = R_2 + \frac{p_a p_b \delta^2 k}{\omega_1^2 + k^2} \tag{43}$$

These results are accurate provided that the spin relaxation decay is dominated by a single exponential damping constant, and are applicable to a wider range of conditions than existing theoretical descriptions. These $R_{1\rho}$, expressions will be useful in analyzing experimental data when exchange is not fast and site populations are unequal. Since this expression involves a chemical-shift difference term that is field-dependent, there will be an increase in $R_{1\rho}$ with field strength. Field-dependent $T_{1\rho}$ relaxation studies can also be used to tease out any contribution from exchange between two chemically shifted nuclei. This exchange model has been used to analyze $T_{1\rho}$ dispersion in cartilage (216).

Scalar relaxation (74). *(a) Scalar relaxation of the first kind:* this is described in the context of two spins, I and S, that are scalar coupled with a spin–spin coupling constant J_{IS}. The exchange time constant between these two spins is denoted by τ_e. If the relaxation time, T_1, of each spin and τ_e is much larger than $1/(2\pi J_{IS})$ then the resonance line of each spin acquires a multiplet structure due to coupling with each other. If $1/T_1$ of either spin or $1/\tau_e$ is much larger than $2\pi J$, then the multiplet structure disappears and each spin will exhibit a single line spectrum and the scalar coupling (J_{IS}) can become a mechanism of relaxation. When the coupling is modulated by (fast) exchange, this type of relaxation is referred to as 'scalar relaxation of the first kind'.

(b) Scalar relaxation of the second kind: if the S spin's T_1 is much shorter than $1/(2^{\pi}J_{IS})$ and τ_e due to anything other than scalar coupling, then the splitting due to scalar coupling is absent and the I spin spectrum will have a single resonance line. This type of situation can occur if S is quadrupolar nuclei. Quadrupolar nuclei couple to the EFG within the molecule in which they are present. In solution state, the fast rotation of the molecules produces a rotating EFG, which leads to a fluctuation of the local magnetic field experienced by the nuclei and results in a short T_1. When the rate of these fluctuating local magnetic fields of quadrupolar nuclei is greater than the coupling constant, the splitting will average to zero. This type of relaxation mechanism is known as 'scalar relaxation of the second kind'.

Contribution of both these types of scalar relaxation leads to broadening of the I spins' spectral lines and an identical effect on the relaxation rate of the I nuclei. An example of scalar relaxation of the first kind is proton relaxation in $H_2{}^{17}O$. The ^{17}O nucleus has spin 5/2 and its T_1 is dominated by quadrupolar relaxation shortening T_1 to ~4 ms. Protons on $H_2{}^{17}O$ are in constant exchange with those on $H_2{}^{16}O$ and at neutral pH $\tau_e \approx 1.0$ ms. Taking into consideration the concentration differences between $H_2{}^{17}O$ and $H_2{}^{16}O$, Meiboom (201) derived equations for proton $T_{1\rho}$ in ^{17}O-enriched water under conditions of [^{17}O–^{1}H] scalar coupling and chemical exchange. In the fast-proton-exchange regime (i.e. $\delta\tau \ll 1$, where 2δ is the J-coupling constant and τ is the proton exchange time), it can be shown that:

$$\frac{1}{T_{1\rho}(\omega_1)} = \frac{1}{T_{1\rho}^0} + \tau \sum_i \frac{p_i \delta_i^2}{(1 + \tau^2 \omega_1^2)} \tag{44}$$

where p_i is the relative intensity of the ith spectral line of an ^{17}O multiplet, and $1/T_{1\rho}^0$ is the rate of all ^{17}O-independent relaxation processes.

Substituting for δ_I and letting $p_i = f/6$, where f is the ^{17}O atom fraction in $H_2{}^{17}O$, the above equation becomes:

$$\frac{1}{T_{1\rho}(\omega_1)} = \frac{1}{T_{1\rho}^0} + \frac{(35/12)\tau J^2 f}{(1 + \tau^2 \omega_1^2)} \tag{45}$$

where $J = 2\delta$.

An imaging method that uses $T_{1\rho}$-weighted images to quantify [$H_2{}^{17}O$] based on this theory has been developed (217). Scalar relaxation of the second kind has been demonstrated in the case of amide protons in farmamide (218). Since quadrupolar relaxation and scalar coupling are both independent of the static field, scalar relaxation of either kind is not field-dependent.

In biological tissue, the protons on amide and amine groups are expected to be influenced by the scalar relaxation (second kind) from the quadrupolar nucleus ^{14}N ($I = 1$) and their exchange with bulk water could influence water $T_{1\rho}$ and T_2 relaxation times.

Nonaveraged or residual dipolar coupling. In biological tissues, the presence of nonaveraged RDI can contribute to '$T_{1\rho}$ dispersion'-variation of $T_{1\rho}$ as a function of the spin-locking field. Since the RDI stems from the ordered structures in the tissues, computation of the residual dipolar coupling (RDC) provides information about the structural integrity of tissue. Previously, different types of multiple quantum (MQ) coherence transfer methods have been developed to characterize this interaction. However, due to an order of magnitude low SNR of MQ filtered methods, their applications have been largely limited to *ex vivo* studies and some imaging experiments that were performed on highly ordered tissue such as tendons (86,219). Spin-locking methods to characterize this interaction offer high SNR (comparable to single quantum coherence) and can be implemented *in vivo* with relative ease.

Recently it has been shown that, because of the changing ratio of the residual dipolar coupling to the B_1 of the spin lock pulse, even in the absence of slow motional frequencies, RDI leads to $T_{1\rho}$ dispersion (220).

Theoretical analysis of the $T_{1\rho}$ relaxation, in the presence of RDI, in the simplest model of two chemically

Copyright © 2006 John Wiley & Sons, Ltd.

DOI: 10.1002/nbm

equivalent dipolar coupled nuclear spins under the influence of spin-locking, has been described (221). During spin-locking, the presence of RDI creates anti-phase magnetization, zero and double quantum coherences and longitudinal two spin-order, some of which evolve into observable coherences with different relaxation rates. The signal expression for a dipolar-coupled spins following spin-locking can be written as (221):

$$S(t) = X_1 \exp(-R_{1\rho}^{\text{app}} t) + X_2 \exp(-R_{1\rho}^{*} t)\cos(2\pi\nu_{\text{osc}} t + \phi) \quad (46)$$

where

$$X_1 = \frac{(R_{1\rho} - R_{1\rho}^{*})^2 + 4\pi^2(\nu_{\text{osc}}^2 - \nu_{\text{d}}^2)}{(R_{1\rho}^{\text{app}} - R_{1\rho}^{*})^2 + 4\pi^2\nu_{\text{osc}}^2} \quad (47)$$

and

$$X_1 + X_2\cos\phi = 1 \quad (48)$$

and

$$\tan\phi = \frac{(R_{1\rho} - R_{1\rho}^{*}) + (R_{1\rho}^{*} - R_{1\rho}^{\text{app}})X_1}{2\pi\nu_{\text{osc}}(1 - X_1)} \quad (49)$$

where

$$x_{\text{o}} = -R_{1\rho}^{\text{app}} = -R_m + \left\{-q/2 + \left[(q/2)^2 + (p/3)^3\right]^{1/2}\right\}^{1/3} + \left\{-q/2 - \left[(q/2)^2 + (p/3)^3\right]^{1/2}\right\}^{1/3} \quad (50)$$

where

$$p = -\frac{(R_{1\rho}^2 + R_{1\rho}'^2 + R_{1\rho}''^2 - R_{1\rho}R_{1\rho}' - R_{1\rho}R_{1\rho}'' - R_{1\rho}'R_{1\rho}'')}{3} + 4\pi^2\nu_{\text{d}}^2 + 16\pi^2\nu_1^2 \quad (51)$$

and

$$q = (R_{1\rho} + R_{1\rho}' + R_{1\rho}'') \times \frac{(2R_{1\rho}^2 + 2R_{1\rho}'^2 + 2R_{1\rho}''^2 - 5R_{1\rho}R_{1\rho}' - 5R_{1\rho}R_{1\rho}'' - 5R_{1\rho}'R_{1\rho}'')}{27} + R_{1\rho}R_{1\rho}'R_{1\rho}'' - \frac{(R_{1\rho} + R_{1\rho}' - 2R_{1\rho}'')4\pi^2\nu_{\text{d}}^2}{3} + \frac{(2R_{1\rho} - R_{1\rho}' - R_{1\rho}'')16\pi^2\nu_1^2}{3} \quad (52)$$

$$x_{1,2} = \frac{-3R_m}{2} - \frac{x_{\text{o}}}{2} \pm 2i\pi\nu_{\text{osc}} \quad (53)$$

where

$$\nu_{\text{osc}} = \frac{1}{4\pi}\sqrt{4p + 3(x_{\text{o}} + R_m)^2} \quad (54)$$

$R_{1\rho}$ is the relaxation rate of single quantum coherence $(I_x + S_x)$, $R_{1\rho}'$ is the relaxation rate of anti-phase two spin order $(2I_yS_z + 2I_zS_y)$ and $R_{1\rho}''$ is the relaxation rate of $(2I_yS_y - 2I_zS_z)$, which is a mixture of zero, double quantum coherences, $2I_yS_y = (I_+S_- + I_-S_+ - I_+S_+ - I_-S_-)/2$, and longitudinal two-spin order.

$$R_m = \frac{(R_{1\rho} + R_{1\rho}' + R_{1\rho}'')}{3} \quad (55)$$

The following three parameters can be measured from the signal expression:

(1) The damping factor of the slowly decaying part of the evolution curve that yields the apparent rotating frame relaxation rate, $R_{1\rho}^{\text{app}}$.
(2) The initial oscillation frequency, ν_{osc}, corresponding to nutation phenomena [due to the presence of two modes: $(2I_yS_y - 2I_zS_z)$ and $(2I_yS_z + 2I_zS_y)$] with respect to the inhomogeneous spin-locking RF field and associated relaxation rate $R_{1\rho}^{*}$ which, is similar to the R_2^{*} when one is dealing with precession with respect to an inhomogeneous B_0 field. When spin-locking field is zero, $R_{1\rho}^{*} \approx R_2^{*}$.
(3) The relative contributions of the fast and slow decaying components X_1 and X_2.

Limiting cases. *Case 1:* when a small molecule is dissolved into a liquid crystalline solvent, the relaxation rates are expected to be much smaller than ν_1 and ν_{d}. In this limiting situation:

$$R_{1\rho}^{\text{app}} = \frac{4\nu_1^2}{4\nu_1^2 + \nu_{\text{d}}^2}R_{1\rho} + \frac{\nu_{\text{d}}^2}{4\nu_1^2 + \nu_{\text{d}}^2}R_{1\rho}'' \quad (56)$$

and

$$\nu_{\text{osc}} = \sqrt{4\nu_1^2 + \nu_{\text{d}}^2} \quad (57)$$

when $\nu_1 \gg \nu_{\text{d}}$, $R_{1\rho}^{\text{app}}$ is equal to the true rotating frame relaxation rate, $R_{1\rho}$, whereas for $\nu_1 \ll \nu_{\text{d}}$, $R_{1\rho}^{\text{app}}$ tends toward the third-mode relaxation rate, $R_{1\rho}''$.

$$X_1 = \frac{R_{1\rho}^{*2} + 16\pi^2\nu_1^2}{R_{1\rho}^{*2} + 4\pi^2\nu_{\text{osc}}^2} \quad (58)$$

and

$$\tan\phi = \frac{-R_{1\rho}^{*}}{2\pi\nu_{\text{osc}}} \quad (59)$$

Case 2: when $\nu_1 \gg \nu_{\text{d}}$ and both are distributed over a range of values as in any polycrystalline, amorphous solid, or in ordered biological tissues. In this limiting situation:

$$R_{1\rho}^{\text{app}} = R_{1\rho} + \frac{\nu_{\text{d}}^2}{4\nu_1^2}(R_{1\rho}'' - R_{1\rho}) \quad (60)$$

Several experiments have shown the feasibility of measuring the residual dipolar coupling using spin-

Copyright © 2006 John Wiley & Sons, Ltd.

DOI: 10.1002/nbm

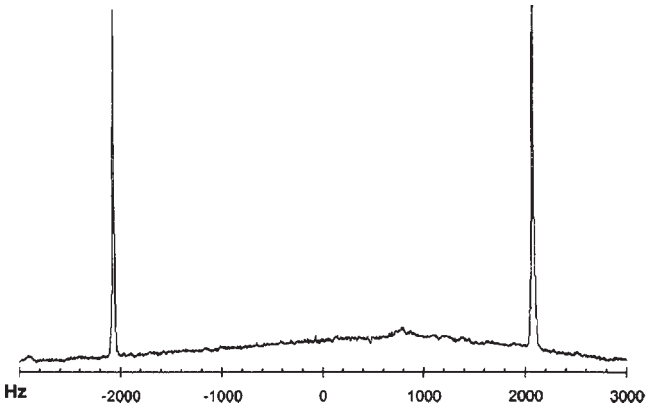


Figure 17. Pulse-acquire proton NMR spectrum of CH_2Cl_2 in a nematic solvent (doublet of 4.2 kHz, arising from the dipolar interaction between the two protons). The distorted baseline is due to the broad NMR spectrum of the liquid crystal (221).

locking techniques in a liquid crystal (Figure 17 and Figure 18 spectra and early portion of oscillations). As shown in this example, in single and liquid crystals the dipolar coupling is manifested as resolved resonance splitting in a pulse-acquired spectrum. Hence, spin-locking or other experiments involving complex pulse sequences are not required to measure RDI. However, biological tissues exhibit a distribution of RDI and it may be difficult to resolve the resulting small splitting. Further, due to RF inhomogeneities during spin-locking, the dipolar oscillation frequency will be damped faster and thereby mask the intrinsic relaxation rates. Dominant bulk water, without any RDI, may mask these small and unresolved splittings. In these cases, the spin-locking experiment is well suited to computing the RDI and associated relaxation rates.

Depending upon the limiting case that is applicable for a given tissue, one has to include the appropriate $R_{1\rho}^{\text{app}}$ in

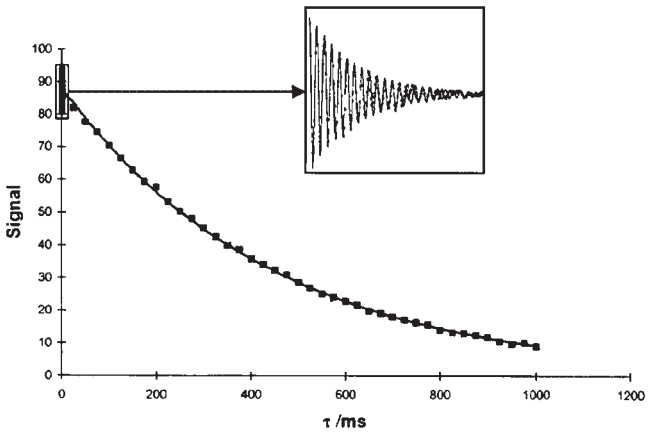


Figure 18. Evolution of dipolar doublet as function of the spin-lock period duration; spin-lock amplitude: $w_1 = 4$ kHz. These experimental results were obtained by subtracting the anti-phase doublet signal. Note the initial rapidly damped oscillations and the mono-exponential decay for the major part of the evolution curve (221).

the expression for observed $T_{1\rho}$ in biological tissues. As long as ω_1 is on the order of a few kHz, dipolar relaxation due to molecular rotational processes such as fluctuating dipolar fields and diffusion do not contribute to the $T_{1\rho}$ dispersion but they add as constants to the overall value of $T_{1\rho}$. The T_1 contribution can either be calculated as mentioned above or treated as a constant. The remaining terms are due to the exchange processes that are associated with water protons and other exchangeable protons on macromolecules (such as -OH and -NH), and residual static dipolar coupling. As discussed above, depending upon the tissue type and limiting cases, appropriate contributions due to dominant exchange interaction and static dipolar interaction terms should be included in the total expression for $T_{1\rho}$. Therefore, the observed $T_{1\rho}$ in biological tissues can expressed as:

$$\left[\frac{1}{T_{1\rho}}\right]_{tissue} = \left[\frac{1}{T_{1\rho}}\right]_{fD} + \left[\frac{1}{T_{1\rho}}\right]_{Diff} + \left[\frac{1}{T_{1\rho}}\right]_{exchange} + \left[\frac{1}{T_{1\rho}}\right]_{RDI} \quad (61)$$

Dipolar interaction in cartilage

Using the approach described above (221), the existence of dipolar oscillation frequency due to static dipolar interaction and its origin in the case of cartilage and model systems is demonstrated (222).

Figure 19 shows the $T_{1\rho}$-weighted spectral intensity from a native bovine cartilage specimen as a function of spin-lock pulse length (for ω_1 of 200 Hz). The inset shows

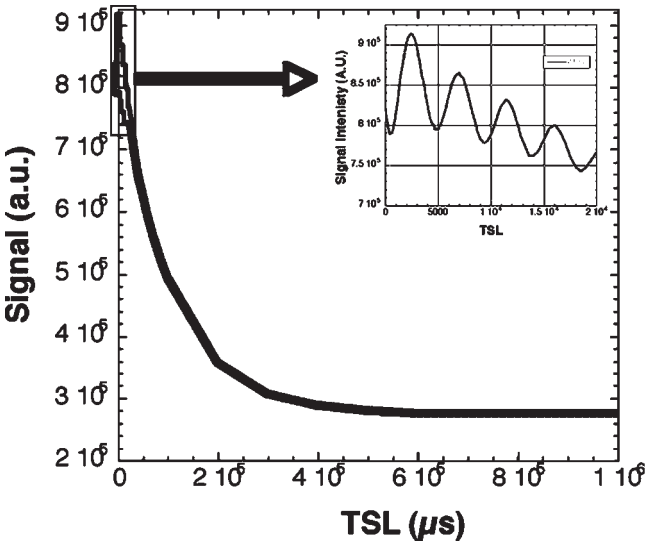


Figure 19. $T_{1\rho}$-weighted signal intensity from a bovine cartilage as a function SL length is shown. The ω_1 used for this study is 250 Hz. The inset shows the expanded version of the initial portion of the signal. The oscillation pattern is characteristic of the presence of RDI in the tissue (240).

Copyright © 2006 John Wiley & Sons, Ltd.

DOI: 10.1002/nbm

the expanded initial portion of the data that has persisting oscillation pattern for ~20 ms. This data, with a fast decaying component with dipolar oscillations and a slow decaying component, has a striking resemblance to the one obtained from liquid crystalline sample with resolved dipolar splitting. This clearly demonstrates the presence of RDI in cartilage. As shown in the inset, in the bovine cartilage the dipolar oscillations lasts ~20 ms during the spin locking. However, since in human cartilage $T_{1\rho}$ relaxation time is about 50% smaller than that in bovine tissue, the oscillation pattern may lasts for about ~10 ms. Since there is a distribution of RDI in cartilage, it should be modeled to fit the observed oscillation pattern to quantify RDI from the tissue similar to the analysis presented by Chaumette *et al*. (221).

Several studies have demonstrated that the static RDI between water molecules associated with fibrillar collagen is the primary source of laminar appearance (alternating bright-dark pattern of signal intensity variation across cartilage) in T_2-weighted images (31,223–225). Given the ~20% (of wet weight) collagen content in cartilage ECM, water proton T_2 relaxation is expected to be dominated by the RDI and therefore masks any small changes in the relaxation times due to alterations in other matrix properties. Further, there are several studies indicating that PG changes in cartilage either do not influence the T_2 or the changes in T_2 do not follow a particular trend (226–228). These observations have led to the argument that T_2 relaxation mapping is either more sensitive to collagen content or only sensitive to changes in collagen (11,228).

$T_{1\rho}$ Dispersion in cartilage

There are only a few studies dealing with $T_{1\rho}$ dispersion in cartilage. In one of the spectroscopic studies of $T_{1\rho}$ dispersion in bovine cartilage, it was suggested that the exchange between protons on -OH and -NH of GAG with bulk water may be the dominant source for the low frequency (0–1.5 kHz) $T_{1\rho}$ dispersion in cartilage (229). Low-frequency dispersion changes are correlated with loss of PG from the ECM of cartilage. Supplementing the experimental data with literature results, logical arguments were presented in support of the mechanism in model systems. However, the data in support of the exchange mechanism in cartilage was extrapolated from that of isolated protein model systems and therefore may not be translated to the case of cartilage with ordered structures. Another problem with this study is that the data was gathered using spectroscopy rather than imaging methods. This will provide an average $T_{1\rho}$ value from the entire sample and could mask subtle regional changes in the tissue characteristics and is highly susceptible to tissue handling (e.g. un-blotted excess water). These experimental and data analysis aspects have to be taken into account when inferring anything from this study.

Recently, $T_{1\rho}$ mapping at two different scanner field strengths was analyzed using a two-site exchange model as described above. It was demonstrated that the $T_{1\rho}$ dispersion is primarily due to RDI and contribution due to chemical exchange between -OH and -NH protons on GAG and bulk water $\leq$3 T is only ~6% (216). Their data also shows that the exchange contribution may increase to ~25% at higher fields of ~7 T. The effect of refocusing the dipolar interaction on the measured T_2 of articular cartilage was also investigated using spectroscopic methods and demonstrated that dipolar interaction contributes significantly to $T_{1\rho}$ dispersion in cartilage. $T_{1\rho}$ dispersion in bovine cartilage and its effect on cartilage contrast, and the effect of spin-locking on the laminar appearance in MRI of cartilage, were also investigated at 4.7 T using orientation-dependent studies (222).

It was found that, when the normal to the surface of cartilage was parallel to B_0, a typical laminar appearance was present in T_2-weighted images but was absent in $T_{1\rho}$-weighted images of the same specimen (Figure 20). At the 'magic angle' orientation (when the surface normal was 54.7° with respect to B_0), neither T_2 nor $T_{1\rho}$ images demonstrated laminae (Figure 21). However, $T_{1\rho}$ values were greater than T_2 at both orientations throughout the cartilage layers. These studies imply that, while RDI contributes to a laminar appearance in T_2 images, its effect is attenuated by spin-locking. Further, if the dipolar interaction is the only contributor to the observed dispersion, then at the magic angle all T_2 values should be equivalent to $T_{1\rho}$ obtained at a spin-lock field at ~2 kHz. They observed significantly higher $T_{1\rho}$ values compared with T_2 even at the magic angle. This may indicate that there are other relaxation mechanisms that contribute to $T_{1\rho}$ in addition to RDI.

Although there are conflicting reports in the literature on the contribution to $T_{1\rho}$ dispersion on cartilage, the bulk of the existing data in the literature and data presented here support the nonaveraged dipolar interaction between water protons associated with collagen being the predominant contributor. However, the dipolar interaction alone cannot account for the complete dispersion observed. Contributions from other sources including exchange cannot be ruled out completely, especially at higher static fields. Further work in this area is required to address this issue.

Small variations in $T_{1\rho}$ dispersion profiles were observed in spectroscopic studies of cartilage specimens (229). However, except for a constant shift, there were no significant changes observed in the $T_{1\rho}$ dispersion curve with varying levels of GAG depletion by trypsin (25). Discrepancy between these results may be due to the measurement of global (spectroscopic) vs (imaging) regional $T_{1\rho}$ and difference in static field strength. In imaging experiments, $T_{1\rho}$ mapping is performed at a particular spin-lock frequency (e.g. 500 Hz) and $T_{1\rho}$ relaxation time, not dispersion, is measured. In spin-locking experiments, as long as the $B_1 > \Delta B_0$, field

Copyright © 2006 John Wiley & Sons, Ltd.

DOI: 10.1002/nbm

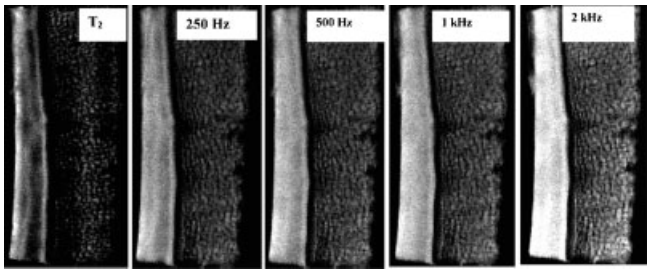


Figure 20. T_2- and $T_{1\rho}$-weighted images of bovine articular cartilage. In T_2-weighted images, laminae of alternating high and low signal intensity pattern are evident. In $T_{1\rho}$-weighted images, the laminar appearance is gradually reduced with increasing ω_1, making the signal more homogeneous across the cartilage (222).

inhomogeneities are refocused. In most of the *in vivo* experiments, this condition is often fulfilled because typical ΔB_0 values are between 100 and 200 Hz and B_1 values used are >250 Hz. At about 500Hz, (i) reduced dipolar interaction by spin-locking minimizes or eliminates laminae (or relaxation effects due to oriented collagen). At this field, it is likely that scalar-relaxation due to proton exchange between $H_2{}^{17}O$ and $H_2{}^{16}O$ and or between -NH and H_2O may also be attenuated substantially (217). As a consequence of the attenuation of the ΔB_0, RDI and exchange broadening increases the dynamic range of the $T_{1\rho}$ relaxation time scale by ~200% in bovine cartilage and by 60% in human cartilage compared with T_2. This improved dynamic range (due to the attenuation of background relaxation of oriented collagen matrix) of $T_{1\rho}$ may facilitate the detection of small changes in relaxation times due to the loss of PG or other matrix component from the tissue. At this point, available data on measured $T_{1\rho}$ in CS phantoms and trypsin-treated cartilage (226) suggest that it may be predominantly due to a combination of changes in [GAG] (221) and, to a lesser extent, from exchange between protons on GAG and bulk water. Further work is required to tease out these contributions. Since the relaxation rate is measured at a fixed B_1 amplitude of the spin-lock pulse, the static dipolar effect adds as a constant. However, $T_{1\rho}$ dispersion maps measured from data obtained as a function of varying B_1 is expected to demonstrate the otherwise dominant dipolar effects and may provide information about the ordered collagen.

Experimental $T_{1\rho}$ studies

***Ex vivo* animal specimens.** Potential of proton $T_{1\rho}$ imaging of cartilage and its applications to study of cartilage degeneration was first proposed by Reddy *et al*. (230). In this study at 2 T, $T_{1\rho}$ mapping and dispersion was

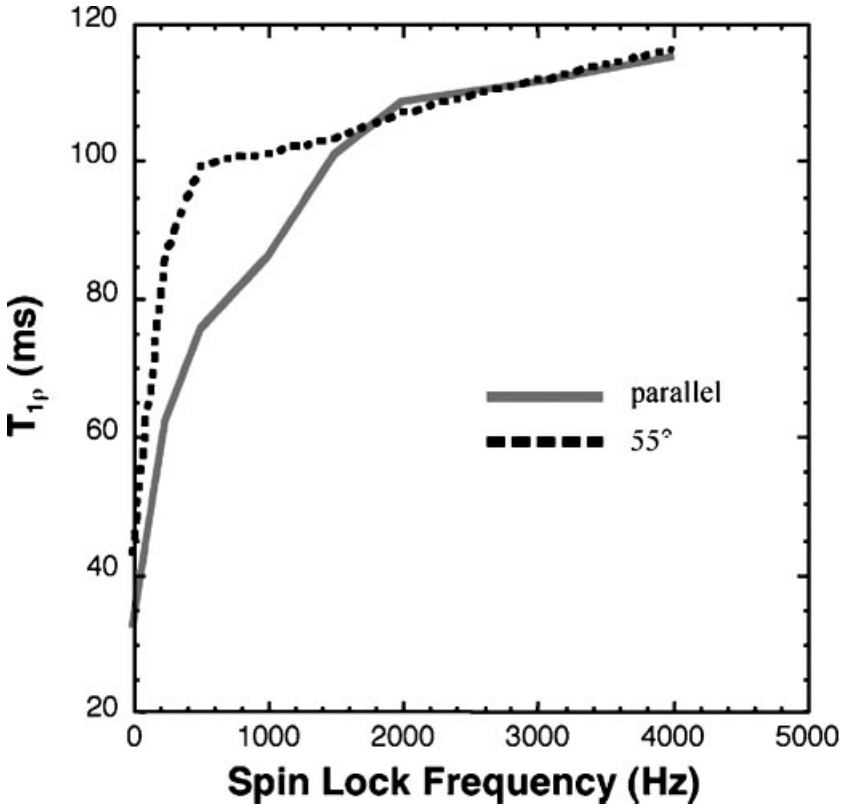


Figure 21. $T_{1\rho}$ dispersion in bovine cartilage; the cartilage surface was oriented parallel to B_0 and at the magic angle ~55°. The data at spin-lock frequency of zero correspond to the respective T_2 values (222).

Copyright © 2006 John Wiley & Sons, Ltd.

DOI: 10.1002/nbm

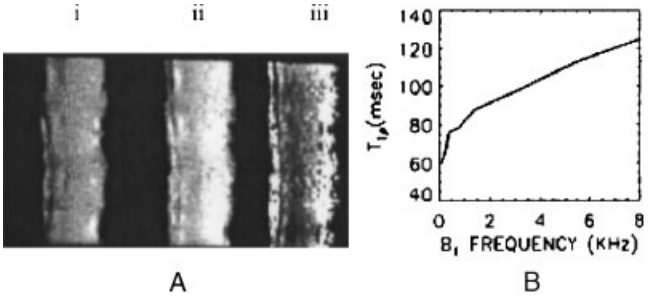


Figure 22. (A) A T_2-weighted (i) and corresponding $T_{1\rho}$-weighted image (ii) and $T_{1\rho}$ map (iii) of a slice through bovine articular cartilage. The $T_{1\rho}$ dispersion collected for spin-lock amplitude (B_1) from 0 to 8 kHz is shown in (B). where a two-fold increase in$T_{1\rho}$ was observed with increasing B_1 amplitude, demonstrating $T_{1\rho}$ dispersion in cartilage (230).

performed on bovine cartilage specimens and the observed dispersion was interpreted by invoking the presence of exchange-modulated dipolar coupling of water protons associated with macromolecules in the tissue (Figure 22). Later studies were performed by subjecting bovine articular cartilage specimens to trypsin- and collagenase-induced PG and collagen degradation, respectively (24). Results demonstrated that the $T_{1\rho}$-weighted images had improved contrast and SNR compared with T_1- and T_2-weighted images and $T_{1\rho}$-weighted images are sensitive to PG change in the tissue. In the same study, it was suggested that collagenase-induced collagen degradation did not exhibit changes in $T_{1\rho}$. However, later it was found that there were errors in the protocol of the collagenase degradation and the conclusions about effect of collagenase on $T_{1\rho}$ were not reliable.

In an elegant study on bovine articular cartilage patellae, sequential trypsin-induced PG depletion was performed (25). Proton $T_{1\rho}$ maps were generated at varying B_1 fields at 4 T using a home-built RF coil. Depleted PG in the medium was quantified using standard dimethyl methylene blue (DMMB) assay and histology. $T_{1\rho}$ computed from region of interest analysis was found to increase linearly with the amount of PG depleted. $T_{1\rho}$ maps clearly demonstrated the PG depleted regions and corresponded well with the histological analysis performed with Safranin-O staining. In another study at 4 T, $T_{1\rho}$ and T_2 relaxation rates were computed from bovine cartilage subjected to sequential PG depletion (226). $T_{1\rho}$ and T_2 maps were correlated with PG in the tissue (Figure 23) and it was found that there was an excellent correlation ($r^2 = 0.89$) between $1/T_{1\rho}$ and [GAG] while the correlation between $1/T_2$ and [GAG] was rather poor ($r^2 = 0.01$). The $T_{1\rho}$ maps reflected clear changes in PG depleted regions of the tissue (Figure 24). Later on, spectroscopic studies were also demonstrated to have the same trend, although as they are based on global relaxation numbers they underestimate the magnitude of the change in the relaxation rates (231). These studies form the basis for using the $T_{1\rho}$ mapping studies in studying cartilage pathology.

$T_{1\rho}$, T_2 and T_1 studies were also performed on osteoarthritic human specimens obtained following the knee replacement surgery (173). In these studies spin-locking frequency used was ~2.5 kHz. It was found that neither T_2 nor $T_{1\rho}$ were significantly changed from studies performed on *ex vivo* human cartilage. These results were in contradiction to the results from several studies described above. The primary reason for this discrepancy appeared to be the status of the osteoarthritic tissue. Prior to the surgery, the patients were intravenously administered $GdDTPA^{2-}$, a contrast agent known to dominate the relaxation mechanism of water protons. Since the tissues were imaged in the presence of the contrast agent it dominates the relaxation contribution to both $T_{1\rho}$ and T_2

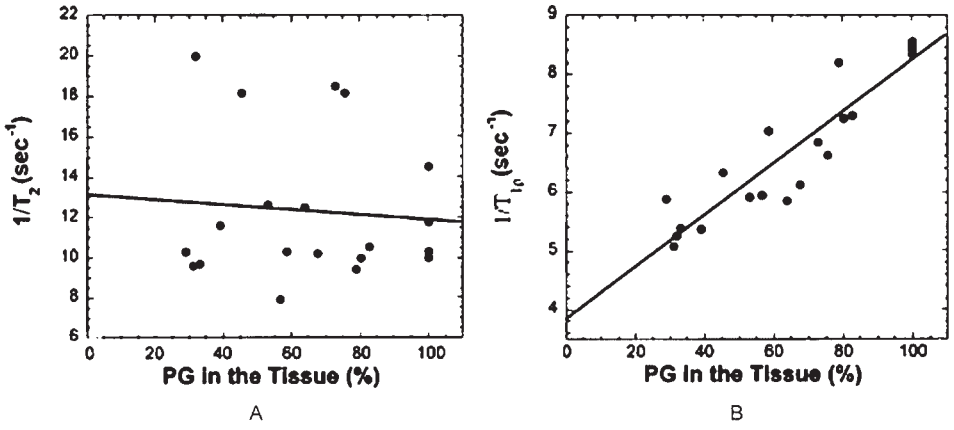


Figure 23. These figures show a plot of $1/T_2$ vs PG and $1/T_{1\rho}$ vs PG loss from a group of bovine cartilage patellae subjected to serial depletion of PG. The solid line indicates the linear fit to the experimental data. Although T_2 did change with PG content, there was no clear trend ($r^2 = 0.01$, $p < 0.7$). $T_{1\rho}$ data from the same set of cartilage specimens, however, demonstrated a strong correlation ($r^2 = 0.9$, $p < 0.001$) between changes in PG and $1/T_{1\rho}$(226).

Copyright © 2006 John Wiley & Sons, Ltd.

DOI: 10.1002/nbm

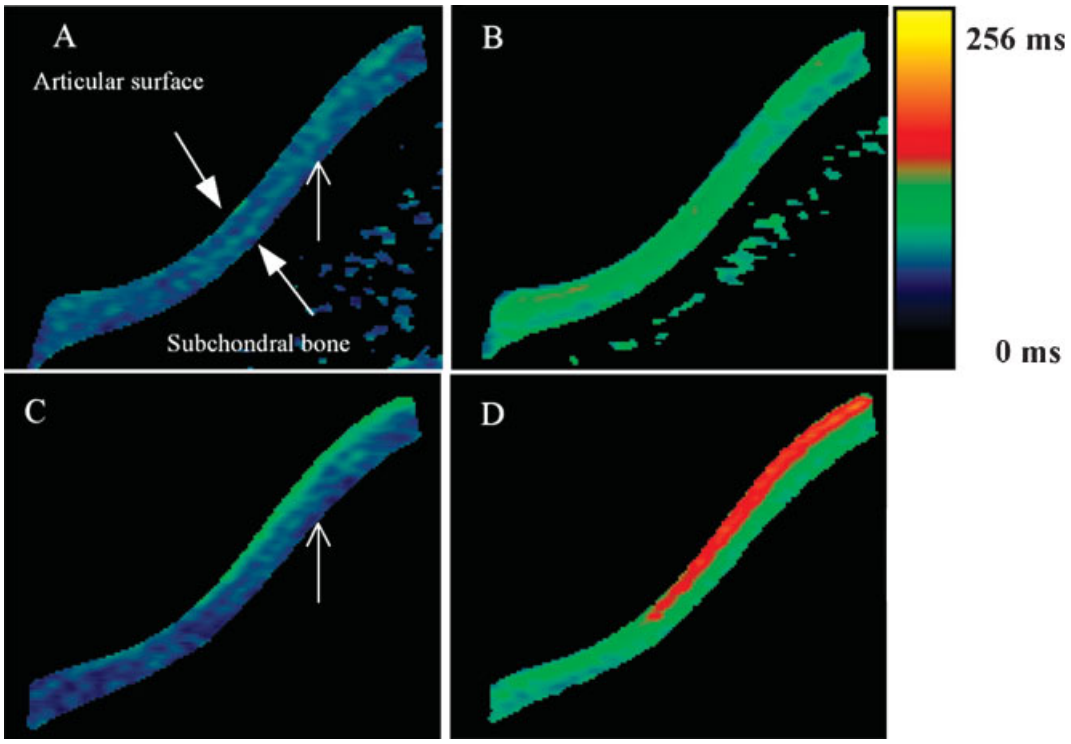


Figure 24. Comparison of T_2, and $T_{1\rho}$ maps of control and 40% of PG depleted bovine patellae. (A) Control T_2 map; (B) control $T_{1\rho}$ map; (C) 40% PG depleted T_2 map; (D) 40% PG depleted $T_{1\rho}$ map. The color scale bar shows the relaxation numbers from 0 to 256 ms (25).

as well and masks any changes due to the loss of PG/macromolecules from the tissue. These studies clearly demand a thorough investigation of the influence of contrast agents like $GdDTPA^{2-}$ on the magnitude of relaxation contribution to $T_{1\rho}$ and T_2

$T_{1\rho}$ and T_2 measurements were made in collagen and GAG suspensions, and an exponential decrease in $T_{1\rho}$ and T_2 was found with the increasing [collagen] and/or [GAG]. Relaxation time measurements were made in native and trypsin- and interleukin-1β-induced bovine cartilage and some human OA specimens as well (227). In these studies, it was found that $T_{1\rho}$ and T_2 are sensitive to biologically meaningful changes in cartilage. However, they are not specific to any one inherent tissue parameter. In this study, data from phantoms show that both PG and collagen contribute to $T_{1\rho}$ rate ($R_{1\rho}$) in a concentration-dependent manner (at low concentrations, $<20\%$, this is almost linear). However, there are several differences between this study and other $T_{1\rho}$ mapping studies in the literature and the following factors should be taken into account when drawing conclusions from this study:

(1) The experiments were performed at a very high (8.5 T) field strength where other mechanisms, e.g. exchange from -OH and -NH to H_2O, will dominate and could contribute to $T_{1\rho}$ [see above and ref. (173)]. Most other $T_{1\rho}$ studies in the literature were performed between 1.5 and 4 T.

(2) Cartilage samples subjected to IL-1β exhibited decreased T_2 but unchanged $T_{1\rho}$ when compared with healthy and trypsin-treated cartilage. This is completely in conflict with several results from IL-1β studies on a larger group of samples and on an *in vivo* animal model where a significant increases in $T_{1\rho}$ (Figure 25) were observed (54,177).

(3) At the higher field (8.5 T), $T_{1\rho}$ should be lower than that at 1.5 T, but the $T_{1\rho}$ numbers measured in human cartilage in this study are almost 50% higher than those observed at 1.5 T. This result was not explained.

(4) In one of the human specimens, the GAG-depleted region shows 19% elevated $T_{1\rho}$ compared with the healthy-appearing region in the same tissue. In fact, even though a suboptimal color scaling was used and there was a possibility of slice mismatch and associated partial volume effects, the $T_{1\rho}$ map almost mirrors the dGEMRIC map, indicating that there is indeed an elevated $T_{1\rho}$ in regions with lower GAG. At the same time, the observed $T_{1\rho}$ values in two other samples [Fig. 2(C) and (D) with more advanced OA] are not consistent with those observed in the GAG-depleted regions. Given the thin sections of the images (2 mm thick) gathered in two different imaging sessions there is a possibility that the slice mismatching and partial voluming effects may be present in the data.

(5) $T_{1\rho}$ imaging on human specimens was performed in multi-slice mode but there are no details of the

Copyright © 2006 John Wiley & Sons, Ltd.

DOI: 10.1002/nbm

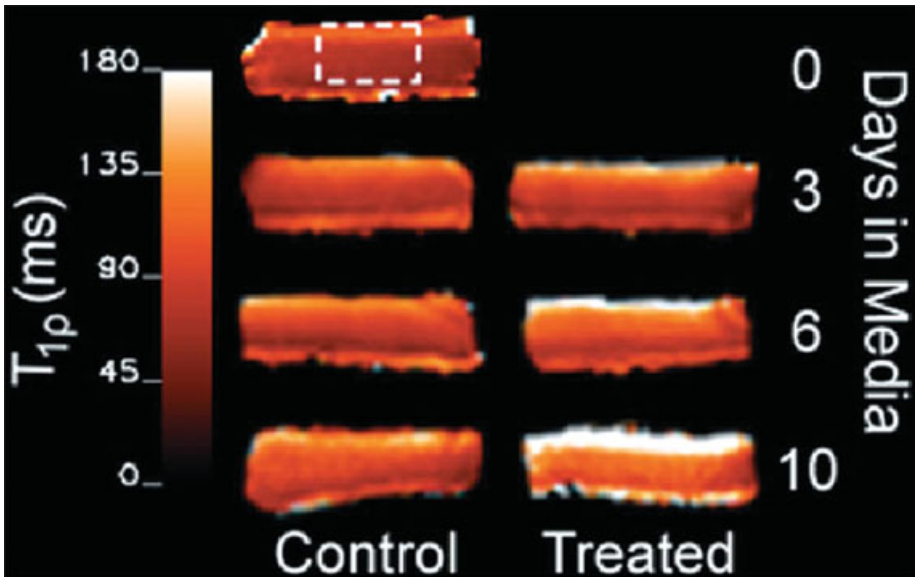


Figure 25. $T_{1\rho}$ maps of representative bovine cartilage specimens in culture media. The treated group represents the treatment with 30 ng/mL of IL-1β over a 10-day period. Significant elevation in $T_{1\rho}$ maps of specimens compared with control specimens is evident (241).

sequence. In fact, in multi-slice mode, there is a substantial $T_{2\rho}$ saturation that, uncorrected, will lead to erroneous results (237).

In direct contradiction to the above study, in human OA specimens ($n = 7$) with different Mankin grades (0–3), a strong correlation between $T_{1\rho}$ rate and FCD measured from sodium MRI was observed (Figure 28), indicating that $T_{1\rho}$ relaxation rate may be useful in studying the OA process in humans (177). Nevertheless, a study on a large group of human osteoarthritic specimens is needed to obtain statistically significant results.

Correlation of changes in cartilage biomechanical and biochemical properties with $T_{1\rho}$ relaxation rate was made in a cytokine-induced model of osteoarthritic condition (54). $T_{1\rho}$ mapping was performed at 4.7 T, and PG, collagen and water content were measured via biochemical assays. Stress-relaxation biomechanical tests were conducted with confined compression apparatus to measure uni-axial aggregate modulus (H_A) and hydraulic permeability (k_0) using linear bi-phasic theory. Results from this study demonstrated that $T_{1\rho}$ relaxation rate was strongly correlated with PG content ($r^2 = 0.93$), H_A ($r^2 = 0.83$) and $\log_{10}k_0$ ($r^2 = 0.86$), demonstrating the potential of $T_{1\rho}$ relaxation as a surrogate index for changes in cartilage biochemical and biomechanical properties as well (Figure 26). These studies clearly provide a link between $T_{1\rho}$ relaxation rate and [GAG] content of the tissue and biomechanical properties. These results are significant because they suggest that non-invasive $T_{1\rho}$ mapping may be used to obtain biomechanical properties of the tissue without subjecting the tissue to compression in magnet, a difficult task to begin with. Results from this work clearly show the potential of $T_{1\rho}$ relaxation mapping in providing information about biomechanical properties *in vivo*.

***Ex vivo* human specimens.** Studies on isolated chondroitin sulfate and collagen suspensions show that $T_{1\rho}$ is sensitive to both the components of cartilage matrix (227). Owing to a well-ordered structure of collagen and the swelling pressure of PG in intact cartilage, the observed proton $T_{1\rho}$ relaxation rates in the intact cartilage cannot be extrapolated to those obtained from isolated PG and collagen suspensions. Therefore, in order to tease out

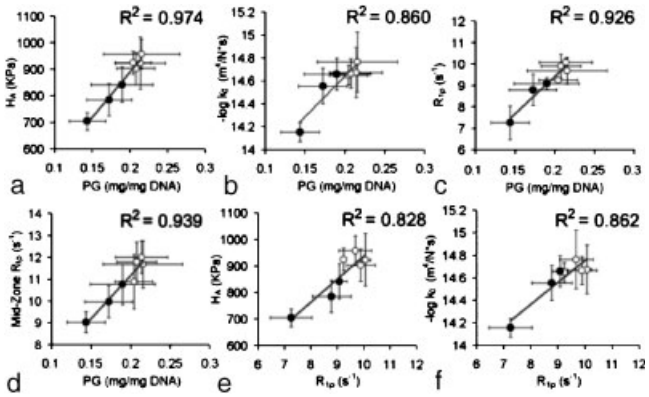


Figure 26. Linear regression plots of average data from each group of (a) H_A vs PG, (b) $\log_{10}k_0$ vs PG, (c) bulk $R_{1\rho}$ vs PG, (d) mid-zone $R_{1\rho}$ vs PG, (e) H_A vs $R_{1\rho}$ and (f) $\log_{10}k_0$ vs $R_{1\rho}$. Open data points represent control groups and closed data points represent IL-1β-treated groups. The correlation coefficient (R^2) is listed on each corresponding plot. Error bars on both axes represent the SD of each measurement (241).

Copyright © 2006 John Wiley & Sons, Ltd.

DOI: 10.1002/nbm

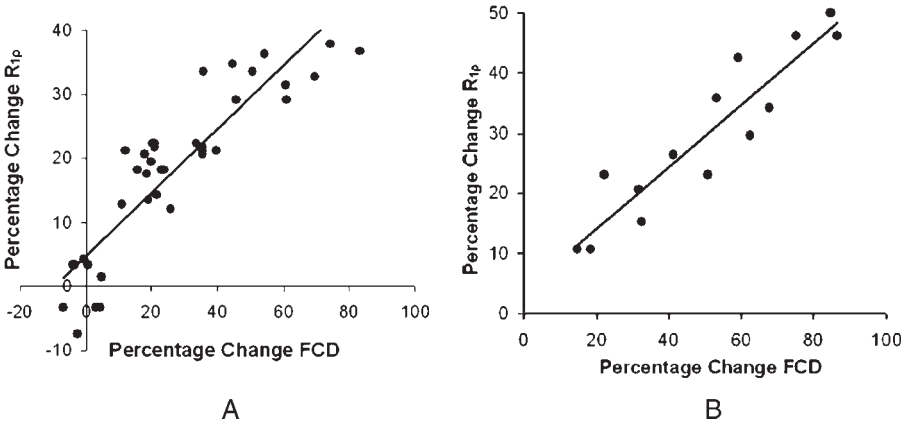


Figure 27. Correlation of normalized FCD and $R_{1\rho}$ data obtained from the trypsin treated model (A). The slope of the linear regression was 0.48 ± 0.004 with $r^2 > 0.75$ ($p < 0.001$). The data are arranged in four clusters representing the four groups of trypsin concentration. The cluster about zero, including negative values, represents the distribution of the mean of the control data. Correlation of normalized FCD and $R_{1\rho}$ data obtained from the natural OA model (B). The slope of the linear regression was 0.51 ± 0.06 with $r^2 > 0.85$ ($p < 0.001$) (177).

the individual contribution of PG and collagen to the observed $T_{1\rho}$, selective depletion studies are needed. It is relatively easy to quantify PG's exclusive contribution to $T_{1\rho}$; however, it is difficult to discern the collagen contribution alone to the $T_{1\rho}$ relaxation. This is because depletion of collagen from cartilage is not feasible without affecting PG content. To overcome this limitation, an indirect approach was used (177) in which spatial maps of proton $T_{1\rho}$ and sodium maps of FCD were computed on bovine specimens subjected to trypsin-induced PG degradation and human OA specimens with different Mankin grade (232). The loss of PG was confirmed by histology in these specimens. Since trypsin predominantly degrades cartilage PG and leaves collagen almost intact, changes induced in $T_{1\rho}$ in this model are primarily from PG loss. In human OA specimens; however, while there may be a predominant contribution from loss of PG, there may also be changes in collagen content and structure depending on the Mankin grade of the tissue. Plots of normalized $1/T_{1\rho}$ rate vs FCD (Figure 27) were found to be strongly correlated with $r^2 > 0.75$ and 0.85, respectively, in both tissue types with nearly identical slope of ~ 0.5 ($p > 0.51$) The strong correlation of the FCD and $T_{1\rho}$ data, with identical slopes, in both the models has been interpreted as that the contributions to $T_{1\rho}$ changes are predominantly from PG and any contribution from collagen may be rather small even in natural OA cartilage. A similar trend is shown in the sodium image and $T_{1\rho}$ map of OA specimen (Figure 28).

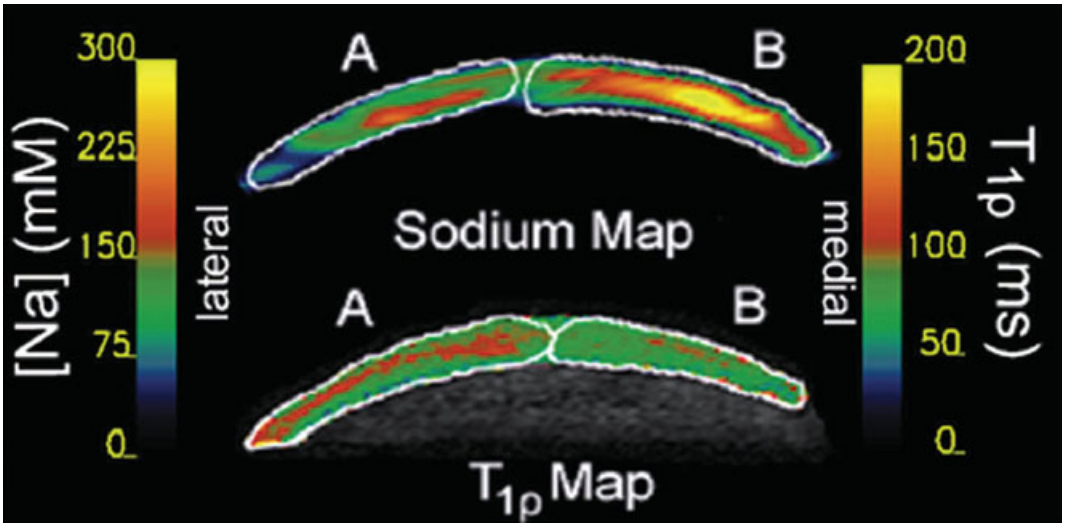


Figure 28. Comparison of sodium concentration and $T_{1\rho}$ maps of a representative *ex vivo* patella from an osteoarthritic joint. The sodium map reveals a distinct reduction in FCD on the lateral side of the patella (ROI A) indicating a reduction of PG content. Elevation of $T_{1\rho}$ in ROI A is observed as an analogous measure of PG loss (177).

Copyright © 2006 John Wiley & Sons, Ltd.

DOI: 10.1002/nbm

Studies on animal models *in vivo*. Animal models serve as a bridge between tissue culture and human disease. The advantage of the animal models is that the disease can be controlled. Therefore, animal models are ideal for research in developing, optimizing and validating therapies, stimulating repair of damaged tissues and understanding the disease process, as well as developing noninvasive diagnostic tools to detect early OA.

The potential of $T_{1\rho}$ mapping in detecting rapidly induced cytokine-mediated cartilage degeneration in porcine animal model *in vivo* was investigated (54). Six Yorkshire pigs were given an intra-articular injection of recombinant porcine interleukin-1β in the knee joints before imaging. The contra-lateral knee joints were given a saline injection to serve as an internal control. Six hours following the injection, $T_{1\rho}$ mapping was performed using $T_{1\rho}$-prepared FSE sequence and sodium imaging was performed using a previously validated method at 4 T. The effect of IL-1β, primarily loss of PG, was confirmed by histological and immunohistochemical analysis (Figure 29). It was found that the average $T_{1\rho}$ rate ($1/T_{1\rho}$) of the IL-1β-treated patella was about 25% lower than that of saline-injected patella. There was an average reduction of 49% in FCD, measured via sodium MRI. These results demonstrate that changes seen in both $T_{1\rho}$ and FCD indicate the loss of PG.

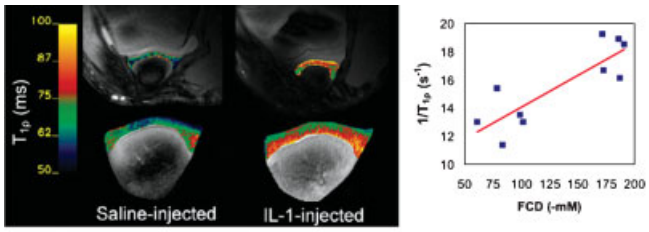


Figure 29. $T_{1\rho}$ maps of saline- and IL-1β-injected patellae of a Yorkshire pig (A) *in vivo* (top row) and the same *ex vivo* (bottom row). Color-coded $T_{1\rho}$ maps corresponding to cartilage are overlaid on the original $T_{1\rho}$-weighted MR image, indicating elevated $T_{1\rho}$ in each IL-1 treated case (54). Also shown is a plot of $1/T_{1\rho}$ measured *in vivo* and FCD measured by post-mortem PG assay from animals (B).

Studies on guinea pig model of spontaneous OA. The advantages of the guinea pig model are that OA occurs spontaneously, it is an inexpensive model compared to anterior cruciate ligament (ACL) transection model, and it has been well studied (233). Initial studies demonstrating the feasibility of performing $T_{1\rho}$ mapping on guinea pig cartilage (Figure 30) exhibited excellent contrast between the cartilage and the surrounding tissues. The in-plane resolution in axial image is 60 μm and that in sagittal images is 117 μm. The signal-to-noise ratio in these images is ~25:1. The color scheme and $T_{1\rho}$ values are shown in the bar-scale. A clear region with elevated $T_{1\rho}$ number (possibly a lesion) can be seen on the femoral cartilage (indicated by an oval shape). In this map, $T_{1\rho}$ numbers of the load-bearing (LB), nonload-bearing (NLB) and lesion regions are: 44 ± 5, 58 ± 5 and 97 ± 14 ms, respectively. The imaging parameters are: spin-lock pulse power = 500 Hz, $TR = 200$ ms, slice thickness = 1 mm. The spin-lock duration varied from 1 to 40 ms. Average $T_{1\rho}$ relaxation

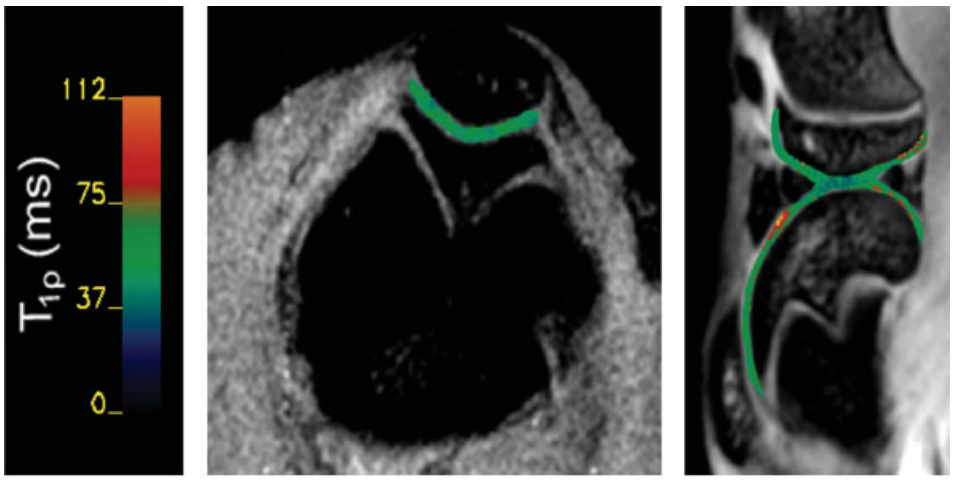


Figure 30. Representative $T_{1\rho}$-weighted images of a guinea pig (age ~4 months) and corresponding color-coded $T_{1\rho}$maps (overlaid on the $T_{1\rho}$-weighted images). (A) An image of the knee joint showing the $T_{1\rho}$ map of patellar cartilage in color. The average $T_{1\rho}$ of patellar cartilage was measured at 57 ± 5 ms. (B) A sagittal slice of the same animal's knee joint showing both femoral and tibial cartilage.

Copyright © 2006 John Wiley & Sons, Ltd.

DOI: 10.1002/nbm

numbers from different regions of guinea pig ($n = 4$) cartilage are as follows: patellar cartilage (59.6 ± 4.4 ms), femoral cartilage load-bearing (43.8 ± 4.6 ms) and femoral cartilage nonload-bearing (65.2 ± 5.4 ms). These results, although preliminary, demonstrate the feasibility of obtaining $T_{1\rho}$ relaxation maps in guinea pig cartilage.

Clinical $T_{1\rho}$ MRI. Proton T_2- and $T_{1\rho}$-weighted images of healthy human knee joint acquired on a 1.5 T clinical scanner with a spin-locking amplitude of 500 Hz are shown in Figure 31. In the T_2-weighted image, the laminar appearance due to different signal intensity patterns corresponding to collagen fiber orientation, although not clearly observed owing to the lack of adequate resolution, is manifested as low signal intensity across the cartilage, whereas in the $T_{1\rho}$-weighted image the laminar appearance is substantially attenuated and results in a more homogeneous appearing and elevated signal intensity across cartilage (222).

Initial $T_{1\rho}$ relaxation studies on healthy human knee joints *in vivo* ($n = 6$) were performed with a $T_{1\rho}$-prepared FSE sequence at 1.5 T (26). Significant $T_{1\rho}$ dispersion (34–50 ms; $T_{1\rho}$ changes with spin-lock frequency) in the frequency range 0–375 Hz was observed. Quantitative comparison of T_2- and $T_{1\rho}$-weighted images has demonstrated a 25% higher signal-difference-to-noise ratio in a chondral lesion, in $T_{1\rho}$-weighted image than in comparable T_2-weighted images *in vivo*.

Clinical $T_{1\rho}$ relaxation mapping studies were also performed in femoral–tibial cartilage and wrist joint *in vivo* at 1.5 T, using home-built bird-cage coils (234,235). In both these studies a single-slice $T_{1\rho}$ prepared FSE sequence was used with a spin locking frequency ranging from 0 to 500 Hz. It was found that the average $T_{1\rho}$ (at $B_1 = 500$ Hz) in the weight-bearing and nonweight-bearing regions of the femoral condyle were 42.2 ± 3.6 and 55.7 ± 2.3 ms, respectively. In wrist joint cartilage, at 500 Hz spin-locking amplitude, $T_{1\rho}$ ranged from 40.5 ± 0.9 to 56.6 ± 4.8 ms. Both studies demonstrated 20–30% higher SNR of cartilage in T_1-weighted images compared with T_2-weighted images. It was suggested that the primary purpose of these studies was to demonstrate the feasibility of quantifying relaxation maps in these complicated structures.

Three-dimensional $T_{1\rho}$ mapping of human knee cartilage was performed at 1.5 T on both healthy and symptomatic osteoarthritic subjects (180,236). Average $T_{1\rho}$ values (at spin locking amplitude of 440 Hz) obtained from eight healthy volunteers (all male with age range 22–45 years) with three-dimensional $T_{1\rho}$ mapping was 49.7 ± 3.2 ms (mean $\pm$ SD) and that obtained from two-dimensional $T_{1\rho}$ mapping was 48.5 ± 2.6 ms (mean $\pm$ SD). In all the symptomatic subjects ($n = 6$, four men and two women, age range 28–63 years) none had radiographic OA except one. $T_{1\rho}$ relaxation times were elevated compared with healthy subjects. In symptomatic subjects, $T_{1\rho}$ values (at 440 Hz spin lock amplitude) varied from 63 ± 4 to 95 ± 12 ms (mean $\pm$ SD) depending on the degree of cartilage degeneration (Table 4). Although this study was performed on a limited number of subjects, it still demonstrates the potential of $T_{1\rho}$ as a surrogate marker for pre-radiographic OA. Study of a larger group of subjects is required to further evaluate the sensitivity and specificity issue of the method.

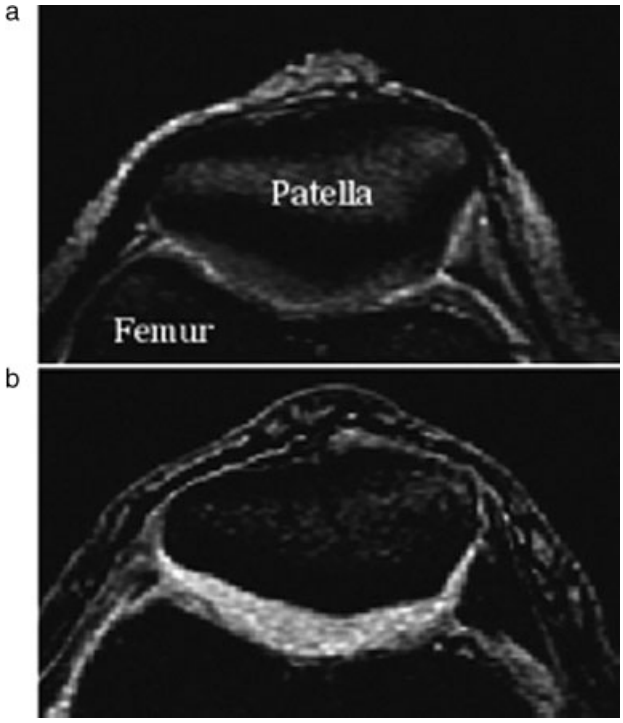


Figure 31. In vivo T_2- and $T_{1\rho}$-weighted images from a healthy human knee joint. The imaging parameters were TR 3 s, FOV = 10 cm × 10 cm, slice thickness = 3 mm, matrix = 256 128 (a) T_2-weighted image, TE = 16 ms (b) $T_{1\rho}$-weighted image, TE +TSL = 16 ms, $B_1 = 500$ Hz.

$T_{1\rho}$ MRI of osteoarthritic subjects. Figure 32 shows a $T_{1\rho}$-weighted image (in gray-scale) of the knee from a clinically-diagnosed OA subject (38-year-old female). These images were read by a radiologist and confirmed the presence of minor irregularities on cartilage surface. In this $T_{1\rho}$-weighted image, $TSL + TE = 60$ ms and the spin-lock power employed is 500 Hz, with an in-plane resolution of ~390 μm and a 3 mm slice. The lateral side of the $T_{1\rho}$ map (overlaid in color) shows larger region of elevated $T_{1\rho}$ values (indicated with an oval). Although, there is an increase in $T_{1\rho}$ across the cartilage compared with the values from healthy controls, in the elliptical ROI, $T_{1\rho}$ is elevated by ~44% compared with the healthy-appearing region.

Figure 33 shows $T_{1\rho}$-weighted images from a clinically diagnosed OA patient (40-year-old female) with an absence of cartilage abnormalities on radiographs. A rheumatologist and an orthopedist diagnosed the subject with osteoarthritis and the subject has been on medication

Copyright © 2006 John Wiley & Sons, Ltd.

DOI: 10.1002/nbm

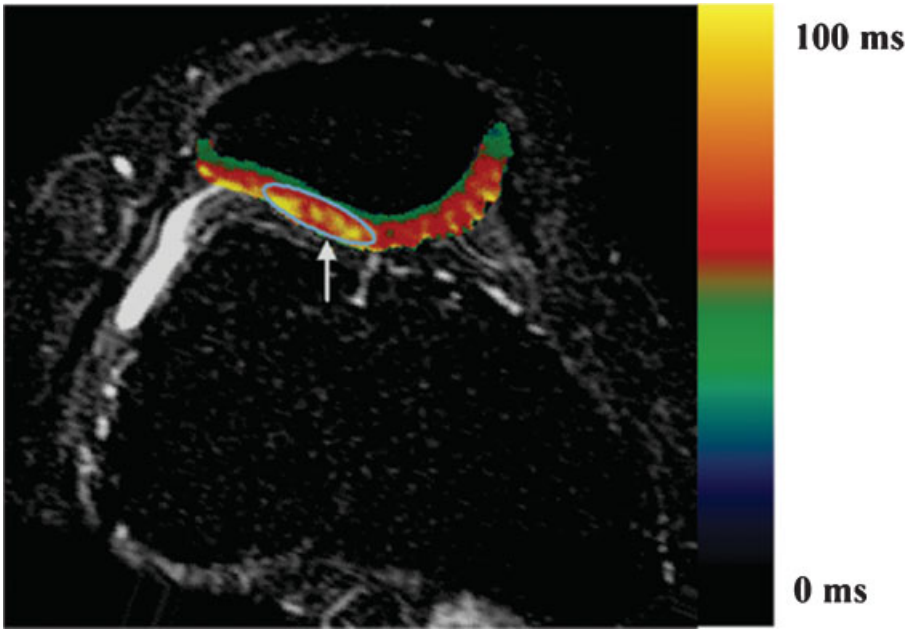


Figure 32. $T_{1\rho}$-weighted image (gray-scale) and corresponding overlaid color map of a clinically diagnosed OA subject's knee joint. This patient *did not* display OA in radiographic images. The region indicated by the oval in the patellar–femoral cartilage indicates a region of elevated $T_{1\rho}$ (>60 ms) and could be a sign of early OA.

for about one year. A practicing radiologist read these images and diagnosed that the patient has cartilage softening on the lateral side without any surface irregularities. Without the knowledge of imaging sequence used, he found that the $T_{1\rho}$ image had superior contrast and excellent delineation of the lesion. Figure 32 (A) and (B) shows $T_{1\rho}$ images acquired with an effective echo time ($TSL + TE$) of 45 and 60ms, respectively. In both $T_{1\rho}$ images, the lateral side of cartilage (indicated by thin arrow) shows elevated signal (in these images, white, yellow and red represent high, medium and low signal intensities, respectively).

$T_{1\rho}$ MRI of a chondromalacia subject. In Figure 34, a three-dimensional surface-rendered $T_{1\rho}$ map and a cross-sectional image of patella of an osteoarthritic human subject who has undergone arthroscopy is presented. At arthroscopy, grade I chondromalacia was identified on the lateral facet of the patellar cartilage while the medial facet was identified with grade 0. The lateral facet of the $T_{1\rho}$ relaxation map (dashed oval indicates the arthroscopically identified chondromalacia region) clearly shows the elevated $T_{1\rho}$ numbers compared with that of medial facet. Red and yellow voxels in this region indicate substantial increase in the $T_{1\rho}$. These data clearly demonstrate that, in cartilage regions of chondromalacia, $T_{1\rho}$ is increased by ~46% compared with healthy cartilage. The cross sectional image shows the $T_{1\rho}$ map of one of the slices overlaid on the $T_{1\rho}$-weighted

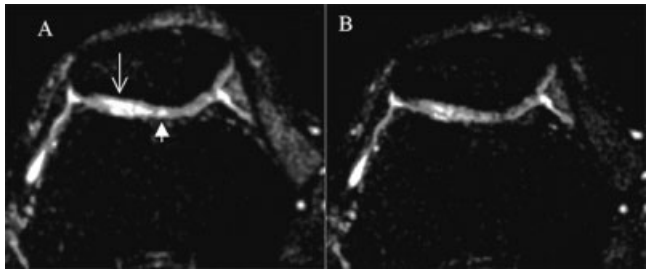


Figure 33. $T_{1\rho}$-weighted images of a symptomatic OA subject without any radiographic OA. (A) and (B) represent the images obtained with an effective weighting of 45 and 60 ms respectively. Elevated signal intensity demonstrates a lesion on cartilage.

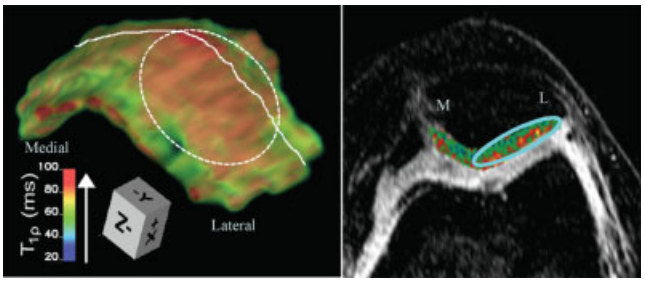


Figure 34. Preliminary results from an OA subject arthroscopically diagnosed with grade I chondromalacia in the lateral facet of the patella. The left-hand side figure shows the three-dimensional $T_{1\rho}$ relaxation map of patellar cartilage. The color scale shows a volume-rendered representation of the$T_{1\rho}$ numbers. The image on the right shows a slice of the $T_{1\rho}$ map at the position indicated by a line on the $T_{1\rho}$ surface (on the left) overlaid on the patellar cartilage of the proton density-weighted image. The dashed elliptical region on image on the left is the arthroscopically confirmed region of chondromalacia.

Copyright © 2006 John Wiley & Sons, Ltd.

DOI: 10.1002/nbm

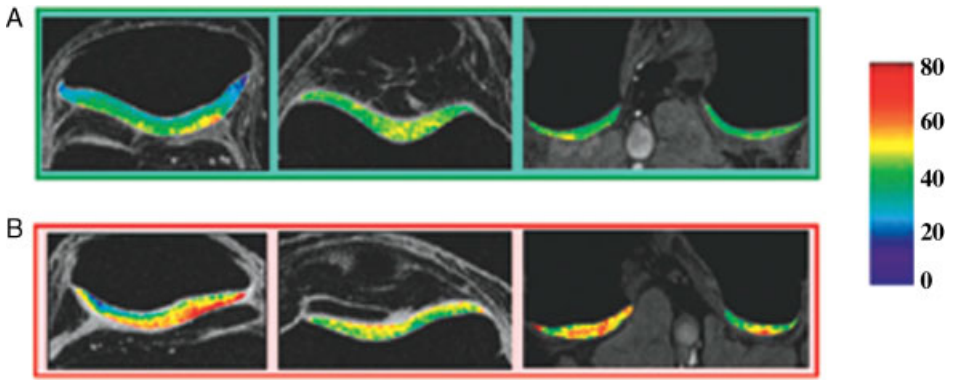


Figure 35. Colour-coded $T_{1\rho}$ maps overlaid on SPGR images. Left: patellar cartilage; middle: anterior femoral (trochlea) cartilage; right: posterior femoral cartilage. (a) a healthy volunteer, male, 30; (b) a patient with early OA, female, 27. The $T_{1\rho}$ values were 40.05 ± 11.43 ms in the volunteer and $50.56\,\text{ms} \pm 19.26$ ms in the patient, respectively.

image. In this map, elevated $T_{1\rho}$ across the cartilage depth can be visualized. These results show the feasibility of computing $T_{1\rho}$ maps of grade I chondromalacia of cartilage *in vivo*. Although arthroscopy is a semi-quantitative technique which provides information about cartilage softening, it is a subjective and invasive procedure and not suitable for longitudinal follow-up studies. However, the relaxation maps presented here are quantitative and noninvasive.

A multi-slice spin-lock (MS-SL) pulse sequence was developed and implemented on clinical scanner. Its utility in a clinical setting was demonstrated by measuring $T_{1\rho}$ maps of the knee joints of six healthy human subjects (237). Since MS-SL $T_{1\rho}$ measurements are confounded by the saturation effects due to the $T_{2\rho}$ process, strategies to compensate for these saturation effects are presented. $T_{2\rho}$-compensated $T_{1\rho}$ maps were computed from multi-slice data from human cartilage tissue. These values differed by 5% when compared with the 'gold-standard' single-slice $T_{1\rho}$ values. Although this sequence is superior in SNR and contrast, when compared with three-dimensional FGRE based sequence, it needs a separate $T_{2\rho}$ map or at least a T_2 map of the same section to compensate for $T_{2\rho}$ saturation and compute the actual $T_{1\rho}$ map. Hence its temporal resolution is lower than that of three-dimensional $T_{1\rho}$ mapping sequence.

Another version of a multi-slice $T_{1\rho}$ MRI pulse sequence was developed by integrating the spin-lock preparation with a spiral readout (183,238). Studies were performed on healthy as well as osteoarthritic human patients on a 3 T clinical scanner (Figure 35). $T_{1\rho}$ values obtained with this sequence were validated by comparison with those obtained with a single-slice version of the sequence. In this study, precision of the $T_{1\rho}$ imaging was shown to be ~4.8%. The increase of average $T_{1\rho}$ in cartilage from controls to the patients was 19.1% [43.9 ms for controls ($n = 5$) and 52.3 ms for osteoarthritic patients ($n = 7$; 52 ± 28 ms)], while the increase of was 9.6% for the average T_2 (34.9 ms for controls and 38.3 ms for patients). The difference in average $T_{1\rho}$ in cartilage between controls and patients was significant ($p = 0.003$), while it was not significant for average T_2 ($p = 0.202$). In this study, although there was significant correlation between $T_{1\rho}$ and T_2, the average $T_{1\rho}$ and T_2 have shown a nonpoint-to-point relationship. This relationship implies that $T_{1\rho}$ and T_2 may give complementary information in detecting cartilage degeneration and injuries. One of the interesting features of this study is that there is a clear demarcation in $T_{1\rho}$ numbers of healthy subjects and OA patients (Figure 36). Results suggest that $T_{1\rho}$ relaxation time may be a promising clinical tool for measuring biochemical changes of the cartilage matrix and treatment monitoring in OA.

Summary

Although early $T_{1\rho}$ experiments on cartilage were spectroscopic, later on these were extended to single-slice imaging and this was followed by the development of three-dimensional and multi-slice imaging methods. Studies on phantoms and isolated matrix components show that both PG and collagen contribute to $T_{1\rho}$. *Ex vivo* studies on bovine specimens subjected to sequential PG depletion have shown a strong correlation between $1/T_{1\rho}$ and [GAG], although correlation between $1/T_2$ and [GAG] was rather poor. *Ex vivo* bovine studies and *in vivo* studies on animal models have shown that treatment with IL-1β elevated the $T_{1\rho}$. In osteoarthritic human specimens, there was a strong correlation between percentage change in FCD measured from sodium MR and percentage change in $1/T_{1\rho}$. The $T_{1\rho}$ rate also strongly correlates with mechanical properties of tissue. However, in studies on a small number of human specimens at 8.5 T, conflicting results were observed. In some specimens elevated $T_{1\rho}$ was observed in GAG-depleted region and in some other specimens it remained almost unchanged. Similarly, in studies (at 8.5 T) on a small group of bovine specimens subjected to IL-1β, $T_{1\rho}$ was found to be unchanged.

Copyright © 2006 John Wiley & Sons, Ltd.

DOI: 10.1002/nbm

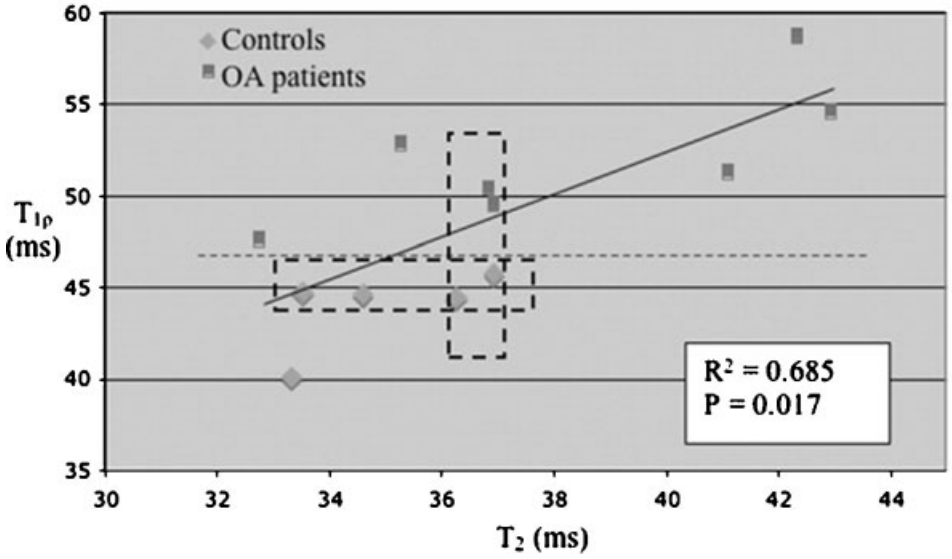


Figure 36. Correlation between $T_{1\rho}$ and T_2 values in 12 subjects (five healthy controls and seven patients with OA). Although the correlation is significant, there is a nonpoint-to-point relationship, that is, patients with similar T_2 values may show different $T_{1\rho}$ values, as shown in the vertical dashed box, or vice versa, as shown in the horizontal dashed box. The dashed line shows a clear-cut difference of the average $T_{1\rho}$ between healthy controls and OA patients, while there is a significant overlap of average T_2 values. A significant difference was found in average $T_{1\rho}$ ($p = 0.003$) but not in T_2 values ($p = 0.2002$) between healthy controls and patients (183).

Existing results to date suggest that contributions to $T_{1\rho}$ dispersion are predominantly due to dipolar interaction of water molecules associated with collagen and they are influenced by the orientation of cartilage. Although the proton exchange between amide and hydroxyl protons on GAG molecules and bulk water may also contribute to the dispersion, its contribution is relatively small at lower fields.

Based on the current data, it appears that the strong correlation between [GAG] and $1/T_{1\rho}$ may be predominantly due to concentration effect in bovine cartilage. The fact that a similar trend is observed in IL-1β-treated specimens, and in human OA specimens, in which some collagen changes are expected, suggests that, in addition to PG contribution, there may be a (small) contribution from collagen as well to the observed $T_{1\rho}$. In other words, $T_{1\rho}$ in addition to measuring PG changes, may also be affected by collagen structural and content changes (if any) present in early OA. Since $T_{1\rho}$ dispersion in cartilage is predominantly due to dipolar interaction of water protons associated with oriented collagen, a dispersion map computed from images obtained as a function of SL pulse amplitude, B_1, at a constant SL length may reflect the changes in collagen structure and content.

When compared with healthy subjects, OA patients presented elevated $T_{1\rho}$ even when their radiographic images did not indicate OA. Measured *in vivo*, $T_{1\rho}$ was found to have a stronger correlation with severity of OA, while differences in T_2 were not statistically significant. $T_{1\rho}$ was also elevated in a patient with arthroscopically confirmed grade I chondromalacia but without radiographic OA. These results clearly indicate that $T_{1\rho}$ may serve as a surrogate marker for molecular changes (preradiographic) in cartilage and may be useful in longitudinal studies. So far the $T_{1\rho}$ studies have been mostly 'demonstration of feasibility' in nature, involving a very limited number of healthy and OA subjects. $T_{1\rho}$ studies on a large group of OA specimens with varying degree of degeneration are needed to determine the correlation between $T_{1\rho}$ rate and OA disease severity as determined by histopathology. Similarly, studies on a large group of OA subjects with mild to moderate OA (with a different degree of radiographic OA) and age-matched healthy subjects are needed to address the issues regarding the precision of $T_{1\rho}$ measurement, the effect of age and disease severity on these measurements and the capability to longitudinally measure OA disease progression.

Acknowledgments

This work was supported by NIH grants R01AR45242, R01AR45404 and R01AR051041 from NIAMS and a P41 grant RR23053 from NCRR. Sampreet Niyogi was supported by NIH training grant T32-EB000814.

REFERENCES

1. Felson DT. Epidemiology of hip and knee osteoarthritis. *Epidemiol. Prev.* 1988; **10**: 1–28.
2. Felson DT. The incidence and natural history of knee osteoarthritis in the elderly. The Farmingham Osteoarthritis Study. *Arthritis Rheum.* 1995; **38**: 1500–1505.

Copyright © 2006 John Wiley & Sons, Ltd.

3. Guccione AA, Felson DT, Anderson JJ, Anthony JM, Zhang Y, Wilson PW, Kelly-Hayes M, Wolf PA, Kreger BE, Kamel WB. The effects of specific medical conditions on the functional limitations of elders in the Farmingham Study. *Am. J. Public Health* 1994; **84**: 351–358.
4. Yelin E. The economics of osteoarthritis. In *Osteoarthritis*, Brandt K, Doherty M, Lohmander LS (eds). Oxford Medical: Oxford, 1998; 23–30.
5. Stanton H, Rogerson FM, East CJ, Golub SB, Lawlor KE, Meeker CT, Little CB, Last K, Farmer PJ, Campbell IK, Fourie AM, Fosang AJ. ADAMTS5 is the major aggrecanase in mouse cartilage *in vivo* and *in vitro*. *Nature* 2005; **434**(7033): 648–652.
6. Glasson SS, Askew R, Sheppard B, Carito B, Blanchet T, Ma HL, Flannery CR, Peluso D, Kanki K, Yang Z, Majumdar MK, Morris EA. Deletion of active ADAMTS5 prevents cartilage degradation in a murine model of osteoarthritis. *Nature* 2005; **434**(7033): 644–648.
7. Smith HE, Mosher TJ, Dardzinski BJ, Collins BG, Collins CM, Yang QX, Schmithorst VJ, Smith MB. Spatial variation in cartilage T_2 of the knee. *J. Magn. Reson. Imag.* 2001; **14**(1): 50–55.
8. Dardzinski BJ, Mosher TJ, Li SZ, VanSlyke MA, Smith MB. Spatial variation of T_2 in human articular cartilage. *Radiology* 1997; **205**(2): 546–550.
9. David-Vaudey E, Ghosh S, Ries M, Majumdar S. T_2 relaxation time measurements in osteoarthritis. *Magn. Reson. Imag.* 2004; **22**(5): 673–682.
10. Glaser C. New techniques for cartilage imaging: T_2 relaxation time and diffusion-weighted MR imaging. *Radiol. Clin. N. Am.* 2005; **43**(4): 641–653, vii.
11. Mosher TJ, Smith H, Dardzinski BJ, Schmithorst VJ, Smith MB. MR imaging and T_2 mapping of femoral cartilage: *in vivo* determination of the magic angle effect. *AJR Am. J. Roentgenol.* 2001; **177**(3): 665–669.
12. Mosher TJ, Dardzinski BJ. Cartilage MRI T_2 relaxation time mapping: overview and applications. *Semin. Musculoskelet. Radiol.* 2004; **8**(4): 355–368.
13. Mosher TJ, Smith HE, Collins C, Liu Y, Hancy J, Dardzinski BJ, Smith MB. Change in knee cartilage T_2 at MR imaging after running: a feasibility study. *Radiology* 2005; **234**(1): 245–249.
14. Van Breuseghem I. Ultrastructural MR imaging techniques of the knee articular cartilage: problems for routine clinical application. *Eur. Radiol.* 2004; **14**(2): 184–192.
15. Van Breuseghem I, Bosmans HT, Elst LV, Maes F, Pans SD, Brys PP, Geusens EA, Marchal GJ. T_2 mapping of human femorotibial cartilage with turbo mixed MR imaging at 1.5 T: feasibility. *Radiology* 2004; **233**(2): 609–614.
16. Van Breuseghem I, Palmieri F, Peeters RR, Maes F, Bosmans HT, Marchal GJ. Combined T_1–T_2 mapping of human femoro-tibial cartilage with turbo-mixed imaging at 1.5 T. *J. Magn. Reson. Imag.* 2005; **22**(3): 368–372.
17. Dunn TC, Lu Y, Jin H, Ries MD, Majumdar S. T_2 relaxation time of cartilage at MR imaging: comparison with severity of knee osteoarthritis. *Radiology* 2004; **232**(2): 592–598.
18. Nieminen MT, Rieppo J, Toyras J, Hakumaki JM, Silvennoinen J, Hyttinen MM, Helminen HJ, Jurvelin JS. T_2 relaxation reveals spatial collagen architecture in articular cartilage: a comparative quantitative MRI and polarized light microscopic study. *Magn. Reson. Med.* 2001; **46**(3): 487–493.
19. Nieminen MT, Menezes NM, Williams A, Burstein D. T_2 of articular cartilage in the presence of Gd-DTPA2. *Magn. Reson. Med.* 2004; **51**(6): 1147–1152.
20. Watrin-Pinzano A, Ruaud JP, Olivier P, Grossin L, Gonord P, Blum A, Netter P, Guillot G, Gillet P, Loeuille D. Effect of proteoglycan depletion on T_2 mapping in rat patellar cartilage. *Radiology* 2005; **234**(1): 162–170.
21. Bashir A, Gray ML, Burstein D. Gd-DTPA^{2-} as a measure of cartilage degradation. *Magn. Reson. Med.* 1996; **36**: 665–673.
22. Bashir A, Gray ML, Boutin RD, Burstein D. Glycosaminoglycan in articular cartilage: *in vivo* assessment with delayed Gd(DTPA)$^{2-}$-enhanced MR imaging. *Radiology* 1997; **205**(2): 551–558.
23. Reddy R, Insko EK, Kaufman JH, Bolinger L, Kneeland JB, Leigh JS. MR imaging of cartilage under spin-locking. In *Proceedings of International Society of Magnetic Resonance Medicine*, Nice, 1995; 1535.
24. Duvvuri U, Reddy R, Patel SD, Kaufman JH, Kneeland JB, Leigh JS. $T_{1\rho}$-relaxation in articular cartilage: effects of enzymatic degradation. *Magn. Reson. Med.* 1997; **38**(6): 863–867.
25. Akella SV, Reddy Regatte R, Gougoutas AJ, Borthakur A, Shapiro EM, Kneeland JB, Leigh JS, Reddy R. Proteoglycan-induced changes in $T_{1\rho}$-relaxation of articular cartilage at 4 T. *Magn. Reson. Med.* 2001; **46**(3): 419–423.
26. Duvvuri U, Charagundla SR, Kudchodkar SB, Kaufman JH, Kneeland JB, Rizi R, Leigh JS, Reddy R. Human knee: *in vivo* $T_{1(\rho)}$-weighted MR imaging at 1.5 T—preliminary experience. *Radiology* 2001; **220**(3): 822–826.
27. Reddy R, Insko EK, Noyszewski EA, Dandora R, Kneeland JB, Leigh JS. Sodium MRI of human articular cartilage *in vivo*. *Magn. Reson. Med.* 1998; **39**(5): 697–701.
28. Borthakur A, Shapiro EM, Beers J, Kudchodkar S, Kneeland JB, Reddy R. Sensitivity of MRI to proteoglycan depletion in cartilage: comparison of sodium and proton MRI. *Osteoarthritis Cartilage* 2000; **8**(4): 288–293.
29. Shapiro EM, Borthakur A, Dandora R, Kriss A, Leigh JS, Reddy R. Sodium visibility and quantitation in intact bovine articular cartilage using high field ^{23}Na MRI and MRS. *J. Magn. Reson.* 2000; **142**(1): 24–31.
30. Wheaton AJ, Borthakur A, Shapiro EM, Regatte RR, Akella SV, Kneeland JB, Reddy R. Proteoglycan Loss in Human Knee Cartilage: Quantitation with Sodium MR Imaging—Feasibility Study. *Radiology* 2004; **231**(3): 900–905.
31. Goodwin DW, Dunn JF. MR imaging and T_2 mapping of femoral cartilage. *AJR Am. J. Roentgenol.* 2002; **178**(6): 1568–1569; author reply 1569–1570.
32. Burstein D, Gray M. New MRI techniques for imaging cartilage. *J. Bone Joint Surg. Am.* 2003; **85**(A Suppl. 2): 70–77.
33. Gray ML, Burstein D. Molecular (and functional) imaging of articular cartilage. *J. Musculoskelet. Neuronal Interact.* 2004; **4**(4): 365–368.
34. Gray ML, Eckstein F, Peterfy C, Dahlberg L, Kim YJ, Sorensen AG. Toward imaging biomarkers for osteoarthritis. *Clin. Orthoped. Relat. Res.* 2004 (427 Suppl): S175–181.
35. Gatehouse PD, Thomas RW, Robson MD, Hamilton G, Herlihy AH, Bydder GM. Magnetic resonance imaging of the knee with ultrashort *TE* pulse sequences. *Magn. Reson. Imag.* 2004; **22**(8): 1061–1067.
36. Gold GE, McCauley TR, Gray ML, Disler DG. What's new in cartilage? *Radiographics* 2003; **23**(5): 1227–1242.
37. Gold GE, Reeder SB, Beaulieu CF. Advanced MR imaging of the shoulder: dedicated cartilage techniques. *Magn. Reson. Imag. Clin. N. Am.* 2004; **12**(1): 143–159, vii.
38. Gold GE, Hargreaves BA, Reeder SB, Vasanawala SS, Beaulieu CF. Controversies in protocol selection in the imaging of articular cartilage. *Semin. Musculoskelet. Radiol.* 2005; **9**(2): 161–172.
39. Hall BK, Newman S. *Cartilage: Molecular Aspects*. CRC Press: Boca Raton, FL, 1991.
40. Recht MP, Goodwin DW, Winalski CS, White LM. MRI of articular cartilage: revisiting current status and future directions. *AJR Am. J. Roentgenol.* 2005; **185**(4): 899–914.
41. Peterfy CG. Imaging of the disease process. *Curr. Opin. Rheumatol.* 2002; **14**(5): 590–596.
42. Young IR, Bydder GM. Magnetic resonance: new approaches to imaging of the musculoskeletal system. *Physiol. Msmt* 2003; **24**(4): R1–23.
43. Winalski CS, Gupta KB. Magnetic resonance imaging of focal articular cartilage lesions. *Top. Magn. Reson. Imag.* 2003; **14**(2): 131–144.
44. Makin HJ, Mow VC, Buckwalter JA. Form and function of articular cartilage. In *Orthopedic Basic Sciences*, Simon SR (ed.). American Academy of Orthopedic Surgeons: Philadelphia, PA, 1994; 3–44.
45. Harris ED, Ruddy S, Kelley WN. *Kelley's Textbook of Rheumatology.* Elsevier/Saunders: Philadelphia, PA, 2005.
46. Pritzker KP, Gay S, Jimenez SA, Ostergaard K, Pelletier JP, Revell PA, Salter D, van den Berg WB. Osteoarthritis cartilage histopathology: grading and staging. *Osteoarthritis Cartilage* 2006; **14**(1): 13–29.

Copyright © 2006 John Wiley & Sons, Ltd.

DOI: 10.1002/nbm

47. Fernandez-Madrid F, Karvonen RL, Teitge RA, Miller PR, Negendank WG. MR features of osteoarthritis of the knee. *Magn. Reson. Imag.* 1994; **12**(5): 703–709.
48. Bonnet CS, Walsh DA. Osteoarthritis, angiogenesis and inflammation. *Rheumatology (Oxford)* 2005; **44**(1): 7–16.
49. Smith RJ, Rohloff NA, Sam LM, Justen JM, Deibel MR, Cornette JC. Recombinant human interleukin–1 alpha and recombinant human interleukin-1 beta stimulate cartilage matrix degradation and inhibit glycosaminoglycan synthesis. *Inflammation* 1989; **13**(4): 367–382.
50. McGuire-Goldring MB, Meats JE, Wood DD, Ihrie EJ, Ebsworth NM, Russell RG. *In vitro* activation of human chondrocytes and synoviocytes by a human interleukin-1-like factor. *Arthritis Rheum.* 1984; **27**(6): 654–662.
51. Meulenbelt I, Seymour AB, Nieuwland M, Huizinga TW, van Duijn CM, Slagboom PE. Association of the interleukin-1 gene cluster with radiographic signs of osteoarthritis of the hip. *Arthritis Rheum.* 2004; **50**(4): 1179–1186.
52. Leppavuori J, Kujala U, Kinnunen J, Kaprio J, Nissila M, Heliovaara M, Klinger N, Partanen J, Terwilliger JD, Peltonen L. Genome scan for predisposing loci for distal interphalangeal joint osteoarthritis: evidence for a locus on 2q. *Am. J. Hum. Genet.* 1999; **65**(4): 1060–1067.
53. Forster T, Chapman K, Marcelline L, Mustafa Z, Southam L, Loughlin J. Finer linkage mapping of primary osteoarthritis susceptibility loci on chromosomes 4 and 16 in families with affected women. *Arthritis Rheum.* 2004; **50**(1): 98–102.
54. Wheaton AJ, Dodge GR, Borthakur A, Kneeland JB, Schumacher HR, Reddy R. Detection of changes in articular cartilage proteoglycan by *T*(1rho) magnetic resonance imaging. *J. Orthoped. Res.* 2005; **23**(1): 102–108.
55. Dinarello CA. The IL-1 family and inflammatory diseases. *Clin. Exp. Rheumatol.* 2002; **20**(5 Suppl. 27): S1–13.
56. Mosley B, Urdal DL, Prickett KS, Larsen A, Cosman D, Conlon PJ, Gillis S, Dower SK. The interleukin-1 receptor binds the human interleukin-1 alpha precursor but not the interleukin-1 beta precursor. *J. Biol. Chem.* 1987; **262**(7): 2941–2944.
57. Lo YY, Conquer JA, Grinstein S, Cruz TF. Interleukin-1 beta induction of c-fos and collagenase expression in articular chondrocytes: involvement of reactive oxygen species. *J. Cell Biochem.* 1998; **69**(1): 19–29.
58. Nietfeld JJ, Wilbrink B, Den Otter W, Huber J, Huber-Bruning O. The effect of human interleukin 1 on proteoglycan metabolism in human and porcine cartilage explants. *J. Rheumatol.* 1990; **17**(6): 818–826.
59. Ku G, Faust T, Lauffer LL, Livingston DJ, Harding MW. Interleukin-1 beta converting enzyme inhibition blocks progression of type II collagen-induced arthritis in mice. *Cytokine* 1996; **8**(5): 377–386.
60. Koshy PJ, Lundy CJ, Rowan AD, Porter S, Edwards DR, Hogan A, Clark IM, Cawston TE. The modulation of matrix metalloproteinase and ADAM gene expression in human chondrocytes by interleukin-1 and oncostatin M: a time-course study using real-time quantitative reverse transcription-polymerase chain reaction. *Arthritis Rheum.* 2002; **46**(4): 961–967.
61. Primakoff P, Myles DG. The ADAM gene family: surface proteins with adhesion and protease activity. *Trends Genet.* 2000; **16**(2): 83–87.
62. Tortorella MD, Burn TC, Pratta MA, Abbaszade I, Hollis JM, Liu R, Rosenfeld SA, Copeland RA, Decicco CP, Wynn R, Rockwell A, Yang F, Duke JL, Solomon K, George H, Bruckner R, Nagase H, Itoh Y, Ellis DM, Ross H, Wiswall BH, Murphy K, Hillman MC Jr, Hollis GF, Newton RC, Magolda RL, Trzaskos JM, Arner EC. Purification and cloning of aggrecanase-1: a member of the ADAMTS family of proteins. *Science* 1999; **284**(5420): 1664–1666.
63. Abbaszade I, Liu RQ, Yang F, Rosenfeld SA, Ross OH, Link JR, Ellis DM, Tortorella MD, Pratta MA, Hollis JM, Wynn R, Duke JL, George HJ, Hillman MC, Jr. Murphy K, Wiswall BH, Copeland RA, Decicco CP, Bruckner R, Nagase H, Itoh Y, Newton RC, Magolda RL, Trzaskos JM, Burn TC. Cloning and characterization of ADAMTS11, an aggrecanase from the ADAMTS family. *J. Biol. Chem.* 1999; **274**(33): 23443–23450.
64. Sandy JD, Neame PJ, Boynton RE, Flannery CR. Catabolism of aggrecan in cartilage explants. Identification of a major cleavage site within the interglobular domain. *J. Biol. Chem.* 1991; **266**(14): 8683–8685.
65. Sandy JD, Flannery CR, Neame PJ, Lohmander LS. The structure of aggrecan fragments in human synovial fluid. Evidence for the involvement in osteoarthritis of a novel proteinase which cleaves the Glu 373–Ala 374 bond of the interglobular domain. *J. Clin. Invest.* 1992; **89**(5): 1512–1516.
66. Bartholomew JS, Handley CJ, Lowther DA. The effects of trypsin treatment on proteoglycan biosynthesis by bovine articular cartilage. *Biochem. J.* 1985; **227**(2): 429–437.
67. Berg A, Singer T, Moser E. High-resolution diffusivity imaging at 3.0 T for the detection of degenerative changes: a trypsin-based arthritis model. *Invest. Radiol.* 2003; **38**(7): 460–466.
68. Malemud CJ, Shuckett R, Goldberg VM. Changes in proteoglycans of human osteoarthritic cartilage maintained in explant culture: implications for understanding repair in osteoarthritis. *Scand. J. Rheumatol. Suppl.* 1988; **77**: 7–12.
69. Gaboriaud C, Serre L, Guy-Crotte O, Forest E, Fontecilla-Camps JC. Crystal structure of human trypsin 1: unexpected phosphorylation of Tyr151. *J. Mol. Biol.* 1996; **259**(5): 995–1010.
70. Basser PJ, Schneiderman R, Bank RA, Wachtel E, Maroudas A. Mechanical properties of the collagen network in human articular cartilage as measured by osmotic stress technique. *Arch. Biochem. Biophys.* 1998; **351**(2): 207–219.
71. Xia Y, Farquhar T, Burtonwurster N, Verniersinger M, Lust G, Jelinski LW. Self-diffusion monitors degraded cartilage. *Arch. Biochem. Biophys.* 1995; **323**(2): 323–328.
72. Duda GN, Kleemann RU, Bluecher U, Weiler A. A new device to detect early cartilage degeneration. *Am. J. Sports Med.* 2004; **32**(3): 693–698.
73. Yoshioka H, Haishi T, Uematsu T, Matsuda Y, Itai Y, Kose K. MR microscopy of the articular cartilage with a 1.0 T permanent magnet portable MR system: preliminary results. *Magn. Reson. Med. Sci.* 2003; **2**(1): 51–55.
74. Abragam A. *The Principles of Nuclear Magnetism*. Clarendon Press: Oxford, 1961.
75. Slichter CP. *Principles of Magnetic Resonance*. Springer: Berlin, 1996.
76. Das TP, Hahn EL. *Nuclear Quadrupole Resonance Spectroscopy.* Academic Press: New York, 1958.
77. Haeberlen U. *High Resolution NMR in Solids: Selective Averaging*, Waugh JH (ed.). Academic Press: London, 1976.
78. Jerschow A. From nuclear structure to the quadrupolar NMR interaction and high-resolution spectroscopy. *Prog. Nucl. Magn. Reson. Spectrosc.* 2005; **46**(1): 63.
79. Mehring M. *High Resolution NMR in Solids*. Springer: Berlin, 1976.
80. Ashbrook SE, Wimperis S. High-resolution NMR of quadrupolar nuclei in solids: the satellite-transition magic angle spinning (STMAS) experiment. *Prog. Nucl. Magn. Reson. Spectrosc.* 2004; **45**(1–2): 53.
81. Donald EW. NMR relaxation of spin-3/2 nuclei: effects of structure, order, and dynamics in aqueous heterogeneous systems. *Conc. Magn. Reson.* 2001; **13**(5): 294–325.
82. Jaccard G, Wimperis S, Bodenhausen G. Multiple quantum NMR spectroscopy of $S = 3/2$ spins in isotropic phase: a new probe for multiexponential relaxation. *J. Chem. Phys.* 1986; **85**(11): 6282–6293.
83. Johan RCvdM. Thermal relaxation and coherence dynamics of spin 3/2. I. Static and fluctuating quadrupolar interactions in the multipole basis. *Conc. Magn. Reson. Pt A* 2003; **19A**(2): 97–116.
84. Johan RCvdM. Thermal relaxation and coherence dynamics of spin 3/2. II. Strong radio-frequency field. *Conc. Magn. Reson. Pt A* 2003; **19A**(2): 117–133.
85. Kemp-Harper R, Wickstead B, Wimperis S. Sodium ions in ordered environments in biological systems: analysis of ^{23}Na NMR spectra. *J. Magn. Reson.* 1999; **140**(2): 351–362.
86. Navon G, Shinar H, Eliav U, Seo Y. Multiquantum filters and order in tissues. *NMR Biomed.* 2001; **14**(2): 112–132.
87. Rooney WD, Springer CS Jr. A comprehensive approach to the analysis and interpretation of the resonances of spins 3/2 from living systems. *NMR Biomed.* 1991; **4**(5): 209–226.

Copyright © 2006 John Wiley & Sons, Ltd.

88. Rooney WD, Springer CS Jr. The molecular environment of intracellular sodium: ^{23}Na NMR relaxation. *NMR Biomed.* 1991; **4**(5): 227–245.
89. Hilal SK, Maudsley AA, Simon HE, Perman WH, Bonn J, Mawad ME, Silver AJ, Ganti SR, Sane P, Chien IC. *In vivo* NMR imaging of tissue sodium in the intact cat before and after acute cerebral stroke. *AJNR Am. J. Neuroradiol.* 1983; **4**(3): 245–249.
90. Hilal SK, Maudsley AA, Ra JB, Simon HE, Roschmann P, Wittekoek S, Cho ZH, Mun SK. *In vivo* NMR imaging of sodium-23 in the human head. *J. Comput. Assist. Tomogr.* 1985; **9**(1): 1–7.
91. Maudsley AA, Hilal SK. Biological aspects of sodium-23 imaging. *Br. Med. Bull.* 1984; **40**(2): 165–166.
92. van der Maarel JRC. Relaxation of spin $S = 3/2$ in the doubly rotating tilted frame. *J. Chem. Phys.* 1989; **91**(3): 1446.
93. Eliav U, Navon G. Analysis of double-quantum-filtered NMR spectra of ^{23}Na in biological tissues. *J. Magn. Reson.* 1994; **B103**(1): 19–29.
94. van der Maarel JRC. Relaxation of spin 3/2 in a non-zero average electric field gradient. *Chem. Phys. Lett.* 1989; **155**: 288–296.
95. Woessner DE, Bansal N. Temporal characteristics of NMR signals from spin 3/2 nuclei of incompletely disordered systems. *J. Magn. Reson.* 1998; **133**: 21–35.
96. Chun-wa C, Wimperis S. Optimum detection of spin–3/2 biexponential relaxation using multiple-quantum filtration techniques. *J. Magn. Reson.* 1990; **88**(2): 440.
97. Muller N, Bodenhausen G, Ernst RR. Relaxation-induced violations of coherence transfer selection rules in nuclear magnetic resonance. *J. Magn. Reson.* 1987; **75**(2): 297.
98. Redfield AG. On the theory of relaxation processes. *IBM J. Res. Devl.* 1957; **1**(1): 19.
99. Redfield AG. The theory of relaxation processes. In *Advances in Magnetic Resonance*, Waugh JS (ed.), Vol. 1. Academic Press: New York, 1965; 1–32.
100. Hubbard PS. Nonexponential relaxation of rotating three-spin systems in molecules of a liquid. *J. Chem. Phys.* 1970; **52**(2): 563–568.
101. Pekar J, Leigh JS Jr. Detection of biexponential relaxation in sodium-23 facilitated by double-quantum filtering. *J. Magn. Reson.* 1986; **69**(3): 582.
102. Pekar J, Renshaw PF, Leigh JS Jr. Selective detection of intracellular sodium by coherence-transfer NMR. *J. Magn. Reson.* 1987; **72**(1): 159.
103. Eliav U, Shinar H, Navon G. The formation of a second-rank tensor in ^{23}Na double-quantum-filtered NMR as an indicator for order in a biological tissue. *J. Magn. Reson.* 1992; **98**(1): 223.
104. Reddy R, Bolinger L, Shinnar M, Noyszewski E, Leigh JS. Detection of residual quadrupolar interaction in human skeletal muscle and brain *in vivo* via multiple quantum filtered sodium NMR spectra. *Magn. Reson. Med.* 1995; **33**(1): 134.
105. Shinar H, Knubovets T, Eliav U, Navon G. Sodium interaction with ordered structures in mammalian red blood cells detected by Na-23 double quantum NMR. *Biophys. J.* 1993; **64**(4): 1273.
106. Reddy R, Shinnar M, Wang Z, Leigh JS. Multiple-quantum filters of spin-3/2 with pulses of arbitrary flip angle. *J. Magn. Reson., Ser. B* 1994; **104**(2): 148.
107. Reddy R, Shuchun L, Noyszewski EA, Kneeland JB, Leigh JSf. *In vivo* sodium multiple quantum spectroscopy of human articular cartilage. *Magn. Reson. Med.* 1997; **38**(2): 207.
108. Kemp-Harper R, Brown SP, Hughes CE, Styles P, Wimperis S. ^{23}Na NMR methods for selective observation of sodium ions in ordered environments. *Prog. Nucl. Magn. Reson. Spectrosc.* 1997; **30**(3–4): 157.
109. Borthakur A, Shapiro EM, Beers J, Kudchodkar S, Kneeland JB, Reddy R. Effect of IL-1beta-induced macromolecular depletion on residual quadrupolar interaction in articular cartilage. *J. Magn. Reson. Imag.* 2002; **15**(3): 315–323.
110. Kemp-Harper R, Wimperis S. Detection of the interaction of sodium ions with ordered structures in biological systems. Use of the Jeener–Broekaert experiment. *J. Magn. Reson. Ser. B* 1993; **102**(3): 326.
111. Hancu I, van der Maarel JRC, Boada FE. Detection of sodium ions in anisotropic environments through spin-lock NMR. *Magn. Reson. Med.* 2002; **47**(1): 68.
112. Eliav U, Keinan-Adamsky K, Navon G. A new method for suppressing the central transition in $I = 3/2$ NMR spectra with a demonstration for ^{23}Na in bovine articular cartilage. *J. Magn. Reson.* 2003; **165**(2): 276–281.
113. Ling W, Jerschow A. Frequency-selective quadrupolar MRI contrast. *Solid St. Nucl. Magn. Reson.* 2006; **29**(1–3): 227–231.
114. Ling W, Jerschow A. Selecting ordered environments in NMR of spin 3/2 nuclei via frequency-sweep pulses. *J. Magn. Reson.* 2005; **176**(2): 234–238.
115. Choy J, Ling W, Jerschow A. Selective detection of ordered sodium signals via the central transition. *J. Magn. Reson.* 2006; **180**(1): 105–109.
116. Thulborn KR, Davis D, Adams H, Gindin T, Zhou J. Quantitative tissue sodium concentration mapping of the growth of focal cerebral tumors with sodium magnetic resonance imaging. *Magn. Reson. Med.* 1999; **41**(2): 351–359.
117. Clayton DB, Lenkinski RE. MR imaging of sodium in the human brain with a fast three-dimensional gradient-recalled-echo sequence at 4 T. *Acad. Radiol.* 2003; **10**(4): 358–365.
118. Bartha R, Menon RS. Long component time constant of ^{23}Na T_2^* relaxation in healthy human brain. *Magn. Reson. Med.* 2004; **52**(2): 407–410.
119. Boada FE, Laverde G, Jungreis C, Nemoto E, Tanase C, Hancu I. Loss of cell ion homeostasis and cell viability in the brain: what sodium MRI can tell us. *Curr. Top. Devl. Biol.* 2005; **70**: 77–101.
120. Stobbe R, Beaulieu C. *In vivo* sodium magnetic resonance imaging of the human brain using soft inversion recovery fluid attenuation. *Magn. Reson. Med.* 2005; **54**(5): 1305–1310.
121. Duvvuri U, Leigh JS, Reddy R. Detection of residual quadrupolar interaction in the human breast *in vivo* using sodium-23 multiple quantum spectroscopy. *J. Magn. Reson. Imag.* 1999; **9**(3): 391–394.
122. Navon G. Complete elimination of the extracellular ^{23}Na NMR signal in triple quantum filtered spectra of rat hearts in the presence of shift reagents. *Magn. Reson. Med.* 1993; **30**(4): 503–506.
123. Neuberger T, Greiser A, Nahrendorf M, Jakob PM, Faber C, Webb AG. ^{23}Na microscopy of the mouse heart in vivo using density-weighted chemical shift imaging. *Magma* 2004; **17**(3–6): 196–200.
124. Pabst T, Sandstede J, Beer M, Kenn W, Neubauer S, Hahn D. Evaluation of sodium T_1 relaxation times in human heart. *J. Magn. Reson. Imag.* 2003; **17**(6): 726–729.
125. Pabst T, Sandstede J, Beer M, Kenn W, Greiser A, von Kienlin M, Neubauer S, Hahn D. Optimization of ECG-triggered 3D (23)Na MRI of the human heart. *Magn. Reson. Med.* 2001; **45**(1): 164–166.
126. Bottomley PA, Lee RF, Constantinides CD, Ouwerkerk R, Weiss RG. Quantification and imaging of myocardial sodium and creatine kinase metabolites. *Magma* 2000; **11**(1–2): 39–41.
127. Constantinides CD, Kraitchman DL, O'Brien KO, Boada FE, Gillen J, Bottomley PA. Noninvasive quantification of total sodium concentrations in acute reperfused myocardial infarction using ^{23}Na MRI. *Magn. Reson. Med.* 2001; **46**(6): 1144–1151.
128. Babsky A, Hekmatyar S, Wehrli S, Doliba N, Osbakken M, Bansal N. Influence of ischemic preconditioning on intracellular sodium, pH, and cellular energy status in isolated perfused heart. *Exp. Biol. Med. (Maywood)* 2002; **227**(7): 520–528.
129. Bansal N, Szczepaniak L, Ternullo D, Fleckenstein JL, Malloy CR. Effect of exercise on (23)Na MRI and relaxation characteristics of the human calf muscle. *J. Magn. Reson. Imag.* 2000; **11**(5): 532–538.
130. Constantinides CD, Gillen JS, Boada FE, Pomper MG, Bottomley PA. Human skeletal muscle: sodium MR imaging and quantification-potential applications in exercise and disease. *Radiology* 2000; **216**(2): 559–568.
131. Aronen HJ, Ramadan UA, Peltonen TK, Markkola AT, Tanttu JI, Jaaskelainen J, Hakkinen AM, Sepponen R. 3D spin-lock imaging of human gliomas. *Magn. Reson. Imag.* 1999; **17**(7): 1001–1010.
132. Kline RP, Wu EX, Petrylak DP, Szabolcs M, Alderson PO, Weisfeldt ML, Cannon P, Katz J. Rapid *in vivo* monitoring of

Copyright © 2006 John Wiley & Sons, Ltd.

DOI: 10.1002/nbm

chemotherapeutic response using weighted sodium magnetic resonance imaging. *Clin. Cancer Res.* 2000; **6**(6): 2146–2156.
133. Schepkin VD, Ross BD, Chenevert TL, Rehemtulla A, Sharma S, Kumar M, Stojanovska J. Sodium magnetic resonance imaging of chemotherapeutic response in a rat glioma. *Magn. Reson. Med.* 2005; **53**(1): 85–92.
134. Reddy R, Insko EK, Leigh JS. Triple quantum sodium imaging of articular cartilage. *Magn. Reson. Med.* 1997; **38**(2): 279–284.
135. Duvvuri U, Kaufman JH, Patel SD, Bolinger L, Kneeland JB, Leigh JS, Reddy R. Sodium multiple quantum spectroscopy of articular cartilage: effects of mechanical compression. *Magn. Reson. Med.* 1998; **40**(3): 370–375.
136. Lesperance LM, Gray ML, Burstein D. Determination of fixed charge-density in cartilage using nuclear-magnetic–resonance. *J. Orthoped. Res.* 1992; **10**(1): 1–13.
137. Borthakur A. *Sodium NMR: a Noninvasive Probe for Proteoglycan Macromolecules*. University of Pennsylvania: Philadelphia, PA, 2000.
138. Horn M. ^{23}Na magnetic resonance imaging for the determination of myocardial viability: the status and the challenges. *Curr. Vasc. Pharmac.* 2004; **2**(4): 329–333.
139. Kohler SJ, Kolodny NH. Sodium magnetic resonance imaging and chemical shift imaging. *Progr. Nucl. Magn. Reson. Spectrosc.* 1992; **24**: 411.
140. Rooney WD, Springer CS, Jr. The molecular environment of intracellular sodium: ^{23}Na NMR relaxation. *NMR Biomed.* 1991; **4**(5): 227.
141. Shapiro E. *Multi-nuclear magnetic resonance methods for evaluating cartilage degeneration*. University of Pennsylvania: Philadelphia, PA, 2001.
142. Reddy R, Insko EK, Leigh JS. Triple quantum sodium imaging of articular cartilage. *Magn. Reson. Med.* 1997; **38**(2): 279–284.
143. Borthakur A, Hancu I, Boada FE, Shen GX, Shapiro EM, Reddy R. *In vivo* triple quantum filtered twisted projection sodium MRI of human articular cartilage. *J. Magn. Reson.* 1999; **141**(2): 286–290.
144. Kemp-Harper R, Wickstead B, Wimperis S. Sodium ions in ordered environments in biological systems: analysis of ^{23}Na NMR spectra. *J. Magn. Reson.* 1999; **140**(2): 351.
145. Maroudas A, Muir H, Wingham J. The correlation of fixed negative charge with glycosaminoglycan content of human articular cartilage. *Biochim Biophys Acta* 1969; **177**(3): 492–500.
146. Paul PK, O'Byrne EM, Gupta RK, Jelicks LA. Detection of cartilage degradation with sodium NMR (letter). *Br. J. Rheumatol.* 1991; **30**: 318.
147. Jelicks LA, Paul PK, O'Byrne E, Gupta RK. H-1, Na-23, and C-13 MR spectroscopy of cartilage degradation *in vitro*. *J. Magn. Reson. Imag.* 1993; **3**(4): 565–568.
148. Insko EK, Kaufman JH, Leigh JS, Reddy R. Sodium NMR evaluation of articular cartilage degradation. *Magn. Reson. Med.* 1999; **41**: 30–34.
149. Granot J. Sodium imaging of human body organs and extremities *in vivo*. *Radiology* 1988; **167**: 547–550.
150. Kaufman JH, Regatte RR, Bolinger L, Kneeland JB, Reddy R, Leigh JS. A novel approach to observing articular cartilage deformation *in vitro* via magnetic resonance imaging. *J. Magn. Reson. Imag.* 1999; **9**(5): 653–662.
151. Borthakur A, Shapiro EM, Beers J, Kudchodkar S, Kneeland JB, Reddy R. Sensitivity of MRI to proteoglycan depletion in cartilage: comparison of sodium and proton MRI. *Osteoarthritis Cartilage* 2000; **8**(4): 288–293.
152. Shapiro EM, Borthakur A, Gougoutas A, Reddy R. ^{23}Na MRI accurately measures FCD in articular cartilage. *Magn. Reson. Med.* 2002; **47**(2): 284–291.
153. Borthakur A, Shapiro EM, Akella SV, Gougoutas A, Kneeland JB, Reddy R. Quantifying sodium in the human wrist *in vivo* by using MR imaging. *Radiology* 2002; **224**: 598–602.
154. Wheaton AJ, Borthakur A, Dodge GR, Kneeland JB, Schumacher HR, Reddy R. Sodium magnetic resonance imaging of proteoglycan depletion in an *in vivo* model of osteoarthritis. *Acad Radiol.* 2004; **11**(1): 21–28.
155. Burstein D, Velyvis J, Scott KT, Stock KW, Kim YJ, Jaramillo D, Boutin RD, Gray ML. Protocol issues for delayed Gd(DTPA)$^{2-}$-enhanced MRI (dGEMRIC) for clinical evaluation of articular cartilage. *Magn. Reson. Med.* 2001; **45**(1): 36–41.
156. Pruessmann KP, Weiger M, Scheidegger MB, Boesiger P. SENSE: sensitivity encoding for fast MRI. *Magn. Reson. Med.* 1999; **42**(5): 952–962.
157. Sodickson DK, Manning WJ. Simultaneous acquisition of spatial harmonics (SMASH): fast imaging with radiofrequency coil arrays. *Magn. Reson. Med.* 1997; **38**(4): 591–603.
158. Hoult DI, Chen CN, Sank VJ. The field dependence of NMR imaging. II. Arguments concerning an optimal field strength. *Magn. Reson. Med.* 1986; **3**(5): 730–746.
159. Chen CN, Sank VJ, Cohen SM, Hoult DI. The field dependence of NMR imaging. I. Laboratory assessment of signal-to-noise ratio and power deposition. *Magn. Reson. Med.* 1986; **3**(5): 722–729.
160. Wen H, Chesnick AS, Balaban RS. The design and test of a new volume coil for high field imaging. *Magn. Reson. Med.* 1994; **32**(4): 492–498.
161. Ugurbil K, Adriany G, Andersen P, Chen W, Garwood M, Gruetter R, Henry PG, Kim SG, Lieu H, Tkac I, Vaughan T, Van De Moortele PF, Yacoub E, Zhu XH. Ultrahigh field magnetic resonance imaging and spectroscopy. *Magn. Reson. Imag.* 2003; **21**(10): 1263–1281 .
162. Wolff SD, Balaban RS. Magnetization transfer contrast (MTC) and tissue water proton relaxation *in vivo*. *Magn. Reson. Med.* 1989; **10**(1): 135–144.
163. Rommel E, Kimmich R, Korperich H, Kunze C, Gersonde K. $T_{1\rho}$ dispersion imaging and localized $T_{1\rho}$ dispersion relaxometry: application *in vivo* to mouse adenocarcinoma. *Magn. Reson. Med.* 1992; **24**(1): 149–157.
164. Santyr GE, Fairbanks EJ, Kelcz F, Sorenson JA. Off-resonance spin locking for MR imaging. *Magn. Reson. Med.* 1994; **32**(1): 43–51.
165. Charagundla SR, Stolpen AH, Leigh JS, Reddy R. Off-resonance proton T_{1r} dispersion imaging of ^{17}O-enriched tissue phantoms. *Magn. Reson. Med.* 1998; **39**(4): 588–595.
166. Palmer AG, 3rd, Kroenke CD, Loria JP. Nuclear magnetic resonance methods for quantifying microsecond-to-millisecond motions in biological macromolecules. *Meth. Enzymol.* 2001; **339**: 204–238.
167. Bull TE. Relaxation in the rotating frame in liquids. *Prog. NMR Spectrosc.* 1992; **24**: 377.
168. Kimmich R. Nuclear magnetic relaxation spectroscopy in solutions of bovine hemoglobin. *Z. Naturforsch. B* 1971; **266**(11): 1168–1170.
169. Santyr GE, Henkelman RM, Bronskill MJ. Spin locking for magnetic resonance imaging with application to human breast. *Magn. Reson. Med.* 1989; **12**(1): 25–37.
170. Lamminen AE, Tanttu JI, Sepponen RE, Pihko H, Korhola OA. T_{1r} dispersion imaging of diseased muscle tissue. *Br. J. Radiol.* 1993; **66**(789): 783–787.
171. Dixon WT, Oshinski JN, Trudeau JD, Arnold BC, Pettigrew RI. Myocardial suppression *in vivo* by spin locking with composite pulses. *Magn. Reson. Med.* 1996; **36**(1): 90–94.
172. Markkola AT, Aronen HJ, Paavonen T, Hopsu E, Sipila LM, Tanttu JI, Sepponen RE. $T_{1\rho}$ dispersion imaging of head and neck tumors: a comparison to spin lock and magnetization transfer techniques. *J. Magn. Reson. Imag.* 1997; **7**(5): 873–879.
173. Mlynarik V, Trattnig S, Huber M, Zembsch A, Imhof H. The role of relaxation times in monitoring proteoglycan depletion in articular cartilage. *J. Magn. Reson. Imag.* 1999; **10**(4): 497–502.
174. Grohn OHJ, Kettunen MI, Makela HI, Penttonen M, Pitkanen A, Lukkarinen JA, Kauppinen RA. Early detection of irreversible cerebral ischemia in the rat using dispersion of the magnetic resonance imaging relaxation time, $T_{1\rho}$. *J. Cereb. Blood Flow Metab.* 2000; **20**(10): 1457–1466.
175. Poptani H, Duvvuri U, Miller CG, Mancuso A, Charagundla S, Fraser NW, Glickson JD, Leigh JS, Reddy R. $T_{1\rho}$ imaging of murine brain tumors at 4 T. *Acad. Radiol.* 2001; **8**(1): 42–47.
176. Borthakur A, Wheaton AJ, Gougoutas AJ, Akella SV, Regatte RR, Charagundla SR, Reddy R. In vivo measurement of $T_{1\rho}$ dispersion in the human brain at 1.5 tesla. *J. Magn. Reson. Imag.* 2004; **19**(4): 403–409.
177. Wheaton AJ, Casey FL, Gougoutas AJ, Dodge GR, Borthakur A, Lonner JH, Schumacher HR, Reddy R. Correlation of $T_{1\rho}$ with fixed charge density in cartilage. *J. Magn. Reson. Imag.* 2004; **20**(3): 519–525.

Copyright © 2006 John Wiley & Sons, Ltd.

178. Hulvershorn J, Borthakur A, Bloy L, Gualtieri EE, Reddy R, Leigh JS, Elliott MA. $T_{1\rho}$ contrast in functional magnetic resonance imaging. *Magn. Reson. Med.* 2005; **54**(5): 1155–1162.
179. Johannessen W, Auerbach JD, Wheaton AJ, Kurji A, Borthakur A, Reddy R, Elliott DM. Assessment of human disc degeneration and proteoglycan content using $T_{1\rho}$-weighted magnetic resonance imaging. *Spine* 2006; **31**(11): 1253–1257.
180. Borthakur A, Wheaton AJ, Charagundla SR, Shapiro EM, Regatte RR, Akella SVS, Kneeland JB, Reddy R. Three-dimensional $T_{1\rho}$-weighted MRI at 1.5 Tesla. *J. Magn. Reson. Imag.* 2003; **17**(6): 730–736.
181. Wheaton AJ, Borthakur A, Charagundla SR, Reddy R. Pulse sequence for multislice $T_{1\rho}$-weighted MRI. *Magn. Reson. Med.* 2004; **51**(2): 362–369.
182. Wheaton AJ. *Quantitative Spin-lock Magnetic Resonance Imaging: Technical Development and Biomedical Applications*. University of Pennsylvania: Philadelphia, PA 2005.
183. Li X, Han ET, Ma CB, Link TM, Newitt DC, Majumdar S. In vivo 3T spiral imaging based multi-slice T(1rho) mapping of knee cartilage in osteoarthritis. *Magn. Reson. Med.* 2005; **54**(4): 929–936.
184. Schmitz B, Hagen T, Reith W. Three-dimensional true FISP for high-resolution imaging of the whole brain. *Eur. Radiol.* 2003; **13**(7): 1577–1582.
185. Collins CM, Li S, Smith MB. SAR and B_1 field distributions in a heterogeneous human head model within a birdcage coil. *Magn. Reson. Med.* 1998; **40**(6): 847–856.
186. Wheaton AJ, Borthakur A, Corbo M, Charagundla SR, Reddy R. Method for reduced SAR $T_{1\rho}$-weighted MRI. *Magn. Reson. Med.* 2004; **51**(6): 1096–1102.
187. Wheaton AJ, Borthakur A, Reddy R. Application of the keyhole technique to $T_{1\rho}$ relaxation mapping. *J. Magn. Reson. Imag.* 2003; **18**(6): 745–749.
188. Redfield AG. Nuclear magnetic resonance saturation and rotary saturation in solids. *Phys. Rev.* 1955; **98**(6): 1787.
189. Redfield AG. Nuclear spin thermodynamics in the rotating frame. *Science* 1969; **164**(3883): 1015.
190. Koenig SH, Brown RD, III. Field-cycling relaxometry of protein solutions and tissue. Implications for MRI. *Prog. NMR Spectrosc.* 1990; **22**(pt 6): 487.
191. Kelly SW, Sholl CA. A relationship between nuclear spin relaxation in the laboratory and rotating frames for dipolar and quadrupolar relaxation. *J. Phys.: Condensed Matter* 1992; **4**(12): 3317.
192. Knispel RR. NMR study of the two-phase equilibrium in cysteine hydrochloride monohydrate. II. *J. Chem. Phys.* 1974; **61**(3): 1125.
193. Meiboom S, Hewitt RC. High resolution NMR probe suitable for use in a superconducting solenoid. *Rev. Sci. Instrum.* 1965; **36**(10): 1509.
194. Carver JP, Richards RE. A general two-site solution for the chemical exchange produced dependence of T_2 upon the Carr-Purcell pulse separation. *J. Magn. Reson.* 1972; **6**(1): 89.
195. Allerhand A, Gutowsky HS. Spin-echo studies of chemical exchange. II. Closed formulas for two sites. *J. Chem. Phys.* 1965; **42**(5): 587.
196. Stevens A, Paschalis P, Schleich T. Sodium-23 and potassium-39 nuclear magnetic resonance relaxation in eye lens. Examples of quadrupole ion magnetic relaxation in a crowded protein environment. *Biophys. J.* 1992; **61**(5): 1061.
197. Chopra S, McClung RED, Jordan RB. Rotating-frame relaxation rates of solvent molecules in solutions of paramagnetic ions undergoing solvent exchange. *J. Magn. Reson.* 1984; **59**(3): 361.
198. Belton PS, Ring SG, Botham RL, Hills BP. Multinuclear NMR studies of water in solutions of simple carbohydrates. II. Oxygen-17 relaxation. *Mol. Phys.* 1991; **72**(5): 1123–1134.
199. Hills BP, Wright KM, Belton PS. Proton NMR studies of chemical and diffusive exchange in carbohydrate systems. *Mol. Phys.* 1989; **67**(6): 1309–1326.
200. Hills BP, Takacs SF, Belton PS. The effects of proteins on the proton NMR transverse relaxation time of water. II. Protein aggregation. *Mol. Phys.* 1989; **67**(4): 919–937.
201. Hills BP, Takacs SF, Belton PS. The effects of proteins on the proton NMR transverse relaxation times of water. I. Native bovine serum albumin. *Mol. Phys.* 1989; **67**(4): 903–918.
202. Hills BP, Duce SL. The influence of chemical and diffusive exchange on water proton transverse relaxation in plant tissues. *Magn. Reson. Imag.* 1990; **8**(3): 321–331.
203. Hills BP. Multinuclear NMR studies of water in solutions of simple carbohydrates. I. Proton and deuterium relaxation. *Mol. Phys.* 1991; **72**(5): 1099–1121.
204. Virta A, Komu M, Kormano M. $T_{1\rho}$ of protein solutions at very low fields: dependence on molecular weight, concentration, and structure. *Magn. Reson. Med.* 1997; **37**(1): 53–57.
205. Virta A, Komu M, Lundbom N, Jaaskelainen S, Kalimo H, Airio A, Alanen A, Kormano M. Low field $T_{1\rho}$ imaging of myositis. *Magn. Reson. Imag.* 1998; **16**(4): 385–391.
206. Trott O, Palmer AG, III. R1rho relaxation outside of the fast-exchange limit. *J. Magn. Reson.* 2002; **154**(1): 157.
207. Trott O, Abergel D, Palmer AG, III. An average-magnetization analysis of R1rho relaxation outside of the fast exchange limit. *Mol. Phys.* 2003; **101**(6): 753.
208. Mlynarik V, Szomolanyi P, Toffanin R, Vittur F, Trattnig S. Transverse relaxation mechanisms in articular cartilage. *J. Magn. Reson.* 2004; **169**(2): 300–307.
209. Reddy R, Stolpen AH, Leigh JS. Detection of ^{17}O by proton T_{1r} dispersion imaging. *J. Magn. Reson. B* 1995; **108**(3): 276–279.
210. Solomon I. Magnetic relaxation in liquids in the presence of a high frequency field. *C. R. Hebdomad. Seances Acad. Sci.* 1959; **249**(17): 1631.
211. Tsoref L, Shinar H, Seo Y, Eliav U, Navon G. Proton double-quantum filtered MRI—a new method for imaging ordered tissues. *Magn. Reson. Med.* 1998; **40**(5): 720–726.
212. Chaumette H, Grandclaude D, Brondeau J, Werbelow L, Canet D. Rotating-frame spin-lattice relaxation measurements $T_{1\rho}$ with weak spin–locking fields in the presence of homonuclear dipolar coupling. *Mol. Phys.* 2003; **101**(12): 1919.
213. Chaumette H, Grandclaude D, Brondeau J, Werbelow L, Canet D. Rotating-frame spin-lattice relaxation measurements $T_{1\rho}$ with weak spin-locking fields in the presence of homonuclear dipolar coupling. *Molecular Physics* 2003; **101**: 1919.
214. Akella SV, Regatte RR, Wheaton AJ, Borthakur A, Reddy R. Reduction of residual dipolar interaction in cartilage by spin-lock technique. *Magn. Reson. Med.* 2004; **52**(5): 1103–1109.
215. Xia Y. Relaxation anisotropy in cartilage by NMR microscopy (μMRI) at 14-μm resolution. *Magn. Reson. Med.* 1998; **39**(6): 941–949.
216. Rubenstein JD, Kim JK, Henkelman RM. Effects of compression and recovery on bovine articular cartilage: appearance on MR images. *Radiology* 1996; **201**(3): 843–850.
217. Mlynarik V, Degrassi A, Toffanin R, Vittur F, Cova M, Pozzi-Mucelli RS. Investigation of laminar appearance of articular cartilage by means of magnetic resonance microscopy. *Magn. Reson. Imag.* 1996; **14**(4): 435–442.
218. Regatte RR, Akella SV, Borthakur A, Kneeland JB, Reddy R. Proteoglycan depletion-induced changes in transverse relaxation maps of cartilage: comparison of T_2 and $T_{1\rho}$. *Acad. Radiol.* 2002; **9**(12): 1388–1394.
219. Menezes NM, Gray ML, Hartke JR, Burstein D. T_2 and $T_{1\rho}$ MRI in articular cartilage systems. *Magn. Reson. Med.* 2004; **51**(3): 503–509.
220. Shinar H, Keinan-Adamsky K, Navon G. The biexponential nature of T_2 decay in articular cartilage. In *Proceedings of the International Society of Magnetic Resonance Medicine*, Kyoto, 2004; 2395.
221. Duvvuri U, Goldberg AD, Kranz JK, Hoang L, Reddy R, Wehrli FW, Wand AJ, Englander SW, Leigh JS. Water magnetic relaxation dispersion in biological systems: the contribution of proton exchange and implications for the noninvasive detection of cartilage degradation. *Proc. Natl Acad. Sci. USA* 2001; **98**(22): 12479–12484.
222. Reddy R, Insko EK, Kaufman JH, Bolinger L, Kneeland JB, Leigh JS. MR imaging of cartilage under spin-locking. In

Copyright © 2006 John Wiley & Sons, Ltd.

Proceedings of the International Society of Magnetic Resonance Medicine, Nice, 1995; 1535.
223. Duvvuri U, Kudchodkar S, Reddy R, Leigh JS. *T*(1rho) relaxation can assess longitudinal proteoglycan loss from articular cartilage *in vitro*. *Osteoarthritis Cartilage* 2002; **10**(11): 838–844.
224. Mankin HJ, Brandt KD. Biochemistry and metabolism of articular cartilage in osteoarthritis. In *Osteoarthritis: Diagnosis and Medical/surgical Management*, Moskowitz RW, Howell DS, Goldberg VM, Mankin HJ (eds). W. B. Saunders: Philadelphia, PA, 1992; 109–154.
225. Watson PJ, Carpenter TA, Hall LD, Tyler JA. MR protocols for imaging the guinea pig knee. *Magn. Reson. Imag.* 1997; **15**(8): 957–970.
226. Regatte RR, Akella SV, Wheaton AJ, Borthakur A, Kneeland JB, Reddy R. *T*1rho-relaxation mapping of human femoral-tibial cartilage *in vivo*. *J. Magn. Reson. Imag.* 2003; **18**(3): 336–341.
227. Akella SV, Regatte RR, Borthakur A, Kneeland JB, Leigh JS, Reddy R. $T_{1\rho}$ MR imaging of the human wrist *in vivo*. *Acad. Radiol.* 2003; **10**(6): 614–619.
228. Regatte RR, Akella SV, Borthakur A, Kneeland JB, Reddy R. *In vivo* proton MR three-dimensional $T_{1\rho}$ mapping of human articular cartilage: initial experience. *Radiology* 2003; **229**(1): 269–274.
229. Wheaton AJ, Borthakur A, Kneeland JB, Regatte RR, Akella SV, Reddy R. *In vivo* quantification of *T*(1rho) using a multislice spin-lock pulse sequence. *Magn. Reson. Med.* 2004; **52**(6): 1453–1458.
230. Lozano J, Li X, Link TM, Safran M, Majumdar S, Ma CB. Detection of posttraumatic cartilage injury using quantitative $T_{1\rho}$ magnetic resonance imaging. A report of two cases with arthroscopic findings. *J. Bone Joint Surg. Am.* 2006; **88**(6): 1349–1352.
231. Regatte RR, Akella SV, Wheaton AJ, Lech G, Borthakur A, Kneeland JB, Reddy R. 3D-*T*(1rho)-relaxation mapping of articular cartilage; *in vivo* assessment of early degenerative changes in symptomatic osteoarthritic subjects(1). *Acad. Radiol.* 2004; **11**(7): 741–749.
232. Akella SV, Regatte RR, Wheaton A, Borthakur A, Reddy R. Measurement of dipolar oscillations in articular cartilage using spin-lock technique. In *Proceedings of the International Society of Magnetic Resonance Medicine*, Kyoto, 2004; 824.
233. Wheaton AJ, Dodge GR, Elliott DM, Nicoll SB, Reddy R. Quantification of cartilage biomechanical and biochemical properties via $T_{1\rho}$ magnetic resonance imaging. *Magn. Reson. Med.* 2005; **54**(5): 1087–1093.

Copyright © 2006 John Wiley & Sons, Ltd.

Gadolinium(III) Chelates as MRI Contrast Agents: Structure, Dynamics, and Applications

Peter Caravan,* Jeffrey J. Ellison, Thomas J. McMurry, and Randall B. Lauffer

EPIX Medical, Inc., 71 Rogers Street, Cambridge, Massachusetts 02142

Received February 22, 1999 (Revised Manuscript Received June 24, 1999)

Contents

I. Introduction 2293
A. Signal Intensity in MRI 2294
B. The Nature of Gadolinium(III) Chelates 2295
C. This Review 2295
II. Solution and Solid State Structures 2295
A. Solid State Structures 2296
B. Solution Methods 2308
C. Solution Structures/Dynamics 2310
D. Gadolinium(III) Chelate Stabilty 2314
E. Solution Equilibria and Contrast Agent Dissociation in Vivo 2314
F. Kinetic Inertness and in Vivo Dissociation of Gadolinium(III) Complexes 2316
G. New Compounds 2316
H. Summary/Future Directions 2320
III. Relaxation Theory 2320
A. Introduction 2320
B. Inner-Sphere Relaxation 2320
C. Outer-Sphere Relaxation 2325
D. Data Fitting of NMRD Curves 2325
IV. Physical Properties of Small Molecule Gadolinium Complexes 2326
A. Water Exchange 2326
B. Proton Exchange 2327
C. Electronic Relaxation 2327
D. Relaxivity 2331
E. Outer- and Second-Sphere Relaxivity 2334
F. Methods of Improving Relaxivity 2336
V. Macromolecular Conjugates 2336
A. Introduction 2336
B. General Conjugation Methods 2336
C. Synthetic Linear Polymers 2336
D. Synthetic Dendrimer-Based Agents 2338
E. Naturally Occurring Polymers (Proteins, Polysaccharides, and Nucleic Acids) 2339
F. Targeted Agents 2340
VI. Relaxivity of Noncovalently Bound Adducts of Gadolinium(III) Complexes 2341
VII. General Physicochemical Properties 2344
VIII. Safety 2345
A. Low Molecular Weight Chelates 2345
B. Macromolecular Agents 2345
IX. Applications 2346
A. Extracellular Agents 2346
B. Blood Pool Agents 2346
C. Hepatobiliary Agents 2346
D. Other Agents 2347
E. Bioactivated Agents 2348
X. Conclusion 2348
XI. Acknowledgments 2348
XII. References 2348

I. Introduction

Gadolinium, an obscure lanthanide element buried in the middle of the periodic table, has in the course of a decade become commonplace in medical diagnostics. Like platinum in cancer therapeutics and technetium in cardiac scanning, the unique magnetic properties of the gadolinium(III) ion placed it right in the middle of a revolutionary development in medicine: magnetic resonance imaging (MRI). While it is odd enough to place patients in large superconducting magnets and noisily pulse water protons in their tissues with radio waves, it is odder still to inject into their veins a gram of this potentially toxic metal ion which swiftly floats among the water molecules, tickling them magnetically.

The successful penetration of gadolinium(III) chelates into radiologic practice and medicine as a whole can be measured in many ways. Since the approval of $[Gd(DTPA)(H_2O)]^{2-}$ in 1988, it can be estimated that over 30 metric tons of gadolinium have been administered to millions of patients worldwide. Currently, approximately 30% of MRI exams include the use of contrast agents, and this is projected to increase as new agents and applications arise; Table 1 lists agents currently approved or in clinical trials. In the rushed world of modern medicine, radiologists, technicians, and nurses often refrain from calling the agents by their brand names, preferring instead the affectionate "gado." They trust this clear, odorless "magnetic light", one of the safest class of drugs ever developed. Aside from the cost ($50−80/bottle), asking the nurse to "Give him some gado" is as easy as starting a saline drip or obtaining a blood sample.

Gadolinium is also finding a place in medical research. When one of us reviewed the field in its infancy,[1] in 1987, only 39 papers could be found for that year in a Medline search for "gado-" and MRI. Ten years later over 600 references appear each year. And as MRI becomes relied upon by different specialties, "gado" is becoming known by neurologists,

* To whom correspondence should be addressed: Tel.: +1 617 250 6127. Fax: +1 617 250 6127. E-mail: pcaravan@epixmed.com.

10.1021/cr980440x CCC: $35.00 © 1999 American Chemical Society
Published on Web 08/20/1999



Peter Caravan grew up in Bay Roberts, Newfoundland. He received a B.Sc. degree in Chemistry from Acadia University in Nova Scotia, Canada, in 1992. He was awarded an NSERC postgraduate scholarship which he took to the University of British Columbia where he studied the coordination chemistry of podand complexes of trivalent metal ions with Chris Orvig. After receiving his Ph.D. in 1996, Peter was awarded an NSERC postdoctoral fellowship to work in the group of André Merbach at the Université de Lausanne. There he probed the dynamics of metal complexes utilizing paramagnetic NMR. In 1998 Peter joined EPIX Medical, Inc., where he is currently investigating various biophysical chemistry problems.



Thomas J. McMurry received his B.S. in Chemistry from Penn State in 1979. He did his graduate work with John T. Groves at the University of Michigan (Ph.D., 1984) where he studied the structure and reactivity of high valent iron porphyrinate models for cytochrome P-450. Tom then moved to Berkeley as an NIH Postdoctoral Fellow in Kenneth N. Raymond's laboratory to work on the synthesis and coordination chemistry of macrobicyclic catechol-based siderophore analogues. In 1987, he joined the NIH as a Staff Fellow in the late Otto Gansow's laboratory and was involved with the development of bifunctional chelating agents for use in radioimmunotherapy. Tom has been employed at EPIX Medical (formerly Metasyn, Inc.) since 1993, where he is currently Senior Director, Chemistry.



Jeff Ellison came to EPIX Medical in 1997. He received a B.S. degree in chemistry from the University of California, Irvine. He earned his Ph.D. at the University of California, Davis, studying the kinetic stabilization of low coordinate metal environments with Phil Power. He did his postdoctoral research with Julie Kovacs at the University of Washington, investigating the role of iron in nitrile hydratase enzymes.



Dr. Lauffer received his Ph.D. in Chemistry from Cornell University in 1983. At the Massachusetts General Hospital, Boston, MA, he served as a National Institutes of Health Postdoctoral Fellow and as director of the NMR Contrast Media Laboratory. He also held positions of Assistant Professor in Radiology at Harvard Medical School and NIH New Investigator. In 1992, Dr. Lauffer founded EPIX Medical, Inc., a developer of MRI contrast agents, and currently serves as Chief Scientific Officer and a member of the board of directors.

cardiologists, urologists, opthamologists, and others in search of new ways to visualize functional changes in the body.

While other types of MRI contrast agents have been approved, namely an iron particle-based agent and a manganese(II) chelate, gadolinium(III) remains the dominant starting material. The reasons for this include the direction of MRI development and the nature of Gd chelates.

A. Signal Intensity in MRI

As described in more detail elsewhere, signal intensity in MRI stems largely from the local value of the longitudinal relaxation rate of water protons, $1/T_1$, and the transverse rate, $1/T_2$. Signal tends to increase with increasing $1/T_1$ and decrease with increasing $1/T_2$. Pulse sequences that emphasize changes in $1/T_1$ are referred to as T_1-weighted, and the opposite is true for T_2-weighted scans.

Contrast agents increase both $1/T_1$ and $1/T_2$ to varying degrees depending on their nature as well as the applied magnetic field. Agents such as gadolinium(III) that increase $1/T_1$ and $1/T_2$ by roughly similar amounts are best visualized using T_1-weighted images since the percentage change in $1/T_1$ in tissue is much greater than that in $1/T_2$. Iron particles, on the other hand, generally lead to a much larger increase in $1/T_2$ than in $1/T_1$ and are best seen with T_2-weighted scans.

The longitudinal and transverse relaxivity values, r_1 and r_2, refer to the amount of increase in $1/T_1$ and $1/T_2$, respectively, per millimolar of agent (often given as per mM of Gd). T_1 agents usually have r_2/r_1 ratios of 1−2, whereas that value for T_2 agents, such as iron oxide particles, is as high as 10 or more.

Table 1. Clinically Relevant Gadolinium(III) Chelates

chemical name	generic name	brand name	company	classification
$[Gd(DTPA)(H_2O)]^{2-}$	gadopentetate dimeglumine	Magnevist[a]	Schering (Germany)	extracellular
$[Gd(DOTA)(H_2O)]^{-}$	gadoterate meglumine	Dotarem[a]	Guerbet (France)	extracellular
$[Gd(DTPA\text{-}BMA)(H_2O)]$	gadodiamide	Omniscan[a]	Nycomed-Amersham (U.K.)	extracellular
$[Gd(HP\text{-}DO3A)(H_2O)]$	gadoteridol	ProHance[a]	Bracco (Italy)	extracellular
$[Gd(DO3A\text{-}butrol)(H_2O)]$	gadobutrol	Gadovist[a]	Schering (Germany)	extracellular
$[Gd(DTPA\text{-}BMEA)(H_2O)]$	gadoversetamide	OptiMARK[b]	Mallinckrodt (U. S.)	extracellular
$[Gd(BOPTA)(H_2O)]^{2-}$	gadobenate dimeglumine	MultiHance[a]	Bracco (Italy)	hepatobiliary/extracellular
$[Gd(EOB\text{-}DTPA)(H_2O)]^{2-}$	gadoxetic acid disodium	Eovist[b]	Schering (Germany)	hepatobiliary
MS-325	gadophostriamine trisodium	AngioMARK[b]	EPIX/Mallinckrodt (U. S.)	blood pool

[a] Approved. [b] In clinical trials.

Advances in MRI have strongly favored T_1 agents and thus gadolinium(III). Faster scans with higher resolution require more rapid radio frequency pulsing and are thus generally T_1-weighted since the MR signal in each voxel becomes saturated. T_1 agents relieve this saturation by restoring a good part of the longitudinal magnetization between pulses. At the same time, a good T_1 agent would not significantly affect the bulk magnetic susceptibility of the tissue compartment in which it is localized, thus minimizing any inhomogeneities which can lead to image artifacts and/or decreased signal intensity. Small iron particles can function as T_1 agents using very T_1-weighted scans, but the resulting changes in magnetic susceptibility are much larger than that for gadolinium(III) chelates.

B. The Nature of Gadolinium(III) Chelates

The choice of Gd(III) would be expected, for no other ion has seven unpaired electrons. But there is a much more subtle reason it performs so well. Two other lanthanide ions, dysprosium(III) and holmium(III), have larger magnetic moments (due to orbital contributions to electron angular momentum) than that of Gd(III), but the asymmetry of these electronic states leads to very rapid electron spin relaxation.[2] The symmetric S-state of Gd(III) is a more hospitable environment for electron spins, leading to a much slower electronic relaxation rate. In the intricate dance that gives rise to relaxivity, water protons hardly feel the effects of ions such as Dy(III), much like a leaf near the incredibly rapid wings of a hummingbird; Gd(III) electrons, on the other hand, are more closely in tune with the proton's frequency.

A bizarre ion does not a drug make. Even with its high relaxivity, how can one inject a whole gram of it into people? This is a toxic heavy metal, with a size approximating calcium(II), but with a higher charge, leading to disruption of critical Ca(II)-required signaling. This is also not cobalt(III) or chromium(III), ions with powerfully bonding orbitals forming chelates that last for years.

The final oddity of gadolinium(III) chelates is that, when proper ligands are chosen, they actually do remain chelated in the body and are excreted intact. Apparently, the off-the-shelf ligands such as DTPA form complexes strong enough so that, for the period that the agent is in the body, there is no detectable dissociation. This is in the face of significant amounts of phosphate, citrate, transferrin, and other chelating substances.

Once the chemist makes the mental leap, however difficult it is, that this exchange-labile metal ion forms essentially inert complexes, then the chelate can be viewed as an intact drug molecule. Traveling over the surface of, say, $[Gd(DTPA)(H_2O)]^{2-}$, it does not look too bad. It is not hydrophobic, so it is unlikely to enter cells. There are no nitrogen mustard or intercalating groups to muck up our DNA. The metal ion is buried in the cage, so it is unlikely to bind to donor groups in proteins and enzymes. There is nothing a good nucleophile or electrophile can attack. It actually does not look like much at all: a little hydrophilic ball, as inocuous as a sugar molecule. And, oddly enough, it appears to be as safe.

C. This Review

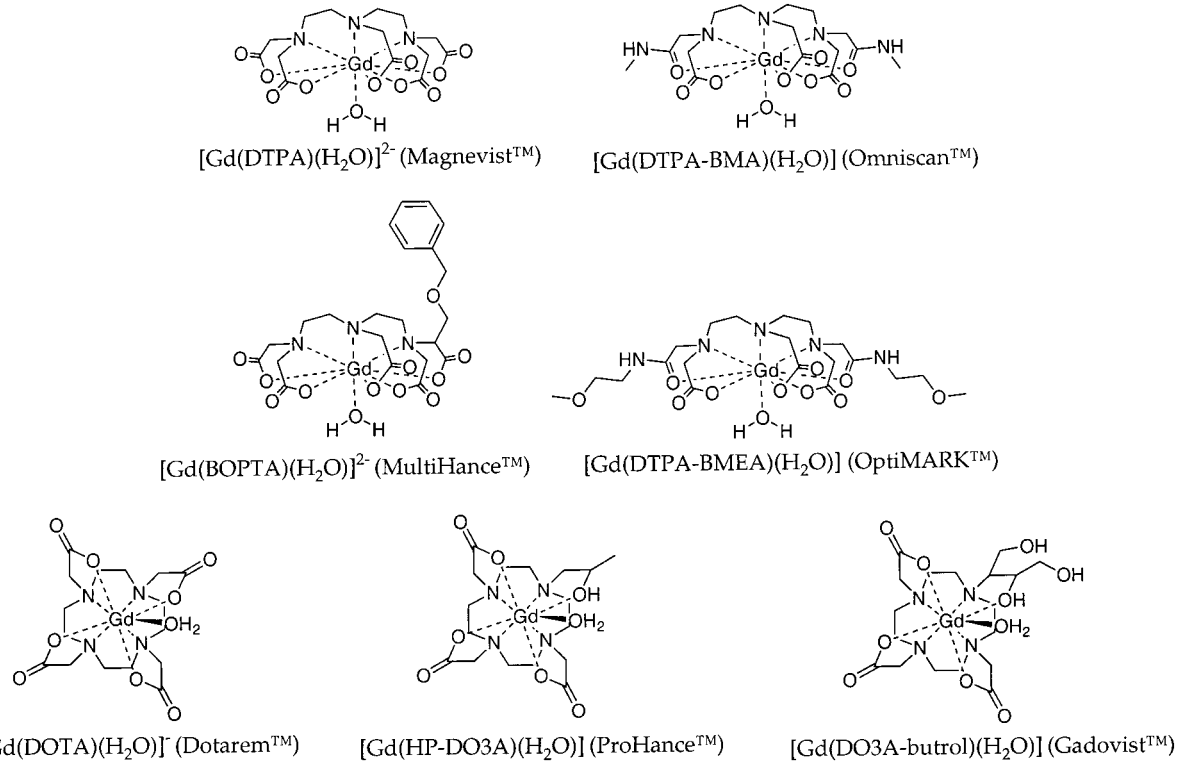
A previous review in this journal,[1] now 12 years old, covered a broad range of topics related to MRI agents. A number of other reviews and perspectives have also appeared.[3−15] The present article is to be more focused, especially on the subtle and unique chemical features of Gd(III) chelates which have not been covered in as much detail. Agents for oral or inhalation use in MRI are omitted from this article. Iron particles and manganese complexes are not discussed here, but good summaries can be found in other sources.[8,16,17] Nor are the other fascinating areas of chemical shift reagents[3,15] and, especially, imaging with the hyperpolarized nuclei of noble gases[18] covered in this review.

With regard to Gd(III) chelates, only brief summaries of safety and applications are provided; more can be found elsewhere.[1,4,8] The chelates discussed are those judged by the authors to be of sufficient stability for in vivo use. As opposed to an exhaustive review of every paper on the subject, our major goal is to communicate the critical points needed to understand the development of clinically relevant agents. We regret if we omitted interesting studies for the sake of conciseness.

II. Solution and Solid State Structures

This first section deals with the solid and solution state structures of gadolinium(III) complexes used in MRI or of interest from an MRI perspective. Structural characterization is the first step in understanding the physicochemical and pharmacologic behavior of these compounds. In the second part of section II, the thermodynamic stability and kinetic inertness of

Chart 1



these complexes is discussed, with particular emphasis on in vivo stability.

A. Solid State Structures

Owing to their large size, lanthanides tend to favor high coordination numbers in aqueous media. Currently, all gadolinium(III)-based chelates approved for use in MRI are nine-coordinate complexes in which a ligand occupies eight binding sites at the metal center and the ninth coordination site is occupied by a solvent water molecule (Chart 1). For nine-coordinate complexes the idealized coordination geometries are tricapped trigonal prism (TTP) and capped square antiprism (CSAP) (Figure 1). In the absence of chelate ring steric effects, Guggenberger and Muetterties identified the tricapped trigonal prism as the most favorable polytopal form for an ML_9 coordination complex.[19] When the square basal plane of a CSAP is bent along the (4,7) diagonal, the CSAP is changed to a TTP geometry (Figure 1). Three useful distinguishing features of the two geometries are the dihedral angle between the trigonal faces

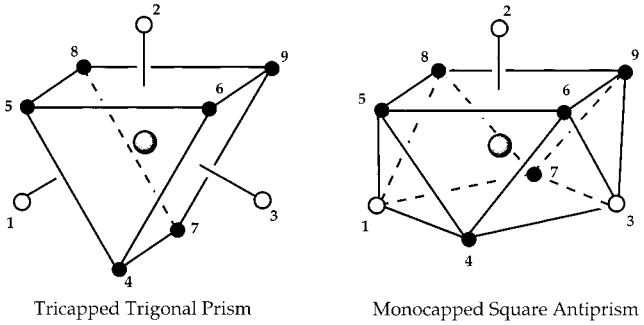


Figure 1. Tricapped trigonal prism (TTP) and monocapped square antiprism (CSAP) geometries.

(4,5,6) and (7,8,9), which in idealized polyhedra is 180° for TTP (coplanar to each other and to the (1,2,3) plane) and 163.5° for CSAP, the dihedral angle between the trigonal faces (1,4,7) and (3,4,7) which should be 26.4° for TTP and 0° for CSAP, and the mean deviation in the basal (1,4,3,7) plane, which should be small in the CSAP case. Nine-coordinate Ln(III) complexes are often described as distorted TTP or distorted CSAP. Because the two geometries are closely related, it is possible that a particular structure is described equally well by both geometries.

X-ray structures for Ln(III) complexes of DTPA (Chart 2) were reported by Gries et al. (Gd(III) complex, Na^+ salt),[20] Stezowski et al. (Nd(III) complex, Ba salt),[21] Jin et al. (Gd(III) complex, Mn salt),[22] Inoue et al. (Gd(III) complex, NH_4^+ salt),[23] Sakagami et al. (Dy(III) complex, Cs salt),[24] and Ruloff et al. (Gd(III) complexes, guanidinium salts).[25] All of these structures contained a nine-coordinate metal ion bonded to three nitrogens and five monodentate carboxylate oxygen atoms of the DTPA ligand. In some cases the observed geometries were distorted from ideal prisms to such a degree that either the TTP or CSAP description is justified. For example, the dihedral angles in the Nd(III) complex (Table 3) were intermediate to those of idealized TTP and CSAP arrangements (Figure 2). In most cases, the geometry is best described as a distorted TTP. The complexes $Na_2[Gd(DTPA)(H_2O)]$, $Mn[Gd(DTPA)(H_2O)]$, $Ba[Nd(DTPA)(H_2O)]$, and $CN_3H_6[Gd(HDTPA)(H_2O)]$ all have similar structures in which the remaining coordination site (position 2 in Figure 1) was occupied by a water molecule. Three examples of dimeric structures, $(NH_4)_4[Gd_2(DTPA)_2]$, $(CN_3H_6)_4[Gd_2(DTPA)_2]$, and $Cs_4[Dy_2(DTPA)_2]$, were also reported.

Chart 2

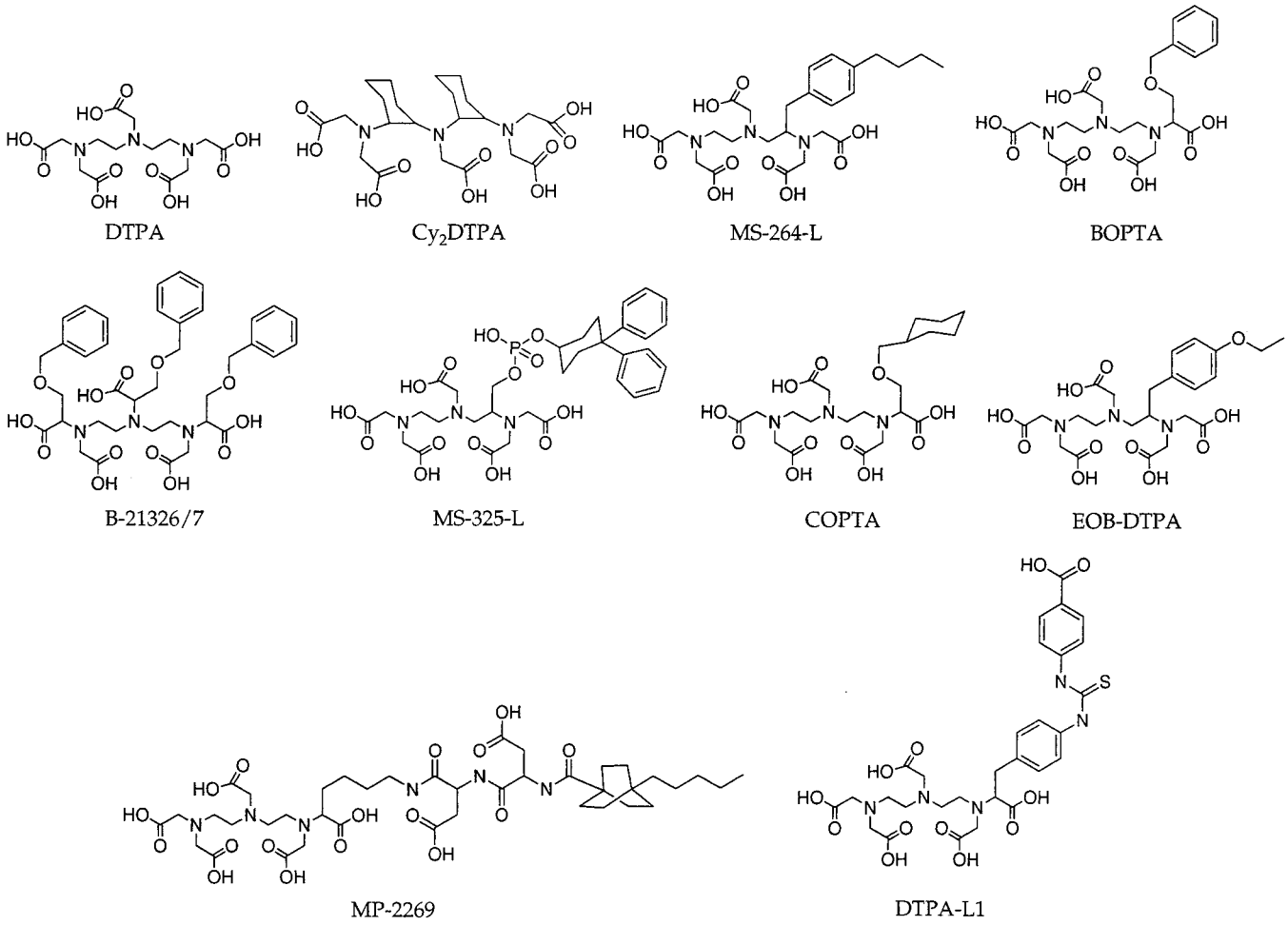


Table 2. Selected Bond Distances (Å) for Ln(III) Complexes of DTPA and Related Ligands

complex	Ln−O_{water}	Ln−$O_{carboxylate}$[a]	Ln−$N_{terminal}$	Ln−$N_{central}$	Ln−O_{amide}	ref
$Na_2[Gd(DTPA)(H_2O)]$	2.490	2.363−2.437	2.629, 2.710	2.582		20
$(NH_4)_4[Gd_2(DTPA)_2]$		2.364−2.413	2.651, 2.728	2.620		23
$(CN_3H_6)_4[Gd_2(DTPA)_2]$		2.371−2.428	2.669, 2.713	2.612		25
$(CN_3H_6)[Gd(HDTPA)(H_2O)]$	2.421[b]	2.340−2.492	(2.659, 2.785)[b]	2.666[b]		25
$Mn[Gd(DTPA)(H_2O)]$	2.441	2.350−2.442	2.588, 2.830	2.621		22
$Ba[Nd(DTPA)(H_2O)]$	2.616	2.361−2.526	2.681, 2.822	2.760		21
$Cs_4[Dy_2(DTPA)_2]$		2.324−2.392	2.648, 2.724	2.609		24
$(NH_4)_2[Gd(Cy_2DTPA)(H_2O)]$	2.434	2.347−2.424	2.622, 2.705	2.800		26
$Na_2[Gd(BOPTA)(H_2O)]$	2.463	2.340−2.416	2.615, 2.800	2.571		28
$Na_2[Gd(MS-264)(H_2O)]$	2.466[b]	2.339−2.419	(2.633, 2.734)[b]	2.605[b]		27
$Na_2[Eu(BOPTA)(H_2O)]$	2.46	2.320−2.437	2.65, 2.81	2.65		29
$[Gd(DTPA\text{-}BBA)(H_2O)]$	2.442	2.368−2.384	2.665, 2.751	2.600	2.427, 2.455	33
$[Gd(DTPA\text{-}BEA)(H_2O)]$	2.423	2.351−2.384	2.702, 2.759	2.645	2.362, 2.425	32
$[Lu(DTPA\text{-}BBA)(H_2O)]$	2.359	2.296−2.308	2.601, 2.739	2.526	2.296, 2.318	35
$[Y(DTPA\text{-}BBA)(H_2O)]$	2.40	2.32−2.34	2.62, 2.74	2.56	2.33, 2.36	36
$[Dy(DTPA\text{-}BMA)(H_2O)]$	2.463	2.318−2.350	2.616, 2.751	2.609	2.348, 2.376	31
$H_2[Eu_2(DTPA-cs124)_2]$		2.35−2.41	2.64, 2.76	2.59	2.50, 2.30	31
$[Gd_2(15\text{-}DTPA-EAM)_2(H_2O)_2]$	2.412	2.380−2.381	2.611, 2.915	2.761	2.406, 2.449	38
$[Gd(16\text{-}DTPA\text{-}PAM)(H_2O)]$	2.474	2.332−2.391	2.664, 2.748	2.618	2.439, 2.451	38
$[Gd(17\text{-}DTPA\text{-}BAM)(H_2O)]$	2.431	2.356−2.387	2.700, 2.785	2.615	2.397, 2.454	40
$[Gd(16\text{-}DTPA\text{-}HPAM)(H_2O)]$	2.408	2.350−2.364	2.695, 2.783	2.643	2.439, 2.454	39
$[Y_2(15\text{-}DTPA-EAM)_2(H_2O)_2]$	2.367	2.320−2.348	2.589, 2.926	2.759	2.403, 2.370	37
$[La_2(15\text{-}DTPA-EAM)_2(H_2O)_2]$	2.534	2.468−2.484	2.718, 2.953	2.842	2.507, 2.559	37
$(CF_3SO_3)_2[La(18\text{-}DTPA-dienH^+)(H_2O)]_2$	2.586	2.555−2.862	2.826, 2.889	2.796	2.615, 2.689	41
$(CF_3SO_3)_2[Eu(18\text{-}DTPA-dienH^+)]_4$		2.361−2.407	2.646, 2.816	2.615	2.408, 2.440	41

[a] Range of observed distances. [b] Average of two independent molecules.

In all three cases a ligand carboxylate donor functions as a bridging bidentate group occupying the ninth coordination site of a neighboring metal center.

The crystal structure of the Gd(III) complex of Cy_2-DTPA (Chart 2), in which the ligand had an all trans configuration in the dicyclohexyltriamine backbone,

Table 3. Selected Dihedral Angles (deg) for Ln(III) Complexes of DTPA and DTPA Derivatives[a]

complexes	(4,5,6) (7,8,9)	(1,7,4) (3,4,7)	ref
idealized CSAP	163.5	0.0	19
$(NH_4)_2$[Gd(Cy$_2$DTPA)(H_2O)]	153.5	0.8	26
Ba[Nd(DTPA)(H_2O)]	166.4	10.2	21
Mn[Gd(DTPA)(H_2O)]	171.7	14.5	22
[Gd(16-DTPA-PAM)(H_2O)]	172.7	14.5	38
[Gd(16-DTPA-HPAM)(H_2O)]	173.9	16.2	39
Na_2[Gd(BOPTA)(H_2O)]	177.0	17.4	28
Na_2[Eu(BOPTA)(H_2O)]	176.9	17.5	29
[Gd(DTPA-BEA)(H_2O)]	175.9	19.8	32
[Dy(DTPA-BMA)(H_2O)]	176.5	22.1	31
[Lu(DTPA-BBA)(H_2O)]	171.2	23.3	35
Na_2[Gd(MS−264)(H_2O)]	178[b]	23[b]	27
idealized TTP	180	26.4	19

[a] Positions are assigned based upon water filling site 2 as described in Figure 11. [b] Average of two independent molecules.

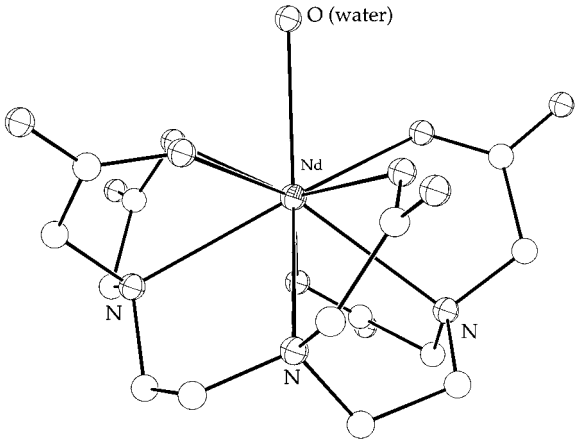


Figure 2. Molecular structure of [Nd(DTPA)(H_2O)]$^{2-}$ (ref 21).

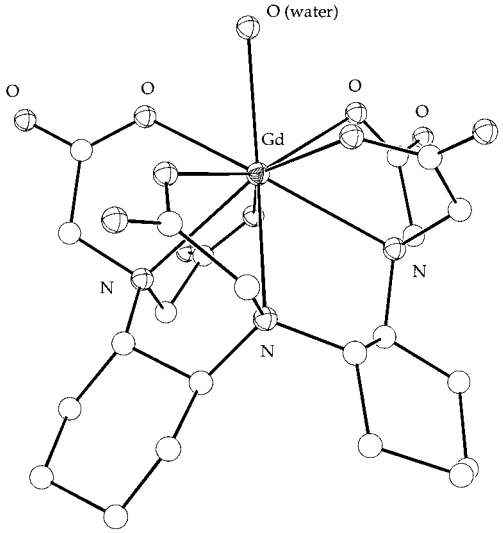


Figure 3. ORTEP drawing of [Gd(Cy$_2$DTPA)(H_2O)]$^{2-}$ (ref 26).

has been reported by Caulfield et al.[26] and is shown in Figure 3. The metal ion was nine-coordinate with the eight donor atoms in a CSAP arrangement. The three amine nitrogens and one carboxylate oxygen were coplanar, forming the basal plane of a prism. The capped plane, comprised of four carboxylate oxygens, was slightly distorted with three of the

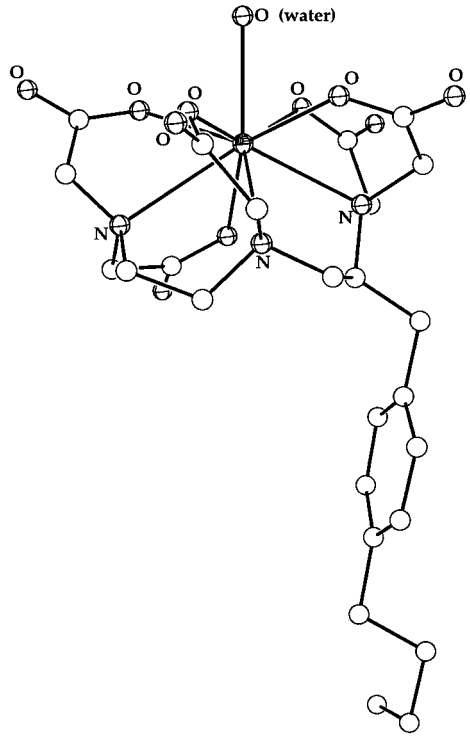


Figure 4. ORTEP drawing of MS-264: one of two independent molecules in the unit cell (ref 27).

oxygens forming a plane that is parallel to the N_3O basal plane. The out of plane carboxylate oxygen was slightly displaced toward the basal plane. The capping position was occupied by a water molecule. The twist angle between the basal and capped planes was ca. 43°. The Gd−N distance to the central nitrogen (2.80 Å) is long relative to those found in Gd(III) complexes of DTPA (2.62 Å average) and likely results from steric constraints of the ligand.

Structures of DTPA derivatives, in which substituents were attached to the acetate arms or diethylenetriamine backbone of the ligand, are known for MS-264 (Gd(III) complex, Na^+ salt)[27] and BOPTA (Gd(III)[28] and Eu(III)[29] complexes, Na^+ salt) (Chart 2). In all four cases the ligand coordinated in the same manner as DTPA, with TTP geometries about the metal centers. As expected for bulky substituents on five-membered rings, these substituents were equatorially positioned from their chelate ring and always directed away from the metal ion. The X-ray crystal structures of the Gd(III) complexes of MS-264 and BOPTA are shown in Figures 4 and 5.

A crystal structure of the Eu(III) complex (Figure 6) of DTPA-cs124 (Chart 3) was reported by Selvin et al.[30] The Eu(III) ion was nine-coordinate with binding sites occupied by three amine nitrogens, four monodentate carboxylate oxygens, and two monodentate amide oxygens. The complex crystallized as an amide bridged dimer in which the ring amide filled a capping position in a distorted TTP arrangement. Interestingly, the Eu−O (bridging amide) distance (2.30 Å) was shorter than the Eu−O (carboxylate) distances. The nonbridging amide distance (Table 2) was 0.2 Å longer.

Several structures of DTPA-bisamide complexes [Dy(DTPA-BMA)(H_2O)],[31] [Gd(DTPA-BEA)(H_2O)],[32]

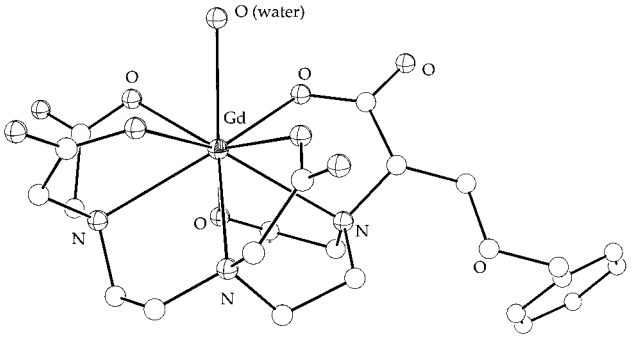


Figure 5. ORTEP drawing of $[Gd(BOPTA)(H_2O)]^{2-}$ (ref 28).

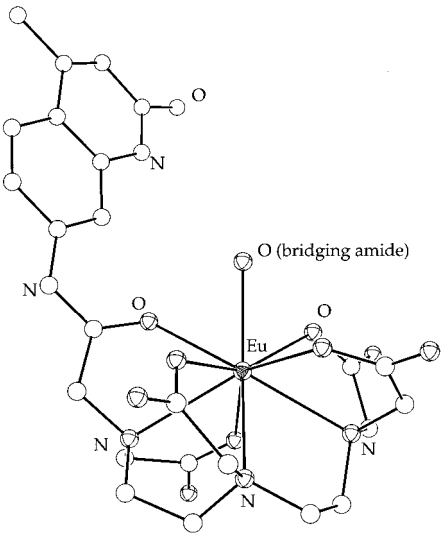


Figure 6. ORTEP drawing of [Eu(DTPA-cs124)]. The capping position is filled by a bridging amide (ref 30).

$[Gd(DTPA\text{-}BBA)(H_2O)]$,[33,34] $[Lu(DTPA\text{-}BBA)(H_2O)]$,[35] and $[Y(DTPA\text{-}BBA)(H_2O)]$[36] were reported (Chart 4). In all of these complexes, nonacoordinate metal ions were observed. The coordination sphere consisted of three nitrogen, three monodentate carboxylate oxygen, two monodentate amide oxygen, and one water oxygen atom donor. There are four possible configurations for placement of the amide groups (syn, cis, anti, and trans), which are illustrated in Figure 7. The Dy(III) complex of DTPA-BMA (Figure 8) and the Gd(III) complex of DTPA-BEA had trans configurations in the solid state. The DTPA-BBA complexes, see Figure 9 for the Gd(III) structure, all exhibited cis configurations. In each case, the geometry was distorted TTP. For $[Dy(DTPA\text{-}BMA)(H_2O)]$, $[Lu(DTPA\text{-}BBA)(H_2O)]$, and $[Y(DTPA\text{-}BBA)(H_2O)]$, the M−O (amide) distances are comparable to those found for M−O (carboxylate), while in the gadolinium complexes $[Gd(DTPA\text{-}BEA)(H_2O)]$ and $[Gd(DTPA\text{-}BBA)(H_2O)]$ the M−O (amide) distances were longer, approaching the M−O (water) distance (Table 2).

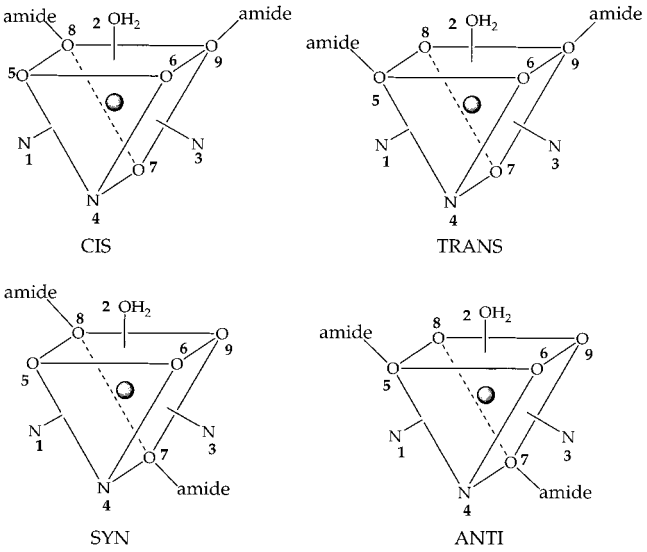


Figure 7. Four possible conformations (cis, trans, syn, and anti) of DTPA-bisamides in a TTP arrangement.

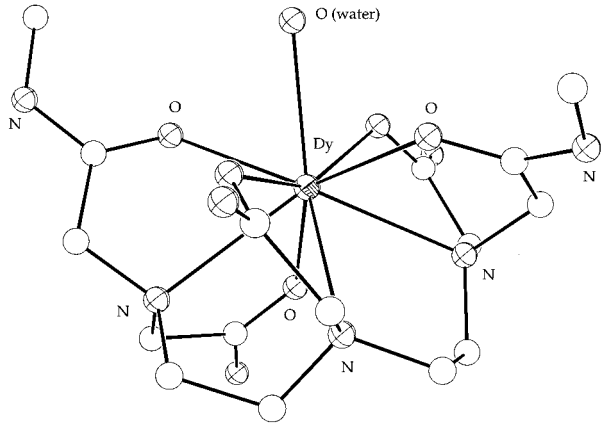


Figure 8. ORTEP drawing of $[Dy(DTPA\text{-}BMA)(H_2O)]$ with the amides in a trans configuration (ref 31).

The isostructural La(III),[37] Y(III),[37] and Gd(III)[38] complexes of 15-DTPA-EAM (Chart 5) crystallized as binuclear centrosymmetric structures with two Ln(III) ions located between two ligand molecules. The Ln(III) ions (CN9) were coordinated to an amide oxygen, two carboxylate oxygens, and two amine nitrogen atom donors from one ligand and an amide oxygen, a carboxylate oxygen, and an amine nitrogen atom donor from the second ligand. The coordination sphere was completed by a water molecule. When the ring is expanded, as with 16-DTPA-PAM,[38] 16-DTPA-HPAM,[39] or 17-DTPA-BAM,[40] the ligand is then able to wrap around the metal center, which resulted in mononuclear structures for the Gd(III) complexes (Chart 5). In the 16-DTPA-PAM (Figure 10), 16-DTPA-HPAM, and 17-DTPA-BAM complexes, the Gd(III) ions were each nine-coordinate, bonded to two amide oxygens, three carboxylate oxygens, three

Chart 3

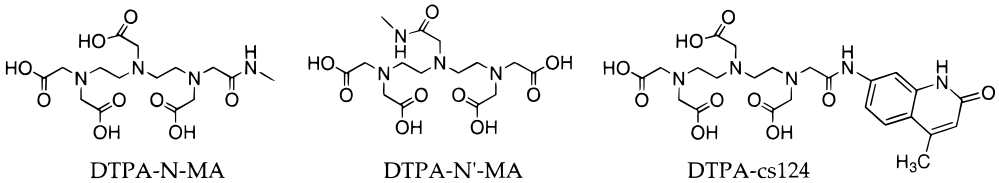
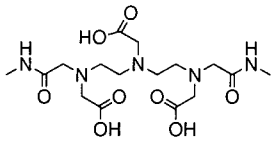
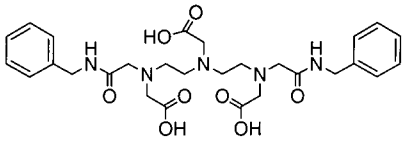


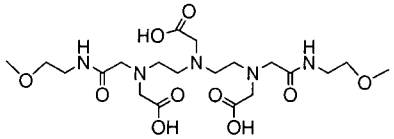
Chart 4



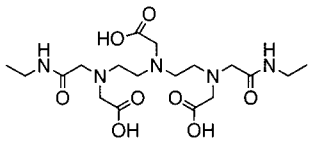
DTPA-BMA



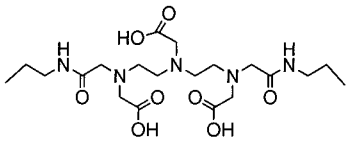
DTPA-BBA



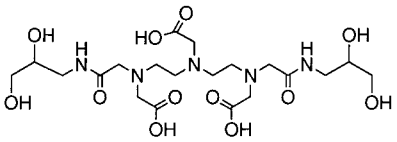
DTPA-BMEA



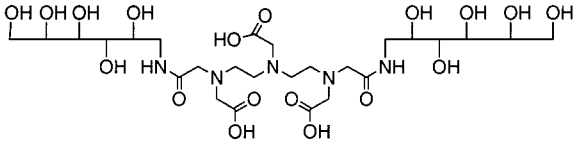
DTPA-BEA



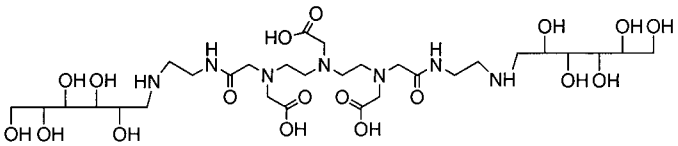
DTPA-B^{n}PA



DTPA-BPDA

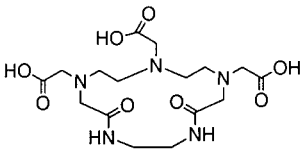


DTPA-BGLUCA

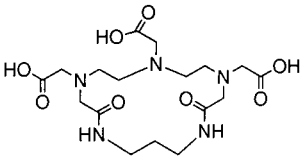


DTPA-BENGALAA

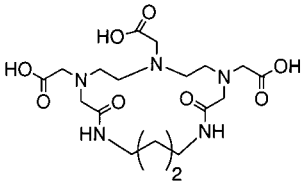
Chart 5



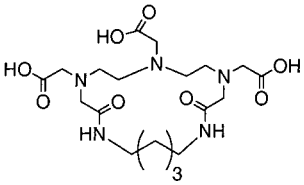
15-DTPA-EAM



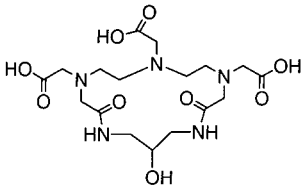
16-DTPA-PAM



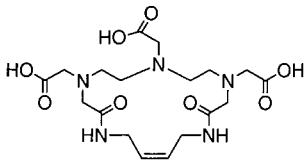
17-DTPA-BAM



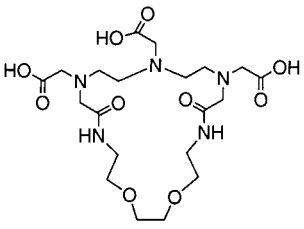
18-DTPA-PenAM



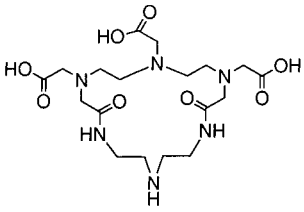
16-DTPA-HPAM



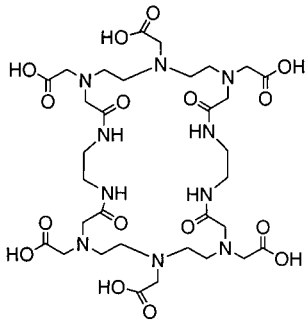
17-DTPA-cisC=CBAM



21-DTPA-OAM



18-DTPA-dien



30-DTPA-en-DTPA-en

amine nitrogens, and a single water molecule. In each structure, the geometry around the metal center was distorted TTP with the amides sitting in a syn configuration. The La(III) complex of 18-DTPA-dien (Chart 5) crystallized as an M_2L_2 dimer in which the metal centers are symmetry related.[41] Each La(III) was eleven-coordinate. Three amine nitrogens, two amide oxygens, three carboxylate oxygens, a bridging bidentate carboxylate, and a water molecule filled the coordination sphere. The Eu(III) complex of 18-DTPA-dien crystallized as a M_4L_4 tetramer[41] in which each metal ion was nine-coordinate. Each 18-DTPA-dien provided eight donor atoms to one metal ion and a bridging carboxylate donor to an adjacent Eu(III). The geometry about each metal ion was distorted TTP with the amide oxygen atoms sitting in a syn configuration. The difference in the solid state structures among the cyclic DTPA-bisamides can be ascribed to steric factors. These steric constraints prevent the formation of anti or trans configurations for the amide oxygen donors.

Several structural features are consistent among the lanthanide complexes in which the backbone of the ligand is diethylenetriamine, as with DTPA,

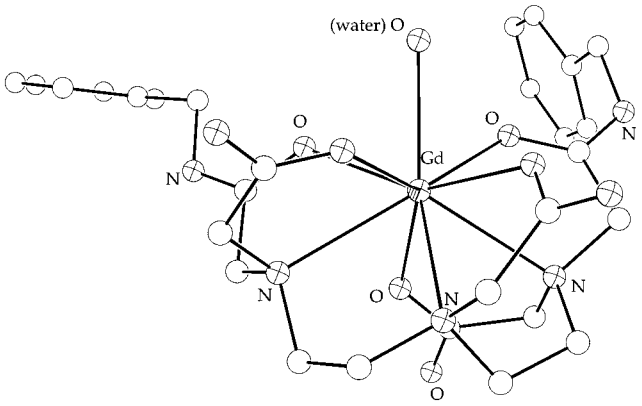


Figure 9. ORTEP drawing of [Gd(DTPA-BBA)(H_2O)] with the amides in a cis configuration (ref 33).

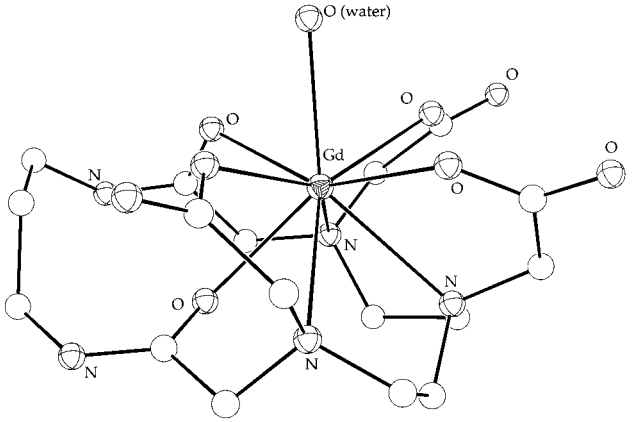


Figure 10. ORTEP drawing of [Gd(16-DTPA-PAM)(H_2O)] with the amides in a syn configuration (ref 38).

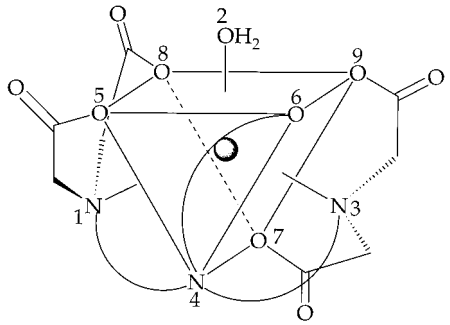


Figure 11. General coordination scheme for complexes of DTPA and DTPA derivatives (one of two wrapping isomers). The terminal backbone nitrogens differ in the position of their pendant acetate/amide groups.

BOPTA, MS-264, DTPA-bisamides (cyclic and linear), and DTPA-cs124. In general, the Ln(III) complexes of these ligands assume distorted TTP geometries. In the TTP arrangement, the neutral donor atoms with longer bond lengths will prefer to occupy a face capping position (positions 1, 2, and 3 in Figure 1) rather than a prismatic corner. However, since it is not possible for all three nitrogens to occupy face capping positions, the central nitrogen of the diethylenetriamine backbone always occupies a prismatic corner, while the terminal backbone nitrogens occupy capping positions (Figure 11). Generally, the shortest Ln(III)−N bond distance belongs to the central backbone nitrogen. The two terminal Ln(III)−N bond distances differ from each other by as much as 9%

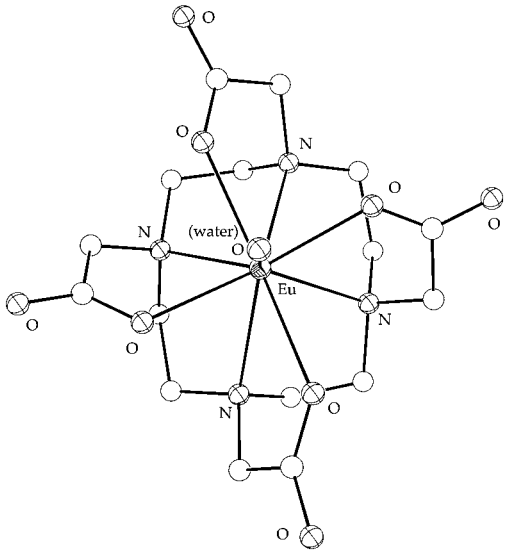


Figure 12. ORTEP drawing of [Eu(DOTA)(H_2O)]$^-$ (CSAP isomer) as viewed looking down the metal−water bond (ref 42).

and exhibit a consistent pattern.[29] The terminal nitrogens are distinguished by the positions of their pendant acetate/amide groups. As shown in Figure 11, at one terminal nitrogen both acetate/amide groups reside at prismatic corners in the (5,6,8,9) plane, while for the other terminal nitrogen one group occupies a prismatic corner in the (5,6,8,9) plane and the other completes the coordination of the basal plane (position 7). The terminal nitrogen associated with the longer Ln(III)−N distance has pendant acetate/amide groups which span the (7,9) edge. The reasons for this bond lengthening are unclear; however, it is worth noting that the trigonal prisms in these structures are very irregular. The (5,8), (6,9), and (4,7) edges tend to be longer than those edges at the triangular faces. The difference in the length of the two edges of interest, (5,8) and (7,9), can be as great as 0.5 Å (for Mn[Gd(DTPA)-(H_2O)] (5,8) = 3.5 Å, (7,9) = 3.0 Å). Dihedral angles for selected complexes are provided in Table 3. Metal−donor atom bond distances are provided in Table 2.

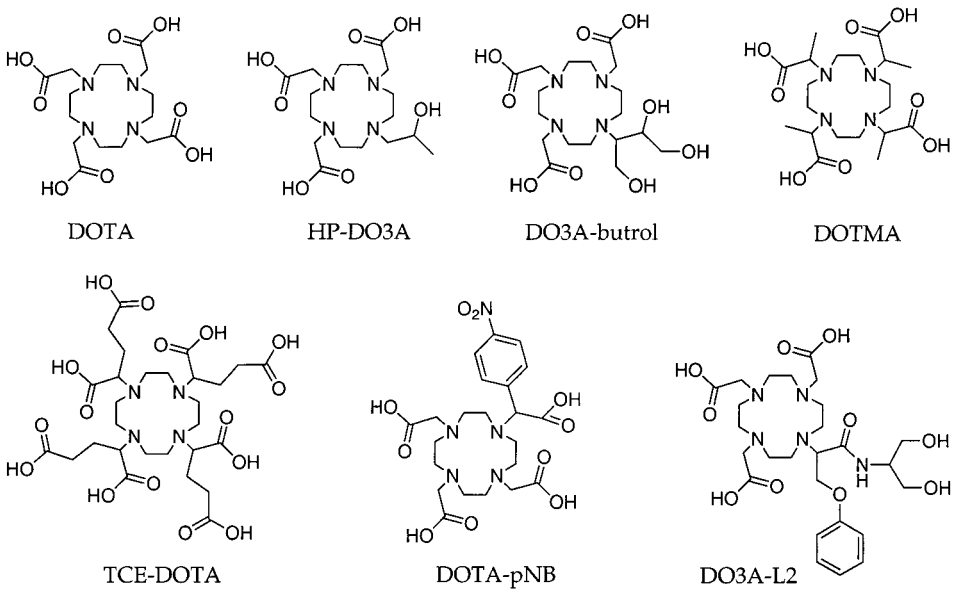
X-ray structures of the Eu(III),[42] Gd(III),[43,44] Y(III),[44] Lu(III),[45] and La(III)[46] complexes of DOTA (Chart 6) showed that the ligand coordinated in an octadentate fashion. Crystals of the Eu(III), Gd(III), Lu(III), and Y(III) complexes were isomorphous; the Eu(III) X-ray structure is shown in Figure 12. These complexes were arranged in a CSAP geometry where the basal plane was occupied by four amine nitrogens, the capped plane was occupied by four carboxylate oxygens, and the capping position was occupied by a water molecule. The twist angle between the basal and capped planes was approximately 39° for these complexes. The La(III) complex crystallized as a helical chain of carboxylate bridged complexes. The asymmetric unit contained two lanthanide chelates in a nine-coordinate monocapped arrangement with capping positions occupied by the bridging carboxylates. In the La(III) complex the twist angle between the basal and capped planes was approximately 22°, halfway between a prismatic (0°) and an antipris-

Table 4. Selected Bond Distances (Å) and Twist Angles (deg) for Ln(III) Complexes of DOTA and Related Macrocycles

complex	Ln−O_{water}	Ln−$O_{carboxylate}$[a]	Ln−N_{amine}[a]	Ln−O	twist angle	ref
Na[Eu(DOTA)(H_2O)]	2.480	2.247−2.511	2.519−2.900		38.9	42
Na[Gd(DOTA)(H_2O)]	2.458	2.362−2.370	2.648−2.679		38.7	43
Na[Y(DOTA)(H_2O)]	2.435	2.316−2.327	2.633−2.666		39.2	44
Na[Lu(DOTA)(H_2O)]	2.416	2.269−2.282	2.597−2.640		39.7	45
{Na[La(DOTA)]}$_n$		2.750−2.806	2.478−2.510		22[c]	46
[Gd(HP-DO3A)(H_2O)]	2.50[c]	2.31−2.38	2.64−2.65	2.33[c,d]	26.0, 37.9	47
[Y(HP-DO3A)(H_2O)]	2.49[c]	2.27−2.35	2.58−2.63	2.36[c,d]	28.1, 37.9	47
[Gd_2(DO3A−butrol)$_2$]		2.342−2.427	2.648−2.741	2.405[d]	27.9	48
H_5[Eu(TCE−DOTA)(H_2O)]	2.445	2.38[i]	2.68[i]		38.4	50
[Gd(DO3A−L2)(H_2O)]	2.429	2.337−2.360	2.627−2.719	2.392[h]	39.1	49
[Gd_2(DO3MA)$_2$(H_2O)$_2$]	2.420, 2.526	2.311−2.392[j]	2.66[k], 2.58[l]		29.7, 38	51
Na_2[{Gd(DO3A)}$_3$(CO_3)]		2.34−2.35[b]	2.61[k], 2.57[l]	2.46[b,e]	38.1[b]	44
[Gd(ODOTRA)(H_2O)]$_n$	2.559	2.327−2.357	2.644−2.674	2.574[f]	30.8	55
[Y(DOTBzP)]$^-$			2.64−2.67	2.20−2.31[g,a]	29.0	52
[Eu(DOTBzP)]$^-$			2.65−2.72	2.30−2.35[g,a]	29.5	53
[Yb(DOTBzP)]$^-$			2.62−2.64	2.22−2.29[g,a]	30.5	53
[La(DOTBzP)(H_2O)]$^-$	2.66		2.69−2.84	2.41−2.50[g,a]	28.8	53

[a] Range of distances. [b] Average of three independent molecules. [c] Average of two independent molecules. [d] M−O (hydroxyalkyl). [e] M−O (carbonate). [f] M−O (ether). [g] M−O (phosphinate). [h] M−O (amide). [i] Average bond distance in molecule. [j] Nonbridging carboxylates. [k] Average M−N distance to tertiary nitrogens. [l] Average M−N distance to secondary nitrogens.

Chart 6



matic (45°) arrangement. This geometry is described as twisted CSAP (also referred to as inverted CSAP). In all five structures the four amine nitrogens were coplanar as were the four carboxylate oxygens in the capped plane.

Neutral Gd(III) complexes of ligands in which one of the acetate arms of DOTA is replaced by a hydroxyalkyl group are approved for use under the brand names ProHance and Gadovist. Crystal structures for both the Gd(III) and Y(III) complexes of HP-DO3A[47] and the Gd(III) complex of DO3A-butrol[48] were reported (Chart 6). In all three structures the metal ion (CN9) was coordinated by four nitrogens, three monodentate carboxylate oxygens, and one hydroxyalkyl oxygen. A water molecule in the capping position completed the coordination sphere in the isostructural HP-DO3A complexes of Gd(III) and Y(III). The unit cell was comprised of two independent molecules with diastereomeric conformations (Figures 13 and 14). The twist angle between the basal and capped planes was ca. 38° in one molecule and ca. 26° in the other. Thus both CSAP (Figure 13) and twisted CSAP (Figure 14) geometries were present in the crystal. The Gd(III) complex of DO3A-butrol crystallized as a carboxylate bridged dimer, with a single unique metal ion in the asymmetric unit. The twist angle between the basal and capped planes was ca. 28° (twisted CSAP geometry). In all three structures, the M−O (hydroxyalkyl) distances were comparable to the M−O (carboxylate) distances (Table 4).

The neutral Gd(III) complex of DO3A-L2 (Chart 6) in which one of the acetate arms of DOTA is replaced by an amide group was reported by Aime et al.[49] The Gd(III) ion was nine-coordinate with bonding to four amine nitrogens, three monodentate carboxylates, one monodentate amide oxygen, and one water molecule. The twist angle between the basal and capped planes was 39.1°, resulting in CSAP geometry (Figure 16). The M−O (amide) distance was compa-

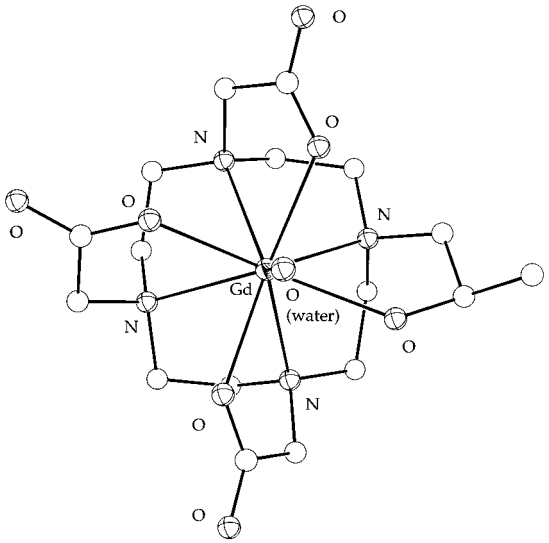


Figure 13. ORTEP drawing of the CSAP diastereomer of [Gd(HP-DO3A)(H_2O)] as viewed looking down the metal−water bond (ref 47).

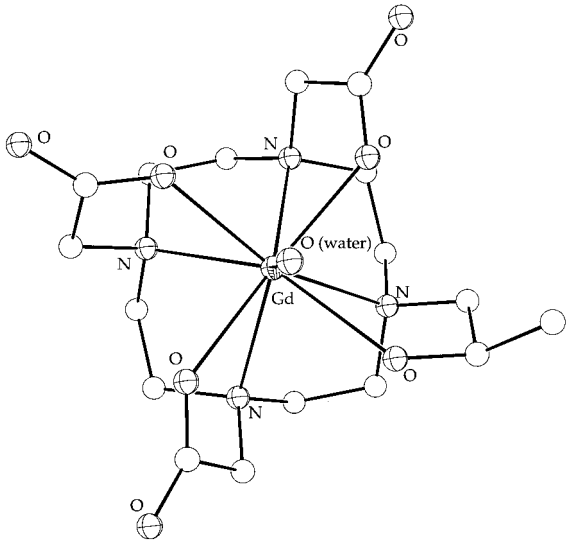


Figure 14. ORTEP drawing of the twisted CSAP diastereomer of [Gd(HP-DO3A)(H_2O)] as viewed looking down the metal−water bond (ref 47).

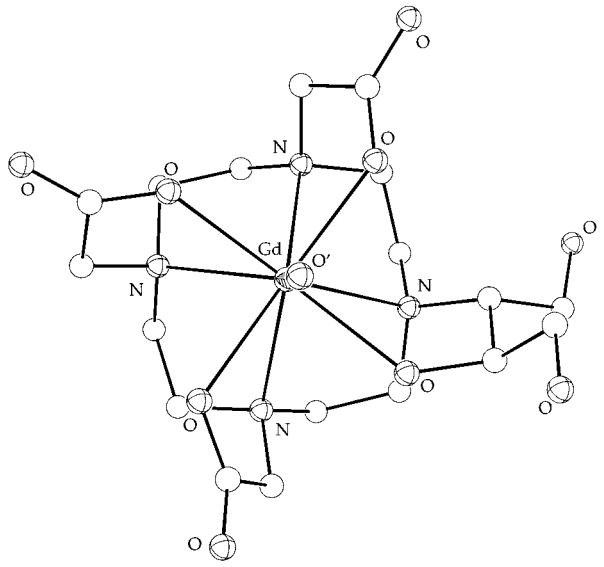


Figure 15. ORTEP drawing of [Gd(DO3A-butrol)] (twisted CSAP isomer). The capping position (O′) is occupied by a bridging carboxylate oxygen (ref 48).

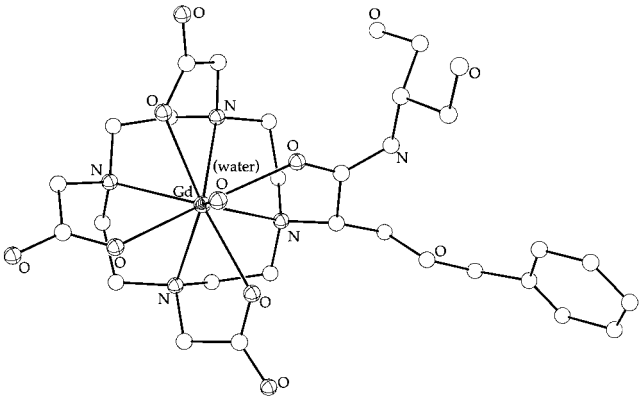


Figure 16. ORTEP drawing of [Gd(DO3A-L2)(H_2O)] (CSAP isomer) as viewed looking down the metal−water bond (ref 49).

rable to the M−O (carboxylate) distances and significantly shorter than the M−O (water) distance (Table 4).

Howard et al. reported the crystal structure for the Eu(III) complex of TCE-DOTA (Chart 6).[50] The ligand was synthesized as a mixture of stereoisomers defined by the absolute configuration at the chiral carbon. Two enantiomers, the (*RRRR*) and (*SSSS*) complexes, with opposite helicities crystallized together. The Eu(III) ion (CN9) was coordinated to four amine nitrogen atoms, four carboxylate oxygen atoms, and a water molecule. The twist angle between the basal and capped planes was 38.4° (CSAP). The X-ray structure for the complex is shown in Figure 17.

Crystal structures of the Gd(III) complexes of DO3A and DO3MA (Chart 7) were reported.[44,51] In both structures, the Gd(III) ions were nine-coordinate with the ligands binding in a heptadentate fashion. The DO3A complex crystallized as a carbonate bridged trimer with three crystallographically independent complexes sharing the same conformation and chirality (Figure 20). The eighth and ninth coordination sites for all three complexes in the trimer were filled by a single carbonate ion. The twist angle between the basal and capped planes was 39° (CSAP). When the ligand is DO3MA, two crystallographically independent complexes formed a dimer, Figures 18 and 19. The remaining two coordination sites in one of the metal centers were occupied by water molecules. The remaining two coordination sites of the second metal center in the dimer were filled by a bidentate carboxylate group which bridged from the first complex. The two complexes have diastereomeric conformations with a twist angle between the basal and capped planes of 38° around one metal center and 29.7° around the other, so that both CSAP and twisted CSAP geometries were present in the structure. In both crystal structures, the four amine nitrogens in each complex were coplanar as were the four oxygens that defined the capped face. The Gd(III)−N distances to the secondary nitrogens were shorter than those to the tertiary nitrogens by ca. 0.1 Å.

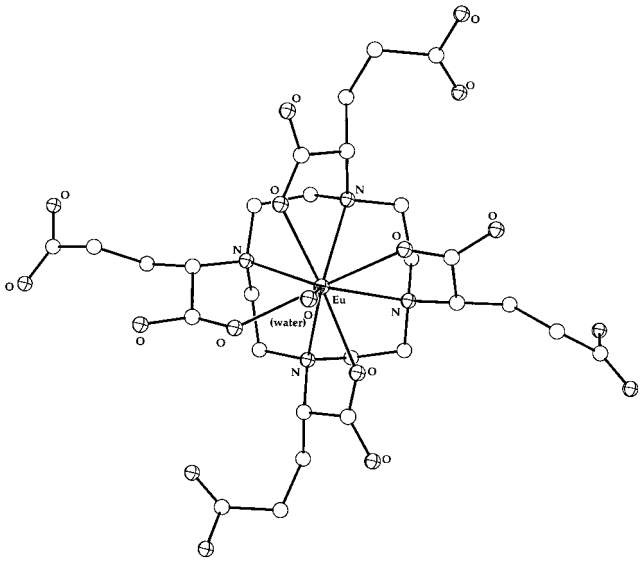


Figure 17. ORTEP drawing of $[Eu(TCE\text{-}DOTA)(H_2O)]^{5-}$ (CSAP isomer) as viewed looking down the metal−water bond (ref 50).

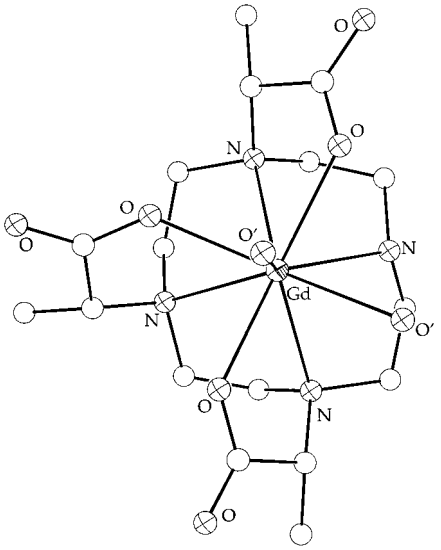


Figure 18. ORTEP drawing of the CSAP diastereomer contained in the dimer $[Gd_2(DO3MA)_2(H_2O)_2]$. Two water molecules (O′) occupy prismatic and capping positions around the metal center (ref 51).

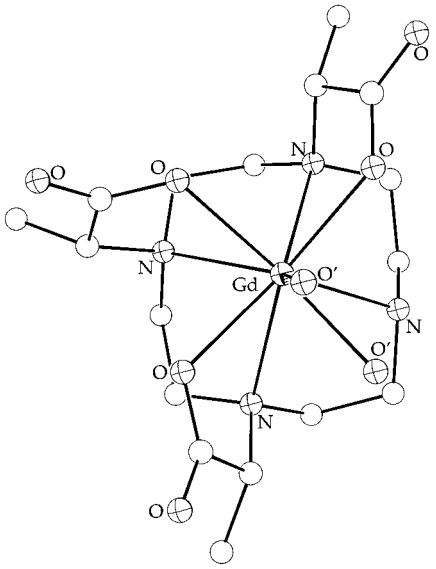


Figure 19. ORTEP drawing of the twisted CSAP diastereomer contained in the dimer $[Gd_2(DO3MA)_2(H_2O)_2]$. Two bridging carboxylates (O′) occupy prismatic and capping positions around the metal center (ref 51).

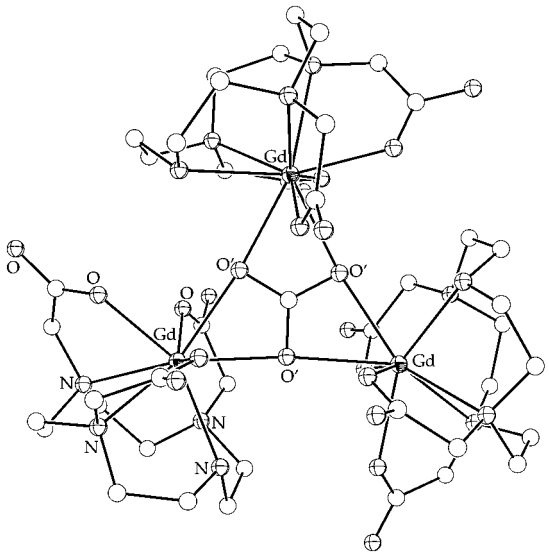


Figure 20. ORTEP drawing of the trimer $\{[Gd(DO3A)]_3[CO_3]\}^{2-}$. Carbonate oxygens (O′) occupy prismatic and capping positions around each metal center (ref 44).

The structures of the Y(III), La(III), Eu(III), and Yb(III) complexes of DOTBzP (Chart 8) were reported.[52,53] The eight-coordinate Y(III), Eu(III), and Yb(III) complexes crystallized without a water molecule in the inner coordination sphere. The X-ray crystal structure for the Y(III) complex is shown in Figure 21. The four amine nitrogens were coplanar, as were the four donor phosphinate oxygens. The twist angle between the nitrogen and oxygen planes was ca. 29°, resulting in twisted square antiprismatic geometries. In contrast, the La(III) complex was nine-coordinate with a water molecule capping the phosphinate oxygen face of the molecule. The four amine nitrogens in this complex were slightly folded at 6.5°. The twist angle between the N_4 and O_4 planes was also ca. 29° (twisted CSAP).

Chart 7

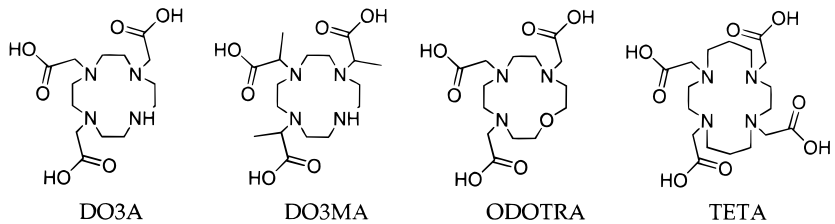
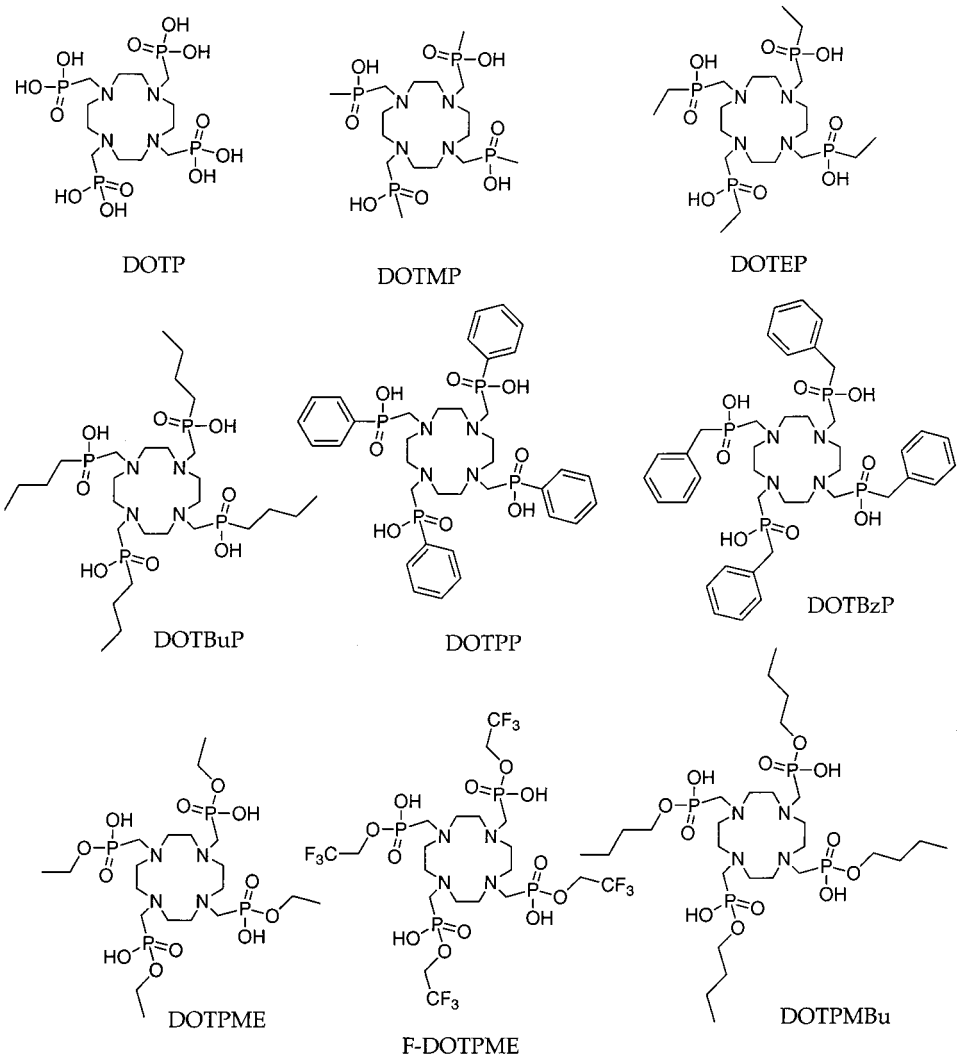


Chart 8



Several structural features are common to the Ln(III) complexes of ligands derived from tetraazacyclododecane. In these structures the macrocycle adopts a square [3333] conformation,[54] forming the basal plane in a square antiprismatic arrangement of donor atoms (see Figure 1). In the examples provided here, the opposite face of the prism is occupied by a planar arrangement of oxygen donors (carboxylate, water, hydroxyalkyl, amide, or phosphinate). As expected for square antiprismatic arrangements, the N_4 plane and the O_4 plane are parallel to each other. The metal ions typically do not occupy the center of the polyhedron, but are shifted toward the O_4 face. This was also observed for the Tb(III) complex of the cyclam-derived ligand TETA and presumably results from differences in donor atom affinity rather than differences in donor atom radii or ligand constraints. One defining feature in these cyclen-derived complexes is the twist angle between the N_4 and O_4 planes. Two angles are possible depending upon the quadrangular conformation of the tetraazacyclododecane ring and the helicity of the complex (see Figures 29 and 31). As a result, two diastereomeric conformations, CSAP and twisted CSAP, are found among the solid state structures. Important bond distances are provided in Table 4.

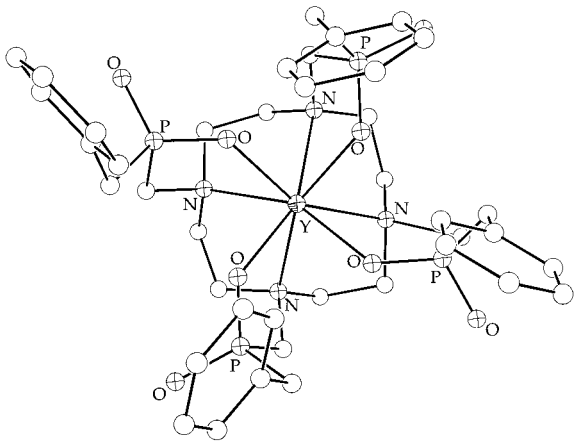


Figure 21. ORTEP drawing of $[Y(DOTBzP)]^-$ (twisted CSAP) as viewed looking down the metal−water bond (ref 52).

Spirlet et al. reported the crystal structure for the Gd(III) complex of ODOTRA (Chart 7).[55] The complex contained a nonacoordinate Gd(III) ion coordinated to three amine nitrogens, one ether oxygen, four carboxylate oxygens, and a water molecule in the capping position (Figure 22). The complex crystallized as an infinite chain with bridging η^1 carboxylate groups shared between adjacent chelates. The three

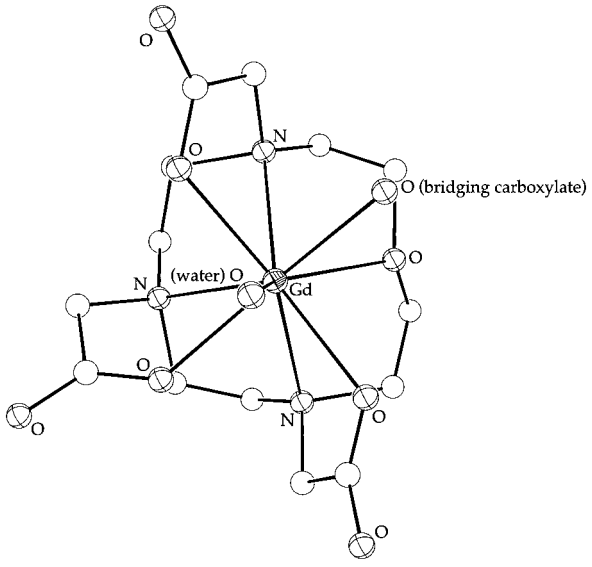


Figure 22. ORTEP drawing of [Gd(ODOTRA)(H_2O)] as viewed looking down the metal−water bond. A prismatic corner is occupied by a bridging carboxylate (ref 55).

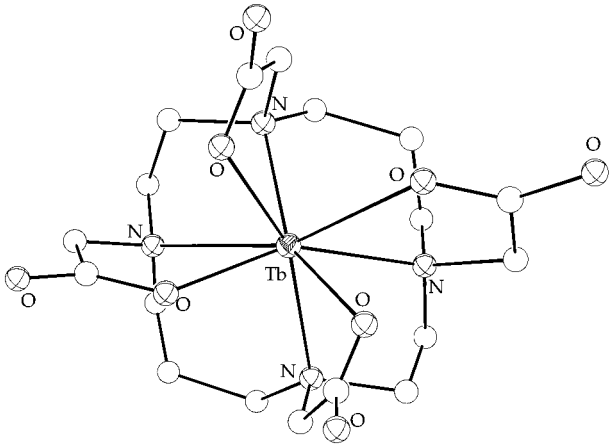


Figure 23. ORTEP drawing of $[Tb(TETA)]^-$ (ref 56).

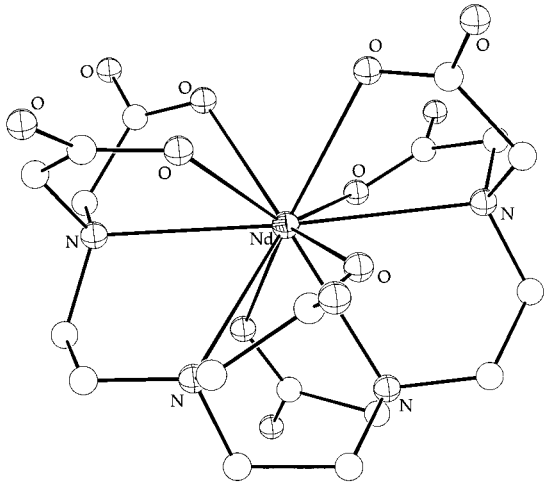


Figure 24. ORTEP drawing of $[Nd(TTHA)]^{3-}$ (ref 62).

amine nitrogens and one ether oxygen were coplanar, forming the basal plane of the prism. The four carboxylates forming the monocapped plane were also coplanar. The twist angle between the faces averaged 30.7° (twisted CSAP).

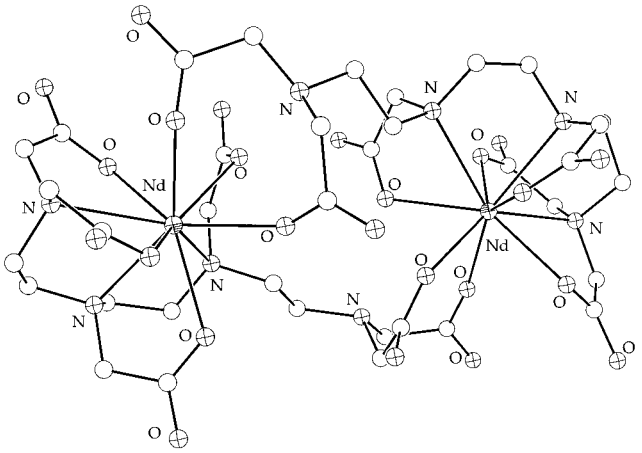


Figure 25. ORTEP drawing of the dimer $[Nd_2(HTTHA)_2]^{4-}$ (ref 60).

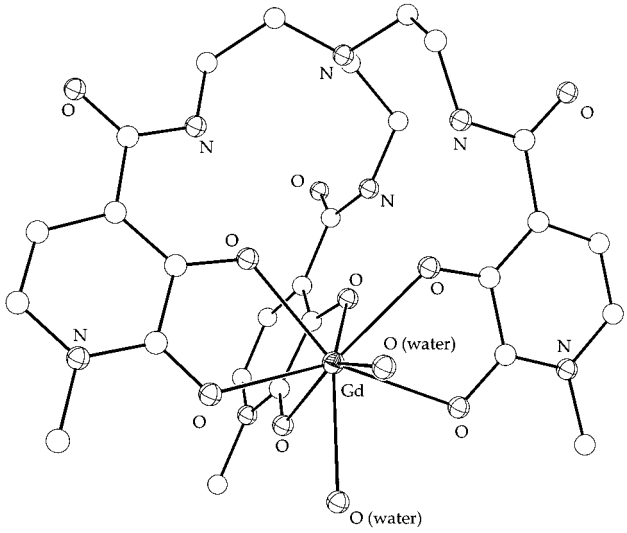


Figure 26. ORTEP drawing of [Gd(HOPO)(H_2O)$_2$] (ref 64).

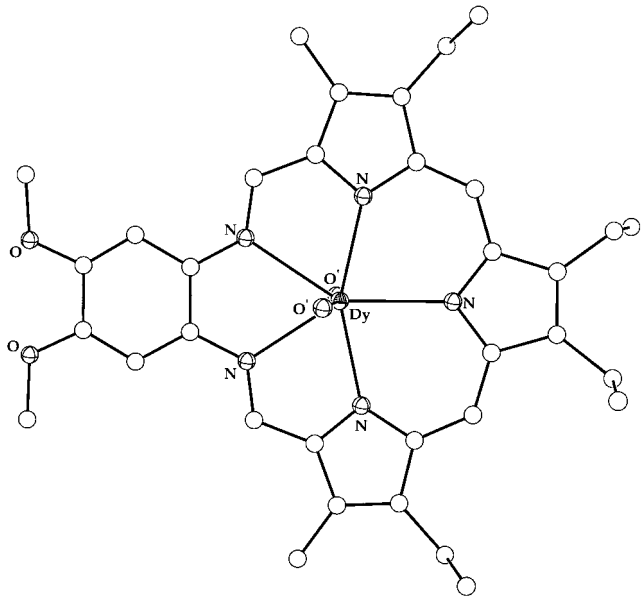
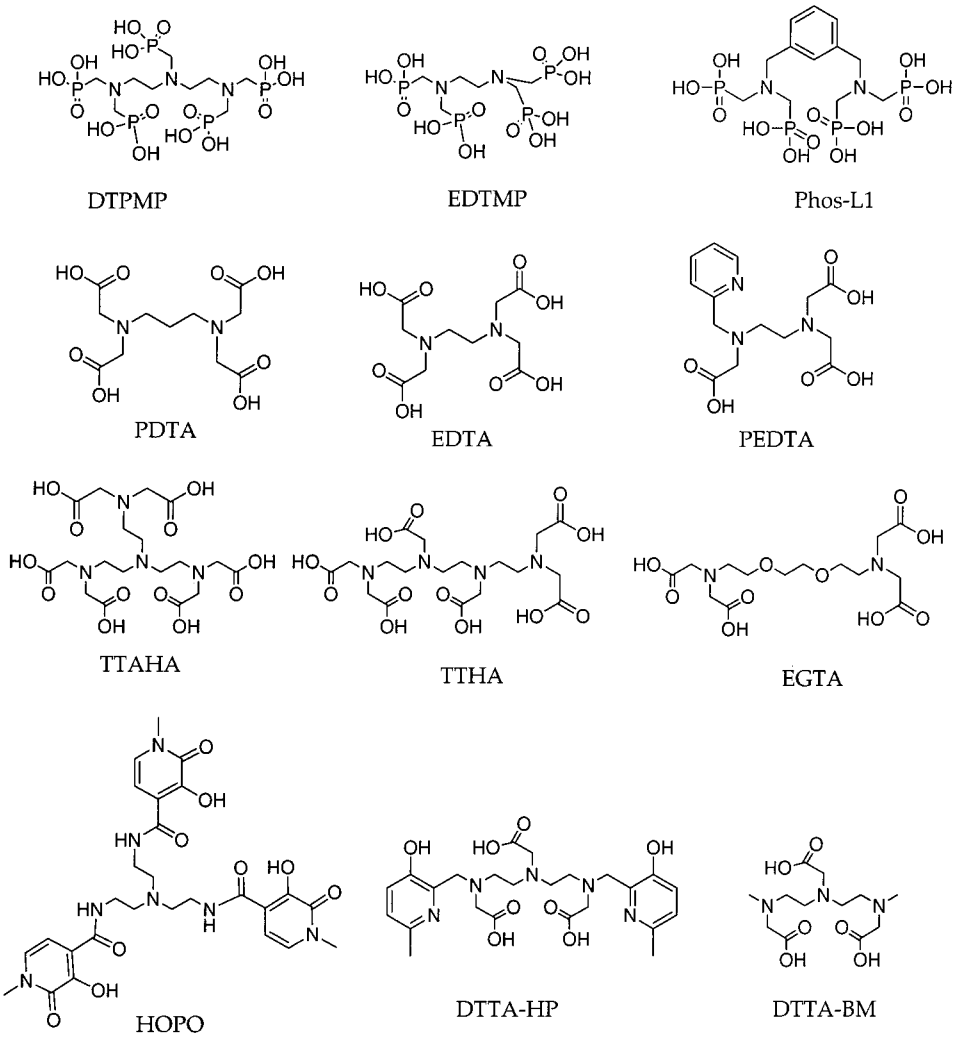


Figure 27. ORTEP drawing of $[Dy((C_6H_5)_2PO_4)_2]$. Two diphenyl phosphate oxygens (O′) occupy axial coordination sites in the complex (ref 66).

The Tb(III) structure of TETA (Chart 7) was reported by Spirlet et al.[56] The Tb(III) ion, which was completely encapsulated by the ligand, was eight-

Chart 9



coordinate with bonds to four amine nitrogens and four carboxylate oxygens. Unlike the related DOTA complexes, the Tb(III) complex of TETA did not have a water molecule in the inner coordination sphere. The geometry about the metal center in the TETA complex approximates a dodecahedron, Figure 23. As expected for such a geometry, a large deviation from planarity in the four nitrogens was observed. Two nitrogens were displaced from the mean plane by 0.28 Å toward the carboxylate oxygens, and two nitrogens are displaced 0.28 Å away from the carboxylate oxygens. The same pattern was observed for the oxygen donor atoms. The metal−donor atom bond distances form pairs of longer (Tb−N = 2.620 and 2.606 Å, Tb−O = 2.322 and 2.330 Å) and shorter (Tb−N = 2.575 and 2.595 Å, Tb−O = 2.302 and 2.304 Å) bonds depending upon their position in the dodecahedron.

Crystal structures of the TTHA (Chart 9) complexes of La(III),[57,58] Dy(III),[57] Gd(III),[59] Nd(III),[60] and Yb(III)[61] were recently reported. The smaller lanthanides, Dy(III), Gd(III), and Yb(III), formed nine-coordinate complexes with coordination to four amine nitrogens and five carboxylate oxygens in a distorted CSAP arrangement. The larger lanthanides, La(III) and Nd(III), formed ten-coordinate complexes involving bonding to all four amine nitrogens and all six carboxylate oxygens of TTHA, Figure 24. The ten-coordinate complexes assumed a distorted bicapped square antiprismatic geometry. In addition to their mononuclear structures, dimeric structures were observed for Nd(III),[62] Figure 25, and Gd(III)[63] complexes as well. In both dimers the metal centers were nine-coordinate with bonding to three amine nitrogens and four carboxylate oxygens from one TTHA ligand. Two free carboxylate oxygens from a ligand molecule in a neighboring complex completed the coordination sphere. Important bond distances are provided in Table 5.

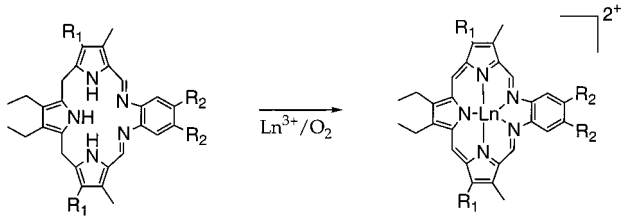
The crystal structure of the Gd(III) complex of TREN-Me-3,2-HOPO (Chart 9) was reported by Xu et al.[64] The structure featured an eight-coordinate Gd(III) center coordinated to six hydroxypyridinone oxygens and two water molecules, Figure 26. The coordination geometry about the metal ion was described as a slightly distorted bicapped trigonal prism in which one water molecule occupied a prismatic corner and the other occupied a capping position. One interesting feature of the structure was the close contact between the amide nitrogen atoms and the coordinated hydroxyl oxygen atoms (2.65 and 2.73 Å), resulting from internal hydrogen bonds (N−H···O) within the complex. The Gd(III)−O (hydroxypyridinone) distances fell in the range of 2.34−2.43

Table 5. Selected Bond Distances (Å) for Ln(III) Complexes of TTHA

complex	Ln−$O_{carboxylate}$[a]	Ln−N_{amine}[a]	ref
Na_3[Nd(TTHA)]	2.430−2.537	2.724−2.823	62
$Na_{0.5}H_{5.5}$[Nd_2(TTHA)$_2$]	2.397−2.471	2.629−2.732	60
$(CN_3H_6)_2$[La(HTTHA)]	2.464−2.535 (2.801)[b]	2.757−2.875	57
K_2[La(HTTHA)]	2.469−2.555 (2.711)[b]	2.788−2.843	58
$(CN_3H_6)_2$[Dy(HTTHA)]	2.317−2.419	2.574−2.712	57
$(CN_3H_6)_2$[Gd(HTTHA)]	2.352−2.437	2.590−2.733	59
K_3[Yb(TTHA)]	2.264−2.365	2.568−2.721	61

[a] Range of observed distances. [b] One significantly longer bond distance is listed in parentheses.

Scheme 1



Tx_1 $R_1 = CH_2CH_3$, $R_2 = OCH_3$
Tx_2 $R_1 = CH_2CH_3$, $R_2 = OCH_2CH_2CH_2OH$
Tx_3 $R_1 = CH_2CH_2CH_2OH$, $R_2 = OCH_2CH_2CH_2OH$ (PCI-0101)
Tx_4 $R_1 = CH_2CH_2CH_2OH$, $R_2 = O(CH_2CH_2O)_3OCH_3$ (PCI-0120)

Å. The Gd(III)−O (water) distances were essentially equal at 2.44 Å.

A series of pyrrole-based ligands of the type shown in Scheme 1 were reported by Sessler and co-workers. The ligand formed 1:1 complexes with Ln(III) ions in the solid state. Oxidation and metalation of the texaphyrin in the presence of a Ln(III) cation yields $[Ln(Tx)]^{2+}$ in which the texaphyrin ring has lost a proton and acts as a monoanion. Structures for the La(III), Gd(III), and Dy(III) (Figure 27) complexes ($R_1 = CH_2CH_3$, $R_2 = OCH_3$), the Lu(III) complex ($R_1 = CH_2CH_3$, $R_2 = OCH_2CH_2CH_2OH$), and the Eu(III) and Gd(III) complexes ($R_1 = CH_2CH_2CH_2OH$, $R_2 = OCH_2CH_2CH_2OH$) were reported.[65,66,244] In the latter instance the crystals of the Eu(III) and Gd(III) complexes were isomorphous. In all of the structures the Ln(III) cations coordinated to all five ring nitrogens of the macrocycle and were axially ligated by counterions and solvent molecules. A buckling of the macrocycle framework was observed which increased with increasing size of the Ln(III) cation. Important bond distances are provided in Table 6.

A comprehensive review of lanthanide complexes of macrocyclic ligands was recently published by Alexander.[67] Lanthanide complexes of EGTA[68−70] as well as Eu(III)[71,72] and Gd(III)[73] complexes of DOTA tetraamides have also been reported.

B. Solution Methods

Contrast agents function in an aqueous environment. Solid state structures provide a wealth of information, but it is imperative to confirm the solution structure in order to to understand the biophysical properties of the molecule. Contrast agents are generally ternary complexes—Gd(III), a multidentate ligand, and one or more water ligands. Determination of the hydration number, q, of a gadolinium complex is crucial to understanding its contrast agent properties. One method to determine q is laser induced luminescence. Horrocks and Sudnick[74] showed that Tb(III) or Eu(III) fluorescence is better quenched in H_2O than in D_2O because of better coupling to the O−H oscillators than to the O−D oscillators. If the fluorescent lifetimes are measured in D_2O and H_2O, the ratio of the fluorescence decay constants in both solvents is proportional to q. Parker and co-workers have extended this approach by applying a correction which allows for the contributions of closely diffusing water molecules and of other proton exchangeable oscillators.[343] Since this method involves the use of Tb(III) or Eu(III), ions which flank Gd(III) in the periodic table and have similar radii, the result should be an excellent indication of the hydration number for the Gd(III) complex. A further benefit of this method is the scant amount (micromolar) of material required. Hydration numbers for selected complexes are provided in Table 7.[75−87]

Any difference in chemical or structural behavior among a series of Ln(III) complexes of a particular ligand can usually be ascribed to the decrease in ionic radius on going from La(III) (1.36 Å) to Lu(III) (1.17 Å).[88] With the gradual change in metal ion radii, it is not uncommon for a ligand to form isostructural chelates within the lanthanide series. The ability to confirm an isostructural relationship between Ln(III) chelates is particularly important since solution studies often involve the use of a surrogate lanthanide to probe the structure and dynamics of a complex.

In the presence of a paramagnetic lanthanide ion, NMR chemical shifts are much larger than in the presence of a diamagnetic ion. This is referred to as the lanthanide induced shift (LIS), $\Delta\omega$. The LIS can be parametrized into a contact, ($\Delta\omega_c$) and a pseudocontact ($\Delta\omega_p$) term, eq 1. The contact term can be

$$\Delta\omega = \Delta\omega_c + \Delta\omega_p \quad (1)$$

$$\Delta\omega = \langle S_Z\rangle F + C_D G \quad (2)$$

written as the product of an entity that is characteristic of the lanthanide ion, $\langle S_Z\rangle$, and one which is characteristic of the ligand in question, F, eq 2. Similarly the pseudocontact term has a lanthanide dependent, C_D, and ligand dependent, G, factor. Calculated values for $\langle S_Z\rangle$ and C_D have been reported.[15] Equation 2 can be rewritten as eqs 3 and 4. If the observed shifts are plotted as $\Delta\omega/\langle S_Z\rangle$ versus $C_D/\langle S_Z\rangle$ (or $\Delta\omega/C_D$ versus $\langle S_Z\rangle/C_D$), the data will fall on a straight line if the lanthanide complexes are isostructural. Any major structural differences in the

$$\left(\frac{\Delta\omega}{\langle S_Z\rangle}\right) = \left(\frac{C_D}{\langle S_Z\rangle}\right)G + F \quad (3)$$

$$\left(\frac{\Delta\omega}{C_D}\right) = \left(\frac{\langle S_Z\rangle}{C_D}\right)F + G \quad (4)$$

series are indicated by a break in the pattern.[15,89]

Table 6. Selected Bond Distances (Å) for Texaphyrin Ln(III) Complexes

complex	Ln−$N_{pyrrole}$[a]	Ln−N_{imine}	Ln−O_{anion}[b]	Ln−O_{MeOH}	ref
[La(III)(Tx_1)(NO_3)$_2$(MeOH)]	2.484−2.615	2.631, 2.685	2.68	2.72	65
[Gd(III)(Tx_1)(NO_3)$_2$(MeOH)]	2.401−2.517	2.564, 2.579	2.60	2.51	65
[Dy(III)(Tx)$_1$(Ph_2PO_4)$_2$]	2.317−2.437	2.438, 2.459	2.23		66
(NO_3)[Lu(III)(Tx_2)(NO_3)(MeOH)]	2.312−2.421	2.428, 2.455	2.37	2.27	65
(NO_3)[Gd(III)(Tx_3)(NO_3)(MeOH)$_2$]	2.383−2.494	2.517, 2.536	2.49	2.49	65
(NO_3)[Eu(III)(Tx_3)(NO_3)(MeOH)$_2$]	2.395−2.500	2.517, 2.538	2.50	2.49	65

[a] Range of observed distances. [b] Average.

Table 7. Hydration Numbers for Selected Eu(III), Tb(III), and Dy(III) Complexes

ligand	q	method	ref
DTPA	1.2 ± 0.5	Eu(III) luminescence	75
DTPA	1.3 ± 0.2	^{17}O Dy.I.S.	76
DTPA	1.2 ± 0.2	Eu(III) luminescence	77
DTPA	1.1	Tb(III) luminescence	78
DTPA	1.08 ± 0.11	Eu(III) luminescence	343
DTPA	1.10 ± 0.11	Tb(III) luminescence	343
BOPTA	1.2 ± 0.5	Eu(III) luminescence	79
DTPA-BPA	1.0 ± 0.2	^{17}O Dy.I.S.	80
DTPA-BPA	1.0 ± 0.2	Eu(III) luminescence	77
15-DTPA-en	1.2 ± 0.2	^{17}O Dy.I.S.	81
15-DTPA-en	2.3 ± 0.5	Eu(III) luminescence	82
30-DTPA-enDTPA-en	0.8 ± 0.2	^{17}O Dy.I.S.	81
30-DTPA-enDTPA-en	1.2 ± 0.5	Eu(III) luminescence	82
DOTA	1.0 ± 0.3	^{17}O LIS	83
DOTA	1.2 ± 0.4	Eu(III) luminescence	84
DOTA	1.2	Eu(III) luminescence	75
DOTA	1.0 ± 0.1	Tb(III) luminescence	85
DOTA	1.2 ± 0.5	Eu(III) luminescence	86
DOTA	0.9 ± 0.5	Tb(III) luminescence	86
DOTA	0.98 ± 0.10	Eu(III) luminescence	343
DOTA	1.05 ± 0.11	Tb(III) luminescence	343
TCE-DOTA	1.06 ± 0.11	Eu(III) luminescence	343
TCE-DOTA	0.60 ± 0.06	Tb(III) luminescence	343
HP-DO3A	1.3 ± 0.1	Tb(III) luminescence	85
DO3A	1.9 ± 0.5	Eu(III) luminescence	79
DO3A	1.8 ± 0.2	Tb(III) luminescence	85
DO3A	1.80 ± 0.18	Eu(III) luminescence	343
DOTP	0.4 ± 0.5	Eu(III) luminescence	79
F-DOPTME	0	^{17}O Dy.I.S.	87
DOTBzP	0	Eu(III) luminescence	343
DOTBzP	0	Tb(III) luminescence	343
DOTMP	0.01	Eu(III) luminescence	343
DOTMP	0.05	Tb(III) luminescence	343
DOTMP-MBBzA	0.58 ± 0.06	Eu(III) luminescence	343
DOTMP-MBBzA	0	Tb(III) luminescence	343
TETA	0.6	Eu(III) luminescence	75
TTHA	0.2	Tb(III) luminescence	78
TTHA	0.2 ± 0.2	^{17}O Dy.I.S.	76

When the chemical shift data for the Ln(III) complexes of DOTBzP were plotted according to eqs 3 and 4, the data fell into two classes: the larger lanthanides, Ce(III) to Nd(III), lay on one line and the smaller ions, Eu(III) to Yb(III) lay on another. This was ascribed to a change in the coordination number at the metal center.[53] Examination of the ^{17}O LIS of water is a ready means of confirming the constancy of a hydration number, q, across the lanthanide series. Geraldes, Peters, and co-workers used this method to show that the Ln(III) complexes of DTPA and DTPA-BPA are all $q = 1$.[80,90,91]

A simple application of using LIS is the method described by Alpoim et al.[76] to determine the number of bound water molecules in a Dy(III) complex. They have shown that the dysprosium induced shift (Dy.I.S.) of the ^{17}O NMR water resonance in Dy(III) chelates is proportional to q. The utility of this method is that natural abundance ^{17}O is measured, there is no need for isotopic enrichment, and the measurements take just minutes. The drawback is sensitivity; millimolar solutions are required.

The LIS effect has an r^{-3} dependence from which structural information about the chelate can be extracted, eq 5.[15] The values of ϕ, θ, and r can be computed directly from crystallographic structures.

$$G = C\left(\frac{3\cos^2\phi - 1}{r^3}\right) + C\left(\frac{\sin^2\theta\cos^2 2\phi}{r^3}\right) \quad (5)$$

Alternately, the internal coordinates of a geometrical model of the complex can be adjusted until the best agreement is reached between the experimental and the calculated NMR shifts. Ytterbium(III) is often selected as a paramagnetic center since this ion induces shifts that are essentially pseudocontact. This avoids the need to dissect the LIS into $\Delta\omega_c$ and $\Delta\omega_p$ contributions.

Paramagnetic lanthanide ions also increase the longitudinal and transverse relaxation rates of ligand nuclei, lanthanide induced relaxation (LIR). This relaxation enhancement has an r^{-6} dependence, making relaxation data useful for obtaining metal−nuclei distances. For example, Nd(III) induced ^{13}C relaxation rate enhancements were used to obtain structural information on DTPA and DTPA-bisamide chelates of Nd(III).[80,90] For paramagnetic lanthanides other than Gd(III), the correlation time which determines nuclear relaxation is the longitudinal electronic relaxation time, T_{1e}, and the dipolar contribution to T_1 for a ^{13}C nucleus is described by eq 6. Here,

$$\frac{1}{T_1} = \frac{4}{3}\left(\frac{\mu_0}{4\pi}\right)^2\left(\frac{\mu_{eff}^2\gamma_I^2\mu_B^2 T_{1e}}{r^6}\right) \quad (6)$$

μ_{eff} is the effective magnetic moment, μ_B is the Bohr magneton, γ_I is the nuclear magnetogyric ratio (^{13}C in this case), $\mu_0/4\pi$ is the magnetic permeability of a vacuum, and r is the electron spin−nuclear spin distance.

Common NMR structure elucidation experiments, e.g., COSY, 1D-NOE, NOESY, have been used to determine solution structures and to confirm their agreement with solid state X-ray crystallographic results for lanthanide complexes. Two-dimensional exchange spectroscopy (EXSY) has proven to be very valuable in the study of the dynamics of conformational equilibria and has been applied to a variety of highly stable lanthanide complexes.[41,92−96] With EXSY, chemical exchange is probed using a standard NOESY pulse sequence, where exchange effects are monitored rather than distance effects. Shukla has ex-

Table 8. Kinetic Data for Rearrangements in Ln(III) Complexes

complex	$\Delta G^{\ddagger}$ (kJ mol^{-1})	$\Delta H^{\ddagger}$ (kJ mol^{-1})	$\Delta S^{\ddagger}$ (J mol^{-1} K^{-1})	k_{ex} (s^{-1})	dynamic process[a]	ref
Pr(DTPA)	56.5(3.6)	35.2(2.0)	−71.4(5.8)	265 (278 K)	A	92
Eu(DTPA)	55.4(4.6)	38.5(2.4)	−56.8(7.0)	360 (278 K)	A	92
Yb(DTPA)	49.4(10)	37.0(5.0)	−41.7(16)	4300 (278 K)	A	92
Nd(DTPA-BPA)	53(1)			350 (283 K)	A	80
Eu(DTPA-dienH^{+})	57.5(0.3)					41
La(DTPA-BPA)	71(1)	47(8)	−84(25)	0.7 (283 K)	B	80
Lu(DTPA-BPA)	67(1)	42(8)	−88(20)	2.4 (283 K)	B	80
La(DTPA-BGLUCA)	66	34	−116	2.7 (283 K)	B	100
La(DTPA-BENGALAA)	65	37	−100	0.7 (283 K)	B	100
Lu(DOTA)	65.9(1.2)	100.5(0.6)	116(2)	18 (298 K)	C	45
Yb(DOTA)	65.9(1.0)	82(12)	52(39)		C	93
La(DOTA)	60.7(1.2)	59.4(0.8)	−4.6(3.3)	23 (278 K)	D	103
La(DOTP)	101(11)				D	105
Lu(TETA)	63.7(7.5)	71.7(5.3)	27(8)	7 (278 K)	E	114

[a] A: exchange between wrapping isomers. B: racemization of terminal backbone nitrogens. C: enantiomerization. D: ring inversion. E: exchange between dodecahedral conformations of TETA.

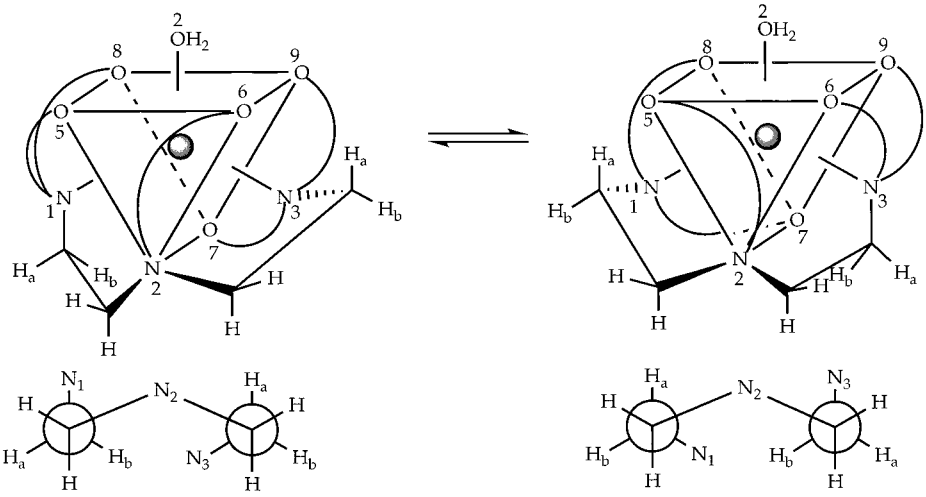


Figure 28. Rapid exchange interconversion between wrapping isomers of Ln(DTPA) results in a psuedo mirror plane, reducing the number of observed proton resonances by half.

ploited rotating-frame exchange spectroscopy (ROESY) to study the exchange dynamics of [Y(HP-DO3A)-(H_2O)].[97]

C. Solution Structures/Dynamics

1. DTPA

The ligation of Ln(III) ions by DTPA were deduced from 2D-EXSY spectroscopy (Pr(III), Eu(III), and Yb(III)) and LIR enhancements of the ^{13}C nuclei in the Nd(III) complex.[91,92] The solution structure was consistent with crystallographic results showing nonadentate coordination at the metal center involving three nitrogens and five monodentate carboxylate oxygens. Luminescence studies on the Eu(III) complex[77] and ^{17}O LIS data for a series of Ln(III) complexes[91] were consistent with a single coordinated water molecule as found in several crystal structures. At low temperatures, the proton NMR spectra for the Pr(III) and Eu(III) chelates exhibited 18 resonances corresponding to 18 nonexchangeable protons. These peaks shift and broaden with temperature until coalescing to nine resonances at 95 °C. At higher temperatures two chiral wrapping isomers exchange rapidly in solution, giving averaged signals for pairs of protons. Activation parameters for the exchange process were obtained for Pr(III), Eu(III), and Yb(III) (Table 8).[92] The major feature of the exchange process involves the shuffling of coordinated acetates accompanied by a flip of the backbone ethylenes between staggered conformations (see Figure 28). This results in a change in the helicity of the complex and leads to the equilibration of two of the acetate arms, which alternate coordination of position 7, and converts axial ethylenediamine protons to equatorial.

2. BOPTA

Uggeri et al. reported the X-ray structure, solution structure, and solution dynamics of Ln(III) complexes of BOPTA.[28] As with the DTPA complexes, BOPTA complexes can adopt two conformations depending upon the helical arrangement of the carboxylate groups around the Ln(III) center. For DTPA complexes this dynamic process involves the interconversion of enantiomers, while for complexes of BOPTA interconverting isomers of opposite helicity are not enantiomerically related. The benzyloxymethyl (BOM) substituent at one acetate group results in two chiral nitrogens upon chelation. This along with the two possible wrapping isomers and the presence of a stereogenic carbon (at the point of substitution) results in 16 possible stereoisomers for

Ln(III) complexes of BOPTA. The observed temperature dependence of the ^{13}C resonances for the La(III) and Lu(III) complexes were consistent with two (or more) couples of interconverting isomers. Activation parameters for exchange processes were not reported, but are expected to reflect the data previously observed for DTPA and DTPA-bisamide complexes. The exchange process involving inversion of the central nitrogen in BOPTA complexes is unusual. This process requires significant decoordination (octadentate to tridentate) of the ligand and is unlikely to be rapid enough to be observable by NMR.

3. EOB-DTPA

Schmitt−Willich et al. have recently reported on the solution behavior of Ln(III) complexes of EOB-DTPA (Chart 2).[98] For the drug substance, the ligand is prepared as the *S* enantiomer at the chiral carbon. The ethoxybenzyl (EOB) substituent in the diethylenetriamine backbone results in chirality at the central nitrogen upon chelation. The presence of two chiral centers (one of which is enantiomerically pure) and the possibility to form two wrappping isomers result in four possible diastereomers for the chelate. ^1H and ^{13}C NMR for the La(III) complex reveal two interconvertable isomers. In both the La(III) and Gd(III) complexes, these isomers exchange very slowly and are readily separated by HPLC. For the Gd(III) complex the equilibrium ratio of the two isomers is 65:35. NMR data collected for the La(III) complex established that the two observed isomers differ in the chirality of the central nitrogen. Similar solution behavior was observed for a DTPA substituted ligand analogous to the Y(III) chelate.[99]

4. DTPA-Bisamides

Upon chelation of a DTPA-bisamide ligand, the two terminal nitrogen atoms become chiral resulting in four diastereomers (see Figure 7). Two enantiomers (wrapping isomers) exist for each diastereomer, resulting in eight possible stereoisomers for their Ln(III) complexes. Geraldes and Peters reported a detailed NMR study on the La(III), Lu(III), and Nd(III) complexes of DTPA-B^{n}PA (Chart 4).[80,90] Consistent with X-ray structures of related Ln(III) complexes (R = Me, Bz, Et), they concluded that DTPA-B^{n}PA binds these Ln(III) cations in an octadentate fashion and that all of the complexes contain one inner sphere water molecule. Eight signals for the β- and γ-^{13}C nuclei of the propyl groups were observed for the Nd(III) complex at −30 °C, indicating that all four diastereomeric pairs of conformers were present in aqueous solution. Activation parameters for the exchange process occurring between the two wrapping isomers were determined for the Nd(III) complex. These are consistent with data reported for DTPA complexes and suggest that the barrier to the exchange is determined by the eclipsing of the ethylene bridges in the transition state, which is unchanged by replacement of carboxylates with amide groups. A racemization of the terminal N-atoms was also observed. The process involves inversion of the terminal backbone nitrogens. This requires partial decoordination of the ligand (octadentate to pentadentate), resulting in a high barrier to exchange. That a similar process was not observed in studies of DTPA complexes was attributed to differences between the coordination strength of carboxylate and amide donors. Activation parameters for the racemization of the terminal nitrogens in La(III) complexes of DTPA-BGLUCA and DTPA-BENGALAA (Chart 4) were reported and were found to be consistent with those reported for DTPA-B^{n}PA.[100] The complexity in the ^{13}C spectrum of the Lu(III) complex of DTPA-BMEA (Chart 4) was attributed to these types of exchange processes.[101] On the basis of the number of resonances observed, it was suggested that at least three unsymmetric conformers of the Lu(III) DTPA-BMEA complex were present in solution. Activation parameters are provided in Table 8.[80,100]

5. Cyclic DTPA-Bisamides

Their are four possible diastereomeric pairs (cis, trans, syn, and anti) for complexes of the linear DTPA-bisamides. The steric requirements of the tether reduce this to two diastereomers (cis and syn) for the cyclic complexes. The crystal structures of the Gd(III), Y(III), and La(III) complexes of 15-DTPA-EAM revealed binuclear structures with one bound water per metal ion and bridging ligands incapable of wrapping around the metal center.[37,38] Luminescence studies on the corresponding Eu(III) complex were suggestive of two bound waters at the metal center.[82] It was postulated that, as these studies are performed under highly dilute conditions (10 μM), a monomer is present in solution and that the ligand binds in a heptadentate fashion, leaving space for two water molecules. In contrast, Dy(III) induced ^{17}O shifts were consistent with one bound water.[81] Multinuclear NMR studies showed that with the smaller Ln(III) ions (Dy(III) to Lu(III)), 15-DTPA-EAM coordinated in an octadentate fashion and monomeric species predominated. ^{13}C NMR of the Lu(III) complex revealed the presence of one diastereomer in rapid exchange with its enantiomer. The ^1H NMR spectra of Ln(III) complexes of 18-DTPA-dien indicated two pairs of isomers.[41] Variable temperature NMR and 2D-EXSY established that one of the isomers (a dynamic isomer) underwent rapid exchange with its enantiomer, while the other isomer remained static. For these complexes two types of diastereomeric pairs were available, cis and syn. The syn enantiomers can undergo exchange by flip of the backbone ethylenes between staggered conformations and shuffling of the donor acetates and amides without changing the chirality of the terminal nitrogens. However, the cis enantiomers cannot undergo exchange without inversion of the terminal nitrogens, requiring partial decoordination of the complex. The static isomer for Ln(III) complexes of 18-DTPA-dien was concluded to comprise of the cis enantiomers, while the dynamic isomer was comprised of the syn enantiomers. For the Ln(III) (Dy(III) to Lu(III)) complexes of 15-DTPA-en only the dynamic syn enantiomers are seen.[81] Because the five atoms, −C−CO−N−C−, of each amide group are constrained to be planar and the tether between amide groups, an

ethylene bridge, is small, a cis configuration is sterically unfavorable for the 15-DTPA-en complexes. The ^{13}C NMR for lanthanide complexes of 30-DTPA-en-DTPA-en revealed several species present in solution. These were assigned to three isomeric pairs; syn−syn (dynamic−dynamic), syn−cis (dynamic−static), and cis−cis (static−static) configurations.

6. DOTA

Solution NMR studies support the presence of two slowly interconverting diastereomers for Ln(III) chelates of DOTA.[93,94,96,102,103] The population of each form is dependent upon the size of the Ln(III) cation, the temperature, and the concentration of added salt. The presence of two diastereomers was supported by luminescence studies of the Eu(III) complex.[104] The structural differences between the two isomers were determined by analysis of the LIS and fitting the NMR results to an axial symmetry model of the chelates based on published X-ray data. The LIS data suggested that the difference between the two isomers arose from the layout of the acetate arms. This was supported by COSY and EXSY experiments. The difference in the arrangement of the acetates gives rise to twisted CSAP (sometimes referred to as inverted CSAP) and CSAP geometries for the two isomers. This difference was described in terms of the relative orientation of the two square planes formed by the eight donor atoms, four nitrogens forming the basal plane, and four acetates forming the monocapped plane (Figure 29). The major isomer has a CSAP geometry with a twist angle between the two planes of ca. 40°. The minor isomer has an twisted CSAP geometry with a twist angle of ca. 30°. There are four stereoisomers, two pairs of enantiomers, which can interconvert in solution by either ring inversion (interconversion of ($\delta\delta\delta\delta$) and ($\lambda\lambda\lambda\lambda$) isomers) or acetate arm rotation (interconversion of Δ and Λ isomers). Either process alone results in exchange between CSAP and twisted CSAP geometries. Both processes combined result in an exchange between enantiomeric pairs as shown in Figure 29. Activation parameters for the exchange processes are provided in Table 8. The structure of the major isomer is consistent with the X-ray analysis of the Eu(III), Gd(III), Y(III), and Lu(III) complexes. The structure of the minor isomer is consistent with the X-ray structure of the La(III) complex.

7. α-Substituted DOTA Derivatives

The introduction of chiral centers of equal configuration (*RRRR* or *SSSS*) to all four acetate arms of DOTA (as with DOTMA and TCE-DOTA), or to one acetate arm of DOTA (as with DOTA-pNB), results in four possible diastereomers upon chelation (Chart 6). The solution structure of the Yb(III) complex of DOTMA, where the configuration at each chiral carbon is (*RRRR*), was reported by Brittain and Desreux.[104] The ^1H NMR spectrum indicated the presence of only two species in solution. This observation was supported by high-resolution luminescence of the Eu(III) complex which indicated two chemically distinct species were present in solution. Two solution isomers were observed for the (*RRRR*)

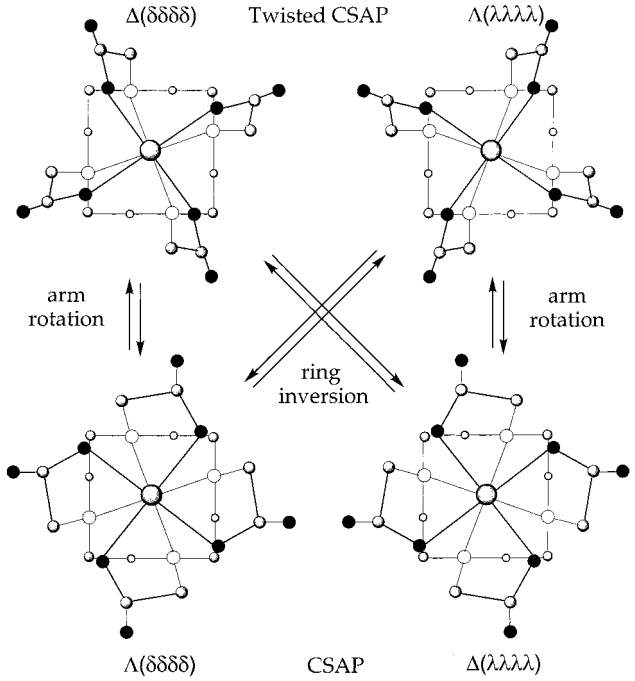


Figure 29. There are two diastereomeric conformations (CSAP and twisted CSAP) for lanthanide complexes of DOTA. Pairs of enantiomers exist for the major isomer (Δ-($\lambda\lambda\lambda\lambda$) and Λ($\delta\delta\delta\delta$)) and for the minor isomer (Δ($\delta\delta\delta\delta$) and Λ($\lambda\lambda\lambda\lambda$)) of $[Ln(DOTA)]^-$.

TCE-DOTA derivative reported by Howard et al.[50] ^1H EXSY established an exchange process between the two isomers that occurred through inversion of the macrocycle ring. Similar observations were made for the Ho(III) and Yb(III) complexes of DOTA-pNB.[95] As with the DOTA complexes, ring inversion results in an exchange between CSAP and twisted CSAP geometries which have the same helicity. Rearrangement of the acetate groups (not observed) would result in exchange between CSAP and twisted CSAP geometries of opposite helicity. The lack of such a dynamic process suggested that the configuration of the stereogenic center at carbon determines the least sterically hindered helical form of the complex. This view was supported by the solid state structures of the Eu(III) complexes (*RRRR*) and (*SSSS*) TCE-DOTA, which revealed a change in the helicity of the complex with the change in the configuration at the carbon center. In both enantiomers the substituent was equatorially positioned (pointing away from the coordination cage). The same observation was made for the Yb(III) complex of DOTA-pNB by analysis of the LIS data, showing that the substituent in both solution species is positioned equatorial from the chelate ring and away from the metal ion. The preference for a particular helicity reduces the number of diastereomers from four to two and is consistent with the NMR data reported for the DOTMA, TCE-DOTA, and DOTA-pNB complexes.

8. HP-DO3A

A number of different isomers are possible for Ln(III) complexes of HP-DO3A. The replacement of an acetate arm with a hydroxypropyl group gives rise to diastereomeric differentiation of the four expected isomers. In addition, the presence of a chiral carbon

Table 9. Rate Constants for HP-DO3A Dynamic Processes[a]

cross-peak	k_i (s^{-1})
ethylene (a)	118.37
ethylene (b)	91.70
ethylene (c)	104.16
hydroxypropyl	33.16
acetate arm (1)	21.13
acetate arm (2)	21.99

[a] For ethylene and acetate assignments, see Figure 30.

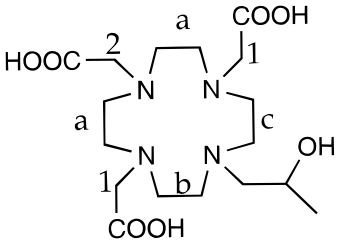


Figure 30. HP-DO3A labeled to show the groups involved in dynamic processes (Table 9).

center in the hydroxypropyl arm doubles the number of possible stereoisomers to eight (four pairs of enantiomers). ROESY analysis of the exchange dynamics for the Y(III) complex of HP-DO3A was reported by Shukla.[97] The presence of the hydroxypropyl arm introduced a site of asymmetry that enabled the chemical shift separation of the acetate arms and ethylene groups. Rearrangement of the acetate groups and inversion of the macrocycle were both observed. Exchange rates were determined using the cross-peak decay between the geminal spin pairs as a function of mixing time. These results showed that exchange of the ethylene groups in the ring is faster than exchange for the pendant arms and exchange for the hydroxypropyl arm is faster than for acetate arms (Table 9 and Figure 30). While resolution was too poor to confirm the presence of multiple diastereomers by counting peaks, the observation of the exchange processes confirmed the presence of multiple species. Two of these diastereomers, found in the crystal structures of the Y(III) and Gd(III) complexes, interconvert by ring inversion. In solution, the presence of diastereomers of opposite helicity was suggested by the observation of an exchange process involving rearrangement of the acetate arms.

9. DOTP

The ^{1}H and ^{13}C NMR spectra of the La(III) and Lu(III) complexes of DOTP (Chart 8) were consistent with a very rigid chelate structure with very long-lived metal−nitrogen and metal−oxygen bonds.[105] The tetraazacyclododecane ring was locked into a single conformation at room temperature. The barrier to inversion, 101 ± 11 kJ mol^{-1}, was considerably higher than that reported for DOTA systems. Unlike the DOTA systems, no fluxional behavior was observed for the phosphonate arms in these complexes. LIS data for ^{1}H, ^{31}P, and ^{13}C nuclei for the entire lanthanide series were reported by Geraldes et al. Analysis of the LIS data for a series of Ln(III) complexes was consistent with eight-coordinate metal ions in an isostructural series.[105,106] The average ionic form of Ln(III) complexes of DOTP at pH = 7.4 is H[Ln(III)(DOTP)].$^{4-}$[107] The highly charged complexes readily form tight ion-paired complexes with alkali and alkaline earth cations. This was exploited in the use of the Tm(III) complex as an in vivo shift reagent for ^{23}Na NMR.[108−111]

10. Phosphinates and Phosphonate Esters

As with DOTA complexes, the Ln(III) complexes of the analogous phosphonate esters and phosphinates have clockwise and counterclockwise wrapping isomers. In addition, coordination of the pendant arm results in an asymmetric center at each phosphorus. Six diastereomers are possible, *RRRR*, *RRRS*, *RRSS*, *RSRS*, *RSSS*, and *SSSS*, each with two possible wrapping isomers resulting six enantiomeric pairs (Δ*RRRR* and Λ*SSSS* are enantiomers).[112] ^{19}F NMR spectra for the Ln(III) complexes of the fluorinated phosphonate ester, F-DOTPME (Chart 8), (Ln = La, Gd, Eu, Dy, Tm, and Yb) revealed up to 16 resolved ^{19}F resonances, consistent with formation of all six possible diastereomers.[87] In contrast, the ^{1}H NMR spectra for the Y(III), Yb(III), and Eu(III) complexes of the tetraphosphinate DOTBzP showed only one species present in solution, with no fluxional behavior observed over a temperature range of 5−80 °C.[52,113] Comparison with Yb(III) data from the corresponding DOTA complex suggested that the DOTBzP complex shares the same twisted square antiprismatic structure found in the minor isomer of the DOTA complex. This is consistent with crystal structure data in which the geometry about the metal centers is twisted CSAP (twist angle ca. 29°). The structure for the Y(III) complex exhibits both *RRRR* and *SSSS* conformations at the stereogenic phosphorus centers in a 1:1 ratio of enantiomers of opposite helicity. Analysis of the ^{31}P LIS for Ln(III) complexes of DOTBzP showed a discontinuity in the structures occurring at Pr(III) (vide supra).[53] This is consistent with crystallographic data which showed a change in coordination number between the heavy and light lanthanide complexes of DOTBzP. The solution properties of the phosphinate complexes and phosphonate ester complexes are very different. While the tetra(benzylphosphinate) complex formed one enantiomeric pair of rigid diastereomers in solution, the F-DOTME complexes formed all of the possible diastereomers.

11. TETA

The solution structure and dynamics of Ln(III) TETA complexes were studied by variable temperature ^{13}C and ^{1}H NMR.[114] A conformational analysis of the Yb(III) complex of TETA using LIS data showed reasonable agreement with the crystal structure of the Tb(III) complex. A temperature dependence in the ^{1}H NMR spectra of the Yb(III) complex and the ^{13}C spectra of the Lu(III) complex was interpreted as arising from an exchange between two equivalent dodecahedral geometries. In a dodecahedral geometry, the Ln(III) complexes contain two different groups of donor atoms (high and low). The exchange was consistent with a dynamic process in which the high and low groups are continuously

moving up and down. Unlike the inversion of ring conformation in DOTA complexes, which required no substantial motion in the ligating atoms, the donor groups for the TETA complexes were rapidly exchanging between two different locations. The heavier lanthanide complexes Eu(III) to Lu(III) behaved similarly. The spectra for the lighter and larger Pr(III) ion were much more complex, indicative of a highly asymmetric structure. Kinetic parameters for the dynamic process in the Lu(III) complex are given in Table 8.

12. TTHA

The La(III), Lu(III), and Y(III) complexes of TTHA were studied by ^{1}H and ^{13}C NMR.[115] ^{13}C data for the La(III) complex showed all of the carboxylate carbon resonances shifted downfield from the free ligand, suggesting that all four amine nitrogens and all six carboxylate oxygens are bound to the metal center. This is consistent with the solid state structure reported for the La(III) complex. The spectra for the Lu(III) and Y(III) complexes were complicated by fluxional processes consistent with multiple 1:1 species present in solution. Absorption spectroscopy for the Eu(III) complex also suggested the presence of two distinct 1:1 species.[116] Monomeric and dimeric X-ray structures of the Nd(III) complex, which differ in coordination number, were reported.[60,62] The f−f transitions in the two crystals were compared to a solution of the Nd(III) complex to determine the solution ratio of monomer to dimer. The results were consistent with a 4:1 ratio of monomeric to dimeric species in solution. Analogous monomeric and dimeric structures were reported for Gd(III) and account for the two distinct species observed for solutions of the Eu(III) complex.

The solution structures of these selected lanthanide complexes generally agree with their solid state structures. Studies of exchange processes in these systems provide a rich description of the solution behavior of these complexes. The occurrence of CSAP and twisted CSAP isomers appears to be a general phenomenon of Ln(III) complexes of DOTA derivatives that naturally results from rotation of the nitrogen donor atoms upon ring inversion (Figure 31). A similar interconversion between gauche conformations in DTPA derivatives also gives rise to multiple isomers in these systems. Another common feature among DOTA and DTPA derivatives is the influence that substituents can have upon the conformational solution equilibria. Several examples have shown that the chiral configuration of a substituent will determine the overall helicity of the complex. A well-placed substituent can reduce the symmetry in these complexes and allowed otherwise unobservable exchange processes to be investigated. For example, with [Y(HPDO3A)(H_2O)] the differentiation of each pendant arm and ethylene group allows the dynamics of each to be monitored separately. For the Gd(III) complex of EOB-DTPA, the exchange between diastereomers which differ only in the chirality of the central backbone nitrogen could be monitored by HPLC.

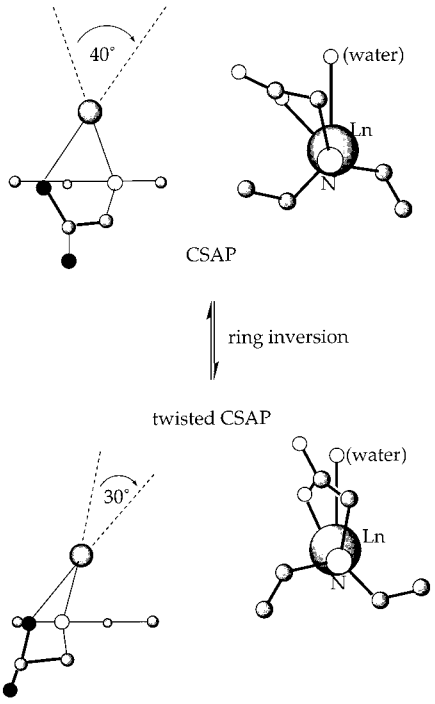


Figure 31. Two positions for the acetate arms of DOTA-type complexes results from the twisting of the macrocycle nitrogens upon ring inversion. On the right, this is viewed looking down the Ln−N bond. On the left, this is viewed looking down the Ln−water bond at one edge of the macrocycle.

D. Gadolinium(III) Chelate Stabilty

It is clear that the integrity of the gadolinium(III) complex must be maintained in vivo in order to create a safe and efficacious MRI agent. Dissociation of Gd(III) from an MRI contrast agent is undesirable, as both the free metal and unchelated ligands are generally more toxic than the complex itself. Free Gd(III) is known to bind with some avidity to serum proteins; eventually much of the released metal comes to reside in the bone, where it becomes tightly and irreversibly associated. Detection of significant amounts of Gd(III), usually by either ICP or gamma counting (in the case of Gd-153 or Gd-159 labeled complexes) in skeletal tissue is the hallmark of gadolinium(III) dissociation from a chelate.[117−119]

The exact prediction of in vivo stability on the basis of fundamental physical properties remains an uncertain science. However a number of significant studies have been published during the past decade which shed light on relevant physical properties, such as solution thermodynamics and dissociation kinetics. This section will focus on compounds for which data have been published since the previous review.[1] An emphasis is placed on clinically relevant chelate systems and those for which combinations of in vitro and in vivo biodistribution data are available.

E. Solution Equilibria and Contrast Agent Dissociation in Vivo

The solution equilibria behavior of gadolinium(III) complexes should be considered in the context of MRI contrast agent medicinal chemistry along with phar-

Table 10. Stability Constants, LD_{50}, and Gd(III) Bone Uptake Data for Selected Complexes

ligand	LD_{50}[f]	%ID[n]/gram	log K_{GdL}	log K^*_{GdL} (pH 7.4)	log K_{sel}	log K_{CaL}	log K_{CuL}	log K_{ZnL}
EDTA	0.3[m]	0.80	17.7[b]	14.70	4.23[m]	10.61[l]	18.78[l]	16.5
			17.37[l]	14.8[b]				
DTPA	5.6[m]	0.005	22.46[l]	17.70	7.04[m]	10.75[l]	21.38[l]	18.29[l]
DTPA-BMA	14.8[m]	0.03	16.85[m]	14.90	9.04	7.17[m]	13.03[m]	12.04[m]
DTPA-BMEA			16.84[b]					
DTPA-BP	2.8[m]		16.83[m]		5.32[m]			
DOTA	11[d]	NDR[o]	25.3[b]	18.33[d]	8.3[a]	17.23[e]	22.63[e]	21.05[e]
			24.6[h]	18.6[b]				
			24.0[i]					
			22.1[k]					
DO3A	7−9[a]	0.0080	21.0[b]	14.97[d]	4.13[a]	11.74[d]	22.87[d]	19.26[d]
				14.5[b]				
DO3MA			25.3[c]		8.3[a]			
HP-DO3A	12[e]	NDR[o]	23.8[b]	17.21[d]	6.95[a]	14.83[d]	22.84[d]	19.37[d]
				17.1[b]				
BOPTA			22.59[j]					

[a] Reference 123, 25.0 °C, μ = 0.1 M $(CH_3)_4NCl$. [b] Reference 47. [c] Reference 51. [d] Reference 124. [e] Reference 125. [f] Intravenous LD_{50} in mice, mmol kg^{-1}. [g] Reference 126. [h] Reference 127. [i] Reference 128. [j] Reference 28. [k] Reference 130. [l] Reference 129. [m] Reference 122. [n] Mean % ID/g in femur at 14 days, estimated from ref 121. [o] NDR = no detectable radioactivity.

macokinetics, protein binding, elimination, and safety. Equilibria between gadolinium(III) and other competing endogenous metals and anions can potentially contribute to the dissociation of gadolinium(III) from the complex, an event which removes the critical magnetic core of the drug. By design, the magnitude of the thermodynamic stability constant K_{GdL}, defined in eq 7,[120] is large for all of the clinically viable

$$M + L = ML \qquad K_{ML} = \frac{[ML]}{[M][L]} \tag{7}$$

contrast agents, ranging from $10^{16.85}$ for [Gd(DTPA-BMA)] to $10^{25.6}$ for [Gd(DOTA)] (Table 10). Clearly, the equilibrium in eq 7 lies heavily to the side of the complex, GdL, and little, if any, free metal is present at equilibrium under conditions where eq 7 is valid.

The coordination chemist will appreciate the fact that protons will compete for the ligand L as the pH is lowered; this competition must be taken into account if one is to understand the solution equilibria at physiological pH. This is critical for the multidentate, multiprotic ligands which are being discussed in this review. Given the protonation constants of the ligands and the formal stability constant K_{ML}, the conditional (or pH dependent) stability constant K^*_{ML} can be calculated using eq 8. The conditional stability constant K^*_{ML} is often used to compare the relative thermodynamic stability of different chelates at pH 7.4. Table 10 also reports the conditional stability constants for the series of clinically relevant contrast agents as well as $[Gd(EDTA)(H_2O)_n]^-$.

$$K^*_{ML} = \frac{K_{ML}}{(1 + K_1[H^+] + K_1K_2[H^+]^2 + ... + K_1K_2K_n[H^+]^n)} \tag{8}$$

where K_1, K_2, K_3, ... K_n are the stepwise protonation constants of the ligand.

Given that there is a difference in the relative thermodynamic stability of these compounds at physiological pH, how do these data correlate with observed in vivo results, particularly the deposition of dissociated gadolinium(III) in the skeleton? To investigate this question, Wedeking et al.[121] have measured the %ID (initial dose)/gram found in the femur at 7 days postinjection (mouse) for a series of clinically relevant extracellular contrast agents (Table 10) with similar pharmacokinetic and elimination characteristics. $[Gd(EDTA)(H_2O)_n]^-$ was not an approved contrast agent, but was included for comparison purposes.

When comparing the complex stability in Table 10 to the amount of gadolinium(III) found in the rodent skeleton at 7 days, it is immediately striking that while thermodynamic (K_{ML}) and conditional stability constants (K^*_{ML}) values for $[Gd(EDTA)(H_2O)_n]^-$ and [Gd(DTPA-BMA)(H_2O)] are relatively similar (for example, K^*_{GdL} = 14.9 and 14.7, respectively, for L = EDTA and L = DTPA-BMA), the amount of Gd(III) deposited in the mouse at 7 days is rather significant (~0.8%ID/gram) for $[Gd(EDTA)(H_2O)_n]^-$ and small for [Gd(DTPA-BMA)(H_2O)] (~0.03%ID/gram).[121] Likewise, the amount of Gd(III) found in the bone for $[Gd(DO3A)(H_2O)_n]$ is surprisingly small given the rather low conditional stability constant. Thus, it is clear that thermodynamics, i.e., the gadolinium(III) stability constant alone, is not sufficient to explain in vivo stability trends.

Cacheris et al. evaluated the relationship between thermodynamics and toxicity for a series of gadolinium(III) complexes and also concluded thermodynamic stability of the Gd(III) complexes in itself was insufficient to correlate observed acute toxicity (not bone deposition) for a series of Gd-153 labeled DTPA derivatives examined in rodents. In their study, the authors assumed that acute toxicity was related to the dissociation of gadolinium(III). Consideration of the relative affinity of the ligands for Gd^{3+} as well as biologically relevant cations such as Ca^{2+}, Zn^{2+}, and Cu^{2+} led the authors to propose the use of a "selectivity" factor, log K_{sel}, to accommodate the biological data. Table 10 shows the observed LD_{50} in mice,[122−125] stability constants for the ligands with Gd(III), Ca(II), Cu(II), and Zn(II),[28,47,51,126−130] as well as a selectivity factor, log K_{sel}, which was calculated using eq 9. This factor takes into account the ligand

equilibria for H^+, Gd^{3+}, Ca^{2+}, Zn^{2+}, and Cu^{2+}. At equilibrium, a ligand with a higher selectivity factor will bind Gd(III) more strongly in the presence of the competing metal ions (Ca(II), Cu(II), Zn(II)) than a ligand with a lower selectivity factor.

$$K_{sel} = K_{ML}(\alpha_H^{-1} + \alpha_{CaL}^{-1} + \alpha_{CuL}^{-1} + \alpha_{ZnL}^{-1})^{-1} \quad (9)$$

where the α's are defined below

$$\alpha_H^{-1} = 1 + K_1[H^+] + K_1K_2[H^+]^2 + K_1K_2K_3[H^+]^3 + ...K_1K_2K_3K_n[H^+]^n \quad (10)$$

$$\alpha_{CaL}^{-1} = K_{CaL}[Ca^{2+}] \quad (11)$$

$$\alpha_{CuL}^{-1} = K_{CuL}[Cu^{2+}] \quad (12)$$

$$\alpha_{ZnL}^{-1} = K_{ZnL}[Zn^{2+}] \quad (13)$$

Examination of Table 10 reveals that the compound with the highest selectivity factor, GdDTPA-BMA, also has the highest LD_{50}. Cacheris and coworkers suggested that an increase in selectivity for Gd(III) over endogenous cations substantially contributes to the high LD_{50} (indicating a lack of acute toxicity) for DTPA-BMA, and they calculate that all four complexes become toxic to 50% of the mice when approximately 13−15 μM Gd(III) is released. On the basis of these calculations, [Gd(DTPA-BMA)(H_2O)] is expected to release half of its Gd(III) as compared with $[Gd(DTPA)(H_2O)]^{2-}$. However, the studies of Wedeking[121] and others[131,132] contradict this prediction, and consistently indicate that less Gd(III) is dissociated from DTPA than from DTPA-BMA as measured by skeletal uptake or by transmetalation.

It is also noteworthy that the selectivity arguments failed for the Gd(III) complex of the macrocyclic polyaminocarboxylate ligand DOTA, presumably because of the kinetic inertness of the macrocyclic complex. This result highlights a key point: the thermodynamic selectivity index can be considered only for those complexes which have sufficiently fast dissociation and substitution kinetics such that transmetalation occurs during the time in which the gadolinium(III) complex remains in vivo.

F. Kinetic Inertness and in Vivo Dissociation of Gadolinium(III) Complexes

As noted above, dissociation and transmetalation kinetics play a key role in determining the fate of a complexed Gd(III) ion in vivo.[133] While fast kinetics are characteristic of metal complexes derived from acyclic ligands, an accumulated body of literature has shown that macrocylic complexes tend to be significantly more inert.[113,130,134−136] This is clearly the case for the polyaminocarboxylate analogues of DOTA, which form Gd(III) complexes that are exceptionally inert as well as thermodynamically stable.[137,138] These properties were exploited in the design of [Gd(HP-DO3A)(H_2O)], which is a commercially available neutral macrocyclic extracellular agent (see ProHance, Charts 1 and 6).

Table 11. Acid Dissociation Rate Constants, k_{obs}, ($[H^+]$ = 0.1 M)

ligand	Log K_{GdL}	%ID/g @ 24 h	k_{obs} (10^3 s^{-1})	$t_{1/2}$ (h)
EDTA	17.70		140000[f]	
DTPA-BMA	16.85[b]		> 20	0.18[e]
DTPA	22.2	0.3[e]	1.2	
DO3A	21.0[g]		2.37 (2)[b]	
NP-DO3A	16.0		> 20	
HP-DO3A	23.8[h]		0.064 (9)[b]	
HE- DO3A	22.3[h]		0.466[c]	
HIP-DO3A	23.9[h]		0.0582[c]	
DOTA	25.3[g]		0.021	60.2[d]
			0.0032 (3)[d]	
BOPTA	22.59[i]	0.22[e]		
DTPA-BMEA	16.84[a]			
DOTBzP		<0.05[e]	0.0239 (2)[d]	8.1[d]
DOTMP		0.08[e]	0.0104 (1)[d]	18.5[d]
DOTBuP			0.0369 (6)[d]	5.2[d]
DOTMP-MBBzA		<0.05[e]	0.00430 (8)[d]	44.9[d]
DOTMP-MBuA			0.00130 (2)[d]	153[d]
DOTBuP-MMA		0.09[e]	0.00410 (9)[d]	47[d]
DOTPP			0.0777 (6)[d]	2.5[d]

[a] Reference 126. [b] Reference 134, 25 °C, μ = 1.0 M NaCl. [c] Reference 138, Supporting Information. [d] Reference 113. [e] Reference 139. [f] Reference 121. [g] Reference 47. [h] Reference 138. [i] Reference 28.

As noted in Table 10, small but measurable differences in in vivo Gd(III) dissociation are observed for this class of complex, which have similar pharmacokinetic characteristics. To explain these variations, the Tweedle group explored the use of acid-catalyzed dissociation rates as a predictor for in vivo loss of gadolinium(III).[121] Table 11 lists acid-catalyzed dissociation constants for a series of macrocyclic and acyclic gadolinium(III) complexes. Wedeking et al. report that a good correlation exists between the acid dissociation constant determined in 0.1 M HCl and the amount of Gd(III) deposited in the bone at 7 days for the first nine entries in Table 10. Parker and coworkers have also reported a correlation between the acid-catalyzed dissociation rate and in vivo loss of Gd(III) for the series of phosphinate compounds shown in Chart 10.[113,139] These data are consistent with the accumulated body of research which has established that the macrocyclic gadolinium(III) complexes discussed here, such as GdDOTA (Chart 1), are remarkably kinetically inert.

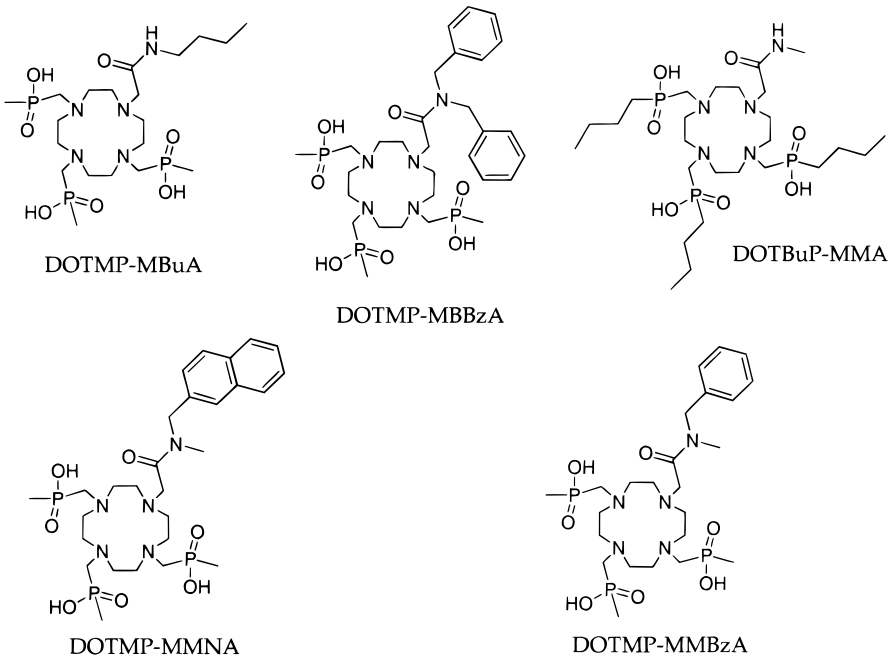
For relatively inert complexes, such as the macrocyclic agents, transmetalation is not anticipated to be an important mechanism for release of Gd(III), and acid-catalyzed dissociation should be minimal in the extracellular environment. It is not surprising that acute toxicity could result from one or more other pharmacological effects besides gadolinium(III) release. It is an important scientific goal to minimize the in vivo dissociation of gadolinium(III) from contrast agents; however, the notion that acute toxicity results predominantly from Gd(III) release is probably an oversimplification.

G. New Compounds

1. Stability Constants

The hypothesis that a high thermodynamic selectivity of a ligand system for Gd(III) over endogenous

Chart 10



ions may enhance the safety of MRI contrast agents has resulted in fundamental research efforts directed at understanding how to modulate selectivity. Consequently, a number of papers have appeared which detail the synthesis and solution equilibria of acyclic ligand systems with Gd(III), Ca(II), Cu(II), and Zn(II) (see Table 12).[123,140−144] The effect of various donor groups on metal ion selectivity is of particular relevance to the design of new contrast agents, as exemplified by the study of Paul-Roth and Raymond comparing the effect of amide vs carboxylate substitution.[145] In that report, the authors studied the effect of the amide substitution for acetate on Gd/Ca selectivity using two diethylenetriamine derivatives: DTPA-BMA, a diethylenetriaminepentaacetic acid diamide ligand, and DTTA-BM, a diethylenetriaminetriacetic acid ligand. The contribution of amide substitution to stability was found to produce selectivity for Gd(III) over Ca(II) by approximately 3.4 log units per amide group. The selectivity should be quantified by the decrease in free metal ion concentration under specified conditions and not the formation constant, because ligands have different proton basicity as well as different metal ion stability constants. Paul-Roth and Raymond used the difference in pM value, (ΔpM), as a measure of the metal ion free energy. The pM value of a complex specifies the degree of metal chelation at a given pH and is defined as −log[free metal ion] under stated conditions of total metal, total ligand, pH, and ionic strength.[146] The pM value incorporates the protonation competition effect and is useful to directly compare the relative affinities of different ligand systems for a given metal ion.

The contribution of various neutral donors to the stability of lanthanide chelation is summarized in Figure 32 (after Caravan et al.[147] and Thompson et al.[148]). The term Δlog *K* here refers to a free energy difference in binding after taking into account the difference in ligand basicity. The neutral donors which give the most increase in stability are alchoholic oxygen, pyridyl nitrogen, and amide oxygen.

The relatively low pK_a of the hydroxypyridinone functional group (Chart 9) has been exploited in the design of new contrast agents. The HOPO ligands coordinate in a hexadentate fashion to Gd(III). In these complexes, the gadolinium ion is eight-coordinate with two coordinated waters. The Gd(III) complex was found to be more stable than DTPA at pH 7.4 and to be more selective than DTPA for Gd/Ca.[64]

A significant amount of fundamental macrocyclic chemistry has been reported during the last 10 years.[28,47,49,51,107,122,126,132,140,144,145,149−155] Table 12 shows the solution equilibrium data collected for these compounds (see Charts 11−13 for ligands). There are large discrepancies in the reported values for the stability constant of some macrocyclic compounds, particularly $[Gd(DOTA)(H_2O)]^-$. These problems arise from two sources: (1) the relatively high pK_1 of the ligand, which is strongly depressed in sodium electrolyte due to cation binding,[47] and (2) the slow kinetics of the macrocyclic systems.[134] A number of competition methods have been used to determine the stability constants, including the use of competing ligands—arzenazo dye or DTPA, and metals such as Eu(III).[156,157] The latter appears to be a powerful technique, as it combines the use of a well-characterized competing ligand (DTPA) with sensitive, direct quantification of the different Eu(III) species using luminescence techniques.

Macrocyles containing amide donors have also been prepared and charcterized[49,158] and are of particular interest as a similar structure has recently been incorporated into a new macromolecular dendrimer-based agent, Gadomer 17 (see section V). One disadvantage of chelates containing amide donors is the fact that the water exchange rate is slow relative to the acetate analogues, resulting in exchange-limited relaxivity. This will be further discussed in sections IV and V.

Table 12. Stability Constants for Various Cyclic and Acyclic Gd(III) Complexes

ligand	ligand denticity	log K_{GdL}	log K_{GdL*}	pM	ΔH (kJ/mol)	ΔS (J K^{-1} mol^{-1})	ref
DTPA	8	22.46			−32.6	321	126
DTPA-BMEA	8	16.84[a]			−27.5	231	126
					−25.3[a]	238[a]	
DTPA-BMMEA	8	17.68[a]			−35.3	220	126
DTPA-BHMEA	8	17.49[a]			−35.1	217	126
DTPA-BMA	8	16.85		15.83			145
DTTA-BM	6	13.12		9.08			145
DTTA-HP	8	23.65					149
DOTA-MPA	8	20.1	16.2				158
DO3A−L2	8	25.9					49
DO3A−L1	8	26.4					49
DTPA-BGLUCA	8	16.54	15.7				132
BOPTA	8	22.59					28
DOTA	8	25.3					47
DO3MA	7	25.3					51
DO3A	7	21.1	14.5				47
DOTP	8	28.8					107
HP-DO3A	8	23.8	17.1				138
HIP-DO3A	8	23.9	16.7				138
HE-DO3A	8	22.3	16.7				138
DTPA-EAM	8	11.15					144
DTPA-PAM	8	14.49					144
DTPA-BAM	8	15.39					144
DTPA-cis$^{C=C}$BAM	8	15.56					144
DTPA-PenBAM	8	15.94					144
DTPA-OAM	8	17.44					144
NOTA	6	13.7					155
DETA	6	15.1					155
Me-DETA	6	14.7					155
Me_2−DETA	6	10.4					155
PC2A	6	16.6					152
BP2A	6	14.5					152
N_3O_6−L1	9	16.27					153
N_3O_5−L1	8	11.49					129
N_3O_6−L2	9	18.07					149
N_3O_5−L2	8	17.23					129
ODOTRA	7	21.6					154
TTAHA	10	19.00					150
PEDTA	6	15.56					150

[a] Reference 140.

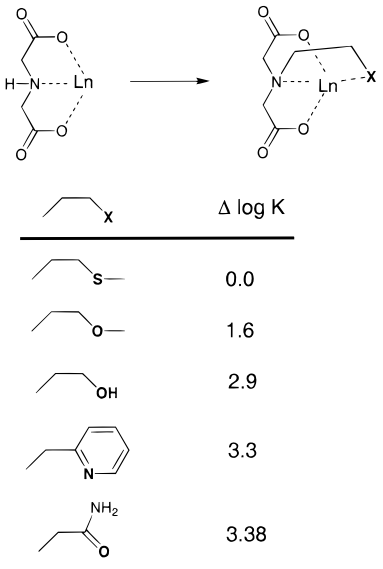


Figure 32. Relative affinity of different donor atoms for Ln(III) ions.

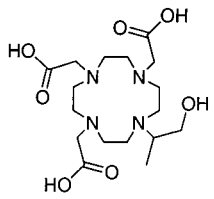
Phosphinate derivatives of macrocyclic chelates have been explored in detail by Parker and Sherry.[52,107,112,113,159−164] Many of these complexes have high thermodynamic stability to compliment their kinetic inertness.

2. Kinetic Inertness

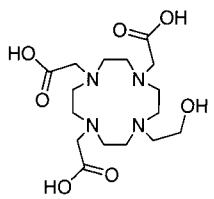
Phosphinate derivatives of the tetraazacyclododecane ring system are quite inert to acid dissociation. Table 11 shows some data obtained for a series of functionalized phosphinate derivatives. The data show that the triphosphinate monoamide macrocycles are more inert to acid dissociation than the tetraphosphinate analogues (see Charts 8 and 10 for ligand structures).

In principle, rigid acyclic ligand systems, as exemplified by the classic *trans*-cyclohexylethylendiaminetetraacetic acid (CDTA) ligand, also provide enhanced kinetic inertness relative to flexible parent ligands. For example, Choppin reported the acid dependent dissociation constant of $[Eu(EDTA)(H_2O)_n]^-$ to be 230 M^{-1} s^{-1} as compared with 6.3 M^{-1} s^{-1} for $[Ce(CDTA)(H_2O)_n]^-$, indicating that substantial differences in dissociation rates can be expected.[165] Similarly, for a series of Y(III) complexes of eight-coordinate DTPA-type ligands which included cyclohexyl and benzyl moieties in the backbone, the observed acid-catalyzed

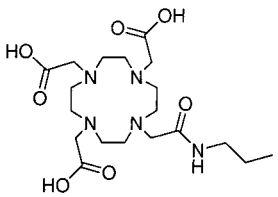
Chart 11



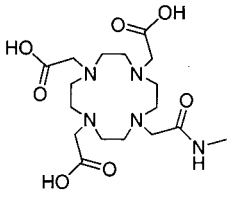
HIP-DO3A



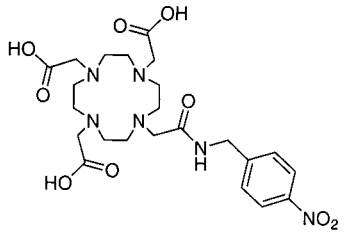
HE-DO3A



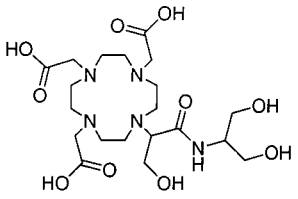
DO3A-MPA



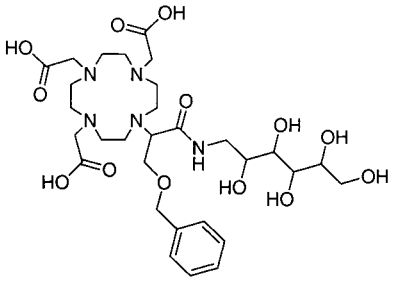
DO3A-MMA



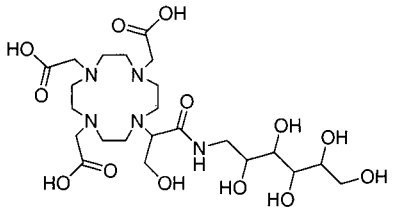
DO3A-MNBA



DO3A-L4

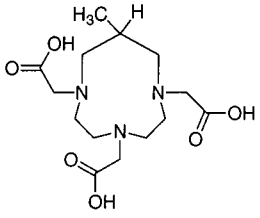


DO3A-L1

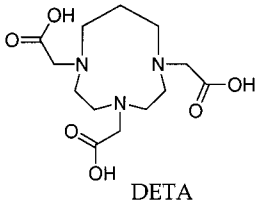


DO3A-L3

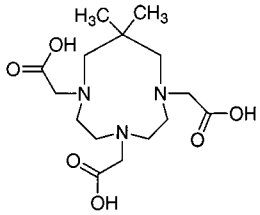
Chart 12



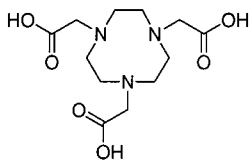
MeDETA



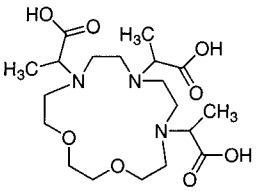
DETA



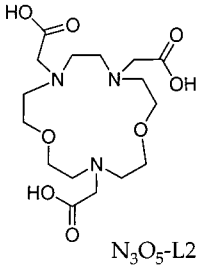
Me_2DETA



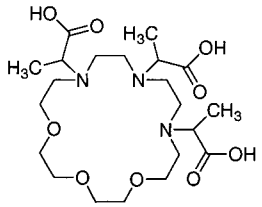
NOTA



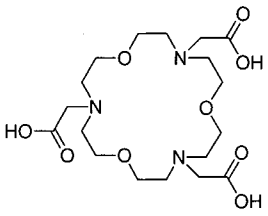
N_3O_5-L1



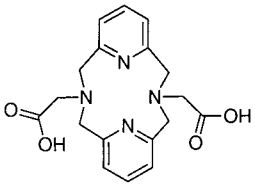
N_3O_5-L2



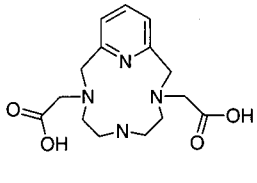
N_3O_6-L1



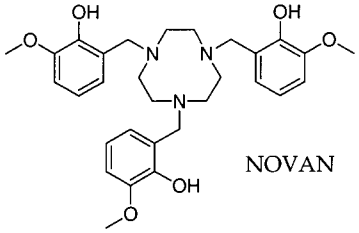
N_3O_6-L2



BP2A



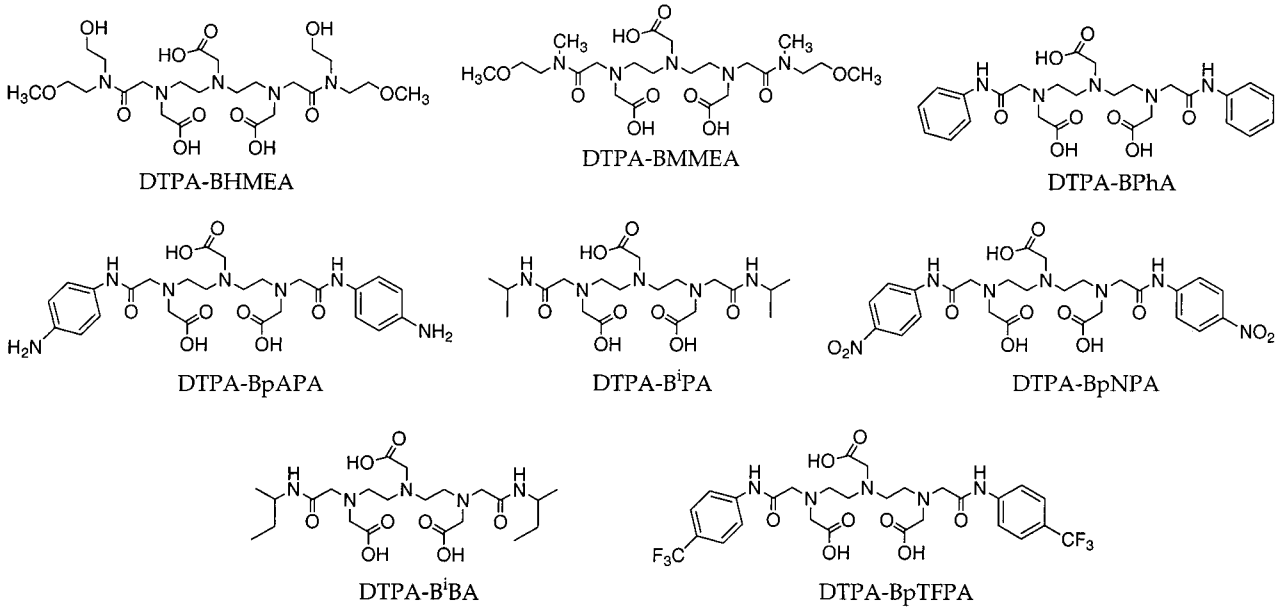
PC2A



NOVAN

dissociation rate constants varied by up to 3 orders of magnitude.[166] Too much emphasis should not be placed on acid-catalyzed dissociation; it was noted in this report that the compound with the slowest observed acid dissociation rate actually had the highest loss of radioactive Y(III) in vivo. Although the principles are general, much of this work has not yet been extended to include studies with gadolinium(III).

Chart 13



H. Summary/Future Directions

Data accumulated over the past 10 years indicate that all of the chelates utilized in the commercially available products are remarkably stable with respect to dissociation in vivo. Chemical factors which contribute to the stability include the multidentate nature of the ligand systems, high thermodynamic stability, and in some cases, remarkable kinetic inertness. In examples where significant dissociation is evident, such as the noncommercial but well-studied $[Gd(EDTA)(H_2O)_n]^-$, multiple solvent coordination sites accessible to various competing anions undoubtedly contribute to the loss of gadolinium(III). Given the interest in imaging low-concentration receptors, a significant challenge for coordination chemists in the future is to balance the need for higher relaxivity with acceptable stability.

III. Relaxation Theory

A. Introduction

Relaxation theory was discussed in detail in the previous review,[1] but will be reintroduced because it is essential to a discussion of gadolinium(III)-based contrast agents. The presence of a gadolinium(III) complex will increase the longitudinal and transverse relaxation rates, $1/T_1$ and $1/T_2$, respectively, of solvent nuclei. Diamagnetic and paramagnetic relaxation rates are additive and given by eq 14 where $(1/T_i)_{obs}$

$$(1/T_i)_{obs} = (1/T_i)_d + (1/T_i)_p \qquad i = 1, 2 \quad (14)$$

is the observed solvent relaxation rate and the subscripts "*d*" and "*p*" refer to diamagnetic and paramagnetic, respectively. The paramagnetic contribution is dependent on the concentration of paramagnetic species. Relaxivity, r_i, is defined as the slope of the concentration dependence, eq 15. Thus a plot

$$(1/T_i)_{obs} = (1/T_i)_d + r_i[Gd] \qquad i = 1, 2 \quad (15)$$

of $(1/T_i)_{obs}$ versus concentration would give the relaxivity as the slope. Relaxivity is normally expressed in units of $mM^{-1}\ s^{-1}$; however, molal concentrations should be used when dealing with nondilute systems (see section VI).

The origin of paramagnetic relaxation enhancement is generally divided into two components, inner-sphere and outer-sphere, eq 16. Inner-sphere relaxation refers to relaxation enhancement of a solvent molecule directly coordinated to the paramagnetic ion, and outer-sphere relaxation refers to relaxation enhancement of solvent molecules in the second coordination sphere and beyond (i.e., bulk solvent). This separation is used in an attempt to explain observed relaxivities in terms of existing theories. As in the previous review, the emphasis will be on the longitudinal relaxation rate $(1/T_1)$ enhancement of water hydrogen atoms since this is the effect which is of most interest in MRI.

$$(1/T_i)_p = (1/T_i)_{inner-sphere} + (1/T_i)_{outer-sphere} \qquad i = 1, 2 \quad (16)$$

B. Inner-Sphere Relaxation

The equations relating the lifetime, chemical shift, and relaxation rates of solvent molecules in the inner-sphere to NMR observables are given[167,168] in eqs 17−19.

$$\frac{1}{T_1^{IS}} = \frac{qP_m}{T_{1m} + \tau_m} \quad (17)$$

$$\frac{1}{T_2^{IS}} = qP_m \frac{1}{\tau_m}\left[\frac{T_{2m}^{-1}(\tau_m^{-1} + T_{2m}^{-1}) + \Delta\omega_m^2}{(\tau_m^{-1} + T_{2m}^{-1})^2 + \Delta\omega_m^2}\right] \quad (18)$$

$$\Delta\omega_{obs}^{IS} = qP_m\left[\frac{\Delta\omega_m}{(1+\tau_m T_{2m}^{-1})^2+\tau_m^2\Delta\omega_m^2}\right] \quad (19)$$

The IS superscript refers to inner-sphere, P_m is the mole fraction of bound solvent nuclei, q is the number of bound water (or solvent) nuclei per metal ion (i.e., the hydration number), τ_m is the lifetime of the solvent molecule in the complex (τ_m is the reciprocal of the solvent exchange rate, k_{ex}). The "m" subscript refers to the shift or relaxation rate of the solvent molecule in the inner-sphere. $\Delta\omega$ refers to the chemical shift difference between the paramagnetic complex and a diamagnetic reference.

From eq 17, one sees that if the water exchange rate is fast enough such that $\tau_m \ll T_{1m}$, then the relaxation rate enhancement experienced by the bulk solvent will depend on the relaxation rate enhancement for the coordinated solvent molecule ($1/T_{1m}$). The approach generally used to calculate the bound relaxation rates is through the Solomon−Bloembergen−Morgan equations outlined below. Further details can be obtained from the review by Kowalewski and co-workers,[169] or by consulting the books by Bertini and co-workers.[2,170]

$$\frac{1}{T_{im}} = \frac{1}{T_i^{DD}} + \frac{1}{T_i^{SC}} \qquad i = 1, 2 \quad (20)$$

$$\frac{1}{T_1^{DD}} = \frac{2}{15}\frac{\gamma_I^2 g^2 \mu_B^2 S(S+1)}{r^6}\left[\frac{3\tau_{c1}}{(1+\omega_I^2\tau_{c1}^2)} + \frac{7\tau_{c2}}{(1+\omega_s^2\tau_{c2}^2)}\right] \quad (21)$$

$$\frac{1}{T_1^{SC}} = \frac{2}{3}S(S+1)\left(\frac{A}{\hbar}\right)^2\left[\frac{\tau_{e2}}{(1+\omega_s^2\tau_{e2}^2)}\right] \quad (22)$$

$$\frac{1}{T_2^{DD}} = \frac{1}{15}\frac{\gamma_I^2 g^2 \mu_B^2 S(S+1)}{r^6}\left[\frac{3\tau_{c1}}{(1+\omega_I^2\tau_{c1}^2)} + \frac{13\tau_{c2}}{(1+\omega_s^2\tau_{c2}^2)} + 4\tau_{c1}\right] \quad (23)$$

$$\frac{1}{T_2^{SC}} = \frac{1}{3}S(S+1)\left(\frac{A}{\hbar}\right)^2\left[\frac{\tau_{e2}}{(1+\omega_s^2\tau_{e2}^2)} + \tau_{e1}\right] \quad (24)$$

$$\frac{1}{\tau_{ci}} = \frac{1}{T_{ie}} + \frac{1}{\tau_m} + \frac{1}{\tau_R} \qquad i = 1, 2 \quad (25)$$

$$\frac{1}{\tau_{ei}} = \frac{1}{T_{ie}} + \frac{1}{\tau_m} \qquad i = 1, 2 \quad (26)$$

For protons, the two relaxation mechanisms operative are the dipole−dipole (DD) mechanism and the scalar (SC) or contact mechanism. The correlation times that define dipole−dipole and scalar relaxation are τ_{ci} and τ_{ei}, respectively. At high field strengths with slowly rotating molecules the Curie spin relaxation mechanism may become important, but it is negligible at the low fields used in MRI (typically up to 1.5 T). For deuteron or ^{17}O relaxation, quadrupolar mechanisms must also be considered. Equations 21−24 apply to ions with $S > {}^1/_2$ such as Gd(III) ($S = {}^7/_2$). Here, γ_I is the nuclear gyromagnetic ratio, g is the electronic g factor, μ_B is the Bohr magneton, r is the electron spin−solvent nuclear spin distance, ω_s and ω_I are the electron and nuclear Larmor precession frequencies, respectively, and $A/\hbar$ is the electron − nuclear hyperfine coupling constant. These equations describe relaxation as a function of magnetic field (recall that nuclear or electron Larmor frequency is related to magnetic field, B, by the gyromagnetic ratio, γ, $\omega = \gamma B$). In each equation there is a characteristic correlation time, which is related to the different dynamic processes occurring on the molecular level. τ_R is the rotational correlation time related to the reorientation of the metal ion−solvent nucleus vector. T_{1e} and T_{2e} are the electronic longitudinal and transverse relaxation times for the metal ion, sometimes referred to as τ_{s1} and τ_{s2}.

To make matters more complex, the electronic relaxation rates themselves are field dependent. For Gd(III), the electronic relaxation rate is usually ascribed to a transient zero field splitting (ZFS) brought about by solvent collisions or molecular vibrations. This is described by an equation such as eq 27 where the constant B is related to the magnitude of the transient ZFS and τ_v is a correlation time for the modulation of this transient ZFS. Sometimes one sees B written as ${}^1/_5\tau_{s0}$ where τ_{s0} refers to the electronic relaxation time at zero field. Other workers use $B = (1/25)\Delta^2[4S(S+1) - 3]\tau_v$, where Δ is the trace of the ZFS tensor. For T_{2e} an analogous equation exists, where there is also a field independent term, eq 28. The validity of these expressions will be discussed further.

$$\frac{1}{T_{1e}} = B\left[\frac{1}{1+\omega_s^2\tau_v^2} + \frac{4}{1+4\omega_s^2\tau_v^2}\right] \quad (27)$$

$$\frac{1}{T_{2e}} = B\left[\frac{5}{1+\omega_s^2\tau_v^2} + \frac{2}{1+4\omega_s^2\tau_v^2} + 3\right]$$

$$B = \frac{1}{10\tau_{s0}} = \frac{\Delta^2}{50}[4S(S+1) - 3]\tau_v \quad (28)$$

At this point it may be useful to calculate some proton $1/T_1$ relaxation rates as a function of field to show the interplay between the various parameters. In eq 21, the two terms inside the square bracket (the "3 term" and the "7 term") have field dependence. The "3 term" is a function of the nuclear precession frequency while the "7 term" is a function of the electron precession frequency. Since the magnetogyric ratio is much larger for an electron than for a proton ($\gamma_s/\gamma_H = 658$), $\omega_s^2\tau_{c2}^2$ will become much greater than 1 at a much lower magnetic field than $\omega_I^2\tau_{c2}^2$.

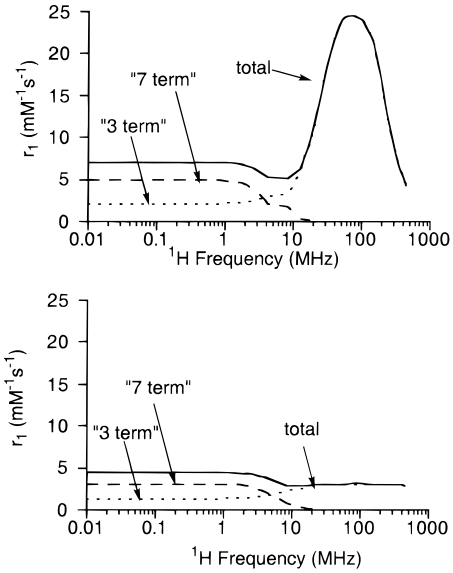


Figure 33. Simulated inner-sphere relaxivities. Top: $\tau_R = 1$ ns. Bottom: $\tau_R = 0.1$ ns. See text for other parameters.

At the field where $\omega_s^2\tau_{c2}^2$ becomes greater than 1, the "7 term" disperses away to approach zero. This is shown in Figure 33. In Figure 33 (top), where the rotational correlation time is lengthened (and hence τ_{c1} as well), the "3 term" dispersion can also be observed. It interesting to note how increasing the overall correlation times, τ_{ci}, increases the bound relaxation rate ($1/T_{1m}$). The relaxation enhancement will approach a maximum as the inverse of the correlation time, $1/\tau_{ci}$, approaches the Larmor precession frequency, ω_I.

Nuclear magnetic relaxation dispersion (NMRD), or the measurement of relaxation rates as a function of magnetic field, is widely used for characterizing contrast agents. Most often reported are proton $1/T_1$ rates for water in the presence of a Gd(III) chelate. The inner-sphere relaxation rate is described by eqs 17, 21, and 22. Because of the ionic nature of bonding in Gd(III) compounds, and the fact that the water proton is separated from the Gd(III) ion by two bonds, the hyperfine coupling constant, $A/\hbar$, is quite small. Thus the scalar mechanism, eq 22, is not very efficient; furthermore because of its $1/\omega_s^2$ dependence it has dispersed at frequencies below 10 MHz. $1/T_1^{IS}$ is determined by $1/T_1^{DD}$ (eq 21) and τ_m (eq 17). The variables in eqs 17 and 21 are: τ_m, τ_R, q, r, T_{1e}, and T_{2e}. The electronic relaxation times, T_{1e} and T_{2e}, are defined by Δ^2 and τ_v. An understanding of how these parameters influence the appearance of the NMRD curve is essential to optimizing relaxivity for a given field strength.

1. Hydration Number and Electron–Nuclear Spin Distance

From eq 17, it is clear that increasing the hydration number, q, will increase the inner-sphere relaxivity. However an increase in q is often accompanied by a decrease in thermodynamic stability and/or kinetic inertness. In attempting to understand the magnitude of relaxivity of a given compound, it is imperative to know its hydration number. Methods for determining q have been outlined in section II.

Table 13. Lanthanide(III)−Oxygen and −Deuterium Distances in Solution

complex	CN	r_{Ln-O} (Å)	r_{Ln-D} (Å)	method
$[Nd(H_2O)_9]^{3+}$	9	2.50	3.14	ND[a]
$[Sm(H_2O)_{8.5}]^{3+}$	8.5	2.46	3.11	ND[a]
$[Dy(H_2O)_8]^{3+}$	8	2.50	3.03	ND[a]
$[Yb(H_2O)_8]^{3+}$	8	2.50	2.98	ND[a]
$Gd^{3+}_{(aq)}$	7.6	2.43		XAFS[b]
$Gd^{3+}_{(aq)}$	8.0	2.37		XRD[c]
$Gd^{3+}_{(aq)}$	8.7	2.41		XAFS[d]
$[Gd(DTPA)(H_2O)]^{2-}$	9	2.490		XAFS[d]
$[Gd(DOTA)(H_2O)]^{2-}$	9	2.447		XAFS[d]

[a] ND = neutron diffraction, ref 171. [b] XAFS = X-ray absorption fine structure, ref 174. [c] XRD = X-ray diffraction, ref 175. [d] Reference 173.

The distance between the water proton and the unpaired electron spin, r, is a difficult parameter to measure and to control. Because of the $1/r^6$ dependence, a decrease of about 0.2 Å would result in a 50% increase in relaxivity according to eq 8. The Gd(III) water oxygen distance ranges from 2.41 to 2.50 Å for monomeric complexes in the solid state (vide supra). Merbach and co-workers [171,172] performed neutron diffraction first-order difference studies on the lanthanide aqua ions Nd^{3+}, Sm^{3+}, Dy^{3+}, and Yb^{3+} using the isotope substitution technique in D_2O. They concluded that Nd^{3+} was nine-coordinate, Sm^{3+} had a coordination number of 8.5 (i.e., there was a dynamic CN9−CN8 equilibrium), and Dy^{3+} and Yb^{3+} were eight-coordinate. The Ln−O and Ln−D distances are given in Table 13. The distances are shorter for the smaller (heavier) ions. This is a consequence of charge-to-radius ratio, but also of differing coordination number. For Gd^{3+}, one would expect a decrease in the Gd−O distance by decreasing the overall CN. Gadolinium−oxygen distances in solution can also be measured by X-ray measurements—X-ray absorption fine structure (XAFS) on relatively dilute solutions[173,174] and by X-ray diffraction (XRD) on more concentrated solutions.[175] It is unlikely that the change from solid state to solution would change the Gd−O bond distance, and this has been verified[173] for $[Gd(DTPA)(H_2O)]^{2-}$ and $[Gd(DOTA)(H_2O)]^{-}$.

Although Gd−O distances are relatively well defined, Gd−H distances are not. This is because the angle between the plane of the water molecule and the Gd−O vector is unknown; neutron diffraction studies, both in the solid and solution state, demonstrate that this angle can be quite varied for aqua complexes. Gd−H distances could, in principle, be measured by solution neutron diffraction. Clarkson et al.[176] used electron spin−echo envelope modulation (ESEEM) spectroscopy to examine Gd(III) complexes of TTHA, DTPA, and EDTA in deuterium oxide solution. The authors report a Gd−D distance of 2.7 Å for the coordinated water distance. This seems very short in light of the neutron diffraction studies.

Electron delocalization onto the ligand to shorten r is not a possibility for Gd(III) complexes. The bonding in Gd(III) complexes is predominantly ionic in nature, and this is reflected in the low $A/\hbar$ values for $H_2{}^{17}O$ coordinated to Gd^{3+} compared with transition metal ions. [170]

2. Rotation

Rotation is perhaps the most critical variable in these equations. It was recognized early[1] that the rotational correlation time of small Gd(III) chelates was the dominant contributor to the effective correlation time τ_{ci}. Strategies to slow rotation in order to improve relaxivity have had varying degrees of success (vide infra). Figure 33 shows calculated r_1^{IS} NMRD curves for two values of τ_R with the other parameters in eqs 17 and 21 being fixed[177] at values reported for $[Gd(DTPA)(H_2O)]^-$. The top NMRD curve is for a rotational correlation time of 1 ns and the bottom for 0.1 ns.

Rotational correlation times can be estimated in a number of ways. Equation 29 can be used for spherical molecules if a good estimate of the radius, a, and the viscosity, η, are known. The problem here is the value of a and also that, in microheterogeneous solutions, the microviscosity may differ from the measured macroscopic viscosity.

$$\tau_R = 4\pi a^3 \eta / 3kT \tag{29}$$

Other magnetic resonance techniques could be employed. Clarkson and co-workers have substituted the vanadyl ion, VO^{2+}, for Gd(III) in a variety of chelates.[178,179] The line shapes observed in the EPR spectra of VO^{2+} containing chelates are very sensitive to rotation. Simulation of the spectrum can afford a τ_R for the vanadyl ion. The problem with this technique is obvious: VO^{2+} is not Gd^{3+}. However, EPR is a very sensitive technique which can allow observation of vanadyl at physiological concentrations (sub-millimolar). Furthermore, the simulation of vanadyl EPR line shapes can distinguish between isotropic and anisotropic motion. In principle, a nitroxide spin label could be incorporated into the ligand, and similar measurements be carried out on a diamagnetic analogue of the chelate. To our knowledge, this approach has not been reported.

Merbach and co-workers often use $H_2{}^{17}O$ T_1 measurements to ascertain τ_R. ^{17}O is a quadrupolar nucleus that is dominantly relaxed via the quadrupolar relaxation mechanism (eq 30)[180] as well as by

$$\frac{1}{T_{q1}} = \frac{3\pi^2}{10}\frac{2I+3}{I^2(2I-1)}\chi^2(1+\eta^2/3)\left[\frac{0.2\tau_R}{1+\omega_I^2\tau_R^2} + \frac{0.8\tau_R}{1+4\omega_I^2\tau_R^2}\right] \tag{30}$$

dipolar relaxation in the presence of Gd(III). Here I is the nuclear spin, χ^2 is the quadrupolar coupling constant, and η is an asymmetry parameter. Gd(III) is not an efficient T_1 relaxation agent for ^{17}O. A small effect is observed, and another unknown is introduced, the $\chi^2(1+\eta^2/3)$ term. In terms of the quadrupolar coupling constant, the value for acidified water is often used. Yet there is no reason to believe that the quadrupolar coupling constant for an oxygen atom in a water molecule directly coordinated to a (+3) metal ion should be the same as that of an oxygen atom in acidified water. If the $\chi^2(1+\eta^2/3)$ term was known for a series of Gd(III) chelates (perhaps from NQR), then this method possesses some advantages. First, the measurement is being made on the Gd(III) complex—there are no metal ion substitutions. In addition, the rotation rate of the Gd(III)$-^{17}O$ vector is being probed, which is directly analogous to that of the Gd(III)$-^1H$ vector in ^1H NMRD.

Carbon-13 relaxation measurements have been made on carbon atoms in the ligand.[100,181] This technique employs a diamagnetic surrogate for Gd(III) such as Y(III), La(III), or Lu(III). The primary drawback here is the inherent insensitivity of ^{13}C NMR. High concentrations or ^{13}C labeling must be employed. High concentrations often preclude working at physiological conditions, while ^{13}C labeling may introduce synthetic challenges.

Recently, Vander Elst et al.[182] have advocated the use of deuterium labeling of the chelate and determining τ_R on a diamagnetic analogue of the Gd(III) complex. The problems here are the same as for ^{13}C: low sensitivity (although the T_1 values are shorter, leading to quicker measurements) and the synthetic challenge of deuterium labeling. In their study, [182] Vander Elst et al. labeled the α-acetate carbons of DTPA by refluxing the ligand overnight in a deuterated K_2CO_3 solution. This is not an alternative for chelates with chemically sensitive functional groups.

Fluorescence polarization spectroscopy[183] is another method of determining τ_R. This method requires the chelate to contain a fluorophore which fluoresces anisotropically and possesses a fluorescent lifetime of the same order of magnitude as τ_R. The problem here is introduction of a suitable fluorophore.

3. Water Exchange

The rate of water exchange between an inner-sphere water molecule and the bulk can usually be estimated by ^{17}O NMR by measuring the transverse relaxation rate of water in the presence and absence of a Gd(III) chelate. Merbach and co-workers[184] have shown that outer-sphere contributions to observed ^{17}O relaxation rates for Gd(III) complexes which contain inner-sphere water molecules are negligible; the observed relaxation rate is the inner-sphere relaxation rate. Because of the time scales involved and the relatively small values of chemical shifts reported for Gd(III)-aqua oxygen atoms, eq 18 reduces to eq 31. Since the oxygen is directly coordinated to the gadolinium(III) ion, $1/T_{2m}$ is dominated by the scalar term, which at high fields reduces to eq 32. A plot of $(1/T_2)_p$ vs reciprocal temperature has

$$\left(\frac{1}{T_2}\right)_p = \frac{1}{T_2^{IS}} = qP_m\left[\frac{1}{\tau_m + T_{2m}}\right] \tag{31}$$

$$\frac{1}{T_{2m}} = \frac{1}{T_2^{SC}} = \frac{1}{3}S(S+1)\left(\frac{A}{\hbar}\right)^2\left(\frac{1}{T_{1e}} + \frac{1}{\tau_m}\right)^{-1} \tag{32}$$

the form of Figure 34. It is useful to obtain data at at least two magnetic fields since $1/T_{1e}$ is field dependent, but $1/\tau_m$ is not. For very fast exchange rates, $T_{2m} \ll \tau_m$, and the $1/\tau_m$ side of the curve may not be observed. Under these conditions the residency

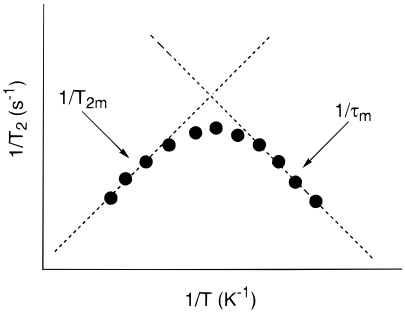


Figure 34. Contributions to the ^{17}O transverse relaxation rate for water coordinated to Gd(III). The circles represent the observed effect, and the dashed lines represent the contributions of $1/T_{2m}$ and $1/\tau_m$.

time cannot be estimated from ^{17}O relaxation measurements alone; some knowledge of T_{1e} is required.

Under neutral pH conditions, the water exchange rate and the proton exchange rate are usually equal. Determining proton exchange rates by NMR is more difficult since dipolar relaxation and outer-sphere relaxation also contribute to $(1/T_2)_p$. Aime et al. have shown that measuring relaxivity as a function of pH can be a good indicator of changes in proton residency time since this is an acid- or base-catalyzed event.[185]

4. Electronic Relaxation

T_{1e} and T_{2e} are the most difficult parameters to determine independently because of their field dependence. Equations 27 and 28 are valid only in the limit (extreme narrowing) $\omega_s^2\tau_v^2 \ll 1$.[2] This represents a monoexponential electronic relaxation process. Outside the extreme narrowing condition, electronic relaxation for an $S = {}^7/_2$ ion (e.g., Gd^{3+}) becomes multiexponential.[186] It has been proposed that at higher frequencies (fields) electronic relaxation can be described by an "average" monoexponential[2] which has the form of eqs 27 and 28. Strandberg and Westlund[186] have derived closed analytical expressions for electronic relaxation under nonextreme narrowing conditions.

The groups of Sharp,[187−195] Westlund,[196,197] Bertini,[2,198] and Kowalewski[169,199,200] have shown that when the energy of the ZFS interaction is larger than that of Zeeman energy, the SBM equations are no longer valid (the so-called low-field region). Physically, in the Zeeman (SBM) limit, the electron spin precesses about the direction of the external magnetic field axis (i.e., in the laboratory reference frame). In the ZFS limit the electron spin precesses about the principal axis of the ZFS tensor (i.e., in the molecular frame). Under these conditions (ZFS limit), nuclear relaxation is strongly dependent upon the angle, θ, between the electron spin−nuclear spin vector and the principal axis of the ZFS tensor. It is also dependent upon the symmetry of the molecule; rhombicity in the ZFS can greatly diminish nuclear relaxation. Qualitatively, the magnetic field dispersion profiles of nuclear relaxation generated using low-field theories look similar to those generated using SBM.

Electronic relaxation parameters of small molecules are often estimated by fitting NMRD curves to the SBM equations from ^1H frequencies ranging from 0.01 to 50 MHz and higher. At some point the ZFS energy will become larger than the Zeeman energy, and the SBM equations will become invalid. Low-field NMRD data fit to the SBM equations may well be "fit", but the parameters obtained may be physically meaningless.

5. Influence of Various Parameters on Inner-Sphere Relaxivity

Relaxivity will reach a maximum when the correlation time τ_{c1} is the inverse of the proton Larmor frequency. For a 0.5 T imaging spectrometer (21 MHz ^1H frequency), the optimum τ_{c1} is 7.4 ns; while for a 1.5 T magnet (64.5 MHz), the optimum τ_{c1} is 2.5 ns. Since τ_m enters into both eqs 17 and 21, there is a trade-off. From eq 17, one wants $\tau_m \ll T_{1m}$; however, if τ_m is too short, it will begin to influence T_{1m}. The optimum value for τ_m is about 10 ns. In Figure 35, the influence of T_{1e}, τ_R, and τ_m on relaxivity at two common imaging fields is displayed. At these field strengths, the "7 term" has dispersed such that T_{2e} is unimportant. These results are simulated with $q = 1$ and $r = 3.1$ Å. Doubling q would double r_1^{IS} and decreasing r would increase r_1^{IS} in an obvious manner. There are two points of interest here. The first is that the maximum relaxivity attainable will decrease with increasing field strength. The second is that as one parameter begins to be optimized, the other parameters become more critical; the slope about the relaxivity maximum is very large. A decline in maximum relaxivity with increasing field strength is offset by an increase in resolution and sensitivity at higher field. Also, T_{1e} is getting longer as field strength increases. At 0.5 T, T_{1e} may be a limiting factor, but at 1.5 T it may have lengthened to the point where it does not influence r_1. At higher fields, contrast agent design need depend on only τ_m and τ_R. The approved contrast agents lie somewhere on the front of these plots; τ_R is on the order of 0.1 ns. It is clear from Figure 35 that there is room for improvement.

6. Some Caveats Concerning SBM

Most of the preceding discussion has been based upon the Solomon−Bloembergen−Morgan equations. The validity of the description of electronic relaxation has been questioned above. A second point not addressed is that of anisotropic rotation. Strategies to increase τ_R include incorporation of a Gd(III) chelate into a polymer, dendrimer, or binding to a macromolecule. Under these circumstances there may be fast internal motion (e.g., side chain rotation) coupled with the overall rotation of the macromolecule. It can be shown that the correlation function that defines relaxation is a function of the overall motion of the macromolecule and the internal motion. This may be approximated using the model free approach of Lipari and Szabo[201] whereby a second spectral density term is added to account for the fast motion. The degree to which fast motion limits relaxation is given by an order parameter.

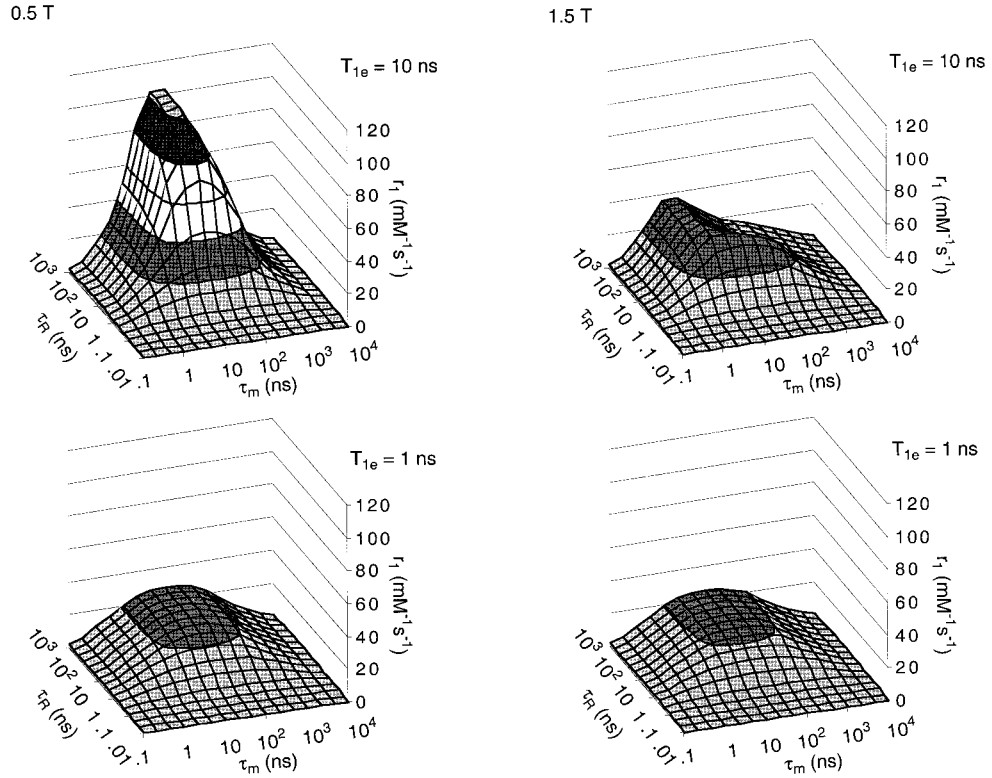


Figure 35. Inner-sphere relaxivities calculated as a function of τ_m and τ_R for various values of T_{1e} at 0.5 T (~21 MHz) and 1.5 T (~64.5 MHz).

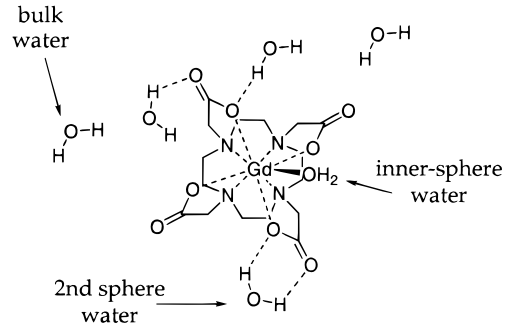


Figure 36. Three classes of water: inner-sphere (directly coordinated to Gd(III)), second-sphere (H-bonded to the complex), and bulk water.

C. Outer-Sphere Relaxation

Coordinatively saturated Gd(III) complexes also enhance relaxivity. This occurs by two mechanisms: second-sphere relaxation and outer-sphere relaxation. Second-sphere relaxation occurs when water molecules in the second coordination sphere (H-bonded to lone pairs on the carboxylate oxygen atoms), see Figure 36, are relaxed via a dipolar mechanism. This can also be described by eqs 17 and 21 where the relevant parameters are usually denoted with a prime, q', r', etc. This is difficult to quantify since the number of second-sphere water molecules is unknown, the Gd−H distance is unknown, and τ_m is very short and the likely limiting parameter in determining T_{1m}.

Outer-sphere relaxation arises from the translational diffusion of water molecules near the Gd(III) complex. Water molecules and the Gd(III) complex are often treated as hard spheres,[202,203] and the outer-sphere relaxation rates are described by eqs 33 and 34

$$\frac{1}{T_1^{OS}} = C[3j(\omega_I) + 7j(\omega_S)] \quad (33)$$

$$\frac{1}{T_2^{OS}} = C[2 + 1.5j(\omega_I) + 6.5j(\omega_S)] \quad (34)$$

$$C = \left(\frac{32\pi}{405}\right)\gamma_I^2\gamma_S^2\hbar^2 S(S+1)\frac{N_A M}{1000aD}$$

$$j(\omega) = \mathrm{Re}\{[1 + {}^1/_4[i\omega\tau_D + (\tau_D/T_{1e})]^{1/2}]/[1 + [i\omega\tau_D + (\tau_D/T_{1e})]^{1/2} + {}^4/_9[i\omega\tau_D + (\tau_D/T_{1e})] + {}^1/_9[i\omega\tau_D + (\tau_D/T_{1e})]^{3/2}]\}$$

where N_A is Avogadro's number, M is the concentration of the complex, a is the distance of closest approach of the water molecule and the complex, D is the sum of the diffusion constants of water and the complex, and τ_D is a diffusional correlation time given by $\tau_D = a^2/D$.

Separation of the two contributions in a $q = 0$ chelate is not obvious. An approach often taken in determining the inner-sphere relaxivity is to subtract the relaxivity of a $q = 0$ complex such as $[Gd(TTHA)]^{3-}$ or $[Gd(TETA)]^-$ from the observed r_1 and hope that this a reasonable estimation of outer-sphere plus second-sphere relaxivity.[77,204] Often the second-sphere contribution is ignored and the observed r_1 fit to the sum of eqs 17 and 33.

D. Data Fitting of NMRD Curves

It is apparent from the previous discussion of the complexity of the parameters determining proton

Table 14. Kinetic Parameters for Water Exchange at Various Gd(III) Complexes

ligand	k_{ex}^{25} (10^6 s^{-1})	τ_m^{37} (ns)	$\Delta H^{\ddagger}$ (kJ mol^{-1})	$\Delta S^{\ddagger}$ (J K^{-1} mol^{-1})	$\Delta V^{\ddagger}$ (cm^3 mol^{-1})	ref
aqua	804	0.94	15.3	−23.1	−3.3	177
DTPA	3.30	130	51.6	53	12.5	177
EOB-DTPA	3.60	124	49.1	45.2	12.3	215
MP-2269	4.20	102	51.6	55.8		220
COPTA	3.40					228
DTPA-N′-MA	1.90	230	50.6	40.2	10.6	215
DTPA-N-MA	1.30	346	48.6	35.7	12.7	215
DTPA-BMA	0.45	1000	47.6	22.9	7.3	177
DTPA-BMEA	0.39	1130	49.8	27	7.4	217
DTPA-BPDA	0.36	1400	41	−1.1	6.7	100
DTPA-BGLUCA	0.38	1200	47.6	21.7	6.8	100
DTPA-BENGALAA	0.22	2252	42.5	0	5.6	100
DOTA	4.10	108	49.8	48.5	10.5	177
DO3A-MNBA	1.60	317	40.9	11.1	7.7	212
$(DO3A)_2L2$	1.00	602	30	−29	0.5	177
$(DO3A)_2L6$	1.50	376	34.2	−11.7		213
$(DO3A)_2L7$	1.40	377	38.5	1.7	2.3	177
DO3A	6.25	77	44	33		225
PCTP-[13]	125	3	58	105		231
PCTA-[12]	14	34	45	43		225
PCTP-[12]	170	5	14	−40		225
EGTA	31	16	42.7	42	10.5	215
PDTA	100	8	11	−54.6	−1.5	207
taci	11	34	59.8	−89	−12.7	217

relaxation as a function of magnetic field. Assuming that SBM equations are valid and that there is no second-sphere relaxation and that outer-sphere relaxation can be described by eq 20, there are still eight parameters to be fit: τ_m, τ_R, τ_v, Δ^2, q, r, D, and a. Fitting a rather featureless curve like the NMRD profile of $[Gd(DTPA)(H_2O)]^{2-}$ to eight parameters is meaningless. Often what one sees is that certain parameters are arbitrarily fixed and a limited number fit. Unfortunately ranges of values or values with errors representing a 95% confidence limit are rarely given so that it is difficult for the reader to ascertain which parameters strongly influence the fit. For example, values of τ_m may vary over 3 orders of magnitude and still produce an identical NMRD curve for a small molecule, whereas τ_R may be limited to values within a factor of 2. Only when several of these parameters can be determined independently can any credence be given to the result of an NMRD fit.[205] Operating on this principle, the next section will discuss the relaxivities and relevant physical parameters for small molecule Gd(III) chelates.

IV. Physical Properties of Small Molecule Gadolinium Complexes

A. Water Exchange

It had been assumed that water exchange rates for Gd(III) complexes were very fast, on the order of 10^9 s^{-1}, similar to that of $[Gd(H_2O)_8]^{3+}$.[206] In 1993 Micskei et al.[184] showed that the water exchange rates for $[Gd(DTPA)(H_2O)]^{2-}$ and $[Gd(DOTA)(H_2O)]^{-}$ (Chart 1) were lower by about 3 orders of magnitude compared with the Gd^{3+} aqua ion. The Merbach group has since shown that Gd(III) water exchange rates can vary over 4 orders of magnitude.[100,177,184,207−220] Recently a tripositive europium complex was shown to have an exceedingly slow water exchange rate in a water−acetonitrile mixture.[221] If the analogous Gd(III) complex has a similar rate (which is likely), then the rate of water exchange would vary by almost 7 orders of magnitude for known complexes! In Table 14 the water exchange rates, water residency times, activation parameters, and volumes of activation determined from ^{17}O NMR are given for a host of Gd(III) complexes.

Table 15. Kinetic Parameters for Water Exchange at Ln(III)-DTPA-BMA Complexes[222]

Ln(III)	k_{ex}^{25} (10^6 s^{-1})	τ_m^{37} (ns)	$\Delta H^{\ddagger}$ (kJ mol^{-1})	$\Delta S^{\ddagger}$ (J K^{-1} mol^{-1})	$\Delta V^{\ddagger}$ (cm^3 mol^{-1})
Nd	0.53	922	43.4	10.2	−0.8
Eu	0.66	676	49.2	31.5	8.5
Gd	0.45	1000	47.6	22.9	7.3
Tb	1.61	272	50.3	42.6	9.8
Dy	3.53	127	48.9	44.4	7.3
Ho	5.98	69	54.2	66.6	9.4

The complexes clinically available are all nine-coordinate, with the polyaminopolycarboxylato ligand providing eight donors, and a water molecule occupying the ninth coordination site. These complexes all have large positive values of $\Delta V^{\ddagger}$ which is indicative of a dissociative mechanism. This is also suggested by the positive entropies of activation for these complexes, $\Delta S^{\ddagger}$.

There are two studies[222,223] on the effect of varying the lanthanide ion on the water exchange rate, and these are summarized in Tables 15 and 16. In the case of DTPA-BMA (Chart 4), water exchange at Nd(III) is the slowest and the volume of activation suggests an interchange, I, process (Table 15). The exchange rate increases by a factor of 10 on going from Nd(III) to Ho(III). In the PDTA system, where $q = 2$, the exchange rate decreases from Gd(III) to Yb(III) by almost 2 orders of magnitude. The mechanism also appears to change as $\Delta V^{\ddagger}$ is negative from Gd(III) to Tm(III) but positive for Yb(III). This suggests a change from an I_A (or A) mechanism for the gadolinium complex to an I_D (or D) mechanism

Table 16. Kinetic Parameters for Water Exchange at Ln(III)-PDTA Complexes[223]

Ln(III)	k_{ex}^{25} (10^6 s^{-1})	τ_m^{37} (ns)	$\Delta H^{\ddagger}$ (kJ mol^{-1})	$\Delta S^{\ddagger}$ (J K^{-1} mol^{-1})	$\Delta V^{\ddagger}$ (cm^3 mol^{-1})
Gd	100	8	11	−54.6	−1.5
Tb	24	30	19	−47.6	−7.6
Dy	6.6	100	24.2	−33.1	−5.5
Er	0.56	890	42.1	6.3	−6.5
Tm	0.35	1340	46	15.5	−1.2
Yb	0.28	2000	34.8	−23.6	7.4
Er(EDTA)	9.8	69	22.7	34.8	ND

for the ytterbium complex. The results are summarized in Table 16.

It is clear that changing the size of the ion can dramatically alter k_{ex}. This is not neccessarily true for altering substituents on a given ligand. The kinetic parameters for Gd(III) complexes of DTPA, COPTA, MP-2269, and EOB-DTPA (Chart 2) are all very similar. Likewise the various bisamides of DTPA all have similar kinetic parameters. This suggests that the water exchange rates for these types of chelates incorporated into macromolecules will not vary significantly, and in some instances this has been shown (see section V).

Coincidentally, $[Gd(DOTA)(H_2O)]^-$ has very similar water exchange parameters to $[Gd(DTPA)(H_2O)]^{2-}$. Replacement of one carboxylato donor by an amide donor results in a decrease in the exchange rate by a factor of 3−4.[224] The bisamides of DTPA have exchange rates which are slower still. The effect of this is that for compounds such as $[Gd(DTPA\text{-}BMA)(H_2O)]^-$ τ_m is of the same magnitude as T_{1m}. Since $r_1 \alpha 1/(T_{1m} + \tau_m)$, the relaxivity of these compounds can become limited by the slow water exchange rate. This is especially true in instances when T_{1m} can be shortened by slowing down the tumbling time of the molecule. The Eu(III) complex of the tetraamide DOTAM (Chart 14) has the slowest water exchange rate reported to date for a lanthanide. The complex $[Gd(DTMA)(H_2O)]^{3+}$ is another instance of a tetraamide ligand with an exceedingly slow water exchange rate.[185] Indeed, the relaxivity of this $q = 1$ complex is more consistent with a $q = 0$ complex at neutral pH, since for relaxivity purposes it is exchange inert.

A few other ligand systems have been studied. The $[Gd(EGTA)(H_2O)]^-$ complex exchanges faster than $[Gd(DTPA)(H_2O)]^{2-}$, dispelling simple-minded notions that complex charge dictates water exchange dynamics.[214] The pyridine-based macrocycles have different dynamic properties as well.[225,226] There is clearly room for more study to delineate the factors which influence water exchange at Gd(III).

B. Proton Exchange

Water exchange measurements give a lower limit for proton exchange, $\tau_m^O \geq \tau_m^H$. Proton exchange of a bound water molecule with the bulk is likely to be acid- or base-catalyzed as it is for proton transfer in pure water. One way to observe this is to measure proton relaxivity as a function of pH. This is best observed at low temperatures where τ_R will be longer, making T_{1m} comparable to τ_m. Aime and co-workers have observed this phenomenon for a bisamide derivative of DTPA with gadolinium(III)[227] and with the complex $[Gd(DTMA)(H_2O)]^{3+}$ noted above.[185] This may be a more widespread phenomenon, but not readily observable in chelates with shorter water residency times since $\tau_m \ll T_{1m}$. A recent report on the $[Gd(COPTA)(H_2O)]^{2-}$ complex supports this hypothesis.[228]

C. Electronic Relaxation

Electronic relaxation parameters for a selection of Gd(III) complexes (see Charts 14−16 for additional ligand structures) are listed in Table 17. The NMRD literature tends to use τ_{s0} while the EPR literature usually refers to Δ^2. Both are listed in the table with the conversion factor being given in eqs 27 and 28. A selection of EPR line widths are given in Table 18 to give a sense of T_{2e} at a given field strength.

Most of the information on electronic relaxation is indirect, coming from NMRD studies.[28,53,95,100,160,177,204,225,228−239] These data must be viewed with caution in light of the previous discussion on the uncertainty of the contribution of outer-sphere relaxation, the magnitude of r, the validity of the Bloembergen−Morgan equations describing the field dependence of T_{1e} and T_{2e} (especially at low fields), and of the large number of parameters used in fitting the data. Some generalizations can be made. DOTA-type chelates and monoamide or monohydroxyl derivatives of DOTA all have longer τ_{s0} (smaller Δ^2) values than all other Gd(III) compounds studied. Physically this translates to a higher low-field (0.01 MHz) relaxivity, and this is shown in Figure 37 along with the NMRD profiles of $[Gd(DTPA)(H_2O)]^{2-}$ and $[Gd(DTPA\text{-}BMA)(H_2O)]$. Interestingly, symmetric phosphonate, phosphinate, and phosphonic ester derivatives of DOTA do not show this effect (long τ_{s0}), suggesting that there may be another effect besides molecular symmetry which influences low-field relaxivity.

X-band line widths range from 90 to over 1200 G which is indicative of the disparate relaxation behavior of the Gd(III) ion in different environments.[237] The X-band data seem to correlate with low field relaxivity. As expected from Bloembergen−Morgan, Gd(III) EPR line widths decrease with increasing field strength, Table 18. It is interesting perhaps that the great difference in low-field electronic relaxation rate between $[Gd(DOTA)(H_2O)]^-$ and $[Gd(DTPA)(H_2O)]^{2-}$ is not nearly as marked at high field. At X-band $1/T_{2e}$ is 6−7 times faster for $[Gd(DTPA)(H_2O)]^{2-}$, but only twice as fast at Q-band, and at the highest field (5 T), only one-third as fast.

Subtle changes in solvation can have a dramatic effect on electronic relaxation. Sur and Bryant[240] showed that the addition of nitrite to a gadolinium chloride solution causes a marked decrease in X-band line width. The authors showed that this was consistent with the formation of a second-sphere nitrite complex. Addition of carbonate ion had the opposite effect.

Shukla et al.[241] carried out a pulsed EPR study at X-band over the temperature range 18−100 K and

Table 17. Electronic, Rotation, Gd(III)−H Distances, and Hydration Numbers for a Selection of Gd(III) Complexes

ligand	temp (°C)	τ_v (ps)	τ_R (ps)	τ_{s0} (ps)	Δ^2 (10^{19} s^{-2})	r	q	o.s. model	method	ref
aqua	25	7.3	41	96	11.90	3.13	1	fit	NMRD/O-17	177
DOTA	37	65	56	650	0.20	3.13	1.15	TTHA	NMRD	160
	5	9	100	430	2.15	3.13	1.15	TTHA	NMRD	160
	25	11	77	473	1.60	3.13	1	fit	NMRD/O-17	177
DOTA-pNB	39	4.9	58	497	3.42	3.02	1	fit	NMRD	95
DOTA-pNB	25	7.4	81	420	2.68	3.02	1	fit	NMRD	95
DOTA-pNB	10	15	113	271	2.05	3.02	1	fit	NMRD	95
DO3A	25	14	66	129	4.6	3.15	2	fit	NMRD	225
$(DO3A)_2L6$	25	19	171	258	1.70	3.13	1	fit	NMRD/O-17	177
$(DO3A)_2L7$	25	15	106	265	2.10	3.13	1	fit	NMRD/O-17	177
DOTEP	35	20	72	86	4.84	3.26	1	fit	NMRD	235
	25	27	107	92	3.35	3.26	1	fit	NMRD	235
	5	33	189	96	2.63	3.26	1	fit	NMRD	235
	37	18	65	49	9.45	3.13	0.7	TTHA	NMRD	160
	37	15	57	41	13.55	3.13	0.8	TTHA	NMRD	160
	5	33	180	120	2.10	3.13	0.7	TTHA	NMRD	160
	5	26	160	100	3.21	3.13	0.8	TTHA	NMRD	160
DOTPME	37	11	53	86	8.81	3.13	0.6	TTHA	NMRD	160
	37	10	43	80	10.42	3.13	0.7	TTHA	NMRD	160
	5	8.4	140	150	6.61	3.13	0.7	TTHA	NMRD	160
	5	8.4	120	140	7.09	3.13	0.8	TTHA	NMRD	160
DOTPMB	37	9.4	130	67	13.23	3.13	0.2	TTHA	NMRD	160
	37	8.2	82	41	24.79	3.13	0.3	TTHA	NMRD	160
	5	11	160	480	1.58	3.13	0.2	TTHA	NMRD	160
	5	17	110	330	1.49	3.13	0.3	TTHA	NMRD	160
DOTMP-MMBzA	37	9	61	91	10.18	3.4	1	fit	NMRD	230
DOTMP-MMBzA	25	18	100	122	3.79	3.4	1	fit	NMRD	230
DOTMP-MMNA	37	8.4	60	113	8.78	3.44	1	fit	NMRD	230
DOTMP-MMNA	25	16	91	124	4.20	3.44	1	fit	NMRD	230
DOTMP-MMNA	5	24	190	118	2.94	3.44	1	fit	NMRD	230
DTPA	25	25	58	72	4.60	3.13	1	fit	NMRD/O-17	177
EOB-DTPA	25	4	178	91	23	NA	1	NA	O-17	215
COPTA	25	25	80	83	4	2.96	1	fit	NMRD	228
BOPTA	25	26	88	76	4.22	2.96	1	fit	NMRD	28
DTPA-N′-MA	25	3.1	155	87	31	NA	1	NA	O-17	215
DTPA-N-MA	25	3	143	107	26	NA	1	NA	O-17	215
DTPA-N-MBA	25	17	98	70	7.00	3.10	1	TTHA	NMRD	238
DTPA-BMA	25	25	66	81	4.10	3.13	1	fit	NMRD/O-17	177
	35	15	58	72	7.72	3.1	1	fit	NMRD	234
	25	17	72	65	7.54	3.1	1	fit	NMRD	234
	5	21	107	89	4.46	3.1	1	fit	NMRD	234
	37	13	77	50	12.82	3.1	1	TTHA	NMRD	204
	5	2.4	>100	15	231.48	3.1	1	TTHA	NMRD	204
DTPA-BPDA	25	15	162	116	4.8	3.1	1	fit	NMRD/O-17	100
DTPA-BGLUCA	25	14	183	94	6.3	3.1	1	fit	NMRD/O-17	100
DTPA-BENGALAA	25	16	265	98	5.3	3.1	1	fit	NMRD/O-17	100
DTPA-BPhA	25	19	80	93	4.72	3.14	1	NG	NMRD	232
DTPA-B^{n}PA	37	26	81	57	5.62	3.1	1	TTHA	NMRD	204
DTPA-BBuA	37	25	93	53	6.29	3.1	1	TTHA	NMRD	204
DTPA-BMEA	37	21	88	53	7.49	3.1	1	TTHA	NMRD	204
DTPA-BHpA	37	60	120	85	1.63	3.1	1	TTHA	NMRD	204
DTPA-BMPEA	37	32	86	57	4.57	3.1	1	TTHA	NMRD	204
DTPA-BDHEA	37	46	84	76	2.38	3.1	1	TTHA	NMRD	204
DTPA-B^{n}PA	5	11.4	223	12	60.92	3.1	1	TTHA	NMRD	204
DTPA-BBuA	5	20	66	12	34.72	3.1	1	TTHA	NMRD	204
DTPA-BMEA	5	9	28	9	102.88	3.1	1	TTHA	NMRD	204
DTPA-BHpA	5	60	240	270	0.51	3.1	1	TTHA	NMRD	204
DTPA-BMPEA	5	2.4	56	1.9	1827.49	3.1	1	TTHA	NMRD	204
DTPA-BDHEA	5	20	22	0.8	520.83	3.1	1	TTHA	NMRD	204
PC2A	37	23	40	96	3.77	3.06	3.3	BPO4A	NMRD	229
	25	27	54	93	3.32	3.06	3.3	BPO4A	NMRD	229
	15	14	79	75	7.94	3.06	3.3	BPO4A	NMRD	229
	5	27	96	71	4.35	3.06	3.3	BPO4A	NMRD	229
PCTA-[12]	37	15	44	87	6.39	3.06	2.4	BPO4A	NMRD	229
	25	21	60	104	3.82	3.06	2.4	BPO4A	NMRD	229
	15	19	80	85	5.16	3.06	2.4	BPO4A	NMRD	229
	5	24	106	87	3.99	3.06	2.4	BPO4A	NMRD	229
PCTA-[12]	25	28	70	106	2.8	3.1	2	fit	NMRD	225
PCTP-[12]	25	19	106	56	7.8	3.06	1	fit	NMRD	225
PCTA-[13]	25	32	NG	141	1.85	3.2	1	fit	NMRD	255
PCTP-[13]	25	31	102	90	3	3	1	DOTP	NMRD	231
BP2A	37	19	47	119	3.69	3.06	3.5	BPO4A	NMRD	229
	25	42	64	140	1.42	3.06	3.5	BPO4A	NMRD	229
	15	37	87	104	2.17	3.06	3.5	BPO4A	NMRD	229
	5	35	102	89	2.68	3.06	3.5	BPO4A	NMRD	229

Table 17 (Continued)

ligand	temp (°C)	τ_v (ps)	τ_R (ps)	τ_{s0} (ps)	Δ^2 (10^{19} s^{-2})	r	q	o.s. model	method	ref
NOVAN	35	41	166	105	1.94	3.1	4	TTHA	NMRD	237
NOVAN	5	31	143	80	3.36	3.1	4	TTHA	NMRD	237
Tx	37	46	120	140	1.29	3.13	3.5	TTHA	NMRD	236
Tx	25	62	160	145	0.93	3.13	3.5	TTHA	NMRD	236
Tx	5	42	295	130	1.53	3.13	3.5	TTHA	NMRD	236
N_6–L1	39	9.1	87	46	19.91	2.91	3	fit	NMRD	239
N_6–L1	25	13	105	59	10.86	2.91	3	fit	NMRD	239
N_6–L1	4	21	192	73	5.44	2.91	3	fit	NMRD	239

[a] NA = not applicable; ND = not determined; NG = not stated; o.s. = outer-sphere.

Chart 14

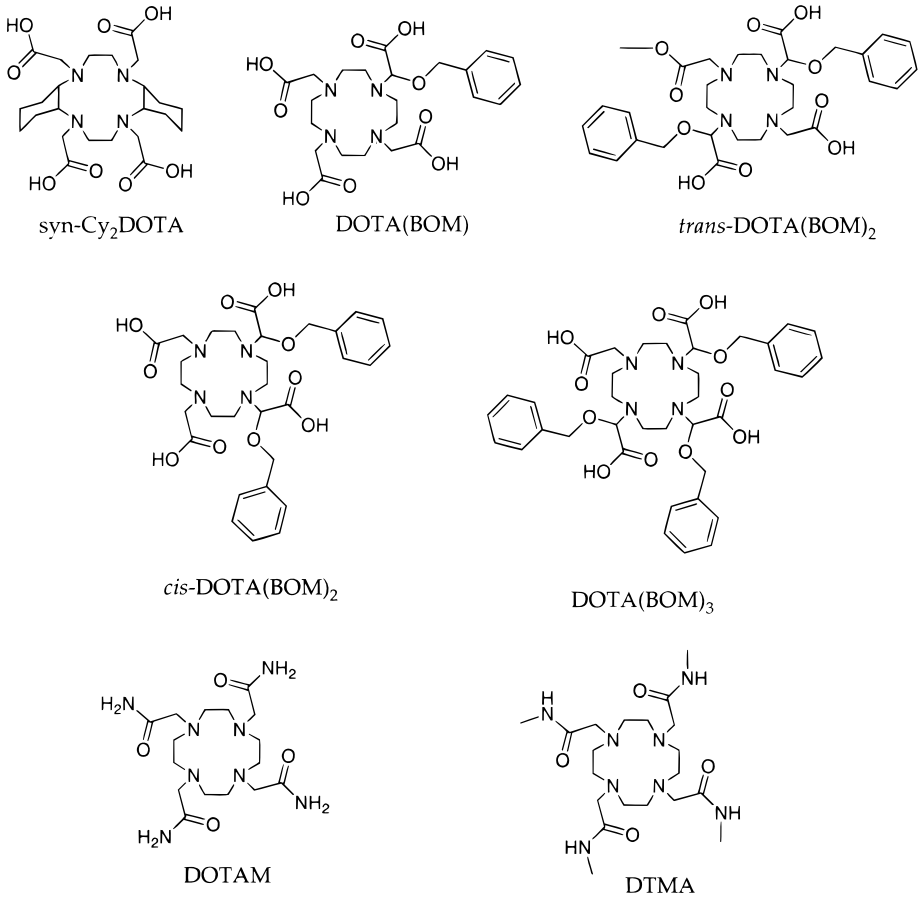


Table 18. EPR Line Widths for Selected Gd(III) Complexes at Three Magnetic Fields

ligand	X-band (0.34 T) line width (G)	Q-band (1.2 T) line width (G)	2 mm (5.0 T) line width (G)
DTPA[a]	604	103	16.1
DOTA[a]	91	57	11.7
DTPA-BMA[a]	428	75	18.0
DOTP[b]	531		
aqua	527,[a] 492[c]	195	52.5
aqua + CO_3^{2-}	890[c]		
aqua + NO_2^-	173[c]		

[a] Reference 177. [b] Reference 237. [c] Reference 240.

measured T_{1e} using an inversion recovery method. The results correlate roughly with the low-field (0.01−0.1 MHz) r_1 values for these complexes. It would appear that increasing structural rigidity slows down the longitudinal electronic relaxation rate, at least at very low temperatures (Table 19). This is likely an effect of minimizing the static ZFS. It would be interesting to estimate the T_{1e} values at a higher field by ^{17}O NMR to determine whether this trend still holds.

Merbach and co-workers performed several variable field EPR studies in conjunction with ^{17}O NMR measurements and sometimes ^1H NMRD. They find that $1/T_{2e}$ as determined by line width measurements can be well described by the semiempirical expression in eq 35.[242] Longitudinal ($1/T_{1e}$) values are inferred

$$\frac{1}{T_{2e}} = \Delta^2\tau_v\left[\frac{5.26}{1 + 0.372\omega_s^2\tau_v^2} + \frac{7.18}{1 + 1.24\omega_s\tau_v}\right] \quad (35)$$

from ^{17}O NMR transverse relaxation rates via eq 32, and from ^1H NMRD via eq 8. The field dependence of $1/T_{1e}$ is given by eq 27. All the relaxation data are then fitted simultaneously.[177] This is a usefull method since it allows the field dependence of $1/T_{ie}$ to be probed over a broad field range. At high fields it was

Chart 15

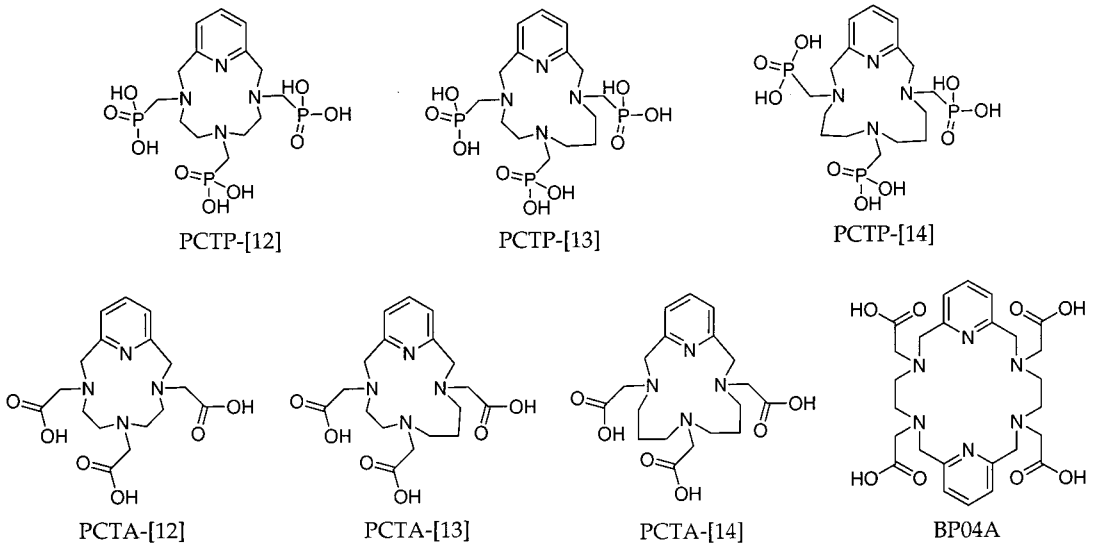


Chart 16

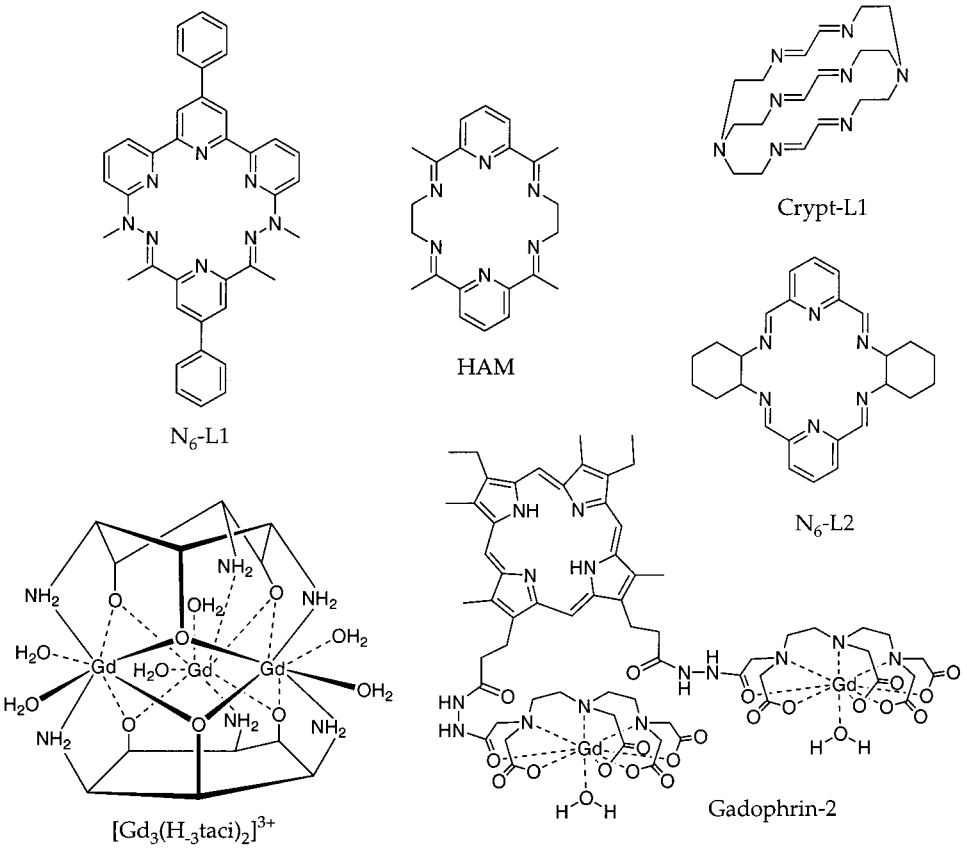


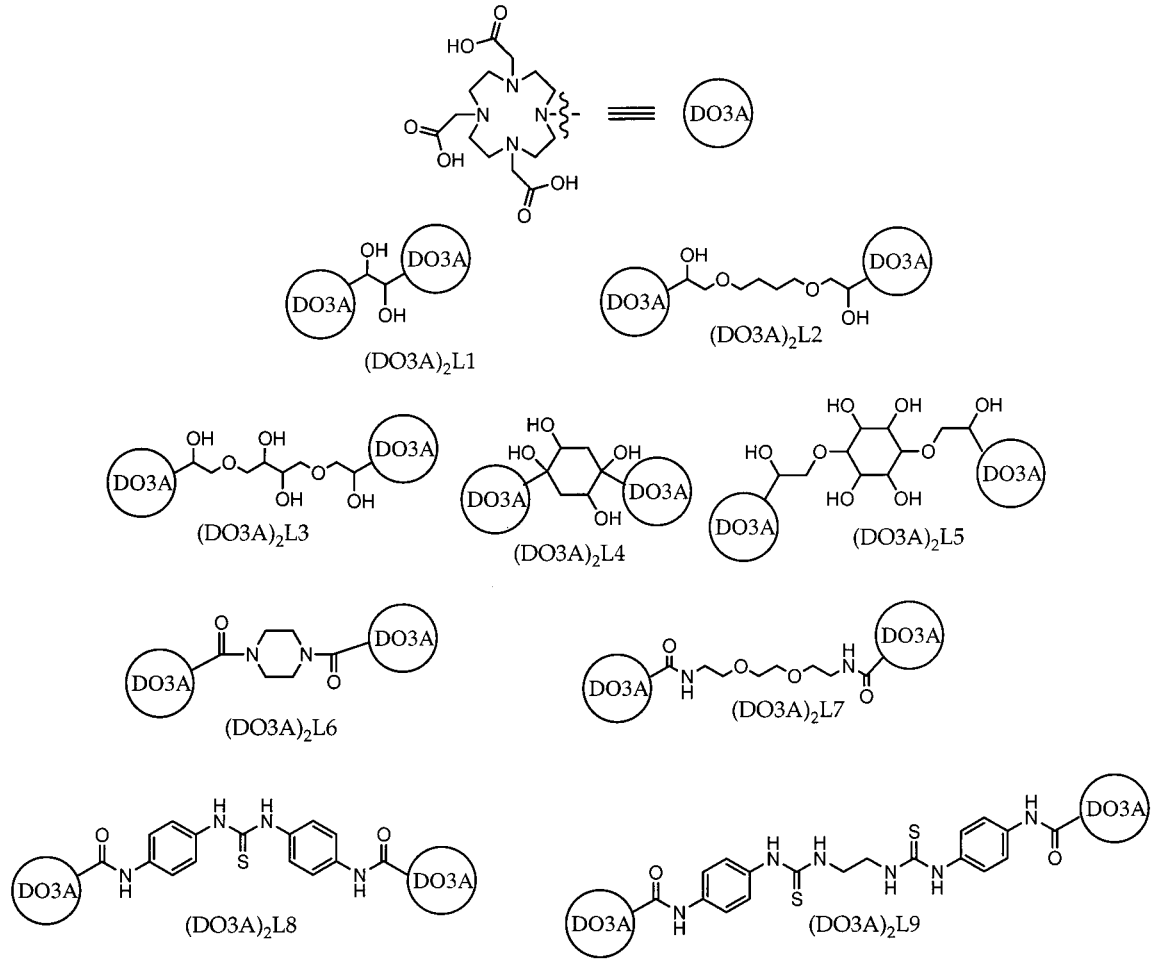
Table 19. Directly Measured T_{1e} Values (X-band) for Four Gd(III) Complexes at Low Temperature[241]

ligand	T_{1e} at 17.9 K (μs)	T_{1e} at 100 K (μs)
DTPA	58.5	0.81
DOTA	56.8	1.27
Cy_2DOTA	82.0	1.37
DOTMA	90.2	1.34

sometimes necessary to include a second relaxation mechanism, which the Lausanne group ascribed to a spin rotation mechanism which is field independent. This is perhaps not surprising given that $1/T_{1e}$ is predicted to decrease with the square of the field and these ^{17}O NMR measurements were made at 14.1 T. Since relaxation times are much longer at high fields (approaching microseconds), the advent of pulsed high-field EPR may illuminate the mechanisms underlying electronic relaxation of Gd(III) complexes.

Merbach and co-workers have also examined several systems in which there exist more than one Gd(III) ion. These are the dimers[177] $[Gd_2(DO3A)_2L6(H_2O)_2]$ and $[Gd_2(DO3A)_2L7(H_2O)_2]$ and the trinuclear $[Gd_3(H_{-3}taci)_2(H_2O)_6]^{3+}$ complex (Charts 16 and 17).[217] Here a dipolar coupling relaxation mechanism was

Chart 17



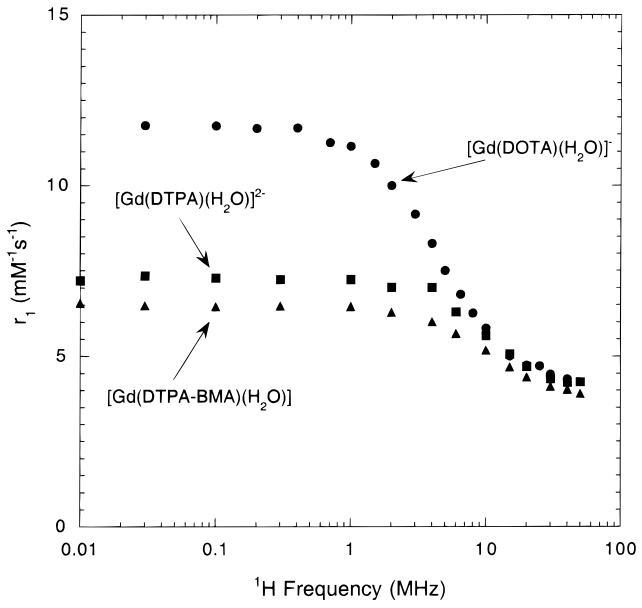


Figure 37. NMRD curves for three clinically approved gadolinium(III) chelates at 25 °C.

invoked to account for the relaxation of one Gd(III) ion by another. The taci system is of particular interest because of the close proximity of the Gd(III) ions, 3.7 Å. There is very little magnetic exchange in this system, $J = -0.092$ cm^{-1}, and the electronic relaxation could be accounted for by a dipolar mechanism modulated on a vibrational time scale. However this mechanism only dominated at high magnetic fields; the consequence for contrast agent design is that aggregation of Gd(III) centers in a multimeric environment is unlikely to limit ^{1}H relaxivity.

D. Relaxivity

The relaxivity of these low molecular weight species is dominated by rotation, especially at ^{1}H Larmor frequencies greater than 10 MHz. Most of the 20 MHz relaxivities can be accounted for by assuming an approximately equal contribution to outer- and second-sphere relaxivity with the inner-sphere relaxivity determined by a fast rotational rate. As noted in the previous section, electronic relaxation can influence low field (<1 MHz) relaxivities; however, the similarity in relaxivity at 20 MHz for [Gd(DOTA)(H$_2$O)]$^-$, [Gd(DTPA)(H$_2$O)]$^{2-}$, and [Gd(DTPA-BMA)(H$_2$O)] can be attributed to the similar rotational correlation times of the three complexes. In Tables 20 and 21, relaxivities are collected for a variety of gadolinium(III) chelates.[23,28,33−35,40,49,51,64,65,85,87,144,150,152,159,160,162,185,204,225−227,231,239,243−264] Tweedle and co-workers[265] have shown that relaxivity per gadolinium(III) correlates well with molecular weight for a series of monomeric and multimeric gadolinium(III) chelates (Charts 17−19) and this is shown in Figure 38 (data in Table 21). For spheroidal molecules, increases in relaxivity increase approxi-

Table 20. Relaxivities for Various Gd(III) Complexes

compound	r_1 ($mM^{-1}\,s^{-1}$)	r_2 ($mM^{-1}\,s^{-1}$)	^{1}H freq (MHz)	temp (°C)	pH[a]	ref
		DTPA Derivatives				
DTPA	4.3		20	25	7.4	253
DTPA	3.8		20	25		241
BOPTA	5.2		20	25	7.4	253
EOB	5.3		20	37		260
MP-2269	6.2		20	40		258
B-21326/7	6.78	7.77	20	39	7.0	246
MS-325	6.6		20	37	7.4	301
DTPA-L1	3.7		20			252
BOPTA	4.39	5.56	20	39	7.4	28
		DOTA Derivatives				
DOTA	4.2		20	25	7.4	253
DOTA	3.56	4.75	20	39	7.3	49
DOTA	4.8		20	40		257
DOTA	3.5		20	25		241
syn-Cy_2DOTA	4.5		20	25		241
DOTMA	3.8		20	25		241
DOTA-pNB	5.4		20	25		95
DOTA(BOM)	5.4		20	25	7.4	243
cis-$DOTA(BOM)_2$	6.8		20	25	7.4	243
trans-$DOTA(BOM)_2$	6.5		20	25	7.4	243
$DOTA(BOM)_3$	7.5		20	25	7.4	243
DOTA(BOM)	5.4		20	25	7.4	253
cis-$DOTA(BOM)_2$	5.7		20	25	7.4	253
trans-$DOTA(BOM)_2$	5.8		20	25	7.4	253
$DOTA(BOM)_3$	6.7		20	25	7.4	253
		DTPA-Monoamides				
DTPA-MpNPA	5.08		20	25		261
		DTPA-Bisamides				
DTPA-BMA	4.58		20	5		177
DTPA-BMA	4.39		20	25		177
DTPA-BMA	3.96		20	35		177
DTPA-BMEA	4.7		20	40		259
DTPA-BPA	4.66		20	25		261
DTPA-BPA	4.86			25		33
DTPA-BpAPA	4.12		20	25		261
DTPA-BpNPA	3.78		20	25		261
DTPA-BpTFPA	3.71		20	25		261
DTPA-B^{i}PA	4.27			25		33
DTPA-B^{i}BA	5.09			25		33
DTPA-BMMEA	4.1		20	40		259
DTPA-BHMEA	4.2		20	40		259
DTPA-BBA	4.50			25		33
DTPA-BBA	4.8		20	25	7	227
DTPA-BBA	6.5		20	25	12	227
DTPA-BBA	4.08	6.01	20	37	7	34
		DTPA Cyclic Amides				
DTPA-*cis*-BAM	3.2		20	40		144
DTPA-PenAM	3.6		20	40		144
DTPA-OAM	4.2		20	40		144
16-DTPA-PN	2.8		64	24		40
16-DTPA-PN	3.7		250	24		40
17-DTPA-BN	2.5		64	24		40
17-DTPA-BN	3.4		250	24		40
16-DTPA-PN−OH	3.5	4.4	250	23		39
		DO3A Derivatives				
HP-DO3A	3.7		20	40		257
HP-DO3A	3.65		20	40		85
HP-DO3A	3.7		20	40		51
DO3MA	4.4		20	40		51
DO3A	4.8		20	40		51
DO3A−L2	4.49	5.99	20	39	7.3	49
DO3A−L1	4.03	5.35	20	39	7.3	49
DO3A−L4	5.19	7.29	20	39	7.3	49
DO3A−L3	4.33	6.36	20	39	7.3	49
		$q = 0$ Compounds				
DOTPMB	2.8					160
BPO4A	1.71	1.74	40	25	7	229
BPO4A	1.66	1.83	40	25	12	229
DOTPMe	2.09	2.34	64	25		162
DOTMP-MBBzA	3.09		20	25		256
DOTMP-MPA	3.08		20	25		256
$CF_3CH_2PO_3$DOTA	2.5		40	25	6.8	87
DOTEP	5.1		40	25	7	159

Table 20 (Continued)

compound	r_1 ($mM^{-1}\,s^{-1}$)	r_2 ($mM^{-1}\,s^{-1}$)	^1H freq (MHz)	temp (°C)	pH[a]	ref
			Pyridine Containing Macrocycles			
PCTP-[13]	7.7		20	25	7.5	231
PCTA-[13]	6.3		20	25		255
PCTA-[12]	6.9		20	25		225
PCTP-[12]	7.5		20	25		225
PC2A	7.5	8.3	40	25	7	229
PCTA-[12]	5.42	6.52	40	25	7	229
BP2A	8.27	8.63	40	25	7	229
PC2A	3.7	3.9	40	25	12	229
PCTA-[12]	3.43	3.11	40	25	12	229
BP2A	4.51	4.91	40	25	12	229
PCTA-[12]	6.9		20	25	7	226
PCTA-[13]	6.3		20	25	7	226
PCTA-[14]	5.9		20	25	7	226
			Other Macrocyclics			
Tx	18		50	25		236
Tx	5.3		50	25	P_i	236
Tx	19.0		20	25		65
Tx	16.9		50	25		65
Tx	5.3		50	20	P_i	65
HAM	9.7		300	25	7.4	266
HAM	9.7		20	30	7.4	266
N_6−L1	12.8		20	25	6	239
N_6−L1	~2		20	25	12	239
N_6−L2	11.0		20	37	6	248
N_6−L2	4.7		20	37	P_i	248
Crypt-L1	5.8		10	25	6	251
Crypt-L1	3.5		10	25	9	251
			Other Acyclics			
TTAHA	9.5	10.5	300	25	7.4	150
PEDTA	8.8	9.6	300	25	7.4	150
EDMP	11.1	15.9	10	37	7	249
Phos-L1	10.0	14.3	10	37	7	249
DTPMP	8.6	11.8	10	37	7	249
HOPO	10.5		20	37		64

[a] P_i = phosphate buffer. If a pH is not specified, the compound was often dissolved in water or saline solution.

Table 21. Relaxivities (20 MHz, 40 °C) and Molecular Weights for Multimeric Gd(III) Complexes[265]

ligand	MW (Da)	r_1 ($mM^{-1}\,s^{-1}$)	ligand	MW (Da)	r_1 ($mM^{-1}\,s^{-1}$)
HP-DO3A	588	3.7	$(DO3A)_3L2$	2259	8.5
DO3A-MA	585	3.5	$(DO3A)_3L1$	2285	8.8
DO3A-PA	647	4.1	$(DO3A)_4L4$	2417	8.4
$(DO3A)_2L2$	1231	5.1	$(DO3A)_4L1$	2229	8.5
$(DO3A)_2L5$	1257	5.4	$(DO3A)_4L2$	2461	9.6
$(DO3A)_2L3$	1103	6.4	$(DO3A)_4L3$	2501	9.8
$(DO3A)_2L4$	1201	6.6	$(DO3A)_4L5$	2597	10.2
$(DO3A)_2L8$	1367	6.2	$(DO3A)_6L1$	4390	11.2
$(DO3A)_2L9$	1469	6.9	$(DO3A)_8L1$	4998	13

mately with increasing molecular weight. It should be noted that it is the rotational correlation time of the Gd(III)−H vector which determines relaxation and this rotational correlation time may be much shorter than one computed using eq 29 for the molecule as a whole.

Figure 38 is comprised of monomers, dimers, trimers, tetramers, a hexamer, and an octamer. It has been recognized that rigidity plays a role in determining the relaxivity of multimeric gadolinium(III) chelates.[265] For instance, the relaxivity of dimer $[Gd_2(DO3A)_2L4]$ is 6.6 $mM^{-1}\,s^{-1}$ while that of $[Gd_2(DO3A)_2L5]$ is 5.4 $mM^{-1}\,s^{-1}$. Both compounds have identical chelate structures and almost identical molecular weight, but $[Gd_2(DO3A)_2L4]$ has a much less flexible linker between the two gadolinium(III) chelates. Even for compounds with molecular weights

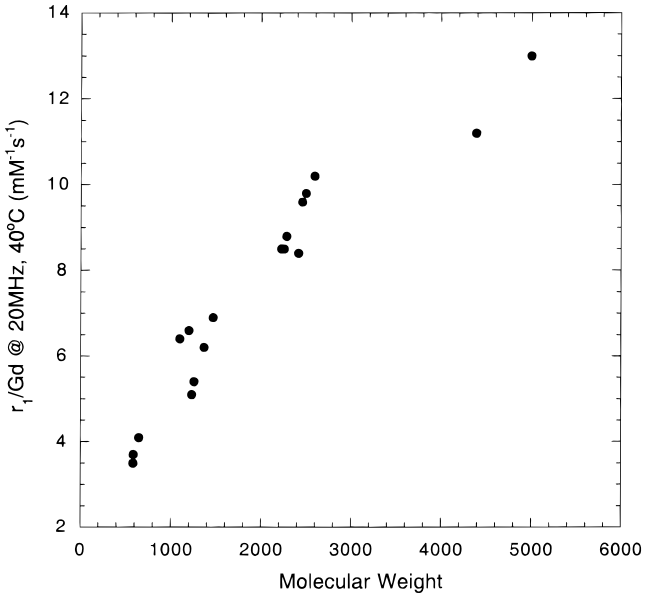
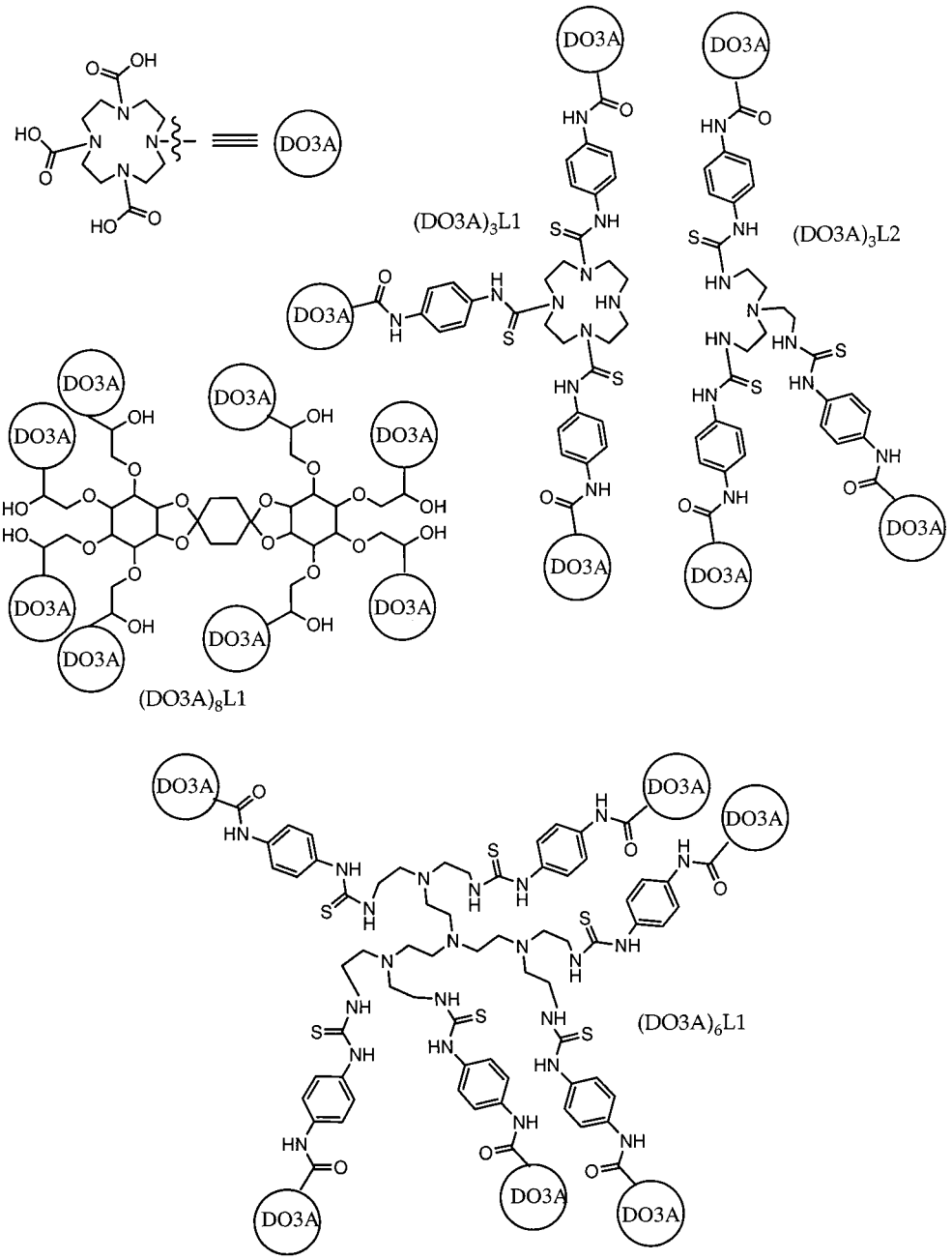


Figure 38. Relaxivity per Gd(III) vs molecular weight for various Gd(III) multimeric complexes.

in the 3000 Da range, the difference in rotational correlation times between rigid and "floppy" multimers is not likely to be large. The effect of internal motion becomes dramatic for polymeric conjugates.

The hydration number plays an important role in determining relaxivity. Notable examples of thermodynamically stable/kinetically inert complexes with

Chart 18



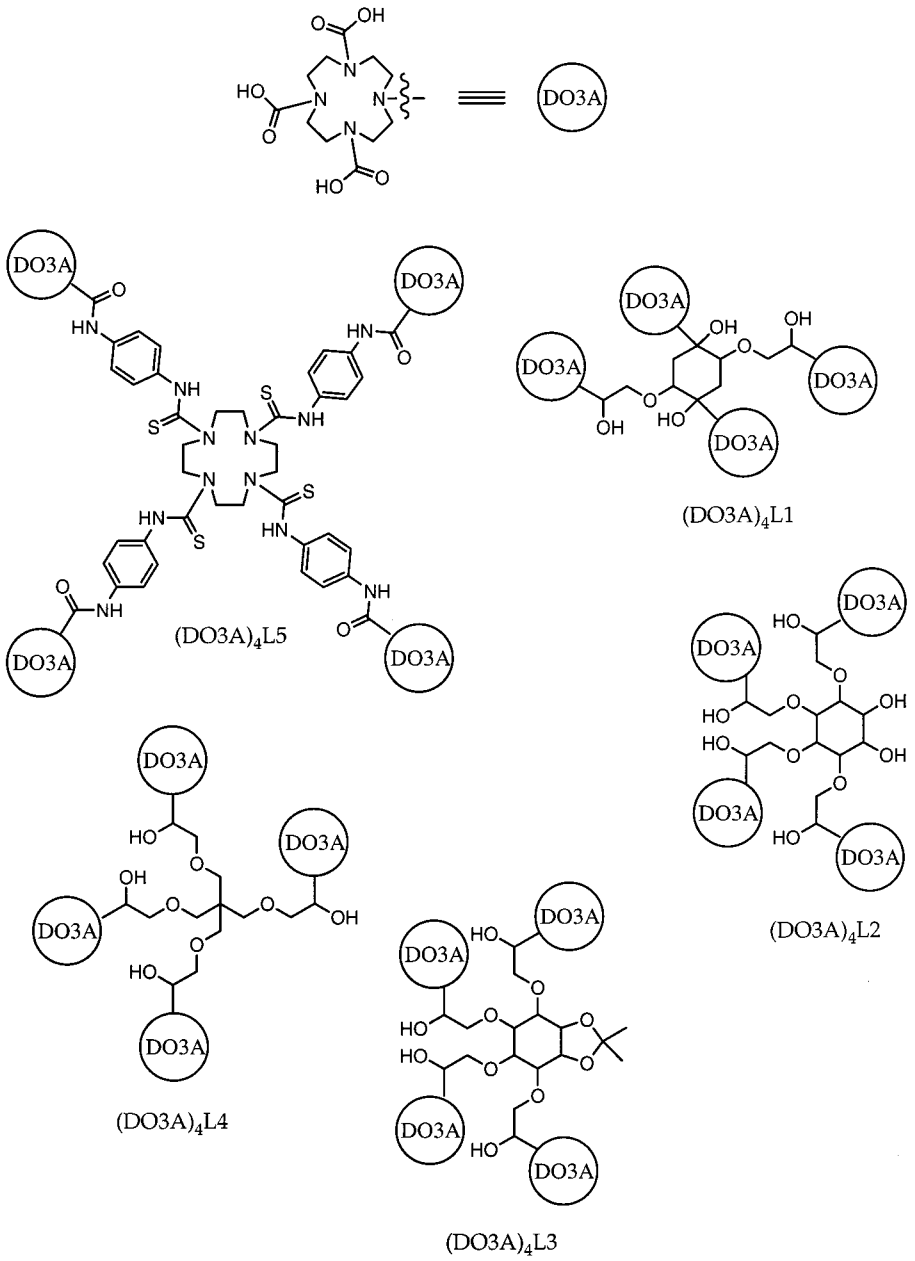
$q > 1$ are $[Gd(TX)(H_2O)_3]^{2+}$, $[Gd(HOPO)(H_2O)_2]$, $[Gd(DO3A)(H_2O)_2]$, $[Gd(HAM)(H_2O)_3]^{3+}$, and $[Gd(N_6\text{-L1})(H_2O)_3]^{3+}$.[64,85,236,239,244,266] These complexes (Charts 7, 9, 16 and Scheme 1) represent dramatic improvements in small molecule contrast agent design. One hurdle that remains in these systems is the coordination of endogenous anions, a factor that is generally not a problem for $q = 1$ complexes.[267] In Table 20 there are some values reported in the presence and absence of phosphate buffer (P_i). Lower relaxivity in the presence of phosphate is an indicator of ternary complex formation which decreases q and lowers relaxivity. Bicarbonate is another endogenous anion present in rather large concentration in vivo which is known to coordinate to [Gd(DO3A)] and reduce relaxivity.[44]

Relaxivities tend to increase at lower temperatures for low molecular weight chelates. This is a consequence of slower molecular tumbling rates. Exceptions can occur for molecules with long water residency times. Activation energies for rotation tend to be in the 20 kJ mol^{-1} range[177] while the energy barrier to water exchange is usually about 50 kJ mol^{-1}. Thus τ_m increases faster than τ_R with decreasing temperature, and this may bring about the limiting condtion $\tau_m > T_{1m}$.

E. Outer- and Second-Sphere Relaxivity

Outer-sphere relaxivity can vary from complex to complex. It is often assumed that the relaxivity exhibited by $q = 0$ complexes can be described by Freed's equation (eq 33) for outer-sphere relaxation. While the NMRD curves of complexes such as $[Gd(TETA)]^-$ and $[Gd(TTHA)]^{3-}$ (Charts 7 and 9) can be modeled by eq 33, it does not neccessarily follow that the values for τ_{s0}, τ_v, a (distance of closest

Chart 19



approach), and *D* (diffusion constant) are physically meaningful. As in the preceding section, electronic relaxation may not be well described by the BM equation in the low-field limit. There is also the question of second-sphere relaxivity.

The NMRD curves of $[Gd(TTHA)]^{3-}$ and $[Gd(DOTP)]^{5-}$ are shown in Figure 39. Both ions are $q = 0$ and are of similar size. The increased relaxivity for $[Gd(DOTP)]^{5-}$ (Chart 8) cannot be due to pure outer-sphere relaxation alone. This is likely because of second-sphere relaxivity. This is not surprising considering that lanthanide complexes of DOTP have been used as shift reagents for sodium and other metal ions.[112]

The existence of a second coordination sphere is well established for such species as the aqua complexes of tripositive ions. Neutron diffraction, X-ray diffraction, and LAXS (large angle X-ray scattering) studies of tripositive ions such as $Cr^{3+}_{(aq)}$, $Al^{3+}_{(aq)}$, $Ga^{3+}_{(aq)}$, $In^{3+}_{(aq)}$, and $Rh^{3+}_{(aq)}$ show well-defined second-sphere structure in solution.[268] Bleuzen et al.[269] estimated a residency time of 128 ps at 25 °C for a water molecule in the second sphere of the $Cr^{3+}_{(aq)}$ ion from both ^{17}O NMR relaxation and molecular dynamics. This is long enough to cause a relaxivity enhancement via an SBM dipolar mechanism.

Chen et al. have used VO^{2+} EPR of various polyaminocarboxylates to study second-sphere hydration.[178,179] They determine τ_R and τ_v from EPR solution simulations at various temperatures. From the τ_R data, the hydrodynamic radius is determined, and the distance of closest approach, *a*, is estimated. Fitting the NMRD curves of $[VO(EDTA)]^{2-}$ and other complexes to only the outer-sphere equation gave values for *a* that are physically too small, leading to the conclusion that a second-sphere process was also contributing to the observed r_1. The authors went on to study $[Gd(TTHA)]^{3-}$ assuming that it had a similar

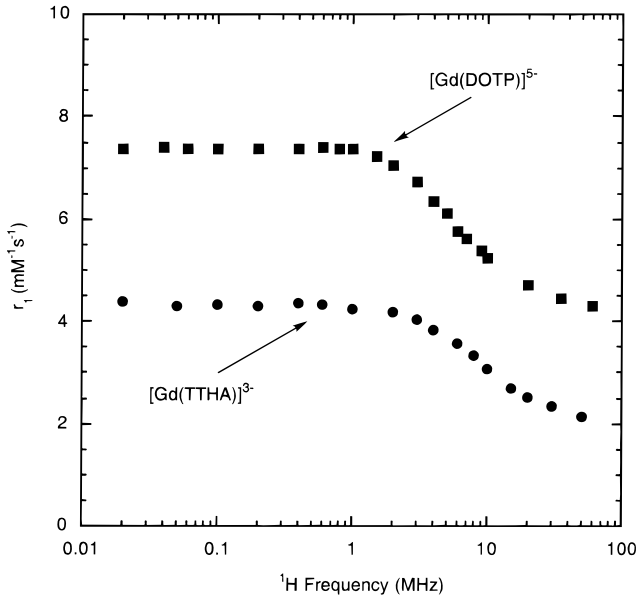


Figure 39. NMRD curves for two $q = 0$ complexes, $[Gd(DOTP)]^{5-}$ and $[Gd(TTHA)]^{3-}$ at 25 °C, showing that all "outer-sphere" complexes are not created equal.

rotational correlation time as $[VO(TTHA)]^{4-}$ and a similar value for a. This lead to a description in which the second-sphere mechanism contributed between 20 and 25% of the observed relaxivity. NMRD curves of $[Gd(DTPA)]^{2-}$ and $[Gd(EOB\text{-}DTPA)]^{2-}$ were also trisected into inner-, second-, and outer-sphere contributions, but the large number of parameters and assumptions makes the analysis statistically questionable.

F. Methods of Improving Relaxivity

The obvious way to ameliorate relaxivity is to increase τ_R, and this will be discussed in depth in the next two sections. It is likely that rigidity will play a role in optimizing τ_R as a function of molecular weight. The limitations of slow water exchange on relaxation have been recognized, and there is a growing body of evidence to aid in optimizing τ_m. Increasing the hydration number poses some interesting challenges to maintain thermodynamic stability/kinetic inertness and, at the same time, be resistant to formation of ternary complexes with endogenous ligands such as phosphate and carbonate. However increasing q offers a large reward in terms of relaxivity. Outer-sphere relaxation is still a misunderstood entity receiving little attention.

Although a large body of data has been accumulated since the previous review, most of this centers around polyaminopolycarboxylate ligands. This bias is understandable considering the composition of the clinically available complexes coupled with the need for thermodynamically stable complexes. It would behove the coordination chemist to examine the physical properties of Gd(III) complexes with a variety of donor atoms in order to ascertain the factors which influence water exchange, electronic relaxation, and outer-sphere relaxation.

V. Macromolecular Conjugates

A. Introduction

The conjugation of low molecular weight chelates such as GdDTPA or GdDOTA to macromolecules alters the biophysical and pharmacological properties of low molecular weight agents.[270] From the biophysical perspective, the conjugation of gadolinium(III) chelates to polymeric materials was anticipated to increase the rotational correlation time and, hence, to improve the relaxivity per gadolinium atom. Combined with tissue-specific targeting moieties, polymeric conjugates were also envisioned to provide MRI with the ability to image low-concentration receptors by delivering a large payload of gadolinium(III) chelates. High molecular weight conjugates are retained in the vascular space by virtue of molecular size and thus facilitate blood pool imaging. However the goal of imaging receptors using MRI in the clinic has been elusive.[271]

The most common approaches which have been used to prepare macromolecular structures containing gadolinium(III) chelates involve conjugation of functionalized chelates to polymers, dendrimers, or biological molecules. In addition, macromolecules with multiple ligands have been prepared by polymerization. The intent of this portion of the review is to survey the synthesis and chemical structure of representative macromolecular conjugates as well as to survey their biophysical properties.

B. General Conjugation Methods

Conjugation methods for linking chelates to macromolecules are well established in the literature.[272] Typical chemistries include the functionalization of primary amines using acylation, alkylation, ureas or thiourea formation, and reductive amination. The majority of papers have been published using commercially available reagents, such as DTPA itself or DTPA-dianhydride, to functionalize macromolecules. Reaction of these reagents with a reactive primary amine on the macromolecule generates an amide bond using one of the DTPA carboxylates (see for example, Figure 40). While still an eight-coordinate ligand, the donor set has been modified as compared with DTPA itself: one acetate donor has been replaced with an amide oxygen. Because the substitution of an amide for a carboxylate has significant relaxivity implications, the tables will explicitly note the chemical structure of the ligand donor set (for example, DTPA vs DTTA-MA, diethylenetriamine tetraacetic acid monoamide).

C. Synthetic Linear Polymers

Polylysine is commercially available in a variety of molecular weight ranges and has been derivatized with gadolinium chelates.[273−277] The reactive epsilon amino groups of the lysine backbone are typically modified with acyclic and macrocyclic polyaminocarboxylate derivatives as shown in Figure 40. Conjugates containing up to 70 Gd(IIII) chelates have been reported (Table 22). Polylysine has also been co-

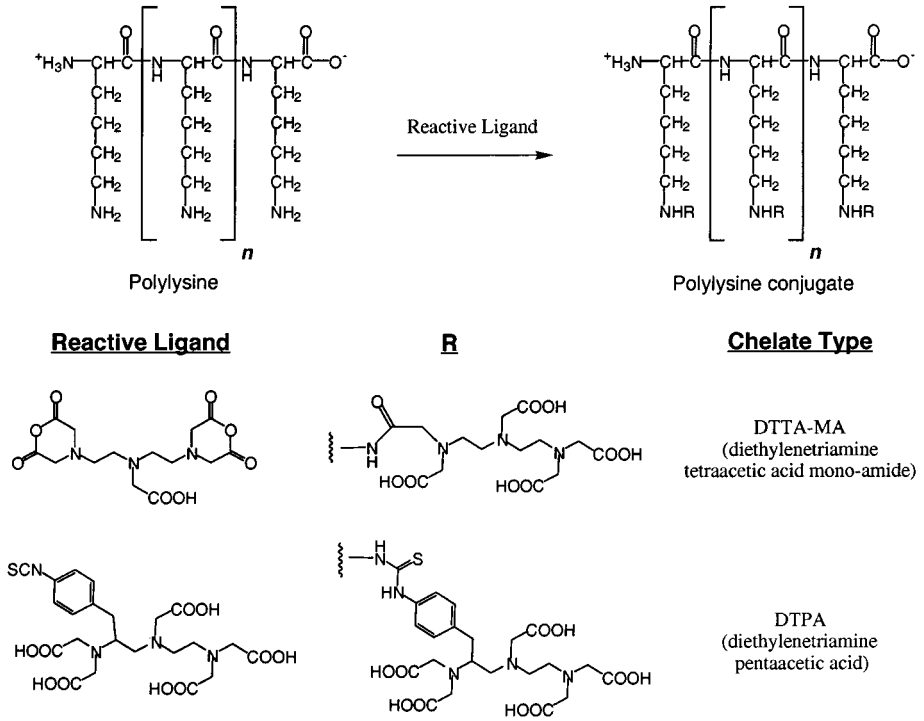


Figure 40. Chemical structure of polylysine and representative chelate conjugates.

Table 22. Synthetic Polymer-Based Macromolecular Contrast Agents

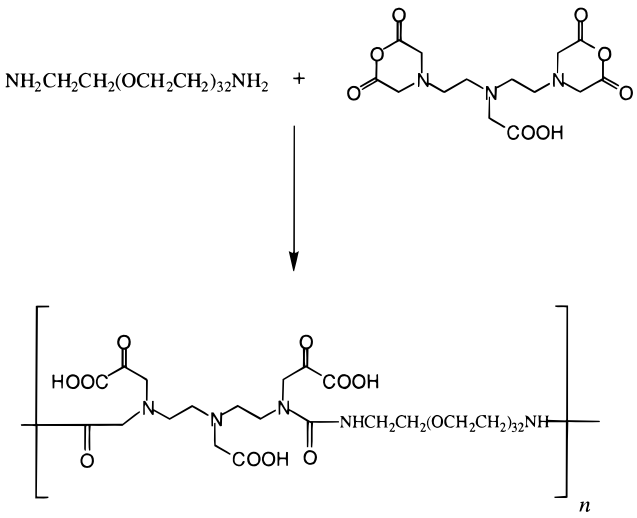
macromolecular contrast agent	chelate type	MW (Da)	no. Gd(III)	% Gd content	ion r_1 (mM^{-1} s^{-1})[a,b]	mol. r_1 (mM^{-1} s^{-1})[a]	freq (MHz)	T (°C)	ref
polylysine-GdDTPA	Gd-DTTA-MA	48 700	60−70		13.1	850	20	39	273
PL-GdDTPA	Gd-DTTA-MA	50 000			10.8		10	37	274
PL-GdDTPA	Gd-DTTA-MA	238 100			11.74		100	37	275
PL-GdDTPA	Gd-DTTA-MA	89 900			11.58		100	37	275
PL-GdDTPA	Gd-DTTA-MA	56 000			10.56		100	37	275
PL-GdDTPA	Gd-DTTA-MA	7 700			11.67		100	37	275
PL-GdDOTA	Gd-DO3A-MA	65 000			13.03		10	37	274
MPEG- PL-GdDTPA	Gd-DTTA-MA	320 000	110	5.5	18	2000−2500	20	37	277, 278
Gd-DTPA-PEG I-polylysine	Gd-DTTA-MA	10 800	6−7	9.64	6.0	39	20	37	276
Gd-DTPA-PEG II-polylysine	Gd-DTTA-MA	13 600	8−9	9.85	6.0	51	20	37	276
Gd-DTPA-PEG III-polylysine	Gd-DTTA-MA	18 500	9−10	7.75	6.0	57	20	37	276
Gd-DTPA-PEG IV-polylysine	Gd-DTTA-MA	21 900	11−12	8.42	6.0	69	20	37	276
Gd-DTPA-PEG V-polylysine	Gd-DTTA-MA	31 500	7−8	3.73	6.0	45	20	37	276
Gd-DTPA-PEG VI-polylysine	Gd-DTTA-MA	39 600	9−10	3.93	6.0	57	20	37	276
Gd-DTPA-PEG VII-polylysine	Gd-DTTA-MA	83 400	35−36	6.65	6.0	213	20	37	276
(DTPA-BA)-PEG	triacetate bisamide	20 000			6.13		20	37	281
(DTPA-BA) α,ω alkyldiamine $(CH_2)_n$, where $n = 4$	triacetate bisamide	8 000		26.2	8*		20	35	280
(DTPA-BA) α,ω alkyldiamine $(CH_2)_n$, where $n = 5$	triacetate bisamide	8 300		25.6	9*		20	35	280
(DTPA-BA) α,ω alkyldiamine $(CH_2)_n$, where $n = 6$	triacetate bisamide	19 400		21.75	10*		20	35	280
(DTPA-BA) α,ω alkyldiamine $(CH_2)_n$, where $n = 10$	triacetate bisamide	10 300		19.92	15*		20	35	280
(DTPA-BA) α,ω alkyldiamine $(CH_2)_n$, where $n = 12$	triacetate bisamide	15 700		20.06	18*		20	35	280

[a] Water. [b] Asterisk (*) indicates values estimated from NMRD curve.

modified with PEG to modulate the pharmacokinetic properties of the agents.[278,279] The relaxivity of polylysine derivatives range from 15 to 20 mM^{-1} s^{-1} at 20 MHz (Table 22), lower than anticipated for a truly immobilized monoamide DTPA chelate. This is likely because of the flexible nature of the linear polymeric backbone and the epsilon amino side chain.

A series of linear copolymers of bisamide chelates linked by α,ω-alkyldiamides with a varying number (n) of methylenes[280] or poly(ethylene glycol) (PEG) diamines [219] have been prepared. These compounds differ from those described above in that the chelates are incorporated directly into the polymeric chain instead of being conjugated to an existing polymer. An example synthetic route and structure of one representative copolymer incorporating poly(ethylene glycol) units are shown in Figure 41.

Variable temperature EPR, variable temperature, pressure, multiple field ^{17}O NMR, and variable temperature NMRD studies were reported for the linear



[α-ω-poly(ethyleneglycol)diamine]-DTPA copolymer)

Figure 41. Chemical synthesis and structure of a linear DTPA derivative copolymer: [α-*ω*-poly(ethyleneglycol)-diamine]-DTPA copolymer.

Gd(DTPA-bisamide)-poly(ethylene glycol) copolymer.[219] This work demonstrated for the first time that the water exchange rate ($k_{ex}^{298} = 4.8 \times 10^5\ s^{-1}$) and mechanism (dissociatively activated) were identical for the polymer and the corresponding small molecule chelate. As a result of the slow water exchange and relatively fast rotational correlation time, the relaxivities for this polymer were low and independent of temperature at all field strengths.

Relaxivity studies were also reported for the related series of copolymers which were prepared from DTPA dianhydride and α,*ω*-alkyldiamines without the poly(ethylene glycol) spacers.[280] Contrary to expectations, r_1 was higher than the PEG containing copolymers and increased with increasing *n*, the number of methylene units between each chelate. This was explained by postulating the presence of intramolecular aggregates which made the linear polymers less rodlike and more globular, thereby increasing the rotational correlation time. Again, the water exchange rate of the monomer was identical to that of the polymer, indicating that the relaxivity of these compounds was limited by a slow water exchange rate (τ_m limited).[281] Toth et al.[281] showed that the relaxivity differences between polymers with varying *n* could be explained by fitting the ^{17}O longitudinal relaxation rates to a Lipari-Szabo model to separate local fast motions within the polymer from the global tumbling time of the entire molecule. The local motional rates and the extent to which they contributed to relaxivity were found to be similar (as in the case of the PEG-based copolymers); however, the slower global motion of the larger polymers accounted for the difference in observed relaxivity.

D. Synthetic Dendrimer-Based Agents

Dendrimers are three-dimensional, oligomeric structures prepared by reiterative reaction sequences starting from smaller "core" molecules, as shown schematically in Figure 42. The highly branched, nearly monodisperse structure of dendrimers have led to a number of interesting molecular attributes for this relatively new class of macromolecule. Several excellent reviews describing the evolution of dendrimer chemistry have appeared.[282,283]

A number of workers have explored the potential use of conjugated dendrimers as a new class of macromolecular MRI agents. The potential advantages of Gd(III) chelate dendrimer conjugates include the fact that dendrimers, such as the Starburst polyamidoamine (PAMAM) dendrimers (Figure 42), have uniform surface chemistry and minimal molecular weight distribution and shape variation. In contrast to linear polymers, dendrimers have a relatively rigid structure and the overall tumbling of the molecule contributes to the rotational correla-

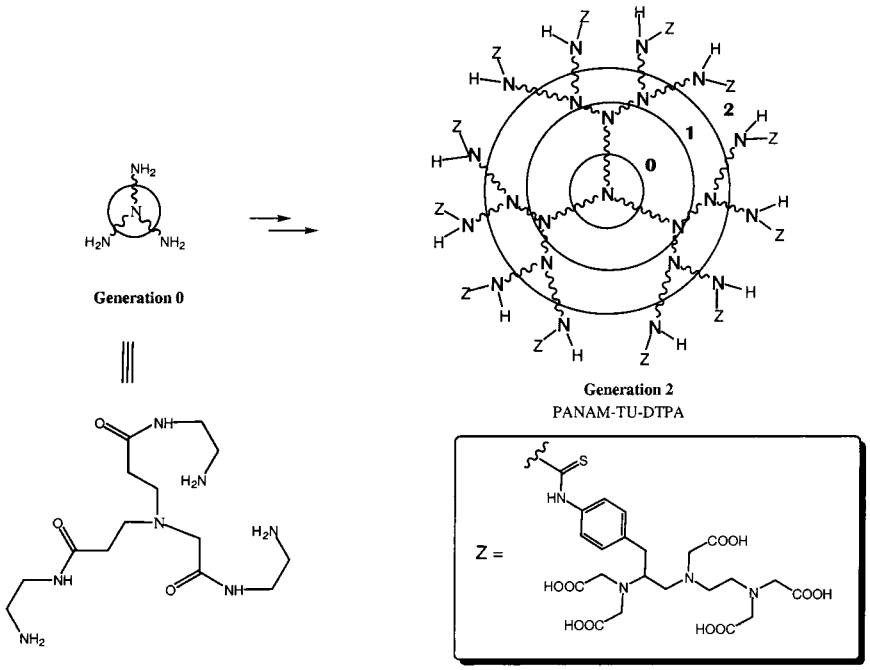


Figure 42. Schematic drawing of a generation 2 PAMAM thiourea DTPA dendrimer.

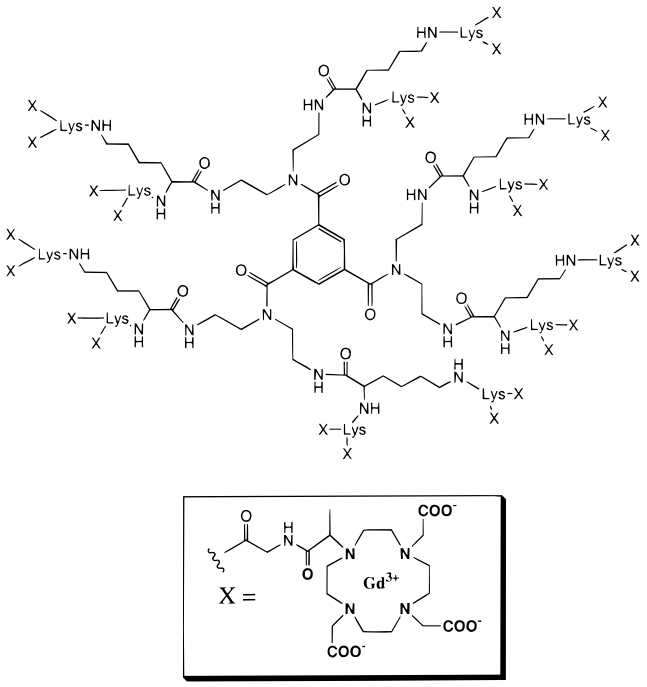


Figure 43. Chemical structure of Gadomer 17.

tion time. The rotational correlation times of the carbon atoms in PAMAM-type dendrimers was measured by ^{13}C NMR. These studies found that the correlation time of the internal carbons increased by several orders of magnitude between generation 0 and 10, and doubled for carbons on the surface.[284] Provided chelates can be attached in a manner which limits rapid rotation of the chelate itself, the relaxivity should benefit from conjugation to a dendrimeric structure.

A dendrimer-based MRI agent was prepared by linking p-NCS-Bz-DTPA to a G = 2 and G = 6 PAMAM Starburst dendrimer (Figure 42). The resulting G = 2 and G = 6 conjugates of DTPA contained, on average, 11 and 170 chelates, respectively. This work has recently been extended to include larger dendrimers (up to G = 9) and DOTA chelates, which appear to provide materials with the largest number of Gd(III) ions per macromolecule yet reported.[285]

Margerum and co-workers have employed an analogous approach to link the macrocyclic monoamide chelate DO3A-monoamide to PAMAM dendrimers of generation 2−5.[286] In addition, these authors report the incorporation of PEG subunits, which have a pronounced effect on the pharacokinetic properties.

Schering AG has reported the preparation and characterization of two types of dendrimer-based MRI agents: GdDTPA-cascade-24-polymer[287−289] and Gadomer 17.[290,291] GdDTPA-cascade-24-polymer is a PAMAM dendrimer which has been functionalized with 24 Gd-DTPA chelates, whereas Gadomer 17 is derived from a lysine-functionalized 1,3,5-benzene tricarboxylic acid core (Figure 43). Comparisons of the pharmacokinetics of GdDTPA-cascade-24-polymer with Gd-DTPA-polylysine in the rat indicate that the dendrimer-based agents are eliminated much more readily than the linear polylysine polymer, presumably due to the globular nature of the dendrimer.[292]

The reported relaxivity values of the dendrimer conjugates range from ∼14 mM^{-1} s^{-1} to 36 mM^{-1} s^{-1} at 25 MHz, 37 °C depending on the nature of the chelate and the dendrimer structure. These values are higher than those observed for the linear analogues for two reasons. First, most of the linear polymer work has been reported using mono- or diamide polyaminocarboxylate derivatives, both of which are now known to have relaxivities limited by slow water exchange. Second, the dendrimers are inherently more rigid than their linear analogues, leading to fewer degress of freedom for the conjugated gadolinium chelate.

Tóth and Merbach have reported an ^{17}O NMR and NMRD study of a series of functionalized PAMAM dendrimers.[212] Importantly, these experiments demonstrated for the first time that the attachment of the macrocyclic DO3A-monoamide chelate to the dendrimer did not significantly influence water exchange on the complex. The water exchange and relaxivity results of this study are summarized in Table 23. The NMRD profiles of the dendritic contrast agents G_3Gd_{52} and G_3Gd_{23} showed a high-field peak characteristic of contrast agents with long rotational correlation times. However, the relaxivity improvement at 20 MHz is relatively modest as compared with that reported by Weiner et al. for the DTPA and DOTA functionalized PAMAM dendrimers.[285,293] Given the discussion in section IV, one can appreciate that the relaxivity of the DO3A-monoamide chelates studied by Tóth and Merbach is limited by the long water residency time (τ_m) of the mono amide ligand system. These results have important implications for the design of optimized macromolecular contrast agents.

E. Naturally Occurring Polymers (Proteins, Polysaccharides, and Nucleic Acids)

A significant amount of exploratory research has been performed using Gd-DTPA derivatives of human or bovine serum albumin (HSA or BSA).[294] Because of the intravascular retention of the macromolecule, Gd-DTPA-BSA/HSA is used as a "gold standard" blood pool agent and has been used to demonstrate the benefits of MR angiography.[295] Conjugates containing up to about 30 ligands are readily formed by the reaction of DTPA-dianhydride with BSA or HSA in buffered aqueous solution.

Dextran has also been explored as a scaffold for the attachment of various chelates.[296,297] As with polylysine, dextrans are available in a variety of molecular weight ranges and can be modified to include chelating agents.[298−302] Of relevance to potential human use is the fact that dextrans have been successfully employed as plasma volume expanders.[303]

Dextran-based macromolecular contrast agents have been investigated as blood pool MRI contrast agents. An example of well-studied macrocyclic conjugates is CMD-A2-Gd-DOTA, shown in Figure 44.[300] This macromolecular contrast agent is prepared by a three-step modification of dextran by alkylation

Table 23. Dendrimeric Macromolecular Contrast Agents

macromolecular contrast agent	dendrimer type	chelate	MW (Da)	no. of Gd(III)	ion r_1 ($mM^{-1}\,s^{-1}$)	mol. r_1 ($mM^{-1}\,s^{-1}$)	freq (MHz)	T (°C)	ref
G_9(N[CS]N-bz−GdDTPA)$_{1331}$	PANAM	Gd-DOTA	1 600 000	1 331	36	47 916	25	23	285
G_7(N[CS]N-bz−GdDTPA)$_{383}$	PANAM	Gd-DOTA	375 000	383	34	13 022	25	23	285
G_6(N[CS]N-bz−GdDTPA)$_{170}$	PANAM	Gd-DTPA	139 000	170	34	5 800	25	20	293
G_6(N[CS]N-bz−GdDTPA)$_{170}$	PANAM	Gd-DTPA	139 000	170	34	5 800	25	35	293
G_6(N[CS]N-bz−GdDTPA)$_{170}$	PANAM	Gd-DTPA	139 000	170	23.1	3 900	10	20	293
G_6(N[CS]N-bz−GdDTPA)$_{170}$	PANAM	Gd-DTPA	139 000	170	23.5	4 000	10	35	293
G_2(N[CS]N-bz−GdDTPA)$_{11}$	PANAM	Gd-DTPA	8 508	11	21.3	234	25	20	293
G_2(N[CS]N-bz−GdDTPA)$_{11}$	PANAM	Gd-DTPA	8 508	11	16.7	184	10	20	293
G_5(N[CS]N-bz−GdDO3A)$_{57}$	PAMAM	Gd-DO3A- MA	61 775	57	18.8	1 072	25	37	286
G_4(N[CS]N-bz−GdDO3A)$_{38}$	PAMAM	Gd-DO3A- MA	37 420	38	16.9	642	20	37	286
G_3(N[CS]N-bz−GdDO3A)$_{24}$	PAMAM	Gd-DO3A- MA	22 074	24	14.8	355	25	37	286
G_4(N[CS]N-bz−GdDO3A)$_{11}$	PAMAM	Gd-DO3A- MA	18 385	11	16.0	176	25	37	286
G_3(N[CS]N-bz−GdDO3A)$_{13}$	PAMAM	Gd-DO3A- MA	14 319	13	12.3	160	20	37	286
G_3(N[CS]N-bz−GdDO3A)$_{10}$(PEG_{5000})$_{12}$	PAMAM	Gd-DO3A- MA	69 352	10	13.8	138	20	37	286
G_3(N[CS]N-bz−GdDO3A)$_{15}$(PEG_{2000})$_9$	PAMAM	Gd-DO3A- MA	33 330	15	13.7	205	20	37	286
G_2(N[CS]N-bz−GdDO3A)$_9$(PEG_{5000})$_3$	PAMAM	Gd-DO3A- MA	23 760	9	12.4	112	20	37	286
G_2(N[CS]N-bz−GdDO3A)$_5$(PEG_{2000})$_7$	PAMAM	Gd-DO3A- MA	20 587	5	11.0	55	20	37	286
Gd-DTPA-cascade-polymer	PAMAM	Gd-DTPA	<30 000	24	11.9	289	20	40	292
Gadomer 17	polyamide	Gd-DO3A- MA	17 453	24	15.2[a]	365	64.5	37	291
Gadomer 17	polyamide	Gd-DO3A- MA	17 453	24	18.7[a]	449	20	39	291
Gadomer 17	polyamide	Gd-DO3A- MA	17 453	24	17.3	415	20	39	291

[a] In plasma.

Table 24. Natural Polymer-Based Macromolecular Contrast Agents

macromolecular contrast agent	chelate type	MW (Da)	no. of Gd(III)	% Gd	ion r_1 ($mM^{-1}\,s^{-1}$)[a]	mol. r_1 ($mM^{-1}\,s^{-1}$)[a]	freq (MHz)	T (°C)	ref
albumin-GdDTPA	Gd-DTTA-MA	90 000	90		14	420	10	25	274
CMD-A2-DOTA-Gd	Gd-DO3A-MA	52 100			10.59		20	37	296
dextran-alanine-GdDTPA	Gd-DTTA-MA			1.7	9.4		10	37	
dextran-alanine-GdDTPA	Gd-DTTA-MA			2.2	8.7		10	37	
dextran-alanine-GdDTPA	Gd-DTTA-MA			3.4	8.7		10	37	
CMD-Gd-DTPA (carboxymethyldextran-GdDTPA, carbamate linked)	Gd-DTTA-MA	28 000			7.8		20	37	297
CMD-Gd-DTPA (carboxymethyldextran-GdDTPA, carboxymethyl linked)	Gd-DTTA-MA	39 900			9.8				299
CMD-Gd-DTPA	Gd-DTTA-MA	66 000			7.62		20	37[b]	301
CMD$_n$-Gd−DTPA where $n = 2$	Gd-DTTA-MA				9.4		20	37	302
CMD$_n$-Gd−DTPA where $n = 3$	Gd-DTTA-MA				9.5		20	37	302
CMD$_n$-Gd−DTPA where $n = 4$	Gd-DTTA-MA				9.4		20	37	302
CMD$_n$-Gd−DTPA where $n = 6$	Gd-DTTA-MA				8.9		20	37	302

[a] Water. [b] Plasma.

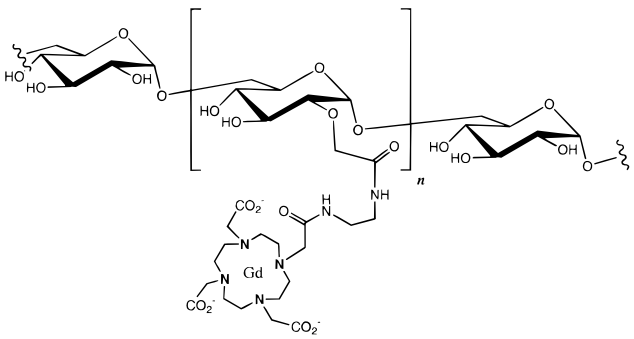


Figure 44. Chemical structure of CMD-A2-Gd-DOTA, a modified dextran polymer.

with chloroacetic acid, the introduction of an ethylenediamine spacer, followed by EDCI-mediated coupling of DOTA. The resulting conjugate has been investigated as an intravascular MR contrast agent for myocardial perfusion [296]

The relaxivity properties of CMD-A2-Gd-DOTA and related derivatives are shown in Table 24. The derivatives have modest 20 MHz relaxivity values (6−11 $mM^{-1}\,s^{-1}$ at 37 °C). Interestingly, the relaxivity data for a series of compounds differing by the number of methylene units linking the chelate to the dextran backbone are essentially identical. In addition, there was little dependence on molecular weight.

F. Targeted Agents

Conceptually, antibodies or other tissue-specific molecules may be combined with paramagnetic centers to provide disease-specific MRI agents. The challenge with regard to delivering sufficient quantity of paramagnetic label is substantial.[271] However, a number of interesting reports have appeared describing the preparation and characterization of targeted agents which contain a significant number of gadolinium atoms.

Curtet and co-workers have described the improved conjugation of polylysine-gadolinium chelates to anticarcinoembryonic antigen (CEA) monoclonal antibodies.[304] In this example, paramagnetic loading as high

Table 25. Targeted Macromolecular Contrast Agents

macromolecular contrast agent	conjugate	chelate type	target	MW (Da)	ion r_1 (mM^{-1} s^{-1})[a]	mol r_1 (mM^{-1} s^{-1})[a]	freq (MHz)	T (°C)	no. of Gd(III)	ref
Gd−PL-DTPA-HSA	HSA	DTTA-MA	vascular	140 000	∼10.8[b]		10	37	60−90	274
Gd−PL-DOTA-HSA	HSA	DO3A-MA	vascular	140 000	∼13.0[b]		10	37	60−90	274
f-PANAM-TU-DTPA	folic acid	DTPA	folate receptor	NR	NR	NR[c]	NR[c]	NR[c]	NR[c]	306
PL-Gd-DTPA$_{24-28}$−anti CEA	anti-CEA Fab(ab′)$_2$	DTTA-MA	Colorectal carcinoma	113 000	14.5	348−406	20	39	24−28 per antibody	304
PL-Gd-DOTA$_{24-28}$−anti CEA	anti-CEA Fab(ab′)$_2$	DO3A-MA	Colorectal carcinoma	114 000	16	384−448	20	39	24−28 per antibody	304

[a] Water. [b] Molar relaxivity of the polymeric chelate (reported to be essentially identical to that of the HSA conjugate). [c] NR = not reported.

as 24 to 28 metal ions per antibody was obtained without sacrificing immunoreactivity (80−85%) for conjugates PL-Gd-DTPA$_{24-28}$F(ab′)$_2$ and PL-Gd-DOTA$_{24-28}$F(ab′). The bipohysical data for these conjugates are listed in Table 25. The relatively low relaxivity for the antibody conjugates (r_1 = 13 to 16 mM^{-1} s^{-1}) is thought to be a consequence of fast segmental motion and/or slow water exchange. In vivo studies were performed in nude mice grafted with human colorectal carcinoma LS 174T. For one group of animals, 24 h after injection of 0.001 mmol/kg of gadoliunium-labeled immunoconjugate, the tumor uptake in was 10−15% and a corresponding r_1 increase of 15−20% was noted. However, in another "MRI negative group" of mice, no difference was found between the control and injected mice.

Wu and co-workers have reported the preparation of metal-chelate-dendrimer-antibody constructs for use in imaging and radioimmunotherapy.[305] Dendrimers have the advantage of uniform surface chemistry and low polydispersity ratios, which in theory should make their conjugates more well-defined chemically than their polymeric counterparts. In this work, generation 2 polyamidoamine (PAMAM) dendrimers were modified by reaction with bifunctional DTPA or DOTA chelators followed by conjugation to monoclonal antibody. No significant effect on immunoreactivity was noted. While this work was primarily directed toward radioimmunotherapy, the approach was noted to be useful for gadolinium as well. Subsequently, Wiener reported the preparation of folate-conjugated MRI imaging agents using the dendrimer conjugation approach.[306] In this work, folic acid was attached to a generation four ammonia core dendrimer, which was then reacted with an isothiocyanate DTPA derivative to form the polymeric chelate f-PAMAM-TU-DTPA. Cells accumulated the folate-conjugated dendrimer in a receptor specific manner. When treated with 28 nM folate-conjugated PAMAM-TU-GdDTPA for 40 min, the longitudinal relaxation rate at 50 MHz increased by 109% as compared with ∼20% for the control. These data indicate that cellular relaxation rates can be modified by targeting receptors in vitro. However, as noted by the authors, layers of targeting and pharmacokinetic challenges remain before receptor-based MRI agents can be used in vivo.

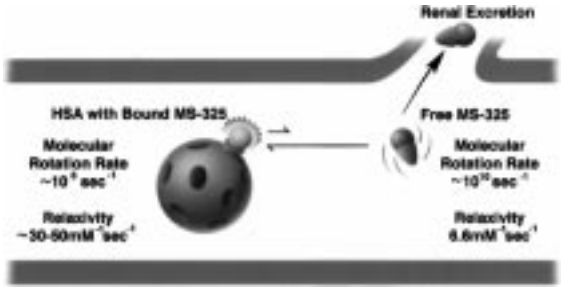


Figure 45. RIME mechanism of action for MS-325. The agent is shown schematically as consisting of two parts: a circular gadolinium chelate and a bullet-shaped protein-binding moiety. Within the bloodstream, MS-325 binds, on average, to one of many available sites on HSA. The bound form is in equilibrium with a small amount of the free form which is renally excreted steadily over time. The bound form of MS-325 has greatly enhanced relaxivity by virtue of its slower molecular tumbling rate.

VI. Relaxivity of Noncovalently Bound Adducts of Gadolinium(III) Complexes

Gadolinium(III) complexes that noncovalently bind to substrates have certain inherent advantages from a biophysical viewpoint over their bioconjugate cousins. This is the basis of the receptor induced magnetization enhancement (RIME) philosophy.[307] In this approach, a contrast agent is targeted to a particular protein or receptor molecule. The binding causes an increased concentration and retention of the Gd(III) complex in the area of the receptor molecule. Binding to a macromolecule also allows the Gd(III) complex to take on a rotational correlation time that is similar to that of the macromolecule. This increase in τ_R can cause a dramatic increase in relaxivity. Furthermore, the high relaxivity of the bound complex is much greater than that of the unbound, which leads to a high target-to-background ratio.

The RIME concept was articulated[307] in 1991 and is diagrammed schematically in Figure 45, using MS-325 (Chart 2) as an example. Relaxivity enhancement in the tissue of interest occurs not only by compartmentalization of the agent but also by improved relaxivity upon binding. This is a mechanism that is unique to MRI contrast agents and is unavailable to diagnostic nuclear medicine or ultrasound. Some of the early work in this area involved the binding of iron(III) complexes to HSA.[308]

MS-325 was the first complex to fully exploit the RIME concept. MS-325 was designed as a contrast agent for imaging the blood pool using serum albu-

min as the targeted binding molecule.[309,310] HSA is an attractive target for blood pool imaging. It constitutes about 4.5% of plasma (~ 0.67 mM) and is known to bind a variety of small molecules at multiple sites on the protein. In 4.5% HSA at 37 °C, MS-325 was highly bound at a contrast agent concentration of 0.1 mM. Under these conditions, the observed 20 MHz relaxivity was 42.0 mM^{-1} s^{-1}. The relaxivity of MS-325 in phosphate buffered saline (PBS) is only 6.6 mM^{-1} s^{-1}. This represents an almost 7-fold increase upon binding.

It was shown that MS-325 binds to more than one site on HSA and that the calculated bound relaxivity ($r_1^{bound} = \{r_1^{obs} - x^{free}r_1^{free}\}/x^{bound}$; x = mole fraction) is dependent on the binding binding site. As the MS-325 concentration increased, r_1^{bound} decreased from 45 to 30 mM^{-1} s^{-1}. These two points suggest that the use of the proton relaxation enhancement (PRE) method alone for determining binding constants is not a useful method for HSA ligand interactions.[311] With HSA there are often multiple nonidentical binding sites which can give rise to varying degrees of relaxation enhancement. Scatchard plots cannot be unambiguously fit, making the interpretation of data rather dubious.

It should also be noted at this point that defining relaxivity in terms of mM^{-1} s^{-1} in protein solutions can be misleading. Several reports use HSA concentrations greater than 3 mM; because of the high molecular weight of HSA, these solutions are more than 20% protein and hence less than 80% water. The molar concentration of 1 mmol of Gd(III) in a liter of 20% HSA is 1 mM, but the molal concentration would be 1.25 mmolal—the reported relaxivity is overestimated by 25%. A relaxivity enhancement has been reported for $[Gd(DOTA)(H_2O)]^-$ as a function of HSA concentration.[243] Although $[Gd(DOTA)(H_2O)]^-$ does not bind to HSA there is an apparent linear increase in r_1 with increasing HSA concentration which can be ascribed to the misleading definition of relaxivity.

MP-2269 (Chart 2) is another example of a blood pool agent which binds to HSA and exhibits enhanced relaxivity.[258] The relaxivity of MP-2269 was found to be about 3 times greater in the presence of 4% HSA versus its relaxivity in pure H_2O. Toth et al.[220] have studied MP-2269 in the presence and absence of 20% w/v bovine serum albumin (BSA) with NMRD and ^{17}O NMR. Their results suggest that the water exchange rate of MP-2269 does not change upon binding to BSA. They estimate the rotational correlation time of the bound complex to be about 1 ns which is about 7 times longer than the unbound complex. A 1 ns correlation time suggests that there is still some rotational flexibility within the bound complex.

Cavagna et al. have shown that increasing the number of benzyloxymethyl (BOM) groups on a DTPA or DOTA core (Charts 2 and 14) leads to increased relaxation enhancement in the presence of HSA. The multipurpose agent $[Gd(BOPTA)(H_2O)]^{2-}$ contains one BOM, group and B-21326/7 contains three BOM groups.[246] Both compounds showed enhanced relaxivity in plasma. B-21326/7 had a higher enhancement and appeared to be more rigidly bound

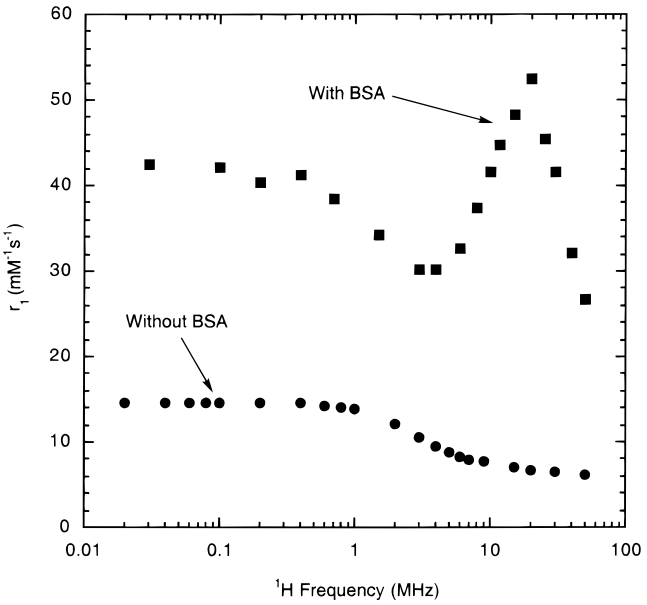


Figure 46. NMRD curves $[Gd\{(DOTA(BOM)_3\}(H_2O)]^-$ in the presence and absence of BSA. Note the large increase in relaxivity upon binding to the protein.

based on an NMRD profile. Aime et al. reported relaxation enhancements of $[Gd(DOTA\{BOM\}_n(H_2O)]^-$ complexes with HSA.[243] The relaxation enhancement increased with the number of BOM units added. Their data was fit to a two equal site binding model.

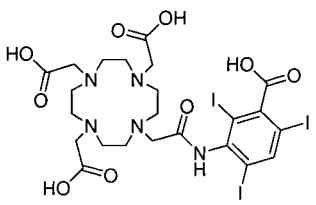
The NMRD curve of $[Gd(DOTA(BOM)_3)(H_2O)]^-$ is shown in Figure 46.[243] The calculated NMRD curve of $[Gd(DOTA(BOM)_3)(H_2O)]^-$ bound to BSA is also shown. The authors used the K_a from their PRE study to calculate how much complex was bound to BSA under these conditions. They then used these data to determine a bound relaxivity. The increase in r_1 upon binding is remarkable.

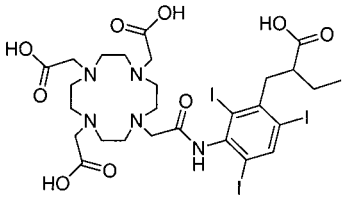
Anelli et al. have also reported a series of monoamide derivatives of DOTA in which the amide group is linked to an iodinated aryl ring.[263] They report six derivatives and use two aryl groups which find use in hepatobiliary X-ray contrast imaging, Chart 20. These compounds also bind to HSA. In a study at 20 MHz, the relaxivity of these compounds in saline and reconstituted human serum were compared. There is a 2- to 3-fold increase in r_1 and r_2 in serum compared to saline (Table 26).

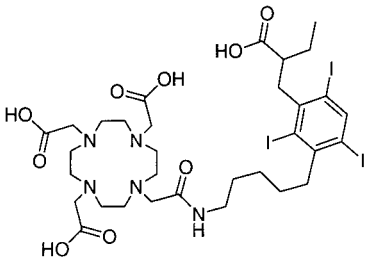
The complex $[Gd(PCTP\text{-}[13])(H_2O)]^{3-}$ binds weakly to HSA with an association constant of 600 M^{-1} reported.[231] The authors claim a relaxivity of 45 mM^{-1} s^{-1} for the bound agent. They have also calculated a "bound" NMRD profile based on the association constant and used $[Gd(DOTP)]^{5-}$ as an outer-sphere model. The authors fit the NMRD curve to a rotational correlation time of 30 ns and a water residency time of 290 ns at 25 °C. On the basis of this analysis, the water exchange rate slows by about 2 orders of magnitude upon protein binding.

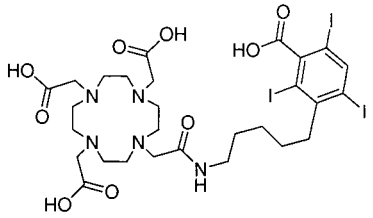
Aime and co-workers have also examined the q = 0 complex $[Gd(DOTPMBu)]^-$ (Chart 8) in the presence of HSA.[52] The butyl groups appear to enhance HSA binding (the ethyl analogue does not bind well), and they estimate a K_d of 1 mM. The relaxivity of $[Gd(DOTPMBu)]^-$ increases from 2.8 to 13.4 mM^{-1}

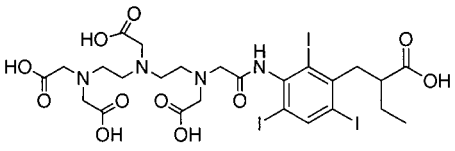
Chart 20


DO3A-L5


DO3A-L6


DO3A-L7


DO3A-L8


DTPA-L2

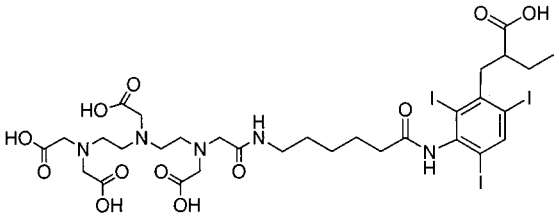

DTPA-L3

Table 26. Relaxivities (20 MHz, 39 °C) of Gd(III) Complexes Containing Iodinated Aryl Rings in Saline and in Seronorm (Reconstituted Human Plasma)[263]

ligand	r_1 (saline)	r_2 (saline)	r_1 (Seronorm)	r_2 (Seronorm)
DO3A-L5	5.01	7.01	10.57	12.08
DO3A-L6	5.59	7.33	14.23	16.57
DO3A-L7	5.07	6.60	18.19	21.50
DO3A-L8	4.80	6.25	10.51	12.51
DTPA-L2	5.91	7.96	12.92	14.46
DTPA-L3	5.48	6.17	18.39	21.12

s^{-1} on going from saline to 5% HSA solution. This is a very significant result to consider when trying to estimate the amount of inner-sphere relaxivity for a given compound. For systems with long τ_R, outer-sphere (second-sphere) relaxivity cannot be estimated from a small molecule such as $[Gd(TTHA)]^{3-}$.

Targeting of other macromolecules should increase relaxivity via the RIME mechanism. Two complexes which were designed with hepatobiliary contrast in mind are $[Gd(BOPTA)(H_2O)]^{2-}$ and $[Gd(EOB\text{-}DTPA)(H_2O)]^{2-}$. $[Gd(BOPTA)(H_2O)]^{2-}$ has a relaxivity of 4.4 $mM^{-1}\ s^{-1}$ in water, 6.9 $mM^{-1}\ s^{-1}$ in rat plasma, and $\sim$30 $mM^{-1}\ s^{-1}$ in rat hepatocytes.[312] $[Gd(EOB\text{-}DTPA)(H_2O)]^{2-}$ has a relaxivity (20 MHz, 37 °C) of 5.3 $mM^{-1}\ s^{-1}$ in water, 8.7 $mM^{-1}\ s^{-1}$ in rat plasma, and 16.9 $mM^{-1}\ s^{-1}$ in rat hepatocytes. [313]

Wiener and co-workers have prepared a folate conjugate of their PAMAM-tu-DTPA dendrimer (vide supra).[306] This compound was designed to target tumor cells which express the high-affinity folate receptor (hFR). They established that the complex binds to tumor cells with the hFR and that upon binding a 2-fold increase in relaxivity was observed.

Martin et al.[252] described the preparation of some DTPA-based dimers and tetramers (Chart 21). The authors also report relaxivities in water and in 4% BSA solution and observe an increase upon measuring r_1 in the protein solution (see Table 27).

Incorporation of a contrast agent into a liposome or membrane is another means of slowing tumbling times and increasing relaxivity.[314−319] The majority of studies have employed a DTPA-bisamide ligand where the amide group contains a long chain fatty acid such as a stearyl or myristyl derivative. This is largely a result of the synthetic ease of preparing symmetric bisamides from DTPA anhydride. Unfortunately, as outlined in sections IV and V, Gd(III) complexes of DTPA-bisamides have very slow water exchange rates and relaxivity can be limited by long τ_m values. Nevertheless, relaxivities in the teens to mid-twenties range have been reported for various liposome and membrane containing contrast agents. Liposomes have also been used to encapsulate contrast agents as a means of drug delivery;[320,321] encapsulated chelates do not show the same r_1 enhancement as those which form part of the liposome itself.

Aime and co-workers have reported several studies on the formation of ternary complexes between β-cyclodextrin and contrast agents. [35,95,228,253,256] Cyclodextrin binding serves to slow the molecular tumbling time and increase relaxivity. The relaxivity increases are modest compared to some of the systems mentioned above, but this is a much more well-defined system and more amenable to quantitative study.

Chart 21

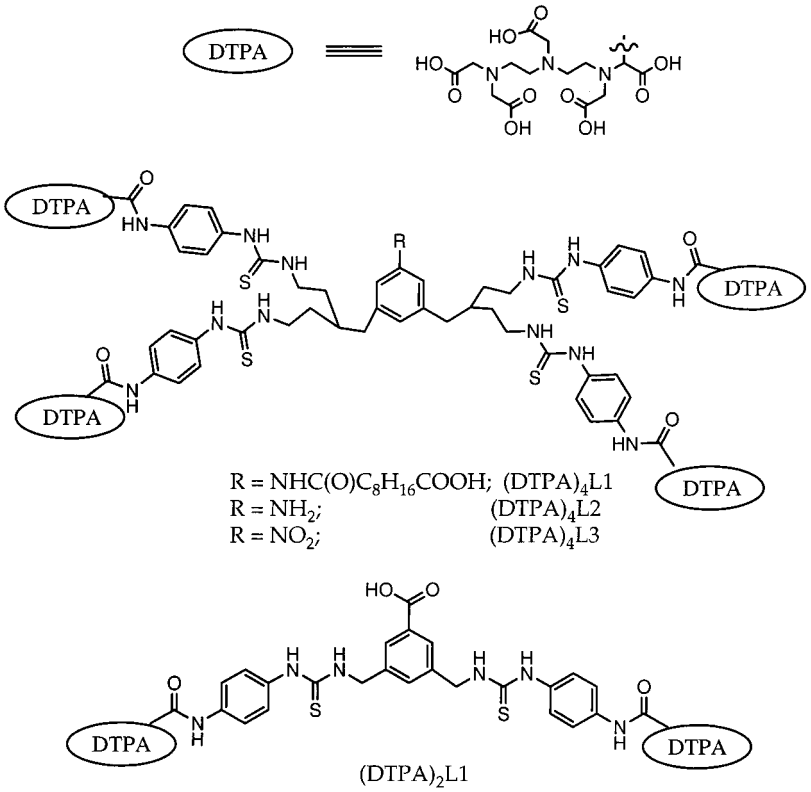


Table 27. Relaxivities (20 MHz) of DTPA Multimers in Water and in 4% Bovine Serum Albumin Solution[252]

ligand	r_1/Gd (H_2O)	r_1/mol (H_2O)	r_1/Gd (BSA)	r_1/mol (BSA)
DTPA-L1	3.7	3.7	12.6	12.6
$(DTPA)_2L1$	4.7	9.4	9.3	18.6
$(DTPA)_4L1$	10.4	41.6	24.6	98.4
$(DTPA)_4L2$	9.1	36.4	19.2	76.8
$(DTPA)_4L3$	13.3	53.2	20.4	81.6

The use of noncovalent binding to a macromolecular target is a field that shows a great deal of promise. Many impressive gains in relaxivity have already been reported. The quantitation of the parameters influencing relaxivity is even more difficult than in sections IV and V because a new variable—binding—is introduced. What is more difficult still is that proteins such as HSA do not have a single well-defined binding site. In many reports to date several assumptions have been made regarding binding. It is often assumed that multiple binding sites have the same binding constant and that the relaxivity at each site is the same, but this has never been proven. Intuitively one would expect contrast agents to bind to HSA with varying affinities to multiple sites on the protein since this is what happens with fatty acids and other small molecules.[322] Likewise, it is dangerous to assume that binding offers a uniform relaxivity. Because of these two discrepancies, proton relaxation enhancement curves cannot be uniquely fit to one model.[311] Until the speciation of the contrast agent−protein system is established by direct techniques, the interpretation of relaxation data is questionable.

VII. General Physicochemical Properties

Beyond the relatively esoteric functional attribute of relaxivity, MRI contrast agents exist and function in the body as drugs. As such, their in vivo properties, including biodistribution, pharmacokinetics, and safety, are dependent on the same combination of properties that determine drug behavior. These properties do not vary tremendously among the agents currently approved or in clinical trials. However, their cataloging does illuminate subtle differences, some of which have functional consequences. Table 28 shows the most frequently measured parameters for the relevant i.v. formulations.[323] Variations in hydrophobicity lead to the greatest differences in in vivo behavior, with potential to alter biodistribution, pharmacokinetics, and safety. Osmolality and viscosity are mainly discussed in reference to safety and ease of injection.

Hydrophobicity can be measured using traditional octanol/water or butanol/water partition experiments or HPLC.[324] Butanol/water coefficients are shown in Table 28 since they are more available in the literature and because very little of the more hydrophilic agents, such as $[Gd(DTPA)(H_2O)]^{2-}$, partition into octanol. The results show that MRI contrast agents are generally hydrophilic, a property that was well known to give rise to limited cell penetration and good tolerability. A more mundane advantage of hydrophilicity is good water solubility; this permits the substantial doses to be administered in small volumes.

The extracellular agents have log *P* values over a very limited range (−2 to −3.2). The lack of any substantial difference in in vivo properties among these agents seems to correlate with these measurements. The addition of aromatic or conjugated ring systems increases hydrophobicity and allows for varying degrees of targeting to proteins or cells (see

Table 28. Physicochemical Properties of MRI Contrast Agents[6,8,323,324]

chemical name	concn (M)	osmolality[a] (osmol kg^{-1})	viscosity (mP s)	log *P* ($BuOH/H_2O$)
$[Gd(DTPA)(H_2O)]^{2-}$	0.5	1.96	2.9	−3.16
$[Gd(DOTA)(H_2O)]^{-}$	0.5	1.35	2.0	
$[Gd(DTPA\text{-}BMA)(H_2O)]$	0.5	0.65	1.4	−2.13
$[Gd(HP\text{-}DO3A)(H_2O)]$	0.5	0.63	1.3	−1.98
$[Gd(DO3A\text{-}butrol)(H_2O)]$	0.5	0.57	1.43	−2
$[Gd(DO3A\text{-}butrol)(H_2O)]$	1.0	1.39	3.9	−2
$[Gd(DTPA\text{-}BMEA)(H_2O)]$	0.5			
$[Gd(BOPTA)(H_2O)]^{2-}$	0.5	1.97	5.3	−2.23
$[Gd(EOB\text{-}DTPA)(H_2O)]^{2-}$	0.25	0.89	1.22	−2.11
MS-325	0.25			−2.11

[a] Osmolality and viscosity measured at 37 °C.

section IX). Nonetheless, the agents remain very hydrophilic.

Osmolality is frequently measured for MRI contrast media more as a holdover from iodinated X-ray contrast agents than for any critical safety reason. Since very large doses of X-ray agents are used, some improvement in tolerability was obtained by switching from charged agents to neutral molecules which required no counterions and thus exhibited much lower osmolality. It was thought that the newer formulations were less irritating to the vascular system and kidneys since the solutions were much closer to the osmolality of serum. These notions guided commercial activities in MRI as well.[8]

Table 28 shows that similar reductions in osmolality have been achieved for the neutral extracellular MRI agents which require no positively charged counterions. While these neutral agents have been shown to have higher LD_{50}s in animals, the mechanisms responsible have not been elucidated. Moreover, some of the mild and reversible effects of ionic agents, such as vacuolization of the kidney tubular cells, were thought at one time to be osmotic in nature, but these effects were produced by the neutral agents as well.[325] Most importantly, clinical trials repeatedly showed no significant difference in adverse events between any of the extracellular agents.[326,327]

In addition to lower osmolality, the formulations of neutral agents also have lower viscosity. This could have some benefit in applications requiring rapid injection, although power injectors have largely replaced human hands for these applications. It was also thought that the injection of a less viscous solution would minimize sheer forces in the vein, but there is no evidence of any difference in vascular toxicity among the extracellular agents.

VIII. Safety

A. Low Molecular Weight Chelates

The extracellular class of MRI agents are widely known to be among the safest drugs ever introduced.[4,326−328] The reported adverse event rates range from 1 to 3%, including such mild effects as headache, nausea, and taste perversion (oddly, a "metallic" taste despite the fact that the chelates do not dissociate in vivo). As with any widely used drug, there are scattered reports of more serious reactions such as anaphylaxis, but the reported rates are extremely low (0.0003−0.01%). The hepatobiliary and blood pool chelates in development appear to have comparable safety.[329−334]

An important contributory factor to the safety of these agents is their efficient excretion from the body. This minimizes exposure to the drug and reduces the chance that slow uptake processes such as endocytosis might internalize the agents in cells. In addition, the agents are largely excreted unaltered by oxidation or conjugation.

There is no evidence that any of the clinical effects of gadolinium(III) chelates stem from free gadolinium(III). Most likely the effects are due to the intact, foreign molecule or the small amount of free ligand added in the formulation. As discussed earlier, both metal ions and ligands tend to be more toxic than their stable chelates. The lack of any metal-based toxicity in humans is consistent with biodistribution studies in animals showing no significant bone uptake of free gadolinium(III).[6,334]

Investigators have tried to use animal and in vitro studies to discriminate among the extracellular agents,[6,8,334] especially using LD_{50} values, zinc chelation results, or metal ion release data (vide supra, section II). As mentioned above, neutral chelates have higher LD_{50}s. Macrocyclic chelates, such as $[Gd(DOTA)(H_2O)]^{-}$ and $[Gd(HP\text{-}DO3A)(H_2O)]$, release somewhat less gadolinium(III) in vivo. However, none of these differences appear to be relevant clinically.

B. Macromolecular Agents

As opposed to the free excreted small molecules, macromolecular conjugates tend to have much longer dwell times in the body and less complete elimination. This increases the odds of cellular uptake and processing, leading potentially to the release of toxic byproducts including free gadolinium(III). Franano et al.[117] have shown that albumin-Gd-DTPA conjugates can be metabolized in vivo to form lysine-Gd-DTPA monomers. Since this is likely to occur in the low pH environment of a lysosome, it is not suprising that, depending on the strength of the chelate, a significant fraction of the chelates dissociated, and gadolinium was found in the bone.

Moreover, large multivalent molecules are more likely to be antigenic than small molecules, leading to drug-directed antibodies and potentially anaphy-

laxis. Probably as a result of these concerns, no macromolecular agents have progressed to human trials.

IX. Applications

Due to the appreciable concentrations of paramagnetic label required for MRI enhancement (10−100 μM), novel applications involving true "magic bullet" targeting to receptors have not emerged, at least clinically. As outlined 12 years ago,[1] the dominant classes of agents in use or in development stem from bulk biodistribution rather than any elegant uptake mechanism. Still, there are molecular features which are critical to their function and interesting to explore.

A. Extracellular Agents

This class of agents represents the dominant use of MRI contrast media in radiology. After injection, the agents distribute nonspecifically throughout the plasma and interstitial space of the body. The agents are excreted by the kidneys with an elimination half-life of 1.5 h. A typical use is the detection of tumors in the brain. New applications involve faster imaging during injection to obtain images of arteries or of blood flow to the heart.

B. Blood Pool Agents

After extracellular agents, the next largest class of applications may involve blood pool agents that enhance vascular structures for the entire period of the MRI exam. The clinical need for these types of agents stems largely from the desire for a noninvasive alternative to X-ray angiography, the standard, but potentially dangerous, procedure for obtaining high-resolution pictures of arterial blockages in the body. In X-ray angiography, an artery, such as the femoral artery in the groin, is punctured and a long cathether fed to the site of interest. Large volumes of iodinated X-ray contrast agent are rapidly injected to highlight arteries during X-ray exposure. In addition to high cost to the health care system, side effects include pain, damage to the puncture site, kidney damage, and occasionally limb loss or death.

MRI represents a more attractive procedure for patients and doctors. Images of enhanced vessels can be obtained easily using intravenous injections of contrast agents rather than arterial injections. In addition, gadolinium agents are used in lower doses than X-ray agents and do not cause kidney dysfunction.

MS-325 (AngioMARK) is the prototype MR angiographic agent.[310,333] In addition to high relaxivity, its strong binding to albumin in serum reduces the free concentration available for glomerular filtration in the kidneys, thus slowing the renal excretion rate and prolonging the blood half-life and imaging window. Animal (Figure 47) and human studies showed that vessels were strongly enhanced with MS-325 for over 1 h in comparison to the very short window available with extracellular agents (0.5−3 min). The added time available with MS-325 permits the use of very high-resolution MR pulse sequences, affording stunningly detailed images of the vascular system (Figure 48).

A critical element in the design of MS-325 was pharmacokinetic tuning. The same chemical features which give rise to albumin binding, hydrophobic groups, also lead to liver uptake which can decrease blood half-life. A structure−activity analysis afforded a general solution to this problem,[335] and the hydrophilic phosphodiester group in MS-325 is representative. Despite causing a decrease in the overall lipophilicity, this moiety, placed in a critical position between the hydrophobic diphenylcyclohexyl group and the chelate, allowed for high albumin binding affinity. Presumably, the critical positioning of this anionic group leads to electrostatic interactions with known cationic side chains in the albumin binding sites. At the same time, however, the decreased overall lipophilicity leads to decreased liver uptake and prolonged blood half-life.

The alternative approach to blood pool agents, using macromolecules with covalently attached chelates, has been plagued with manufacturing and safety concerns.[4] None of these agents has progressed to clinical trials to date.

C. Hepatobiliary Agents

The presence of hydrophobic groups on metal chelates can lead to hepatocellular uptake and excretion into the bile ducts, gall bladder, and intestines. This class of MRI agents has been actively investigated for years,[14] and the first gadolinium-based agent, $[Gd(BOPTA)(H_2O)]^{2-}$ (MultiHance), is approved in Europe.[329,330] Interestingly, the perceived clinical applications of this agent mirror the biochemical consequences of its chemical structure. The presence of an aromatic ring gives rise to both albumin binding in serum and liver uptake (with cytosolic binding inside hepatocytes), so the agent is being pursued as both a liver agent and a general agent with higher relaxivity due to albumin binding. Latter applications include the same uses as the extracellular agents, especially the temporary enhancement of vascular structures. Thus $[Gd(BOPTA)(H_2O)]^{2-}$ is the first RIME agent to be approved for human use.

A related chelate, $[Gd(EOB\text{-}DTPA)(H_2O)]^{2-}$ (Eovist), is currently in phase III clinical trials.[331,332] This agent is excreted to a greater extent via the liver (roughly 50% for $[Gd(EOB\text{-}DTPA)(H_2O)]^{2-}$ vs 2−4% for $[Gd(BOPTA)(H_2O)]^{2-}$), resulting in stronger liver enhancement.

The mechanism for chelate uptake by the liver has not been clarified. Presumably it occurs from passive dissolution in the hepatocyte membrane or via discrete receptors. However, studies with MRI agents have confirmed that the transport from the hepatocyte into bile occurs via a specific organic anion transporter critical in the excretion of bilirubin, the toxic heme breakdown product. In the case of $[Gd(EOB\text{-}DTPA)(H_2O)]^{2-}$, prolonged trapping in the liver

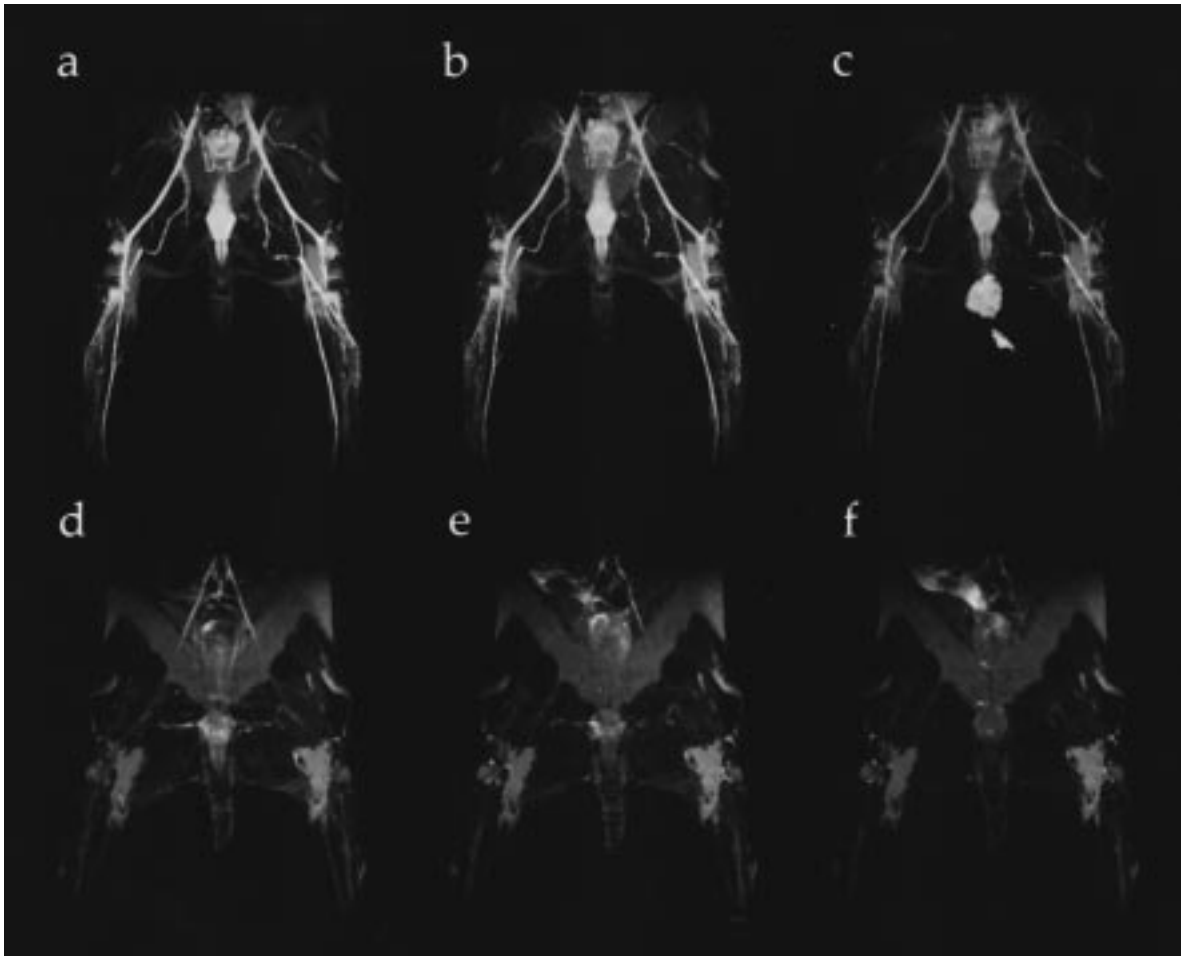


Figure 47. MR images (FISP 40/10/60 deg) of rabbit hindquarters after injection of either MS-325 (0.025 mmol/kg; a−c) or Gd-DTPA (0.1 mmol/kg; d−f). Images shown are 5 (a, d), 30 (b, e), and 60 min postinjection (c, f). Strong, persistent vascular enhancement is evident for MS-325 compared to transient enhancement available with Gd-DTPA.

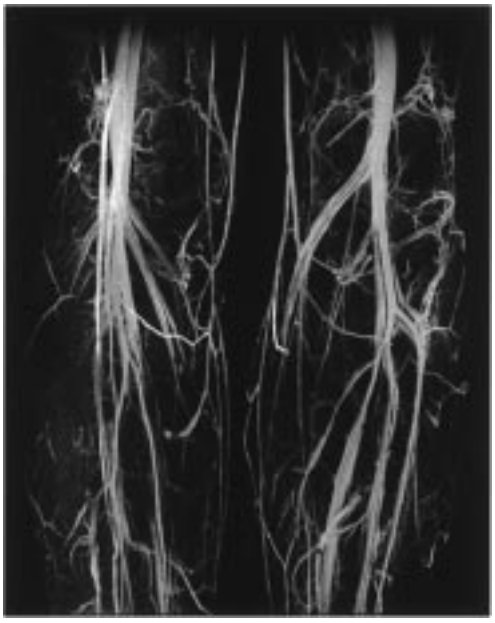


Figure 48. MRI image of the legs in a volunteer after injection of AngioMARK (MS-325). The prolonged increase in blood $1/T_1$ and signal enables noninvasive, high-resolution imaging of the vascular system, including detailed depictions of artery/vein pairs.

and strongly reduced biliary excretion were observed in mutant rats lacking this transporter.[336]

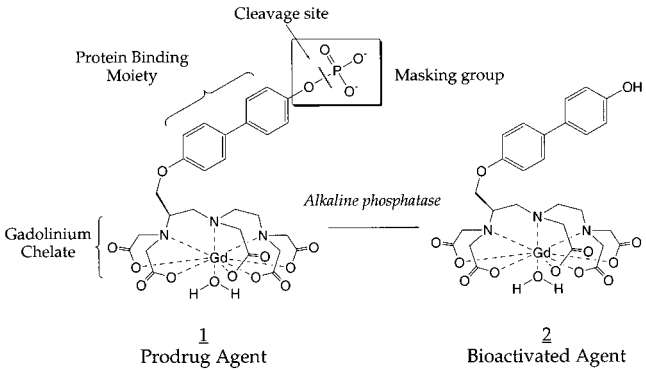
D. Other Agents

Many targeted contrast agents for MRI have been proposed and studied in vitro and in animals. Most of these have not progressed to advanced development or clinical trials due to metal chelate instability, insufficient targeting, high cost, toxicity, or small perceived market. An interesting discussion by Nunn et al. analyzes the reasons in more detail.[271] The following discussion summarizes a few notable areas that have attracted the most attention.

Metalloporphyrins have been evaluated as MRI agents for many years. The nonspecific binding of porphyrins to the interstitial space in tumors, known for over 50 years, attracted early interest in tumor imaging. One expanded porphyrin, PCI-120 ([Gd-(Tx)]$^{2+}$), is currently in clinical trials as a radiation sensitizer for brain cancer,[337] properties that stem from the unique delocalized ring structure, not the metal ion (see Scheme 1 for ligand structure). As a side benefit, the presence of a gadolinium(III) ion in the agent also creates prolonged enhancement of the tumors on MRI images. There are no reports that the agent has any advantages over extracellular agents for tumor detection, however.

One application for porphyrins that may have more promise is the prolonged enhancement of necrotic tissue, especially of myocardial infarcts. Schering AG has developed gadophrin-2, a Gd-DTPA chelate teth-

Scheme 2



ered to a mesoporphrin (see Chart 16).[338,339] The mechanism for the avidity to necrosis is unknown, but may involve binding to cellular proteins released upon cell death or even to albumin which fills the necrotic area.

E. Bioactivated Agents

Recent reports show the potential of MRI agents which sense their biochemical environment, either through enzyme-induced relaxivity changes or changes due to the concentration of a particular substance. Once these strategies are made practical by proper choices of chelates, biochemical targets, and clinical indications, this approach may permit the detailed images of biological function.

Two recent reports show the potential to MRI agents which sense the presence of particular enzymes via enzyme-induced relaxivity changes. Meade and co-workers[340] synthesized (4,7,10-tri(acetic acid)-1-(2-β-galactopyranosylethoxy)-1,4,7,10-tetraazacyclododecane)gadolinium(III), a substrate for β-galactosidase. The galactose group coordinates to the Gd(III), lowering the relaxivity. The enzyme cleaves the galactopyranose group, increasing q from 0.7 to 1.2 and increasing the relaxivity by 20%.

McMurry and co-workers[341] used protein binding changes to increase relaxivity. This is shown schematically in Scheme 2. A substrate for alkaline phosphatase, prodrug **1**, was selected for its low binding affinity for HSA. Reaction with the enzyme yielded a 70% increase in $1/T_1$ in 4.5% HSA. Hydrolysis of the phosphate moiety increases the hydrophobicity of the aryl group, permitting stronger HSA binding affinity. Higher binding of **2**, the bioactivated agent, increases relaxivity.

Finally, Li et al.[342] sythesized a calcium-responsive agent, DOPTA-Gd, based on well-known calcium-chelating EGTA fluorophores. In the presence of low concentrations of calcium, the aromatic iminoacetate groups may coordinate in some fashion to the gadolinium ions, maintaining low (outer sphere?) relaxivity. As the concentration of calcium approaches micromolar, the EGTA chelate binds calcium, possibly releasing the Gd(III) coordinated iminoacetates, and increases relaxivity from 3.26 to 5.76 mM^{-1} s^{-1}. This interesting compound certainly merits more attention. The mechanism of relaxivity increase is speculative, and a detailed study of hydration is warranted.

X. Conclusion

MRI contrast media represent a complex field of technical endeavor. Much like other multidisciplinary areas such as high-temperature superconductors, the progress is at once encouraging but frustratingly slow.

We have seen great progress in understanding why different complexes have different relaxivities, yet we have been unable to drastically increase the values to enable targeting low-concentration receptors. The structure−activity relationships seen with water exchange behavior are most notable, but this is just a tuning fork, not the ultimate answer. In addition, the structure of the transition states and, thus, the real reasons why each complex has a different τ_m are unknown.

Most frustrating has been the lack of hard data and new theories regarding electron spin relaxation and its field dependent effects on relaxivity. Why are there countless dissertations on the electronic properties of obscure metalloenzymes and essentially none on gadolinium?

The ultimate beneficiaries of this hard work are, of course, patients. MRI, with the help of contrast agents, can eliminate painful, invasive procedures and provide diagnostic information earlier in the clinical workup. The authors have heard countless stories of clinical trial patients comparing a torturous X-ray angiography procedure to a safe, painless AngioMARK MRI. The efforts of chemists, along with their colleagues in other disciplines, have a lot to do with this progress.

It will be interesting to see how much more we can say in another decade.

XI. Acknowledgments.

The authors acknowledge Prof. André Merbach and Dr. Éva Tóth for providing data and a preprint of ref 281. Professor Silvio Aime is thanked for providing the NMRD data in Figures 39 and 46. Professor Bill Armstrong is kindly acknowledged for the use of his software and facilities in preparing the ORTEP drawings used throughout.

XII. References

(1) Lauffer, R. B. *Chem. Rev.* **1987**, *87*, 901−927.
(2) Banci, L.; Bertini, I.; Luchinat, C. *Nuclear and Electron Relaxation*; VCH: Weinheim, 1991.
(3) Aime, S.; Botta, M.; Fasano, M.; Terreno, E. *Chem. Soc. Rev.* **1998**, *27*, 19−29.
(4) Brasch, R. C. *Radiology* **1992**, *183*, 1−11.
(5) Tweedle, M. F. *J. Alloys Compd.* **1992**, *180*, 317−23.
(6) Tweedle, M. F. *Invest. Radiol.* **1992**, *27*, 2−6.
(7) Lauffer, R. B. *Magn. Reson. Quart.* **1990**, *6*, 65−84.
(8) Rocklage, S. M.; Watson, A. D.; Carvlin, M. J. In *Magnetic Resonance Imaging*; Stark, D. D., Bradley, W. G., Eds.; Mosby: St. Louis, 1992; Vol. 1.
(9) Øksendal, A. N.; Hals, P.-A. *Magn. Reson. Imaging* **1993**, *3*, 157−165.
(10) Mathur-De Vré, R.; Lemort, M. *Brit. J. Radiol.* **1995**, *68*, 225−247.
(11) Mitchell, D. G. *J. Magn. Reson. Imaging* **1997**, *7*, 1−4.
(12) Low, R. N. *J. Magn. Reson. Imag.* **1997**, *7*, 56−67.
(13) Mahfouz, A.-E.; Hamm, B.; Taupitz, M. *Eur. Radiol.* **1997**, *7*, 507−513.
(14) Schuhmann-Giampieri, G. *Invest. Radiol.* **1993**, *8*, 753−761.
(15) Peters, J. A.; Huskens, J.; Raber, D. J. *Prog. Nucl. Magn. Reson. Spectrosc.* **1996**, *28*, 283−350.

(16) Weissleder, R.; Papisov, M. *Rev. Magn. Reson. Med.* **1992**, *4*, 1−20.
(17) Gupta, H.; Weissleder, R. *MRI Clinics of North America* **1996**, *4*, 171.
(18) Albert, M. S.; Cates, G. D.; Driehuys, B.; Happer, W.; Saam, B.; Springer, C. S., Jr.; Wishnia, A. *Nature* **1994**, *370*, 199.
(19) Guggenberger, L. J.; Muetterties, E. L. *J. Am. Chem. Soc.* **1976**, *98*, 7221−5.
(20) Gries, H.; Miklautz, H. *Physiol. Chem. Phys. Med. NMR* **1984**, *16*, 105−12.
(21) Stezowski, J. J.; Hoard, J. L. *Isr. J. Chem.* **1984**, *24*, 323−34.
(22) Jin, T.; Zhao, S.; Xu, G.; Han, Y.; Shi, N.; Ma, Z. *Huaxue Xuebao* **1991**, *49*, 569−75.
(23) Inoue, M. B.; Inoue, M.; Fernando, Q. *Inorg. Chim. Acta* **1995**, *232*, 203−6.
(24) Sakagami, N.; Homma, J.-i.; Konno, T.; Okamoto, K.-i. *Acta Crystallogr., Sect. C: Cryst. Struct. Commun.* **1997**, *C53*, 1378−1381.
(25) Ruloff, R.; Gelbrich, T.; Hoyer, E.; Sieler, J.; Beyer, L. *Z. Naturforsch., B: Chem. Sci.* **1998**, *53*, 955−959.
(26) Caulfield, T. J.; Guo, P.; Illig, C. R.; Kellar, K. E.; Liversidge, E.; Shen, J.; Wellons, J.; Ladd, D.; Peltier, N.; Toner, J. L. *Bioorg. Med. Chem. Lett.* **1995**, *5*, 1657−62.
(27) Tyeklar, Z.; Midelfort, K.; Dunham, S.; Lauffer, R.; McMurry, T.; Hollander, F. Unpublished results.
(28) Uggeri, F.; Aime, S.; Anelli, P. L.; Botta, M.; Brocchetta, M.; de Haën, C.; Ermondi, G.; Grandi, M.; Paoli, P. *Inorg. Chem.* **1995**, *34*, 633−42.
(29) Dapporto, P.; Fedelli, F.; Paoli, P.; Uggeri, F. *Acta Crystallogr., Sect. C: Cryst. Struct. Commun.* **1996**, *C52*, 1438−1441.
(30) Selvin, P. R.; Jancarik, J.; Li, M.; Hung, L.-W. *Inorg. Chem.* **1996**, *35*, 700−5.
(31) Ehnebom, L.; Fjaertoft Pedersen, B. *Acta Chem. Scand.* **1992**, *46*, 126−30.
(32) Konings, M. S.; Dow, W. C.; Love, D. B.; Raymond, K. N.; Quay, S. C.; Rocklage, S. M. *Inorg. Chem.* **1990**, *29*, 1488−91.
(33) Bligh, S. W. A.; Chowdhury, A. H. M. S.; McPartlin, M.; Scowen, I. J.; Bulman, R. A. *Polyhedron* **1995**, *14*, 567−9.
(34) Wang, Y.-M.; Cheng, T.-H.; Sheu, R.-S.; Chen, I.-T.; Chiang, M. Y. *J. Chin. Chem. Soc. (Taipei)* **1997**, *44*, 123−128.
(35) Aime, S.; Benetollo, F.; Bombieri, G.; Colla, S.; Fasano, M.; Paoletti, S. *Inorg. Chim. Acta* **1997**, *254*, 63−70.
(36) Parker, D.; Pulukkody, K.; Smith, F. C.; Batsanov, A.; Howard, J. A. K. *J. Chem. Soc., Dalton Trans.* **1994**, 689−93.
(37) Inoue, M. B.; Inoue, M.; Fernando, Q. *Acta Crystallogr., Sect. C: Cryst. Struct. Commun.* **1994**, *C50*, 1037−40.
(38) Inoue, M. B.; Inoue, M.; Munoz, I. C.; Bruck, M. A.; Fernando, Q. *Inorg. Chim. Acta* **1993**, *209*, 29−34.
(39) Inoue, M. B.; Navarro, R. E.; Inoue, M.; Fernando, Q. *Inorg. Chem.* **1995**, *34*, 6074−9.
(40) Inoue, M. B.; Oram, P.; Inoue, M.; Fernando, Q.; Alexander, A. L.; Unger, E. C. *Magn. Reson. Imaging* **1994**, *12*, 429−32.
(41) Franklin, S. J.; Raymond, K. N. *Inorg. Chem.* **1994**, *33*, 5794−804.
(42) Spirlet, M. R.; Rebizant, J.; Desreux, J. F.; Loncin, M. F. *Inorg. Chem.* **1984**, *23*, 359−63.
(43) Dubost, J. P.; Leger, J. M.; Langlois, M. H.; Meyer, D.; Schaefer, M. *C. R. l'Academie Sci., Ser. II Univers* **1991**, *312*, 349−54.
(44) Chang, C. A.; Francesconi, L. C.; Malley, M. F.; Kumar, K.; Gougoutas, J. Z.; Tweedle, M. F.; Lee, D. W.; Wilson, L. J. *Inorg. Chem.* **1993**, *32*, 3501−8.
(45) Aime, S.; Barge, A.; Botta, M.; Fasano, M.; Ayala, J. D.; Bombieri, G. *Inorg. Chim. Acta* **1996**, *246*, 423−429.
(46) Aime, S.; Barge, A.; Benetollo, F.; Bombieri, G.; Botta, M.; Uggeri, F. *Inorg. Chem.* **1997**, *36*, 4287−4289.
(47) Kumar, K.; Chang, C. A.; Francesconi, L. C.; Dischino, D. D.; Malley, M. F.; Gougoutas, J. Z.; Tweedle, M. F. *Inorg. Chem.* **1994**, *33*, 3567−75.
(48) Platzek, J.; Blaszkiewicz, P.; Gries, H.; Luger, P.; Michl, G.; Mueller-Fahrnow, A.; Raduechel, B.; Suelzle, D. *Inorg. Chem.* **1997**, *36*, 6086−6093.
(49) Aime, S.; Anelli, P. L.; Botta, M.; Fedeli, F.; Grandi, M.; Paoli, P.; Uggeri, F. *Inorg. Chem.* **1992**, *31*, 2422−8.
(50) Howard, J. A. K.; Kenwright, A. M.; Moloney, J. M.; Parker, D.; Woods, M.; Port, M.; Navet, M.; Rousseau, O. *Chem. Commun.* **1998**, 1381−1382.
(51) Kang, S. I.; Ranganathan, R. S.; Emswiler, J. E.; Kumar, K.; Gougoutas, J. Z.; Malley, M. F.; Tweedle, M. F. *Inorg. Chem.* **1993**, *32*, 2912−18.
(52) Aime, S.; Batsanov, A. S.; Botta, M.; Howard, J. A. K.; Parker, D.; Senanayake, K.; Williams, G. *Inorg. Chem.* **1994**, *33*, 4696−706.
(53) Aime, S.; Batsanov, A. S.; Botta, M.; Dickins, R. S.; Faulkner, S.; Foster, C. E.; Harrison, A.; Howard, J. A. K.; Moloney, J. M.; Norman, T. J.; Parker, D.; Royle, L.; Williams, J. A. G. *J. Chem. Soc., Dalton Trans.* **1997**, 3623−3636.
(54) Dale, J. *Isr. J. Chem.* **1980**, *20*, 3−11.
(55) Spirlet, M.-R.; Rebizant, J.; Wang, X.; Jin, T.; Gilsoul, D.; Comblin, V.; Maton, F.; Muller, R. N.; Desreux, J. F. *J. Chem. Soc., Dalton Trans.* **1997**, 497−500.
(56) Spirlet, M. R.; Rebizant, J.; Loncin, M. F.; Desreux, J. F. *Inorg. Chem.* **1984**, *23*, 4278−83.
(57) Ruloff, R.; Prokop, P.; Sieler, J.; Hoyer, E.; Beyer, L. *Z. Naturforsch., B: Chem. Sci.* **1996**, *51*, 963−968.
(58) Wang, R.-Y.; Li, J.-R.; Jin, T.-Z.; Xu, G.-X.; Zhou, Z.-Y.; Zhou, X.-G. *Polyhedron* **1997**, *16*, 1361−1364.
(59) Ruloff, R.; Gelbrich, T.; Sieler, J.; Hoyer, E.; Beyer, L. *Z. Naturforsch., B: Chem. Sci.* **1997**, *52*, 805−809.
(60) Mondry, A.; Starynowicz, P. *Inorg. Chem.* **1997**, *36*, 1176−1180.
(61) Wang, R.-Y.; Li, J.-R.; Jin, T.-Z.; Xu, G.-X.; Zhou, Z.-Y.; Zhou, X.-G. *Polyhedron* **1997**, *16*, 2037−2040.
(62) Mondry, A.; Starynowicz, P. *J. Chem. Soc., Dalton Trans.* **1998**, 859−863.
(63) Chen, D.-F.; Yang, W.-C.; Wang, R.-Y.; Jin, T.-Z. *Huaxue Xuebao* **1997**, *55*, 672−677.
(64) Xu, J.; Franklin, S. J.; Whisenhunt, D. W., Jr.; Raymond, K. N. *J. Am. Chem. Soc.* **1995**, *117*, 7245−6.
(65) Sessler, J. L.; Mody, T. D.; Hemmi, G. W.; Lynch, V. *Inorg. Chem.* **1993**, *32*, 3175−87.
(66) Lisowski, J.; Sessler, J. L.; Lynch, V.; Mody, T. D. *J. Am. Chem. Soc.* **1995**, *117*, 2273−85.
(67) Alexander, V. *Chem. Rev.* **1995**, *95*, 273−342.
(68) Schauer, C. K.; Anderson, O. P. *J. Chem. Soc., Dalton Trans.* **1989**, 185−91.
(69) Morita, K.; Yukawa, Y.; Inomata, Y.; Howell, F. S.; Takeuchi, T. *Kidorui* **1996**, *28*, 218−219.
(70) Okamura, D.; Inomata, Y.; Howell, F. S. *Kidorui* **1997**, *30*, 324−325.
(71) Amin, S.; Voss, D. A., Jr.; Horrocks, W. D.; Lake, C. H.; Churchill, M. R.; Morrow, J. R. *Inorg. Chem.* **1995**, *34*, 3294−300.
(72) Dickins, R. S.; Howard, J. A. K.; Lehmann, C. W.; Moloney, J.; Parker, D.; Peacock, R. D. *Angew. Chem., Int. Ed. Engl.* **1997**, *36*, 521−523.
(73) Alderighi, L.; Bianchi, A.; Calabi, L.; Dapporto, P.; Giorgi, C.; Losi, P.; Paleari, L.; Paoli, P.; Rossi, P.; Valtancoli, B.; Virtuani, M. *Eur. J. Inorg. Chem.* **1998**, 1581−1584.
(74) Horrocks, W. D., Jr.; Sudnick, D. R. *J. Am. Chem. Soc.* **1979**, *101*, 334−40.
(75) Bryden, C. C.; Reilley, C. N. *Anal. Chem.* **1982**, *54*, 610−15.
(76) Alpoim, M. C.; Urbano, A. M.; Geraldes, C. F. G. C.; Peters, J. A. *J. Chem. Soc., Dalton Trans.* **1992**, 463−7.
(77) Geraldes, C. F. G. C.; Sherry, A. D.; Cacheris, W. P.; Kuan, K. T.; Brown, R. D., III.; Koenig, S. H.; Spiller, M. *Magn. Reson. Med.* **1988**, *8*, 191−9.
(78) Chang, C. A.; Brittain, H. G.; Telser, J.; Tweedle, M. F. *Inorg. Chem.* **1990**, *29*, 4468−73.
(79) Anelli, P. L.; Balzani, V.; Prodi, L.; Uggeri, F. *Gazz. Chim. Ital.* **1991**, *121*, 359−64.
(80) Geraldes, C. F. G. C.; Urbano, A. M.; Hoefnagel, M. A.; Peters, J. A. *Inorg. Chem.* **1993**, *32*, 2426−32.
(81) Bovens, E.; Hoefnagel, M. A.; Boers, E.; Lammers, H.; van Bekkum, H.; Peters, J. A. *Inorg. Chem.* **1996**, *35*, 7679−7683.
(82) Frey, S. T.; Chang, C. A.; Carvalho, J. F.; Varadarajan, A.; Schultze, L. M.; Pounds, K. L.; Horrocks, W. D., Jr. *Inorg. Chem.* **1994**, *33*, 2882−9.
(83) Bryden, C. C.; Reilley, C. N.; Desreux, J. F. *Anal. Chem.* **1981**, *53*, 1418−25.
(84) Albin, M.; Horrocks, W. D., Jr.; Liotta, F. J. *Chem. Phys. Lett.* **1982**, *85*, 61−4.
(85) Zhang, X.; Chang, C. A.; Brittain, H. G.; Garrison, J. M.; Telser, J.; Tweedle, M. F. *Inorg. Chem.* **1992**, *31*, 5597−600.
(86) Murru, M.; Parker, D.; Williams, G.; Beeby, A. *J. Chem. Soc., Chem. Commun.* **1993**, 1116−18.
(87) Kim, W. D.; Kiefer, G. E.; Huskens, J.; Sherry, A. D. *Inorg. Chem.* **1997**, *36*, 4128−4134.
(88) Shannon, R. D. *Acta Crystallogr., Sect. A* **1976**, *A32*, 751−67.
(89) Peters, J. A. *J. Magn. Reson.* **1986**, *68*, 240−51.
(90) Geraldes, C. F. G. C.; Urbano, A. M.; Alpoim, M. C.; Hoefnagel, M. A.; Peters, J. A. *J. Chem. Soc., Chem. Commun.* **1991**, 656−8.
(91) Peters, J. A. *Inorg. Chem.* **1988**, *27*, 4686−91.
(92) Jenkins, B. G.; Lauffer, R. B. *Inorg. Chem.* **1988**, *27*, 4730−8.
(93) Jacques, V.; Desreux, J. F. *Inorg. Chem.* **1994**, *33*, 4048−53.
(94) Hoeft, S.; Roth, K. *Chem. Ber.* **1993**, *126*, 869−73.
(95) Aime, S.; Botta, M.; Ermondi, G.; Terreno, E.; Anelli, P. L.; Fedeli, F.; Uggeri, F. *Inorg. Chem.* **1996**, *35*, 2726−36.
(96) Aime, S.; Botta, M.; Ermondi, G. *Inorg. Chem.* **1992**, *31*, 4291−9.
(97) Shukla, R. B. *J. Magn. Reson., Ser. A* **1995**, *113*, 196−204.
(98) Schmitt−Willich, H.; Brehm, M.; Ewers, Ch. L. J.; Michl, G.; Müller−Fahrnow, A.; Petrov, O.; Platzek, J.; Radüchel, B.; Sülzle, D. *Inorg. Chem.* **1999**, *38*, 1134−1144.
(99) Cummins, C. H.; Rutter, E. W., Jr.; Fordyce, W. A. *Bioconjugate Chem.* **1991**, *2*, 180−186.

(100) Lammers, H.; Maton, F.; Pubanz, D.; Van Laren, M. W.; Van Bekkum, H.; Merbach, A. E.; Muller, R. N.; Peters, J. A. *Inorg. Chem.* **1997**, *36*, 2527−2538.
(101) White, D. H.; DeLearie, L. A.; Dunn, T. J.; Rizkalla, E. N.; Imura, H.; Choppin, G. R. *Invest. Radiol.* **1991**, *28*, S229−S231.
(102) Aime, S.; Botta, M.; Fasano, M.; Marques, M. P. M.; Geraldes, C. F. G. C.; Pubanz, D.; Merbach, A. E. *Inorg. Chem.* **1997**, *36*, 2059−2068.
(103) Desreux, J. F. *Inorg. Chem.* **1980**, *19*, 1319−24.
(104) Brittain, H. G.; Desreux, J. F. *Inorg. Chem.* **1984**, *23*, 4459−66.
(105) Geraldes, C. F. G. C.; Sherry, A. D.; Kiefer, G. E. *J. Magn. Reson.* **1992**, *97*, 290−304.
(106) Ren, J.; Sherry, A. D. *J. Magn. Reson., Ser. B* **1996**, *111*, 178−182.
(107) Sherry, A. D.; Ren, J.; Huskens, J.; Bruecher, E.; Toth, E.; Geraldes, C. F. C. G.; Castro, M. M. C. A.; Cacheris, W. P. *Inorg. Chem.* **1996**, *35*, 4604−4612.
(108) Sherry, A. D.; Malloy, C. R.; Jeffrey, M. H.; Cacheris, W. P.; Geraldes, C. F. G. C. *J. Magn. Reson.* **1988**, *76*, 528−533.
(109) Buster, D. C.; Castro, M. M. C. A.; Geraldes, C. F. G. C.; Malloy, C. R.; Sherry, A. D.; Siemers, T. C. *Magn. Reson. Med.* **1990**, *15*, 25−32.
(110) Bansal, N.; Germann, M. J.; Seshan, V.; Shires, G. T., III.; Malloy, C. R.; Sherry, A. D. *Biochemistry* **1993**, *32*, 5638−43.
(111) Seshan, V.; Germann, M. J.; Preisig, P.; Malloy, C. R.; Sherry, A. D.; Bansal, N. *Magn. Reson. Med.* **1995**, *34*, 25−31.
(112) Sherry, A. D. *J. Alloys Compd.* **1997**, *249*, 153−157.
(113) Pulukkody, K. P.; Norman, T. J.; Parker, D.; Royle, L.; Broan, C. J. *J. Chem. Soc., Perkin Trans. 2* **1993**, 605−20.
(114) Loncin, M. F.; Desreux, J. F.; Merciny, E. *Inorg. Chem.* **1986**, *25*, 5, 2646−8.
(115) Holz, R. C.; Horrocks, W. D., Jr. *Inorg. Chim. Acta* **1990**, *171*, 193−8.
(116) Mondry, A.; Riehl, J. P. *Acta Phys. Pol., A* **1993**, *84*, 969−74.
(117) Franano, F. N.; Edwards, W. B.; Welch, M. J.; Brechbiel, M. W.; Gansow, O. A.; Duncan, J. R. *Magn. Reson. Imaging* **1995**, *13*, 201−14.
(118) Wedeking, P.; Tweedle, M. *Nucl. Med. Biol.* **1988**, *15*, 395−402.
(119) Wedeking, P.; Kumar, K.; Tweedle, M. F. *Nucl. Med. Biol.* **1993**, *20*, 679−91.
(120) Smith, R. M.; Martell, A. E. *Critical Stability Constants*; Plenum: New York, 1974.
(121) Wedeking, P.; Kumar, K.; Tweedle, M. F. *Magn. Reson. Imaging* **1992**, *10*, 641−8.
(122) Cacheris, W. P.; Quay, S. C.; Rocklage, S. M. *Magn. Reson. Imaging* **1990**, *8*, 467−81.
(123) Kumar, K.; Tweedle, M. F.; Malley, M. F.; Gougoutas, J. Z. *Inorg. Chem.* **1995**, *34*, 6472−80.
(124) Meyer, D.; Schaefer, M.; Doucet, D. *Invest. Radiol.* **1990**, *25*, S53−S55.
(125) Runge, V. M.; Gelblum, D. Y.; Jacobson, S. *Magn. Reson. Imaging* **1991**, *9*, 79−87.
(126) White, D. H.; DeLearie, L. A.; Moore, D. A.; Wallace, R. A.; Dunn, T. J.; Cacheris, W. P.; Imura, H.; Choppin, G. R. *Invest. Radiol.* **1991**, *26*, S226−S228.
(127) Cacheris, W. P.; Nickle, S. K.; Sherry, A. D. *Inorg. Chem.* **1987**, *26*, 958−60.
(128) Clarke, E. T.; Martell, A. E. *Inorg. Chim. Acta* **1991**, *190*, 37−46.
(129) Smith, R. M.; Motekaitis, R. J.; Martell, A. E. *NIST Standard Reference Database #46*, 3.0 ed.; National Institute of Standards and Technology: Washington, DC, 1997.
(130) Wang, X.; Jin, T.; Comblin, V.; Lopez-Mut, A.; Merciny, E.; Desreux, J. F. *Inorg. Chem.* **1992**, *31*, 1095−9.
(131) Puttagunta, N. R.; Gibby, W. A.; Smith, G. T. *Invest. Radiol.* **1996**, *31*, 739−742.
(132) Puttagunta, N. R.; Gibby, W. A.; Puttagunta, V. L. *Invest. Radiol.* **1996**, *31*, 619−624.
(133) Tweedle, M. F.; Hagan, J. J.; Kumar, K.; Mantha, S.; Chang, C. A. *Magn. Reson. Imaging* **1991**, *9*, 409−15.
(134) Kumar, K.; Tweedle, M. F. *Inorg. Chem.* **1993**, *32*, 4193−9.
(135) Brucher, E.; Sherry, A. D. *Inorg. Chem.* **1990**, *29*, 1555−9.
(136) Choi, K.-Y.; Kim, K. A.; Kim, J. C. *Polyhedron* **1994**, *13*, 567−571.
(137) Kumar, K.; Chang, C. A.; Tweedle, M. F. *Inorg. Chem.* **1993**, *32*, 587−93.
(138) Kumar, K.; Jin, T.; Wang, X.; Desreux, J. F.; Tweedle, M. F. *Inorg. Chem.* **1994**, *33*, 3823−9.
(139) Harrison, A.; Walker, C. A.; Pereira, K. A.; Parker, D.; Royle, L.; Pulukkody, K.; Norman, T. J. *Magn. Reson. Imaging* **1993**, *11*, 761−70.
(140) Rizkalla, E.; Choppin, G.; Cacheris, W. *Inorg. Chem.* **1993**, *32*, 582−586.
(141) Wang, Y.-M.; Cheng, T.-H.; Liu, G.-C.; Sheu, R.-S. *J. Chem. Soc., Dalton Trans.* **1997**, 833−837.
(142) Wang, Y.-M.; Lin, S.-T.; Wang, Y.-J.; Sheu, R.-S. *Polyhedron* **1998**, *17*, 2021−2028.
(143) Wang, Y.-M.; Lee, C.-H.; Liu, G.-C.; Sheu, R.-S. *J. Chem. Soc., Dalton Trans.* **1998**, 4113−4118.
(144) Varadarajan, J. A.; Crofts, S. P.; Carvalho, J. F.; Fellmann, J. D.; Kim, S.-H.; Chang, C. A.; Watson, A. D. *Invest. Radiol.* **1994**, *29*, S18−S20.
(145) Paul-Roth, C.; Raymond, K. N. *Inorg. Chem.* **1995**, *34*, 1408−12.
(146) Harris, W. R.; Raymond, K. N.; Weitl, F. L. *J. Am. Chem. Soc.* **1981**, *103*, 2667−75.
(147) Caravan, P.; Mehrkhodavandi, P.; Orvig, C. *Inorg. Chem.* **1997**, 13166-1321.
(148) Thompson, L.; Shafer, B.; Edgar, J.; Mannila, K. *Adv. Chem. Ser.* **1967**, *71*, 169−179.
(149) Wiegers, C. B.; Welch, M. J.; Sharp, T. L.; Brown, J. J.; Perman, W. H.; Sun, Y.; Motekaitis, R. J.; Martell, A. E. *Magn. Reson. Imaging* **1992**, *10*, 903−11.
(150) Wagner, M.; Ruloff, R.; Hoyer, E.; Grunder, W. *Z. Naturforsch., C: Biosci.* **1997**, *52*, 508−515.
(151) Sherry, A. D. *J. Less-Common Met.* **1989**, *149*, 133−41.
(152) Kim, W. D.; Hrncir, D. C.; Kiefer, G. E.; Sherry, A. D. *Inorg. Chem.* **1995**, *34*, 2225−32.
(153) Hong, C.; Kim, D. W.; Choi, K.-Y. *Bull. Korean Chem. Soc.* **1997**, *18*, 1158−1161.
(154) Delgado, R.; Sun, Y.; Motekaitis, R. J.; Martell, A. E. *Inorg. Chem.* **1993**, *32*, 3320−6.
(155) Brucher, E.; Cortes, S.; Chavez, F.; Sherry, A. D. *Inorg. Chem.* **1991**, *30*, 2092−7.
(156) Wu, S. L.; Horrocks, W. D., Jr. *J. Chem. Soc., Dalton Trans.* **1997**, 1497−1502.
(157) Wu, S. L.; Horrocks, W. D., Jr. *Anal. Chem.* **1996**, *68*, 394−401.
(158) Sherry, A. D.; Brown, R. D., III; Geraldes, C. F. G. C.; Koenig, S. H.; Kuan, K. T.; Spiller, M. *Inorg. Chem.* **1989**, *28*, 620−2.
(159) Lazar, I.; Sherry, A. D.; Ramasamy, R.; Brucher, E.; Kiraly, R. *Inorg. Chem.* **1991**, *30*, 5016−19.
(160) Geraldes, C. F. G. C.; Sherry, A. D.; Lázár, I.; Miseta, A.; Bogner, P.; Berenyi, E.; Sumegi, B.; Kiefer, G. E.; McMillan, K.; Maton, F.; Muller, R. N. *Magn. Reson. Med.* **1993**, *30*, 696−703.
(161) Geraldes, C. F. G. C.; Brown, R. D., III; Cacheris, W. P.; Koenig, S. H.; Sherry, A. D.; Spiller, M. *Magn. Reson. Med.* **1989**, *9*, 94−104.
(162) Parker, D.; Pulukkody, K.; Norman, T. J.; Harrison, A.; Royle, L.; Walker, C. *J. Chem. Soc., Chem. Commun.* **1992**, 1441−3.
(163) Broan, C. J.; Cole, E.; Jankowski, K. J.; Parker, D.; Pulukkody, K.; Boyce, B. A.; Beeley, N. R. A.; Millar, K.; Millican, A. T. *Synthesis* **1992**, 63−8.
(164) Aime, S.; Botta, M.; Parker, D.; Williams, J. A. G. *J. Chem. Soc., Dalton Trans.* **1996**, 17−23.
(165) Choppin, G. R. *J. Alloys Compd.* **1995**, *225*, 242−245.
(166) McMurry, T. J.; Pippin, C. G.; Wu, C.; Deal, K. A.; Brechbiel, M. W.; Mirzadeh, S.; Gansow, O. A. *J. Med. Chem.* **1998**, *41*, 3546−3549.
(167) Luz, Z.; Meiboom, S. *J. Chem. Phys.* **1964**, *40*, 2686.
(168) Swift, T. J.; Connick, R. E. *J. Chem. Phys.* **1962**, *37*, 307.
(169) Kowalewski, J.; Nordenskioeld, L.; Benetis, N.; Westlund, P. O. *Prog. Nucl. Magn. Reson. Spectrosc.* **1985**, *17*, 141−85.
(170) Bertini, I.; Luchinat, C. *Coord. Chem. Rev.* **1996**, *150*, 1−295.
(171) Cossy, C.; Helm, L.; Powell, D. H.; Merbach, A. E. *New J. Chem.* **1995**, *19*, 27−35.
(172) Helm, L.; Merbach, A. E. *Eur. J. Solid State Inorg. Chem.* **1991**, *28*, 245−50.
(173) Benazeth, S.; Purans, J.; Chalbot, M.-C.; Nguyen-van-Duong, M. K.; Nicolas, L.; Keller, F.; Gaudemer, A. *Inorg. Chem.* **1998**, *37*, 3667−3674.
(174) Yamaguchi, T.; Nomura, M.; Wakita, H.; Otaki, H. *J. Chem. Phys.* **1988**, *89*, 5153−9.
(175) Steele, M. L.; Wertz, D. L. *J. Am. Chem. Soc.* **1976**, *98*, 4424−8.
(176) Clarkson, R. B.; Hwang, J. H.; Belford, R. L. *Magn. Reson. Med.* **1993**, *29*, 521−7.
(177) Powell, D. H.; Ni Dhubhghaill, O. M.; Pubanz, D.; Helm, L.; Lebedev, Y. S.; Schlaepfer, W.; Merbach, A. E. *J. Am. Chem. Soc.* **1996**, *118*, 9333−9346.
(178) Chen, J. W.; Auteri, F. P.; Budil, D. E.; Belford, R. L.; Clarkson, R. B. *J. Phys. Chem.* **1994**, *98*, 13452−9.
(179) Chen, J. W.; Belford, R. L.; Clarkson, R. B. *J. Phys. Chem. A* **1998**, *102*, 2117−2130.
(180) Halle, B.; Wennerström *J. Magn. Reson.* **1981**, *44*, 89.
(181) Aime, S.; Nano, R. *Invest. Radiol.* **1988**, *23*, S264−S266.
(182) Vander Elst, L.; Laurent, S.; Muller, R. N. *Invest. Radiol.* **1998**, *33*, 828−834.
(183) Lakowicz, J. R. *Principles of Fluorescence Spectroscopy*; Plenum: New York, 1983.
(184) Micskei, K.; Helm, L.; Brucher, E.; Merbach, A. E. *Inorg. Chem.* **1993**, *32*, 3844−50.
(185) Aime, S.; Barge, A.; Botta, M.; Parker, D.; De Sousa, A. S. *J. Am. Chem. Soc.* **1997**, *119*, 4767−4768.
(186) Strandberg, E.; Westlund, P.-O. *J. Magn. Reson., Ser. A* **1996**, *122*, 179−191.
(187) Abernathy, S. M.; Miller, J. C.; Lohr, L. L.; Sharp, R. R. *J. Chem. Phys.* **1998**, *109*, 4035−4046.
(188) Abernathy, S. M.; Sharp, R. R. *J. Chem. Phys.* **1997**, *106*, 9032−9043.

(189) Abernathy, S. M.; Sharp, R. R. *J. Phys. Chem. A* **1997**, *101*, 3692−3698.
(190) Sharp, R.; Abernathy, S. M.; Lohr, L. L. *J. Chem. Phys.* **1997**, *107*, 7620−7629.
(191) Sharp, R. R. *J. Chem. Phys.* **1993**, *98*, 912−21.
(192) Sharp, R. R. *J. Chem. Phys.* **1993**, *98*, 2507−15.
(193) Sharp, R. R. *J. Chem. Phys.* **1993**, *98*, 6092−101.
(194) Sharp, R. R. *J. Magn. Reson.* **1992**, *100*, 491−516.
(195) Bovet, J. M.; Sharp, R. R. *J. Chem. Phys.* **1993**, *99*, 18−26.
(196) Westlund, P.-O. *J. Chem. Phys.* **1998**, *108*, 4945−4953.
(197) Westlund, P. O.; Larsson, T. P.; Teleman, O. *Mol. Phys.* **1993**, *78*, 1365−84.
(198) Banci, L.; Bertini, I.; Briganti, F.; Luchinat, C. *J. Magn. Reson.* **1986**, *66*, 58−65.
(199) Benetis, N.; Kowalewski, J.; Nordenskioeld, L.; Wennerstroem, H.; Westlund, P. O. *Mol. Phys.* **1983**, *48*, 329−46.
(200) Larsson, T.; Westlund, P.-O.; Kowalewski, J.; Koenig, S. H. *J. Chem. Phys.* **1994**, *101*, 1116−28.
(201) Lipari, G.; Szabo, A. *J. Am. Chem. Soc.* **1982**, *104*, 4546−4559.
(202) Freed, J. *J. Chem. Phys.* **1978**, *68*, 4034.
(203) Pfeifer, H. *Ann. Phys. (Leipzig)* **1961**, *8*, 1.
(204) Geraldes, C. F. G. C.; Urbano, A. M.; Alpoim, M. C.; Sherry, A. D.; Kuan, K.-T.; Rajagopalan, R.; Maton, F.; Muller, R. N. *Magn. Reson. Imaging* **1995**, *13*, 401−20.
(205) Koenig, S. H. *Invest. Radiol.* **1994**, *29*, S127−S130.
(206) Southwood-Jones, R. V.; Earl, W. L.; Newman, K. E.; Merbach, A. E. *J. Chem. Phys.* **1980**, *73*, 5909−18.
(207) Micskei, K.; Powell, D. H.; Helm, L.; Brucher, E.; Merbach, A. E. *Magn. Reson. Chem.* **1993**, *31*, 1011−20.
(208) Gonzalez, G.; Powell, D. H.; Tissieres, V.; Merbach, A. E. *J. Phys. Chem.* **1994**, *98*, 53−9.
(209) Powell, D. H.; Gonzalez, G.; Tissieres, V.; Micskei, K.; Bruecher, E.; Helm, L.; Merbach, A. E. *J. Alloys Compd.* **1994**, *207−208*, 20−4.
(210) Helm, L.; Powell, D. H.; Merbach, A. E. *High-Pressure Research* **1994**, *13*, 109−113.
(211) Powell, D. H.; Favre, M.; Graeppi, N.; Dhubhghaill, O. M. N.; Pubanz, D.; Merbach, A. *J. Alloys Compd.* **1995**, *225*, 246−252.
(212) Toth, E.; Pubanz, D.; Vauthey, S.; Helm, L.; Merbach, A. E. *Chem. Eur. J.* **1996**, *2*, 1607−1615.
(213) Toth, E.; Vauthey, S.; Pubanz, D.; Merbach, A. E. *Inorg. Chem.* **1996**, *35*, 3375−9.
(214) Aime, S.; Barge, A.; Borel, A.; Botta, M.; Chemerisov, S.; Merbach, A. E.; Mueller, U.; Pubanz, D. *Inorg. Chem.* **1997**, *36*, 5104−5112.
(215) Toth, E.; Burai, L.; Brucher, E.; Merbach, A. E. *J. Chem. Soc., Dalton Trans.* **1997**, 1587−1594.
(216) Toth, E.; Connac, F.; Helm, L.; Adzamli, K.; Merbach, A. E. *Eur. J. Inorg. Chem.* **1998**, 2017−2021.
(217) Toth, E.; Helm, L.; Merbach, A. E.; Hedinger, R.; Hegetschweiler, K.; Janossy, A. *Inorg. Chem.* **1998**, *37*, 4104−4113.
(218) Ruloff, R.; Muller, R. N.; Pubanz, D.; Merbach, A. E. *Inorg. Chim. Acta* **1998**, *275−276*, 15−23.
(219) Toth, E.; Van Uffelen, I.; Helm, L.; Merbach, A. E.; Ladd, D.; Briley-Saebo, K.; Kellar, K. E. *Magn. Reson. Chem.* **1998**, *36*, S125−S134.
(220) Toth, E.; Connac, F.; Helm, L.; Adzamli, K.; Merbach, A. E. *J. Biol. Inorg. Chem.* **1998**, *3*, 606−613.
(221) Aime, S.; Barge, A.; Botta, M.; De Sousa, A. S.; Parker, D. *Angew. Chem., Int. Ed. Engl.* **1998**, *37*, 2673−2675.
(222) Pubanz, D.; Gonzalez, G.; Powell, D. H.; Merbach, A. E. *Inorg. Chem.* **1995**, *34*, 4447−53.
(223) Graeppi, N.; Powell, D. H.; Laurenczy, G.; Zekany, L.; Merbach, A. E. *Inorg. Chim. Acta* **1995**, *235*, 311−26.
(224) Toth, E.; Burai, L.; Brucher, E.; Merbach, A. *J. Chem Soc. Dalton Trans.* **1997**, 1587−1594.
(225) Aime, S.; Botta, M.; Crich, S. G.; Giovenzana, G.; Pagliarin, R.; Sisti, M.; Terreno, E. *Magn. Reson. Chem.* **1998**, *36*, S200−S208.
(226) Aime, S.; Botta, M.; Crich, S. G.; Giovenzana, G. B.; Jommi, G.; Pagliarin, R.; Sisti, M. *Inorg. Chem.* **1997**, *36*, 2992−3000.
(227) Aime, S.; Botta, M.; Fasano, M.; Paoletti, S.; Terreno, E. *Chem. Eur. J.* **1997**, *3*, 1499−1504.
(228) Aime, S.; Crich, S. G.; Gianolio, E.; Terreno, E.; Beltrami, A.; Uggeri, F. *Eur. J. Inorg. Chem.* **1998**, 1283−1289.
(229) Kim, W. D.; Kiefer, G. E.; Maton, F.; McMillan, K.; Muller, R. N.; Sherry, A. D. *Inorg. Chem.* **1995**, *34*, 2233−43.
(230) Aime, S.; Botta, M.; Dickins, R. S.; Maupin, C. L.; Parker, D.; Riehl, J. P.; Williams, J. A. G. *J. Chem. Soc., Dalton Trans.* **1998**, 881−892.
(231) Aime, S.; Botta, M.; Crich, S. G.; Giovenzana, G. B.; Pagliarin, R.; Piccinini, M.; Sisti, M.; Terreno, E. *J. Biol. Inorg. Chem.* **1997**, *2*, 470−479.
(232) Aime, S.; Fasano, M.; Paoletti, S.; Terreno, E. *Gazz. Chim. Ital.* **1995**, *125*, 125−31.
(233) Aime, S.; Botta, M.; Nonnato, A.; Terreno, E.; Anelli, P. L.; Uggeri, F. *J. Alloys Compd.* **1995**, *225*, 274−8.
(234) Aime, S.; Botta, M.; Fasano, M.; Paoletti, S.; Anelli, P. L.; Uggeri, F.; Virtuani, M. *Inorg. Chem.* **1994**, *33*, 4707−11.
(235) Aime, S.; Botta, M.; Terreno, E.; Anelli, P. L.; Uggeri, F. *Magn. Reson. Med.* **1993**, *30*, 583−91.
(236) Geraldes, C. F. G. C.; Sherry, A. D.; Vallet, P.; Maton, F.; Muller, R. N.; Mody, T. D.; Hemmi, G.; Sessler, J. L. *Magn. Reson. Imaging* **1995**, *5*, 725−729.
(237) Geraldes, C. F. G. C.; Brown, R. D., III; Brucher, E.; Koenig, S. H.; Sherry, A. D.; Spiller, M. *Magn. Reson. Med.* **1992**, *27*, 284−95.
(238) Aime, S.; Botta, M.; Dastru, W.; Fasano, M.; Panero, M.; Arnelli, A. *Inorg. Chem.* **1993**, *32*, 2068−71.
(239) Hall, J.; Haner, R.; Aime, S.; Botta, M.; Faulkner, S.; Parker, D.; de Sousa, A. S. *New J. Chem.* **1998**, *22*, 627−631.
(240) Sur, S. K.; Bryant, R. G. *J. Magn. Reson.* **1996**, *B 111*, 105−108.
(241) Shukla, R. B.; Kumar, K.; Weber, R.; Zhang, X.; Tweedle, M. *Acta Radiologica* **1997**, *38*, 121−123.
(242) Powell, D. H.; Merbach, A. E.; Gonzalez, G.; Bruecher, E.; Micskei, K.; Ottaviani, M. F.; Koehler, K.; von Zelewsky, A.; Grinberg, O. Y.; Lebedev, Y. S. *Helv. Chim. Acta* **1993**, *76*, 2129−46.
(243) Aime, S.; Botta, M.; Fasano, M.; Crich, S. G.; Terreno, E. *J. Biol. Inorg. Chem.* **1996**, *1*, 312−319.
(244) Sessler, J. L.; Mody, T. D.; Hemmi, G. W.; Lynch, V.; Young, S. W.; Miller, R. A. *J. Am. Chem. Soc.* **1993**, *115*, 10368−9.
(245) Smith, P. H.; Reyes, Z. E.; Lee, C. W.; Raymond, K. N. *Inorg. Chem.* **1988**, *27*, 4154−65.
(246) Cavagna, F. M.; Maggioni, F.; Castelli, P. M.; Dapra, M.; Imperatori, L. G.; Lorusso, V.; Jenkins, B. G. *Invest. Radiol.* **1997**, *32*, 780−796.
(247) Zhang, X.; Pillai, R.; Shukla, R.; Ranganathan, R. S.; Tweedle, M. *Invest. Radiol.* **1994**, *29*, S69−S70.
(248) Bligh, S. W. A.; Choi, N.; Evagorou, E. G.; McPartlin, M.; Cummins, W. J.; Kelly, J. D. *Polyhedron* **1992**, *11*, 2571−3.
(249) Bligh, S. W. A.; Harding, C. T.; McEwen, A. B.; Sadler, P. J.; Kelly, J. D.; Marriott, J. A. *Polyhedron* **1994**, *13*, 1937−43.
(250) Bligh, S. W. A.; Choi, N.; Geraldes, C. F. G. C.; Knoke, S.; McPartlin, M.; Sanganee, M. J.; Woodroffe, T. M. *J. Chem. Soc., Dalton Trans.* **1997**, 4119−4126.
(251) Bligh, S. W. A.; Drew, M. G. B.; Martin, N.; Maubert, B.; Nelson, J. *J. Chem. Soc., Dalton Trans.* **1998**, 3711−3714.
(252) Martin, V. V.; Ralston, W. H.; Hynes, M. R.; Keana, J. F. W. *Bioconjugate Chem.* **1995**, *6*, 616−23.
(253) Aime, S.; Botta, M.; Panero, M.; Grandi, M.; Uggeri, F. *Magn. Reson. Chem.* **1991**, *29*, 923−7.
(254) Aime, S.; Botta, M.; Ermondi, G. *J. Magn. Reson.* **1991**, *92*, 572−80.
(255) Aime, S.; Botta, M.; Crich, S. G.; Giovenzana, G. B.; Jommi, G.; Pagliarin, R.; Sisti, M. *J. Chem. Soc., Chem. Commun.* **1995**, 1885−6.
(256) Aime, S.; Botta, M.; Parker, D.; Williams, J. A. G. *J. Chem. Soc., Dalton Trans.* **1995**, 2259−66.
(257) Shukla, R.; Fernandez, M.; Pillai, R. K.; Ranganathan, R.; Ratsep, P. C.; Zhang, X.; Tweedle, M. F. *Magn. Reson. Med.* **1996**, *35*, 928−931.
(258) Wallace, R. A.; Haar, J. P., Jr.; Miller, D. B.; Woulfe, S. R.; Polta, J. A.; Galen, K. P.; Hynes, M. R.; Adzamli, K. *Magn. Reson. Med.* **1998**, *40*, 733−739.
(259) Periasamy, M.; White, D.; DeLearie, L.; Moore, D.; Wallace, R.; Lin, W.; Dunn, J.; Hirth, W.; Cacheris, W. *Invest. Radiol.* **1991**, *26*, S217−S220.
(260) Weinmann, H. J.; Schuhmann-Giampieri, G.; Schmitt-Willich, H.; Vogler, H.; Frenzel, T.; Gries, H. *Magn. Reson. Med.* **1991**, *22*, 233−7.
(261) Geze, C.; Mouro, C.; Hindre, F.; Le Plouzennec, M.; Moinet, C.; Rolland, R.; Alderighi, L.; Vacca, A.; Simonneaux, G. *Bull. Soc. Chim. Fr.* **1996**, *133*, 267−272.
(262) Claire, P. P. K.; Jones, C. J.; Chiu, K. W.; Thornback, J. R.; McPartlin, M. *Polyhedron* **1992**, *11*, 499−500.
(263) Anelli, P. L.; Calabi, L.; de Haen, C.; Fedeli, F.; Losi, P.; Murru, M.; Uggeri, F. *Gazz. Chim. Ital.* **1996**, *126*, 89−97.
(264) Adzamli, I. K.; Blau, M. *Magn. Reson. Med.* **1991**, *17*, 141−8.
(265) Ranganathan, R. S.; Fernandez, M. E.; Kang, S. I.; Nunn, A. D.; Ratsep, P. C.; Pillai, K. M. R.; Zhang, X.; Tweedle, M. F. *Invest. Radiol.* **1998**, *33*, 779−797.
(266) Smith, P. H.; Brainard, J. R.; Morris, D. E.; Jarvinen, G. D.; Ryan, R. R. *J. Am. Chem. Soc.* **1989**, *111*, 7437−43.
(267) Burai, L.; Hietapelto, V.; Kiraly, R.; Toth, E.; Brucher, E. *Magn. Reson. Med.* **1997**, *38*, 146−150.
(268) Lindqvist-Reis, P.; Muñoz-Páez, A.; Díaz-Moreno, S.; Pattanaik, S.; Persson, I.; Sandström, M. *Inorg. Chem.* **1998**, *37*, 6675−6683.
(269) Bleuzen, A.; Foglia, F.; Furet, E.; Helm, L.; Merbach, A.; Weber, J. *J. Am. Chem. Soc.* **1996**, *118*, 12777.
(270) Brasch, R. C. *Magn. Reson. Med.* **1991**, *22*, 282−7.
(271) Nunn, A. D.; Linder, K.; Tweedle, M. *Quart. J. Nuc. Med.* **1997**, *41*, 155−62.
(272) Brinkley, M. *Bioconjugate Chem.* **1992**, *3*, 2−13.

(273) Schuhmann-Giampieri, G.; Schmitt-Willich, H.; Frenzel, T.; Press: W. R.; Weinmann, H. J. *Invest. Radiol.* **1991**, *26*, 969−74.
(274) Sieving, P. F.; Watson, A. D.; Rocklage, S. M. *Bioconjugate Chem.* **1990**, *1*, 65−71.
(275) Spanoghe, M.; Lanens, D.; Dommisse, R.; Van der Linden, A.; Alder Weireldt, F. *Magn. Reson. Imaging* **1992**, *10*, 913−17.
(276) Desser, T.; Rubin, D.; Muller, H.; Qing, F.; Khodor, S.; Zanazzi; Young, S.; Ladd, D.; Wellons, J.; Kellar, K.; Toner, J.; Snow, R. *J. Magn. Reson. Imaging* **1994**, *4*, 467−472.
(277) Frank, H.; Weissleder, R.; Bogdanov, A.; Brady, T. *Am. J. Radiol.* **1994**, 1041−1046.
(278) Bogdanov, A. A.; Weissleder, R.; Frank, H. W.; Bogdanova, A. V.; Nossif, N.; Schaffer, B. K.; Tsai, E.; Papisov, M. I.; Brady, T. J. *Radiology* **1993**, *187*, 701−6.
(279) Bogdanov, A. A. J.; Weissleder, R.; Brady, T. J. *Adv. Drug Delivery Rev.* **1995**, *16*, 335−48.
(280) Kellar, K. E.; Henrichs, P. M.; Hollister, R.; Koenig, S. H.; Eck, J.; Wei, D. *Magn. Reson. Med.* **1997**, *38*, 712−716.
(281) Toth, E.; Helm, L.; Kellar, K. E.; Merbach, A. E. *Chem. Eur. J.* **1999**, *5*, 1202−1211.
(282) Tomalia, D.; Naylor, A.; Goddard, W., III. *Angew. Chem., Int. Ed. Engl.* **1990**, *29*, 138−175.
(283) Tomalia, D. A.; Durst, H. D. *Top. Curr. Chem.* **1993**, *165*, 193−313.
(284) Wiener, E. C.; Auteri, F. P.; Chen, J. W.; Brechbiel, M. W.; Gansow, O. A.; Schneider, D. S.; Belford, R. L.; Clarkson, R. B.; Lauterbur, P. C. *J. Am. Chem. Soc.* **1996**, *118*, 7774−7782.
(285) Bryant, L. H., Jr.; Brechbiel, M. W.; Wu, C.; Bulte, J. W. M.; Herynek, V.; Frank, J. A. Proceedings of the 6th International Society of Magnetic Resonance in Medicine Conference, Sydney, Australia, 1998.
(286) Margerum, L. D.; Campion, B. K.; Koo, M.; Shargill, N.; Lai, J.-J.; Marumoto, A.; Sontum, P. C. *J. Alloys Compd.* **1997**, *249*, 185−190.
(287) Tacke, J.; Adam, G.; Claben, H.; Muhler, A.; Prescher, A.; Gunther, R. W. *Magn. Reson. Imaging* **1997**, *7*, 678−682.
(288) Roberts, H. C.; Saeed, M.; Roberts, T. P. L.; Muhler, A.; Shames, D. M.; Mann, J. S.; Stiskal, M.; Demsar, F.; Brasch, R. C. *Magn. Reson. Imaging* **1997**, *7*, 331−338.
(289) Roberts, H. C.; Saeed, M.; Roberts, T. P. L.; Brasch, R. C. *Acad. Radiol.* **1998**, *5*, S31−S33.
(290) Raduechel, B.; Schmitt-Willich, H.; Platzek, J.; Ebert, W.; Frenzel, T.; Misselwitz, B.; Weinmann, H.-J. *Book of Abstracts*; 216th ACS National Meeting, Boston, August 23−27, 1998; p PMSE−278.
(291) Dong, Q.; Hurst, D. R.; Weinmann, H. J.; Chenevert, T. L.; Londy, F. J.; Prince, M. R. *Invest. Radiol.* **1998**, *33*, 699−708.
(292) Adam, G.; Neuerburg, J.; Spuntrup, E.; Muhler, A.; Scherer, K.; Gunther, R. W. *Magn. Reson. Imaging* **1994**, *4*, 462−466.
(293) Wiener, E. C.; Brechbiel, M. W.; Brothers, H.; Magin, R. L.; Gansow, O. A.; Tomalia, D. A.; Lauterbur, P. C. *Magn. Reson. Med.* **1994**, *31*, 1−8.
(294) Lauffer, R. B.; Brady, T. J. *Magn. Reson. Imaging* **1985**, *3*, 11−16.
(295) Schmiedl, U.; Ogan, M.; Paajanen, H.; Marotti, M.; Crooks, L. E.; Brito, A. C.; Brasch, R. C. *Radiology* **1987**, *162*, 205−10.
(296) Casali, C.; Janier, M.; Canet, E.; Obadia, J. F.; Benderbous, S.; Carot, C.; Revel, D. *Acad Radiol* **1998**, *5*, S214−S218.
(297) Meyer, D.; Schaeffer, M.; Bouillot, A.; Beaute, S.; Chambon, C. *Invest. Radiol.* **1991**, *26*, S50−S52.
(298) Armitage, F. E.; Richardson, D. E.; Li, K. C. P. *Bioconjugate Chem.* **1990**, *1*, 365−74.
(299) Rebizak, R.; Schaefer, M.; Dellacherie, E. *Bioconjugate Chem.* **1997**, *8*, 605−610.
(300) Corot, C.; Schaefer, M.; Beaute, S.; Bourrinet, P.; Zehaf, S.; Benize, V.; Sabatou, M.; Meyer, D. *Acta Radiologica* **1997**, *38*, 91−99.
(301) Siauve, N.; Clement, O.; Cuenod, C.-A.; Benderbous, S.; Frija, G. *Magn. Reson. Imaging* **1996**, *14*, 381−390.
(302) Rebizak, R.; Schaefer, M.; Dellacherie, E. *Bioconjugate Chem.* **1998**, *9*, 94−99.
(303) Dellacherie, É. In *Polysaccharides in Medicinal Applications*; Dumitriu, S., Ed.; Marcel Dekker: New York, 1996.
(304) Curtet, C.; Maton, F.; Havet, T.; Slinkin, M.; Mishra, A.; Chatal, J.-F.; Muller, R. N. *Invest. Radiol.* **1998**, *33*, 752−761.
(305) Wu, C.; Brechbiel, M. W.; Kozak, R. W.; Gansow, O. A. *Bioorg. Med. Chem. Lett.* **1994**, *4*, 449−54.
(306) Wiener, E. C.; Konda, S.; Shadron, A.; Brechbiel, M.; Gansow, O. *Invest. Radiol.* **1997**, *32*, 748−754.
(307) Lauffer, R. B. *Magn. Reson. Med.* **1991**, *22*, 339.
(308) Jenkins, B. G.; Armstrong, E.; Lauffer, R. B. *Magn. Reson. Med.* **1991**, *17*, 164−178.
(309) Parmelee, D. J.; Walovitch, R. C.; Ouellet, H. S.; Lauffer, R. B. *Invest. Radiol.* **1997**, *32*, 741−747.
(310) Lauffer, R. B.; Parmelee, D. J.; Dunham, S. U.; Ouellet, H. S.; Dolan, R. P.; Witte, S.; McMurry, T. J.; Walovitch, R. C. *Radiology* **1998**, *207*, 529−538.
(311) Dwek, R. A. *Nuclear Magnetic Resonance (N.M.R.) in Biochemistry*; Oxford University Press: Oxford, 1973.
(312) Cavagna, F.; Tirone, P.; Felder, E.; De Haen, C. In *Liver Imaging: Current Trends and New Techniques*; Ferrucci, J. T., Stark, D. D., Eds.; Andover Medical Publishers: Boston, 1990.
(313) Schuhmann-Giampieri, G.; Schmitt-Willich, H.; Press: W.-R.; Negishi, C.; Weinmann, H. J.; Speck, U. *Radiology* **1992**, *183*, 59−64.
(314) Kim, S. K.; Pohost, G. M.; Elgavish, G. A. *Magn. Reson. Med.* **1991**, *22*, 57−67.
(315) Tilcock, C.; Ahkong, Q. F.; Koenig, S. H.; Brown, R. D., III.; Davis, M.; Kabalka, G. *Magn. Reson. Med.* **1992**, *27*, 44−51.
(316) Kabalka, G. W.; Davis, M. A.; Moss, T. H.; Buonocore, E.; Hubner, K.; Holmberg, E.; Maruyama, K.; Huang, L. *Magn. Reson. Med.* **1991**, *19*, 406−15.
(317) Kim, S. K.; Pohost, G. M.; Elgavish, G. A. *Bioconjugate Chem.* **1992**, *3*, 20−6.
(318) Kabalka, G. W.; Davis, M. A.; Holmberg, E.; Maruyama, K.; Huang, L. *Magn. Reson. Imaging* **1991**, *9*, 373−7.
(319) Zhao, X.; Zhuo, R.; Lu, Z.; Liu, W. *Polyhedron* **1997**, *16*, 2755−2759.
(320) Fossheim, S. L.; Colet, J.-M.; Mansson, S.; Fahlvik, A. K.; Muller, R. N.; Klaveness, J. *Invest. Radiol.* **1998**, *33*, 810−821.
(321) Unger, E.; Fritz, T.; Wu, G.; Shen, D.; Kulik, B.; New, T.; Crowell, M.; Wilke, N. *J. Liposome Res.* **1994**, *4*, 811−34.
(322) Peters, T. J. *All About Albumin: Biochemistry, Genetics, and Medical Applications*; Academic Press: San Diego, 1996.
(323) Vogler, H.; Platzek, J.; Schuhmann-Giampieri, G.; Frenzel, T.; Weinmann, H.-J.; Radüchel, B.; Press: W.-R. *Eur. J. Radiol.* **1995**, *21*, 1−10.
(324) Kumar, K.; Sukumaran, K.; Taylor, S.; Chang, C. A.; Nunn, A. D.; Tweedle, M. F. *J. Liq. Chromatogr.* **1994**, *17*, 3735−46.
(325) Harpur, E. S.; Worah, D.; Hals, P.-A.; Holtz, E.; Furuhama, K.; Nomura, H. *Invest. Radiol.* **1993**, *28*, S28−S-43.
(326) Hieronim, D. E.; Kanal, E.; Swanson, D. P. *Am. J. Health-Syst. Pharm.* **1995**, *52*, 2556.
(327) Murphy, K. J.; A., B. J.; Cohan, R. H. *Am. J. Radiol.* **1996**, *167*, 847.
(328) Nelson, K. L.; Gifford, L. M.; Lauber-Huber, C.; Gross, C. A.; Lasser, T. A. *Radiology* **1995**, *196*, 439−443.
(329) Vogl, T. J.; Pegios, W.; McMahon, C. *AJR* **1992**, *158*, 887−892.
(330) Rosati, G.; Pirovano, G.; Spinazzi, A. *Invest. Radiol.* **1994**, *29*, S183.
(331) Hamm, B.; Staks, T.; Muhler, A.; Bollow, M.; Taupitz, M.; Frenzel, T.; Wolf, K.-J.; Weinmann, H.-J.; Lange, L. *Radiology* **1995**, *195*, 785−792.
(332) Reimer, P.; Rummeny, E. J.; Shamsi, K.; Balzer, T.; Daldrup, H. E.; Peters, P. E. *Radiology* **1996**, *199*, 177−183.
(333) Grist, T. M.; Korosec, F. R.; Peters, D. C.; Witte, S.; Walovitch, R. C.; Dolan, R. P.; Bridson, W. E.; Yucel, E. K.; Mistretta, C. A. *Radiology* **1998**, *207*, 539−544.
(334) Tweedle, M. F.; Wedeking, P.; Kumar, K. *Invest. Radiol.* **1995**, *30*, 372−80.
(335) McMurry, T. J.; Sajiki, H.; Scott, D. M.; Lauffer, R. B. PCT Int. Appl. WO9623526 1996; *Chem. Abstr.* **1996**, *125*, 230822.
(336) Mühler, A.; Oulde Elferink, R. P. J.; Weinmann, H.-J. *MAGMA* **1993**, *1*, 134−139.
(337) Young, S. W.; Qing, F.; Harriman, A.; Sessler, J. L.; Dow, W. C.; Mody, T. D.; Hemmi, G. W.; Hao, Y.; Miller, R. A. *Proc. Natl. Acad. Sci.* **1996**, *93*, 6610−6615.
(338) Ni, Y.; Pislaru, C.; Bosmans, H.; Pislaru, S.; Miao, Y.; Dymarkowski, S.; Bogaert, J.; Van de Werf, F.; Semmler, W.; Marchal, G. Proceedings of the 6th International Society of Magnetic Resonanace in Medicine Conference, Sydney, Australia, 1998; p 551.
(339) Kraitchman, D. L.; Oznur, I.; Faranesh, A. Z.; McVeigh, E. R.; Weinmann, H.-J. Proceedings of the 6th International Society of Magnetic Resonanace in Medicine Conference, Sydney, Australia, 1998; p 552.
(340) Moats, R. A.; Fraser, S. E.; Meade, T. J. *Angew. Chem., Int. Ed. Engl.* **1997**, *36*, 726−728.
(341) Lauffer, R. B.; McMurry, T. J.; Dunham, S. O.; Scott, D. M.; Parmelee, D. J.; Dumas, S. PCT Int. Appl. WO9736619, 1997; *Chem. Abstr.* **1997**, *127*, 316334.
(342) Li, W.-h.; Fraser, S. E.; Meade, T. J. *J. Am. Chem. Soc.* **1999**, *121*, 1413−1414.
(343) Beeby, A.; Clarkson, I. M.; Dickins, R. S.; Faulkner, S.; Parker, D.; Royle, L.; de Sousa, A. S.; Williams, J. A. G.; Woods, M. *J. Chem. Soc., Perkin Trans. 2* **1999**, 493−504.

CR980440X

Biotechnology Advances xxx (2015) xxx–xxx

Contents lists available at ScienceDirect

Biotechnology Advances

journal homepage: www.elsevier.com/locate/biotechadv

Research review paper

Tailored functionalization of iron oxide nanoparticles for MRI, drug delivery, magnetic separation and immobilization of biosubstances

Katerina Hola, Zdenka Markova, Giorgio Zoppellaro, Jiri Tucek, Radek Zboril *

Regional Centre of Advanced Technologies and Materials, Department of Physical Chemistry, Faculty of Science, Palacky University, 17. listopadu 1192/12, 771 46 Olomouc, Czech Republic

ARTICLE INFO

Available online xxxx

Keywords:
Biomedical applications
Nanoengineering
Surface design
Magnetic separation
SERS
Hyperthermia
Magnetic resonance imaging
Antibacterial
Water treatment

ABSTRACT

In this critical review, we outline various covalent and non-covalent approaches for the functionalization of iron oxide nanoparticles (IONPs). Tuning the surface chemistry and design of magnetic nanoparticles are described in relation to their applicability in advanced medical technologies and biotechnologies including magnetic resonance imaging (MRI) contrast agents, targeted drug delivery, magnetic separations and immobilizations of proteins, enzymes, antibodies, targeting agents and other biosubstances. We review synthetic strategies for the controlled preparation of IONPs modified with frequently used functional groups including amine, carboxyl and hydroxyl groups as well as the preparation of IONPs functionalized with other species, e.g., epoxy, thiol, alkane, azide, and alkyne groups. Three main coupling strategies for linking IONPs with active agents are presented: (i) chemical modification of amine groups on the surface of IONPs, (ii) chemical modification of bioactive substances (e.g. with fluorescent dyes), and (iii) the activation of carboxyl groups mainly for enzyme immobilization. Applications for drug delivery using click chemistry linking or biodegradable bonds are compared to non-covalent methods based on polymer modified condensed magnetic nanoclusters. Among many challenges, we highlight the specific surface engineering allowing both therapeutic and diagnostic applications (theranostics) of IONPs and magnetic/metallic hybrid nanostructures possessing a huge potential in biocatalysis, green chemistry, magnetic bioseparations and bioimaging.

© 2015 Elsevier Inc. All rights reserved.

Contents

1. Introduction — basic properties and synthetic strategies towards IONPs . . . 0
2. Principles and specific requirements for applications of IONPs in biomedicine and biotechnologies . . . 0
   2.1. Contrast agents in MRI . . . 0
   2.2. Targeted drug delivery . . . 0
   2.3. Magnetic separation . . . 0
   2.4. Application of IONPs conjugated with enzymes . . . 0
   2.5. Applications of magnetic/metallic hybrid nanostructures . . . 0
3. Surface design of magnetic nanoparticles . . . 0
   3.1. Immobilization of proteins, enzymes, antibodies and targeting agents . . . 0
   3.2. Biodegradable bonds for targeted drug delivery . . . 0
   3.3. Functionalization for magnetic separation . . . 0
   3.4. IONP/metal hybrid synthesis . . . 0
4. Concluding remarks . . . 0
Acknowledgments . . . 0
References . . . 0

* Corresponding author. Tel.: +420 585634337; fax: +420 585634167.
E-mail address: radek.zboril@upol.cz (R. Zboril).

http://dx.doi.org/10.1016/j.biotechadv.2015.02.003
0734-9750/© 2015 Elsevier Inc. All rights reserved.

Please cite this article as: Hola K, et al, Tailored functionalization of iron oxide nanoparticles for MRI, drug delivery, magnetic separation and immobilization of biosubsta..., Biotechnol Adv (2015), http://dx.doi.org/10.1016/j.biotechadv.2015.02.003

1. Introduction — basic properties and synthetic strategies towards IONPs

The properties of iron oxide nanoparticles (IONPs) – a flexible and modular design combined with low toxicity – lend themselves to numerous technological applications in applied nanoscience (Gupta and Gupta, 2005a). The bottom-up engineering of IONPs generates excellent platforms in biomedical research for magnetically controllable drug delivery systems (Sun et al., 2008), biosensors and contrast agents for medical diagnostics (Xie et al., 2011). Research in biotechnology, the environmental sciences and green (environmentally friendly) chemistry has shown that IONPs' high magnetic response under an external magnetic field allows them to act as efficient carriers in the magnetic separation of various biosubstances or environmentally important species (e.g., proteins, low molecular weight agents, ions, inorganic or organic pollutants etc.), be tailored to work as separable and renewable nanocarriers for catalysis (Gawande et al., 2013) and be used as magnetically drivable platforms for enzyme immobilization (Ansari and Husain, 2012).

The six non-hydrated crystalline iron oxide phases identified so far (Cornell and Schwertmann, 2003) are most frequently classified according to the valence state of iron in their crystal structure. FeO, known mineralogically as wüstite, has only Fe^{2+} ions in its cubic crystal structure, and is thermodynamically unstable and paramagnetic at room temperature. On the other hand, Fe_2O_3, or ferric oxide, contains only Fe^{3+} ions and displays polymorphism, that is, the existence of further isochemical phases with different physical properties revealed by their different crystal structures. So far, four Fe_2O_3 polymorphs have been described (Machala et al., 2007, 2011; Tucek et al., 2010; Zboril et al., 2002): (i) α-Fe_2O_3, known mineralogically as hematite, with a rhombohedrally centered hexagonal crystal structure (space group $R\bar{3}c$); (ii) β-Fe_2O_3 with a cubic-body-centered crystal structure of a bixbyite type (space group $Ia\bar{3}$); (iii) γ-Fe_2O_3 with a cubic crystal structure of inverse spinel type (space group $Fd3m$); and (iv) ε-Fe_2O_3 with an orthorhombic crystal structure (space group $Pna2_1$). The last non-hydrated iron oxide phase, Fe_3O_4 (known mineralogically as magnetite) has both Fe^{2+} and Fe^{3+} ions distributed over a cubic inverse spinel crystal structure. However, only Fe_3O_4 and γ-Fe_2O_3 have been found to be functional and promising candidates in biomedical and biotechnological applications due to their favorable magnetic properties (Gupta and Gupta, 2005b; Laurent et al., 2008; Pankhurst et al., 2003; Tucek et al., 2014). They are both strong ferrimagnetic materials with two magnetic sublattices mirroring tetrahedral (T) and octahedral (O) sites, the two non-equivalent cation positions in their crystal lattice (Machala et al., 2011; Zboril et al., 2002). In stoichiometric Fe_3O_4, Fe^{3+} ions are distributed over all T-sites and half the O-sites whereas Fe^{2+} ions occupy the remaining O-sites leaving no vacant places. On the other hand, in stoichiometric γ-Fe_2O_3, Fe^{3+} ions are located at all the T-sites and 5/3 of O-sites; the remaining 1/3 of O-sites are left vacant (with virtual negative charge) to establish the neural charge in the γ-Fe_2O_3 crystal lattice. O-site vacancies can appear in a random manner, or be partially or fully ordered changing the crystal symmetry from high (cubic) to low (tetragonal). Replacing iron cations with foreign (non-iron) cations in the γ-Fe_2O_3 or Fe_3O_4 crystal structure alters the γ-Fe_2O_3 or Fe_3O_4 hysteresis parameters (magnetic hardness), thus modifying their magnetic properties and requirements for a given application. More importantly, if the size of γ-Fe_2O_3 or Fe_3O_4 nanoparticles falls below a certain threshold (usually below ~15 nm), they display superparamagnetism, a relaxation phenomenon associated with thermally activated spontaneous oscillations of nanoparticle superspin among the orientations along easy axes of magnetization energetically favored by nanoparticle magnetic anisotropy (Tucek et al., 2006). In a superparamagnetic regime (i.e., above a size-determined temperature), γ-Fe_2O_3 and Fe_3O_4 nanoparticles exhibit a remarkably high MRI contrast effect, are easily controlled by a magnetic field gradient, and display a strong magnetic response in a relatively low applied magnetic field (less than 1 T). Like all other iron oxide phases, γ-Fe_2O_3 and Fe_3O_4 are non-toxic (at low dosage), biodegradable and biocompatible, significantly raising their application potential in bio-related fields (Gupta and Gupta, 2005b).

For biomedical and biotechnological applications, the γ-Fe_2O_3 and Fe_3O_4 nanoparticle surface must be covered by a suitable biocompatible compound to (i) prevent the degradation of iron oxide nanoparticles in an unfriendly and aggressive environment (e.g., blood), (ii) suppress the aggregation of iron oxide nanoparticles by suppressing their magnetic interactions and (iii) provide functional groups for bioactive compound (e.g., drug) attachment (Gupta and Gupta, 2005b). The resulting inorganic/organic complex has a core/shell nanoarchitecture, which may be functionalized by adding various compounds. Added functions include prolonging the recognition time by the immune system or treating unhealthy cells and tissues. Such a functional complex has theranostic properties in that it can be used in both diagnostic and therapeutic procedures (e.g., MRI imaging, targeted drug delivery, cell labeling and separation, or magnetically-assisted hyperthermia) (Gupta and Gupta, 2005b).

The chemistry of a core-shell IONP's magnetic core and surface dictates its function and working environments (Veiseh et al., 2010). A functionalization of the surface enables a fine modulation of IONP behavior in solution, such as colloidal stability, pH response, overall toxicity and proclivity to bind and transport active substances. The design of the magnetic core (chemical nature and crystal lattice), on the other hand, allows the nanoparticle's magnetic response (ferrimagnetic/superparamagnetic, magnetic hardness) to be adjusted by modifying the core size and chemical composition (e.g., upon using admixture of other metals diverse from Fe). It is not a surprise that in the last 20 years, a tremendous research effort has been devoted towards the exploration and the development of different routes for controlling the chemical and physical properties of IONPs.

Thus, many synthetic routes for the preparation of IONPs of various shapes and morphologies have been described. These synthetic approaches can be shortly classified as (i) synthesis in constrained-environments, (ii) hydrothermal synthesis, (iii) sol–gel reactions, (iv) flow injections, (v) microwave assisted processes, and (vi) co-precipitation processes. In addition to the solvent or thermal degradation-based methods, IONPs can be also obtained via biomineralization in living organisms from magnetotactic bacteria (Blakemore, 1975; Markova et al., 2012a). However, the most commonly used synthetic procedures rely on the co-precipitation processes of IONPs from suitable admixtures of metal salts, a method first reported by Massart (1981), the thermal decomposition of iron precursors in organic solvents (Fang et al., 2009; Gautier et al., 2013), and solid-state thermal decompositions of iron precursors under controlled conditions (Machala et al., 2011; Zboril et al., 2004).

A graphical overview that collects several types of IONP architectures with different core/shell arrangements is depicted in Fig. 1, examples that help to illustrate the tremendous creativity-driven-design beneath this field of research. The size of IONPs can vary from a few nm up to several hundred nm in some condensed IONP assemblies and they also exhibit diverse structural shapes. The ultrasmall superparamagnetic iron oxide nanoparticles, called USPIOS, usually exhibit a spherical shape and small size, from 4 to 13 nm (Park et al., 2005), whereas nanoclusters obtained from condensed IONPs (Bakandritsos et al., 2010; Kim et al., 2008; Zoppellaro et al., 2014) are much larger (>50 nm), but can also adopt a nearly spherical morphology. Apart from the spherical motif, other IONP shapes have been described such as iron oxide nanocubes (Guardia et al., 2012; Lee et al., 2011), tetrahedral nanoparticles (Arndt et al., 2014), magnetic nanostars (Li et al., 2014), and nanorods (Xiao et al., 2012). The chemical behavior of IONPs is determined and driven not only by their shape and size but also by their surface passivation, which regulates the hydrodynamic diameter, solvent dispersability, surface charge, colloidal

Please cite this article as: Hola K, et al, Tailored functionalization of iron oxide nanoparticles for MRI, drug delivery, magnetic separation and immobilization of biosubsta..., Biotechnol Adv (2015), http://dx.doi.org/10.1016/j.biotechadv.2015.02.003

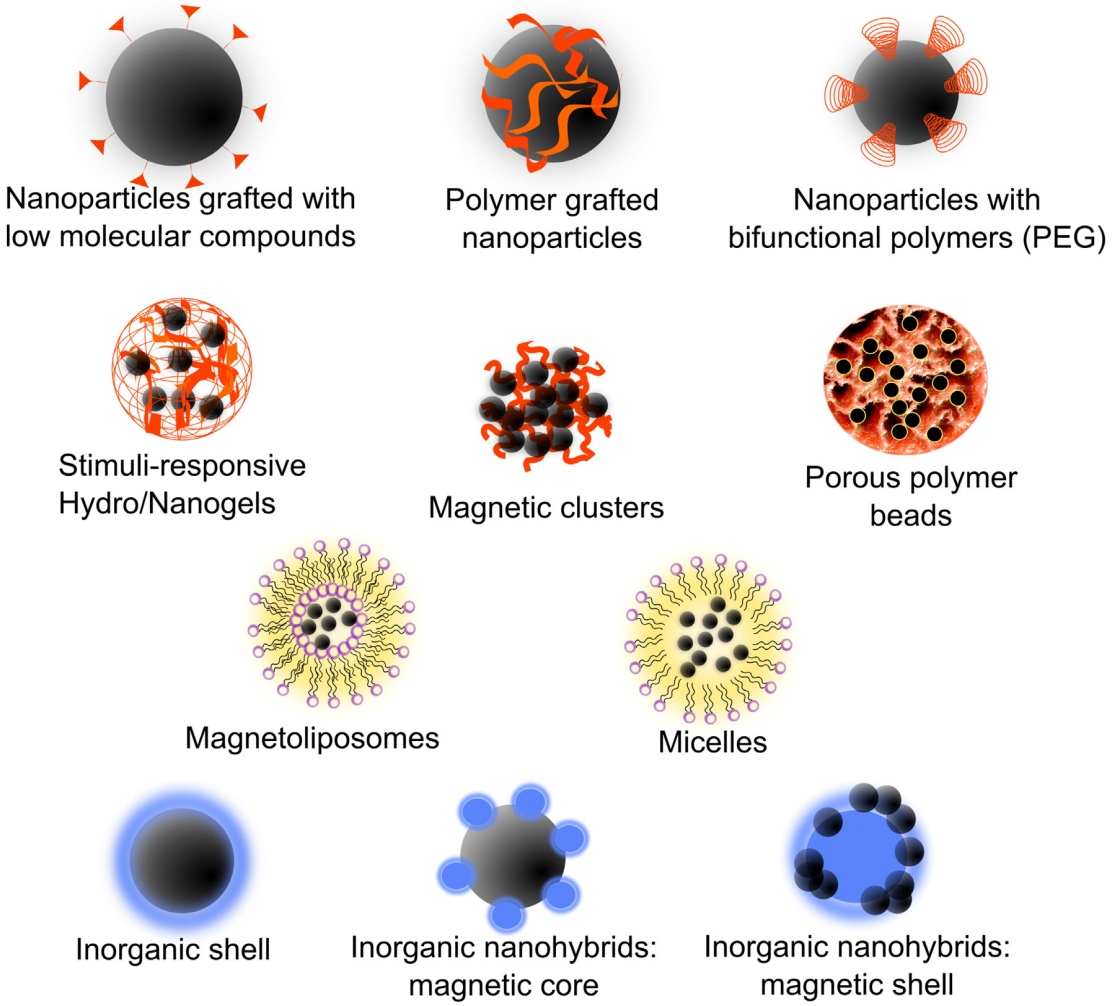


Fig. 1. General types of IONP arrangements with polymers, molecules and inorganic nanoparticles. Nanoparticles/hybrids are not depicted to scale.

stability or the speed of response to an external magnetic field. Further IONP characteristics and various surface shells are summarized and discussed in the next section.

Herein, we provide an overview of the physical and morphological IONP characteristics that dictate their applications in biological environments, soil or water. We illustrate the interplay of IONP design (size, shape, composition, and surface chemistry) that allows the assembly of versatile and truly multifunctional magnetic platforms. Most importantly, we critically discuss the principal requirements of IONP properties, their surface chemistry, and conjugation methods used in selected bioapplications, namely MRI contrast agents, drug delivery, magnetic separation and immobilization of enzymes and other biosubstances. The conjugation routes and applications potential of IONPs/metal hybrids are also highlighted.

2. Principles and specific requirements for applications of IONPs in biomedicine and biotechnologies

IONPs have found their application in various fields of biomedicine and biotechnology. Owing to their small size, they are an ideal platform for use as nanocarriers in drug delivery. A further advantage of IONPs is that due to their magnetic properties, mainly superparamagnetism, they can be used as contrast agents for nuclear magnetic resonance imaging (MRI). Their magnetic response on the external magnetic field can be even used for local overheating of cancer tissues known as hyperthermia therapy. Among these biomedical applications, magnetic properties of IONPs can be also fully explored in separation techniques of various (bio)substances or pollutants. Magnetic separation attracts a big scientific interest mainly because of its speed and effectiveness. This is also a reason why IONPs have been employed as a support for enzyme immobilization. The renewable magnetic-enzyme platform is very promising for various industrial applications and even proteomics. The overview of utilization of IONPs is depicted in Fig. 2. In the following subchapters, all of the mentioned areas of IONPs use will be addressed in greater details.

2.1. Contrast agents in MRI

MRI is a powerful and non-invasive technique used in diagnostics, characterized by ultrahigh spatial resolution based on the detection of proton relaxation in an external magnetic field. The relaxation and the enhancement of the signal/contrast can be increased with the aid of contrast agent material. Those based on superparamagnetic iron oxides (SPIOs) are able to substantially alter the spin–spin relaxation of water molecules (T2 relaxation) near the magnetic nanoparticle and to enhance the negative contrast of the image (Wang et al., 2001). The contrast properties can also be influenced by the size and hydrophilicity of the nanoparticles (Duan et al., 2008) or by the thickness of the surface shell (LaConte et al., 2007; Veiseh et al., 2010). The water relaxivity can also be enhanced when low molecular-weight compounds used in the

Please cite this article as: Hola K, et al, Tailored functionalization of iron oxide nanoparticles for MRI, drug delivery, magnetic separation and immobilization of biosubsta..., Biotechnol Adv (2015), http://dx.doi.org/10.1016/j.biotechadv.2015.02.003

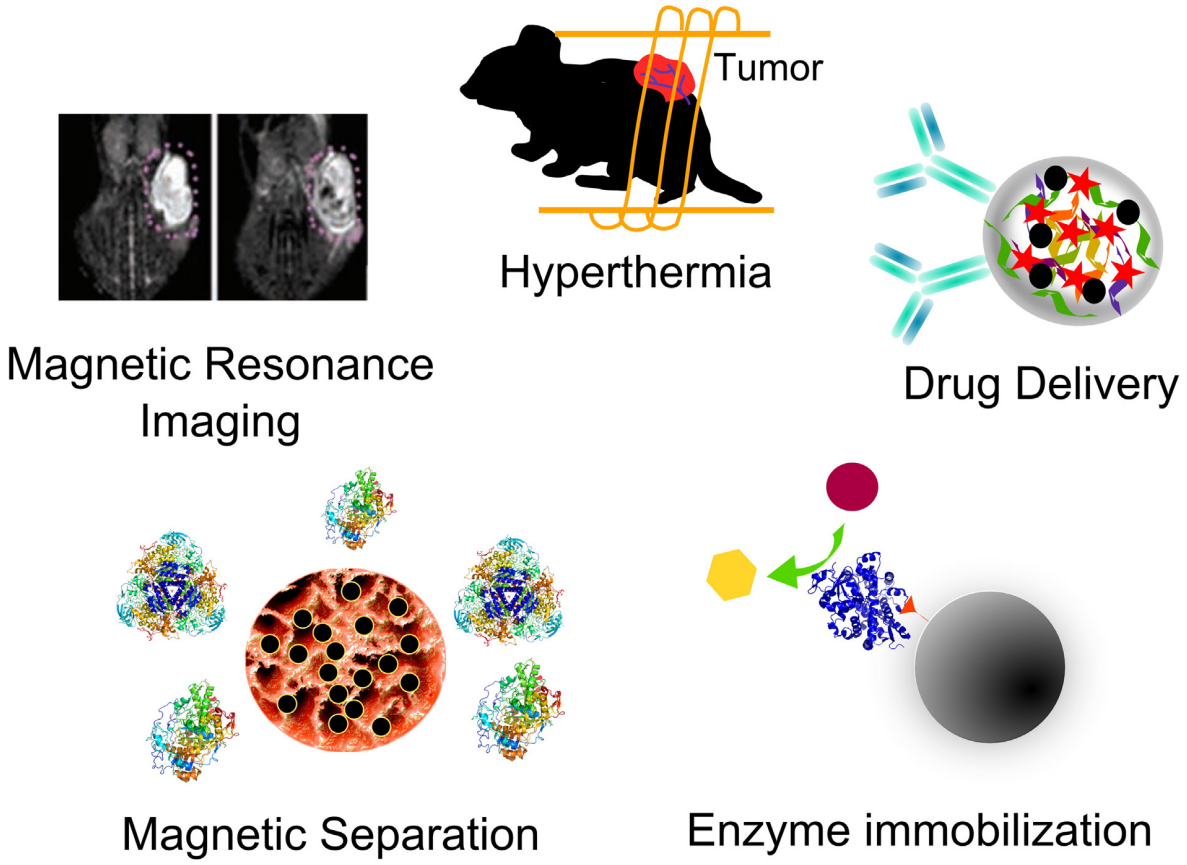


Fig. 2. Schematic representation of biomedical and biotechnological applications of IONPs. The image for magnetic resonance imaging was reprinted with permission from Yang et al. (2009).

IONP shell encode π-conjugation paths that allow an effective spin transfer from the magnetic core to the surrounding water (Maity et al., 2012).

Two general types of negative contrast agents (CAs) based on IONPs can be found in literature; the peroral CAs for imaging of digestive system (Kluchova et al., 2009) and CAs used through intravenous administrations. The key characteristics of peroral CAs are their low toxicity combined with the good stability to withstand the acidic environment of the stomach (Kluchova et al., 2009). The precise design of the surface coating materials is not so essential for peroral CA preparations. In contrast, IONPs used for intravenous administration are much more challenging to design.

The basic requirements for the application of IONPs as intravenous CA in MRI are: (i) low toxicity, (ii) colloidal stability at physiological conditions (37 °C, PBS buffer, pH = 7.4, 0.154 M ionic strength) (Qiao et al., 2009; Veiseh et al., 2010), (iii) low and stable hydrodynamic diameter in plasma, (iv) little proclivity towards aggregation, (v) well controlled surface charges (Chapman et al., 2013), and (vi) low nonspecific protein adsorption (Nie, 2010). All these variables determine the nanoparticle's biodistribution and its ability to overcome biological barriers in vivo (Chapman et al., 2013; Veiseh et al., 2010). In general, nanoparticles with hydrodynamic sizes of up to 5–8 nm (similar to the size of 30–50 kDa serum proteins) and low molecular weight contrast agents can undergo renal excretion (Choi et al., 2007; Liu et al., 2013; Longmire et al., 2012; Nie, 2010). IONPs below 5 nm are quite unusual (Wang et al., 2014) and they are much more prone to extravasation processes, thus are cleared very fast. The majority of functional IONPs have larger hydrodynamic diameters and are captured by the reticuloendothelial system (RES, e.g., in liver and spleen) (Weissleder et al., 1989). This is also the reason why IONPs were originally used for imaging and detection of hepatic (Weissleder et al., 1987) and splenic tumors (Weissleder et al., 1988). Nanoparticles from 20/30 nm up to 100/150 nm (Elsabahy and Wooley, 2012; Veiseh et al., 2010) can also accumulate in the stomach (Banerjee et al., 2002), bones and kidneys (Lee et al., 2010). However, these medium size nanoparticles have a high potential for cancer imaging as well as for drug delivery, due to their prolonged circulation time in blood vessels and their tendency to passively target tumors due to the Enhanced Permeation and Retention (EPR) effect of solid tumors (Elsabahy and Wooley, 2012; Tanaka et al., 2004). These medium-sized particles can escape the renal clearance and are not so big as to be immediately opsonized (coated with serum proteins) and captured by the RES. Another important parameter for avoiding a fast opsonization of the IONPs is the surface charge of the nanoparticle. Neutral nanoparticles with coats containing hydrophilic polymers, for example polyethylene glycol or dextran (Hong et al., 2008), do not strongly interact with opsonin proteins such as albumins, immunoglobulins, fibronectins, and complement proteins (Nie, 2010; Roser et al., 1998). The IONP's surface charge can be reduced by assembling complex surface architectures combining two types of polymeric coating (e.g., polyethylene glycol branched chitosan (Veiseh et al., 2009) or polyacrylic acid with polyethylene glycol (Pothayee et al., 2013)). In contrast, positively or negatively charged IONPs strongly interact with plasma proteins and are rapidly removed from the bloodstream by macrophages, a process activated by the enhanced stimulation of the immune system (Dobrovolskaia and McNeil, 2007).

The advantage of using IONPs as contrast agents over other types of metal oxide is their excellent biocompatibility, even if they end up localized in the spleen or liver and are metabolically degraded (Jain et al., 2008). In vitro studies show that IONP surface coverage strongly affects its cytotoxicity, cellular uptake, and mechanism of endocytosis (Gupta

Please cite this article as: Hola K, et al, Tailored functionalization of iron oxide nanoparticles for MRI, drug delivery, magnetic separation and immobilization of biosubsta..., Biotechnol Adv (2015), http://dx.doi.org/10.1016/j.biotechadv.2015.02.003

and Gupta, 2005a). Coated IONPs exhibit much lower cytotoxicity and are almost nontoxic in comparison with the particles without surface coverage. Nevertheless, it has been shown that the IC50 of IONPs without surface coverage was around 0.5 mg/mL, which is still better than the values reported for other nanomaterials used for biomedical applications (Lewinski et al., 2008). The particles without surface coverage can, e.g., determine the organization of the cytoskeleton, ability of cells to adhesion (Gupta and Gupta, 2005a) or the kinetics of their biological degradation (Lartigue et al., 2013). The cytotoxicity of IONP degradation in a biological environment also needs to be taken into account. IONP degradation follows, in general, the path of lysosomal digestion (Lartigue et al., 2013). Lysosomal enzymes degrade nanoparticles with a simultaneous release of iron cations. The kinetics of degradation is strongly determined by the "active" surface of IONPs in terms of enzyme recognition, the surface polymer's hydrophilicity or the ability of particles not to aggregate in the lysosomes (Lartigue et al., 2013). The release of iron cations can potentially promote severe oxidative reactions in cells. However, iron homeostasis is highly regulated and excess iron is quickly stored in ferritin proteins (Lartigue et al., 2013), one of the enzymatic systems that help to control the iron level in the body (Jain et al., 2008).

The effective application of IONPs for MRI imaging and preventive medicine is also associated to their ability of an early detection of cancers in various organs, following their preferential localization in such areas due to the EPR effect. While the passive targeting has proven to be an effective tool for the early diagnostic, the active tumor targeting approach became in recent years one of the leading strategies that directed the IONP chemical design. In this context, the surface engineering of functional IONPs can be augmented by specific cancer markers, such as antibodies and glycoproteins (Tanaka et al., 2004). These bioactive compounds are usually immobilized onto IONPs in a late synthetic step, via coupling reactions following an initial coating of the nanoparticle surface with polymeric materials that contain functional groups responsive to the coupling. An overview of polymers/molecules for coating IONP systems suitable for MRI is presented in Fig. 3. Coupling methods for immobilizing targeting compounds are discussed in the third part of this review.

2.2. Targeted drug delivery

Drug delivery refers to pharmaceutical approaches to transporting drugs to a desired place in the body. Nanotechnology is used mostly for intravenous delivery, in particular, to cancer tissues. The goals of targeted drug delivery are to reduce the toxic dose for non-cancerous tissues and increase the therapeutic effect of the drug in the desirable places. Nanoparticles are the ideal candidates for drug delivery because they do not only act as a nanocarrier for passive tumor targeting but can be coated for active tumor targeting and, in the case of IONPs, can be delivered to cancer tissues by magnetic targeting (Chertok et al., 2008).

IONP systems have the potential to act as magnetic nanocarriers because IONP surfaces may be coated with diverse organic polymers (see Fig. 3) that, in turn, are capable of interacting with or binding pharmaceutically active molecules. Such properties create biomedical applications for IONPs, especially in cancer therapies.

Morphological differences in the physical surroundings of healthy and cancer tissues gives rise to a selective penetration by IONPs of

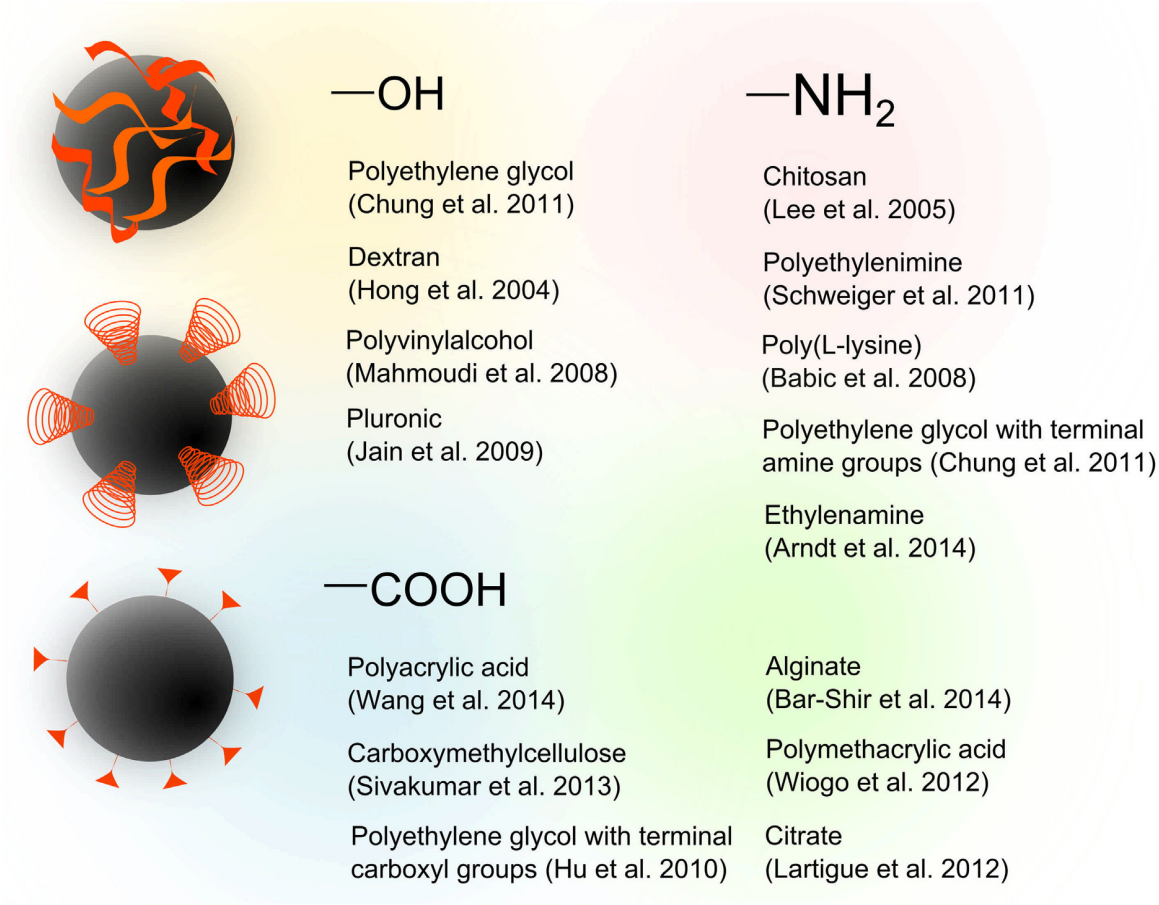


Fig. 3. Polymers and organic molecules (sorted by functional group) typically used for primary coating and stabilization of IONPs for MRI. The appropriate coating/functionalization method can be found in given literature (Arndt et al., 2014; Babic et al., 2008; Bar-Shir et al., 2014; Chung et al., 2011; Hong et al., 2004; Hu et al., 2010; Jain et al., 2009; Lartigue et al., 2012; Lee et al., 2005; Mahmoudi et al., 2008; Schweiger et al., 2011; Sivakumar et al., 2013; Wang et al., 2014; Wiogo et al., 2012).

Please cite this article as: Hola K, et al, Tailored functionalization of iron oxide nanoparticles for MRI, drug delivery, magnetic separation and immobilization of biosubsta..., Biotechnol Adv (2015), http://dx.doi.org/10.1016/j.biotechadv.2015.02.003

tumor regions. Solid tumors are usually characterized by a compromised leaky vasculature that promotes extravasation of the IONPs from the blood and their subsequent retention in the tumor interstitium. In contrast, the densely packed endothelial cells in healthy-tissue vessels form effective barriers that prevent IONP extravasation. Selective penetration can be combined with magnetic gated-delivery of IONPs (Cole et al., 2011).

The therapeutic effect can then be triggered by local overheating of the cancer cells via hyperthermia (Guardia et al., 2012) and/or upon the IONP's gated-delivery of cancer drugs. The hyperthermia effect, namely, the ability of magnetic nanoparticles to adsorb alternating current (AC) energy and to convert it into heat, although very promising as a therapeutical approach, may suffer from difficulties in controlling the effect of overheating effects in both the tumor region and its healthy surroundings. If local overheating by hyperthermia is in the temperature range from 41 to 46 °C, the cancer cells undergo apoptosis, programmed cell death caused by thermal stress (Deatsch and Evans, 2014; Kumar and Mohammad, 2011). Higher temperatures can cause dangerous necrosis or coagulation of tissues often associated with inflammation (Gnant et al., 2000). Against this background, IONPs used for cancer drug delivery may be safer, although a combination of drug-delivery and hyperthermia may provide the ultimate solution for therapy.

For this reason, various synthetic strategies have been explored to obtain drug–IONP conjugates where the triggered release can benefit from the heating of IONPs. Various drugs have been successfully incorporated into IONPs to achieve these properties, such as paclitaxel, doxorubicin and methotrexate, photoactivated agents and even radiochemicals.

A variety of methods are used to attach a drug to the IONPs. The drug molecule can be loaded in the polymer interspace of magnetic nanoclusters (Bakandritsos et al., 2012), encapsulated in stimuli responsive hydrogel/polymer frameworks (Jaiswal et al., 2014), linked to the activated surface of IONPs (Magro et al., 2014) or trapped in magnetoliposomes (Tai et al., 2009). In addition, drugs can be connected to the IONP's organic canopy by covalent linkages that are susceptible to degradation (e.g., by hydrolysis) as part of the cell's metabolism (see Fig. 4).

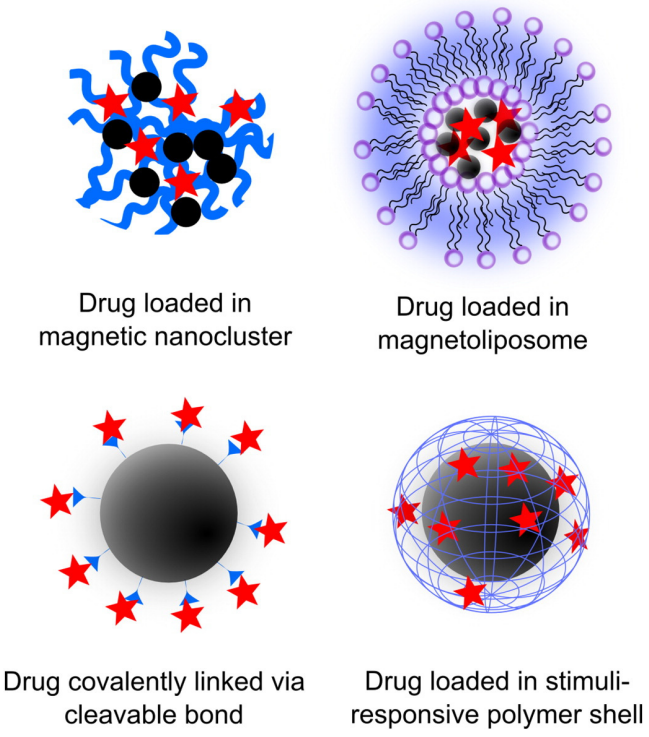


Fig. 4. Schematic representation of various IONP–drug nanosystems for targeted magnetic drug delivery.

The in vivo kinetics of drug release is a key factor that can be tailored by successful drug–IONP conjugate design. Drug release can be induced not only by external stimuli such as a local temperature increase but also by low pH, typical for cancer tissues. Tai et al. (2009) reported the preparation of thermosensitive magnetoliposomes that were able to release the loaded compounds after exposure to alternating magnetic field and following a local temperature increase. Another example of controlled drug (doxorubicin) release by magnetic IONPs has been described in condensed IONP nanoclusters containing alginate chains as polymer-coronas (Zoppellaro et al., 2014). These clusters exhibited very high loading capacity of anticancer drug (doxorubicin, 26% in weight) and were able to release almost 70% of the loaded drug within 5 min after exposure to an alternating magnetic field. A similar study was performed by Deka et al. (2011), using IONPs in the form of nanobeads that were surface-functionalized with thermoresponsive N-isopropylacrylamide (PNIPAM). Such systems were capable of loading doxorubicin molecules up to 45% in weight. In this case, the drug release topped 85% after 110 h at 37 °C. It is important to note that a slower sustained release of the drug can sometimes be considered a therapeutical advantage, since it may mitigate several of the side-effects typically observed in the patient undergoing the chemotherapy; in fact, Ponta and colleagues recently reported that a more effective cancer treatment can be obtained using a slower release of the active drug from micelles (Ponta and Bae, 2014). Another effective IONP drug-delivery therapy was reported by Lim and co-authors. In their study, the magnetic nanoparticles were encapsulated into a pH-responsive nanoparticle, conjugated with HER2/neu antibody (HER = Herceptin) and loaded with doxorubicin (Lim et al., 2011). The system exhibited an excellent selectivity for targeted tumor tissues. A nearly 100% release of the drug doxorubicin was observed in the tumor regions characterized by an acidic environment (pH = 5.5) over 5 days. In contrast, just 50% release of the drug was observed in healthy tissues where pH is nearly neutral (~7.4). As mentioned earlier, the drug can also be attached to the surface of IONPs by pH degradable bonds. Banerjee and colleagues reported the successful linkage of doxorubicin to IONPs coated with arabic gum via pH-sensitive hydrazone bonds (Banerjee and Chen, 2008). The loaded doxorubicin (80%) was found to be released fast, within 4 h, when the environmental pH was made acidic enough (pH = 5.0). From these examples, the research on drug delivery is well on its way to generate highly tailored IONPs; as such, they will provide in the close future better plasma pharmacokinetics, tumor selectivity and, in general, a truly personalized platform for medical therapies.

2.3. Magnetic separation

Another highly effective technological application of IONPs is their use in the magnetic separation processes of various substances. Suitably modified IONPs efficiently separate ions (Liu et al., 2009), pollutants (Ambashta and Sillanpää, 2010), cells (Borlido et al., 2013), proteins/antibodies (Heebøll-Nielsen et al., 2004; Safarik and Safarikova, 2004), and various bioactive substances (Müller-Schulte and Brunner, 1995).

The advantages of using magnetic separation techniques in comparison to more conventional procedures such as chromatography, are their (i) high versatility, (ii) the possibility to work without pre-treatment of the active material even in heterogeneous crude media, (iii) fast, highly cost-effective and straightforward methodology, and (iv) the reusability of sorbents after the magnetic separation. Today, several ready-to-use magnetic sorbents are available commercially, some containing an activation reagent for the immobilization of various substances, such as magnetic Sepharose®, Dynabeads® and Chemicell®. Two types of magnetic sorbents have been reported, (i) IONPs coated with specific functional groups and

Please cite this article as: Hola K, et al, Tailored functionalization of iron oxide nanoparticles for MRI, drug delivery, magnetic separation and immobilization of biosubsta..., Biotechnol Adv (2015), http://dx.doi.org/10.1016/j.biotechadv.2015.02.003

(ii) IONPs encapsulated in the porous matrix of a polymer bead (polymer microsphere). The separation of different substances can be finely tailored by the synthetic design for use in processes such as ion-exchange, hydrophobic interactions, affinity adsorptions, and even specific interaction through antibody–antigen interactions. Fig. 5 shows these two types of architectures in IONPs used in magnetic separation processes.

From the more general perspective, the key requirement for magnetic sorbents is a large amount of functional groups per mass of magnetic material in combination with an appreciable saturation magnetization value (Franzreb et al., 2006). These properties are pivotal for obtaining both high binding proclivity for the target substances and a fast magnetic response of the composite. Magnetic microspheres (Fig. 5a) fulfill these requirements by caging a high content of magnetic material and having a porous polymer framework. Similarly, core-shell magnetic nanoparticles (Fig. 5b) have both a high surface area and the ability to incorporate a large amount of functional groups in the polymeric or inorganic shell.

Magnetic microspheres are usually prepared by adding IONPs to the polymer solution during formation (spraying or microemulsion method) of the polymer bead (Yang et al., 2008). IONPs can also be synthesized within the pores of the polymer microspheres in situ (Luo et al., 2009). The choice of polymer coating material is dictated by the type of compound that needs to be separated. An overview of the synthesis techniques used for surface modification of IONPs is given in the third section of this review. Krizova and colleagues prepared magnetic microspheres from methacrylates with low porosity and a carboxylic acid functional group for the separation of genomic DNA (Krizova et al., 2005). In the case of proteins, separation can be achieved by using highly porous microspheres coated with hydrophilic polymers such as cellulose (Safarik et al., 2007), agarose (Zhang et al., 1999) or poly(vinylalcohol) (Yang et al., 2008). The hydrophilicity of these polymers prevents any denaturation of the proteins. Other types of magnetic microsphere include the ion-exchange resins. These composites are suitable for separation of ions and low molecular organic substances and are usually composed of microspheres prepared by the polymerization of styrene in the presence of IONPs (Lee et al., 2003).

In addition to the separation methods based on specific interactions, IONPs can also be used for non-specific sorption such as the sorption of heavy metals (Hua et al., 2012). This separation is partly based on electrostatic interaction but, more importantly, uses the large surface of IONPs (Xu et al., 2012). Hu and colleagues used IONPs for the removal of hexavalent chromium. The particles had a surface area of 178 $m^2 g^{-1}$ and a very high sorption capacity for chromium amounting to 19.2 mg g^{-1} (Hu et al., 2005). Similarly, superparamagnetic IONPs are highly efficient for arsenate removal from an aqueous environment (Kilianova et al., 2013). Apparently, even IONPs without specific surface coverage can be used to separate or remove pollutants in waste water through non-specific interactions.

2.4. Application of IONPs conjugated with enzymes

Magnetic nanosystems combining enzymes and IONPs via biopolymer immobilization are another fast expanding area of biotechnology research. Such nanocomposites are potentially useful to the food industry, in the form of food processing units. As renewable "bio-catalysts", they can also be implemented for the greener generation of biofuels (Ansari and Husain, 2012). There are several technological advantages to immobilize enzymes onto IONPs. Above all, the magnetic recovery of the active material decreases the cost of production. Furthermore, immobilized enzymes often exhibit better temperature stability, pH stability and/or higher activity compared to unsupported proteins (Khoshnevisan et al., 2011; Pecova et al., 2013).

An example of a highly cost-effective industrial implementation of enzyme–IONP conjugates can be found in the immobilization of the enzyme lactase onto IONPs. The conjugate is used to deplete milk of lactose for use by lactose intolerant individuals (Talbert and Goddard, 2013). Another potential application of enzyme–IONP conjugates is the green synthesis of cellulosic ethanol. The degradation of cellulose into glucose by cellulase is, however, not yet as cost-effective as the production of ethanol from glucose in yeast, but such a platform may enable a further development of the process (Jordan et al., 2011).

The conjugation of enzymes to IONPs can be achieved by various synthetic approaches and an overview of strategies is provided in Section 3. In general, the enzyme can be attached to the magnetic polymer microspheres or simply to the magnetic nanoparticles that contain suitable surface functionalities (e.g., amino groups, thiol moieties, carboxylate residues). Compared to antibody–IONPs for drug delivery, there is no strict requirement for colloidal stability of the enzyme–IONP system because of the needed faster response of IONP aggregates to an external magnetic field. Importantly, the enzymatic activity in the supported nanocomposite must be carefully preserved.

Enzyme–IONP conjugates can also be used in other applications such as biosensing or proteomics. For example, trypsin conjugated IONPs are regarded as a promising platform for proteomic analysis (Lin et al., 2008). In this case, immobilization of trypsin onto magnetic nanoparticles decreases autolysis of the enzyme and increases its re-usability (Lin et al., 2008; Pecova et al., 2013). Trypsin's conjugation with IONPs even

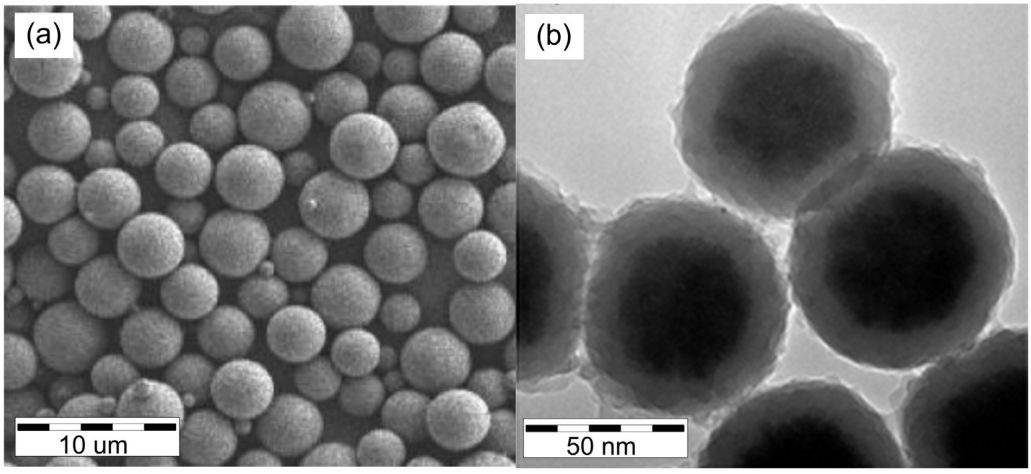


Fig. 5. Examples of sorbents for magnetic separation. (a) Magnetic microspheres and (b) magnetic nanoparticles with surface coating; (a) scanning electron microscope image of porous microspheres from poly(vinylalcohol) with IONPs encapsulated in the matrix (reprinted with permission from (Yang et al., 2008)). (b) Transmission electron microscope micrograph of superparamagnetic IONPs with polymer-silica shell (reprinted with permission from (Fang et al., 2010b)).

Please cite this article as: Hola K, et al, Tailored functionalization of iron oxide nanoparticles for MRI, drug delivery, magnetic separation and immobilization of biosubsta..., Biotechnol Adv (2015), http://dx.doi.org/10.1016/j.biotechadv.2015.02.003

improves its thermal stability such that trypsin-induced digestion of various proteins can take place at a higher temperature. Enzyme–IONP conjugates have also been used for biosensing, enabling the detection of various analytes (gases, glucose, drugs, cells, metabolic products, contaminants, etc.). The various biosensing systems based on IONPs have been excellently reviewed elsewhere (Xu and Wang, 2012).

2.5. Applications of magnetic/metallic hybrid nanostructures

Another class of magnetic nanostructure is the IONP/metal hybrid nanostructure, which can be obtained by merging two or more nanometer-scale components, allowing complex technological features to exist in a single unit. Such materials can be multifunctional (magnetic, electronic, optical), since the functionality of each component can be fully integrated into the merged unit. The different components' material and size parameters can be independently optimized in order to fine-tune their function or to induce synergistic phenomena (Zeng and Sun, 2008).

The IONP/metal nanocomposites have demonstrated the huge application potential and real possibility to obtain a large variety of catalytic, magnetic, electric, optical, and plasmonic properties. Of all the IONP/metal nanohybrids, those combining IONPs with noble metals (mainly silver, gold, and palladium) represent the most promising superstructures with a versatile portfolio of applications.

IONP/Ag nanocomposites are successfully used as hydrogen peroxide sensors in electrochemistry. They are also used as substrates in magnetically assisted surface enhanced Raman scattering (SERS) for the chemical analysis of organic species, bioactive substances or toxic molecules with record detection limits (Choi et al., 2010; Han et al., 2013; Ranc et al., 2014). Moreover, IONP/Ag hybrid nanostructures also exhibit antibacterial, antifungal and even antiviral properties and they are utilized in antimicrobial targeting (Chudasama et al., 2011; Nangmenyi et al., 2011; Prucek et al., 2011).

The IONP/Au nanohybrids can serve as multimodal contrast agents for MRI and CT bioimaging (Narayanan et al., 2012). Furthermore, they can be used in bioseparation and immunoassays based on surface-enhanced Raman spectroscopy at favorably low detection levels (Bao et al., 2009; Ranc et al., 2014). The magnetic-gold hybrids possess a highly tunable plasmon resonance, a property that may be exploited in photothermal therapy for selective destruction of target carcinoma cells (Salgueirino-Maceira et al., 2006).

IONP/Au hybrid nanostructures are also being used as magnetically separable catalysts. Gawande and colleagues demonstrated that highly tuneable catalytic processes can be obtained from magnetite–gold nanoparticles in oxidative esterification and hydrogen transfer reactions (Gawande et al., 2013, 2014). Nanocatalysts based on magnetite and palladium nanoparticles were successfully applied in the Buchwald–Hartwing reactions for arylation of amines and amides (Sa et al., 2014). Similarly, palladium-supported magnetic materials have successfully catalyzed the hydrodechlorination of the chlorohydrocarbons trichloroethene or chlorobenzene, as described by Hildebrand et al. (2009).

Several other mixed metal composites have been reported, such as magnetite–nickel (Costa et al., 2014), magnetite–platinum (Wu et al., 2012) or magnetite–ruthenium (Baig and Varma, 2014) nanocatalysts. These are but a few applications of magnetic/metallic hybrid nanostructures for catalysis, a popular research topic for material chemists in recent years. The wide range of applications for IONP/noble metal hybrids is illustrated in Fig. 6.

3. Surface design of magnetic nanoparticles

The manner in which active substances/groups/nanomaterials are immobilized onto the surface of IONPs is pivotal to their function. Primary functional groups prevent nanoparticle aggregation and provide suitable binding sites for further conjugation with biosubstances. Usually, primary functional groups can be attached to IONPs via adsorbed polymer/small molecules or covalently linked to the particle via polymerized silane structures with an attached functional group (e.g., amine group via APTES 3-aminopropyltriethoxysilane). Typical functional groups used for primary functionalization are hydroxyl groups (e.g., polysaccharides, PEG), amine groups (e.g., chitosan, polyethylenimine), and carboxylic groups (e.g., polyacrylic acid, alginate, citrate). Other types of functional groups such as epoxy, sulfhydryl (thiol), alkyne, azide, and carbonyl are very often used for specific conjugation methods such as "click" chemistry. The synthetic strategies used for functionalization of IONPs with various types of functional groups are depicted in Fig. 7.

3.1. Immobilization of proteins, enzymes, antibodies and targeting agents

The suitable synthetic strategy for immobilizing active substances ("vectorization") is crucial in IONP design. Many conjugation techniques exist, each with specific characteristics and requirements. Immobilization should neither affect the active agent's recognition site nor the required IONP characteristics (e.g., colloidal stability for drug delivery). Proteins, enzymes and even antibodies contain multiple functional groups such as amine, carboxyl, thiol (sulfhydryl) or hydroxyl groups, in the case of glycoproteins. In general, any of these functional groups can be used for attachment to the IONP surface. The optimal conjugation strategy must also take the number of particular groups into account.

There are three approaches for covalently conjugating IONPs with bioactive substances (antibodies, peptides, fluorescent dyes, molecules expressed by cancer cells). The first involves a chemical modification of the functional group on the IONP's surface followed by its attachment to the specified bioactive substance's functional group. The second approach uses an activation of the IONP's functional groups and the third strategy relies on a chemical modification of the bioactive substance.

The modification of suitable IONP functional groups (mainly the amine group) is a very efficient strategy for immobilization of proteins, enzymes and antibodies with thiol functional groups (Laurent et al., 2008; Veiseh et al., 2010). The advantage of this strategy is the selectivity of the covalent bonds and the reduced probability of aggregation for proteins with few thiol groups. Several examples of the chemical modification of IONPs (with maleimide, pyridyl disulfide, iodoacetate and hydrazine) for the attachment of thiol-active compounds are given in Fig. 8.

Another way of chemically modifying IONPs is to attach bifunctional aldehydes (e.g., glutaraldehyde) to their amine groups (Kluchova et al., 2009). Thus, aldehydes are used to immobilize another amine containing compound. However, the formed condensed Schiff-base is not stable in acidic pH and should be stabilized via a reducing agent such as cyanoborohydride. This conjugation technique is not very selective due to the high amount of amine groups in proteins and is suitable mainly for enzyme immobilization where colloidal stability is not necessary. However, the slightly modified approach based on condensing a Schiff-base can be used to immobilize antibodies for drug delivery. Pereira and colleagues treated the antibody with sodium periodate, which oxidized the minor sugar units of the antibody into the aldehyde functional group (Pereira and Lai, 2008). The aldehyde functional groups were next coupled with a hydrazine bond that was covalently attached to particles via adipic acid dihydrazide (see Fig. 8d) (Pereira and Lai, 2008).

Bioactive substances may also be attached by activating an IONP's functional group. This strategy is used mainly for immobilizing small molecules onto carboxylic group-containing IONPs. The carboxylic group is activated to be more reactive for the covalent attachment of various substances. Compared to the chemical modification described above, the activation agent does not become part of the final conjugate. Carboxylic acid can be activated via a reaction with thionyl chloride followed by coupling with a hydroxyl group (McCarthy and Weissleder, 2008). However, this strategy is not suitable for

Please cite this article as: Hola K, et al, Tailored functionalization of iron oxide nanoparticles for MRI, drug delivery, magnetic separation and immobilization of biosubsta..., Biotechnol Adv (2015), http://dx.doi.org/10.1016/j.biotechadv.2015.02.003

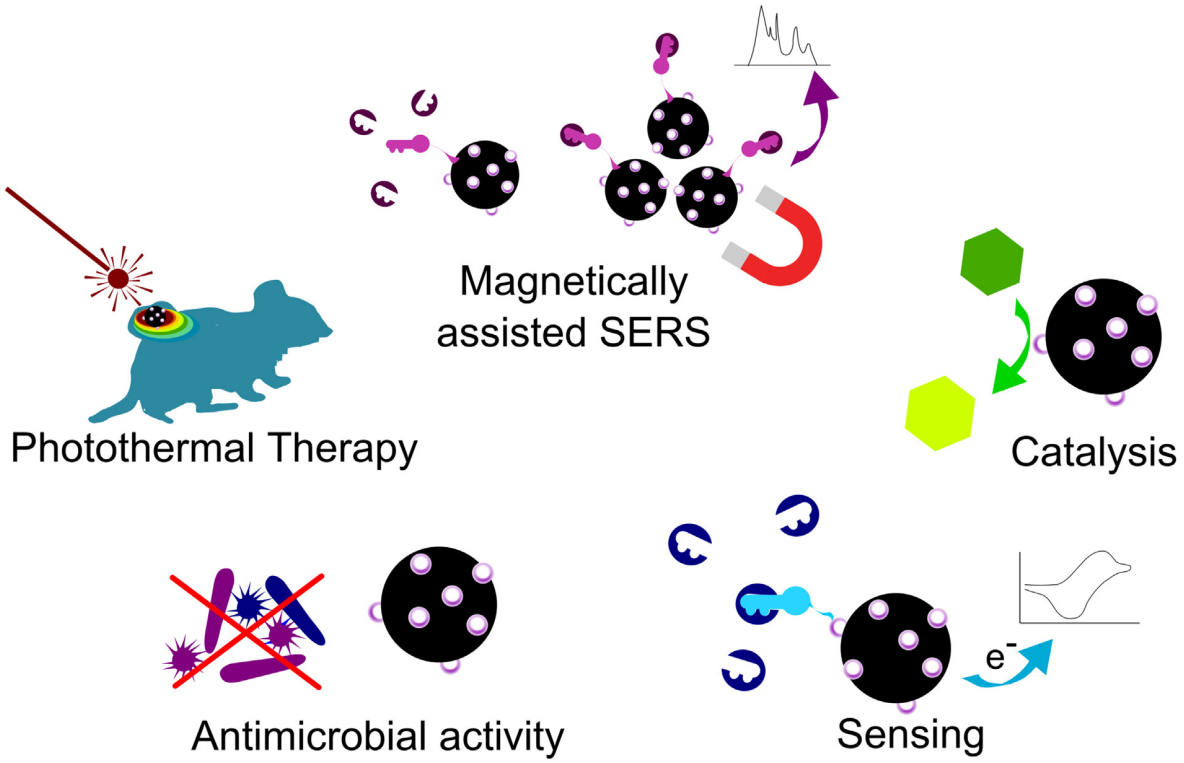


Fig. 6. Schematic illustration of various applications of IONP/noble metal hybrids.

immobilizing antibodies or enzymes because the reaction has to be performed under anhydrous conditions, e.g., in DMSO (Aksoy et al., 1998; McCarthy and Weissleder, 2008). Another example of this conjugation strategy is the activation of the carboxyl group via a reaction with EDC (1-ethyl-3-(3-dimethylaminopropyl)carbodiimide) and NHS (N-hydroxosuccinimide) (Veiseh et al., 2010). This activation is suitable mainly for small molecules containing one amine group or for enzyme immobilization because of the possible aggregation of IONPs via crosslinking of the particles (not suitable for immobilization of proteins/antibodies to IONPs for biomedical applications).

The direct modification of bioactive substances is another method used for their conjugation with IONPs (see Fig. 8). Some compounds such as fluorescent dyes are commercially available in the activated form, e.g., fluorescein isothiocyanate or rhodamine B isothiocyanate. Such compounds may be used for reactions with amine groups, aldehydes or even polysaccharides modifying the surface of IONPs. The main conjugation possibilities are depicted in Fig. 8.

"Click" chemistry, as shown in Fig. 9, is a special conjugation strategy. The alkyne/azide and thiol/alkene groups can be attached to bioactive substances using the same strategies summarized in Fig. 7. The key advantages of this conjugation strategy include high yield and selectivity, and also good physiological stability. The possibility of perfectly controlling the conjugation route makes "click" chemistry one of the most powerful tools for surface nanoengineering (Nandivada et al., 2007). Finally, the above mentioned linking techniques represent an overview of the basic principles of conjugation chemistry and many other conjugation alternatives exist (Biju, 2014).

3.2. Biodegradable bonds for targeted drug delivery

One of the challenges in drug delivery is to design nanocarriers that release the attached drug in the desired place. In addition to the non-covalent techniques discussed in Section 2.2, the most promising nanosystems for this purpose consist of nanoparticles with a drug covalently attached via biologically degradable or cleavable bonds.

Several types of biologically cleavable bonds exist: the hydrazone bond that is cleavable at low pH (cancer tissue, lysosomal environment), the S–S bond that is enzymatically degradable by thiol reductase in the lysosomes (Arunachalam et al., 2000), the peptide sequence Gly–Phe–Leu–Gly cleavable by lysosomal cathepsin (proteinase) (Hanessian et al., 2008) or the biologically cleavable ester bond that has been used for linking drugs to carbon nanotubes (Liu et al., 2008) or polymers (Kopecek and Kopeckova, 2011). An overview of these bonds is given in Fig. 9.

Although enzymatically cleavable bonds are highly promising they have not yet been fully explored for use with IONPs. The main advantage lies in their selectivity for drug release. They can be degraded (with the drug being released) just after internalization into the cell. By comparison, pH-triggered drug release is less selective because the pH differences between the bloodstream and the lysosomal environment are not so dramatic and can cause unwanted slow drug release in the bloodstream or a slow hydrolysis in the lysosomes (Kopecek and Kopeckova, 2011).

3.3. Functionalization for magnetic separation

Magnetic separations based on IONPs offer enormous variability in applications and even in preparation techniques of magnetic sorbent. IONPs can be used to separate cells via a conjugated antibody (Borlido et al., 2013) as well as separate ions via electrostatic interaction. The antibodies are attached to the magnetic sorbent using methods similar to those mentioned in the previous section. Magnetic separation is also used to isolate antibodies from crude media. For example, boronic acid can capture antibodies via the formation of a bond with the antibodies' cis-diol (glycol) units (Borlido et al., 2011). The conjugation of boronic acid to IONPs can be performed, for example, by thiol-en click chemistry (Zhang et al., 2014a, 2014b).

The functionalization of magnetic microspheres with typical ion-exchange separation groups such as diethylaminoethyl (DEAE), carboxymethyl (CM), sulfopropyl (SP) and hydrophobic groups (pentyl, octyl) can be performed in a manner similar to the typical

Please cite this article as: Hola K, et al, Tailored functionalization of iron oxide nanoparticles for MRI, drug delivery, magnetic separation and immobilization of biosubsta..., Biotechnol Adv (2015), http://dx.doi.org/10.1016/j.biotechadv.2015.02.003

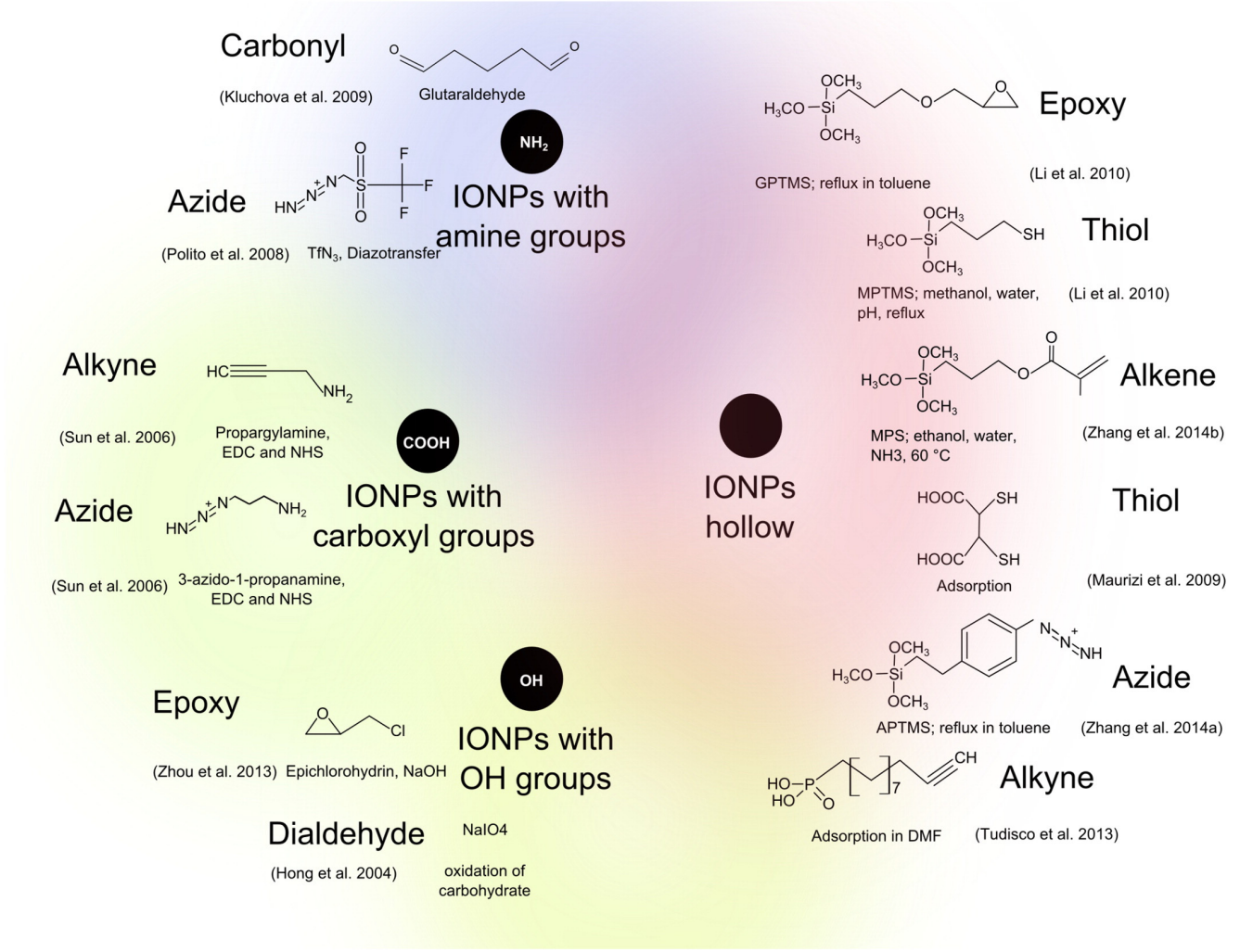


Fig. 7. Strategies for functionalization of IONPs with specific functional groups. GPTMS: 3-(glycidoxy)propyltrimethoxylsilane, MPTMS: 3-(mercapto) propyltrimethoxysilane, MPS: 3-(methacryloyloxy)propyltrimethoxylsilane, NHS: (N-hydroxosuccinimide), APTMS: 4-(azidomethyl)phenethyltrimethoxysilane, EDC: (1-ethyl-3-(3-dimethylaminopropyl) carbodiimide). The appropriate coating/functionalization method can be found in given literature (Hong et al., 2004; Kluchova et al., 2009; Li et al., 2010; Maurizi et al., 2009; Polito et al., 2008; Sun et al., 2006; Tudisco et al. 2013; Zhou et al., 2013; Zhang et al., 2014a; Zhang et al., 2014b).

functionalization of agarose/cellulose microspheres. These synthetic strategies are based on the activation of the polysaccharide in sodium hydroxide followed by the addition of a compound with a Cl–C bond such as chloroacetic acid or 2-chlorethyl-diethylamine (Boeden et al., 1991; Peška et al., 1976). The hydrophobic group can be there attached via n-alkylamines/carbonyl Schiff base coupling (Boeden et al., 1991).

3.4. IONP/metal hybrid synthesis

There are several approaches for preparing multicomponent nanomaterials containing IONPs and metallic nanoparticles of various arrangements (see Fig. 10), namely, the raspberry like structure, dumbbell like structure or core-shell arrangement. The first and most widely used synthesis involves the heterogeneous nucleation and growth of a metallic component onto seed nanoparticles. The seed nanoparticles are usually magnetite or maghemite cores. They can be pristine (Sa et al., 2014) or surface functionalized by amines (APTES (Liu et al., 2010)), dopamine (Chin et al., 2009), or chitosan (Markova et al., 2012b), carboxylic groups/polyacrylate acid (Prucek et al., 2011), thiol (APTMS (Han et al., 2013; Odio et al., 2014)), or hydroxide groups (TEOS (Choi et al., 2010)). The reduction of metals on a magnetic seed surface is mediated by common reducing agents such as $NaBH_4$ (Tamer et al., 2010), reducing sugars (Iglesias-Silva et al., 2007; Mandal et al., 2005), butylamine (Choi et al., 2010), amine groups on the surface of IONPS in a basic environment (Gawande et al., 2014; Sa et al., 2014) and others. This type of reaction usually results in raspberry like structures of nanocomposites.

The second type of preparation is based on a physico-chemical approach. Gu and colleagues described heterodimeric magnetite–Ag nanoparticles prepared at a liquid–liquid interface of "colloidosomes" provided by ultrasonication (Gu et al., 2005). A dumbbell-like structure is formed due to the limited number of catalytic centers available for the reduction of Ag^+ onto the magnetite surface. The solution-phase route supported by heating to prepare magnetite–Ag colloidal dimer nanoparticles with a dumbbell-like shape was also described by Lopes et al. (2010). Furthermore, sonochemical irradiation of iron(II) acetate solution in the presence of silver nanopowder can result in the deposition of magnetic nanoparticles on metal nanocrystals and the formation of metal@magnetite raspberry like structures, as described by Perkas et al. (2009).

The last category of IONP/metal hybrid synthesis involves non-covalent electrostatic or Van der Waals interactions between separately prepared magnetic and metal nanoparticles. An electrostatic interaction causes the formation of hydrides in syntheses described by Liu et al. (2010) where mixing of aminated magnetic nanoparticles and citrate

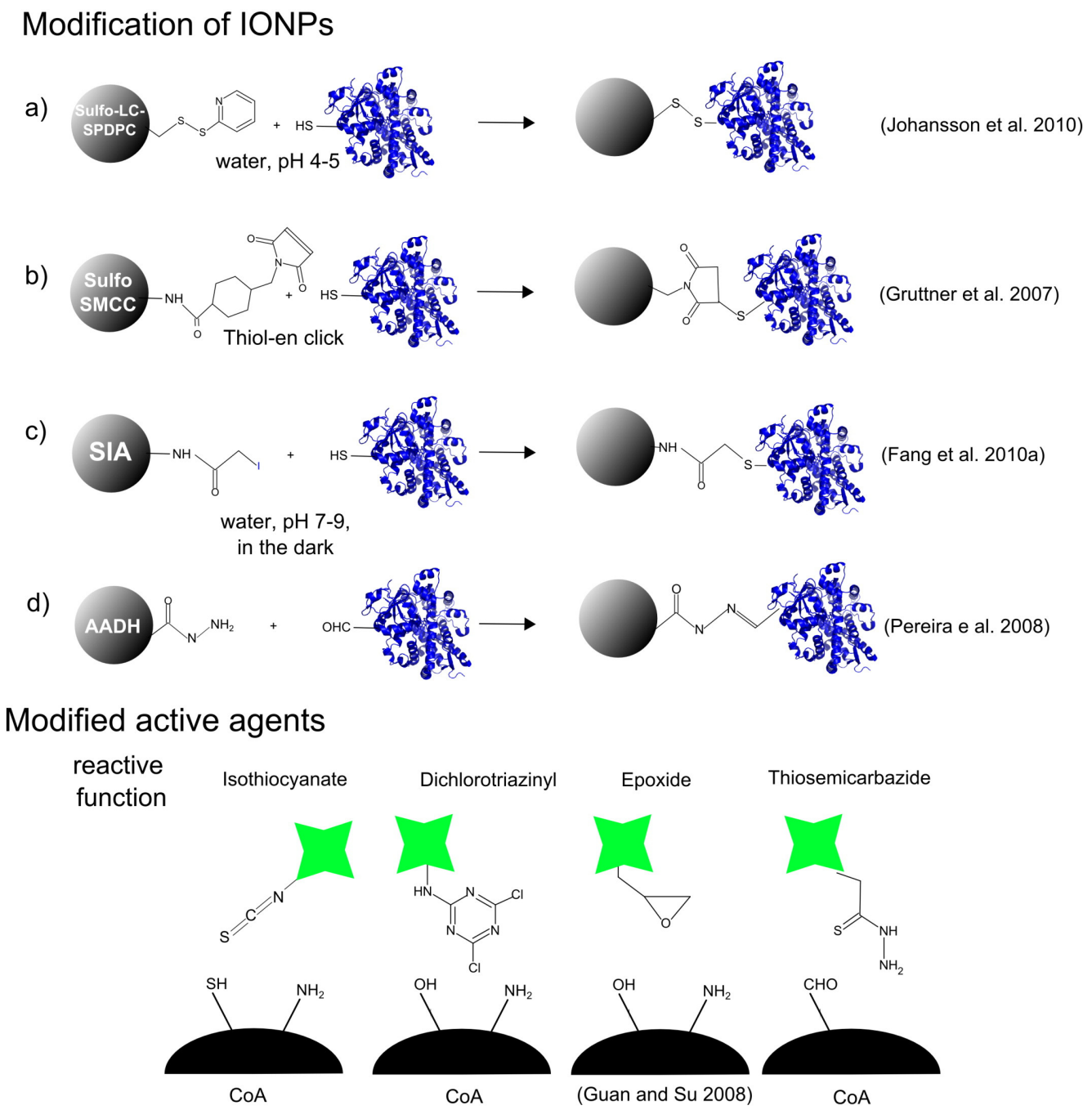


Fig. 8. Coupling strategies for linking IONPs with bioactive substances. Modification of the IONP's surface for immobilization of active compounds (a) via Sulfo-LC-SPDP: sulfosuccinimidyl 6-[3´(2-pyridyldithio)-propionamido] hexanoate, (b) Sulfo-SMCC: sulfosuccinimidyl-4-N-(maleimidomethyl)cyclohexyne-1-carboxylate, (c) SIA: succinimidyl iodoacetate. (d) Hydrazine strategy (AASH: adipic acid dihydrazide) for immobilization of antibodies. All of the reagents are commercially available. Modified active agents: commercially available activated agents (mainly fluorescent dyes); CoA: commercially available. The appropriate details for these coupling strategies can be found in given literature (Fang et al., 2010a; Grüttner et al., 2007; Guan and Su, 2008; Johansson et al., 2010; Pereira and Lai, 2008).

stabilized Ag nanoparticles led to magnetite–Ag submicrospheres. The Van der Waals interactions play a crucial role in impregnating the magnetite surface with Ni and NiPd nanoparticles, as described by Costa et al. (2014) or in the simple adsorption of Au seed on silica coated magnetite nanoparticles prepared in the study by Maciera (Salgueirino-Maceira et al., 2006). However, the covalent interaction can also be used to attach metallic nanoparticles to thiol-capped magnetite nanoparticles as described by Odio (Odio et al., 2014) or Han (Han et al., 2013). The deposited metal seeds on magnetic core can form a template for growing the shell. Salgueirino-Maceira et al. (2006) developed a shell of gold on magnetic silica spheres decorated with Au nanoparticulate seeds in a step-by-step reduction of $HAuCl_4$ aliquots with ascorbic acid. Similarly, a silver shell is formed by the addition of $AgNO_3$ solution instead of gold salt, as described by Chin (Chin et al., 2009) or Liu (Liu et al., 2010).

4. Concluding remarks

Much research has been devoted to the surface modification of magnetic IONPs. The biocompatibility, biodegradability, colloidal

Please cite this article as: Hola K, et al, Tailored functionalization of iron oxide nanoparticles for MRI, drug delivery, magnetic separation and immobilization of biosubsta..., Biotechnol Adv (2015), http://dx.doi.org/10.1016/j.biotechadv.2015.02.003

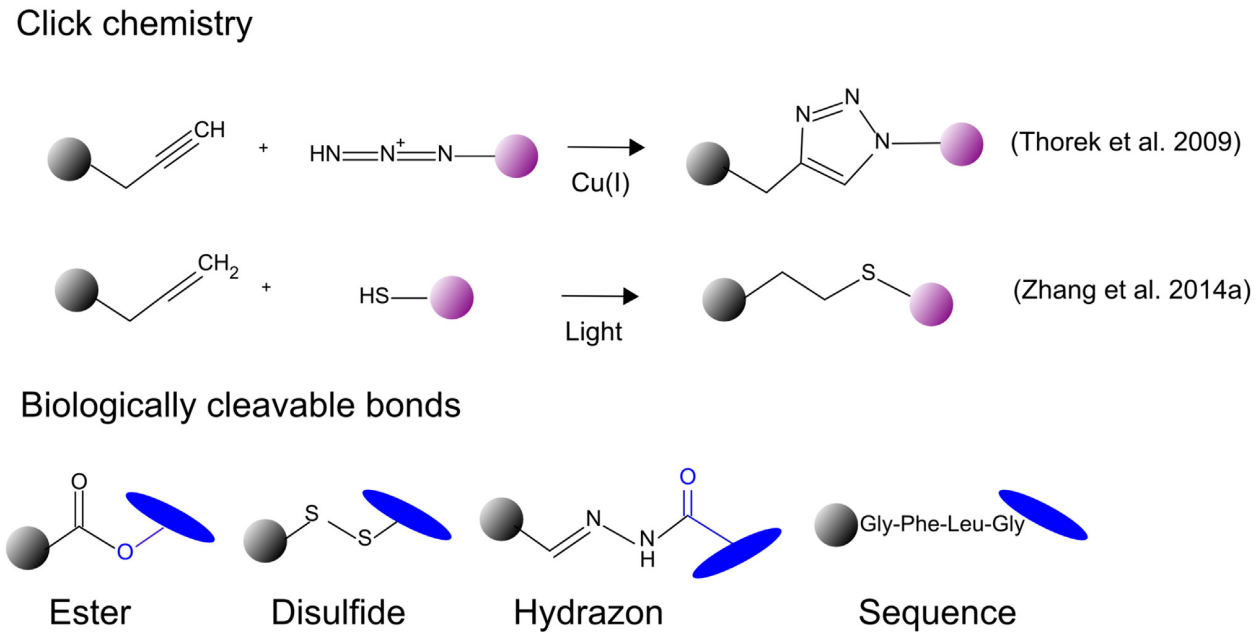


Fig. 9. Click chemistry linking approaches and biodegradable bonds for drug delivery. The appropriate details for these click chemistry coupling strategies can be found in given literature (Thorek et al., 2009; Zhang et al., 2014a).

stability, magnetic separability, nanometer scale and contrast enhancing in MRI make IONPs one of the most promising tools in various fields of biomedicine and biotechnology. In this short critical review, we summarize and critically discuss the principles, functionalization procedures, and conjugation strategies for applications of IONPs in magnetic resonance imaging, drug delivery, magnetic separation, and immobilization of various biosubstances (e.g., proteins, enzymes, drugs, antibodies). This review demonstrates that despite many similarities, each nanosystem application requires specific core-shell properties, and as a result, tailored functionalization and conjugation procedures. Because of this, a challenge in this field is to develop universal systems and functionalization procedures that allow simultaneous diagnostic (MRI) and therapeutic (drug delivery, hyperthermia) applications of IONPs. In addition to these so called theranostic agents,

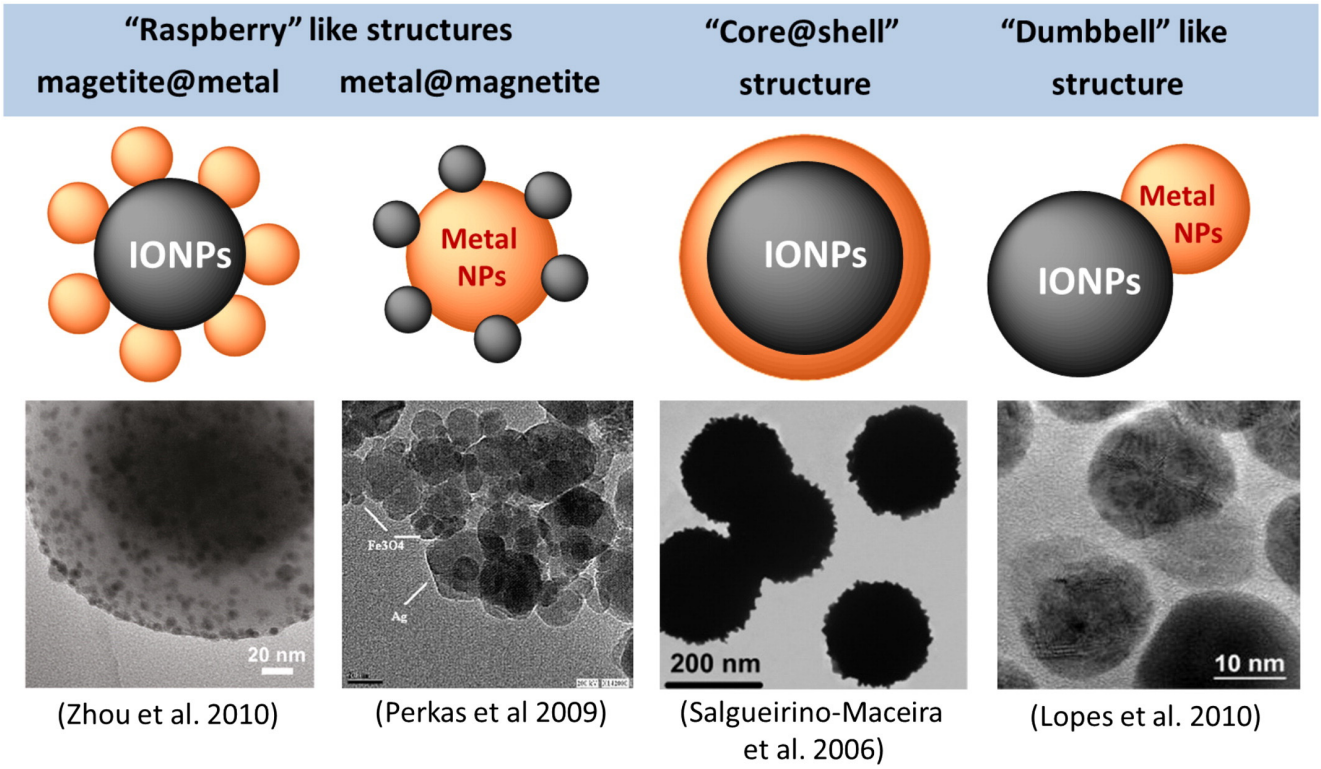


Fig. 10. Schematic illustration of IONPs/metal NP (nanoparticle) assemblies.
Reprinted with permissions from Lopes et al. (2010), Perkas et al. (2009), Salgueirino-Maceira et al. (2006), and Zhou et al. (2010).

Please cite this article as: Hola K, et al, Tailored functionalization of iron oxide nanoparticles for MRI, drug delivery, magnetic separation and immobilization of biosubsta..., Biotechnol Adv (2015), http://dx.doi.org/10.1016/j.biotechadv.2015.02.003

multicomponent hybrids combining the properties of magnetic IONPs and metallic nanoparticles represent another type of biomaterial with a huge potential in biocatalysis, biosensing, analytical chemistry, bioimaging, and environmental and antibacterial technologies.

In the field of biomedical application of IONPs, huge progress has been made so far. We now understand the in vivo toxicity of the particles, their bioprocesses, how to avoid opsonization and RES-uptake and how to target the particles to desired places by surface functionalization. However, to fully harness the potential of IONPs for targeted healthcare, the pharmacokinetics of drug release from the particles must be explored for specific diseases. The combination of targeted delivery, controlled drug release/therapy and parallel MRI imaging makes IONPs an excellent platform for personalized medicine. Challenges are also found in the areas of magnetic separations or enzyme immobilization. Much attention is focused on upscaling systems in an economically viable manner. Research is also focused on the new and emerging applications of magnetic/metallic hybrid nanostructures, for example, in heterogeneous catalysis or in new technologies for early detection of disease based on surface-enhanced Raman spectroscopy. These highly sophisticated nanosystems and their applications can expect enormous development in the future.

Acknowledgments

The authors gratefully acknowledge the support by the project LO1305 of the Ministry of Education, Youth and Sports of the Czech Republic and the Operational Program “Education for Competitiveness — European Social Fund” CZ.1.07/2.3.00/20.0155 and CZ.1.05/3.1.00/14.0302 of the Ministry of Education, Youth and Sports of the Czech Republic. The Student Project IGA_PrF_2014023 of Palacký University is also gratefully acknowledged.

References

Aksoy S, Tumturk H, Hasirci N. Stability of alpha-amylase immobilized on poly(methyl methacrylate-acrylic acid) microspheres. J Biotechnol 1998;60:37–46.
Ambashta RD, Sillanpää M. Water purification using magnetic assistance: a review. J Hazard Mater 2010;180:38–49.
Ansari SA, Husain Q. Potential applications of enzymes immobilized on/in nano materials: a review. Biotechnol Adv 2012;30:512–23.
Arndt D, Zielasek V, Dreher W, Bäumer M. Ethylene diamine-assisted synthesis of iron oxide nanoparticles in high-boiling polyolys. J Colloid Interface Sci 2014;417:188–98.
Arunachalam B, Phan UT, Geuze HJ, Cresswell P. Enzymatic reduction of disulfide bonds in lysosomes: characterization of a gamma-interferon-inducible lysosomal thiol reductase (GILT). Proc Natl Acad Sci U S A 2000;97:745–50.
Babic M, Horák D, Trchová M, Jendelová P, Glogarová K, Lesný P, et al. Poly(L-lysine)-modified iron oxide nanoparticles for stem cell labeling. Bioconjug Chem 2008;19:740–50.
Baig RBN, Varma RS. Magnetic carbon-supported palladium nanoparticles: an efficient and sustainable catalyst for hydrogenation reactions. ACS Sustainable Chem Eng 2014;2:2155–8.
Bakandritsos A, Mattheolabakis G, Zboril R, Bouropoulos N, Tucek J, Fatouros DG, et al. Preparation, stability and cytocompatibility of magnetic/PLA-PEG hybrids. Nanoscale 2010;2:564–72.
Bakandritsos A, Papagiannopoulos A, Anagnostou EN, Avgoustakis K, Zboril R, Pispas S, et al. Merging high doxorubicin loading with pronounced magnetic response and bio-repellent properties in hybrid drug nanocarriers. Small 2012;8:2381–93.
Banerjee SS, Chen D-H. Multifunctional pH-sensitive magnetic nanoparticles for simultaneous imaging, sensing and targeted intracellular anticancer drug delivery. Nanotechnology 2008;19:505104.
Banerjee T, Mitra S, Kumar Singh A, Kumar Sharma R, Maitra A. Preparation, characterization and biodistribution of ultrafine chitosan nanoparticles. Int J Pharm 2002;243:93–105.
Bao F, Yao J-L, Gu R-A. Synthesis of magnetic Fe_2O_3/Au core/shell nanoparticles for bioseparation and immunoassay based on surface-enhanced Raman spectroscopy. Langmuir 2009;25:10782–7.
Bar-Shir A, Avram L, Yariv-Shoushan S, Anaby D, Cohen S, Segev-Amzaleg N, et al. Alginate-coated magnetic nanoparticles for noninvasive MRI of extracellular calcium. NMR Biomed 2014;27:774–83.
Biju V. Chemical modifications and bioconjugate reactions of nanomaterials for sensing, imaging, drug delivery and therapy. Chem Soc Rev 2014;43:744–64.
Blakemore R. Magnetotactic bacteria. Science 1975;190:377–9.
Boeden HF, Pommerening K, Becker M, Rupprich C, Holtzhauer M, Loth F, et al. Bead cellulose derivatives as supports for immobilization and chromatographic purification of proteins. J Chromatogr 1991;552:389–414.
Borlido L, Azevedo AM, Roque ACA, Aires-Barros MR. Potential of boronic acid functionalized magnetic particles in the adsorption of human antibodies under mammalian cell culture conditions. J Chromatogr A 2011;1218:7821–7.
Borlido L, Azevedo AM, Roque ACA, Aires-Barros MR. Magnetic separations in biotechnology. Biotechnol Adv 2013;31:1374–85.
Chapman S, Dobrovolskaia M, Farahani K, Goodwin A, Joshi A, Lee H, et al. Nanoparticles for cancer imaging: the good, the bad, and the promise. Nano Today 2013;8:454–60.
Chertok B, Moffat BA, David AE, Yu F, Bergemann C, Ross BD, et al. Iron oxide nanoparticles as a drug delivery vehicle for MRI monitored magnetic targeting of brain tumors. Biomaterials 2008;29:487–96.
Chin SF, Iyer KS, Raston CL. Facile and green approach to fabricate gold and silver coated superparamagnetic nanoparticles. Cryst Growth Des 2009;9:2685–9.
Choi HS, Liu W, Misra P, Tanaka E, Zimmer JP, Itty Ipe B, et al. Renal clearance of quantum dots. Nat Biotechnol 2007;25:1165–70.
Choi J-Y, Kim K, Shin KS. Surface-enhanced Raman scattering inducible by recyclable Ag-coated magnetic particles. Vib Spectrosc 2010;53:117–20.
Chudasama B, Vala AK, Andhariya N, Upadhyay RV, Mehta RV. Antifungal activity of multifunctional Fe_3O_4–Ag nanocolloids. J Magn Magn Mater 2011;323:1233–7.
Chung HJ, Lee H, Bae KH, Lee Y, Park J, Cho S-W, et al. Facile synthetic route for surface-functionalized magnetic magnetic resonance imaging studies. ACS Nano 2011;5:4329–36.
Cole AJ, David AE, Wang J, Galbán CJ, Yang VC. Magnetic brain tumor targeting and biodistribution of long-circulating PEG-modified, cross-linked starch-coated iron oxide nanoparticles. Biomaterials 2011;32:6291–301.
Cornell RM, Schwertmann U. The Iron Oxides: Structure, Properties, Reactions, Occurrence and Uses. Weinheim, Germany: Wiley-VCH Publishers; 2003.
Costa NJS, Guerrero M, Collie V, Teixeira-Neto E, Landers R, Philippot K, et al. Organometallic preparation of Ni, Pd, and NiPd nanoparticles for the design of supported nanocatalysts. ACS Catal 2014;4:1735–42.
Deatsch AE, Evans BA. Heating efficiency in magnetic nanoparticle hyperthermia. J Magn Magn Mater 2014;354:163–72.
Deka SR, Quarta A, Di Corato R, Riedinger A, Cingolani R, Pellegrino T. Magnetic nanobeads decorated by thermo-responsive PNIPAM shell as medical platforms for the efficient delivery of doxorubicin to tumour cells. Nanoscale 2011;3:619–29.
Dobrovolskaia M a, McNeil SE. Immunological properties of engineered nanomaterials. Nat Nanotechnol 2007;2:469–78.
Duan H, Kuang M, Wang X, Wang YA, Mao H, Nie S. Reexamining the effects of particle size and surface chemistry on the magnetic properties of iron oxide nanocrystals: new insights into spin disorder and proton relaxivity. J Phys Chem C 2008;112:8127–31.
Elsabahy M, Wooley KL. Design of polymeric nanoparticles for biomedical delivery applications. Chem Soc Rev 2012;41:2545–61.
Fang C, Bhattarai N, Sun C, Zhang M. Functionalized nanoparticles with long-term stability in biological media. Small 2009;5:1637–41.
Fang C, Veiseh O, Kievit F, Bhattarai N, Wang F, Stephen Z, et al. Functionalization of iron oxide magnetic nanoparticles with targeting ligands: their physicochemical properties and in vivo behavior. Nanomedicine 2010a;5:1357–69.
Fang W, Chen X, Zheng N. Superparamagnetic core-shell polymer particles for efficient purification of his-tagged proteins. J Mater Chem 2010b;20:8624–30.
Franzreb M, Siemann-Herzberg M, Hobley TJ, Thomas ORT. Protein purification using magnetic adsorbent particles. Appl Microbiol Biotechnol 2006;70:505–16.
Gautier J, Allard-Vannier E, Hervé-Aubert K, Soucé M, Chourpa I. Design strategies of hybrid metallic nanoparticles for theragnostic applications. Nanotechnology 2013;24:432002.
Gawande MB, Branco PS, Varma RS. Nano-magnetite (Fe_3O_4) as a support for recyclable catalysts in the development of sustainable methodologies. Chem Soc Rev 2013;42:3371–93.
Gawande MB, Rathi AK, Tucek J, Safarova K, Bundaleski N, Teodoro OMND, et al. Magnetic gold nanocatalyst (nanocat-Fe–Au): catalytic applications for the oxidative esterification and hydrogen transfer reactions. Green Chem 2014;16:4137–43.
Gnant MF, Turner EM, Alexander HR. Effects of hyperthermia and tumour necrosis factor on inflammatory cytokine secretion and procoagulant activity in endothelial cells. Cytokine 2000;12:339–47.
Grüttner C, Müller K, Teller J, Westphal F, Foreman A, Ivkov R. Synthesis and antibody conjugation of magnetic nanoparticles with improved specific power absorption rates for alternating magnetic field cancer therapy. J Magn Magn Mater 2007;311:181–6.
Gu H, Yang Z, Gao J, Chang CK, Xu B. Heterodimers of nanoparticles: formation at a liquid–liquid interface and particle-specific surface modification by functional molecules. J Am Chem Soc 2005;127:34–5.
Guan X, Su Z. Synthesis and characterization of fluorescent starch using fluorescein as fluorophore: potential polymeric temperature/pH indicators. Polym Adv Technol 2008;19:385–92.
Guardia P, Di Corato R, Lartigue L, Wilhelm C, Espinosa A, Garcia-Hernandez M, et al. Water-soluble iron oxide nanocubes with high values of specific absorption rate for cancer cell hyperthermia treatment. ACS Nano 2012;6:3080–91.
Gupta AK, Gupta M. Cytotoxicity suppression and cellular uptake enhancement of surface modified magnetic nanoparticles. Biomaterials 2005a;26:1565–73.
Gupta AK, Gupta M. Synthesis and surface engineering of iron oxide nanoparticles for biomedical applications. Biomaterials 2005b;26:3995–4021.
Han XX, Schmidt AM, Marten G, Fischer A, Weidinger IM, Hildebrandt P. Magnetic silver hybrid nanoparticles for surface-enhanced resonance Raman spectroscopic detection and decontamination of small toxic molecules. ACS Nano 2013;7:3212–20.
Hanessian S, Grzyb JA, Cengelli F, Juillerat-Jeanneret L. Synthesis of chemically functionalized superparamagnetic nanoparticles as delivery vectors for chemotherapeutic drugs. Bioorg Med Chem 2008;16:2921–31.

Please cite this article as: Hola K, et al, Tailored functionalization of iron oxide nanoparticles for MRI, drug delivery, magnetic separation and immobilization of biosubsta..., Biotechnol Adv (2015), http://dx.doi.org/10.1016/j.biotechadv.2015.02.003

Heebøll-Nielsen A, Dalkiaer M, Hubbuch JJ, Thomas ORT. Superparamagnetic adsorbents for high-gradient magnetic fishing of lectins out of legume extracts. Biotechnol Bioeng 2004;87:311–23.
Hildebrand H, Mackenzie K, Kopinke F-D. Highly active Pd-on-magnetite nanocatalysts for aqueous phase hydrodechlorination reactions. Environ Sci Technol 2009;43:3254–9.
Hong X, Guo W, Yuan H, Li J, Liu Y, Ma L, et al. Periodate oxidation of nanoscaled magnetic dextran composites. J Magn Magn Mater 2004;269:95–100.
Hong RY, Feng B, Chen LL, Liu GH, Li HZ, Zheng Y, et al. Synthesis, characterization and MRI application of dextran-coated Fe_3O_4 magnetic nanoparticles. Biochem Eng J 2008;42:290–300.
Hu J, Chen G, Lo IMC. Removal and recovery of Cr(VI) from wastewater by maghemite nanoparticles. Water Res 2005;39:4528–36.
Hu F, Macrenaris KW, Waters EA, Schultz-Sikma EA, Eckermann AL, Meade TJ. Highly dispersible, superparamagnetic magnetite nanoflowers for magnetic resonance imaging. Chem Commun 2010;46:73–5.
Hua M, Zhang S, Pan B, Zhang W, Lv L, Zhang Q. Heavy metal removal from water/wastewater by nanosized metal oxides: a review. J Hazard Mater 2012;211–212:317–31.
Iglesias-Silva E, Rivas J, León Isidro LM, López-Quintela MA. Synthesis of silver-coated magnetite nanoparticles. J Non Cryst Solids 2007;353:829–31.
Jain TK, Reddy MK, Morales MA, Leslie-Pelecky DL, Labhasetwar V. Biodistribution, clearance, and biocompatibility of iron oxide magnetic nanoparticles in rats. Mol Pharm 2008;5:316–27.
Jain TK, Foy SP, Erokwu B, Dimitrijevic S, Flask CA, Labhasetwar V. Magnetic resonance imaging of multifunctional pluronic stabilized iron-oxide nanoparticles in tumor-bearing mice. Biomaterials 2009;30:6748–56.
Jaiswal MK, Gogoi M, Dev Sarma H, Banerjee R, Bahadur D. Biocompatibility, biodistribution and efficacy of magnetic nanohydrogels in inhibiting growth of tumors in experimental mice models. Biomater Sci 2014;2:370–80.
Johansson L, Gunnarsson K, Bijelovic S, Eriksson K, Surpi A, Göthelid E, et al. A magnetic microchip for controlled transport of attomole levels of proteins. Lab Chip 2010;10:654–61.
Jordan J, Kumar CSSR, Theegala C. Preparation and characterization of cellulase-bound magnetite nanoparticles. J Mol Catal B: Enzym 2011;68:139–46.
Khoshnevisan K, Bordbar A-K, Zare D, Davoodi D, Noruzi M, Barkhi M, et al. Immobilization of cellulase enzyme on superparamagnetic nanoparticles and determination of its activity and stability. Chem Eng J 2011;171:669–73.
Kilianova M, Prucek R, Filip J, Kolarik J, Kvitek L, Pnacek A, et al. Remarkable efficiency of ultrafine superparamagnetic iron(III) oxide nanoparticles toward arsenate removal from aqueous environment. Chemosphere 2013;93:2690–7.
Kim J, Lee JE, Lee SH, Yu JH, Lee JH, Park TG, et al. Designed fabrication of a multifunctional polymer nanomedical platform for simultaneous cancer-targeted imaging and magnetically guided drug delivery. Adv Mater 2008;20:478–83.
Kluchova K, Zboril R, Tucek J, Pecova M, Zajoncova L, Safarik I, et al. Superparamagnetic maghemite nanoparticles from solid-state synthesis — their functionalization towards peroral MRI contrast agent and magnetic carrier for trypsin immobilization. Biomaterials 2009;30:2855–63.
Kopecek J, Kopeckova P. Drug delivery in oncology, from basic research to cancer therapy, 17. Design of Polymer–Drug Conjugates. Wiley-VCH Verlag GmbH & Co. KGaA; 2011. p. 483–512.
Krizova J, Spanova A, Rittich B, Horak D. Magnetic hydrophilic methacrylate-based polymer microspheres for genomic DNA isolation. J Chromatogr A 2005;1064:247–53.
Kumar CSSR, Mohammad F. Magnetic nanomaterials for hyperthermia-based therapy and controlled drug delivery. Adv Drug Deliv Rev 2011;63:789–808.
LaConte LEW, Nitin N, Zurkiya O, Caruntu D, O'Connor CJ, Hu X, et al. Coating thickness of magnetic iron oxide nanoparticles affects R_2 relaxivity. J Magn Reson Imaging 2007;26:1634–41.
Lartigue L, Hugounenq P, Alloyeau D, Clarke SP, Lévy M, Bacri J-C, et al. Cooperative organization in iron oxide multi-core nanoparticles potentiates their efficiency as heating mediators and MRI contrast agents. ACS Nano 2012;6:10935–49.
Lartigue L, Alloyeau D, Kolosnjaj-Tabi J, Javed Y, Guardia P, Riedinger A, et al. Biodegradation of iron oxide nanocubes: high-resolution in situ monitoring. ACS Nano 2013;7:3939–52.
Laurent S, Forge D, Port M, Roch A, Robic C, Vander Elst L, et al. Magnetic iron oxide nanoparticles: synthesis, stabilization, vectorization, physicochemical characterizations, and biological applications. Chem Rev 2008;108:2064–110.
Lee Y, Rho J, Jung B. Preparation of magnetic ion-exchange resins by the suspension polymerization of styrene with magnetite. J Appl Polym Sci 2003;89:2058–67.
Lee HS, Hee Kim E, Shao H, Kook Kwak B. Synthesis of SPIO-chitosan microspheres for MRI-detectable embolotherapy. J Magn Magn Mater 2005;293:102–5.
Lee MJ-E, Veiseh O, Bhattarai N, Sun C, Hansen SJ, Ditzler S, et al. Rapid pharmacokinetic and biodistribution studies using cholorotoxin-conjugated iron oxide nanoparticles: a novel non-radioactive method. PLoS One 2010;5:e9536.
Lee N, Kim H, Hong S, Park M, Kim D, Kim H. Magnetosome-like ferrimagnetic iron oxide nanocubes for highly sensitive MRI of single cells and transplanted pancreatic islets. Proc Natl Acad Sci U S A 2011;108:2662–7.
Lewinski N, Colvin V, Drezek R. Cytotoxicity of nanoparticles. Small 2008;4:26–49.
Li D, Teoh WY, Gooding JJ, Selomulya C, Amal R. functionalization strategies for protease immobilization on magnetic nanoparticles. Adv Funct Mater 2010;20:1767–77.
Li Z, Ma Y, Qi L. Controlled synthesis of $Mn_xFe_{1-x}O$ concave nanocubes and highly branched cubic mesocrystals. CrystEngComm 2014;16:600.
Lim E-K, Huh Y-M, Yang J, Lee K, Suh J-S, Haam S. pH-triggered drug-releasing magnetic nanoparticles for cancer therapy guided by molecular imaging by MRI. Adv Mater 2011;23:2436–42.
Lin S, Yun D, Qi D, Deng C, Li Y, Zhang X. Novel microwave-assisted digestion by trypsin-immobilized magnetic nanoparticles for proteomic analysis technical notes. J Proteome Res 2008;7:1297–307.
Liu Z, Chen K, Davis C, Sherlock S, Cao Q, Chen X, et al. Drug delivery with carbon nanotubes for in vivo cancer treatment. Cancer Res 2008;68:6652–60.
Liu X, Hu Q, Fang Z, Zhang X, Zhang B. Magnetic chitosan nanocomposites: a useful recyclable tool for heavy metal ion removal. Langmuir 2009;2:3–8.
Liu Z, Zhao B, Shi Y, Guo C, Yang H, Li Z. Novel nonenzymatic hydrogen peroxide sensor based on iron oxide-silver hybrid submicrospheres. Talanta 2010;81:1650–4.
Liu J, Yu M, Zhou C, Zheng J. Renal clearable inorganic nanoparticles: a new frontier of bionanotechnology. Mater Today 2013;16:477–86.
Longmire M, Choyke PL, Kobayashi H. Clearance properties of nano-sized particles and molecules as imaging agents: consideration and caveats, 3; 2012. p. 703–17.
Lopes G, Vargas M, Sharma SK, Be F, Pirota KR, Knobel M, et al. Ag–Fe_3O_4 dimer colloidal nanoparticles: synthesis and enhancement of magnetic properties. J Phys Chem C 2010;114:10148–52.
Luo X, Liu S, Zhou J, Zhang L. In situ synthesis of Fe_3O_4/cellulose microspheres with magnetic-induced protein delivery. J Mater Chem 2009;19:3538–45.
Machala L, Zboril R, Gedanken A. Amourphous iron(III) oxide — a review. J Phys Chem B 2007;111:4003–18.
Machala L, Tucek J, Zboril R. Polymorphous transformations of nanometric iron(III) oxide: a review. Chem Mater 2011;23:3255–72.
Magro M, Campos R, Baratella D, Lima G, Holà K, Divoky C, et al. A magnetically drivable nanovehicle for curcumin with antioxidant capacity and MRI relaxation properties. Chem Eur J 2014;20:11913–20.
Mahmoudi M, Simchi A, Imani M, Milani AS, Stroeve P. Optimal design and characterization of superparamagnetic iron oxide nanoparticles coated with polyvinyl alcohol for targeted delivery and imaging. J Phys Chem B 2008;112:14470–81.
Maity D, Zoppellaro G, Sedenkova V, Tucek J, Safarova K, Polakova K, et al. Surface design of core-shell superparamagnetic iron oxide nanoparticles drives record relaxivity values in functional MRI contrast agents. Chem Commun 2012;48:11398–400.
Mandal M, Kundu S, Ghosh SK, Panigrahi S, Sau TK, Yusuf SM, et al. Magnetite nanoparticles with tunable gold or silver shell. J Colloid Interface Sci 2005;286:187–94.
Markova Z, Bourlinos AB, Safarova K, Polakova K, Tucek J, Medrik I, et al. Synthesis and properties of core–shell fluorescent hybrids with distinct morphologies based on carbon dots. J Mater Chem 2012a;22:16219–23.
Markova Z, Siskova K, Filip J, Safarova K, Prucek R, Panacek A, et al. Chitosan-based synthesis of magnetically-driven nanocomposites with biogenic magnetite core, controlled silver size, and high antimicrobial activity. Green Chem 2012b;14:2550–8.
Massart R. Preparation of aqueous magnetic liquids in alkaline and acidic media. IEEE Trans Magn 1981;17:1247–8.
Maurizi L, Bisht H, Bouyer F, Millot N. Easy route to functionalize iron oxide nanoparticles via long-term stable thiol groups. Langmuir 2009;25:8857–9.
McCarthy JR, Weissleder R. Multifunctional magnetic nanoparticles for targeted imaging and therapy. Adv Drug Deliv Rev 2008;60:1241–51.
Müller-Schulte D, Brunner H. Novel magnetic microspheres on the basis of poly(vinyl alcohol) as affinity medium for quantitative detection of glycated haemoglobin. J Chromatogr A 1995;711:53–60.
Nandivada H, Jiang X, Lahann J. Click chemistry: versatility and control in the hands of materials scientists. Adv Mater 2007;19:2197–208.
Nangmenyi G, Li X, Mehrabi S, Mintz E, Economy J. Silver-modified iron oxide nanoparticle impregnated fiberglass for disinfection of bacteria and viruses in water. Mater Lett 2011;65:1191–3.
Narayanan S, Sathy BN, Mony U, Koyakutty M, Nair SV, Menon D. Biocompatible magnetite/gold nanohybrid contrast agents via green chemistry for MRI and CT bioimaging. ACS Appl Mater Interfaces 2012;4:251–60.
Nie S. Understanding and overcoming major barriers in cancer nanomedicine. Nanomedicine 2010;5:523–8.
Odio OF, Mart R, Reguera E. Sorption of gold by naked and thiol-capped magnetite nanoparticles: an XPS approach. J Phys Chem C 2014;118:2776–91.
Pankhurst QA, Connolly J, Jones SK, Dobson J. Applications of magnetic nanoparticles in biomedicine. J Phys D Appl Phys 2003;36:R167–81.
Park J, Lee E, Hwang N-M, Kang M, Kim SC, Hwang Y, et al. One-nanometer-scale size-controlled synthesis of monodisperse magnetic iron oxide nanoparticles. Angew Chem 2005;117:2932–7.
Pecova M, Sebela M, Markova Z, Polakova K, Cuda J, Safarova K, et al. Thermostable trypsin conjugates immobilized to biogenic magnetite show a high operational stability and remarkable reusability for protein digestion. Nanotechnology 2013;24:125102.
Pereira M, Lai EP. Capillary electrophoresis for the characterization of quantum dots after non-selective or selective bioconjugation with antibodies for immunoassay. J Nanobiotechnol 2008;6:10.
Perkas N, Amirian G, Rottman C, de la Vega F, Gedanken A. Sonochemical deposition of magnetite on silver nanocrystals. Ultrason Sonochem 2009;16:132–5.
Peška J, Štamberg J, Hradil J. Chemical transfomation of polymers, XIX. Ion exchange derivatives of bead cellulose. Angew Macromol Chem 1976;53:73–80.
Polito L, Monti D, Caneva E, Delnevo E, Russo G, Prosperi D. One-step bioengineering of magnetic nanoparticles via a surface diazo transfer/azide-alkyne click reaction sequence. Chem Commun 2008;5:621–3.
Ponta A, Bae Y. Tumor-preferential sustained drug release enhances antitumor activity of block copolymer micelles. J Drug Target 2014;22:619–28.
Pothayee N, Balasubramaniam S, Pothayee N, Jain N, Hu N, Lin Y, et al. Magnetic nanoclusters with hydrophilic spacing for dual drug delivery and sensitive magnetic resonance imaging. J Mater Chem B 2013;1:1142.

Please cite this article as: Hola K, et al, Tailored functionalization of iron oxide nanoparticles for MRI, drug delivery, magnetic separation and immobilization of biosubsta..., Biotechnol Adv (2015), http://dx.doi.org/10.1016/j.biotechadv.2015.02.003

Prucek R, Kvítek L, Filip J, Kolar M, Zboril R. The targeted antibacterial and antifungal properties of magnetic nanocomposite of iron oxide and silver nanoparticles. Biomaterials 2011;32:4704–13.
Qiao R, Yang C, Gao M. Superparamagnetic iron oxide nanoparticles: from preparations to in vivo MRI applications. J Mater Chem 2009;19:6274.
Ranc V, Markova Z, Hajduch M, Prucek R, Kvitek L, Kaslik J, et al. Magnetically assisted surface-enhanced Raman scattering selective determination of dopamine in an artificial cerebrospinal fluid and a mouse striatum using Fe_3O_4/Ag nanocomposite. Anal Chem 2014;86:2939–46.
Roser M, Fischer D, Kissel T. Surface-modified biodegradable albumin nano- and microspheres. II: effect of surface charges on in vitro phagocytosis and biodistribution in rats. Eur J Pharm Biopharm 1998;46:255–63.
Sa S, Gawande MB, Velhinho A, Veiga JP, Bundaleski N, Trigueiro J, et al. Magnetically recyclable magnetite–palladium (Nanocat-Fe–Pd) nanocatalyst for the Buchwald–Hartwig reaction. Green Chem 2014;16:3494.
Safarik I, Safarikova M. Magnetic techniques for the isolation and purification of proteins and peptides. BioMagn Res Technol 2004;2:7.
Safarik I, Sabatkova Z, Tokar O, Safarikova M. Magnetic cation exchange isolation of lysozyme from native hen egg white. Food Technol Biotechnol 2007;45:355–9.
Salgueirino-Maceira V, Correa-Duarte MA, Farle M, Lopez-Quintela A, Sieradzki K, Diaz R. Bifunctional gold-coated magnetic silica spheres. Chem Mater 2006;18:2701–6.
Schweiger C, Pietzonka C, Heverhagen J, Kissel T. Novel magnetic iron oxide nanoparticles coated with poly(ethylene imine)-g-poly(ethylene glycol) for potential biomedical application: synthesis, stability, cytotoxicity and MR imaging. Int J Pharm 2011;408:130–7.
Sivakumar B, Aswathy RG, Nagaoka Y, Suzuki M, Fukuda T, Yoshida Y, et al. Multifunctional carboxymethyl cellulose-based magnetic nanovector as a theragnostic system for folate receptor targeted chemotherapy, imaging, and hyperthermia against cancer. Langmuir 2013;29:3453–66.
Sun EY, Josephson L, Weissleder R. "Clickable" nanoparticles for targeted imaging. Mol Imaging 2006;5:122–8.
Sun C, Lee JSH, Zhang M. Magnetic nanoparticles in MR imaging and drug delivery. Adv Drug Deliv Rev 2008;60:1252–65.
Tai L-A, Tsai P-J, Wang Y-C, Wang Y-J, Lo L-W, Yang C-S. Thermosensitive liposomes entrapping iron oxide nanoparticles for controllable drug release. Nanotechnology 2009;20:135101.
Talbert JN, Goddard JM. Characterization of lactase-conjugated magnetic nanoparticles. Process Biochem 2013;48:656–62.
Tamer U, Gündoğdu Y, Boyacı İH, Pekmez K. Synthesis of magnetic core–shell Fe_3O_4–Au nanoparticle for biomolecule immobilization and detection. J Nanoparticle Res 2010;12:1187–96.
Tanaka T, Shiramoto S, Miyashita M, Fujishima Y, Kaneo Y. Tumor targeting based on the effect of enhanced permeability and retention (EPR) and the mechanism of receptor-mediated endocytosis (RME). Int J Pharm 2004;277:39–61.
Thorek DLJ, Elias DR, Tsourkas A. Comparative analysis of nanoparticle-antibody conjugations: carbodiimide versus click chemistry. Mol Imaging 2009;8:221–9.
Tucek J, Zboril R, Petridis D. Maghemite nanoparticles by view of Mossbauer spectroscopy. J Nanosci Nanotechnol 2006;6:926–47.
Tucek J, Zboril R, Namai A, Ohkoshi S. ε-Fe_2O_3: an advanced nanomaterial exhibiting giant coercive field, millimeter-wave ferromagnetic resonance, and magnetoelectric coupling. Chem Mater 2010;22:6483–505.
Tucek J, Kemp KC, Kim KS, Zboril R. Iron-oxide-supported nanocarbon in lithium-ion batteries, medical, catalytic, and environmental applications. ACS Nano 2014;8:7571–612.
Tudisco C, Bertani F, Cambria MT, Sinatra F, Fantechi E, Innocenti C, et al. Functionalization of PEGylated Fe_3O_4 magnetic nanoparticles with tetraphosphonate cavitand for biomedical application. Nanoscale 2013;5:11438–46.
Veiseh O, Sun C, Fang C, Bhattarai N, Gunn J, Kievit F, et al. Specific targeting of brain tumors with an optical/magnetic resonance imaging nanoprobe across the blood–brain barrier. Cancer Res 2009;69:6200–7.
Veiseh O, Gunn JW, Zhang M. Design and fabrication of magnetic nanoparticles for targeted drug delivery and imaging. Adv Drug Deliv Rev 2010;62:284–304.
Wang YX, Hussain SM, Krestin GP. Superparamagnetic iron oxide contrast agents: physicochemical characteristics and applications in MR imaging. Eur Radiol 2001;11:2319–31.
Wang G, Zhang X, Skallberg A, Liu Y, Hu Z, Mei X, et al. One-step synthesis of water-dispersible ultra-small Fe_3O_4 nanoparticles as contrast agents for T1 and T2 magnetic resonance imaging. Nanoscale 2014;6:2953–63.
Weissleder R, Stark DD, Wittenberg J, Ferrucci T. Ferrite-enhanced MR imaging of hepatic lymphoma: an experimental study in rats. Am J Roentgenol 1987;149:1161–5.
Weissleder R, Hahn PF, Stark DD, Elizondo G, Saini S, Todd LE, et al. Superparamagnetic iron oxide: enhanced detection of focal splenic tumors with MR imaging. Radiology 1988;169:399–403.
Weissleder R, Stark DD, Engelstad BL, Bacon BA, Compton CC, White DL, et al. Superparamagnetic iron oxide: pharmacokinetics and toxicity. Am J Roentgenol 1989;152:167–73.
Wiogo HTR, Lim M, Bulmus V, Gutiérrez L, Woodward RC, Amal R. Insight into serum protein interactions with functionalized magnetic nanoparticles in biological media. Langmuir 2012;28:4346–56.
Wu S, Kaiser J, Guo X, Li L, Lu Y, Ballauff M. Recoverable platinum nanocatalysts immobilized on magnetic spherical polyelectrolyte brushes. Ind Eng Chem Res 2012;51:5608–14.
Xiao Z, Xia Y, Ren Z, Liu Z, Xu G, Chao C, et al. Facile synthesis of single-crystalline mesoporous α-Fe_2O_3 and Fe_3O_4 nanorods as anode materials for lithium-ion batteries. J Mater Chem 2012;22:20566–73.
Xie J, Liu G, Eden HS, Ai H, Chen X. Surface-engineered magnetic nanoparticle platforms for cancer imaging and therapy. Acc Chem Res 2011;44:883–92.
Xu Y, Wang E. Electrochemical biosensors based on magnetic micro/nano particles. Electrochim Acta 2012;84:62–73.
Xu P, Zeng GM, Huang DL, Feng CL, Hu S, Zhao MH, et al. Use of iron oxide nanomaterials in wastewater treatment: a review. Sci Total Environ 2012;424:1–10.
Yang C, Guan Y, Xing J, Shan G, Liu H. Preparation and characterization of monodisperse superparamagnetic poly (vinylalcohol) beads by reverse spray suspension crosslinking. J Polym Sci A Polym Chem 2008;46:203–10.
Yang L, Peng X-H, Wang YA, Wang X, Cao Z, Ni C, et al. Receptor-targeted nanoparticles for in vivo imaging of breast cancer. Clin Cancer Res 2009;15:4722–32.
Zboril R, Maslan M, Petridis D. Iron(III) oxides from thermal processes — synthesis, structural and magnetic properties, mossbauer spectroscopy characterization, and applications. Chem Mater 2002;14:969–82.
Zboril R, Machala L, Mashlan M, Sharma V. Iron(III) oxide nanoparticles in the thermally induced oxidative decomposition of Prussian Blue, $Fe_4[Fe(CN)_6]_3$. Cryst Growth Des 2004;4:1317–25.
Zeng H, Sun S. Syntheses, properties, and potential applications of multicomponent magnetic nanoparticles. Adv Funct Mater 2008;18:391–400.
Zhang Z, Sullivan DAO, Lyddiatt A. Magnetically stabilised fluidised bed adsorption: practical benefit of uncoupling bed expansion from fluid velocities in the purification of a recombinant protein from *Escherichia coli*. J Chem Technol Biotechnol 1999;74:270–4.
Zhang L, Li P, Liu C, Yang J, Wang M, Wang L. A highly efficient and recyclable Fe_3O_4 magnetic nanoparticle immobilized palladium catalyst for the direct C-2 arylation of indoles with arylboronic acids. Catal Sci Technol 2014a;4:1979–88.
Zhang S, He X, Chen L, Zhang Y. Boronic acid functionalized magnetic nanoparticles via thiol–ene click chemistry for selective enrichment of glycoproteins. New J Chem R Soc Chem 2014b;38:4212–8.
Zhou L, Gao C, Xu W. Robust Fe_3O_4/SiO_2–Pt/Au/Pd magnetic nanocatalysts with multifunctional hyperbranched polyglycerol amplifiers. Langmuir 2010;26:11217–25.
Zhou J, Zhang J, David AE, Yang VC. Magnetic tumor targeting of β-glucosidase immobilized iron oxide nanoparticles. Nanotechnology 2013;24:375102.
Zoppellaro G, Kolokithas-Ntoukas A, Polakova K, Tucek J, Zboril R, Loudos G, et al. Theranostics of epitaxially condensed colloidal nanocrystal clusters, through a soft biomineralization route. Chem Mater 2014;26:2062–74.

Please cite this article as: Hola K, et al, Tailored functionalization of iron oxide nanoparticles for MRI, drug delivery, magnetic separation and immobilization of biosubsta..., Biotechnol Adv (2015), http://dx.doi.org/10.1016/j.biotechadv.2015.02.003

Annu. Rev. Biomed. Eng. 2008.10:391-411. Downloaded from www.annualreviews.org
Access provided by Stanford University - Main Campus - Lane Medical Library on 03/16/15. For personal use only.



ANNUAL REVIEWS **Further**

Click here for quick links to Annual Reviews content online, including:

- Other articles in this volume
- Top cited articles
- Top downloaded articles
- Our comprehensive search

Chemical Exchange Saturation Transfer Contrast Agents for Magnetic Resonance Imaging

A. Dean Sherry[1,2] and Mark Woods[1]

[1]Department of Chemistry, University of Texas at Dallas, Richardson, Texas 75080; email: sherry@utdallas.edu

[2]Advanced Imaging Research Center, University of Texas Southwestern Medical Center, Dallas, Texas 75390-8568; email: dean.sherry@utsouthwestern.edu

Annu. Rev. Biomed. Eng. 2008. 10:391–411

First published online as a Review in Advance on April 18, 2008

The *Annual Review of Biomedical Engineering* is online at bioeng.annualreviews.org

This article's doi: 10.1146/annurev.bioeng.9.060906.151929

Copyright © 2008 by Annual Reviews. All rights reserved

1523-9829/08/0815-0391$20.00

Key Words

MRI contrast agents, CEST, PARACEST

Abstract

Magnetic resonance imaging (MRI) contrast agents have become an important tool in clinical medicine. The most common agents are Gd^{3+}-based complexes that shorten bulk water T_1 by rapid exchange of a single inner-sphere water molecule with bulk solvent water. Current gadolinium agents lack tissue specificity and typically do not respond to their chemical environment. Recently, it has been demonstrated that MR contrast may be altered by an entirely different mechanism based on chemical exchange saturation transfer (CEST). CEST contrast can originate from exchange of endogenous amide or hydroxyl protons or from exchangeable sites on exogenous CEST agents. This has opened the door for the discovery of new classes of responsive agents ranging from MR gene reporter molecules to small molecules that sense their tissue environment and respond to biological events.

Annu. Rev. Biomed. Eng. 2008.10:391-411. Downloaded from www.annualreviews.org
Access provided by Stanford University - Main Campus - Lane Medical Library on 03/16/15. For personal use only.

Contents

MAGNETIC RESONANCE IMAGING CONTRAST AGENTS: HISTORICAL ASPECTS 392
THE BASICS OF CHEMICAL EXCHANGE SATURATION TRANSFER 392
ENDOGENOUS CHEMICAL EXCHANGE SATURATION TRANSFER 394
EXOGENOUS CHEMICAL EXCHANGE SATURATION TRANSFER AGENTS 397
Paramagnetic Chemical Exchange Saturation Transfer Agents 399
Sensitivity-Enhanced Chemical Exchange Saturation Transfer Agents 404
CONCLUDING REMARKS 407

MAGNETIC RESONANCE IMAGING CONTRAST AGENTS: HISTORICAL ASPECTS

Paramagnetic complexes of Gd^{3+} are now widely used as magnetic resonance imaging (MRI) contrast agents in clinical medicine. These low-molecular-weight Gd^{3+} complexes alter image contrast via changes in the spin-lattice relaxation rate (T_1) of tissue water, which translates to brighter intensities in T_1 weighted images. The physical properties of Gd^{3+}-based contrast agents have been thoroughly studied in recent years and the mechanisms that determine the efficiency of such agents are reasonably well understood (1, 2). These detailed studies have formed the basis of numerous efforts to create responsive or smart MRI agents: Gd^{3+}-based agents that respond to changes in pH (3–9); Zn^{2+} and Ca^{2+} ion concentrations (10–12), a variety of anions (13, 14), enzymes (15–17), and proteins (18) have been reported. Although new Gd^{3+}-based agents continue to be widely investigated, they do have some limitations as a platform for responsive MRI agents. The effectiveness of a Gd^{3+} contrast agent is measured in terms of its relaxivity, defined as the increase in water proton relaxation rate per unit concentration of contrast agent (per millimolar per second). The relaxivity of a complex is dependent on multiple physical constants, including the magnetic properties of the Gd^{3+} complex, constants related to electron-spin relaxation, rotational mobility, and the number of metal-bound water molecules (q) (1, 2). The net result is that all Gd^{3+} complexes relax water to some extent and their presence always affects what is observed in the MR image. So, even though the off form of a responsive Gd^{3+} agent affects an MR image less than the on form, it continues to have some effect. It is therefore necessary to account for the concentration of the agent if these Gd^{3+}-based agents are used in vivo (19, 20).

Responsive agent: a contrast agent that affects image contrast differently depending on the presence of another biological species or a change in some physiological or biochemical parameter, such as pH, O_2 tension, or enzyme activity

Chemical exchange saturation transfer (CEST): causes a reduction in the signal intensity of an NMR resonance that is in chemical exchange with another resonance to which a low-power irradiation or presaturation pulse has been applied

THE BASICS OF CHEMICAL EXCHANGE SATURATION TRANSFER

Gd^{3+} agents are widely used in clinical imaging and have been successful in that setting. However, their limitations and drawbacks, particularly in association with responsive agents, suggest that an alternative mechanism for generating image contrast may be able to provide additional information that may improve diagnosis by MRI. Chemical exchange saturation transfer, or CEST, is a technique that has been used in nuclear magnetic resonance (NMR) for more than four decades and is now generating increasing interest as a means of generating contrast in MR images.

The phenomenon of chemical exchange has been studied by NMR spectroscopy for many years. In 1957, McConnell & Thompson (21) modified the NMR Bloch equations to include terms for chemical exchange and reported proton transfer rates between the ammonium ion and water (22). But the first example of a CEST experiment was performed by Forsén & Hoffman (23),

Annu. Rev. Biomed. Eng. 2008.10:391-411. Downloaded from www.annualreviews.org
Access provided by Stanford University - Main Campus - Lane Medical Library on 03/16/15. For personal use only.

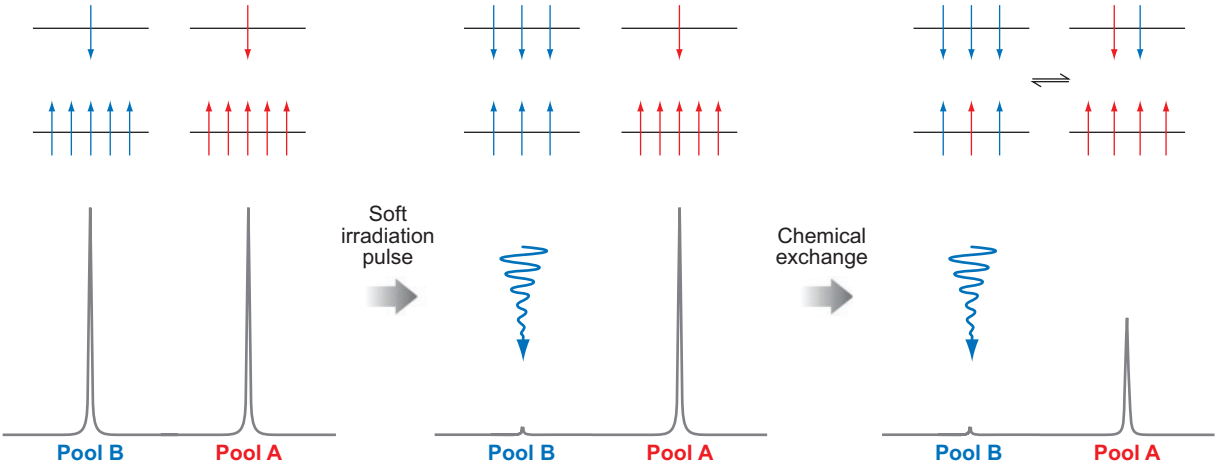


Figure 1

Schematic representations of the distribution of spins, aligned with and against the field (upper and lower energy levels, respectively) (*above*) and simulated NMR spectra (*below*) for two chemically distinct pools of nuclei (*left*), two spins after a saturation pulse has been applied to one pool (*middle*), and for a system undergoing chemical exchange after a saturation pulse has been applied to one pool (*right*).

who used the method to measure proton transfer rates between salicylaldehyde and water. This CEST technique is also referred to as saturation transfer (ST) or magnetization transfer (MT) in some publications. Nevertheless, general methods such as this have been widely applied in both chemistry and biology to determine unidirectional rate constants of simple reactions for many years.

To have CEST, the system must be in chemical exchange. These chemical exchange processes might be exchange of the γ-phosphate of ATP and the phosphate group of creatine phosphate (PCr) catalyzed by the enzyme creatine kinase, the two methyl groups attached to a nitrogen atom in an asymmetrical molecule that exchange their spatial positions via nitrogen inversion, or, for the purposes of the current discussion, an exchangeable proton of a molecule that exchanges with those of the solvent water. Consider two general exchanging pools, A and B, perturbed by application of a saturation pulse to pool B (**Figure 1**). Saturation is the process by which the Boltzmann distribution of nuclear spins, aligned either with or against the magnetic field, is temporarily altered by applying a soft (low-power) irradiation pulse at the resonance frequency of a nucleus of interest. The number of spins aligned against the field is increased at the expense of those aligned with the field (**Figure 1**). Once the number of spins aligned with and against the field is equal, the system is said to be saturated, the net magnetization is zero, and no signal is observed in the NMR spectrum. The nuclei in Pool A are in exchange with the saturated nuclei in Pool B. This exchange transfers spins that are aligned against the field from Pool B to Pool A and spins aligned with the field from Pool A to Pool B. The net result is transfer of saturation from Pool B to Pool A and a concomitant decrease in the signal intensity of the nuclei in Pool A (**Figure 1**). Longitudinal relaxation returns each system to its equilibrium distribution of spins, so eventually the system reaches steady state. The steady-state intensity ($M_{A\infty}/M_{A0}$) of the nuclei in Pool A is given by Equation 1. We refer readers interested in a more in-depth description of the mechanism of CEST to an earlier review (24).

$$\frac{M_{A\infty}}{M_{A0}} = \frac{1}{(1 + k_2 T_{1B})} \quad (1)$$

Saturation: a condition wherein the number of nuclear spins aligned against the field is increased at the expense of those aligned with the field, leading to a decrease in signal intensity

Boltzmann distribution: the ratio of the spins aligned with the field over those aligned against $= e^{(-\Delta E/kT)}$

Annu. Rev. Biomed. Eng. 2008.10:391-411. Downloaded from www.annualreviews.org
Access provided by Stanford University - Main Campus - Lane Medical Library on 03/16/15. For personal use only.

$\Delta\omega$: the difference between the resonance frequencies of two pools involved in chemical exchange

LRP: lysine-rich protein

The model presented in **Figure 1** also implies that the chemical shift of the two exchanging pools must differ substantially. For diamagnetic compounds, the chemical shift difference ($\Delta\omega$) between exchangeable protons and bulk water is typically <5 ppm, which corresponds to 315 Hz at 1.5T and 630 Hz at 3T. Assuming the slow-to-intermediate exchange condition ($k_{ex} \leq \Delta\omega$) represents a rough boundary condition for CEST, this means that exchange must be slower than ~1980 s^{-1} using a 1.5T scanner or slower than ~3960 s^{-1} using a 3T scanner to observe CEST. As $\Delta\omega$ is small in diamagnetic systems, the applied presaturation frequency must by definition be close to that of solvent water so partial direct off-resonance saturation of the solvent water can occur (25). This problem is accentuated in vivo where the bulk water signal tends to be broader. To extract the effects of a diamagnetic CEST agent then, whether it is an endogenous compound or an exogenous agent, it is often necessary to subtract the effects of direct off-resonance saturation by measuring the effect of presaturation at equal frequency offset difference on each side of the central bulk water peak and report the difference as an asymmetry ratio (26). In an imaging sense, one collects two images, one after presaturation at the exchange site of interest and another at an equivalent frequency offset on the opposite side of bulk water. The difference between these two image intensities should then report only the effects of the exchanging CEST agent. Although the CEST effect generated from diamagnetic endogenous CEST agents often does not differ much from that due to direct off-resonance saturation of bulk water, it is nonetheless large enough to be useful in a number of applications.

ENDOGENOUS CHEMICAL EXCHANGE SATURATION TRANSFER

Because the effect of CEST is to reduce magnetization in Pool A, the bulk water pool, the net result is a loss of signal intensity and a darkening of the image, or negative contrast. This is in contrast to Gd^{3+} agents, which typically serve as positive contrast agents by brightening images. As a general rule, positive contrast is preferable simply because the human eye can more easily discriminate a slight increase in brightness than a slight increase in darkness. The image darkening effect of adding a presaturation magnetization transfer pulse has proven useful, however, in a number of applications. One such example is time-of-flight magnetic resonance angiography (TOF-MRA; **Figure 2**). Here a presaturation pulse is applied directly to the bulk water signal in the image slice of interest, thereby eliminating the water signal. A small time delay then allows any mobile water protons, such as those in blood, to move out of the slice and be replaced by new blood containing spins that were not saturated. An image is then acquired in which the signal from the stationary tissue is darkened by saturation, whereas the signal of blood appears at normal intensity. The result is dramatic, showing a nice delineation of the vascular space from the surrounding tissue (**Figure 2**). More recently, Gd^{3+}-based T_1 agents that enhance the blood signal by binding to albumin have been introduced for contrast enhanced MR angiography (CE-MRA), providing an additional option for imaging the vasculature (27, 28).

One recent challenge has been the development of new imaging agents for cell tracking. Exogenous paramagnetic agents of various types have been loaded into cells at levels sufficient to alter T_1 or T_2 without overt loss of biological function (29–32). However, these contrast effects tend to fade with time either because of cell leakage or cell division. van Zijl and coworkers reported an ingenious approach to circumvent these problems by genetically altering glioma cells to express a lysine-rich protein (LRP) that can then be detected by CEST imaging (33). The large number of equivalent amide protons in the LRP appearing 3.76 ppm downfield of the water resonance were used to initiate CEST (34). Genetically modified giloma cells, implanted into a mouse brain, were easily differentiated from control cells by CEST imaging by applying a selective presaturation pulse at the resonant frequency of the LRP amide resonance (**Figure 3**).

Annu. Rev. Biomed. Eng. 2008.10:391-411. Downloaded from www.annualreviews.org
Access provided by Stanford University - Main Campus - Lane Medical Library on 03/16/15. For personal use only.

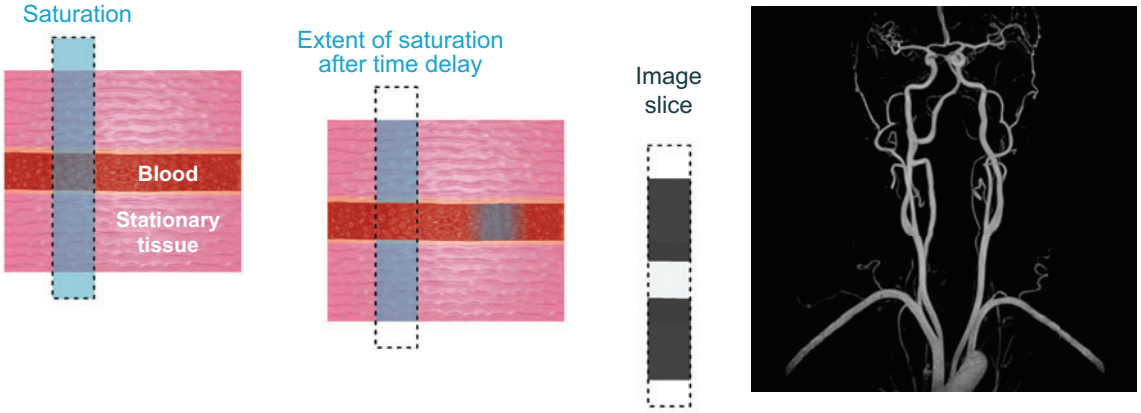


Figure 2

Angiography by TOF-MRA is a form of saturation transfer experiment. An image slice, represented by the dotted line, is acquired by saturating the bulk water protons only in that image slice (*left*, the saturation is represented in *blue*). After a short time delay, the saturation of water protons in blood has been transferred out of the slice and replaced by unsaturated spins (*middle*). Thus, when the image is acquired, the stationary tissue appears dark but the blood is bright. In this way, angiograms may be acquired, such as the one of the carotid arteries shown (*right*).

The images show CEST contrast only in the region where the engineered cells had been implanted, demonstrating that unique CEST activation systems such as this may be useful for cell tracking. Because the LRP is produced by the genetic machinery of the cell, its concentration should, in principle, be maintained even after many cell divisions. Furthermore, different cells could be encoded to produce different markers for CEST that require different activation frequencies. This would allow two, or more, types of cells to be tracked simultaneously by applying an appropriate frequency-selective presaturation pulse to follow the cells of interest.

This example demonstrates one of the main advantages of CEST imaging—CEST contrast can be turned on selectively by simply adding a presaturation pulse to an imaging sequence. The apparent negative image contrast generated by CEST activation is not a drawback in this case because a control CEST image that uses a different activation frequency (typically at an equal frequency offset on the opposite side of the water frequency) must be gathered so the difference image can be displayed as a positive image, a negative image, or a colorized image.

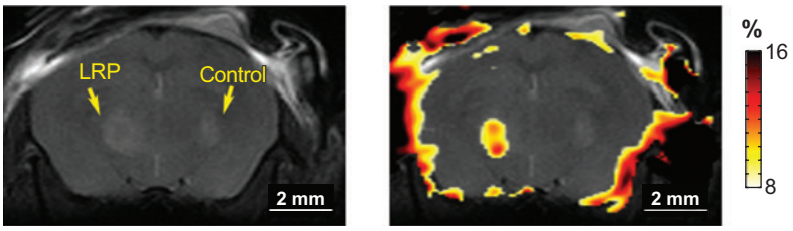


Figure 3

An image of a mouse brain implanted with glioma cells expressing LRP (*left hemisphere*) and glioma cells (*right hemisphere*). On the left is an anatomical image, on the right a colorized difference image of the areas that exhibit CEST has been overlaid on the anatomical image. The LRP gives rise to a significant change in water signal intensity, allowing the genetically modified cells to be easily identified and tracked by CEST imaging. The area of CEST intensity around the skull is thought to be due to field inhomogeneities. Images reproduced, with permission, from Nature Biotechnology.

Annu. Rev. Biomed. Eng. 2008.10:391-411. Downloaded from www.annualreviews.org
Access provided by Stanford University - Main Campus - Lane Medical Library on 03/16/15. For personal use only.

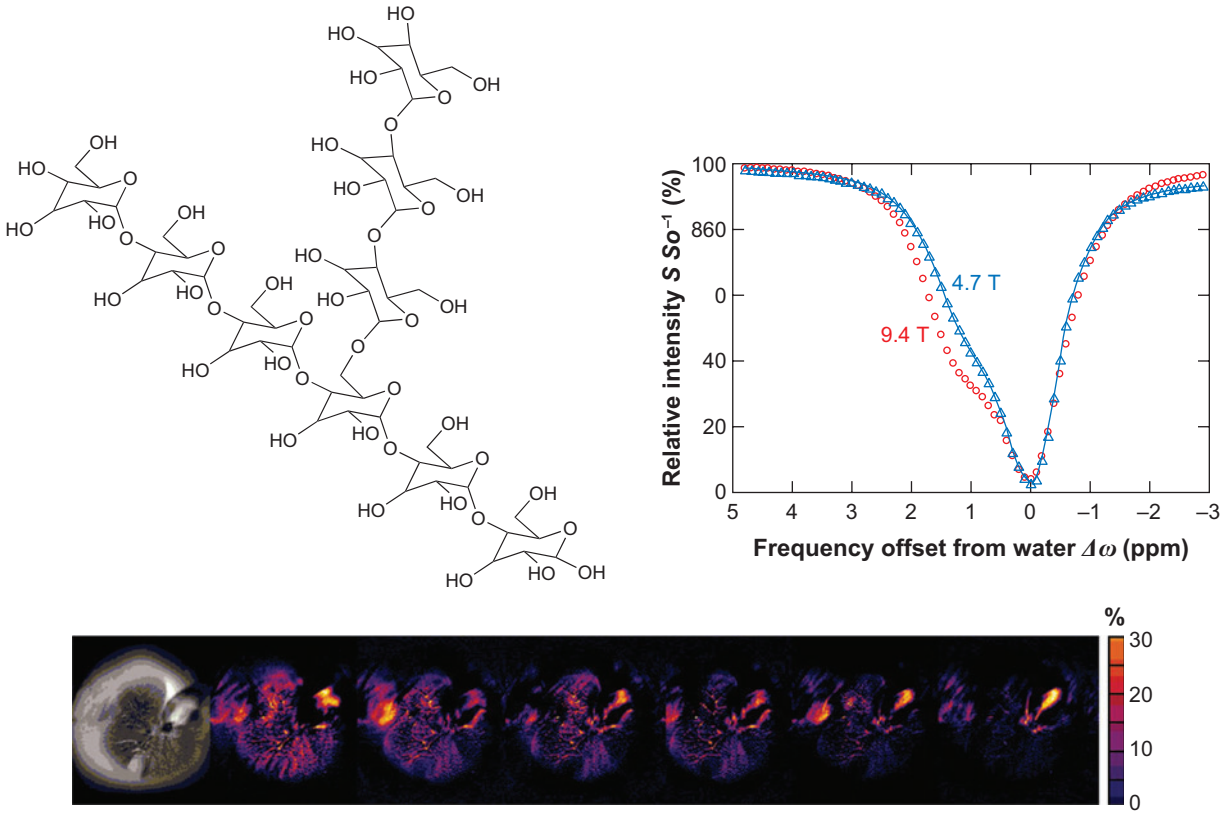


Figure 4

The structure of glycogen (*top left*) and its CEST spectra recorded at 200 and 400 MHz (*top right*). An anatomical image, with a presaturation pulse applied at +1 ppm, shows a darkening of the image due to the presence of glycogen (*bottom left*). Colorized CEST difference images acquired at 0, 20, 40, 60, 80, 100, and 120 min after administration of glucagon become progressively less orange, reflecting depletion of glycogen (*bottom*). MR images and CEST spectra reproduced from *Proceedings of the National Academy of Sciences*.

In mammalian tissue, excess glucose is stored in the form of the branching polymer glycogen (**Figure 4**). The body uses glycogen to replenish blood glucose levels as necessary, so a noninvasive method of tracking the distribution, synthesis, and breakdown of glycogen could have a major impact as a diagnostic tool in humans with glycogen storage disease or diabetes. The size and degree of branching of glycogen can vary but typically it has a molecular weight of several million and, by definition, a large number of exchangeable hydroxyl protons. Presaturation of glycogen –OH resonances ~1 ppm downfield of water enables these hydroxyl protons to be used as CEST antennae (35). The CEST spectra of glycogen recorded at 4.7 T and 9.4 T shown in **Figure 4** nicely illustrate the advantage of working at higher magnetic fields for CEST detection. The value of $\Delta\omega$ (measured in Hertz) is larger at the higher field, and this renders the slow-to-intermediate exchange condition more favorable as well.

CEST arising from glycogen (glycoCEST) can be used to follow glycogen breakdown (glycogenolysis) stimulated by the hormone glucagon. The liver of a fed mouse has a substantial amount of glycogen that can easily be degraded and exported for use by other tissues. During periods of starvation, blood glucose levels begin to drop and the pancreas responds by releasing glucagon. Glucagon, in turn, binds to specific receptors on the surface of liver cells, and through

Annu. Rev. Biomed. Eng. 2008.10:391-411. Downloaded from www.annualreviews.org
Access provided by Stanford University - Main Campus - Lane Medical Library on 03/16/15. For personal use only.

a cascade of intracellular events, this stimulates glycogenolysis and export of glucose. These same events occur when glucagon is presented to an isolated perfused liver, but, in this case, glucose is simply exported to the surrounding perfusate. A series of colorized glycoCEST images of liver from a fed mouse are shown (**Figure 4**, bottom). The color variations in these images suggest that glycogen may not be uniformly distributed throughout the liver, or that proton exchange rates may vary depending on the location or size of the glycogen particle. Differentiating between these possibilities will require further detailed studies of the CEST properties of various chemical forms of glycogen. Nevertheless, glycoCEST images acquired at time intervals after administration of glucagon demonstrate that the magnitude of CEST is reduced as glycogen is broken down and glucose is released from the liver.

Although glycogen can be detected by CEST activation of a large population of hydroxyl protons, the protons of many alcohols and amines are not generally amenable to CEST because chemical exchange from these types of functional groups is often too fast (34, 36). Amide protons, however, exchange more slowly and represent an attractive means of generating CEST contrast (37). We have already seen the effect of irradiating the amide protons of LRP in cells modified to overexpress that protein. However, naturally occurring amide protons are abundant in all tissue and can be used to obtain information about the state of the tissue through CEST imaging. The rate of amide proton exchange is highly dependent on pH; above approximately pH 5, the presence of base catalyses exchange, so the higher the pH, the faster the exchange rate. This difference in exchange rate can be used to assess pH because the magnitude of CEST is strongly influenced by the exchange rate. Ischemic regions of rat brain tissues have been imaged by applying a presaturation pulse at 3.5 (sat-on) and –3.5 ppm (sat-off) to probe the CEST arising from naturally abundant amide protons (38). Regions of ischemia were clearly distinguished in the CEST images, presumably reflecting pH differences due to a loss of tissue oxygenation and aerobic metabolism. No such tissue differentiation was observed in T_2-weighted control images, demonstrating that CEST imaging could provide additional diagnostic utility over conventional imaging methods.

EXOGENOUS CHEMICAL EXCHANGE SATURATION TRANSFER AGENTS

The CEST applications discussed so far have focused on the use of endogenous species having a component in exchange with the solvent water. However, there are circumstances when one may wish to obtain information that cannot be gained from an endogenous CEST probe. Here, it may be desirable to administer an exogenous CEST agent that can respond to some biological event or change in physiology. We describe later how exogenous agents can be used to effect changes in the water signal intensity, but we first consider a recently reported example of CEST that uses an NMR nucleus not naturally found in tissue (39). ^{129}Xe has a favorable NMR spin quantum number of 1/2, its chemical shift is extremely sensitive to its chemical environment, and it has an unusually long T_1. Xenon gas can be inhaled safely and because there is zero background signal in tissue, it has been considered for use in lung imaging. Xenon is soluble in both water and fat, so this inert substance distributes to some extent in all tissues (40). Because the chemical shift of ^{129}Xe is exquisitely sensitive, gaseous xenon, xenon dissolved in blood, and xenon in various tissue compartments are easily discriminated. Unfortunately, ^{129}Xe is not the most sensitive of NMR nuclei (similar sensitivity as ^{13}C), so the amount that can be delivered as a gas barely provides enough signal for imaging. However, the sensitivity of this nucleus can be improved dramatically by first hyperpolarizing the ^{129}Xe, typically by optical pumping of rubidium gas followed by polarization transfer (spin exchange) to ^{129}Xe (40, 41). The effect of hyperpolarization is the reverse of saturation; the number of spins aligned with the magnetic field is increased, relative to

Hyperpolarization: a condition wherein the number of nuclear spins aligned with the field is increased at the expense of those aligned against the field, leading to an increase in signal intensity

Annu. Rev. Biomed. Eng. 2008.10:391-411. Downloaded from www.annualreviews.org
Access provided by Stanford University - Main Campus - Lane Medical Library on 03/16/15. For personal use only.

the normal Boltzmann distribution, and thus the net magnetization is also considerably enhanced. The sensitivity of ^{129}Xe can be increased up to 100,000-fold making it possible to image inhaled xenon gas with exquisite image resolution. Of course, the magnetization of a hyperpolarized nucleus returns to steady-state Boltzmann levels with a rate constant of $1/T_1$, so the amount of time one has available for imaging heavily depends on the T_1 relaxation rate of the nucleus. Because ^{129}Xe has a long T_1 over one minute in water at 9.4 T, there is considerable interest in the possibility of pulmonary imaging with hyperpolarized ^{129}Xe.

Xe is considered to be chemically inert because it is not easily oxidized or reduced and only forms stable covalent bonds with certain elements. However, Xe can be encapsulated by chemical cages of appropriate size via van der Waals interactions, and such caged complexes can, in principle, be covalently linked to a targeting motif for delivery of hyperpolarized ^{129}Xe to a specific tissue target. Encapsulated Xe experiences a sizable shift in resonance frequency of more than 100 ppm, so it is easy to discriminate between encapsulated and free Xe. Although these cages may be able to localize Xe to a specific tissue type, even with the benefits of hyperpolarization many biologically relevant targets, such as cell receptors, are present in such low concentrations (often nanomolar or lower) that direct detection of the target-bound encapsulated Xe would not be possible. However, the rate of exchange between free and encapsulated forms of Xe was found to be slow on the NMR timescale, and this raised the possibility of performing CEST experiments with hyperpolarized Xe to detect the minor species (caged Xe) through the signal of the more abundant species (free Xe) (39).

Figure 5 shows images of a phantom system of agarose beads, one half of which are plain agarose beads and the other half of which are avadin-agarose beads. The beads were treated with crytophanes conjugated, through a water-soluble linker, to biotin, which selectively binds with avidin. The system was then perfused with hyperpolarized Xe-saturated water and images collected. When the phantom was imaged after presaturation of the encapsulated Xe (65.4 ppm), a significant decrease in the signal of free Xe (193.6 ppm) was observed (**Figure 5**). This system nicely demonstrates that this hyperCEST technique is able to differentiate the more abundant free Xe at sensitivity levels characteristic of hyperpolarized nuclei even though the caged atoms are barely detectable by direct ^{129}Xe NMR spectroscopy. Furthermore, xenon biosensors such as this could be preloaded to allow time for tissue targeting prior to diffusion of hyperpolarized Xe.

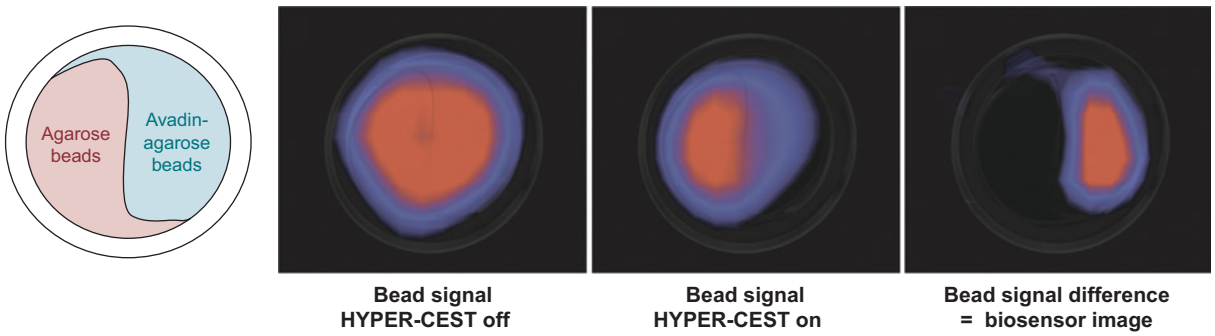


Figure 5

The setup of the phantom system used to image the CEST properties of hyperpolarized ^{129}Xe (*far left*). Images of the phantom system showing the signal arising from free ^{129}Xe (*left*) and free ^{129}Xe after presaturation of the encapsulated xenon (*right*). The difference image (*far right*) shows that the CEST effect is only generated for those regions in which the avadin target is found. MR images from Reference 39. Reprinted with permission from AAAS.

Annu. Rev. Biomed. Eng. 2008.10:391-411. Downloaded from www.annualreviews.org
Access provided by Stanford University - Main Campus - Lane Medical Library on 03/16/15. For personal use only.

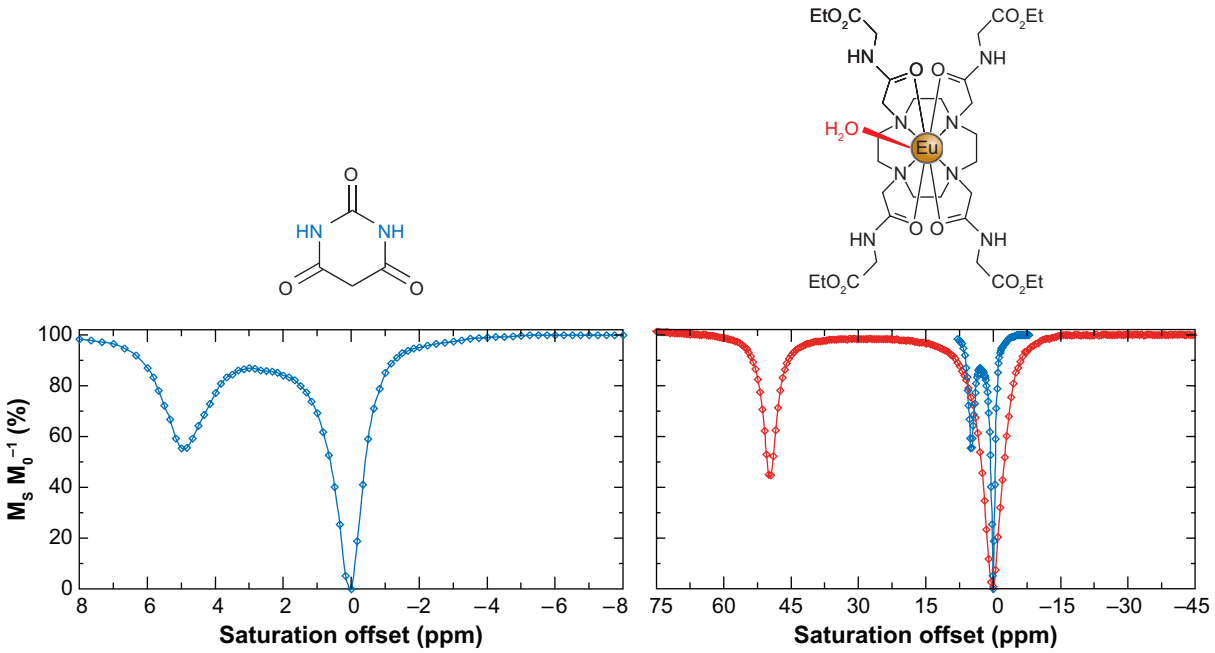


Figure 6

The CEST spectra of barbituric acid (*left*) and a Eu^{3+} complex, EuDOTA-(glycine ethyl ester)$_4$ (*right*). The CEST spectrum of barbituric acid is shown on the same scale as that of the Eu^{3+} complex (*blue*, *right*) for comparative purposes.

Paramagnetic Chemical Exchange Saturation Transfer Agents

The development of hyperpolarization technologies and hyperCEST present new and exciting opportunities for MRI using a wide range of NMR active nuclei. However, clinical MR imaging largely involves detection of protons, so it is important to remain focused on CEST agents that can provide useful clinical information by altering contrast in water proton images. Balaban and coworkers were first to propose using low-molecular-weight, diamagnetic molecules with exchangeable protons as exogenous CEST agents (42, 43). A number of sugars, metabolites, amino acids, and other small molecules were evaluated by recording a CEST spectrum in which the intensity of the bulk water signal is plotted as a function of the presaturation frequency. Many of these small diamagnetic molecules showed a significant ability to alter the solvent water signal intensity at the relatively high concentrations of CEST agent (10–100 mM). The CEST spectrum of barbituric acid, a typical diamagnetic agent, is shown in **Figure 6**. From this spectrum, it is clear that the shift difference between the two exchanging pools is small, ~5 ppm. This limits the CEST experiment in two ways: (*a*) application of a presaturation pulse even 5 ppm away from the bulk water signal will result in some off-resonance saturation of the water so there are limitations in the amount of power that can be applied, and (*b*) the slow exchange condition ($k_{ex} < \Delta\omega$) means that very slow exchange rates are required for diamagnetic CEST agents of this sort. Both problems can be alleviated by using an agent that has a larger chemical shift separation between the two exchanging pools, much like the Xe example described above. This allows a broader spectrum of suitable exchange agents to be investigated and, intuitively, more rapid chemical exchange will increase the number of saturated spins that can be transferred to the solvent water in any given time frame, thereby increasing the observed CEST effect.

Annu. Rev. Biomed. Eng. 2008.10:391-411. Downloaded from www.annualreviews.org
Access provided by Stanford University - Main Campus - Lane Medical Library on 03/16/15. For personal use only.

Paramagnetic CEST (PARACEST): chemical exchange saturation transfer that arises from presaturation of exchangeable protons on a paramagnetic molecule or complex

DOTA-tetraamide: an octadentate ligand based on the structure 1,4,7,10-tetraazacyclododecane-1,4,7,10-tetraacetamide

Arrhenius's law: $k_{ex} = Ae^{(-E_a/RT)}$

The rate of water exchange in the Gd^{3+} complexes used as T_1-shortening MRI contrast agents is quite fast ($1/k_{ex} \ll 1$ μs) and certainly too fast for CEST (1, 44). However, the structure of these complexes can be modified in such a way that favors much slower exchange kinetics while retaining the stability of the complex required for in vivo applications (45–47). The discovery of such slow water exchange complexes suggested to us that such lanthanide-based chelates might be used as paramagnetic CEST agents (PARACEST) (48, 49). The Gd^{3+} ion is isotropic (seven unpaired electrons in seven 4f orbitals) so it cannot act as a shift reagent, but other paramagnetic lanthanide ions with anisotropic distributions of their f-electrons can induce very large shifts in the resonance frequencies of proximate protons (50–52). Some of those other lanthanides, when complexed with DOTA-tetraamide ligands, exhibit a single, highly shifted metal ion-bound water resonance in their ^{1}H NMR spectra due to slow water exchange (49). The chemical shift of this metal ion-bound water molecule can vary from +500 to –720 ppm depending on which lanthanide ion is coordinated (53). The first paramagnetic complex that showed a water-exchange peak in its CEST spectrum was in EuDOTA-(glycine ethyl ester)$_4$ (**Figure 6**) (48). Here, an exchange peak near +50 ppm was easily assigned to a water molecule that exchanges between an inner-sphere coordination position on the Eu^{3+} and bulk solvent. The exchange peak observed in this spectrum was consistent with models presented earlier, suggesting that water-exchange rates would vary with the bulkiness of the appended amide side chain groups (45). Highly shifted exchange peaks such as this offer a distinct advantage for CEST activation in that direct off-resonance saturation of the bulk water pool is largely eliminated, in dramatic contrast to diamagnetic CEST agents (**Figure 6**). Such large $\Delta\omega$ values also expand the range of k_{ex} values allowable for CEST. Although the hyperfine shifted exchange resonances seen in Eu^{3+} complexes are smaller than those found in the analogous Tm^{3+} (+500 ppm) and Dy^{3+} (–720 ppm) complexes, Eu^{3+} complexes have been more widely studied as PARACEST agents. The reasons for this popularity relate to the fact that water exchange is found to be slowest in Eu^{3+} complexes in comparison to all other lanthanides (54) and to the poor relaxation properties of Eu^{3+} that result in long relaxation times, which in turn favor CEST.

As other ligands and metal ions have been studied, it has been found that CEST can be achieved by presaturating other exchangeable protons in lanthanide complexes, in particular, coordinating alcohol protons (55), coordinating amide protons (56–58), and proximate noncoordinating amide protons (59, 60). These discoveries have had important consequences for the development of PARACEST agents as an imaging tool. The primary advantage of CEST agents, and in particular PARACEST agents, over conventional T_1-shortening agents is in the amount and type of information that can be obtained. In particular, metabolic information, which we have already seen is difficult to acquire with Gd^{3+}-based contrast agents, is more easily obtained using a PARACEST agent. Because CEST is extremely sensitive to exchange rates, any change in the prevailing conditions that alters the exchange rate is likely to have a profound effect on CEST. We first examine the practical advantages of these agents before discussing some design features that provide the basis for these responsive agents.

Two experimental conditions are intrinsically linked to the rate of proton and water exchange, sample temperature and pH. The exchange rate of all species increases with increasing temperature according to Arrhenius's law, so PARACEST agents such as these have potential as MRI temperature probes (57, 61). In contrast, the relationship between exchange rate and pH can be more complex (57). For example, the rate of metal-bound water proton exchange is unaffected by changes in pH between 2 and 8 but increases at higher pH, whereas the rate of coordinated amide proton exchange increases significantly between pH 5 and 8. Aime and coworkers have proposed methods by which the pH dependence of CEST from the amide protons in lanthanide DOTA-tetraamide complexes might be used to assess pH by MRI in a concentration-independent

Annu. Rev. Biomed. Eng. 2008.10:391-411. Downloaded from www.annualreviews.org
Access provided by Stanford University - Main Campus - Lane Medical Library on 03/16/15. For personal use only.

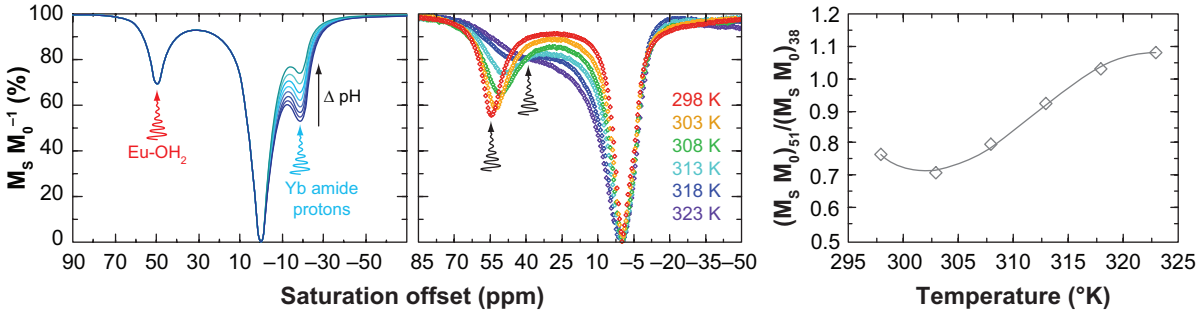


Figure 7

CEST imaging allows ratiometric determination of biologically relevant parameters such as pH and temperature. (*Left*) simulated CEST spectra of a cocktail of Eu^{3+} and Yb^{3+} DOTA-tetraamide complexes with varying pH. The insensitivity of CEST from the metal-bound water of the Eu^{3+} complex can be used as a concentration marker, whereas the pH-sensitive amide protons of the Yb^{3+} complexes can be used to measure pH. (*Right*) The CEST spectra of an Eu^{3+} DOTA-tetraamide complex at different temperatures.

manner (58). The CEST effect arising from metal-bound water exchange in EuDOTA-tetraamide complexes (+50 ppm) is unaffected by changes in pH over the physiological pH range so it has been proposed as a concentration marker. In contrast, the CEST effect from the coordinating amide protons of the Yb^{3+} complex of the same ligand (–20 ppm) will report changes in pH. Eu^{3+} and Yb^{3+} complexes are isostructural so one might anticipate they would distribute in tissue identically. Hence, a cocktail of Eu^{3+} and Yb^{3+} complexes with the same ligand could be administered simultaneously and CEST activation at +50 ppm would report the agent concentration without activating the pH reporter, whereas CEST activation at –20 ppm would report the pH (**Figure 7*a***). The large difference in irradiation frequency between the amide and metal-bound water protons allows each pool to be activated selectively without influencing the other exchange site. CEST from both the amide and water protons can be observed for many Eu^{3+} DOTA-tetraamide complexes so it may not be necessary to use two lanthanide ions complexes to achieve this goal. However, the intensity of each CEST peak, water and amide, must be comparable if one is to be used as a concentration marker. For Eu^{3+} complexes this condition is not met, but by using a mixture of two complexes, the composition of the cocktail can be tuned to achieve the desired balance. Aime and co-workers have subsequently reported that a single complex can provide the desired balance in CEST intensities between the two presaturation sites (57). They showed that a DOTA-tetraamide complex of Pr^{3+} is able to provide a pH sensing function through its amide protons and a concentration determination through its coordinated water molecule. Although these two site probes for metabolic information are quite viable in an imaging context, a simpler, more elegant solution that requires only a single exchanging pool has been proposed by Wegh and coworkers (62). In their work, changes in pH were assessed using a dendrimer-like compound with several YbDOTA-tetraamide complexes appended, the amide protons of which have pH-sensitive CEST properties (63). However, their approach to measuring changes in pH can, in principle, be extended to any responsive CEST agent. As an example, **Figure 7** shows the CEST spectra of a EuDOTA-tetraamide complex recorded at different temperatures (61). It can be seen that the CEST peak corresponding to the metal-bound water decreases in intensity as the temperature increases, but, as it does so, it also broadens and shifts toward the bulk water peak. This NMR signature is characteristic of a system undergoing more rapid chemical exchange with increasing temperature. If the magnitude of the CEST effect is measured by presaturation at +51 ppm, it will decrease with increasing temperature. However, a significant CEST effect can also be generated by presaturating closer to the solvent water frequency, say

Isostructural: having identical structures despite differences in chemical composition

Annu. Rev. Biomed. Eng. 2008.10:391-411. Downloaded from www.annualreviews.org
Access provided by Stanford University - Main Campus - Lane Medical Library on 03/16/15. For personal use only.

+38 ppm, and the response of the CEST magnitude after presaturation at this frequency is completely different from that at +51 ppm. So by taking the ratio of the change in solvent water signal intensity after presaturation at +51 ppm and +38 ppm, both acting on the metal-bound water, a concentration-independent method of determining temperature can be obtained (**Figure 7*c***). The benefit of this method is that only one exchanging pool that responds to the parameter of interest is required.

Clearly, the insensitivity of the metal-bound water-exchange peak in EuDOTA-tetraamide complexes to changes in pH makes this an ideal platform to design agents that respond to other physiological or biological parameters. To design such an agent, one must first choose a complex in which the exchange rate of the metal-bound water is affected by its interaction with the species under consideration. In principle, there are three routes to achieving this goal: (*a*) alter the steric encumbrance around the water molecule, (*b*) introduce a group that catalyzes proton or water exchange, or (*c*) alter the interaction binding energy between the metal ion and the water molecule. Let's consider each in turn. A PARACEST agent may be designed in such a way that the species under analysis binds, either covalently or noncovalently, to the complex above the coordination site of metal-bound water. In doing so, it makes it harder for the metal-bound water molecule to exchange with the bulk simply because the analyte is impeding departure of the water molecule from its metal-binding site. This should result in a decreased water-exchange rate in response to exposure to the analyte of interest. One example of such as system is a recently reported glucose-responsive PARACEST agent (64, 65) in which the glucose, binding to two phenyl boronates, sits above the water coordination site and slows water exchange. In this example, water exchange slows by approximately a factor of two when glucose is bound and this is sufficient to switch on CEST from the metal-bound water. **Figure 8*a*** shows images of the binding event in phantom systems but monitoring glucose distribution in isolated, perfused mouse livers has also been performed (J. Ren & A.D. Sherry, unpublished data).

Certain proximate groups, such as phosphonates, can catalyze the exchange of metal-bound water protons, a feature that has been used to design pH responsive Gd^{3+} agents (3). If, upon binding, the chosen analyte introduces a suitably located group that is capable of catalyzing water proton exchange, then the resulting increase in apparent water-exchange rate will be reflected in the CEST properties of the PARACEST agent. A PARACEST agent with four pyridyl groups was designed to bind the Zn^{2+} ion above the water coordination site (66), but unlike the glucose sensor described above, at physiological pH the Zn^{2+} ion bound to this complex presents a coordinated hydroxyl group just above the Eu^{3+}-bound water molecule, which catalyzes acceleration of water proton exchange, thereby affording very large changes in the CEST spectrum upon binding of Zn^{2+}. In this case, the CEST was on initially in the absence of Zn^{2+} but was turned off when the catalytic –OH group was introduced by the Zn^{2+}.

Water exchange in EuDOTA-tetraamide complexes such as these is known to occur by a dissociative mechanism, whereby the single bound water molecule must leave the Eu^{3+} coordination sphere before a different water molecule can enter (67). Consequently, the strength of the interaction between the Eu^{3+} and its bound water molecule essentially determines the water-exchange rate. If the strength of this interaction can be subtly altered in response to changes in concentration of a parameter of interest, then this might also be reflected in the water-exchange rate and, ultimately, in the CEST properties of the complex. To test this hypothesis, a series of complexes were prepared in which one amide substituent was systematically altered to vary the electron-donating power of that amide ligand (68). The magnitude of the CEST effect was found to vary with the nature of the amide substituent, supporting the hypothesis that these electronic effects can be used to design responsive PARACEST agents. As shown in **Figure 8*c***, when the amide substituent was varied from a *p*-NO_2-phenyl (electron-withdrawing) to a *p*-NH_2-phenyl (electron-donating)

Annu. Rev. Biomed. Eng. 2008.10:391-411. Downloaded from www.annualreviews.org
Access provided by Stanford University - Main Campus - Lane Medical Library on 03/16/15. For personal use only.

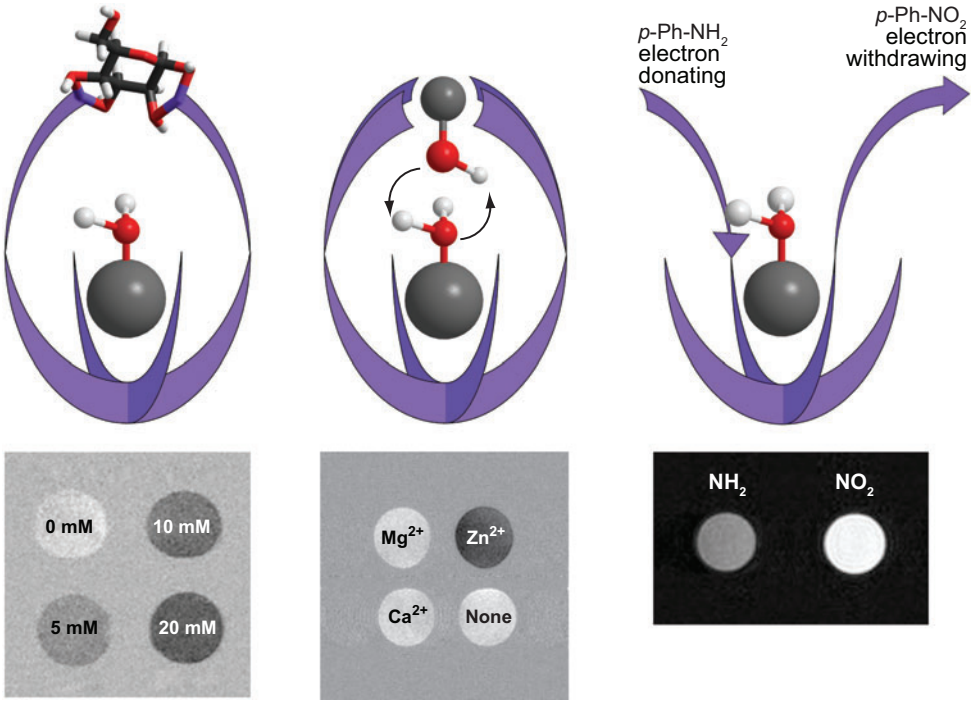


Figure 8

Illustrating different methods of designing responsive PARACEST agents. (*Left*) The binding of glucose hinders water exchange, increasing CEST. (*Middle*) At physiological pH, binding of Zn^{2+} at its binding site above the Eu^{3+}-OH_2 molecule results in catalysis of proton exchange, altering the CEST properties. (*Right*) Altering the electronic effects of substituents can affect the interaction between the metal and water, which may be observed as a change in CEST.

substituent, a significant difference in CEST image intensity is observed in phantom systems after presaturation of the metal-bound water molecule. This suggests that a generalized approach to the design of responsive agents may be possible that would even allow for assessment of parameters, such as tissue redox, for which it may otherwise have been difficult to design a responsive agent.

The design of responsive PARACEST agents is not restricted to examining changes in the signal arising from the metal-bound water protons or the coordinated amide protons. Pagel and coworkers adopted a somewhat different approach in developing a PARACEST agent that responds to the action of an enzyme (60). Rather than begin with a DOTA-tetraamide complex, as in the previous examples, the authors started with DOTA modified by a primary amine in the α-position of one pendant arm. This amine was then used to attach a peptide chain that could be cleaved by caspase-3. The amide NH in the α-position of DOTA could then be used as a CEST antennae in the same way we have seen amide protons used to generate CEST; however, in this case, its effectiveness was increased by incorporating a lanthanide with good shifting properties, Tm^{3+}, to shift the –NH resonance as far away from water as possible, thereby magnifying $\Delta\omega$. A sizable CEST effect was observed for a 25 mM solution of the complex arising from this single amide proton. However, after one hour in the presence of 48 nM caspase-3, most of the peptide had been cleaved, leaving behind a primary amino group that showed no CEST because proton exchange was too fast in this case. The advantage of this approach is that the agent does

Annu. Rev. Biomed. Eng. 2008.10:391-411. Downloaded from www.annualreviews.org
Access provided by Stanford University - Main Campus - Lane Medical Library on 03/16/15. For personal use only.

not require stoichiometric binding of a substrate but rather the CEST magnitude depends only on the amount of time the agent is exposed to the enzyme and the enzyme turnover number or activity. The disadvantage of course is that such systems are not reversible. Nevertheless, the idea of creating enzyme-specific CEST agents that are activated by enzymatic cleavage of a specific bond is a good one and should provide added value to the arsenal of biological information provided by MRI.

One further development in the field of PARACEST agents worthy of mention at this point is targeted CEST agents. Eu^{3+} and Yb^{3+} complexes of DOTA-tetraamide ligands having one or more benzyloxy ether substituents for binding to serum albumin (69–71) have been reported (72). A number of Gd^{3+}-based agents that bind to serum albumin have been observed to exhibit a decrease in the water-exchange rate upon binding (69, 70, 73, 74), and a similar effect was anticipated in the case of CEST agents. Quite unexpectedly, the rate of water exchange in these PARACEST agents was found to increase upon binding to serum albumin, likely due to catalysis of proton exchange by protein surface residues. This agent showed a detectable CEST effect at concentrations as low as 0.75 mM when bound to albumin. This may be too high to allow these complexes to function as fully fledged blood-pool agents, but there may be some potential advantages to using CEST agents in other targeted contrast media applications. Conventional T_1 or T_2 MR contrast agents require image collection pre- and postcontrast so any motion artifacts can contribute to registration errors. CEST contrast agents offer the opportunity to interleave images by acquiring each projection with and without presaturation. The two images can effectively be acquired at the same time, reducing the effects of motion on any resulting difference image. This is the great advantage of being able to turn a contrast medium on/off at will by turning on/off the presaturation pulse.

Sensitivity-Enhanced Chemical Exchange Saturation Transfer Agents

One of the current limitations of exogenous CEST agents is their relatively low sensitivity, typically requiring 1–10 mM of agent for detection. In an attempt to generate systems that are capable of operating at much lower detection limits and potentially image biologically relevant targets, several approaches to enhance the sensitivity of CEST agents have been proposed. Unlike Gd^{3+}-based contrast agents, which require complicated design features to improve relaxivity, CEST agents can be made more sensitive by simply increasing the number of exchangeable groups on the agent. Lanza, Wickline, and coworkers used perfluorocarbon-filled nanoparticles, modified with a targeting ligand, to deliver large payloads of Gd^{3+} to specific sites (75–77). Recently, this work was extended by using an appropriately functionalized Eu^{3+} complex (78) to load the particles with CEST agents (79). Upward of 10^5 chelates could be loaded onto the surface of each nanoparticle (77), thereby dramatically increasing the number of water-exchanging sites. This model PARACEST-loaded nanoparticle has been used to demonstrate that fibrin is easily detected in blood clots by CEST imaging (79).

Another strategy that has been used to increase the sensitivity of CEST agents is to encapsulate a small volume of highly shifted water within the core of a semipermeable membrane. Liposomes are ideal for this purpose because water exchange between the intra- versus extraliposomal compartments can be adjusted by varying the membrane composition. The first such example was a liposome in which the encapsulated water was shifted using the shift reagent, TmDOTMA (80). Tm^{3+} induced a significant downfield shift of the intraliposomal water, which could then be used as a CEST antenna. With an average liposome internal volume of 9.2×10^{-18} liters, the number of exchanging sites available for CEST is increased from 2 (for a single water molecule) to approximately 1.1×10^{10} in the liposome (**Figure 9*b***). This lowered the detection limit for a LIPOCEST

Annu. Rev. Biomed. Eng. 2008.10:391-411. Downloaded from www.annualreviews.org
Access provided by Stanford University - Main Campus - Lane Medical Library on 03/16/15. For personal use only.

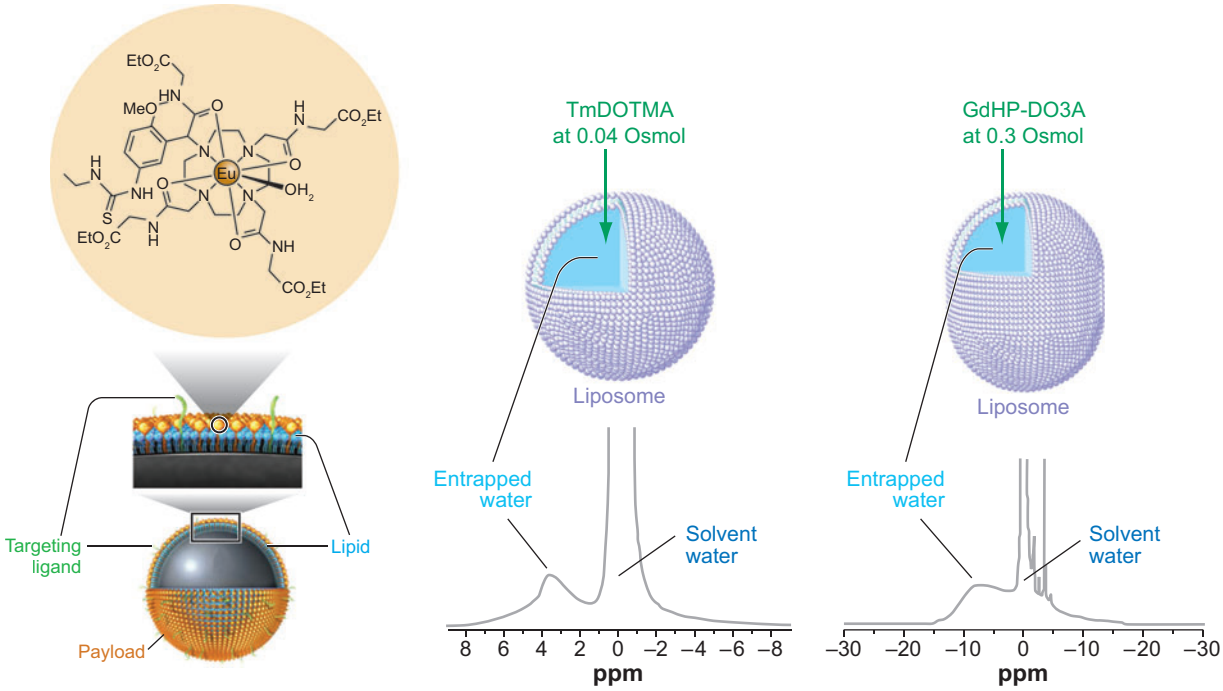


Figure 9

Three examples of ways to enhance CEST sensitivity. (*Left*) A perfluorocarbon-filled nanoparticle has a large number of CEST agents incorporated onto the surface of the nanoparticle. (*Middle*) A spherical liposome is filled with a high concentration of TmDOTMA, a reagent that exchanges water rapidly and shifts the average position of the intraliposomal water downfield by nearly 4 ppm. (*Right*) An osmotically shrunk liposome filled with a high concentration of GdHP-DO3A, a clinically approved agent, results in a highly shifted intraliposomal water peak due to bulk susceptibility differences between the two water compartments.

agent of this type to ~90 pM. This concept of using liposomes as CEST agents was extended recently by encapsulating the clinically approved contrast agent, ProHance (GdHP-DO3A), into liposomes (81). As indicated previously, the isotropic Gd^{3+} ion does not induce paramagnetic shifts, so no shift is observed for spherical liposomes containing the agent. However, the liposome shape can be altered through changes in osmolality; adding sodium chloride to the external water causes the liposome to expel water from its inner core, shrinking and deforming the liposomes into nonspherical shapes. By increasing the osmolality of the external solution in this way, the liposomes themselves become anisotropic and this results in a shift in the intraliposomal water resonance induced by the isotropic Gd^{3+} agent (**Figure 9*c***). Such liposomes can be considered a dual modality MR contrast agent because they act both as an effective CEST agent and as a T_1-shortening agent. At isotonic concentrations of sodium chloride (300 mOsmol), the liposomes were estimated to have a detection limit of ~30 nM by CEST imaging, a reasonable range to facilitate imaging of some cell receptors.

An alternative to increasing the number of small molecules with exchanging sites, e.g., water or metal-bound water, is to use a system that inherently has an extremely large number of exchangeable protons. Clearly this requires the use of macromolecular structures, although in certain applications, it is these very macromolecules that are of interest. One such example is the field of gene therapy, where the in vivo fate of therapeutic nucleic acids is of considerable interest.

Annu. Rev. Biomed. Eng. 2008.10:391-411. Downloaded from www.annualreviews.org
Access provided by Stanford University - Main Campus - Lane Medical Library on 03/16/15. For personal use only.

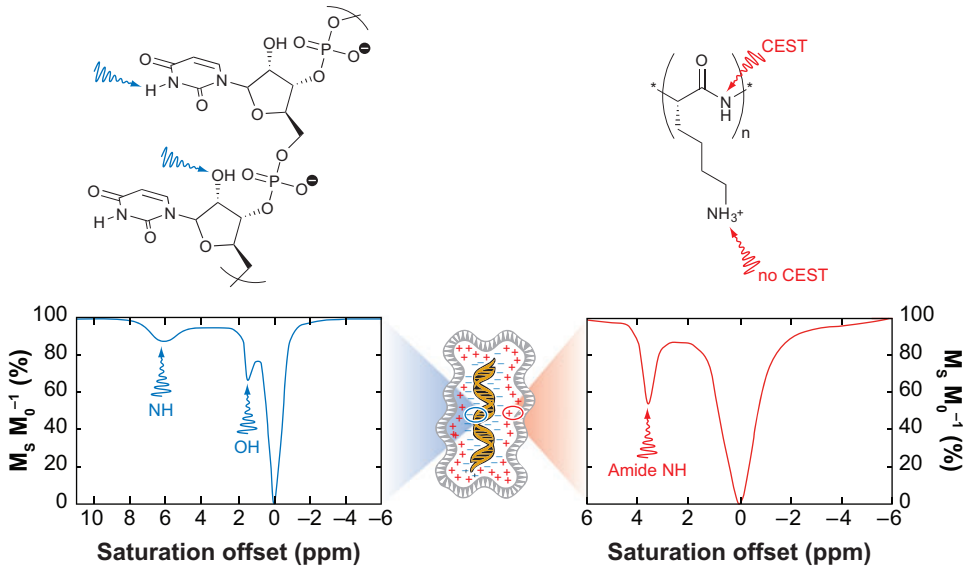


Figure 10

A schematic representation of a gene therapy bundle of nucleic acids and cationic polymers. The RNA strand poly(rU) (*left*) has two sites that give rise to CEST. The amide protons in cationic polymers, such as PLL (*right*), can also give rise to a CEST effect.

Nucleic acids are anionic polymers, and thus a delivery system is typically required to transport the nucleic acid polymer across the cell membrane and into the cell nucleus. Often viruses are used for this purpose, but nucleic acids may also be delivered by bundling them with cationic polymers. These cationic polymers may contain several kinds of exchanging protons; most contain a protonated amine, which exchanges protons too rapidly for CEST (34, 36), but a number of polymers used for gene therapy also contain amides. Polycations, such as poly-L-lysine (PLL) and starburst PAMAM dendrimers, contain amide groups and both examples have been considered for use in gene delivery (34, 36). A representative CEST spectrum of PLL is shown in **Figure 10**. The large numbers of amide groups present in these structures means that even at concentrations of 0.1 mM, the solvent water signal can be reduced in intensity by almost half. This opens the possibility of using a cationic delivery system as a method of tracking nucleic acids during gene therapy. However, a more direct approach to tracking gene delivery that would not limit the choice of delivery platform may be available. Snoussi et al. subsequently examined poly(rU) to see if any of the exchangeable groups present in the nucleic acid strand could be used to activate CEST contrast (26). Two protons in a strand of poly(rU) were found to give rise to CEST, the hydroxyl group of the ribose moiety and the NH of the uracil base. The CEST effects arising from these two protons are clearly identifiable in the CEST spectrum (**Figure 10**). Like the cationic polymers, large numbers of these protons are present in the nucleic acids used for gene therapy, so the detection limit for CEST agents of this type is likely to be quite low. Interestingly, the CEST effects from poly(rU) could be detected even with the nucleic acid bundled with a PAMAM dendrimer (26). Using the exchangeable pools of the nucleic acid as antennae, the dendrimer-poly(rU) bundle has proven even more sensitive than PLL, providing a comparable change in water signal intensity at just 10 μM.

Annu. Rev. Biomed. Eng. 2008.10:391-411. Downloaded from www.annualreviews.org
Access provided by Stanford University - Main Campus - Lane Medical Library on 03/16/15. For personal use only.

CONCLUDING REMARKS

Although Gd^{3+}-based T_1 agents are widely accepted both in basic research and in clinical medicine, the era of molecular medicine will require new information that is not typically provided by anatomical imaging. A new class of paramagnetic lanthanide complexes having slowly exchanging water molecules or other types of -NH or -OH protons provides a new avenue to introduce tissue contrast via a CEST mechanism. Because MR contrast provided by PARACEST agents is determined by chemical features, such as water molecule exchange or proton exchange, rather than by physical characteristics of the paramagnetic center, they offer new opportunities for creating responsive CEST agents capable of reporting significant biological or physiology events by MRI. Early studies have shown that exchange in these systems is easily modulated by simple chemical manipulation, so applying fundamental chemical principles, such as molecular recognition or self-assembly, to these systems should prove invaluable in creating novel systems for reporting molecular events by MRI.

SUMMARY POINTS

1. A new class of MRI contrast agents based on a chemical exchange saturation transfer (CEST) mechanism offers new opportunities for development of MR gene reporters and biologically responsive imaging agents.
2. CEST contrast can arise from multiple types of proton exchange groups, so molecules endogenous to tissues as well as exogenous agents are potential imaging candidates.
3. A large chemical shift difference between an exchanging proton site and solvent water ($\Delta\omega$) is highly advantageous for CEST contrast because the exchange site can be activated using a selective RF pulse without indirectly partially saturating water.
4. Paramagnetic lanthanide ions that induce large hyperfine shifted resonances in nearby protons are especially useful for CEST contrast because large $\Delta\omega$ values allow access to a wider variety of faster exchanging chemical systems. Lanthanide-based agents of this type are referred to as PARACEST agents.
5. Numerous biological and chemical approaches are being taken to enhance the sensitivity of both endogenous and exogenous CEST agents.

DISCLOSURE STATEMENT

The authors are not aware of any biases that might be perceived as affecting the objectivity of this review.

ACKNOWLEDGMENTS

This review was supported in part by grants from the National Institutes of Health (CA-115531, DK-058398 and RR-02584) and the Robert A. Welch Foundation (AT-584).

LITERATURE CITED

1. Caravan P, Ellison JJ, McMurry TJ, Lauffer RB. 1999. Gadolinium(III) chelates as MRI contrast agents: structure, dynamics, and applications. *Chem. Rev.* 99:2293–352

Annu. Rev. Biomed. Eng. 2008.10:391-411. Downloaded from www.annualreviews.org
Access provided by Stanford University - Main Campus - Lane Medical Library on 03/16/15. For personal use only.

2. Toth E, Merbach AE. 2001. *Chemistry of Contrast Agents in Medical Magnetic Resonance Imaging*. New York: Wiley
3. Kalman FK, Woods M, Caravan P, Jurek P, Spiller M, et al. 2007. Potentiometric and relaxometric properties of a gadolinium-based MRI contrast agent for sensing tissue pH. *Inorg. Chem.* 46:5260–70
4. Aime S, Barge A, Botta M, Howard JAK, Kataky R, et al. 1999. Dependence of the relaxivity and luminescence of gadolinium and europium amino-acid complexes on hydrogencarbonate and pH. *Chem. Commun.* 1999:1047–48
5. Lowe MP, Parker D. 2000. Controllable pH modulation of lanthanide luminescence by intramolecular switching of the hydration state. *Chem. Commun.* 2000:707–8
6. Aime S, Crich SG, Botta M, Giovenzana G, Palmisano G, Sisti M. 1999. A macromolecular Gd(III) complex as pH-responsive relaxometric probe for MRI applications. *Chem. Commun.* 1999:1577–78
7. Hovland R, Glogard C, Aasen AJ, Klaveness J. 2001. Gadolinium DO3A derivatives mimicking phospholipids; preparation and in vitro evaluation as pH responsive MRI contrast agents. *J. Chem. Soc., Perkin Trans.* 2:929–33
8. Glogard C, Hovland R, Fossheim SL, Aasen AJ, Klaveness J. 2000. Synthesis and physicochemical characterisation of new amphiphilic gadolinium DO3A complexes as contrast agents for MRI. *J. Chem. Soc., Perkin Trans.* 25:1047–52
9. Woods M, Kiefer GE, Bott S, Castillo-Muzquiz A, Eshelbrenner C, et al. 2004. Synthesis, relaxometric and photophysical properties of a new pH-responsive MRI contrast agent: the effect of other ligating groups on dissociation of a p-nitrophenolic pendant arm. *J. Am. Chem. Soc.* 126:9248–56
10. Hanaoka K, Kikuchi K, Urano Y, Nagano T. 2001. Selective sensing of zinc ions with a novel magnetic resonance imaging contrast agent. *J. Chem. Soc., Perkin Trans.* 2:1840–43
11. Li W-H, Fraser SE, Meade TJ. 1999. A calcium-sensitive magnetic resonance imaging contrast agent. *J. Am. Chem. Soc.* 121:1413–14
12. Li W-H, Parigi G, Fragai M, Luchinat C, Meade TJ. 2002. Mechanistic studies of a calcium-dependent MRI contrast agent. *Inorg. Chem.* 41:4018–24
13. Dickins RS, Gunnlaugsson T, Parker D, Peacock RD. 1998. Reversible anion binding in aqueous solution at a cationic heptacoordinate lanthanide center: selective bicarbonate sensing by time-delayed luminescence. *Chem. Commun.* 1998:1643–44
14. Dickins RS, Love CS, Puschmann H. 2001. Bidentate lactate binding in aqueous solution in a cationic, heptadentate lanthanide complex: an effective chiral derivatising agent. *Chem. Commun.* 2001:2308–9
15. **Moats RA, Fraser SE, Meade TJ. 1997. A "smart" magnetic resonance imaging agent that reports on specific enzymatic activity. *Angew. Chem. Int. Ed.* 36:726–28**
16. Anelli PL, Bertini I, Fragai M, Lattuada L, Luchinat C, Parigi G. 2000. Sulfonamide-functionalized gadolinium DTPA complexes as possible contrast agents for MRI: a relaxometric investigation. *Eur. J. Inorg. Chem.* 2000(4):625–30
17. Nivorozhkin AL, Kolodziej AF, Caravan P, Greenfield MT, Lauffer RB, McMurry TJ. 2001. Enzyme-activated Gd^{3+} magnetic resonance imaging contrast agents with a prominent receptor-induced magnetization enhancement. *Angew. Chem. Int. Ed.* 40:2903–6
18. De Leon-Rodriguez LM, Ortiz A, Weiner AL, Zhang S, Kovacs Z, et al. 2002. Magnetic resonance imaging detects a specific peptide-protein binding event. *J. Am. Chem. Soc.* 124:3514–15
19. Garcia-Martin ML, Martinez GV, Raghunand N, Sherry AD, Zhang S, Gillies RJ. 2006. High resolution pH imaging of rat glioma using pH-dependent relaxivity. *Magn. Reson. Med.* 55:309–15
20. Raghunand N, Howison C, Sherry AD, Zhang S, Gillies RJ. 2003. Renal and systemic pH imaging by contrast-enhanced MRI. *Magn. Reson. Med.* 49:249–57
21. McConnell HM, Thompson DD. 1957. Molecular transfer of nonequilibrium nuclear spin magnetization. *J. Chem. Phys.* 26:958–59

A seminal paper that first brought the idea of responsive contrast agents to light.

Annu. Rev. Biomed. Eng. 2008.10:391-411. Downloaded from www.annualreviews.org
Access provided by Stanford University - Main Campus - Lane Medical Library on 03/16/15. For personal use only.

22. McConnell HM, Thompson DD. 1959. Molecular transfer of nonequilibrium nuclear spin magnetization. *J. Chem. Phys.* 31:85–88
23. Forsén S, Hoffman RA. 1963. Study of moderately rapid chemical exchange reactions by means of nuclear magnetic resonance double resonance. *J. Chem. Phys.* 39:2892–901
24. Woods M, Woessner DE, Sherry AD. 2006. Paramagnetic lanthanide complexes as PARACEST agents for medical imaging. *Chem. Soc. Rev.* 35:500–11
25. Woessner DE, Zhang S, Merritt M, Sherry AD. 2005. Numerical solution of the Bloch equations provides insights into the optimum design of PARACEST agents for MRI. *Magn. Reson. Med.* 53:790–99
26. Snoussi K, Bulte JWM, Gueron M, van Zijl PCM. 2003. Sensitive CEST agents based on nucleic acid imino proton exchange: detection of poly(rU) and of a dendrimer-poly(rU) model for nucleic acid delivery and pharmacology. *Magn. Reson. Med.* 49:998–1005
27. Meaney JF. 2003. Magnetic resonance angiography of the peripheral arteries: current status. *Eur. Radiol.* 13:836–52
28. Eiberg JP, Lundorf E, Thomsen C, Schroeder TV. 2001. Peripheral vascular surgery and magnetic resonance arteriography—a review. *Eur. J. Vasc. Endovasc. Surg.* 22:396–402
29. Bhakoo K, Chapon C, Jackson J, Jones W. 2006. Application of MRI to cell tracking. In *Modern Magnetic Resonance*, ed. G Webb, pp. 873–84. New York: Springer
30. Rogers WJ, Meyer CH, Kramer CM. 2006. Technology insight: in vivo cell tracking by use of MRI. *Nat. Clin. Pract. Cardiovasc. Med.* 3:554–62
31. Arbab AS, Liu W, Frank JA. 2006. Cellular magnetic resonance imaging: current status and future prospects. *Expert Rev. Med. Devices* 3:427–39
32. Bulte JWM, Kraitchman DL. 2004. Monitoring cell therapy using iron oxide MR contrast agents. *Curr. Pharm. Biotechnol.* 5:567–84
33. Gilad AA, McMahon MT, Walczak P, Winnard PT Jr, Raman V, et al. 2007. Artificial reporter gene providing MRI contrast based on proton exchange. *Nat. Biotech.* 25:217–19
34. Goffeney N, Bulte JWM, Duyn J, Bryant LH Jr, van Zijl PCM. 2001. Sensitive NMR detection of cationic-polymer-based gene delivery systems using saturation transfer via proton exchange. *J. Am. Chem. Soc.* 123:8628–29
35. van Zijl PCM, Jones CK, Ren J, Malloy CR, Sherry AD. 2007. MRI detection of glycogen in vivo by using chemical exchange saturation transfer imaging (glycoCEST). *Proc. Natl. Acad. Sci. USA* 104:4359–64
36. McMahon MT, Gilad AA, Zhou J, Sun PZ, Bulte JWM, van Zijl PCM. 2006. Quantifying exchange rates in chemical exchange saturation transfer agents using the saturation time and saturation power dependencies of the magnetization transfer effects on the magnetic resonance imaging signal (QUEST and QUESP): pH calibration for poly-L-lysine and a starburst dendrimer. *Magn. Reson. Med.* 55:836–47
37. Jones CK, Schlosser MJ, van Zijl PCM, Pomper MG, Golay X, Zhou J. 2006. Amide proton transfer imaging of human brain tumors at 3T. *Magn. Reson. Med.* 56:585–92
38. Zhou J, Payen J-F, Wilson DA, Traystman RJ, van Zijl PCM. 2003. Using the amide proton signals of intracellular proteins and peptides to detect pH effects in MRI. *Nat. Med.* 9:1085–90
39. Schroeder L, Lowery TJ, Hilty C, Wemmer DE, Pines A. 2006. Molecular imaging using a targeted magnetic resonance hyperpolarized biosensor. *Science* 314:446–49
40. Oros AM, Shah NJ. 2004. Hyperpolarized xenon in NMR and MRI. *Phys. Med. Biol.* 49:R105–53
41. Bouchiat MA, Carver TR, Varnum CM. 1960. Nuclear polarization in ^{3}He gas induced by optical pumping and dipolar exchange. *Phys. Rev. Lett.* 5:373–75
42. Ward KM, Aletras AH, Balaban RS. 2000. A new class of contrast agents for MRI based on proton chemical exchange dependent saturation transfer (CEST). *J. Magn. Reson.* 143:79–87
43. Ward KM, Balaban RS. 2000. Determination of pH using water protons and chemical exchange dependent saturation transfer (CEST). *Magn. Reson. Med.* 44:799–802
44. Powell DH, Ni Dhubhghaill OM, Pubanz D, Helm L, Lebedev YS, et al. 1996. High-pressure NMR kinetics. Part 74. Structural and dynamic parameters obtained from ^{17}O NMR, EPR, and NMRD studies

A useful review for a more basic, and also more thorough, discussion of the theory behind CEST.

Presents a numerical solution of the Bloch equations used to fit CEST spectra.

Introduced the idea of using exogenous compounds as CEST agents for MRI.

Annu. Rev. Biomed. Eng. 2008.10:391-411. Downloaded from www.annualreviews.org
Access provided by Stanford University - Main Campus - Lane Medical Library on 03/16/15. For personal use only.

of monomeric and dimeric Gd^{3+} complexes of interest in magnetic resonance imaging: an integrated and theoretically self-consistent approach. *J. Am. Chem. Soc.* 118:9333–46

This important observation opened the way for the development of slow water-exchange agents as imaging agents.

45. Aime S, Barge A, Botta M, De Sousa AS, Parker D. 1998. Direct NMR spectroscopic observation of a lanthanide-coordinated water molecule whose exchange rate is dependent on the conformation of the complexes. *Angew. Chem. Int. Ed.* 37:2673–75

46. Aime S, Barge A, Botta M, Parker D, De Sousa AS. 1997. Prototropic vs whole water exchange contributions to the solvent relaxation enhancement in the aqueous solution of a cationic Gd^{3+} macrocyclic complex. *J. Am. Chem. Soc.* 119:4767–68

47. Aime S, Barge A, Bruce JI, Botta M, Howard JAK, et al. 1999. NMR, relaxometric, and structural studies of the hydration and exchange dynamics of cationic lanthanide complexes of macrocyclic tetraamide ligands. *J. Am. Chem. Soc.* 121:5762–71

The first demonstration of a paramagnetic CEST agent as a MRI agent.

48. Zhang S, Winter P, Wu K, Sherry AD. 2001. A novel europium(III)-based MRI contrast agent. *J. Am. Chem. Soc.* 123:1517–18

49. Zhang S, Wu K, Biewer MC, Sherry AD. 2001. ^{1}H and ^{17}O NMR detection of a lanthanide-bound water molecule at ambient temperatures in pure water as solvent. *Inorg. Chem.* 40:4284–90

50. Bleaney B. 1972. Nuclear magnetic resonance shifts in solution due to lanthanide ions. *J. Magn. Reson.* 8:91–100

51. Bleaney B, Dobson CM, Levine BA, Martin RB, Williams RJP, Xavier AV. 1972. Origin of lanthanide nuclear magnetic resonance shifts and their uses. *J. Chem. Soc. Chem. Commun.* 1972:791–93

52. Mironov VS, Galyametdinov YG, Ceulemans A, Gorller-Walrand C, Binnemans K. 2002. Room-temperature magnetic anisotropy of lanthanide complexes. A model study for various coordination polyhedra. *J. Chem. Phys.* 116:4673–85

Introduced the term PARACEST to describe paramagnetic CEST agents.

53. Zhang S, Merritt M, Woessner DE, Lenkinski RE, Sherry AD. 2003. PARACEST agents: modulating MRI contrast via water proton exchange. *Acc. Chem. Res.* 36:783–90

54. Zhang S, Wu K, Sherry AD. 2002. Unusually sharp dependence of water exchange rate versus lanthanide ionic radii for a series of tetraamide complexes. *J. Am. Chem. Soc.* 124:4226–27

55. Woods M, Woessner DE, Zhao P, Pasha A, Yang M-Y, et al. 2006. Europium(III) macrocyclic complexes with alcohol pendant groups as chemical exchange saturation transfer agents. *J. Am. Chem. Soc.* 128:10155–62

56. Zhang S, Michaudet L, Burgess S, Sherry AD. 2002. The amide protons of an ytterbium(III) dota tetraamide complex act as efficient antennae for transfer of magnetization to bulk water. *Angew. Chem. Int. Ed.* 41:1919–21

57. Terreno E, Castelli DD, Cravotto G, Milone L, Aime S. 2004. Ln(III)-DOTAMGly complexes: a versatile series to assess the determinants of the efficacy of paramagnetic chemical exchange saturation transfer agents for magnetic resonance imaging applications. *Investig. Radiol.* 39:235–43

58. Aime S, Barge A, Castelli DD, Fedeli F, Mortillaro A, et al. 2002. Paramagnetic Lanthanide(III) complexes as pH-sensitive chemical exchange saturation transfer (CEST) contrast agents for MRI applications. *Magn. Reson. Med.* 47:639–48

59. Yoo B, Pagel MD. 2007. Peptidyl molecular imaging contrast agents using a new solid-phase peptide synthesis approach. *Bioconjug. Chem.* 18:903–11

60. Yoo B, Pagel MD. 2006. A PARACEST MRI contrast agent to detect enzyme activity. *J. Am. Chem. Soc.* 128:14032–33

61. Zhang S, Malloy CR, Sherry AD. 2005. MRI thermometry based on PARACEST agents. *J. Am. Chem. Soc.* 127:17572–73

62. Wegh RT, Pikkemaat JA, Willard NP. 2006. *WO Patent No. 2006-IB51237, 2006114739*

63. Willard NP, Wegh RT, Pikkemaat JA, Gruell H. 2006. *WO Patent No. 2006-IB51235, 2006114738*; Pikkemaat JA, Wegh RT, Lamerichs R, van de Molengraaf RA, Langereis S, et al. 2007. Dendritic PARACEST contrast agents for magnetic resonance imaging. *Contrast Media Mol. Imaging* 2:229–39

64. Trokowski R, Zhang S, Sherry AD. 2004. Cyclen-based phenylboronate ligands and their Eu^{3+} complexes for sensing glucose by MRI. *Bioconjug. Chem.* 15:1431–40

65. Zhang S, Trokowski R, Sherry AD. 2003. A paramagnetic CEST agent for imaging glucose by MRI. *J. Am. Chem. Soc.* 125:15288–89

Annu. Rev. Biomed. Eng. 2008.10:391-411. Downloaded from www.annualreviews.org
Access provided by Stanford University - Main Campus - Lane Medical Library on 03/16/15. For personal use only.

66. Trokowski R, Ren JM, Kalman FK, Sherry AD. 2005. Selective sensing of zinc ions with a PARACEST contrast agent. *Angew. Chem. Int. Ed.* 44:6920–23
67. Micskei K, Helm L, Brucher E, Merbach AE. 1993. Oxygen-17 NMR study of water exchange on gadolinium polyaminopolyacetates $[Gd(DTPA)(H_2O)]^{2-}$ and $[Gd(DOTA)(H_2O)]^{-}$ related to NMR imaging. *Inorg. Chem.* 32:3844–50
68. Ratnakar J, Woods M, Lubag AJM, Kovacs Z, Sherry AD. 2008. Modulation of water exchange in europium(III) DOTA-tetraamide complexes via electronic substituent effects. *J. Am. Chem. Soc.* 130:6–7
69. Aime S, Botta M, Fasano M, Crich SG, Terreno E. 1996. Gd(III) complexes as contrast agents for magnetic resonance imaging: a proton relaxation enhancement study of the interaction with human serum albumin. *J. Biol. Inorg. Chem.* 1:312–19
70. Aime S, Chiaussa M, Digilio G, Gianolio E, Terreno E. 1999. Contrast agents for magnetic resonance angiographic applications: ^{1}H and ^{17}O NMR relaxometric investigations on two gadolinium(III) DTPA-like chelates endowed with high binding affinity to human serum albumin. *J. Biol. Inorg. Chem.* 4:766–74
71. Hovland R, Aasen AJ, Klaveness J. 2003. Preparation and in vitro evaluation of $GdDOTA-(BOM)_4$; a novel angiographic MRI contrast agent. *Org. Biomol. Chem.* 1:1707–10
72. Ali M, Woods M, Suh E, Kovacs Z, Tircsó G, et al. 2007. Albumin-binding PARACEST agents. *J. Biol. Inorg. Chem.* 12:855–65
73. Caravan P, Cloutier NJ, Greenfield MT, McDermid SA, Dunham SU, et al. 2002. The interaction of MS-325 with human serum albumin and its effect on proton relaxation rates. *J. Am. Chem. Soc.* 124:3152–62
74. Zech SG, Eldredge HB, Lowe MP, Caravan P. 2007. Protein binding to lanthanide(III) complexes can reduce the water exchange rate at the lanthanide. *Inorg. Chem.* 46:3576–84
75. Winter PM, Cai KJ, Chen J, Adair CR, Kiefer GE, et al. 2006. Targeted PARACEST nanoparticle contrast agent for the detection of fibrin. *Magn. Reson. Med.* 56:1384–88
76. Winter PM, Caruthers SD, Kassner A, Harris TD, Chinen LK, et al. 2003. Molecular imaging of angiogenesis in nascent vx-2 rabbit tumors using a novel $a_n b_3$-targeted nanoparticle and 1.5 Tesla magnetic resonance imaging. *Cancer Res.* 63:5838–43
77. Flacke S, Fischer S, Scott MJ, Fuhrhop RJ, Allen JS, et al. 2001. Novel MRI contrast agent for molecular imaging of fibrin implications for detecting vulnerable plaques. *Circulation* 104:1280–85
78. Adair C, Woods M, Zhao PY, Pasha A, Winters PM, et al. 2007. Spectral properties of a bifunctional PARACEST europium chelate: an intermediate for targeted imaging applications. *Contrast Media Mol. Imaging* 2:55–58
79. Schmieder AH, Winter PM, Caruthers SD, Harris TD, Williams TA, et al. 2005. Molecular MR imaging of melanoma angiogenesis with $a_n b_3$-targeted paramagnetic nanoparticles. *Magn. Reson. Med.* 53:621–27
80. Aime S, Castelli DD, Terreno E. 2005. Highly sensitive MRI chemical exchange saturation transfer agents using liposomes. *Angew. Chem. Int. Ed.* 44:5513–15
81. Aime S, Castelli DD, Lawson D, Terreno E. 2007. Gd-loaded liposomes as T_1, susceptibility, and CEST agents, all in one. *J. Am. Chem. Soc.* 129:2430–31

RELATED RESOURCES

Owing to the relative youth of this field of research, a wide range of background texts are not yet available. For more information, the reader may wish to consult Modo MJM & Bulte JWM. 2007. *Molecular and Cellular MR Imaging.* Boca Raton, FL: CRC Press

Annu. Rev. Biomed. Eng. 2008.10:391-411. Downloaded from www.annualreviews.org
Access provided by Stanford University - Main Campus - Lane Medical Library on 03/16/15. For personal use only.

Annual Review of Biomedical Engineering
Volume 10, 2008

Contents

Fluorescence Proteins, Live-Cell Imaging, and Mechanobiology: Seeing Is Believing
Yingxiao Wang, John Y.-J. Shyy, and Shu Chien 1

Catch Bonds in Adhesion
Wendy Thomas 39

Current and Future Considerations in the Use of Mechanical Circulatory Support Devices
Marc A. Simon, John Watson, J. Timothy Baldwin, William R. Wagner, and Harvey S. Borovetz 59

Injury Biomechanics and Child Abuse
Mary Clyde Pierce and Gina Bertocci 85

Point-of-Care Diagnostics for Global Health
Paul Yager, Gonzalo J. Domingo, and John Gerdes 107

Bacterial Quorum Sensing: Signals, Circuits, and Implications for Biofilms and Disease
Arul Jayaraman and Thomas K. Wood 145

Molecular Engineering of Viral Gene Delivery Vehicles
David V. Schaffer, James T. Koerber, and Kwang-il Lim 169

Targeted Drug-Aerosol Delivery in the Human Respiratory System
C. Kleinstreuer, Z. Zhang, and J.F. Donohue 195

Intracranial and Abdominal Aortic Aneurysms: Similarities, Differences, and Need for a New Class of Computational Models
J.D. Humphrey and C.A. Taylor 221

Ultralow-Power Electronics for Biomedical Applications
Anantha P. Chandrakasan, Naveen Verma, and Denis C. Daly 247

Neural Stimulation and Recording Electrodes
Stuart F. Cogan 275

Fluorescence Imaging of Membrane Dynamics
Jay T. Groves, Raghuveer Parthasarathy, and Martin B. Forstner 311

Psychophysical Evaluation for Visual Prosthesis
Gislin Dagnelie 339

Quantitative Imaging of Musculoskeletal Tissue
Peter Augat and Felix Eckstein 369

Chemical Exchange Saturation Transfer Contrast Agents for Magnetic Resonance Imaging
A. Dean Sherry and Mark Woods 391

Indexes

Cumulative Index of Contributing Authors, Volumes 1–10 413

Cumulative Index of Chapter Titles, Volumes 1–10 417

Errata

An online log of corrections to *Annual Review of Biomedical Engineering* articles may be found at http://bioeng.annualreviews.org/

Annu. Rev. Biomed. Eng. 2008.10:391-411. Downloaded from www.annualreviews.org
Access provided by Stanford University - Main Campus - Lane Medical Library on 03/16/15. For personal use only.

ANNUAL REVIEWS

It's about time. Your time. It's time well spent.

New From Annual Reviews:

Annual Review of Statistics and Its Application

Volume 1 • Online January 2014 • http://statistics.annualreviews.org

Editor: **Stephen E. Fienberg,** *Carnegie Mellon University*

Associate Editors: **Nancy Reid,** *University of Toronto*

Stephen M. Stigler, *University of Chicago*

The *Annual Review of Statistics and Its Application* aims to inform statisticians and quantitative methodologists, as well as all scientists and users of statistics about major methodological advances and the computational tools that allow for their implementation. It will include developments in the field of statistics, including theoretical statistical underpinnings of new methodology, as well as developments in specific application domains such as biostatistics and bioinformatics, economics, machine learning, psychology, sociology, and aspects of the physical sciences.

Complimentary online access to the first volume will be available until January 2015.

TABLE OF CONTENTS:

- *What Is Statistics?* Stephen E. Fienberg
- *A Systematic Statistical Approach to Evaluating Evidence from Observational Studies,* David Madigan, Paul E. Stang, Jesse A. Berlin, Martijn Schuemie, J. Marc Overhage, Marc A. Suchard, Bill Dumouchel, Abraham G. Hartzema, Patrick B. Ryan
- *The Role of Statistics in the Discovery of a Higgs Boson,* David A. van Dyk
- *Brain Imaging Analysis,* F. DuBois Bowman
- *Statistics and Climate,* Peter Guttorp
- *Climate Simulators and Climate Projections,* Jonathan Rougier, Michael Goldstein
- *Probabilistic Forecasting,* Tilmann Gneiting, Matthias Katzfuss
- *Bayesian Computational Tools,* Christian P. Robert
- *Bayesian Computation Via Markov Chain Monte Carlo,* Radu V. Craiu, Jeffrey S. Rosenthal
- *Build, Compute, Critique, Repeat: Data Analysis with Latent Variable Models,* David M. Blei
- *Structured Regularizers for High-Dimensional Problems: Statistical and Computational Issues,* Martin J. Wainwright
- *High-Dimensional Statistics with a View Toward Applications in Biology,* Peter Bühlmann, Markus Kalisch, Lukas Meier
- *Next-Generation Statistical Genetics: Modeling, Penalization, and Optimization in High-Dimensional Data,* Kenneth Lange, Jeanette C. Papp, Janet S. Sinsheimer, Eric M. Sobel
- *Breaking Bad: Two Decades of Life-Course Data Analysis in Criminology, Developmental Psychology, and Beyond,* Elena A. Erosheva, Ross L. Matsueda, Donatello Telesca
- *Event History Analysis,* Niels Keiding
- *Statistical Evaluation of Forensic DNA Profile Evidence,* Christopher D. Steele, David J. Balding
- *Using League Table Rankings in Public Policy Formation: Statistical Issues,* Harvey Goldstein
- *Statistical Ecology,* Ruth King
- *Estimating the Number of Species in Microbial Diversity Studies,* John Bunge, Amy Willis, Fiona Walsh
- *Dynamic Treatment Regimes,* Bibhas Chakraborty, Susan A. Murphy
- *Statistics and Related Topics in Single-Molecule Biophysics,* Hong Qian, S.C. Kou
- *Statistics and Quantitative Risk Management for Banking and Insurance,* Paul Embrechts, Marius Hofert

Access this and all other Annual Reviews journals via your institution at www.annualreviews.org.

ANNUAL REVIEWS | Connect With Our Experts

Tel: 800.523.8635 (US/CAN) | Tel: 650.493.4400 | Fax: 650.424.0910 | Email: service@annualreviews.org

Annu. Rev. Biomed. Eng. 2008.10:391-411. Downloaded from www.annualreviews.org
Access provided by Stanford University - Main Campus - Lane Medical Library on 03/16/15. For personal use only.

MAGNETIC RESONANCE IN MEDICINE **14,** 68–78 (1990)

Oxygenation-Sensitive Contrast in Magnetic Resonance Image of Rodent Brain at High Magnetic Fields

SEIJI OGAWA, TSO-MING LEE, ASHA S. NAYAK,* AND PAUL GLYNN

AT&T Bell Laboratories, Murray Hill, New Jersey 07974

Received November 30, 1988; accepted June 20, 1989

At high magnetic fields (7 and 8.4 T), water proton magnetic resonance images of brains of live mice and rats under pentobarbital anesthetization have been measured by a gradient echo pulse sequence with a spatial resolution of 65 × 65-μm pixel size and 700-μm slice thickness. The contrast in these images depicts anatomical details of the brain by numerous dark lines of various sizes. These lines are absent in the image taken by the usual spin echo sequence. They represent the blood vessels in the image slice and appear when the deoxyhemoglobin content in the red cells increases. This contrast is most pronounced in an anoxy brain but not present in a brain with diamagnetic oxy or carbon monoxide hemoglobin. The local field induced by the magnetic susceptibility change in the blood due to the paramagnetic deoxyhemoglobin causes the intra voxel dephasing of the water signals of the blood and the surrounding tissue. This oxygenation-dependent contrast is appreciable in high field images with high spatial resolution.
© 1990 Academic Press, Inc.

INTRODUCTION

Magnetic resonance imaging of tissue water in brain provides anatomical details of high image quality which are capable of distinguishing a variety of pathological conditions. This high image quality is achieved only in water proton images. Water is the most abundant compound in most biological tissues and the proton is the nucleus with the highest NMR sensitivity. On the other hand, the water proton concentration, around 75 *M* in tissue, is so high that the resonance signal is insensitive to normal metabolic reactions which involve reactants at concentrations of a few m*M*. Therefore, direct reflection of physiological events in water images has not been observed. If proton MRI from water is to be used for physiological studies of brain, then some indirect effects of physiology must occur. Regional blood flow measurements (*1*) with water images can be one such example since the metabolic activity of brain tissue is well correlated with the oxygen supply and hence to the blood flow.

In this article some new observations of oxygenation level-sensitive contrast in water images are presented as another example of such indirect reflection of physiology. Using high field instruments, we obtained very high spatial resolution brain images with high contrast which are capable of detecting blood vessels as small as 50 to 100 μm in diameter. Such images may provide a means to monitor regional brain activity

* From Department of Biochemistry, Florida State University, Tallahassee, FL 32306 and on AT&T Bell Laboratories Summer Research program (1988).

0740-3194/90 $3.00

Copyright © 1990 by Academic Press, Inc.
All rights of reproduction in any form reserved.

in situ in a similar way as positron emission tomography (*2*) is used to map regional oxygen consumption rates in the brain. With a similar objective oxygen level mapping by ^{19}F magnetic resonance imaging of a blood substitute in cat brain has been reported (*3*).

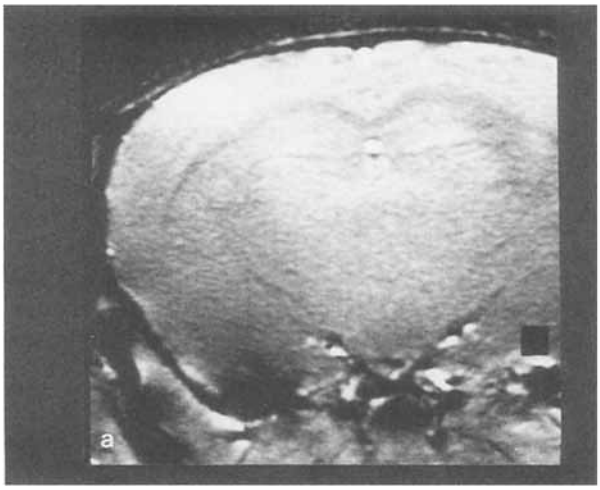
MATERIALS AND METHODS

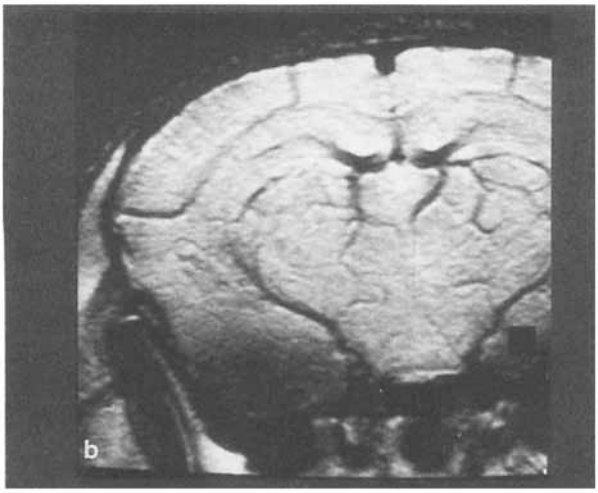
High resolution images of rodent brains were measured both with a microimaging apparatus attached to a Bruker 360 MHz wide bore spectrometer with a vertical bore magnet and with a 300 MHz imaging spectrometer with a 183-mm horizontal bore magnet (Spectroscopy Imaging Systems Inc.). The field gradients used were up to 4 to 5 G/cm and the slice thickness was 700 μm. The pixel size in the slice plane was 65×65 μm in the data acquisition. In order to get the sensitivity of the probe as high as possible, 15 to 20-mm-diameter saddle coils and surface coils were used. The width of the water peak was 20 to 30 Hz after shimming on a 5-mm-thick slice.

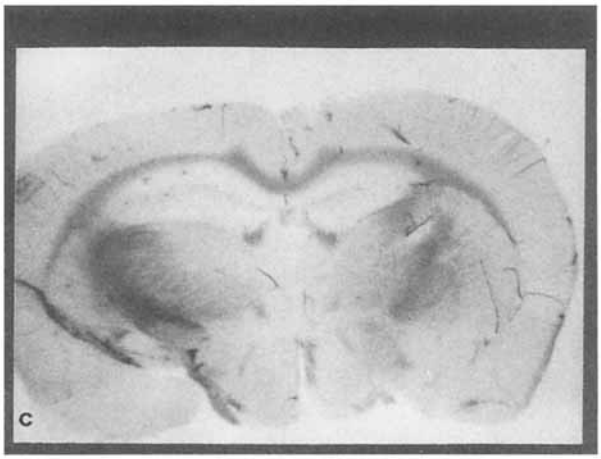
A/J mice (Jackson Laboratory, Bar Harbor, ME) and Sprague–Dawley rats (local commercial source) were anesthetized with interperitoneal injections of pentobarbital (50 mg/kg) and in most cases with an additional 25 mg/kg of the drug subcutaneously. With the vertical magnet (360 MHz), a mouse or a rat (85 to 100 g) held in a vessel was placed upside down in the probe. The heart rate of the animal was monitored by attaching wire electrodes near the chest. A typical heart rate of an anesthetized mouse was 300 to 340 beats/min. When the animal was placed in the probe and breathing 100% oxygen, the rate was near 300 beats/min and when breathing air it was around 250 beats/min. Although the mouse was breathing without assistance, the oxygen uptake in the lungs seemed to be rather inefficient under this anesthetic condition. When the mouse was breathing air, the image of the carotid arteries had much lower signal intensities than the image of the mouse breathing 100% oxygen. This indicated a low oxygenation level of the blood as one would expect from the loss of redness in skin color observed in the mouse breathing air. Although we did not measure the oxygenation level of the circulating blood in these animals, the anesthetizing condition, dependent on such factors as the type of drug and its dosage, seemed to have a strong influence on the oxygenation level in these murine animals. The signal acquisition was not synchronized to the heart beat.

RESULTS

The effect of the blood oxygenation on the mouse brain image is shown in Fig. 1. The images, coronal slices of a mouse head, were obtained with a simple gradient echo pulse sequence. The main magnetic field was normal to these slice image planes. When the mouse, anesthetized with pentobarbital, was breathing 100% oxygen with a heart rate of 280 beats/min, the image (Fig. 1a) showed some features of the brain tissue organization but the contrast was quite poor. However, dramatic changes in the brain image (Fig. 1b) were observed when the oxygen content in the breathing gas was reduced to 20% (the heart rate was 235 beats/min). This change in the contrast was completely reversible. Many dark lines appeared in the image. The prominent ones were along the boundaries of the organizational elements of the brain. Optical microscopy of fixed slices prepared from an excised brain showed many blood


a


b


c

vessels in these boundaries. In the region of the cerebral cortex, numerous small blood vessels were seen in the photograph of a fixed slice (Fig. 1c). Correspondingly in these coronal slice images (Fig. 1b and also Fig. 3a described later) there were many narrow dark lines running perpendicular to the arachnoid surface in the cerebral cortex. When the content of oxygen in the breathing gas was incrementally changed from 50 to 20% in experiments at 360 MHz, the contrast of these images changed gradually. Similar images of rat and mouse brains were also obtained with the 7 T horizontal bore magnet where these animals were placed in their natural position relative to the gravitational field.

The contrast of these images was dependent on the length of the echo time in the image acquisition sequence, especially when the oxygen supply was low. With a longer echo time, the widths of some dark lines and the size of dark regions became enlarged. This indicated that there was a distribution of the signal decay time around these dark regions. In Fig. 2, plots of signal intensities at various locations in such images as shown in Figs. 1a and 1b vs the echo time are shown. Two of these locations in the images were in the hippocampal region (*4*), one was on the dark line (between CA1 and CA3) and the other was in the light part (CA1). A spot in the cerebral cortex was on one of the dark lines. The signal decay rates (the slopes of the plots) were strongly dependent on the oxygenation in the dark regions seen in Fig. 1b and the signal from cerebral spinal fluid, as identified by a long T_2 value, was insensitive to the blood oxygenation.

As a further test for determining the cause of the contrast enhancement, an anesthetized mouse was sacrificed by keeping it in a carbon monoxide atmosphere until the color of the lips turned pink and its heart stopped. Most of the contrast seen in Fig. 1b disappeared from the image of the brain. On the other hand, when a mouse was left under an anoxic condition, the image contrast (Fig. 3a) was very high. In this case the flow of the blood was absent and the level of blood oxygenation was presumably very low as the purple color of the lips indicated. These observations strongly indicate that the image contrast was caused by the magnetic susceptibility difference between the blood with paramagnetic deoxyhemoglobin and the surrounding tissues. With diamagnetic oxy or carbon monoxy hemoglobin, the contrast was absent.

There was a striking difference in the image contrast between the gradient echo image (Fig. 3a) and the spin echo image (Fig. 3b) both with a 10 ms echo time at the same slice location in the brain of a dead mouse. The dark lines seen in the gradient echo image (Fig. 3a) were mostly absent in the spin echo image and only faint lines were recognizable at their corresponding locations. Since the process of "time reversal" by the 180° pulse in the spin echo sequence prevented the signal decay during

---

FIG. 1. Coronal slice images of a mouse brain at 360 MHz (a, b). These were gradient echo images and the slice plane was perpendicular to the B_0 field. The pixel size and the slice thickness were 65 × 65 and 700 μm at the data acquisition. The black square in the image is 500 × 500 μm in size. These images were acquired with a 6 ms echo time and a repetition time of 1 s with 256 phase encoding steps. The signals were accumulated four times. (a) Breathing 100% oxygen with the heart rate of 280 beats/min. (b) Breathing air with the heart rate of 235 beats/min. (c) A fixed slice (300 μm thick) of an exercised mouse brain. Most of the dark lines corresponded to blood vessels except those fibrous structures in the region of the thalamus nucleus.

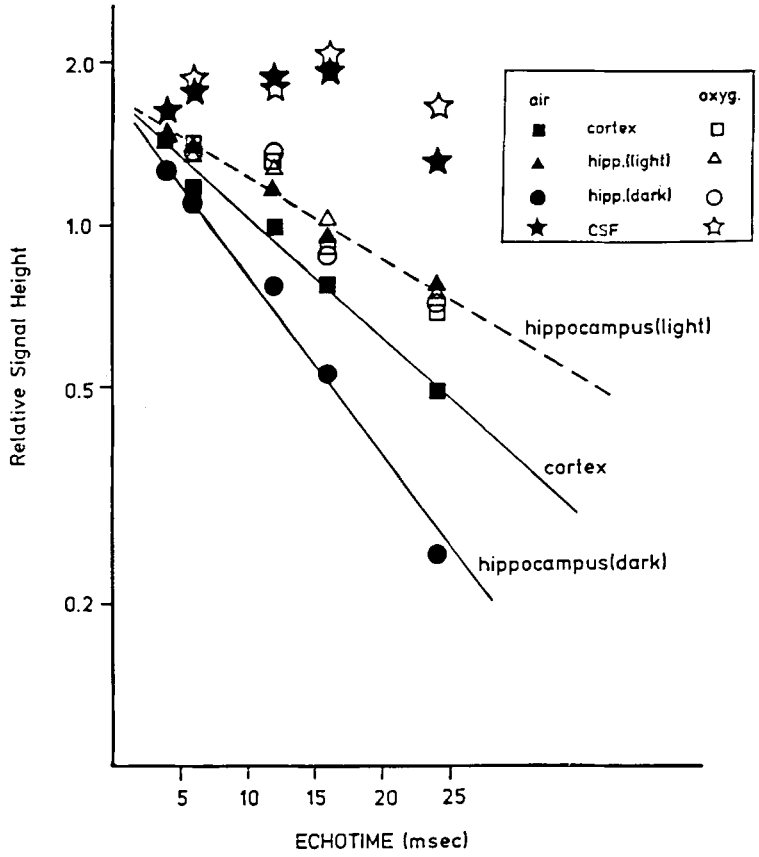


FIG. 2. Signal decays as a function of echo time in gradient echo images of a mouse brain. The open and the closed symbols are used for the image signals of a mouse breathing 100% oxygen and 20% oxygen, respectively. Various symbols are for those spots selected at a dark region between CA1 and CA3 (○) and a light region in CA1 (△) of the hippocampal region (4). Other symbols in this figure are from a dark line in the cerebral cortex (□) and at a region with cerebral spinal fluid (☆) in such slice images as the one shown in Fig. 1b.

the echo time, the cause of the contrast could not be a dynamic phenomenon such as blood flow or water diffusion (the shortening of T_2 of blood water due to the red cells with deoxyhemoglobin) (*5*), but a static phenomenon such as chemical-shift difference or field inhomogeneity. Furthermore, the signal that decayed quickly and gave these dark lines in the gradient echo image was not all coming from the water in blood vessels. The contribution of the blood water was only a small part of it (see Discussion). Otherwise, the spin echo image would have had the same contrast.

It is well known that upon deoxygenation the magnetic susceptibility of blood changes and the T_2 value of blood water becomes short (*6, 7*). We examined those values at the 360 MHz resonant frequency and tested the images of blood samples. The T_2 value measured by 90–t–180–t–sequence was 4 ms for deoxygenated blood (guinea pig blood, hematocrit 0.35) and was 50 ms for oxygenated blood. The mag-

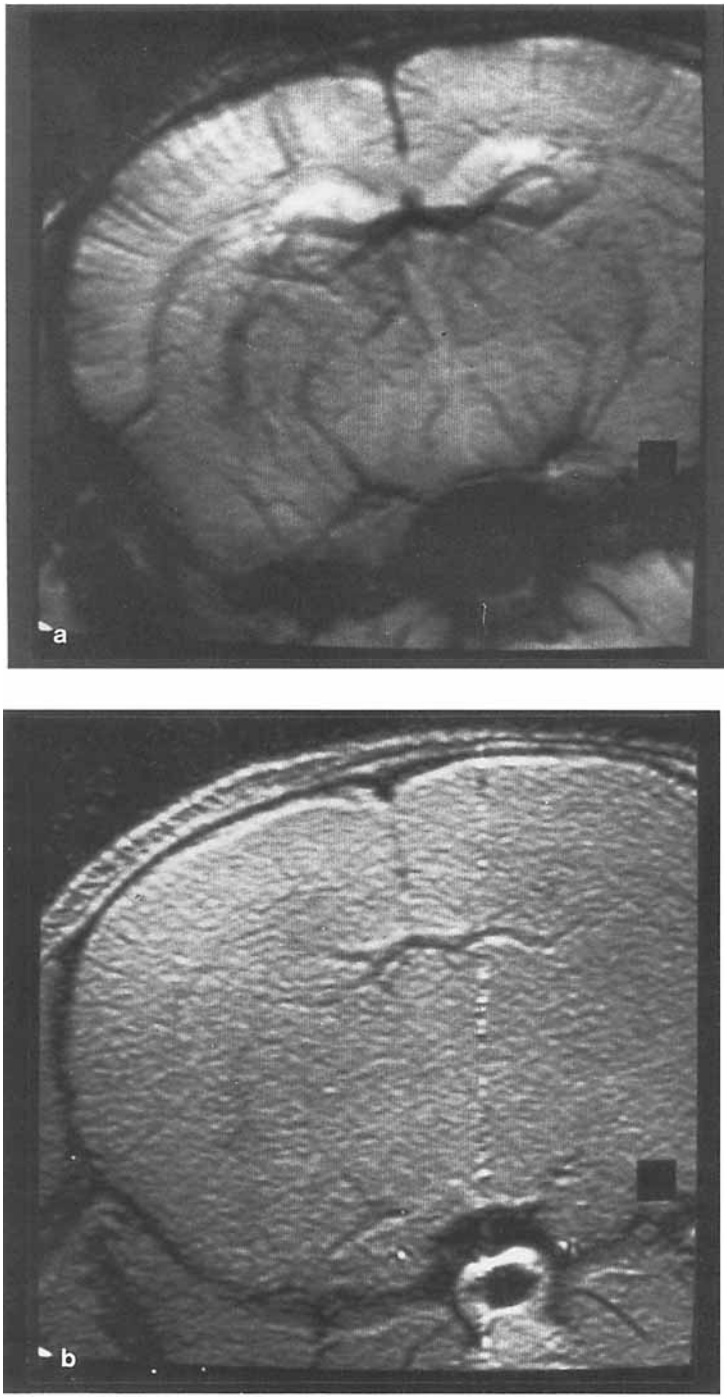


FIG. 3. A comparison of the gradient echo (a) and the spin echo (b) images of an anoxic mouse brain. The coronal slice images were at a different location from those in Fig. 1.

netic susceptibility change was examined in a concentric double tube (blood in the center capillary and saline in the outer tube), the axis of which was placed parallel to the static magnetic field. The shift of the blood water peak relative to the peak of the saline water was essentially zero with oxygenated blood and −150 Hz (down field) with deoxygenated blood. The corresponding volume magnetic susceptibility change was 0.1×10^{-6} as reported by Thulborn *et al.* (*6*). The width of the blood water peak was 250 Hz at the half height.

We obtained several images of a capillary tube (1.4 mm o.d. and 1.0 mm i.d.) filled with blood and placed in a saline bath in order to examine the susceptibility effect in the blood vessel images. To avoid red cell sedimentation during the experiment, heparinized blood from a rat was spun down to have a hematocrit of 65% prior to being filled into the tube. The tube was placed perpendicular to the main field and the slice plane was chosen to be perpendicular to the tube axis. With oxygenated blood in the tube, the spin echo image and the gradient echo image (Figs. 4a and 4b) of the cross section of the tube were quite similar to each other, showing a proper size and shape. The effect of the thin glass wall was minimal. When the tube was filled with deoxygenated blood, the two types of images (Figs. 4c and 4d) became quite different from each other and also from those with oxygenated blood. The signal of the blood water was very weak because of the much shorter T_2 compared with the echo time of the image acquisition, and it should appear black in the images. In the spin echo image, there was a shape distortion due to the shift of the resonance frequency of the nearby water in the saline bath. In the gradient echo image, the dark area extended far beyond the cross-sectional area of the tube. When the slice plane was parallel to the tube axis but the tube orientation relative to the main field was kept the same, the gradient echo image had a much wider dark area in the radial direction of the tube than the spin echo image, which had a width close to the normal size. When the capillary tube with deoxygenated blood was placed parallel to the main field, the spin echo and the gradient echo images did not show any difference in their shapes and displayed the proper size. The signal of the blood water was too weak to be observable, leaving a void space (black area) in the image. Figure 4e shows the gradient echo image of a slice whose plane was perpendicular to the tube axis and therefore also to the main field. The displayed image size is smaller by a factor of 2 than the other images in Fig. 4. There were air bubbles on the side of the bath wall and they had dark halo circles around their images, the origin of which was also the susceptibility effect.

DISCUSSION

The high resolution *in vivo* brain images of a mouse or rat (Fig. 1b and Fig. 3a) show the anatomical details of the brain organization and closely resemble histological slice pictures published in the rat brain atlas (*4*). In the image, the boundaries of various elements of the brain are depicted by dark lines which enhance the contrast. At these boundaries (ventricles and fissures) there are many large blood vessels observable in excised brain slices under an optical microscope. Numerous small blood vessels running perpendicular to the arachnoid surface in the cerebral cortex (Fig. 1c) are also seen. One can find many narrow dark lines with a similar geometry in

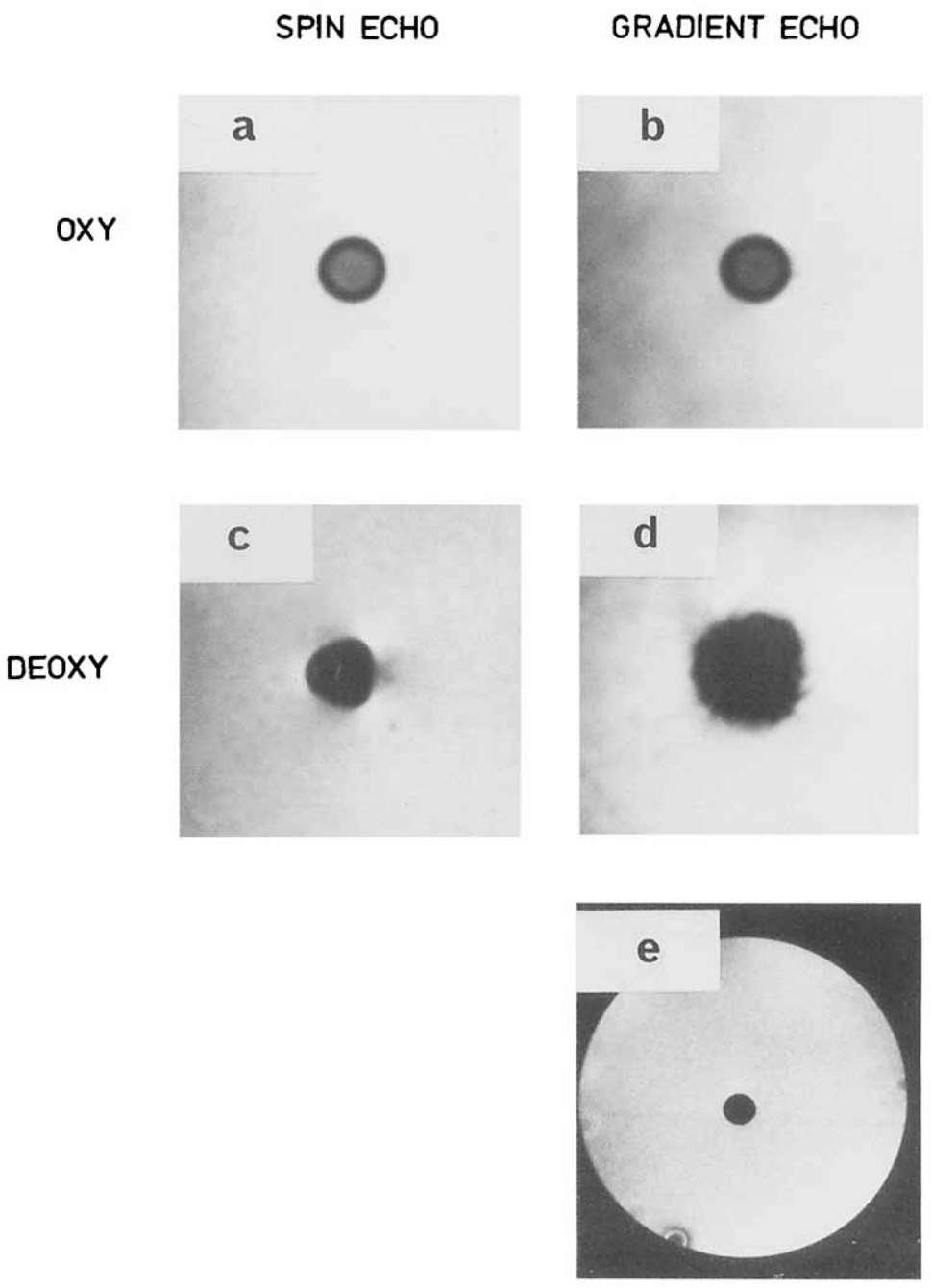


FIG. 4. The spin echo and gradient echo images of a capillary tube with blood in a saline bath. (a–d) The tube axis was perpendicular to the main field and to the slice plane. The tube (1.4 mm o.d. and 1 mm i.d.) was filled with either oxygenated or deoxygenated blood (hematocrit 65%). The spatial resolution of these images was 133 × 133 μm in pixel size. The echo time was 10 ms for a and b and 24 ms for c and d. (e) The tube axis was parallel to the main field and perpendicular to the slice plane. A tube of the same size was filled with deoxygenated blood. The spatial resolution was 66 × 66 μm in pixel size. The echo time was 10 ms. This gradient echo image was displayed to show the size of the tube to be a factor of 2 smaller than the other images.

the MR images (Figs. 1b and 3a). The appearance of these dark lines was dependent on the blood oxygenation level and they disappeared when the blood was completely oxygenated (Fig. 1). The presence of paramagnetic deoxyhemoglobin (the high spin ferrous state) in blood was responsible for the appearance of dark lines, while diamagnetic oxy or CO hemoglobin (the zero spin ferrous state) did not give the contrast. The contrast was observed in gradient echo images but not in spin echo images. From these observations, the cause of the contrast was thought to be the magnetic susceptibility change in blood relative to the surrounding tissues.

It is well known that the field homogeneity is degraded at the boundary of two materials which have different magnetic susceptibilities. Due to the susceptibility difference, the boundary can appear with higher contrast in a gradient echo image (*8, 9*) than in a spin echo image. In deoxygenated blood, large field inhomogeneities are generated inside and around red cells (*5*). These field inhomogeneities or field gradients within the diffusion distance of water molecules are responsible for the shortening of the blood water T_2. In addition to this, the averaged magnetic susceptibility of deoxygenated blood is still significantly different from the susceptibility of surrounding tissues and therefore the field variation can also extend beyond the boundary of a blood vessel.

When a blood vessel is running parallel to the main magnetic field, there is no field variation around the vessel as shown in the *in vitro* experiment with a blood sample described earlier (Fig. 4e). In the coronal slice images of Fig. 1 (normal to the main field), one can see the cross sections of the blood vessels, various arteries at the base of the brain, and the sagical sinus at the top of the brain where venus blood flows. When a blood vessel which contains paramagnetic deoxyhemoglobin is normal to the main magnetic field, there is a region with a varying magnetic field around it. The variation of the field (ω_s) near a blood vessel (a long cylinder with an inner radius a) at the distance of r from the its center ($r \geq a$) can be expressed by

$$\omega_s/\omega_0 = 2\pi\Delta\chi\left(\frac{a}{r}\right)^2(2\cos^2\theta - 1). \qquad [1]$$

In Eq. [1] $\Delta\chi$ is the difference of the volume magnetic susceptibilities of the blood and the surrounding tissue and θ is the angle which the radial vector **r** makes with the main field and ω_0 is the resonance frequency of the tissue water far away from the blood vessel (*10–13*). The value of $\Delta\chi$ is proportional to the degree of deoxygenation of the blood. Taking the degree of the deoxygenation to be 50% and $\Delta\chi$ to be 0.05×10^{-6}, the variation in ω_s/ω_0 is estimated to be ± 0.08 ppm at a distance of $r = 2a$. With this field variation, the echo signal develops a phase difference of $\omega_s \cdot t_e$ during the echo time (t_e) relative to the echo signal without the extra field. The tissue water signal $S(x', y')$ at a pixel (x', y') in the slice image can be expressed in the following way after taking the two dimensional Fourier transform where the T_2 decay term is neglected:

$$S(x', y') = A\left|\int_{\text{voxel}} dv \exp(i\omega_s \cdot t_e)\delta(\omega_x + \omega_s - \omega_{x'})\right|. \qquad [2]$$

In Eq. [2], ω_x and $\omega_{x'}$, are the angular frequencies at x and x' along the read gradient

axis in the object space and in the image space, respectively, and δ is a delta function which has a value of 1 for the signal at x when $\omega_x + \omega_s$ falls within the frequency range of the voxel centered at $\omega_{x'}$ and has a value of zero otherwise. When ω_s is larger than the pixel size in frequency, the signal is shifted along the read gradient axis to a nearby voxel. The volume integral in Eq. [2] is over the voxel of $\omega_{x'}$, counting all the signals in the voxel. This includes those shifted into it from various positions of x. The summing should be a vectorial addition with the phase term $\exp(i\omega_s \cdot t_e)$. In spin echo image acquisition, the phase inversion by the 180° pulse makes the dephasing factor zero provided that the 180° pulse is at the center of the total echo time period in the sequence. All the signals in the voxel are then in phase, but the above-mentioned chemical-shift artifact induced by the shift ω_s appears in the image (Fig. 4c). In the gradient echo acquisition the vectorial summation in the voxel causes some signal cancellation (intra-voxel dephasing effect) and the tissue water image shows dark regions around the vessel cylinder in addition to the chemical-shift artifact (Fig. 4d).

We have made calculations of the above dephasing effect to simulate the images obtained from the blood samples mentioned earlier (*14*). The point to be made here is that the region which contributes the intra-voxel dephasing extends as far as two times the vessel diameter, and in some case greater, as judged by the dark area in the calculated image. This means that the volume which contributes to the dephasing is four times that vessel volume if one treats a cylinder as a two-dimensional object. The direction of the slice gradient, if it is not parallel to the cylinder axis, is one linear dimension of the two. This could be the reason why the dark lines representing the blood vessels in the slice plane were observable despite the slice thickness of several hundred microns (Figs. 1 and 3). In the other linear dimension, normal to the cylinder axis in the slice plane, the width of the dark lines could be twice as large as the actual blood vessel sizes. In other words, the dark lines in the gradient echo image were exaggerated. In the comparison of the spin echo image with the gradient echo image in Fig. 3, the lines seen in the spin echo image are much narrower and less distinct than those in the gradient echo image. This exaggeration or contrast enhancement is dependent on the value of ω_s and therefore ω_0. At a lower field strength the contrast would be hard to observe and at much higher fields the contrast becomes overly exaggerated or the image distortion may become unacceptable. We have tested two frequencies (360 and 300 MHz) so far.

Although the contrast described above is sensitive to the blood oxygenation, it is difficult to estimate the degree of the oxygenation from the extent of the contrast. The intra-voxel dephasing or the apparent signal decay rate, such as the one shown in Fig. 2, would depend not only on the oxygenation level but also on the size and geometry of the blood vessels in the magnetic field. When blood vessels are parallel to the main field, the blood oxygenation level could be estimated from the relaxation time T_2 of the blood water, since it is strongly dependent on the degree of oxygenation (*15*). These subjects need further study.

In conclusion, gradient echo images of the brain at high fields give a high image contrast which is sensitive to the blood oxygenation level. Although we have not shown the distinction between arterial blood vessels and venus blood vessels at various locations in the brain, we expect this oxygenation-sensitive contrast could be used to monitor regional oxygen usages in the brain. When some region in a brain is much

more active than other regions, the active region could show darker lines in the image because of the increased level of deoxyhemoglobin resulting from higher oxygen consumption. The oxygen usage in the brain is supposed to be tightly coupled to the metabolic activity of the brain cells (*16*). Therefore, in addition to the anatomy of the brain, one aspect of its physiology can be studied by the MRI of water.

REFERENCES

1. C. L. DUMOULIN, S. P. SOUZA, AND H. R. HART, *Magn. Res. Med.* **5,** 238 (1987).
2. M. E. RAICHLE, M. A. MINTUM, AND P. HERSCOVITCH, *in* "Brain Imaging and Brain Function" (L. Sokoloff, Ed.), pp. 51–59, Raven Press, New York, 1985.
3. D. EIDELBERG, G. JOHNSON, D. BARNES, P. S. TOFTS, D. DELPY, D. PLUMMER, AND W. I. MCDONALD, *Magn. Res. Med.* **6,** 244 (1988).
4. G. PAXINOS AND C. WATSON, *in* "The Rat Brain," Figure 36, Academic Press, Orlando, 1986.
5. K. M. BRINDLE, F. F. BROWN, I. D. CAMPBELL, C. GRATHWOHE, AND P. W. KUCHEL, *Biochem. J.* **180,** 37 (1979).
6. K. R. THULBORN, J. C. WATERTON, P. M. MATHEWS, AND G. K. RADDA, *Biochim. Biophy. Acta* **714,** 265 (1982).
7. R. A. BROOKS AND G. DI CHIRO, *Med. Phys.* **14,** 903 (1987).
8. I. J. COX, G. M. BYDDER, D. G. GADIAN, I. R. YOUNG, E. PROCTOR, S. R. WILLIAMS, AND I. HART, *J. Magn. Res.* **70,** 163 (1986).
9. J. FRAHM, K. D. MERBOLDT, AND W. HAENICKE, *Magn. Res. Med.* **6,** 474 (1988).
10. C. A. REILLY, H. M. MCCONNELL, AND R. G. MEISENHEIMER, *Phys. Rev.* **98,** 264A (1955).
11. M. G. MORIN, G. PAULETT, AND M. E. HOBBS, *J. Phys. Chem.* **60,** 1594 (1956).
12. D. C. DOUGLASS AND A. FRATIELLO, *J. Chem. Phys.* **39,** 3161 (1963).
13. J. D. JACKSON, *in* "Classical Electrodynamics," pp. 110–119, Wiley, New York, 1963.
14. S. OGAWA AND T. M. LEE, *Magn. Reson. Med.*, in press.
15. K. R. THULBORN, C. J. WATERTON, AND G. K. RADDA, *J. Magn. Res.* **45,** 188 (1981).
16. B. K. SIESJÖ, *in* "Brain Energy Metabolism" p. 106, Wiley, New York, 1978.

Original Research

1991 I. I. Rabi Award

Estimating Oxygen Saturation of Blood in Vivo with MR Imaging at 1.5 T[1]

Graham A. Wright, MSc • Bob S. Hu, MD • Albert Macovski, PhD

The use of magnetic resonance (MR) imaging is investigated for noninvasively estimating the oxygen saturation of human blood ($\%HbO_2$) in vivo by means of relaxation characteristics identified in earlier MR spectrometry studies. To this end, a sequence is presented for determining the T2 of vascular blood in regions in which motions of the body and of the blood itself present a major challenge. With use of this sequence on a commercial 1.5-T whole-body imager, the relationship between the T2 and $\%HbO_2$ of blood is calibrated in vitro for the conditions expected in vivo. T2 varies predictably from about 30 to 250 msec as $\%HbO_2$ varies from 30% to 96%. T2 values measured in situ for vascular blood in the mediastinum of several healthy subjects qualitatively reflected the behavior observed in vitro. Estimates of $\%HbO_2$ for these vessels obtained with the in vitro calibration appear reasonable, particularly for venous blood, although difficulties arise in selecting the appropriate calibration factors. These encouraging initial results support a more systematic study of potential sources of error and an examination of the accuracy of in vivo measurements by comparison with direct measurements of $\%HbO_2$ in vessels.

Index terms: Blood, MR studies, 94.1214 • Oxygen • Phantoms • Physics • Pulse sequences • Relaxometry

JMRI 1991; 1:275–283

Abbreviations: CPMG = Carr-Purcell-Meiboom-Gill, RF = radio frequency, S/N = signal-to-noise ratio, STIR = short inversion time inversion recovery, TI = inversion time, TR_e = effective recovery time, 2DFT = two-dimensional Fourier transform.

[1] From the Magnetic Resonance Systems Research Laboratory, 120 Durand, Stanford University, Stanford, CA 94305 (G.A.W., A.M.); and the Division of Cardiovascular Medicine, Stanford University Hospital, Stanford, Calif (B.S.H.). Received November 8, 1990; revision requested January 16, 1991; revision received and accepted February 11. Supported by the GE Medical Systems Group, the National Institutes of Health (contracts 1R01-HL-39478 and CA-50948) and the National Science Foundation (contract ECS-8801708). G.A.W. also supported by the Natural Sciences and Engineering Research Council of Canada. **Address reprint requests to** G.A.W.

© SMRI, 1991

THE DETERMINATION OF BLOOD OXYGEN saturation finds application in assessing cardiac output, consumption of oxygen in perfused organs, and the severity of vascular shunts such as those found in congenital heart diseases. Available oximetry methods are based primarily on optical transmittance and reflectance differences between oxy- and deoxyhemoglobin. The resulting measure of blood oxygen saturation is the percentage of hemoglobin that is oxygenated, abbreviated as $\%HbO_2$. The poor penetration of tissue by light, however, limits the noninvasive monitoring of $\%HbO_2$ to superficially accessible regions. The determination of oxygen saturation in deep vascular structures currently must be made via direct sampling of the blood of interest. In this report, we extend the current work relating the T2 of blood ($T2_b$) in magnetic resonance (MR) studies to its oxygen saturation (1–3) for the purpose of noninvasively estimating $\%HbO_2$ of vascular blood in vivo with a commercial whole-body imager.

Earlier investigators speculated that this goal should be attainable (1); however, to our knowledge, only qualitative in vivo signal variations attributed to the dependence of $T2_b$ on $\%HbO_2$ have been reported (4–6). Quantitative in vivo work demands a calibration of the $T2_b$ versus $\%HbO_2$ relationship for the specific experimental setup. The variations among experimental data fits for this relationship derived under a wide range of conditions with MR spectrometers (2,3,7,8) demonstrate that the underlying mechanism is not adequately understood. In particular, the parametric fit of the $T2_b$ versus $\%HbO_2$ relationship appears to be sensitive to field strength and the time between refocusing pulses in a way not predicted by the Luz-Meiboom model (9) used by most investigators (3). To our knowledge, only one study has directly measured $T2_b$ for a wide range of $\%HbO_2$. This study examined rat blood on a 4.3-T spectrometer that refocused the signal every 2 msec (2). Thus, for in vivo $\%HbO_2$ estimation, this relationship must be experimentally quantified for conditions resembling

as closely as possible those to be used for human in vivo studies.

Before performing this calibration, we must address a more basic challenge: accurate estimation of $T2_b$ in vivo in a manner consistent with the estimation of $\%HbO_2$. Difficulties that arise include (*a*) isolation of the blood signal of interest, (*b*) variation in signal strengths of blood at different TEs due to effects of flow such as wash-in of unexcited spins and dephasing, (*c*) artifacts due to motion (breathing and blood pulsatility), and (*d*) the poorer B_0 and B_1 homogeneity combined with weaker B_0 and B_1 fields available on whole-body imagers compared with those of spectrometers. This challenge is exacerbated because the vessels of interest include those of the mediastinum, where imaging conditions are the most demanding.

Here, we briefly review the available literature on the $T2_b$ versus $\%HbO_2$ effect to derive a reasonable parametric model to fit to experimentally measured variations of $T2_b$ with $\%HbO_2$ and to identify the basic structure for the in vivo sequence. From this foundation, we enhance the sequence to address the above practical issues. We then describe a series of experiments (*a*) to examine potential sources of bias in T2 measurements that might be introduced by the enhanced in vivo sequence or by the presence of flow, (*b*) to quantify the effect of $\%HbO_2$ on $T2_b$ in vitro for the current setup, and (*c*) to measure $T2_b$ in vivo (particularly in the mediastinum) in healthy volunteers. Finally, with the in vitro calibration, we estimate the $\%HbO_2$ of the in vivo blood from the $T2_b$ measurements and discuss factors affecting the accuracy and precision of such estimates.

• THEORY AND BACKGROUND

From work currently available in the literature, we identified the basic form of the relationship to be expected between $T2_b$ and $\%HbO_2$ and the approximate sensitivity of $T2_b$ to $\%HbO_2$ and to controllable sequence parameters. The latter is particularly useful for sequence design.

Functional Relationship between $T2_b$ and $\%HbO_2$

The origin of the $\%HbO_2$ effect on $T2_b$ is the irreversible dephasing of spins undergoing exchange and/or bounded diffusion through gradient fields in and around intact red blood cells. These gradients are established when B_0 is shifted for water inside the red blood cells due to the presence of paramagnetic deoxyhemoglobin. This frequency shift is proportional to the concentration of deoxyhemoglobin, found only therein (2,10), directly reflecting blood oxygen saturation. Rapidly and regularly applying 180° pulses reduces the range of frequencies a spin experiences before it is "refocused" and hence reduces the degree to which this loss of coherence is irreversible.

The Luz-Meiboom model of relaxation in the presence of exchange between two sites at different frequencies (9) is a good starting point for describing how this situation affects $T2_b$:

$$\frac{1}{T2_b} = \frac{1}{T2_o} + (P_A)(1 - P_A)\tau_{ex}\left[\left(1 - \frac{\%HbO_2}{100\%}\right)\alpha\omega_0\right]^2 \times \left(1 - \frac{2\tau_{ex}}{\tau_{180}}\tanh\frac{\tau_{180}}{2\tau_{ex}}\right). \quad (1)$$

$T2_o$ is the T2 of fully oxygenated blood; τ_{ex} is a measure of the average time required for a proton to move between the two sites; ω_0 is the resonant proton frequency; α is a dimensionless value related to the susceptibility of deoxyhemoglobin and the geometry of the erythrocyte, so that $\alpha\omega_0[1 - (\%HbO_2/100\%)]$ can be considered the frequency difference between the two "sites" at which the protons exchange according to the Luz-Meiboom model; P_A is the fraction of protons resident at one of the sites under exchange; τ_{180} is the interval between refocusing 180° pulses in the MR imaging sequence. The strength of the $\%HbO_2$ effect depends on field strength through the ω_0 term, increasing quadratically with B_0 and therefore favoring the use of high-field-strength imagers for the study. The sensitivity of $T2_b$ to $\%HbO_2$ increases as τ_{180} increases, particularly when τ_{180} is on the order of τ_{ex}. Although the Luz-Meiboom model was developed with the assumption of many short refocusing pulses for which τ_{180} is much less than T2, simulations of the underlying exchange equations (11) indicate that the model is equally valid even when τ_{180} is equal to $T2_o$, as long as α remains relatively small (as it should in the current situation).

We do not require all the degrees of freedom given in the Luz-Meiboom model. We are interested in parameterizing the $T2_b$ versus $\%HbO_2$ relationship in healthy subjects for a particular setup, not in exploring the details of the underlying mechanism as reflected by the parameters α, τ_{ex}, and P_A (3,8,12,13). These parameters can therefore be lumped into a single parameter K, which depends on the controllable variable τ_{180}. ω_0 is also subsumed under K for one field strength. Thus, measurements of $T2_b$ for a range of $\%HbO_2$ will be fitted to a simplified Luz-Meiboom model for a small set of practical τ_{180} values:

$$\frac{1}{T2_b} = \frac{1}{T2_o} + K(\tau_{180}, \omega_0)\left(1 - \frac{\%HbO_2}{100\%}\right)^2. \quad (2)$$

Sensitivity of $T2_b$ to $\%HbO_2$ and τ_{180}: Design Issues

Although we may not be able to establish from the literature the specific parameters relating $\%HbO_2$ to $T2_b$, we can glean information about the order of magnitude of effects that will be valuable in designing our studies. The most basic issue is whether the $\%HbO_2$ effect is great enough to be useful for our purposes. The size of the effect increases with operating field strength. Our studies are performed on a 1.5-T Signa unit (GE Medical Systems, Milwaukee). Apart from availability, it is well suited to this study because it is among the

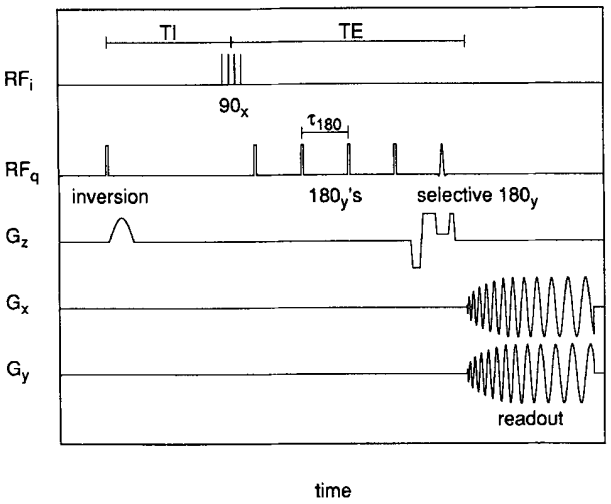


Figure 1. Pulse sequence for the in vivo estimation of $T2_b$. *TI* = inversion time. RF_i and RF_q are the in-phase and quadrature components of the RF field, respectively; G_x, G_y, and G_z are the field gradients applied along the corresponding spatial axes. As shown, the sequence images an axial section.

highest-field-strength whole-body imagers that are widely used.

In Equation (2), the size of the $\%HbO_2$ effect is reflected in the parameters $T2_o$ and K (for sufficiently large τ_{180}). When examining these parameters, we will consider only human blood under normal physiologic conditions—specifically, intact red blood cells suspended in plasma with a hematocrit around 45% and at 37°C. Temperature and hematocrit (7) affect $T2_o$ and, to a lesser extent, K. Complete cell lysis eliminates the oxygen effect ($K = 0$), while the development of methemoglobin in intact cells found in clots will increase K (2,3). Under normal conditions, $T2_o$ is approximately 220 msec ± 30, per studies of oxygenated blood in a 1.4-T field (3,7). On the basis of the data fits of both Thulborn et al (2) and Bryant et al (7), $K(\tau_{180} \rightarrow \infty, B_0 = 1.5\ T)$ is approximately 40 sec^{-1}. $T2_b$ should be between 60 and 100 msec for sufficiently long τ_{180} when $\%HbO_2$ is about 50%, the minimum level that is likely of interest for studies of vascular blood. This indicates that $T2_b$ variations should be sufficient to reflect relatively small changes in $\%HbO_2$.

A second question is how fast one can refocus the signal while still realizing most of the $\%HbO_2$ effect (longer τ_{180} results in greater $\%HbO_2$ effect). More rapid refocusing (shorter τ_{180}) is desirable to maintain spin coherence in the presence of complicated flow (14) and to provide a sufficient range of TEs to accurately estimate $T2_b$. The full Luz-Meiboom model indicates that the dependence of $1/T2_b$ on τ_{180} is greatest for $\tau_{180} \approx \tau_{ex}$ and saturates as τ_{180} increases beyond about $5\tau_{ex}$. Ideally, we would use the value of τ_{180} at which this saturation begins. Independent of the above concerns, the minimum achievable τ_{180} is about 6 msec with the current experimental setup, limited by power absorption concerns and technical limitations of the radio-frequency (RF) amplifier.

A reasonable τ_{180} is determined in part by the magnitude of the $\%HbO_2$ effect. To accurately measure TE, τ_{180} should be at most on the order of half of the $T2_b$ of interest. This suggests that we need only consider a τ_{180} of less than 50 msec. Where the saturation point for the effect of τ_{180} lies is not clear in the literature. Nonetheless, considering values of τ_{180} only up to 50 msec appears reasonable. From the data fits of Thulborn et al (determined primarily from data acquired at 4.3 T), one would not expect K to vary much with τ_{180} over the range of practical interest (>6 msec). From work performed primarily at 1.4 T (3,7), K should increase significantly as τ_{180} increases from 6 to 50 msec and should then level off slowly for further increases in τ_{180}.

• MATERIALS AND METHODS

As a foundation for the more detailed experimental descriptions, we first identify the complete in vivo sequence and its features and the relevant details of the imager platform used. Materials and methods specific to each of the three experiments proposed in the introduction (checking for bias in T2 estimation, calibrating $T2_b$ dependence on $\%HbO_2$ in vitro, and measuring $T2_b$ in vivo) are then outlined. Since these experiments successively build on each other, it may be convenient for the reader to examine the results of each in the Results section before proceeding to the description of the subsequent experiment.

Sequence for Measurement of $T2_b$ in Vivo

For spectrometer studies of blood, a CPMG (Carr-Purcell-Meiboom-Gill) sequence is used most often to measure $T2_b$. A version of this lies at the heart of the proposed sequence; however, we have made several modifications to address the challenges of the in vivo environment. The resulting sequence (Fig 1) is that originally introduced for the purpose of flow-independent angiography (14), augmented to include (*a*) spatial selectivity without wash-in effects, (*b*) reduced flow dephasing, and (*c*) faster image acquisition (to minimize, where necessary, effects of body motion).

To suppress fat signal, the sequence begins with a short TI inversion recovery (STIR) sequence (TI = 120 msec) followed by a frequency-selective 90° pulse that excites only the water protons (14). Fat is often found surrounding vessels and just under the skin. By eliminating its signal, one can minimize its contribution to signal measured in the vessel caused by partial-volume averaging and by blurring of fat signal (which occurs when one uses time-varying gradients of relatively long duration at data acquisition). Furthermore, artifacts from the normally high-signal-intensity fat in the chest wall that are due to breathing are suppressed. STIR minimizes the fat signal in the longitudinal magnetization at excitation, which has the added advantage of minimizing spurious signal from fat generated by the imperfect hard refocusing pulses that follow. Frequency-selective excitation provides additional fat suppression because it is difficult to

properly tune TI to achieve the desired level of suppression (14).

After excitation, the transverse magnetization is refocused every τ_{180} msec by rectangular 180° pulses. This pulse train establishes the constant refocusing interval required for accurate $T2_b$ estimation in the Luz-Meiboom model. It also restores the coherence of spins dephased because of flow through B_0 inhomogeneities (14). To minimize flow dephasing, spoiling gradients during the refocusing train are not used; however, this could lead to the propagation of spurious signals. One can generate strong spurious signals and lose significant amounts of desired signal because of errors in the axis and amplitude of flip angles, particularly when there are many pulses in the refocusing train. To minimize the effects of these errors, caused by B_0 and B_1 inhomogeneities, we vary the sign of the 180° pulses according to the MLEV pattern (15) whenever there are at least four pulses in the train (14). This pattern of sign variation is more robust than the standard CPMG pattern in the presence of B_0 inhomogeneities; however, under this scheme one should acquire signal only after 2^n pulses, where n is an integer.

As the first step in isolating blood signal by spatial location, the final refocusing 180° pulse is section selective and is bracketed by a pair of spoiling gradients to dephase the out-of-section signal. These gradients and the section-select gradient are flow compensated. Effects of wash-in and of the physical dispersion of tagged spins on blood signal are avoided because this is the only spatially selective pulse in the sequence and it is as close as possible to the data acquisition.

Finally, signal from the section is spatially encoded during data acquisition. We have implemented two variations of this. In the more standard case, we use the two-dimensional Fourier transform (2DFT) encoding of the original flow-independent angiography sequence (14). To minimize flow dephasing with this arrangement, all spatial-encoding gradients (notably the phase-encoding lobe and the dephasing lobe of the readout gradient) are kept compact and close to the data acquisition interval. In the second case, illustrated in Figure 1, spiral gradients rapidly cover k space during data acquisition (16). This version is useful when the duration of image acquisition is an issue. For instance, when imaging the chest, acquiring an entire image in a single breath hold minimizes motion effects. For this gain, we accept poorer signal-to-noise ratios (S/Ns) and greater sensitivity to blurring caused by B_0 inhomogeneity. Each spiral readout begins at the center of k space and at the center of the spin echo to minimize the effects of flow and B_0 inhomogeneities. Furthermore, the spiral trajectory has well-behaved gradient moments, maintaining flow coherence throughout the acquisition (16).

Timing of the data acquisitions can decrease sensitivity to the presence of flow. To prevent loss of coherence in subsequent echoes due to flow effects, signal is acquired at only one TE per excitation. To measure T2, we repeat the sequence at three to four different TEs. To minimize effects of flow pulsatility, the sequence is gated to the cardiac cycle so that readout occurs in the same period of diastole independent of the selected TE. Data are acquired once every other heartbeat to maximize S/N per unit imaging time and to allow adequate T1 recovery to minimize effects of variable R-R intervals (14). Extra rectangular 180° pulses are included after acquisition for all but the longest TE of interest to ensure that the effective recovery time (TR_e) is independent of the TE at which the signal is received.

While the resulting sequence is rather involved, each element is chosen for its simplicity and/or availability with the objective of expeditious implementation. Potential variations include the use of crafted pulses for frequency-selective excitation or more robust refocusing (17,18), as well as alternative rapid acquisition strategies (19,20). These will be explored as the need arises from experimental work.

Imager Considerations

As noted earlier, all experiments were performed on a 1.5-T Signa unit. The system includes superconducting and resistive shims with which field variations of less than 20 Hz can be achieved over a 20-cm field of view in a uniform phantom. No supplementary shimming was done for individual experiments. Good shims minimize flow dephasing and diffusion effects during the refocusing train, as well as blurring when data are acquired with the spiral gradients. B_1 amplitudes are limited to about 625 Hz. The system is equipped with 10-mT/m gradients with which one can generate a 192 × 192 image of a 24-cm field of view in eight 40-msec spiral acquisitions (16). Shielded gradient coils minimize eddy current effects during such acquisitions. All cardiac gating was performed with a plethysmograph.

Experiment 1: Bias in T2 Measurement

Before experimenting on blood, we demonstrated that the features added to the sequence to address in vivo issues do not affect T2 estimation. We also showed that the sequence does not introduce measurement bias in the presence of flowing material. The phantom used in this study was plastic tubing with an inner diameter of 0.6 cm containing a manganese chloride solution with a T1 of approximately 1,200 msec and a T2 of approximately 120 msec. The tubing runs through a pump and settling system so that steady flow of fluid can be achieved. The phantom is a crude model of blood in a vessel. The tubing runs parallel to the main field in the magnet bore to minimize susceptibility effects. With the fluid stationary, we measured its T2 with the following sequences:

Sequence A: a standard multiecho 2DFT sequence with a TR of 2,000 msec and TEs of 48, 96, 144, and 192 msec (21), acquiring axial sections through the tube; TR_e = 1,808 msec.

Sequence B: a simplified version of the proposed sequence with only a rectangular excitation pulse, the train of hard refocusing pulses, each bracketed

Table 1
Estimates of T2 of Phantom under Various Experimental Conditions

Sequence	τ_{180} (msec)	Flow Rate (cm/sec)	T2 (msec)
A	48	0	95
B	48	0	121
B	24	0	122
C	24	0	121
C	24	9	116
C	24	18	117
C	24	28	115
C	12	18	115
C	6	18	120

Note.—See text for explanation of sequences.

by spoiling gradients, and a 2DFT phase encoding and readout to produce coronal projection images (14). One TE is acquired per excitation; τ_{180} = 24 msec; TE = 48, 96, and 192 msec; TR_e = 1,808 msec for each image. This sequence is also repeated with a τ_{180} of 24 msec; TEs of 24, 48, 96, 192, and 384 msec; and a TR_e of 2,000 msec.

Sequence C: the complete proposed sequence, including STIR, frequency-selective excitation, the refocusing train without spoiling gradients, a final spatially selective pulse, and spiral gradients during data acquisition to generate axial sections. τ_{180} = 24 msec; TE = 24, 72, 120, 216, and 408 msec; TR = 2,000 msec. Extra refocusing pulses after data acquisition make the effective T1 recovery time, TR_e, 1,592 msec for each TE.

The effects of flow on $T2_b$ measurement were examined with sequence C in the presence of steady flows of 9, 18, and 30 cm/sec. For a flow of 18 cm/sec, this sequence was repeated with τ_{180} values of 6 and 12 msec to ensure that varying the refocusing rate in the presence of flow does not bias $T2_b$ measurements.

In these and all later experiments, T2 values were estimated with a weighted least-squares fit of a monoexponential decay to the average signal intensities in a small region of the phantom (21,22).

Experiment 2: In Vitro Calibration of $T2_b$ versus $\%HbO_2$

To establish a quantitative relationship between $T2_b$ and $\%HbO_2$, the T2s of human blood oxygenated to varying degrees were measured for a practical range of τ_{180} values. The parameters K and $T2_o$ of Equation (2) were determined by a least-squares fit to the resulting data.

Blood was drawn via venipuncture from five healthy volunteers after their informed consent was obtained. In some cases, the subject's arm was cooled in water (18°C) to reduce oxygen saturation of the venous blood. No chemicals were added to further reduce $\%HbO_2$. The samples were citrated and then aerated to varying levels of $\%HbO_2$ (as measured with a reflectance oximeter [American Optical, Buffalo]), starting at the level at which the blood was drawn. The samples were then stored in evacuated 5-mL glass tubes in which the $\%HbO_2$ levels could be maintained for several hours. This was confirmed by remeasuring the $\%HbO_2$ of each sample after the $T2_b$ measurements. Hematocrit was also measured at this time.

Data for the $T2_b$ measurements were acquired within 2 hours after the original blood drawing. Before imaging, sets of blood-containing tubes were immersed in an insulated bath of water doped with $MnCl_2$ (T2 < 2 msec) at 37°C to minimize B_0 inhomogeneity due to susceptibility and to maintain the blood at body temperature throughout the experiment. A head coil was used for excitation and signal reception. For greater S/N and reduced susceptibility effects, sequence B, the simplified version described in the previous section, was used to measure the $T2_b$ values. Specifically, $T2_b$ values were measured for τ_{180} values of 6, 12, 24, and 48 msec. For each τ_{180}, signals were acquired at TEs ranging from 24 to 384 msec; TR_e was 2,000 msec. Before each set of measurements, the samples were agitated to minimize settling effects. Sequence C was also run in a subset of the experiments to check for any differences when imaging blood.

Experiment 3: In Vivo Studies

Using the complete in vivo sequence (sequence C), we measured $T2_b$ in several vessels of clinical interest—primarily the aorta, superior vena cava, and pulmonary trunk—in several healthy volunteers (with their informed consent). The signals from these vessels were isolated by acquiring an axial section through the pulmonary trunk while the subject lay prone, with a circular surface coil 18 cm in diameter beneath the chest to receive the signal. With use of spiral gradients during readout and reception of signal every other heartbeat during diastole, an image could be acquired in 16 heartbeats, during which the subjects held their breath. This breath-hold interval is quite reasonable for the current study of healthy subjects; however, further development may be required to reduce this interval in patient studies. The resulting image has a resolution of 1.7 × 1.7 × 10 mm. To estimate $T2_b$, we acquired four to five images at TEs ranging from 24 to 408 msec. For most subjects, the signal was refocused every 24 msec (deemed best from the in vitro calibration; see Results). We repeated the studies using τ_{180} values of 6 and 12 msec in three subjects to demonstrate the effect of τ_{180} in vivo. $T2_b$ values were also estimated with 2DFT data acquisition for vessels in an axial section of the arm and for the descending aorta and inferior vena cava in an axial section of the abdomen in individual subjects.

• RESULTS AND DISCUSSION

Experiment 1: Bias in T2 Measurement

T2 estimates for the phantom, obtained with the various sequences, are listed in Table 1. In all cases, monoexponential decay fit the data well. The standard error in repeat measurements of T2 was about 3 msec. The commercial multiecho sequence (A) yielded significantly smaller T2 estimates than the two versions (B and C) of the proposed sequence. When we repeated the measurements with the commercial sequence but used only a single

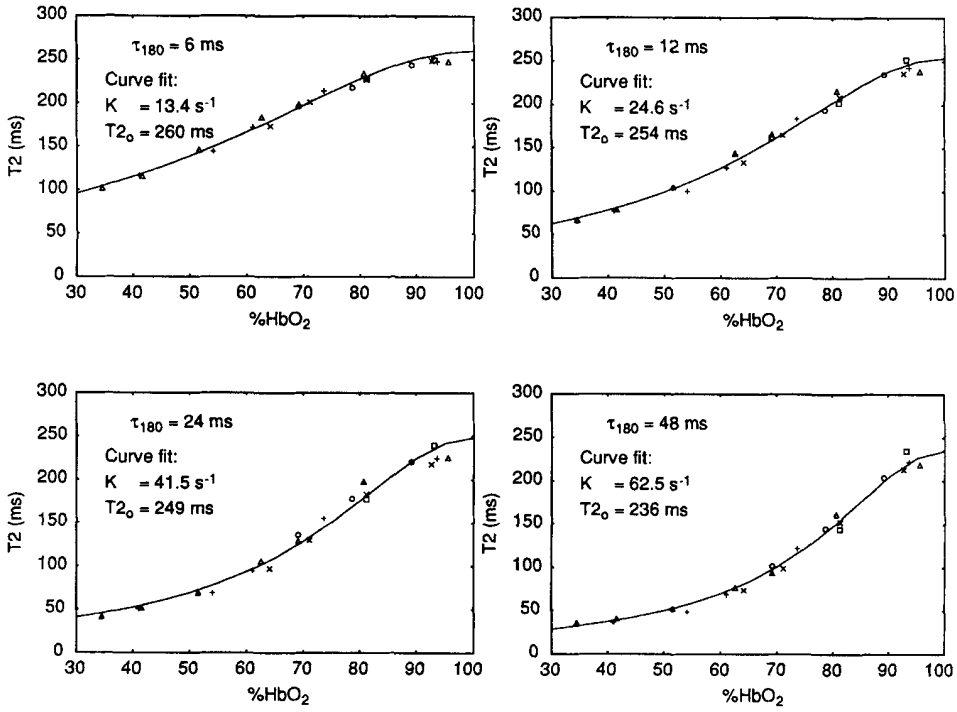


Figure 3. $T2_b$ versus $\%HbO_2$ data fits. Each graph corresponds to a different τ_{180} (as indicated). Different point symbols refer to different subjects. Solid line is the least-squares fit of Equation (2) to the data; corresponding estimates of K and $T2_o$ are indicated.

echo per acquisition and a very long TR, we obtained T2 values comparable with those found with sequences B and C. Hence, the commercial multiecho sequence appears to introduce a biasing error. Further investigation of this problem was beyond the scope of this study; however, potential sources of such errors in multiecho sequences on imagers have been investigated by others (23,24). Both the simplified version (B) and the complete version (C) of the proposed sequence yielded the same T2 values for stationary fluid. T2 measurements with sequence C were relatively independent of velocity for steady flows. Similarly, varying τ_{180} in the presence of steady flow did not affect T2 measurements. Thus, the proposed sequence seems to reflect true transverse relaxation under various conditions. These results also add credence to the use of the relationship between $T2_b$ and $\%HbO_2$—established with in vitro experiments in which stationary blood was imaged with sequence B—in estimating $\%HbO_2$ levels of flowing blood in vivo from $T2_b$ determined with sequence C.

Experiment 2: In Vitro Calibration of $T2_b$ versus $\%HbO_2$

The blood samples used in this experiment had $\%HbO_2$ levels ranging from 30% to 96%. Direct $\%HbO_2$ measurements in the samples, obtained before and after $T2_b$ measurements, differed on average by about 2%. Hematocrits in different subjects ranged from 42% to 47%. The integrity of the erythrocytes was maintained throughout the study, on the basis of examination of centrifuged samples.

Figure 2 depicts one of the images used for the estimation of $T2_b$. The variation in intensity with oxygen saturation of the blood is readily apparent on

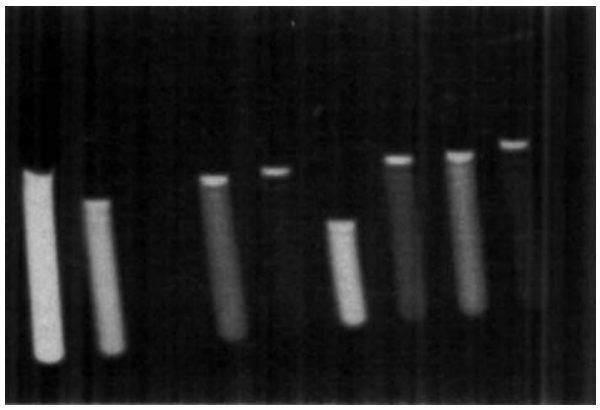


Figure 2. Projection image (τ_{180} = 24 msec, TE = 96 msec) of blood samples from one subject. Test tube at far left contains doped water. Remaining tubes contain blood with varying $\%HbO_2$: from left, 80, 62, 35, 95, 52, 69, and 42.

this T2-weighted image. The $T2_b$ of each sample was estimated from the average signal intensity determined in a small square region at about the center of the sample.

Transverse relaxation of the blood is well described by monoexponential decay. Most errors in fitting this model to the measured signal intensities can be attributed to random noise in the raw data, on the basis of the results of χ^2 tests (21). The resulting estimates of $T2_b$ are plotted in Figure 3 as a function of the $\%HbO_2$ measured for the corresponding samples. Standard errors in the estimates of $T2_b$, based on propagation of random noise in the raw images (25), range from approximately 0.5

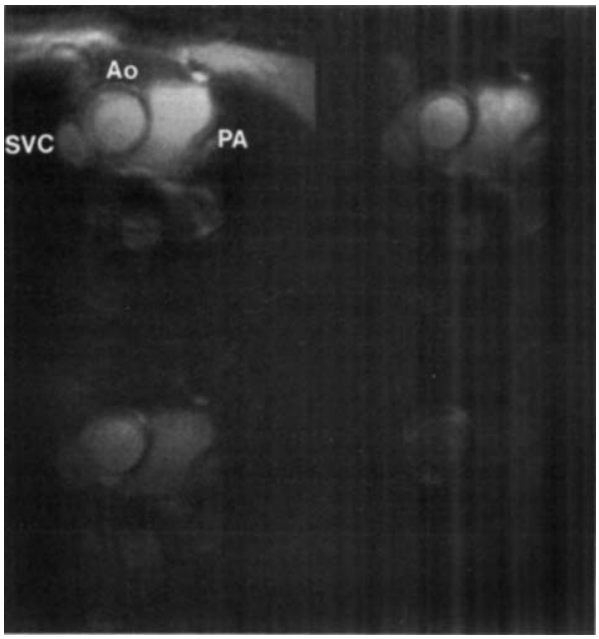


Figure 4. Images used for the estimation of $T2_b$ in vivo. Axial section through the pulmonary trunk is shown at various TEs (clockwise from upper left, 24, 120, 408, and 216 msec). *SVC* = superior vena cava, *Ao* = ascending aorta, *PA* = pulmonary artery.

msec for a $T2_b$ of 30 msec to 5 msec for a $T2_b$ of 250 msec. For each τ_{180}, we estimated K and $T2_o$ via a least-squares fit of Equation (2) to the data, weighted to allow for the expected error in the $T2_b$ values. The resulting parametric values and the corresponding curve fits are presented in Figure 3.

Equation (2) provides a reasonable fit to the data. There is strong evidence that K varies with τ_{180} over the range studied (6–48 msec), in general concurrence with spectrometry studies at about the same field strength (3,7); however, our limited data would yield somewhat lower estimates of τ_{ex} (3–5 msec). As discussed in the Theory and Background section, the minimum τ_{180} value for which K is close to its maximum should be used. The larger K reflects a greater $\%HbO_2$ effect, minimizing the propagation of error from the $T2_b$ measurement to the $\%HbO_2$ estimate. Earlier work, as well as current results, indicates that the influence of τ_{180} on K decreases as τ_{180} increases beyond approximately 24 msec, although we still see a significant change from 24 to 48 msec. Using a τ_{180} of 24 msec gives a reasonable trade-off between maximizing K and minimizing flow effects and provides a sufficient range of TEs for estimating $T2_b$.

Under this arrangement, the standard error in predicting $\%HbO_2$ from $T2_b$ measured in vitro is about 2.5% over the range of clinical interest ($\%HbO_2 < 90\%$). The reflectance oximeter used as our "gold standard" is accurate to ±2% in this range, so this reference is potentially a major source of error. For clinical work, accuracy to within 3% is generally acceptable. For the $\%HbO_2$ range of arterial blood (>90%), the model suggests that $T2_b$ is much less sensitive to $\%HbO_2$ in general, predicting poorer accuracy for such estimates. This may not be a major concern in clinical work because one often simply assumes that arterial blood is fully oxygenated or one uses values of arterial $\%HbO_2$ measured in surface regions with a pulse oximeter. Hence, the current level of accuracy of $\%HbO_2$ estimates would be practically useful if it could be achieved in vivo.

These initial results justified preliminary in vivo studies in healthy volunteers. However, several areas for further development in these calibration studies are in order. For this report, studies were limited to healthy individuals with a narrow range of normal blood characteristics. The effects of variations in blood characteristics among different individuals on the calibration and the accuracy of Equation (2) as a model of the relation between $T2_b$ and $\%HbO_2$ are both areas of interest in expanded studies. As noted in the Theory and Background section, these are subjects of increasing scrutiny in the research community, yielding a growing body of applicable literature.

Of particular interest is the effect of individual differences in hematocrit. There is evidence that $1/T2_o$ varies linearly with hematocrit (7) while K varies quadratically (2). On the basis of these results, for hematocrits ranging from 30% to 50% (an extreme range encompassing many pathologic conditions), changes in K would introduce at most a 3% error in $\%HbO_2$ if not accounted for, while changes in $T2_o$ would yield substantially greater errors. In our work, estimates of K for a given τ_{180} were consistent from subject to subject, while there was weak evidence of individual differences in the parameter $T2_o$ (although these differences did not appear to correlate with the small variations in hematocrit). We will extend our calibration studies in future work to span physiologic or pathologic variations in erythrocyte density (ie, hematocrit) and variations in properties such as erythrocyte size and shape, to determine the need for calibration corrections for particular patients. If such corrections are necessary, they could be realized in a clinical situation by measuring the relevant properties of a patient's blood obtained via venipuncture.

Our current results also raise questions regarding the accuracy of the model. $T2_o$ tends to decrease slightly with increasing τ_{180}, although the theory supporting the model suggests that $T2_o$ should be independent of τ_{180}. No effect of τ_{180} on the T2 of doped water, used as a control in the experiments, was observed; hence, the effect seems to be specific to blood and not easily explained as a reduced diffusion effect. The results of Gomori et al (3) in the measurement of the T2 of fully oxygenated blood for various τ_{180} values reflect this effect, although the authors do not discuss the anomaly. Clearly, further study of $T2_o$ would be of merit, with respect to individual differences and to the accuracy of the model.

Experiment 3: In Vivo Studies

Figure 4 shows a set of images of an axial section through the pulmonary trunk in one volunteer, ac-

Table 2
$\%HbO_2$ Estimates from Measurements of $T2_b$ in Vivo

Subject	$T2_o$ (msec)*	τ_{180} (msec)	Aorta		Superior Vena Cava		Pulmonary Trunk	
			$T2_b$ (msec)	$\%HbO_2$	$T2_b$ (msec)	$\%HbO_2$	$T2_b$ (msec)	$\%HbO_2$
1	224	6	223	97*	185	74	202	81
		24	220	96	138	74	161	80
2	243	12	242	97*	175	75	194	79
		24	230	93	155	76	180	81
3	214	12	213	97*	154	73	162	75
		24	196	90	126	72	147	77
4	196	24	194	97*	139	78	122	73
5	277	24	274	97*	171	77	186	79

* $T2_o$ chosen so that $\%HbO_2$ = 97% for blood in aorta for minimum τ_{180} used.

quired at various TEs. These were used to estimate $T2_b$ values in the aorta, superior vena cava, and pulmonary trunk. One can observe the blurring in off-resonance regions caused by susceptibility effects (primarily at the chest wall and where pulmonary arteries enter the lungs) when the signal is acquired with spiral gradients of relatively long duration. Nonetheless, the signals in the vessels of interest are well isolated; indeed, virtually no flow-dephasing or wash-in effects are observed in the blood signal, even at the late TEs.

The $T2_b$ estimates for this subject and those for several other subjects, determined with the same protocol, are listed in Table 2. Monoexponential decay provides a good fit to the data when estimating the $T2_b$ values, although errors are generally greater than those due to random noise alone. Sources of residual error may include dephasing due to complicated flow, the presence of spurious signals, and variations in average R-R interval and breath-hold position between images with different TEs.

These in vivo results reflect, at least qualitatively, the in vitro results. For each subject, venous blood (pulmonary trunk and vena cava) clearly has a shorter T2 than arterial blood (aorta). In four of the five subjects studied, blood in the pulmonary trunk had a longer T2 than that in the superior vena cava. One might infer that the $\%HbO_2$ in the pulmonary trunk is greater. Whether this is normally true for healthy subjects is not clear from the medical literature. The range of $T2_b$ values is certainly within that measured in vitro. Comparing the $T2_b$ values measured with τ_{180} values of 6 and 24 msec in one subject shows a clearly significant decrease in $T2_b$ for venous blood at the longer refocusing time, as expected on the basis of the in vitro results. When the difference in τ_{180} values was less (12 vs 24 msec), the results were less conclusive, since the $T2_b$ of arterial blood changes almost as much as that of venous blood.

Before one can estimate $\%HbO_2$ from the measured $T2_b$ values, the question remains as to the appropriate parametric values to use in Equation (2). Without evidence to the contrary, we assume that the values of K estimated from in vitro data are equally valid for in vivo studies. In choosing $T2_o$, there are several considerations. In healthy subjects at rest, one would expect that $\%HbO_2$ for aortic blood should always be about 97% (26). This implies that $T2_o$ should be only slightly greater than $T2_b$ in the aorta. If we fix $T2_o$ to the average value obtained from in vitro work, we can expect large errors in estimates of $\%HbO_2$ for arterial blood (eg, estimated $\%HbO_2$ is 83% for a $T2_b$ of 194 msec in subject 4, if $T2_o$ is 250 msec) or meaningless results if $T2_b$ is greater than $T2_o$. If we use measurements of $T2_b$ in the aorta to estimate $T2_o$, we are clearly making assumptions about $\%HbO_2$ in the arteries and hence have no predictive power for these vessels. For expediency, we use the latter approach to study $\%HbO_2$ estimation in the venous blood; however, this clearly unsatisfactory state reinforces the earlier conclusion indicating the need for further study of factors affecting $T2_o$. The results are listed in Table 2. The influence of $T2_o$ is reduced for the T2 of venous blood; hence, the difference between estimates of $\%HbO_2$ obtained with the above two approaches for determining $T2_o$ is on average about 3%. Except for subject 5, the $\%HbO_2$ estimates would be reduced with a $T2_o$ of 250 msec.

The average healthy subject at rest should have an oxygen saturation of about 75% for venous blood (26). The $\%HbO_2$ estimates for the superior vena cava therefore appear reasonable, while those for the pulmonary trunk seem slightly high. In the anecdotal study of τ_{180} effects, predictions of $\%HbO_2$ appear consistent for different refocusing times. These results generally support the applicability of in vitro calibrations to the in vivo measurements. Anecdotal studies of the descending aorta and inferior vena cava in axial images of the abdomen yielded similar results. Still, none of the estimates for deep vessels has been verified by direct, invasive methods of $\%HbO_2$ measurement; therefore, determination of the accuracy of these values remains an important future investigation.

In anecdotal studies of the arm, the relaxation behavior of blood in the deeper arteries and veins paralleled that discussed above. However, for surface veins, estimates of $T2_b$ are significantly higher than expected. Because of the accessibility of these vessels to venipuncture, we were able to directly measure $\%HbO_2$ of samples acquired from one such vessel. This measurement confirmed that with the measured $T2_b$ values and the mapping function derived earlier (Eq [2]), one would overestimate $\%HbO_2$ significantly in this case. Through a series of experiments, we established that $T2_b$ estimates were reduced closer to expected values when the B_0 inhomogeneities due to susceptibility effects

at the skin were eliminated by submerging the arm in water (effects of temperature and different blood flow patterns were factored out through other experiments). We suspect that errors in the quality of signal refocusing in the presence of such inhomogeneities are the source of this effect, prompting further refinement of the train of 180° pulses.

• CONCLUSIONS AND FUTURE WORK

The current work has addressed several challenges in advancing noninvasive estimation of $\%HbO_2$ in vivo by means of relaxation characteristics in MR imaging. The proposed sequence enables accurate measurement of transverse relaxation times in idealized phantom models of vascular blood, even in the presence of steady flow. From in vitro studies with the same imager and effectively the same sequence used for in vivo work, we have quantified the relationship between $T2_b$ and $\%HbO_2$. A simplified version of the Luz-Meiboom model of relaxation in the presence of exchange provides a good two-parameter fit to the data. However, more extensive studies are required to adequately examine factors such as individual differences affecting the calibration, particularly those altering the model parameter $T2_o$. For in vivo studies, the measured $T2_b$ values for venous and arterial blood and their variation with τ_{180} generally correspond to those expected from the in vitro calibration. Some work must be done to improve the quality of the $T2_b$ fits in vivo and to study anomalous $T2_b$ values, particularly in surface veins of the arm. Meanwhile, the consistency between $\%HbO_2$ estimates in deep veins (from $T2_b$ estimates and application of the in vitro calibration) and their expected physiologic values supports the pursuit of correlative studies with direct measurement of $\%HbO_2$ in veins of interest to examine the accuracy of the proposed method. ●

Acknowledgments: We thank Craig Meyer, MSEE, for supplying the gradient waveforms and reconstruction routines for the spiral readouts and the numerous volunteers for their participation in the experimental studies. We also thank Athos Kasapi, MSEE, for his detailed review of the manuscript.

References

1. Thulborn K, Radda G. Correlation of oxygen consumption with energy metabolism by in vivo NMR. J Cereb Blood Flow Metab 1981; 1(suppl 1):S82–S83.
2. Thulborn K, Waterton J, Matthews P, Radda G. Oxygenation dependence of the transverse relaxation time of water protons in whole blood at high field. Biochim Biophys Acta 1982; 714:265–270.
3. Gomori J, Grossman R, Yu-Ip C, Asakura T. NMR relaxation times of blood: dependence on field strength, oxidation state, and cell integrity. J Comput Assist Tomogr 1987; 11:684–690.
4. Hayman L, Ford J, Taber K, Saleem A, Round M, Bryan R. T2 effect of hemoglobin concentration: assessment with in vitro MR spectroscopy. Radiology 1988; 168:489–491.
5. Terrier F, Lazeyras F, Posse S, et al. Study of acute renal ischemia in the rat using magnetic resonance imaging and spectroscopy. Magn Reson Med 1989; 12:114–136.
6. Ogawa S, Lee T, Nayak A, Glynn P. Oxygenation-sensitive contrast in magnetic resonance image of rodent brain at high magnetic fields. Magn Reson Med 1990; 14:68–78.
7. Bryant R, Marill K, Blackmore C, Francis C. Magnetic relaxation in blood and blood clots. Magn Reson Med 1990; 13:133–144.
8. Matwiyoff N, Gasparovic C, Mazurchuk R, Matwiyoff G. The line shapes of the water proton resonances of red blood cells containing carbonyl hemoglobin, deoxyhemoglobin, and methemoglobin. Magn Reson Imaging 1990; 8:295–301.
9. Luz Z, Meiboom S. Nuclear magnetic resonance study of the protolysis of trimethylammonium ion in aqueous solution: order of the reaction with respect to the solvent. J Chem Phys 1963; 39:366–370.
10. Labotka RJ. Measurement of intracellular pH and deoxyhemoglobin concentration in deoxygenated erythrocytes by phosphorus-31 nuclear magnetic resonance. Biochemistry 1984; 23:5549–5555.
11. Allerhand A, Gutowsky H. Spin-echo NMR studies of chemical exchange. II. Closed formulas for two sites. J Chem Phys 1965; 42:1587–1599.
12. Gillis P, Koenig S. Transverse relaxation of solvent protons induced by magnetized spheres: application to ferritin, erythrocytes, and magnetite. Magn Reson Med 1987; 5:323–345.
13. Brooks R, Brunetti A, Alger J, Di Chiro G. On the origin of paramagnetic inhomogeneity effects in blood. Magn Reson Med 1989; 12:241–248.
14. Wright G, Nishimura D, Macovski A. Flow-independent MR projection angiography. Magn Reson Med 1991; 17:126–140.
15. Levitt M, Freeman R, Frenkiel T. Broadband decoupling in high-resolution nuclear magnetic resonance spectroscopy. Adv Magn Reson 1983; 11:47–108.
16. Meyer C, Macovski A, Nishimura D. A comparison of fast spiral sequences for cardiac imaging and angiography (abstr). In: Book of abstracts: Society of Magnetic Resonance in Medicine 1990. Berkeley, Calif: Society of Magnetic Resonance in Medicine, 1990; 403.
17. Pauly J. New approaches to selective excitation for magnetic resonance imaging. Thesis. Stanford University, Stanford, Calif, 1990.
18. Conolly S. Magnetic resonance selective excitation. Thesis, Stanford University, Stanford, Calif, 1989.
19. Mansfield P. Multi-planar image formation using NMR spin echoes. J Phys C Solid State Phys 1977; 10:L55–L58.
20. Haase A. Snapshot FLASH MRI: applications to T1, T2, and chemical-shift imaging. Magn Reson Med 1990; 13:77–89.
21. MacFall J, Wehrli F, Breger R, Johnson G. Methodology for the measurement and analysis of relaxation times in proton imaging. Magn Reson Imaging 1987; 5:209–220.
22. MacFall J, Riederer S, Wang H. An analysis of noise propagation in computed T2, pseudodensity, and synthetic spin-echo images. Med Phys 1986; 13:282–292.
23. Majumdar S, Orphanoudakis S, Gmitro A, O'Donnell M, Gore J. Errors in the measurements of T2 using multiple-echo MRI techniques. I. Effects of radiofrequency pulse imperfections. Magn Reson Med 1986; 3:397–417.
24. Majumdar S, Orphanoudakis S, Gmitro A, O'Donnell M, Gore J. Errors in the measurements of T2 using multiple-echo MRI techniques. II. Effects of static field inhomogeneity. Magn Reson Med 1986; 3:562–574.
25. Bevington P. Data reduction and error analysis for the physical sciences. New York: McGraw-Hill, 1969; 56–64.
26. Ganong W. Review of medical physiology. Los Altos, Calif: Lange Medical, 1981; 520–521.

NIH Public Access
Author Manuscript
Magn Reson Imaging Clin N Am. Author manuscript; available in PMC 2012 May 1.

Published in final edited form as:
Magn Reson Imaging Clin N Am. 2011 May ; 19(2): 249–282. doi:10.1016/j.mric.2011.02.010.

MR Imaging of Articular Cartilage Physiology

Jung-Ah Choi, MD, PhD[1,2,3] and **Garry Gold, MD**[1]

[1] Departments of Radiology, Bioengineering, and Orthopedic Surgery, Stanford University, Stanford, CA, USA

[2] Department of Radiology, Seoul National University Bundang Hospital, Seoul, Korea

[3] Department of Radiology, Seoul National University College of Medicine, Seoul, Korea

Introduction

Osteoarthritis (OA) has become the most prevalent chronic disease of the elderly (1, 2) and is an important cause of disability in our society with increasing incidence not only in the US (3) but in other parts of the world (4–6). It is primarily a disease of the articular cartilage (7–9), which may become pathologic by degeneration or acute injury (10). As the incidence of the disease is on a continual increase, there is a great need for accurate non-invasive evaluation before the onset of irreversible changes (11, 12). There are many diagnostic imaging methods for evaluation of the articular cartilage. (Table 1) Conventional radiography has been used to detect secondary gross changes of the joint cartilage pathology, manifested by the narrowing of the joint space distance (13), and allows visualization of secondary changes such as osteophyte formation (10), but this imaging method only allows detection of later stage of the disease when changes are already irreversible. It does not allow direct visualization of the cartilage. Conventional or CT arthrography has also been used to evaluate surface irregularities of the cartilage; however, it is limited in its invasiveness and provides limited evaluation (14).

MRI has become the best imaging modality for assessment of the articular cartilage (15–19) due to its excellent ability to manipulate contrast to highlight different tissue types (10). Conventional MRI sequences that are currently used for evaluation of cartilage have the ability to depict mostly morphological changes, such as fibrillation and partial-or full thickness defects (10); however, they are limited in their capability for comprehensive assessment of cartilage, with limited spatial resolution (20) and limited information about cartilage physiology.

Commonly used conventional MRI methods include 2D or multi-slice T1-weighted, proton density (PD)-weighted, and T2-weighted imaging with or without fat suppression (10). Then with new developments in imaging hardware and software and improved gradients and radiofrequency coils, fast or turbo spin-echo imaging techniques such as water-only excitation have been used (10). Even though SPGR and GRE techniques have produced excellent quality images with high resolution (0.3×0.6×1.5mm) (21) and 3D-SPGR is considered the current standard for morphologic imaging of cartilage (22, 23), these methods have the disadvantages of lack of reliable contrast between cartilage and fluid and long imaging times (10).

Therefore, newer techniques have emerged for morphologic imaging of cartilage, some of which include dual-echo steady-state (DESS) imaging, driven equilibrium Fourier transform

Correspondence to: Garry Gold, MD, gold@stanford.edu.

NIH-PA Author Manuscript
NIH-PA Author Manuscript
NIH-PA Author Manuscript

NIH-PA Author Manuscript

NIH-PA Author Manuscript

NIH-PA Author Manuscript

(DEFT) imaging, balanced steady-state free precession (SSFP) imaging with fat suppression and its variants, such as fluctuating equilibrium MRI (FEMR), linear combination (LC) SSFP, IDEAL SSFP, phase sensitive SSFP, and vastly interpolated projection reconstruction (VIPR) imaging (10). These newer methods based on SSFP, as well as advances in parallel technology with improved imaging times in 3D FSE imaging, have improved morphologic imaging of cartilage, in terms of contrast, resolution, and acquisition time. However, these techniques are still limited in their ability to depict physiology and biochemistry of cartilage, although allowing time for application of other sequences to explore cartilage physiology (10).

In order to understand the principles of MR imaging of cartilage physiology, we will have to review some of the basic concepts of cartilage anatomy and physiology, which will be reviewed in the following section.

Functional Anatomy and Physiology of Cartilage

Articular cartilage is relatively hypocellular and composed of about 4% chondrocytes by wet weight (24). The main component of the tissue is composed of the extracellular matrix, which is 65% to 85% water, which decreases slightly with depth from the articular surface (24), and solid components, which include type II collagen (15–20%) and large aggregating molecules of proteoglycans (3–10%), which are called aggrecans (25). Most of the extracellular water is associated with the aggrecan molecules and freely exchangeable with synovial fluid (24), whereas a small portion of water is bound in the interfibrillar space of the collagen fibrils (26, 27) (Figure 1A).

The biochemical properties of cartilage are strongly influenced by the content and structure of collagen and proteoglycans in the matrix, which differ from bone interface to the articular surface (25, 28). The orientation and alignment of collagen matrix vary according to the depth from the articular surface as well as regionally within the joint (24). At the most superficial aspect of the articular surface, there is a layer of dense collagen fibers, called the lamina splendens, which has a smooth surface and with proteoglycans such as lubricin (29), surface zone protein, and constituents of synovial fluid help of reduce the friction of the articular surface. Underneath the lamina splendens, tropocollagen molecules, which are components of type II collagen, are organized into a leaflet like structure (30). Then follows the superficial layer, where collagen fibrils tend to have an orientation parallel to the articular surface. The transitional zone is the next layer in depth, which thickens near the periphery of the articular surface (31). In recent studies, the transitional zone has been shown to have anisotropy (32, 33) with a preferential orientation oblique to the articular surface (24). Deeper to the transition zone is the radial zone, where collagen fibrils have a radial or perpendicular orientation to the bone surface and chondrocytes are aligned in a column-like pattern (34). And finally collagen fibrils cross the bone/cartilage interface at the tidemark zone, anchoring the cartilage to the subchondral bone (24) (Figure 1B). The characteristic arrangement of collagen leads to the “magic angle effect” and laminar appearance on proton MR images (35).

There are also regional differences in organization and composition of the collagen within the joint; weight-bearing regions that are frequently exposed to compressive load, such as the femorotibial joint, have a thicker radial zone and a thinner transitional zone (36) and are organized into thicker fibrils at regular intervals (37). This pattern is not seen in areas that are not prone to habitual loading. The transitional zone is thicker near the periphery of the joint, where the cartilage is prone to shear stress, and the direction of the collagen fibers are in the prevailing direction of shear strain (38).

NIH-PA Author Manuscript

NIH-PA Author Manuscript

NIH-PA Author Manuscript

The aggrecans, which are large molecules of aggregating proteoglycans, lie interposed amidst the meshwork of type II collagen fibrils and their concentration varies within the cartilage layer, with the highest levels in the middle section, which decrease near the bone interface and articular surface (39, 40). Aggrecan consists of a protein core with a long extended domain to which many glycosaminoglycan (GAG) side chains are linked; these include chondroitin sulfate (CS) and keratan sulfate (KS) with CS as the predominant GAG molecule in cartilage (35). In turn, several aggrecan molecules are attached to a central core fiber filament of hyaluronic acid (41), to which the aggrecan monomers are bound through a linking protein. A large number of carboxyl and sulfate residues on the GAG side chains are ionized under physiologic conditions and impart a negative charge density (35) (Figure 1C). GAG chains are so densely packed that the concentration of negative charge can be as much as 150mM to 300mM in normal articular cartilage (42). These negative charges allow the GAG molecules to be fixed to the matrix and are referred to as fixed charge, and the concentration of this fixed charge is referred to as fixed charge density (FCD) (42). These negative ions attract positive counter-ions and water molecules and provide a strong electrostatic repulsive force between the proteoglycans, which act together to produce the swelling pressure of cartilage (35). However, swelling of the proteoglycans is constrained by the surrounding collagen meshwork, which produces an interstitial fluid pressure of about 9MPa (43), and this contributes to the compressive stiffness of cartilage which is essential for normal cartilage function (24) (Figures 2A, B). Collagen II fibers, which are the predominant type of collagen in cartilage, provide a tensile force opposing the tendency of the proteoglycans to expand the cartilage and also immobilize the proteoglycans (35). The cartilage interface with the subchondral bone is important to normal cartilage function as well; this area is represented as the subchondral plate, which consists of the tidemark zone, the zone of calcified cartilage, lamellar subchondral cortical bone, and the underlying trabecular bone (24). Type II collagen fibrils pass through the tidemark zone, ending in the zone of calcified cartilage (44), and there is a potential cleavage plane between the zone of calcified cartilage and subchondral cortical bone in response to shear stress (45) (Figure 3). The subchondral plate can remodel in response to altered biomechanics secondary to joint injury or damage to overlying cartilage, and its thickness varies according to joint geometry and other patient factors, such as age, weight, and exercise (46).

Stress is defined as the intensity of force imparted onto the articular surface per unit area, and the deformation of the tissue in response to such stress is called tissue strain (24). The tissue strain that develops within tissue in response to applied stress will vary over time, and such tissues possess viscoelastic properties (24), which are results of interaction between the three main components of cartilage, namely, water, type II collagen matrix, and aggrecan (47). The types of stress imposed on cartilage can be categorized as compression, tension, and shear (24).

Compression causes cartilage to deform and produces a bulk flow of water through the extracellular matrix into the synovial space (48). The ability of cartilage to resist compression is a result of the ability of the extracellular matrix to limit water permeability (49), which is optimal in healthy cartilage where the water flow is able to dissipate most of the energy imparted onto the tissue during compression (Figure 4). This is not the case in degenerative cartilage, where water movement becomes less restricted and more of the compression force is imparted to collagen and aggrecan matrix, which leads to degeneration (24). Cartilage is stiffer toward bone (50) and most of the tissue deformation occurs in the superficial layer of cartilage (24). Tension causes deformity of the contour of cartilage, which is resisted by the fibrillar type II collagen meshwork and hydrated aggrecans (51).

Shear stress is produced when one articular surface passes over the other and at the bone/cartilage interface, where differences in compressive stiffness of tissues result in shear strain

NIH-PA Author Manuscript

NIH-PA Author Manuscript

NIH-PA Author Manuscript

during high compressive loading (24) (Figure 5). In healthy normal cartilage, the smooth surface of the lamina splendens, superficial zone protein, and lubricin, and synovial fluid act together to reduce shear strain (24). Extensive tensile strain may produce cleavage or fractures within the collagen matrix, leading to cartilage fissures along the collagen “leaves” or flap-type tears at the junction of the transitional and radial cartilage zones (24). High compressive forces transmitted to the deep layer of cartilage produce high shear strain in the tidemark zone at the cartilage/bone interface. When this shear strain exceeds the material properties of the tissue, cleavage between calcified cartilage and subchondral bone may occur, leading to cartilage delamination (24).

Osteoarthritis is characterized by following changes in the cartilage biochemistry and microstructure: earliest changes include reduced PG concentration, possible changes in the size of collagen fibril and aggregation of PG, increased water content and increased synthesis and degradation of matrix macromolecules (35) with disorganization of the collagen network (52) (Figure 6). These lead to breakdown and decreased content of the PG matrix, which in turn lead to ulceration with inflow of PG into the synovial fluid with decreased water content of the cartilage, making it less resistive to stress. As osteoarthritis progresses, collagen, PG, and water content are reduced further and the collagen network becomes severely disrupted (53).

MR Imaging of Cartilage Biochemistry and Physiology

Conventional MR imaging methods have demonstrated mostly morphologic changes of cartilage, which probably represent progressed stages of osteoarthritis. Such morphologic changes are preceded by biochemical and structural changes in the extracellular matrix that change the biomechanical properties of the tissue (10). Out of the conventional MRI methods, T2-weighted images are highly sensitive to structural properties of cartilage reflecting the T2 relaxation properties of type II collagen and water associated with it, exhibiting magnetization transfer and magic angle effects. Conventional methods have been based mostly on water content and less commonly on collagen content and orientation. Newer techniques have been developed to map various MRI parameters, assessing proteoglycan content, collagen content and orientation, water mobility, and regional cartilage compressibility. These include sodium MRI, T1 rho, dGEMRIC, T2 mapping, ultrashort TE imaging, magnetization transfer, and diffusion-weighted imaging. Most of these have been studied in vitro using excised specimens; however, some of the techniques have been conducted in human studies. MRI methods to measure proteoglycan depletion of cartilage, which is one of the earliest findings of OA, include sodium MRI, T1 rho mapping, and dGEMRIC (42). Other methods, such as T2 mapping, ultrashort echo time imaging, magnetization transfer, and diffusion-weighted imaging, are mainly based on other biochemical and physiological characteristics of cartilage, such as collagen content and orientation, water content and mobility, and regional cartilage compressibility (10).

Sodium MRI

Any atom with an odd number of protons and/or neutrons possesses a nuclear spin momentum and exhibit the MR phenomenon. Whereas conventional MRI methods have used H to generate signal, the atom ^{23}Na which also has an odd number of protons or neutrons can be used in cartilage imaging. The Larmor frequency of ^{23}Na is 11.262 MHz/T, compared with ^{1}H at 42.575 MHz/T, which means that at 1.5T the resonant frequency of ^{23}Na is 16.9MHz, as compared with 63MHz for ^{1}H (54). In addition to the lower resonance frequency, the concentration of ^{23}Na is 320microM, i.e. relatively lower than that of ^{1}H, with T2 relaxation times between 2 and 10ms (55), often requiring imaging with a non-Cartesian trajectory (56). Due to all of these factors, in vivo imaging using ^{23}Na is

NIH-PA Author Manuscript

NIH-PA Author Manuscript

NIH-PA Author Manuscript

challenging and requires the use of special transmit and receive coils, which are not always available for clinical MRI systems, as well as relatively long imaging times in order to obtain adequate signal-to-noise (54) (Figure 7A, B).

Sodium-23 atoms are associated with the negatively charged GAG side chains and thus the main component of the high fixed-charge density present in the proteoglycan sulfate and carboxylate groups (54) in the extracellular matrix (25, 57) with spatial variation of concentration within the normal cartilage (55). Loss of PG (and hence GAG and FCD) due to cartilage degeneration results in loss of sodium ions from the tissue, which results in lower FCD, thereby releasing positively charged sodium ions (35). Sodium imaging has been shown to be sensitive to small changes in proteoglycan concentration in studies using in vitro cartilage specimen (58–63). Studies have been published on obtaining quantitative measurements of sodium concentration in cartilage (55, 64) and obtaining signal from sodium bound to macromolecules in the extracellular matrix (58, 35, 65–70). With the use of higher field 3.0T (Figure 8) or 7.0T (Figure 9) MRI, better spatial resolution has been achieved and in-vivo studies have been performed (71–75), which suggest Na imaging can be used for physiologic assessment of cartilage with potential application in postoperative patients as well (75). Triple quantum filtered imaging (76), use of 3D cones at high field MRI (74), 3D-radial acquisition with ultrashort echo times (73) and inversion recovery techniques (77) have been shown to be feasible with promising results (Figure 10A, B), but clinical application of ^{23}Na imaging is still limited in many aspects, including the SAR limits.

However, because of its high specificity for PG content and ability to depict cartilage with high contrast without the requirement for exogenous contrast agents, such as in dGEMRIC (78), and with developments in high field MRI, advances in gradient technology and radiofrequency coil technology, and parallel imaging techniques (79, 80), sodium MRI has become more feasible (71–75) and may be used in the future to quantify early physiological and molecular changes associated with osteoarthritis.

T1 rho imaging

T1 rho imaging is made possible when the magnetization is tipped into the transverse plane and then “spin-locked” by a constant radiofrequency (RF) field. Proteoglycan depletion, which is one of the earliest changes in osteoarthritis, affects the physio-chemical interactions within the macromolecular environment, and quantitative T1 rho imaging methods enable probing macromolecular slow motions at high static fields in cartilage (52). Several studies have suggested that with further GAG depletion, T1 rho reflects interaction of collagen with water (81–83).

T1 rho imaging of cartilage with application to study cartilage degeneration was first suggested by Reddy et al (84). Earlier studies using phantom and specimens showed a strong correlation between T1 rho and cartilage PG content (85–90). In a study by Akella et al., a strong correlation was shown between changes in PG and T1 rho, and similar to T2 studies, T1 rho values also showed regional variations within cartilage (89), with the highest values in the superficial zone, decreased in the middle zone, and increased near the subchondral bone (89) (Figure 11). Using sodium MRI, a strong correlation was found between T1 rho and FCD (90). A study of cartilage specimens from patients undergoing total knee arthroplasty suggested T1 rho to be more sensitive to cartilage degeneration as compared with T2 mapping (92) (Figure 12).

Although there have been only few in vivo studies, some studies have shown increased cartilage T1 rho values in OA subjects compared with controls (93, 94), which further suggested the potential application of T1 rho imaging for evaluating cartilage. Studies on T1

NIH-PA Author Manuscript

NIH-PA Author Manuscript

NIH-PA Author Manuscript

rho and T2 have suggested that the values may be complementary and T1 rho may not only reflect PG content, but other biochemical changes that occur in cartilage degeneration (81, 83, 95) and may have a dependence on the angular orientation of collagen fibers (52). Several studies have suggested that the average T1 rho, which has a larger dynamic range, may be a more sensitive indicator of cartilage degeneration than T2 (91, 96).

T1 rho imaging method is a potentially useful technique sensitive to early proteoglycan depletion, one of the earliest changes in osteoarthritis (91, 97, 98) (Figures 13A, B). Initial application of T1 rho in humans was limited to single-slice acquisition (99); however, recent advances in T1 rho imaging techniques have included multi-slice and 3D acquisitions (97, 98, 100, 101), as well as rapid Cartesian acquisition strategies at 3T (102, 103). However, one disadvantage of the T1 rho technique is the relatively large RF power that is applied during the spin-locking preparation pulse, which may result in heating of tissue and problems with SAR; this should be overcome with development of new techniques and is not a significant problem at clinical MRI up to 3.0T (10). Also, implementations of parallel imaging techniques have enabled reduction of imaging times to the range of 5 to 10 minutes (102, 104). Further studies are needed on T1 rho imaging to confirm its reliability in larger patient populations; however, it is a promising technique for investigation of cartilage degeneration and osteoarthritis.

Contrast Enhanced Imaging - Delayed Gadolinium-Enhanced MRI (dGEMRIC)

As described earlier, the proteoglycan components of cartilage has GAG side chains with abundant negatively charged carboxyl and sulfate groups. The negative fixed charge on the cartilage macromolecules is balanced by the net charge of the mobile ions within the extracellular fluid (ECF). The ECF has a lower concentration of anions and a higher concentration of cations than blood or synovial fluid, and the difference between the concentrations of anions and cations in ECF equal the fixed charged density (FCD) (42). GAG or FCD contribute significantly to load-bearing properties or compressive stiffness of cartilage (105–107), so there is a substantial difference in the concentration of mobile ions between normal and GAG depleted cartilage (42). There were many studies attempting to measure GAG, including some of the first quantitative measurements of GAG distribution in relation to the depth from articular surface or topological position or with disease by Maroudas et al (108–111).

MRI enables noninvasive measurement of ion concentrations and simultaneously enables acquisition of spatial images (42). One of the most common MR contrast agents, Magnevist (Berlex, NJ) or $Gd(DTPA)^{2-}$ is a clinically approved MRI contrast agent can be used to indirectly measure FCD by allowing $Gd(DPTA)^{2-}$ to penetrate into cartilage accumulating in high concentration in areas of cartilage with low GAG content (112). Subsequent T1 mapping yields an image depicting GAG distribution, which is referred to as “delayed gadolinium enhanced MRI of cartilage” or “dGEMRIC” with the “delay” meaning the time required for $Gd(DTPA)^{2-}$ to penetrate into cartilage (112). As compared with sodium MRI, which entails a more direct measurement of FCD, dGEMRIC technique using a contrast agent is an indirect method of measuring GAG content in articular cartilage (113, 114). As compared with sodium MRI, the advantages of dGEMRIC is a relatively higher resolution and sensitivity; however, the disadvantages include the need for administration of a contrast agent and the need to convert T1 measurements into $Gd(DTPA)^{2-}$ concentration (42). Areas of low GAG will accumulate a higher concentration of the Gd(DTPA) with more rapid T1 relaxation of adjacent water protons (10). After obtaining a series of images with different degrees of T1 weighting, a T1 map can be calculated to provide a regional assessment of relative Gd(DPTA) concentration that is inversely proportional to the regional GAG content

NIH-PA Author Manuscript

NIH-PA Author Manuscript

NIH-PA Author Manuscript

(115). DGEMRIC index refers to the acquisition of a single T1 map after administration of Gd(DTPA) and has been shown to be similar at both 1.5T and 3.0T field strengths (115).

The dGEMRIC technique has been validated in both in vitro and in vivo studies as reflecting the GAG concentration of cartilage with dGEMRIC measurements corresponding to “gold standard” measures for GAG (115–117). Long-term In vitro studies have been conducted which enabled monitoring changes of GAG distribution over time with high resolution, allowing insight into the process of cartilage degradation, development, and repair (42). For example, in a study by Allen et al. bovine cartilage plugs were monitored over time and showed chondrocytes could replenish GAG after trypsin depletion of GAG (118) and after interleukin-1 (IL-1) treatment (119). GAG measurements have been observed to correlate better in superficial layers of cartilage as compared with deep layers where MRI can overestimate GAG (120). Interobserver and intraobserver variability in the selection and calculation of regional T1 have not been shown to be significant sources of variation for this technique (121).

In vivo studies have provided invaluable clinical insights into cartilage physiology and pathology. Clinical studies have demonstrated the DGEMRIC images show “lesions” in cartilage not observed with administration of a nonionic contrast agent (122), validating the correlation between dGEMRIC and distribution of GAG molecules. Several pilot clinical studies were done using DGEMRIC to evaluate the level of repair in cartilage implants (123–125). Increased uptake of Gd(DTPA) has been observed in arthroscopically correlated regions of cartilage fibrillation and softening (126) and patellar chondrosis (127) and has been associated with joint space narrowing and malalignment within the femorotibial joint of the knee (128). In a recent study, individuals exercising on regular basis were shown to have higher DGEMRIC indices, i.e. higher GAG concentrations, than sedentary subjects, correlating with the level of physical activity (129). In another study, a change in DGEMRIC index was shown 4 months after a meniscal tear, corresponding to the amount of exercise (130). This study provided an insight into the hypothesis that mechanical stimulation could change cartilage biochemistry (42) (Figures 14A, B, C).

The medial femorotibial compartment has been shown to have generally lower DGEMRIC index as compared with the lateral femorotibial compartment of the knee (131), keeping consistent with previous biochemical studies, as well as possibly reflecting a response to different mechanical stress according to the location within the joint. Large variations in DGEMRIC were observed even when no joint space narrowing was observed on radiographs (132), presumably representing biochemical changes preceding morphological changes and actual loss of cartilage (42). The DGEMRIC index also appears to be sensitive to cartilage-modifying injuries, as shown in studies of patients with ACL (133) or PCL injuries (134) who showed lower DGEMRIC values. In another study, cartilage lesions in patients with OA were more apparent using the DGEMRIC technique as compared with the standard MRI scans (135). In a large cross-sectional study of hip dysplasia patients, measures of severity of dysplasia and of pain correlated well with the DGEMRIC index but poorly with the radiological parameter of joint space narrowing (136). DGEMRIC studies exploring the implication for planning and monitoring treatment have shown the DGEMRIC index as the best predictor of failure (137) in osteotomy for hip dysplasia and increased DGEMRIC index in patients postoperatively, suggesting reversibility of cartilage injury (137) (Figure 15).

DGEMRIC may provide a noninvasive way to depict the mechanical properties of cartilage by mapping the biochemical composition (42), as shown in studies with good correlation between decreased GAG content, measured as increased DGEMRIC, and increased cartilage compressibility and site-matched stiffness measurements (120, 138–141). These studies

NIH-PA Author Manuscript

NIH-PA Author Manuscript

NIH-PA Author Manuscript

showed results that could not be explained by GAG measurements alone, suggesting the need for combined GAG/collagen studies (138–141). A preliminary study on osteochondral allografts also showed similar results of low GAG associated with indentation stiffness (125). In a recent study, the in vivo effects of unloading and compression on T1-Gd relaxation times were investigated in healthy knee cartilage at 3.0T, which again showed a relationship between biochemical load response and biomechanical properties of articular cartilage (142) (Figure 16A, B, C). Recent studies have suggested clinical application of DGEMRIC in the assessment of cartilage after repair (124, 143–145) (Figure 17). However, most of the results have shown heterogeneous uptake in repair tissue over time, and so one has to account for the fact that the baseline T1 of the tissue and Gd(DTPA) uptake are influenced not only by GAG content but also by water content and permeability of tissue; therefore, pre- and post contrast measurements of T1 are needed for accurate evaluation of the GAG content (146, 147). In a recent study of autologous chondrocyte implantation with a fibrin-based scaffold in the knee showed DGEMRIC and T2 mapping to provide complementary information on the biochemical properties of repair tissue (148).

Technical issues regarding optimization of the DGEMRIC technique for human clinical application have been investigated and reviewed (78, 149–151). Even though the contrast agent Gd(DTPA) has been approved for clinical use as an MRI contrast agent, the DGEMRIC technique itself is an off-label application. The recommended dose for DGEMRIC studies is 0.2mM/kg or twice the recommended clinical dose but this should be corrected for body mass index (152). Some authors have advocated using a triple dose to improve sensitivity to small changes in GAG (131). According to the DGEMRIC protocol as suggested by Burstein et al., the contrast agent is injected intravenously, the subject exercises the joint for about 10 minutes, and imaging is performed after about 2–3 hours for the knee and 30–90 minutes for the hip (78); reproducibility of this technique was 10–15% for images taken two weeks to two months apart (78).

Safety precautions must be taken when administering gadolinium-based contrast agents, as recently there have been reports linking gadolinium-based contrast media to nephrogenic systemic fibrosis, a highly debilitating condition similar to scleroderma which occurs in patients with moderate to severe renal impairment (153–158). Even though the exact pathogenetic mechanism is still under investigation, it has been hypothesized that renal impairment leads to prolonged circulation of the contrast agent, leading to accumulation of free Gd^{3+} in tissue (154). As there is no cure for this potentially fatal condition, appropriate precautions and screening procedures should be undertaken when administering gadolinium-based contrast agents in all subjects (10).

Other limitations to the DGEMRIC technique include the delay period between injection and imaging and the long imaging time needed to acquire the series to T1-weighted images to calculate the T1 maps, necessitating correction for patient motion between acquisitions (10). More recently, rapid 3D T1 mapping techniques have been developed to reduce acquisition time and improve spatial coverage (146, 149–151, 152, 159, 160). These techniques still need to be validated further. As in all quantitative imaging techniques, there are assumptions and possible error underlying the technique; in DGEMRIC these include the issue of the conditions under which $Gd(DTPA)^{2-}$ fully penetrates cartilage, assumptions inherent in the conversion of T1 to $Gd(DPTA)^{2-}$ concentration, tissue cellularity in young or tissue engineered samples (since $Gd(DPTA)^{2-}$ does not enter cells and cellular volume needs to be corrected for) and better T1 sequences which can cover the joint in a reasonable time frame (112). In spite of these issues and limitations, the biophysical basis of this technique supported by validation studies in vitro and in vivo suggest that the DGEMRIC technique is a valuable tool in investigating cartilage status, disease, and repair and may

NIH-PA Author Manuscript

NIH-PA Author Manuscript

NIH-PA Author Manuscript

shed more light into understanding joint biomechanics in cartilage physiology as well as the role of loading and exercise in cartilage pathology.

T2 relaxation time mapping

One of the earliest physiologic changes in cartilage degeneration is increased permeability of the matrix, which leads to increased content and motion of water. This results in increased stress on cartilage as the hydrodynamic pressure is not sustained by the matrix which leads to proteoglycan-collagen matrix degeneration and subsequently, morphological changes in cartilage. The transverse relaxation time (T2) is constant for a given tissue at a given MR field strength (161), unless altered by tissue pathology or a contrast agent (161); it is sensitive to slow moving protons and is a function of the water content (162, 1, 163–165), collagen content (82, 83, 166–169), and orientation of the highly ordered anisotropic arrangement of collagen fibrils in the extracellular matrix (170, 171, 172–182, 161) (Figure 18). The immobilized water protons in the proteoglycan-collagen matrix promote T2 decay and render the cartilage low in signal intensity (SI) on long-TE (T2-weighted) images, whereas the mobile water protons in synovial fluid maintain high SI (52). As collagen and proteoglycan losses occur, the water molecules are increased in motion and content, manifesting high SI on T2-weighted images (183, 162). High SI in areas of damaged cartilage have been well depicted on conventional T2-weighted images with arthroscopic correlation (184, 185). There is an orientation dependence of T2 in cartilage, which is a result of residual quadripolar relaxation mechanisms due to the aniosotropic arrangement of collagen fibrils (69, 82 186–191), and this is most pronounced in the radial zone where the fibers are aligned in a perpendicular direction to the bone and also varies within the joint (173, 174, 181, 36, 192) (Figures 19A, B, C, D). Several studies have shed light on the significance of the orientation of the collagen matrix in cartilage pathology (193–197); there have been studies suggesting a strong inverse relationship between cartilage T2 and collagen fiber anisotropy (169, 180, 32, 198, 199). Such sensitivity to structural changes in collagen matrix as well as changes in water content and motion renders T2 mapping to be a useful technique to depict early changes in osteoarthritis (200). Loss of collagen matrix anisotropy has been observed to occur early in the disease process of osteoarthritis and has been detected with T2 measurements (201) (Figures 20A, B, C, D). This disruption of collagen organization leads to increased permeability and water content of cartilage (43, 109), leading to increased compressibility of cartilage (49), which in turn, results in greater load-bearing stress on the solid components of the extracellular matrix (202), which finally results in morphological changes in the cartilage. In order to accurately measure the T2 relaxation time, technical concerns are to be taken into account when selecting the MR technique (203). Typically a multiecho spin-echo technique is used with varying echo times (TE) and identical repetition times (TR), and signal levels are fitted to one or more decaying exponentials, depending on whether more than one distribution of T2 is thought to be within the sample (203); T2 is defined as the time at which the signal decays to 37% of maximum signal (52). For conventional MRI, a single exponential fit is usually adequate (161), then an image of the T2 relaxation time is generated with either a color or gray-scale map. For accurate depiction of the depth dependent spatial variation in cartilage T2, high-resolution T2 maps are needed, such that the resolution should be ideally in the range of 2% of total cartilage thickness for each pixel (204), which is impossible with current technologies. However, there have been studies with attempts to decrease image acquisition time, using parallel imaging (102), rapid T2 mapping sequences (205), hybrid gradient-echo/spin-echo (206), and gradient echo T2* mapping techniques (207, 208). Measurements of relaxation times have been shown to be anisotropic with respect to the main magnetic field (172, 170, 188).

NIH-PA Author Manuscript

NIH-PA Author Manuscript

NIH-PA Author Manuscript

In vitro studies have been conducted to investigate the relationship between T2 measurements and biochemical composition of cartilage with results demonstrating a strong correlation between T2 and histologic indicators of cartilage degeneration in tissue samples and animal models (81, 141, 169, 209–213). Such studies showed elevated T2 not only in areas of cartilage damage but also in adjacent areas, suggesting exposure of additional hydrophilic sites leading to a more efficient T2 relaxation and greater magnetization transfer effects (10). Aside from these validation studies mostly conducted in vitro, in vivo studies have been conducted in the human knee joint (203, 205, 214–217) (Figure 21A, B), hip (219, 220), ankle (221), and the proximal interphalangeal joint of the hands (222). High resolution in vivo studies have shown a spatial variation within cartilage with shorter T2 values as the layers get close to the subchondral bone, and higher T2 values as the layers gets more superficial closer to the articular surface (182, 215, 223, 224). Regional variation within the femorotibial joint have also been shown (225), as well as greater entropy of T2 in osteoarthritic cartilage (226). According to results from various studies, regional variation of T2 seems to be affected by age (215, 227, 228, 223), as aging is associated with reorganization and changes of the collagen matrix starting from the superficial layer at the articular surface (10); more significant increases in T2 have been observed in older individuals according to depth (228, 223) and in general throughout the cartilage (228). However, gender does not seem to have a great influence on regional variation of T2 as of yet (229).

In spite of the numerous validation studies of changes in T2 correlating with the biochemical changes in cartilage, there have been relatively limited clinical application studies using quantitative T2 mapping in the evaluation of arthritis. Increased T2 values have been reported in subjects with radiographically evident osteoarthritis of the knee (92, 209, 225, 230, 217); however, the T2 values did not statistically correlate well with the radiographic degree of OA (225). Increased T2 values have been attributed to collagen matrix degeneration in early OA, which are not increased further with progression of the disease, so further investigations are needed to determine the significance of T2 changes and their relationship to disease progression and treatment response (10). However, T2 relaxation time still may provide an insight into the heterogeneous and complex process of cartilage degeneration in OA.

There have been studies investigating the relationship between cartilage morphology and T2, showing an inverse relationship between cartilage T2 and thickness (231, 225), higher cartilage T2 with greater loss of volume (232), increase in mean cartilage T2 at longitudinal follow-up after 12 months in OA groups (231), and increased T2 with cartilage defect regardless of unloading of the knee (233). The study by Apprich et al also explored the effects of biomechanical stress on cartilage, which has also been a subject of interest in recent studies (233).

The effects of joint position and alignment have been investigated in several studies in animal (234) and human studies (235), with increased T2 values in knee flexion (234) and varus alignment (235). There have been other studies exploring the relationship between T2 values and cartilage biomechanics; in initial feasibility studies, decrease in T2 was observed when static compression was applied to the cartilage (236, 237, 238), confirming a strong correlation between change in collagen fiber orientation and T2 values (10). Quantitative T2 mapping in cartilage plugs showed zone-specific changes during compressive loading (198). In a study from the osteoarthritis initiative, physically active individuals had more knee abnormalities and higher patellar T2 values (239). In a recent study by Mosher et al, effect of age and training on knee cartilage were evaluated in response to running. Running resulted in decrease in cartilage thickness and T2 values in the superficial cartilage consistent with greater compressibility in the superficial layer, whereas age and level of

NIH-PA Author Manuscript

NIH-PA Author Manuscript

NIH-PA Author Manuscript

physical activity did not affect the T2 changes in running (240); the changes in the superficial layer were concordant with results from an earlier study (241) (Figures 22, 23A, B). Thus, T2 mapping may be a valuable technique in investigating the role of cartilage biomechanics in cartilage physiology.

T2 mapping has also been used to evaluate cartilage repair tissue after treatment (140, 148, 169, 213, 242–251). In a study by White et al, repair tissue from osteochondral transplantation was shown to have the normal spatial variation of T2 values, which was absent in repair tissue from autologous chondrocyte implantation or microfracture techniques (246) (Figures 24A, B). In a study by Domayer et al, T2 mapping and dGEMRIC provided complementary information on the biochemical properties of repair tissue after autologous chondrocyte implantation with a fibrin-based scaffold in the knee, which resulted in repair tissue with spatial variation of T2 values similar to normal articular cartilage (148) (Figures 25A, B). Another study evaluated cartilage repair tissue using T2 and T2* mapping after matrix-associated autologous chondrocyte transplantation on 3.0T MRI and showed zonal variation (248). In a study by Mamisch et al., differences in response to unloading were evaluated in control and cartilage repair tissue of the knee using T2 mapping, and the results showed differences in early and late unloading T2 values between normal healthy and repaired cartilage (249). Although many of these studies are initial or preliminary studies, the results suggest T2 may be a potentially useful technique in postoperative evaluation of repaired cartilage.

Ultrashort echo time (uTE) imaging

With the higher TEs (greater or equal to 10 milliseconds) used in most conventional T2-weighted sequences on conventional clinical scanners, MR signal from musculoskeletal tissues with short T2 characteristics, such as cortical bone, tendons, ligaments, menisci, and deep radial and calcified layers of cartilage decay rapidly and produce little or no signal (252, 253). With ultrashort-echo time (UTE) MR imaging, signal from tissues with predominantly short T2 (and T2*) can be detected (254, 252, 255, 256) using TEs that are 20–50 times or even 100–1000 times shorter than those used in conventional imaging sequences (252, 257–259), enabling visualization of layers which are not normally depicted well on conventional sequences. The hyaline articular cartilage layer has been depicted as two layers on subtraction images, consisting of a high signal layer and a low signal superficial layer (255). The region of the osteochondral junction consisting of the calcified cartilage layer and subchondral bone, which is important for solute transport between the vasculature and articular cartilage (260), has been implicated to be important in the pathogenesis of osteoarthritis (253) with changes beginning in the calcified layer affecting the more superficial cartilage and subsequently causing cartilage degeneration (261–267). However, the calcified layer of cartilage, due to rapid signal decay, produces little or no signal and is difficult to evaluate with conventional MR imaging sequences. In a study by Gold et al, projection-reconstruction spectroscopic imaging (PRSI) technique and non-Cartesian K-space trajectory 3D cones technique were used to depict articular cartilage at high-resolution in vivo at 5–10 minute scan times (258). A recent study by Bae et al, which used two complementary UTE techniques, suggested that the presence of the calcified layer as well as the deepest layer of uncalcified cartilage, with their short T2 values, contributed to the UTE signal without contribution from the subchondral bone (253) (Figure 26A–D).

Technical challenges related to UTE imaging include distortion of the slice profile, errors in the radial k-space trajectories, and off resonance, which could be improved by gradient calibration, off-resonance correction, efficient long T2 water and fat suppression (268–270) (Figure 27, 28A, B, 29). In spite of the technical challenges and disadvantage of scan time and difficulty in slice selection, UTE imaging may allow evaluation of the calcified layer of

NIH-PA Author Manuscript

NIH-PA Author Manuscript

NIH-PA Author Manuscript

cartilage in osteoarthritis (271). UTE imaging may also be useful for postoperative assessment of cartilage repair, where the removal of calcified layer has been reported to improve surgical outcome (272), and may be the only imaging method thus far which allows examination of the region of osteochondral junction.

Magnetization Transfer

Magnetization transfer (MT) effect is present in any multi-slice MRI technique and is seen in cartilage (170, 273), especially prominent in the radial zone near the bone/cartilage interface (274). It is prominently seen in turbo spin echo (TSE) sequences and can be a source of error in quantitative mapping techniques such as T1 or T2 mapping when multi-slice TSE sequences are used (275–278). In contrast, gradient echo (GRE) sequences exhibit less MT, and by applying an off-resonance RF pulse immediately before the GRE sequence, one can obtain an MT contrast image (10) and by subtracting images, one may obtain an isolated contribution from MT; however, the resulting image is usually prone to artifacts and has poor signal to noise (10). Higher SNR may be achieved using 3.0T MR scanners (279).

As MT is affected by many factors, such as RF power, pulse profile, and offset frequency, quantification of MT is difficult (171, 280). Higher RF power accompanies the problem with SAR, so quantitative MT techniques have been studied in a limited number of human studies (281–284). Therefore, most studies have been conducted using tissue samples (283, 285–290) or animal models (291–293) and have shown that MT is affected mostly by the collagen content and changes in collagen-water interaction. In a study of bovine cartilage specimens, magnetization transfer ratio (MTR) showed depth-dependency and higher values in the radial zone compared with the superficial zone, which suggested that MTR may not only be dependent on collagen content, but other parameters, such as the arrangement of macromolecules, high solid content, bound water fraction, and radial orientation (274) (Figure 30). In spite of the limitations, the technique has been applied to improve contrast between cartilage and fluid and therefore, improve detection of localized cartilage lesions (281, 294–297) (Figure 30). In a study evaluating T1, T2, and magnetization transfer ratios in early diagnosis of patellar cartilage osteoarthritis, MTRs were found to have limitations in early diagnosis of OA (217). There have been also preliminary studies on postoperative cartilage repair tissue, one of which showed too small differences between damaged and repaired cartilage MTR but evolution towards normal MTR in repair tissue, especially after ACI repair (284). Another study showed contrasting results, suggesting MTR to be capable of detecting differences between normal cartilage and areas of cartilage repair and possibly a useful tool in imaging biochemical changes in cartilage after repair (298). Further investigations are needed to validate such studies.

Diffusion-weighted Imaging

Water is abundant within normal cartilage, composing about 65% to 85% of the extracellular matrix, and imaging of water diffusion throughout the cartilage is possible with MRI. In vitro studies have shown diffusion-weighted imaging (DWI) to be sensitive to early cartilage degeneration (175, 299). The apparent diffusion coefficient (ADC) decreases as diffusion times get longer and indicate restriction of the water molecules by solid components of the cartilage, usually collagen network (116). When diffusion-sensitizing gradients are applied, water gains a random amount of phase and does not refocus, which results in signal loss of the tissue undergoing diffusion (112). The amount of diffusion weighting expressed as the *b-value* depends on the amplitude and timing of the diffusion-sensitizing gradients. And a map of the amount of diffusion that has occurred is called the ADC map, which uses the term “apparent” because the values reflect only the bulk water and not the water protons restricted by tissue membranes (112).

NIH-PA Author Manuscript

NIH-PA Author Manuscript

NIH-PA Author Manuscript

In vivo DWI of cartilage is difficult because in order to maximize cartilage signal, TE must be short, but diffusion-sensitizing gradients increase the TE and render the technique sensitive to motion (112). Single-shot techniques have been used for DWI, but they are limited by low SNR and spatial resolution (112); multiple acquisitions improve the SNR and resolution but motion correction is needed (300) (Figures 31A, B). In an in vivo study, ADC measurements of articular cartilage in healthy volunteers showed comparable results to a study using cartilage specimens (301).

Diffusion-weighted imaging has also evaluated in postoperative cartilage repair tissue. In a study by Mamisch et al, repaired cartilage after matrix-associated autologous chondrocyte transplantation at 3.0T using a steady-state precession (FSIP) technique called PSIF showed higher ADC values in the repaired cartilage and a decrease in values at later time point after surgery (302). In another study using high-field MRI, a dedicated multichannel coil, and sophisticated sequences, DWI showed higher ADC values in the repair tissue and was shown to provide additional information than T2 and T2* mapping about cartilage ultrastructure and cartilage repair tissue in the ankle joint (250). Similarly in another study, DWI was able to differentiate between healthy cartilage and cartilage repair tissue in both microfracture therapy and matrix-associated autologous chondrocyte transplantation with good correlation between ADC values and clinical scoring (251). In another recent study, DWI detected changes of diffusion within cartilage repair tissue up to two years after surgery, which then became stabilized with zonal variations (303). Even though the results of most of these studies are preliminary, they suggest DWI to be a potential useful technique in evaluation of the biochemical and physiological changes in postoperative cartilage repair tissue.

Summary

Whereas conventional MR imaging methods were able to depict morphological changes when the disease was already at a progressed state, the newer MR imaging methods are more based and cartilage physiology. Sodium imaging is highly specific for change in PG content without the need for an exogenous contrast agent but requires special transmit and receive coils, long imaging times, and is limited by SAR problems. T1 rho imaging is sensitive to early PG depletion but again is limited by SAR problems because it requires high RF power during the spin-locking preparation pulse. dGEMRIC has relatively high resolution and sensitivity but requires long imaging times, including a delay before imaging, and administration of an exogenous contrast agent, which accompanies a small risk of nephrogenic systemic fibrosis. T2 mapping is relatively straightforward to perform and is sensitive to changes in collagen as well as water content but may be less sensitive in early degeneration than other methods. Ultrashort echo time (UTE) MRI may be the only technique to examine osteochondral junction but technical challenges, such as scan time and difficulty in slice selection, make this challenging. Magnetization transfer provides improved contrast between cartilage and fluid, therefore allowing detection of localized cartilage lesions, but is difficult to quantify and again may have SAR problems. Diffusion weighted imaging may be a valuable tool in postoperative imaging but is limited by low SNR and spatial resolution. There remains much more to be investigated in the field of MR imaging of cartilage physiology, but these promising methods can give researchers important insights into the initiation, progression, and eventual treatment of osteoarthritis.

References

1. Liess C, Lusse S, Karger N, et al. Detection of changes in cartilage water content using MRI T2-mapping in vivo. Osteoarthritis Cartilage. 2002; 10:907–913. [PubMed: 12464550]

NIH-PA Author Manuscript

NIH-PA Author Manuscript

NIH-PA Author Manuscript

2. Felson DT, Zhang Y, Hannan MT, et al. The incidence and natural history of knee osteoarthritis in the elderly. The Framingham Osteoarthritis Study. Arthritis Rheum. 1995; 38(10):1500–1505. [PubMed: 7575700]
3. Lawrence RC, Felson DT, Helmick CG, et al. National Arthritis Data W. Estimates of the prevalence of arthritis and other rheumatic conditions in the United States. Part II. Arthritis Rehum. 2008; 58(1):26–35.
4. Kim I, Kim HA, Seo YI, et al. The prevalence of knee osteoarthritis in elderly community residents in Korea. J Korean Med Sci. 2010; 25(2):293–298. [PubMed: 20119586]
5. Yoshimura N. Progress of research in osteoarthritis. Epidemiology of osteoarthritis in Japanese population. The Road study. Clin Calcium. 2009; 19(11):1572–1577. [PubMed: 19880988]
6. Kang X, Fransen M, Zhang Y, et al. The high prevalence of knee osteoarthritis in a rural Chinese population: the Wuchuan osteoarthritis study. Arthritis Rheum. 2009; 61(5):641–647. [PubMed: 19405001]
7. Poole AR. An introduction to the pathophysiology of osteoarthritis. Front Biosci. 1999; 4:D662–D670. [PubMed: 10525481]
8. Roos H, Adalberth T, Dahlberg L, et al. Osteoarthritis of the knee after injury to the anterior cruciate ligament or meniscus: the influence of time and age. Osteoarthritis Cartilage. 1995; 3:261–267. [PubMed: 8689461]
9. van den Berg WB. Pathophysiology of osteoarthritis. Joint Bone Spine. 2000; 67:555–556. [PubMed: 11195322]
10. Gold, GE.; Mosher, TJ. Arthritis in color: Advanced imaging of arthritis. Bruno, MA.; Mosher, TJ.; Gold, GE., editors. Philadelphia: Elsevier Saunders; 2009. p. 153-192.
11. Helmick CG, Felson DT, Lawrence RC, et al. Estimates of the prevalence of arthritis and other rheumatic conditions in the United States. Part I. Arthritis Rheum. 2008; 58(1):15–25. [PubMed: 18163481]
12. Lawrence RC, Helmick CG, Arnett FC, et al. Estimates of the prevalence of arthritis and selected musculoskeletal disorders in the United States. Arthritis Rheum. 1998; 41(5):778–799. [PubMed: 9588729]
13. Boegard T, Rudling O, Petersson IF, et al. Correlation between radiographically diagnosed osteophytes and magnetic resonance detected cartilage defects in the tibiofemoral joint. Ann Rheum Dis. 1998; 57:401–407. [PubMed: 9797566]
14. Coumas JM, Palmer WE. Knee arthrography: evolution and current status. Radiol Clin North Am. 1998; 36:703–728. [PubMed: 9673648]
15. Disler DG, McCauley TR. Clinical magnetic resonance imaging of articular cartilage. Top Magn Reson Imaging. 1998; 9:360–376. [PubMed: 9894739]
16. Gold GE, McCauley TR, Gray ML, et al. What's new in cartilage? Radiographics. 2003; 23:1227–1242. [PubMed: 14518449]
17. Hodler J, Resnick D. Current status of imaging of articular cartilage. Skeletal Radiol. 1996; 25:703–709. [PubMed: 8958614]
18. McCauley TR, Disler DG. Magnetic resonance imaging of articular cartilage of the knee. J Am Acad Orthop Surg. 2001; 9:2–8. [PubMed: 11174158]
19. Recht MP, Resnick D. Magnetic resonance imaging of articular cartilage: an overview. Top Magn Reson Imaging. 1998; 9:328–336. [PubMed: 9894736]
20. Rubenstein JD, Li JG, Majumdar S, et al. Image resolution and signal-to-noise ratio requirements for MR imaging of degenerative cartilage. AJR Am J Roentgenol. 1997; 169:1089–1096. [PubMed: 9308470]
21. Reeder SB, Hargreaves BA, Yu H, et al. Homodyne reconstruction and IDEAL water-fat decomposition. Magn Reson Med. 2005; 54:586–593. [PubMed: 16086311]
22. Cicuttini F, Forbes A, Asbeutah A, et al. Comparison and reproducibility of fast and conventional spoiled gradient-echo magnetic resonance sequences in the determination of knee cartilage volume. J Orthop Res. 2000; 18:580–584. [PubMed: 11052494]
23. Eckstein F, Westhoff J, Sittek H, et al. In vivo reproducibility of three-dimensional cartilage volume and thickness measurements with MR imaging. AJR Am J Roentgenol. 1998; 170:593–597. [PubMed: 9490936]

NIH-PA Author Manuscript

NIH-PA Author Manuscript

NIH-PA Author Manuscript

24. Mosher, TJ. Arthritis in color: Advanced imaging of arthritis. Bruno, MA.; Mosher, TJ.; Gold, GE., editors. Philadelphia: Elsevier Saunders; 2009. p. 23-32.
25. Venn M, Maroudas A. Chemical composition and swelling of normal and osteoarthrotic femoral head cartilage. I. Chemical composition. Ann Rheum Dis. 1977; 36:121–129. [PubMed: 856064]
26. Torzilli PA. Influence of cartilage conformation on its equilibrium water partition. J Orthop Res. 1985; 3:473–483. [PubMed: 4067706]
27. Maroudas A, Schneiderman R. “Free” and “exchangeable” or ‘trapped” and “non-exchangeable” water in cartilage. J Orthop Res. 1987; 5:133–138. [PubMed: 3819905]
28. Guilak F, Meyer BC, Ratcliffe A, et al. The effects of matrix compression on proteoglycan metabolism in articular cartilage explants. Osteoarthritis Cartilage. 1994; 2:91–101. [PubMed: 11548233]
29. Jay GD, Torres JR, Warman ML, et al. The role of lubricin in the mechanical behavior of synovial fluid. Proc Natl Acad Sci USA. 2007; 104:6194–6199. [PubMed: 17404241]
30. Clark JM. The organization of collagen fibrils in the superficial zones of articular cartilage. J Anat. 1990; 171:117–130. [PubMed: 2081698]
31. Thompson AM, Stockwell RA. An ultrastructural study of the marginal transitional zone in the rabbit knee joint. J Anat. 1983; 136:701–713. [PubMed: 6885623]
32. Xia Y, Moody JB, Burton-Wurster N, et al. Quantitative in situ correlation between microscopic MRI and polarized light microscopy studies of articular cartilage. Osteoarthritis Cartilage. 2001; 9:393–406. [PubMed: 11467887]
33. Clark JM. The organization of collagen in cryofractured rabbit articular cartilage: a scanning elelctron microscopic study. J Orthop Res. 1985; 3:17–29. [PubMed: 3981292]
34. Clark JM. Variation in collagen fiber alignment in a joint surface: a scanning electron microscope study of the tibial plateau in dog, rabbit, and man. J Orthop Res. 1991; 9:246–257. [PubMed: 1992075]
35. Borthakur A, Mellon E, Niyogi S, et al. Sodium and T1 rho MRI for molecular and diagnostic imaging of articular cartilage. NMR Biomed. 2006; 19:781–821. [PubMed: 17075961]
36. Moger CJ, Barrett R, Bleuet P, et al. Regional variations of collagen orientation in normal and diseased articular cartilage and subchondral bone determined using small angle X-ray scattering (SAXS). Osteoarthritis Cartilage. 2007; 15:682–687. [PubMed: 17306566]
37. Gomez S, Toffanin R, Bernstorff S, et al. Collagen fibrils are differently organized in weight-bearing and not-weight-bearing regions of pig articular cartilage. J Exp Zool. 2000; 287:346–352. [PubMed: 10980493]
38. Thompson AM, Stockwell RA. An ultrastructural study of the marginal transitional zone in the rabbit knee joint. J Anat. 1983; 136:701–713. [PubMed: 6885623]
39. Franzen A, Inerot S, Hejderup SO, et al. Variations in the composition of bovine hip articular cartilage with distance from the articular surface. Biochem J. 1981; 195:535–543. [PubMed: 7316972]
40. Bayliss, MT.; Venn, M.; Maroudas, A., et al. Structure of proteoglycans from different layers.
41. Roughley PJ. The structure and function of cartilage proteoglycans. Eur Cell Mater. 2006; 12:92–101. [PubMed: 17136680]
42. Gray ML, Burstein D, Kim YJ, et al. Elizabeth Winston Lanier Award Winner. Magnetic resonance imaging of cartilage glycosaminoglycan: Basic principles, imaging technique, and clinical applications. J Orthop Res. 2007; 26(3):281–291. [PubMed: 17876836]
43. Maroudas AI. Balance between swelling pressure and collagen tension in normal and degenerative cartilage. Nature. 1976; 260:808–809. [PubMed: 1264261]
44. Clark JM, Huber JD. The structure of the human subchondral plate. J Bone Joint Surg Br. 1990; 72:866–873. [PubMed: 2211774]
45. Otterness IG, Chang M, Burkhardt JE, et al. Histology and tissue chemistry of tidemark separation in hamsters. Vet Pathol. 1999; 36:138–145. [PubMed: 10098642]
46. Doube M, Firth EC, Boyde A. Variations in articular calcified cartilage by site and exercise in the 18-month-old equine distal metacarpal condyle. Osteoarthritis Cartilage. 2007; 15:1283–1292. [PubMed: 17517523]

NIH-PA Author Manuscript

NIH-PA Author Manuscript

NIH-PA Author Manuscript

47. Mow, VC.; Huiskes, R. Basic orthopaedic biomechanics & mechano-biology. Philadelphia: Lippincott Williams & Wilkins; 2005.
48. Lu XL, Mow VC. Biomechanics of articular cartilage and determination of material properties. Med Sci Sports Exerc. 2008; 40:193–199. [PubMed: 18202585]
49. Armstrong CG, Mow VC. Variations in the intrinsic mechanical properties of human articular cartilage with age, degeneration, and water content. J Bone Joint Surg Am. 1982; 64:88–94. [PubMed: 7054208]
50. Wong M, Carter DR. Articular cartilage functional histomorphology and mechanobiology: a research perspective. Bone. 2003; 33:1–13. [PubMed: 12919695]
51. Schmidt MB, Mow VC, Chun LE, et al. Effects of proteoglycan extraction on the tensile behavior of articular cartilage. J Orthop Res. 1990; 8:353–363. [PubMed: 2324854]
52. Blumenkrantz G, Majumdar S. Quantitative magnetic resonance imaging of articular cartilage in osteoarthritis. European Cells and Materials. 2007; 13:75–86.
53. Dijkgraaf LC, deBont LG, Boering G, et al. The structure, biochemistry, and metabolism of osteoarthritis cartilage: a review of the literature. J Oral Maxillofac Surg. 1995; 53:1182–1192. [PubMed: 7562173]
54. Gold GE, Hargreaves BA, Stevens KJ, et al. Advanced MR imaging of articular cartilage. Orthop Clin North Am. 2006; 37(3):331–347. vi. [PubMed: 16846765]
55. Shapiro EM, Borthakur A, Gougoutas A, et al. 23Na MRI accurately measures fixed charge density in articular cartilage. Magn Reson Med. 2002; 47(2):284–291. [PubMed: 11810671]
56. Boada FE, Shen GX, Chang SY, et al. Spectrally weighted twisted projection imaging: reducing T2 signal attenuation effects in fast three-dimensional sodium imaging. Magn Reson Med. 1997; 38:1022–1028. [PubMed: 9402205]
57. Maroudas A, Muir H, Wingham J. The correlation of fixed negative charge with glycosaminoglycan content of human articular cartilage. Biochim Biophys Acta. 1969; 177:492–500. [PubMed: 4239606]
58. Borthakur A, Hancu I, Boada FE, et al. In vivo triple quantum filtered twisted projection sodium MRI of human articular cartilage. J Magn Reson. 1999; 141(2):286–290. [PubMed: 10579951]
59. Borthakur A, Shapiro EM, Beers J, et al. Sensitivity of MRI to proteoglycan depletion in cartilage: comparison of sodium and proton MRI. Osteoarthritis Cartilage. 2000; 8(4):288–293. [PubMed: 10903883]
60. Borthakur A, Shapiro EM, Akella SV, et al. Quantifying sodium in the human wrist in vivo by using MR imaging. Radiology. 2002; 224:598–602. [PubMed: 12147862]
61. Insko EK, Kaufman JH, Leigh JS, et al. Sodium NMR evaluation of articular cartilage degradation. Magn Reson Med. 1999; 41:30–34. [PubMed: 10025608]
62. Reddy R, Insko EK, Noyszewski EA, et al. Sodium MRI of human articular cartilage in vivo. Magn Reson Med. 1998; 39:697–701. [PubMed: 9581599]
63. Wheaton AJ, Borthakur A, Dodge GR, et al. Sodium magnetic resonance imaging of proteoglycan depletion in an in vivo model of osteoarthritis. Acad Radiol. 2004; 11:21–28. [PubMed: 14746398]
64. Shapiro EM, Borthakur A, Dandora R, et al. Sodium visibility and quantitation in intact bovine articular cartilage using high field (23)Na MRI and MRS. J Magn Reson. 2000; 142:24–31. [PubMed: 10617432]
65. Choy J, Ling W, Jerschow A. Selective detection of ordered sodium signals via the central transition. J Magn Reson. 2006; 180:105–109. [PubMed: 16469514]
66. Hancu I, van der Maarel JR, Boada FE. A model for the dynamics of spins 3/2 in biological media: signal loss during radiofrequency excitation in triple-quantum-filtered sodium MRI. J Magn Reson. 2000; 147:179–191. [PubMed: 11097809]
67. Ling W, Jerschow A. Selecting ordered environments in NMR of spin 3/2 nuclei via frequency-sweep pulses. J Magn Reson. 2005; 176:234–238. [PubMed: 16027016]
68. Ling W, Regatte RR, Schweitzer ME, et al. Behavior of ordered sodium in enzymatically depleted cartilage tissue. Magn Reson Med. 2006; 56:1151–1155. [PubMed: 17029232]

NIH-PA Author Manuscript

NIH-PA Author Manuscript

NIH-PA Author Manuscript

69. Navon G, Shinar H, Eliav U, et al. Multiquantum filters and order in tissues. NMR Biomed. 2001; 14:112–132. [PubMed: 11320537]
70. Shinar H, Navon G. Multinuclear NMR and microscopic MRI studies of the articular cartilage nanostructure. NMR Biomed. 2006; 19:877–893. [PubMed: 17075957]
71. Speer DP, Dahners L. The collagenous architecture of articular cartilage: correlation of scanning electron microscopy and polarized light microscopy observations. Clin Orthop Relat Res. 1979; 139:267–275. [PubMed: 455843]
72. Jeffery AK, Blunn GW, Archer CW, et al. Three-dimensional collagen architecture in bovine articular cartilage. J Bone Joint Surg Br. 1991; 73:795–801. [PubMed: 1894669]
73. Wang L, Wu Y, Chang G, et al. Rapid isotropic 3D-sodium MRI of the knee joint in vivo at 7T. J Magn Reson Imaging. 2009; 30(3):606–614. [PubMed: 19711406]
74. Staroswiecki E, Bangerter NK, Gurney PT, et al. In vivo sodium imaging of human patellar cartilage with a 3D cones sequence at 3T and 7T. J Magn Reson Imaging. 2010; 32(2):446–451. [PubMed: 20677276]
75. Trattnig S, Welsch GH, Juras V, et al. 23Na MR imaging at 7T after knee matrix-associated autologous chondrocyte transplantation: preliminary results. Radiology. 2010 Aug 16. [Epub ahead of print].
76. Hancu I, Boada FE, Shen GX. Three-dimensional triple-quantum-filtered (23)Na imaging of in vivo human brain. Magn Reson Med. 1999; 42:1146–1154. [PubMed: 10571937]
77. Rong P, Regatte RR, Jerschow A. Clean demarcation of cartilage tissue 23Na by inversion recovery. J Magn Reson. 2008; 193(2):207–209. [PubMed: 18502158]
78. Burstein D, Velyvis J, Scott KT, et al. Protocol issues for delayed Gd(DTPA)$^{2-}$-enhanced MRI (dGEMRIC) for clinical evaluation of articular cartilage. Magn Reson Med. 2001; 45(1):36–41. [PubMed: 11146483]
79. Pruessmann KP, Weiger M, Scheidegger MB, et al. SENSE: sensitivity encoding for fast MRI. Magn Reson Med. 1999; 42(5):952–962. [PubMed: 10542355]
80. Sodickson DK, Manning WJ. Simultaneous acquisition of spatial harmonics (SMASH): fast imaging with radiofrequency coil arrays. Magn Reson Med. 1997; 38(4):591–603. [PubMed: 9324327]
81. Mlynarik V, Trattnig S, Huber M, et al. The role of relaxation times in monitoring proteoglycan depletion in articular cartilage. J Magn Reson Imaging. 1999; 10:497–502. [PubMed: 10508315]
82. Mlynarik V, Szomolanyi P, Toffanin R, et al. Transverse relaxation mechanisms in articular cartilage. J Magn Reson. 2004; 169:300–307. [PubMed: 15261626]
83. Menezes NM, Gray ML, Hartke JR, et al. T2 and T1 rho MRI in articular cartilage systems. Magn Reson Med. 2004; 51:503–509. [PubMed: 15004791]
84. Reddy, R.; Insko, EK.; Kaufman, JH., et al. MR imaging of cartilage under spin-locking. Proceedings of the International Society of Magnetic Resonance Medicine; Nice. 1995. p. 1535
85. Regatte RR, Akella SV, Borthakur A, et al. Proteoglycan depletion-induced changes in transverse relaxation maps of cartilage: comparison of T2 and T1rho. Acad Radiol. 2002; 9:1388–1394. [PubMed: 12553350]
86. Regatte RR, Akella SV, Borthakur A, et al. Proton spin-lock ratio imaging for quantitation of glycosaminoglycans in articular cartilage. J Magn Reson Imaging. 2003; 17:114–121. [PubMed: 12500280]
87. Duvvuri U, Kudchodkar S, Reddy R, et al. T1rho relaxation can assess longitudinal proteoglycan loss from articular cartilage in vitro. Osteoarthritis Cartilage. 2002; 10:838–844. [PubMed: 12435327]
88. Duvvuri U, Reddy R, Patel SD, et al. T1rho-relaxation in articular cartilage: effects of enzymatic degradation. Magn Reson Med. 1997; 38:863–867. [PubMed: 9402184]
89. Akella SV, Regatte RR, Gougoutas AJ, et al. Proteoglycan-induced changes in T1 rho-relaxation of articular cartilage at 4T. Magn Reson Med. 2001; 46:419–423. [PubMed: 11550230]
90. Wheaton AJ, Dodge GR, Borthakur A, et al. Detection of changes in articular cartilage proteoglycan by T(1rho) magnetic resonance imaging. J Orthop Res. 2005; 23:102–108. [PubMed: 15607881]

NIH-PA Author Manuscript

NIH-PA Author Manuscript

NIH-PA Author Manuscript

91. Wheaton AJ, Casey FL, Gougoutas AJ, et al. Correlation of T1rho with fixed charge density in cartilage. J Magn Reson Imaging. 2004; 20:519–525. [PubMed: 15332262]
92. Regatte RR, Akella SV, Lonner JH, et al. T1 rho relaxation mapping in human osteoarthritis (OA) cartilage: comparison of T1rho with T2. J Magn Reson Imaging. 2006; 23:547–553. [PubMed: 16523468]
93. Li, X.; Han, ET.; Crane, JC., et al. Development of in vivo multi-slice spiral T1 rho mapping in cartilage at 3T and its application to osteoarthritis. [abstract 479]. Proc Ann Meeting Int Soc Magn Resonance Med (ISMRM); Miami, Florida. 2005.
94. Regatte RR, Akella SV, Wheaton AJ, et al. 3D-T1 rho-relaxation mapping of articular cartilage: in vivo assessment of early degenerative changes in symptomatic osteoarthritic subjects. Acad Radiol. 2004; 11:741–749. [PubMed: 15217591]
95. Taylor C, Carballido-Gamio J, Majumdar S, et al. Comparison of quantitative imaging of cartilage for osteoarthritis: T2, T1rho, DGEMRIC and contrast-enhanced computed tomography. Magn Reson Imaging. 2009; 27(6):779–784. [PubMed: 19269769]
96. Majumdar S, Li X, Blumenkrantz G, et al. MR imaging and early cartilage degeneration and strategies for monitoring regeneration. J Musculoskelet Neuronal Interact. 2006; 6:382–384. [PubMed: 17185834]
97. Regatte RR, Akella SV, Borthakur A, et al. In vivo proton MR three-dimensional T1rho mapping of human articular cartilage: initial experience. Radiology. 2003; 229:269–274. [PubMed: 14519880]
98. Wheaton AJ, Borthakur A, Kneeland JB, et al. In vivo quantification of T1rho using a multislice spin-lock pulse sequence. Magn Reson Med. 2004; 52:1453–1458. [PubMed: 15562469]
99. Akella SV, Regatte RR, Borthakur A, et al. T1 rho MR imaging of the human wrist in vivo. Acad Radiol. 2003; 10:614–619. [PubMed: 12809414]
100. Pakin SK, Schweitzer ME, Regatte RR. 3D-T1rho quantitation of patellar cartilage at 3.0T. J Magn Reson Imaging. 2006; 24:1357–1363. [PubMed: 17058202]
101. Borthakur A, Wheaton A, Charagundla SR, et al. Three-dimensional T1rho-weighted MRI at 1.5 Tesla. J Magn Reson Imaging. 2003; 17:730–736. [PubMed: 12766904]
102. Zuo J, Li X, Banerjee S, et al. Parallel imaging of knee cartilage at 3 Tesla. J Magn Reson Imaging. 2007; 26:1001–1009. [PubMed: 17896394]
103. Witschey WR, Borthakur A, Elliott MA, et al. T1rho-prepared balanced gradient echo for rapid 3D T1rho MRI. J Magn Reson Imaging. 2008; 28:744–754. [PubMed: 18777535]
104. Pakin SK, Xu J, Schweitzer ME, et al. Rapid 3D-T1rho mapping of the knee joint at 3.0T with parallel imaging. Magn Reson Med. 2006; 56:563–571. [PubMed: 16894582]
105. Maroudas, A. Physicochemical properties of articular cartilage. In: Freeman, M., editor. Adult articular cartilage. 2. London: Pitman Medical; 1979. p. 215-290.
106. Eisenberg SR, Grodzinsky AJ. Swelling of articular cartilage and other connective tissues: electromechanochemical forces. J Orthop Res. 1985; 3:148–159. [PubMed: 3998893]
107. Frank EH, Grodzinsky AJ, Koob TJ, et al. Streaming potentials: a sensitive index of enzymatic degradation in particular cartilage. J Orthop Res. 1987; 5:497–508. [PubMed: 3681524]
108. Maroudas A, Bayliss MT, Venn MF. Further studies on the composition of human femoral head cartilage. Ann Rheum Dis. 1980; 39:514–523. [PubMed: 7436585]
109. Maroudas A, Venn M. Chemical composition and swelling of normal and osteoarthrotic femoral cartilage. II. Swelling. Ann Rheum Dis. 1977; 36:399–406. [PubMed: 200188]
110. Ficat C, Maroudas A. Cartilage of the patella. Topographical variation of glycosaminoglycan content in normal and fibrillated tissue. Ann Rheum Dis. 1975; 34:515–519. [PubMed: 130842]
111. Maroudas A, Evans H, Almeida L. Cartilage of the hip joint. Topographical variation of glycosaminoglycan content in normal and fibrillated tissue. Ann Rheum Dis. 1973; 32:1–9. [PubMed: 4265480]
112. Gold GE, Burstein D, Dardzinski B, et al. MRI of articular cartilage in OA: novel pulse sequences and composition/functional markers. Osteoarthritis Cartilage. 2006; 14 (Suppl A):A76–A86. [PubMed: 16716605]

NIH-PA Author Manuscript

NIH-PA Author Manuscript

NIH-PA Author Manuscript

113. Gray ML, Burstein D, Xia Y. Biochemical (and functional) imaging of articular cartilage. Semin Musculoskelet Radiol. 2001; 5:329–343. [PubMed: 11745049]
114. Gray ML, Burstein D. Molecular (and functional) imaging of articular cartilage. J Musculoskelet Neuronal Interact. 2004; 4:365–368. [PubMed: 15758262]
115. Bashir A, Gray ML, Hartke J, et al. Nondestructive imaging of human cartilage glycosaminoglycan concentration by MRI. Magn Reson Med. 1999; 41:857–865. [PubMed: 10332865]
116. Burstein D, Gray ML, Hartman AL, et al. Diffusion of small solutes in cartilage as measured by nuclear magnetic resonance (NMR) spectroscopy and imaging. J Orthop Res. 1993; 11:465–478. [PubMed: 8340820]
117. Trattnig S, Mlynarik V, Breitenseher M, et al. MRI visualization of proteoglycan depletion in articular cartilage via intravenous administration of Gd-DTPA. Magn Reson Imaging. 1999; 17:577–583. [PubMed: 10231184]
118. Allen RG, Burstein D, Gray ML. Monitoring glycosaminoglycan replenishment in cartilage explants with gadolinium-enhanced magnetic resonance imaging. J Orthop Res. 1999; 17:430–436. [PubMed: 10376734]
119. Williams A, Oppenheimer RA, Gray ML, et al. Differential recovery of glycosaminoglycan after IL-1-induced degradation of bovine articular cartilage depends on degree of degradation. Arthritis Res Ther. 2003; 5:R97–105. [PubMed: 12718753]
120. Nieminen MT, Rieppo J, Silvennoinen J, et al. Spatial assessment of articular cartilage proteoglycans with Gd-DTPA-enhanced T1 imaging. Magn Reson Med. 2002; 48:640–648. [PubMed: 12353281]
121. Tiderius CJ, Tjornstrand J, Akeson P, et al. Delayed gadolinium-enhanced MRI of cartilage (dgemric): intra- and interobserver variability in standardized drawing of regions of interest. Acta Radiol. 2004; 45:628–634. [PubMed: 15587420]
122. Bashir A, Gray ML, Boutin RD, et al. Glycosaminoglycan in articular cartilage: in vivo assessment with delayed Gd(DTPA)(2−)-enhanced MR imaging. Radiology. 1997; 205:551–558. [PubMed: 9356644]
123. Hargreaves BA, Gold GE, Beaulieu CF, et al. Comparison of new sequences for high-resolution cartilage imaging. Magn Reson Med. 2003; 49:700–709. [PubMed: 12652541]
124. Gillis A, Bashir A, McKeon B, et al. Magnetic resonance imaging of relative glycosaminoglycan distribution in patients with autologous chondrocyte transplants. Invest Radiol. 2001; 36:743–748. [PubMed: 11753146]
125. Vasara AI, Nieminen MT, Jurvelin JS, et al. Indentation stiffness of repair tissue after autologous chondrocyte transplantation. Clin Orthop Relat Res. 2005; 433:233–242. [PubMed: 15805963]
126. Tiderius CJ, Olsson LE, Leander P, et al. Delayed gadolinium-enhanced MRI of cartilage (dGEMRIC) in early knee osteoarthritis. Magn Reson Med. 2003; 49:488–492. [PubMed: 12594751]
127. Nojiri T, Watanabe N, Namura T, et al. Utility of delayed gadolinium-enhanced MRI (dgemric) for qualitative evaluation of articular cartilage of patellofemoral joint. Knee Surg Sports Traumatol Arthrosc. 2006; 14:718–723. [PubMed: 16395564]
128. Williams A, Sharma L, McKenzie CA, et al. Delayed gadolinium-enhanced magnetic resonance imaging of cartilage in knee osteoarthritis: findings at different radiographic stages of disease and relationship to malalignment. Arthritis Rheum. 2005; 52:3528–3535. [PubMed: 16255024]
129. Tiderius CJ, Svensson J, Leander P, et al. DGEMRIC (delayed gadolinium-enhanced MRI of cartilage) indicates adaptive capacity of human knee cartilage. Magn Reson Med. 2004; 51:286–290. [PubMed: 14755653]
130. Roos EM, Dahlberg L. Positive effects of moderate exercise on glycosaminoglycan content in knee cartilage: a four-month, randomized, controlled trial in patients at risk of osteoarthritis. Arthritis Rheum. 2005; 52:3507–3514. [PubMed: 16258919]
131. Tiderius CJ, Olsson LE, de Verdier H, et al. Gd-DTPA2-enhanced MRI of femoral knee cartilage: a dose-response study in healthy volunteers. Magn Reson Med. 2001; 46:1067–1071. [PubMed: 11746570]

NIH-PA Author Manuscript NIH-PA Author Manuscript NIH-PA Author Manuscript

132. Williams A, Gillis A, McKenzie C, et al. Glycosaminoglycan distribution in cartilage as determined by delayed gadolinium-enhanced MRI of cartilage (DGEMRIC): potential clinical applications. AJR Am J Roentgenol. 2004; 182:167–172. [PubMed: 14684534]

133. Tiderius CJ, Olsson LE, Nyquist F, et al. Cartilage glycosaminoglycan loss in the acute phase after an anterior cruciate ligament injury: delayed gadolinium-enhanced magnetic resonance imaging of cartilage and synovial fluid analysis. Arthritis Rheum. 2005; 52:120–127. [PubMed: 15641092]

134. Young AA, Stanwell P, Williams A, et al. Glycosaminoglycan content of knee cartilage following posterior cruciate ligament rupture demonstrated by delayed gadolinium-enhanced magnetic resonance imaging of cartilage (Dgemric). A case report. J Bone Joint Surg [Am]. 2005; 87:2763–2767.

135. Stevens K, Hishioka H, Steines D, et al. Contrast enhanced MRI measurement of GAG concentrations in articular cartilage of knees with early osteoarthritis. Proceedings of the Radiological Society of North America. 2001:275.

136. Kim YJ, Jaramillo D, Millis MB, et al. Assessment of early osteoarthritis in hip dysplasia with delayed gadolinium-enhanced magnetic resonance imaging of cartilage. J Bone Joint Surg Am. 2003; 85-A:1987–1992. [PubMed: 14563809]

137. Cunningham T, Jessel R, Zurakowski D, et al. Delayed gadolinium-enhanced magnetic resonance imaging of cartilage to predict early failure of Bernese periacetabular osteotomy for hip dysplasia. J Bone Joint Surg [Am]. 2006; 88:1540–1548.

138. Samosky JT, Burstein D, Eric Grimson W, et al. Spatially-localized correlation of Dgemric-measured GAG distribution and mechanical stiffness in the human tibial plateau. J Orthop Res. 2005; 23:93–101. [PubMed: 15607880]

139. Baldassarri M, Goodwin JS, Farley ML, et al. Relationship between cartilage stiffness and GAG content: correlation and prediction. J Orthop Res. 2007; 25:904–912. [PubMed: 17427215]

140. Kurkijarvi JE, Nissi MJ, Kiviranta I, et al. Delayed gadolinium-enhanced MRI of cartilage (Dgemric) and T2 characteristics of human knee articular cartilage: topographical variation and relationships to mechanical properties. Magn Reson Med. 2004; 52:41–46. [PubMed: 15236365]

141. Nissi MJ, Toyras J, Laasanen MS, et al. Proteoglycan and collagen sensitive MRI evaluation of normal and degenerated articular cartilage. J Orthop Res. 2004; 22:557–564. [PubMed: 15099635]

142. Mayerhoefer ME, Welsch GH, Mamisch TC, et al. The in vivo effects of unloading and compression on T1-Gd (Dgemric) relaxation times in healthy articular knee cartilage at 3.0 Tesla. Eur Radiol. 2010; 20:443–449. [PubMed: 19727756]

143. Trattnig S, Mamisch TC, Pinker K, et al. Differentiating normal hyaline cartilage from post-surgical repair tissue using fast gradient echo imaging in delayed gadolinium-enhanced MRI (Dgemric) at 3 Tesla. Eur Radiol. 2008; 18:1251–1259. [PubMed: 18246356]

144. Kurkijarvi JE, Mattila L, Ojala RO, et al. Evaluation of cartilage repair in the distal femur after autologous chondrocyte transplantation using T2 relaxation time and Dgemric. Osteoarthritis Cartilage. 2007; 15:372–378. [PubMed: 17110135]

145. Miyata S, Homma K, Numano T, et al. Assessment of fixed charge density in regenerated cartilage by Gd-DTPA-enhanced MRI. Magn Reson Med Sci. 2006; 5:73–78. [PubMed: 17008763]

146. Trattnig S, Marlovits S, Gebetsroither S, et al. Three-dimensional delayed gadolinium-enhanced MRI of cartilage (dGEMRIC) for in vivo evaluation of reparative cartilage after matrix-associated autologous chondrocyte transplantation at 3.0T: preliminary results. J Magn Reson Imaging. 2007; 26:974–982. [PubMed: 17896385]

147. Watanabe A, Wada Y, Obata T, et al. Delayed gadolinium-enhanced MR to determine glycosaminoglycan concentration in reparative cartilage after autologous chondrocyte implantation: preliminary results. Radiology. 2006; 239:201–108. [PubMed: 16484349]

148. Domayer SE, Welsch GH, Nehrer S, et al. T2 mapping and dGEMRIC after autologous chondrocyte implantation with a fibrin-based scaffold in the knee: preliminary results. Eur J Radiol. 2010; 73(3):636–642. [PubMed: 19157740]

NIH-PA Author Manuscript

NIH-PA Author Manuscript

NIH-PA Author Manuscript

149. Andreisek G, White LM, Yang Y, et al. Delayed gadolinium-enhanced MR imaging of articular cartilage: Three-dimensional T1 mapping with variable flip angles and B1 correction. Radiology. 2009; 252(3):865–873. [PubMed: 19703855]
150. Studler U, White LM, Andreisek G, et al. Impact of motion on T1 mapping acquired with inversion recovery fast spin echo and rapid spoiled gradient recalled-echo pulse sequences for delayed gadolinium-enhanced MRI of cartilage (Dgemric) in volunteers. J Magn Reson Imaging. 2010; 32:394–398. [PubMed: 20677268]
151. Siversson C, Tiderius C-J, Neuman P, et al. Repeatability of T1-quantification in dGEMRIC for three different acquisition techniques: two-dimensional inversion recovery, three-dimensional look locker, and three-dimensional variable flip angle. J Magn Reson Imaging. 2010; 31:1203–1209. [PubMed: 20432357]
152. McKenzie CA, Williams A, Prasad PV, et al. Three-dimensional delayed gadolinium-enhanced MRI of cartilage (DGEMRIC) at 1.5T and 3.0T. J Magn Reson Imaging. 2006; 24:928–933. [PubMed: 16941612]
153. Bellin MF, Van Der Molen AJ. Extracellular gadolinium-based contrast media: an overview. Eur J Radiol. 2008; 66:160–167. [PubMed: 18358659]
154. Idee JM, Port M, Medina C, et al. Possible involvement of gadolinium chelates in the pathophysiology of nephrogenic systemic fibrosis: a critical review. Toxicology. 2008; 248:77–88. [PubMed: 18440117]
155. Kallen AJ, Jhung MA, Cheng S, et al. Gadolinium-containing magnetic resonance imaging contrast and nephrogenic systemic fibrosis: a case-control study. Am J Kidney Dis. 2008; 51:966–975. [PubMed: 18501784]
156. Marckmann P, Skov L, Rossen K, et al. Nephrogenic systemic fibrosis: suspected causative role of gadodiamide used for contrast-enhanced magnetic resonance imaging. J Am Soc Nephrol. 2006; 17:2359–2362. [PubMed: 16885403]
157. Nainani N, Panesar M. Nephrogenic systemic fibrosis. Am J Nephrol. 2008; 29:1–9. [PubMed: 18663283]
158. Wiginton CD, Kelly B, Oto A, et al. Gadolinium-based contrast exposure, nephrogenic systemic fibrosis, and gadolinium detection in tissue. AJR Am J Roentgenol. 2008; 190:1060–1068. [PubMed: 18356456]
159. Li W, Scheidegger R, Wu Y, et al. Accuracy of T1 measurement with 3-D Look-Locker technique for DGEMRIC. J Magn Reson Imaging. 2008; 27:678–682. [PubMed: 18183573]
160. Kimelman T, Vu A, Storey P, et al. Three-dimensional T1 mapping for dGEMRIC at 3.0T using the Look Locker method. Invest Radiol. 2006; 41:198–203. [PubMed: 16428993]
161. Gold GE, Chen CA, Koo S, et al. Recent advances in MRI of articular cartilage. AJR Am J Roentgenol. 2009; 193:628–638. [PubMed: 19696274]
162. Lehner KB, Rechl HP, Gmeinwieser JK, et al. Structure, function, and degeneration of bovine hyaline cartilage: assessment with MR imaging in vitro. Radiology. 1989; 170:495–499. [PubMed: 2911674]
163. Lusse S, Claassen H, Gehrke T, et al. Evaluation of water content by spatially resolved transverse relaxation times of human articular cartilage. Magn Reson Imaging. 2000; 18:423–430. [PubMed: 10788720]
164. Lusse S, Knauss R, Werner A, et al. Action of compression and cations on the proton and deuterium relaxation in cartilage. Magn Reson Med. 1995; 33:483–489. [PubMed: 7776878]
165. Shapiro EM, Borthakur A, Kaufman JH, et al. Water distribution patterns inside bovine articular cartilage as visualized by 1H magnetic resonance imaging. Osteoarthritis Cartilage. 2001; 9:533–538. [PubMed: 11520167]
166. Fragonas E, Mlynarik V, Jellus V, et al. Correlation between biochemical composition and magnetic resonance appearance of articular cartilage. Osteoarthritis Cartilage. 1998; 6:24–32. [PubMed: 9616436]
167. Nieminen MT, Toyras J, Rieppo J, et al. Quantitative MR microscopy of enzymatically degraded articular cartilage. Magn Reson Med. 2000; 43:676–681. [PubMed: 10800032]
168. Watrin A, Ruaud JP, Olivier PT, et al. T2 mapping of rat patellar cartilage. Radiology. 2001; 219:395–402. [PubMed: 11323463]

NIH-PA Author Manuscript

NIH-PA Author Manuscript

NIH-PA Author Manuscript

169. Watrin-Pinzano A, Ruaud JP, Cheli Y, et al. T2 mapping: an efficient MR quantitative technique to evaluate spontaneous cartilage repair in rat patella. Osteoarthritis Cartilage. 2004; 12:191–200. [PubMed: 14972336]

170. Henkelman RM, Stanisz GJ, Kim JK, et al. Anisotropy of NMR properties of tissues. Magn Reson Med. 1994; 32:592–601. [PubMed: 7808260]

171. Rubenstein JD, Kim JK, Morova-Protzner I, et al. Effects of collagen orientation on MR imaging characteristics of bovine articular cartilage. Radiology. 1993; 188:219–226. [PubMed: 8511302]

172. Grunder W, Wagner M, Werner A. MR-microscopic visualization of anisotropic internal cartilage structures using the magic angle technique. Magn Reson Med. 1998; 39:376–382. [PubMed: 9498593]

173. Xia Y, Farquhar T, Burton-Wurster N, et al. Diffusion and relaxation mapping of cartilage-bone plugs and excised disks using microscopic magnetic resonance imaging. Magn Reson Med. 1994; 31:273–282. [PubMed: 8057798]

174. Xia Y. Relaxation anisotropy in cartilage by NMR microscopy (muMRI) at 14-micron resolution. Magn Reson Med. 1998; 39:941–949. [PubMed: 9621918]

175. Xia Y, Farquhar T, Burton-Wurster N, et al. Origin of cartilage laminae in MRI. J Magn Reson Imaging. 1997; 7:887–894. [PubMed: 9307916]

176. Goodwin DW, Dunn JF. High-resolution magnetic resonance imaging of articular cartilage: correlation with histology and pathology. Top Magn Reson Imaging. 1998; 9:337–347. [PubMed: 9894737]

177. Mlynarik V, Degrassi A, Toffanin R, et al. A method for generating magnetic resonance microimaging T2 maps with low sensitivity to diffusion. Magn Reson Med. 1996; 35:423–425. [PubMed: 8699955]

178. Kim DJ, Suh JS, Jeong EK, et al. Correlation of laminated MR appearance of articular cartilage with histology, ascertained by artificial landmarks on the cartilage. J Magn Reson Imaging. 1999; 10:57–64. [PubMed: 10398978]

179. Xia Y. Heterogeneity of cartilage laminae in MR imaging. J Magn Reson Imaging. 2000; 11:686–693. [PubMed: 10862069]

180. Nieminen MT, Rieppo J, Toyras J, et al. T2 relaxation reveals spatial collagen architecture in articular cartilage: a comparative quantitative MRI an polarized light microscopic study. Magn Reson Med. 2001; 46:487–493. [PubMed: 11550240]

181. Xia Y, Moody JB, Alhadlaq H. Orientational dependence of T2 relaxation in articular cartilage: a microscopic MRI (microMRI) study. Magn Reson Med. 2002; 48:460–469. [PubMed: 12210910]

182. Goodwin DW, Wadghiri YZ, Zhu H, et al. Macroscopic structure of articular cartilage of the tibial plateau: influence of a characteristic matrix architecture on MRI appearance. AJR Am J Roentgenol. 2004; 182:311–318. [PubMed: 14736653]

183. Konig H, Sauter R, Delmling M, et al. Cartilage disorders: a comparison of spin-echo, CHESS, and FLASH sequence MR images. Radiology. 1987; 164:753–758. [PubMed: 3615875]

184. Broderick L, Turner D, Renfrew D, et al. Severity of articular cartilage abnormality in patients with osteoarthritis: evaluation with fast spin-echo MR vs. arthroscopy. AJR Am J Roentgenol. 1994; 162:99–103. [PubMed: 8273700]

185. Peterfy CG. Imaging of the disease process. Curr Opin Rheumatol. 2002; 14:590–596. [PubMed: 12192261]

186. Shinar H, Seo Y, Ikoma K, et al. Mapping of the fiber orientation in articular cartilage at rest and under pressure studied by 2H double quantum filtered MRI. Magn Reson Med. 2002; 48:322–330. [PubMed: 12210941]

187. Keinan-Adamsky K, Shinar H, Navon G. The effect of detachment of the articular cartilage from its calcified zone on the cartilage microstructure, assessed by 2H-spectroscopic double quantum filtered MRI. J Orthop Res. 2005; 23:109–117. [PubMed: 15607882]

188. Xia Y. Magic-angle effect in magnetic resonance imaging of articular cartilage: a review. Invest Radiol. 2000; 35:602–621. [PubMed: 11041155]

189. Krasnosselskaia LV, Fullerton GD, Dodd SJ, et al. Water in tendon: orientational analysis of the free induction decay. Magn Reson Med. 2005; 54:280–288. [PubMed: 16032660]

NIH-PA Author Manuscript

NIH-PA Author Manuscript

NIH-PA Author Manuscript

190. Bydder M, Rahal A, Fullerton GD, et al. The magic angle effect: a source of artifact, determinant of image contrast, and technique for imaging. J Magn Reson Imaging. 2007; 25:290–300. [PubMed: 17260400]
191. Cameron IL, Hunter KE, Ord VA, et al. Relationships between ice crystal size, water content and proton NMR relaxation times in cells. Physiol Chem Phys Med NMR. 1985; 17:371–386. [PubMed: 3836419]
192. Xia Y. Averaged and depth-dependent anisotropy of articular cartilage by microscopic imaging. Semin Arthritis Rheum. 2008; 37:317–327. [PubMed: 17888496]
193. Shirazi R, Shirazi-Adl A. Deep vertical collagen fibrils play a significant role in mechanics of articular cartilage. J Orthop Res. 2008; 26:608–615. [PubMed: 18050338]
194. Korhonen RK, Julkunen P, Wilson W, et al. Importance of collagen orientation and depth-dependent fixed charge densities of cartilage on mechanical behavior of chondrocytes. J Biomech Eng. 2008; 130:021003. [PubMed: 18412490]
195. Julkunen P, Korhonen RK, Nissi MJ, et al. Mechanical characterization of articular cartilage by combining magnetic resonance imaging and finite-element analysis--a potential functional imaging technique. Phys Med Biol. 2008; 53:2425–2438. [PubMed: 18421123]
196. Bae WC, Wong VW, Hwang J, et al. Wear-lines and split-lines of human patellar cartilage: relation to tensile biomechanical properties. Osteoarthrits Cartilage. 2008; 16:841–845.
197. Federico S, Herzog W. On the anisotropy and inhomogeneity of permeability in articular cartilage. Biomech Model Mechanobiol. 2007; 7:367–378. [PubMed: 17619089]
198. Alhadlaq HA, Xia Y. The structural adaptations in compressed articular cartilage by microscopic MRI (microMRI) T(2) anisotropy. Osteoarthritis Cartilage. 2004; 12:887–894. [PubMed: 15501404]
199. Xia Y. Averaged properties of articular cartilage from multidisciplinary microscopic imaging study. Conf Proc IEEE Eng Med Biol Soc. 2005; 3:3161–3164. [PubMed: 17282915]
200. Mosher TJ, Dardzinski BJ. Cartilage MRI T2 relaxation time mapping: overview and applications. Semin Musculoskelet Radiol. 2004; 8:355–368. [PubMed: 15643574]
201. Bi X, Yang X, Bostrom MP, et al. Fourier transform infrared imaging and MR microscopy studies detect compositional and structural changes in cartilage in a rabbit model of osteoarthritis. Anal Bioanal Chem. 2007; 387:1601–1612. [PubMed: 17143596]
202. Mow VC, Holmes MH, Lai WM. Fluid transport and mechanical properties of articular cartilage: a review. J Biomech. 1984; 17:377–394. [PubMed: 6376512]
203. Smith HE, Mosher TJ, Dardzinski BJ, et al. Spatial variation in cartilage T2 of the knee. J Magn Reson Imaging. 2001; 14:50–55. [PubMed: 11436214]
204. Xia Y. Resolution “scaling law” in MRI of articular cartilage. Osteoarthritis Cartilage. 2007; 15:363–365. [PubMed: 17218119]
205. Van Breuseghem I, Bosmans HT, Elst LV, et al. T2 mapping of human femorotibial cartilage with turbo mixed MR imaging at 1.5 T: feasibility. Radiology. 2004; 233:609–614. [PubMed: 15375229]
206. Quaia E, Toffanin R, Guglielmi G, et al. Fast T2 mapping of the patellar articular cartilage with gradient and spin-echo magnetic resonance imaging at 1.5 T: validation and initial clinical experience in patients with osteoarthritis. Skeletal Radiol. 2008; 37:511–517. [PubMed: 18404267]
207. Bittersohl B, Hosalkar HS, Hughes T, et al. Feasibility of T2* mapping for the evaluation of hip joint cartilage at 1.5T using a three-dimensional (3D), gradient-echo (GRE) sequence: a prospective study. Magn Reson Med. 2009; 62(4):896–901. [PubMed: 19645008]
208. Williams A, Qian A, Bear D, et al. Assessing degeneration of human articular cartilage with ultra-short echo time (UTE) T2* mapping. Osteoarthritis Cartilage. 2010; 18(4):539–546. [PubMed: 20170769]
209. David-Vaudey E, Ghosh S, Ries M, et al. T2 relaxation time measurements in osteoarthritis. Magn Reson Imaging. 2004; 22:673–682. [PubMed: 15172061]
210. Gahunia HK, Lemaire C, Cross AR, et al. Osteoarthritis in rhesus macaques: assessment of cartilage matrix quality by quantitative magnetic resonance imaging. Agents Actions Suppl. 1993; 39:255–259. [PubMed: 8456638]

NIH-PA Author Manuscript

NIH-PA Author Manuscript

NIH-PA Author Manuscript

211. Gahunia HK, Babyn P, Lemaire C, et al. Osteoarthritis staging: comparison between magnetic resonance imaging, gross pathology and histopathology in the rhesus macaque. Osteoarthritis Cartilage. 1995; 3:169–180. [PubMed: 8581746]
212. Spandonis Y, Heese FP, Hall LD. High resolution MRI relaxation measurements of water in the articular cartilage of the meniscectomized rat knee at 4.7T. Magn Reson Imaging. 2004; 22:943–951. [PubMed: 15288135]
213. Watrin-Pinzano A, Ruaud JP, Cheli Y, et al. Evaluation of cartilage repair tissue after biomaterial implantation in rat patella using T2 mapping. Magma. 2004; 17:219–228. [PubMed: 15580373]
214. Mosher TJ, Smith H, Dardzinski B, et al. MR imaging and T2 mapping of femoral cartilage: in vivo determination of the magic angle effect. AJR Am J Roentgenol. 2001; 177:665–669. [PubMed: 11517068]
215. Dardzinski BJ, Laor T, Schmithorst VJ, et al. Mapping T2 relaxation time in the pediatric knee: feasibility with a clinical 1.5-T MR imaging system. Radiology. 2002; 225:233–239. [PubMed: 12355010]
216. Dardzinski BJ, Mosher TJ, Li S, et al. Spatial variation of T2 in human articular cartilage. Radiology. 1997; 205:546–550. [PubMed: 9356643]
217. Yao W, Qu N, Lu Z, et al. The application of T1 and T2 relaxation time and magnetization transfer ratios to the early diagnosis of patellar cartilage osteoarthritis. Skeletal Radiol. 2009; 38:1055–1062. [PubMed: 19688346]
219. Watanabe A, Boesch C, Siebenrock K, et al. T2 mapping of hip articular cartilage in healthy volunteers at 3T: a study of topographic variation. J Magn Reson Imaging. 2007; 26:165–171. [PubMed: 17659572]
220. Nishii T, Tanaka H, Sugano N, et al. Evaluation of cartilage matrix disorders by T2 relaxation time in patients with hip dysplasia. Osteoarthritis Cartilage. 2008; 16:227–233. [PubMed: 17644363]
221. Welsch GH, Mamisch TC, Weber M, et al. High-resolution morphological and biochemical imaging of articular cartilage of the ankle joint at 3.0T using a new dedicated phased array coil: in vivo reproducibility study. Skeletal Radiol. 2008; 37:519–526. [PubMed: 18408924]
222. Lazovic-Stojkovic J, Mosher TJ, Smith HE, et al. Interphalangeal joint cartilage: high-spatial-resolution in vivo MR T2 mapping---a feasibility study. Radiology. 2004; 233:292–296. [PubMed: 15317947]
223. Mosher TJ, Dardzinski BJ, Smith MB. Human articular cartilage: influence of aging and early symptomatic degeneration on the spatial variation of T2-preliminary findings at 3 T. Radiology. 2000; 214:259–266. [PubMed: 10644134]
224. Dray, N.; Williams, A.; Prasad, PV., et al. T2 in an OA population: Metrics for reporting data? [abstract 1995]. Proc Ann Meeting Int Soc Magn Resonance Med (ISMRM); Miami, FL. 2005.
225. Dunn TC, Lu Y, Jin H, et al. T2 relaxation time of cartilage at MR imaging: comparison with severity of knee osteoarthritis. Radiology. 2004; 232:592–598. [PubMed: 15215540]
226. Blumenkrantz, G.; Dunn, TC.; Carballido-Gamio, J., et al. Spatial heterogeneity of cartilage T2 in osteoarthritic patients. OARSI; Boston, MA. 2005.
227. Goebel JC, Watrin-Pinzano A, Bettembourg-Brault I, et al. Age-related quantitative MRI changes in healthy cartilage: preliminary results. Biorheology. 2006; 43:547–551. [PubMed: 16912426]
228. Mosher TJ, Liu Y, Yang QX, et al. Age dependency of cartilage magnetic resonance imaging T2 relaxation times in asymptomatic women. Arthritis Rheum. 2004; 50:2820–2828. [PubMed: 15457450]
229. Mosher TJ, Collins CM, Smith HE, et al. Effect of gender on in vivo cartilage magnetic resonance imaging T2 mapping. J Magn Reson Imaging. 2004; 19:323–328. [PubMed: 14994301]
230. Stahl R, Blumenkrantz G, Carballido-Gamio J, et al. MRI-derived T2 relaxation times and cartilage morphometry of the tibio-femoral joint in subjects with and without osteoarthritis during a 1-year follow-up. Osteoarthritis Cartilage. 2007; 15:1225–1234. [PubMed: 17561417]
231. Blumenkrantz G, Lindsey CT, Dunn TC, et al. A pilot, two-year longitudinal study of the interrelationship between trabecular bone and articular cartilage in the osteoarthritic knee. Osteoarthritis Cartilage. 2004; 12:997–1005. [PubMed: 15564067]

NIH-PA Author Manuscript

NIH-PA Author Manuscript

NIH-PA Author Manuscript

232. Blumenkrantz, G.; Dunn, TC.; Ries, MD., et al. Cartilage T2 as a marker of progression of osteoarthritis.[abstract 2004]. Proc Ann Meet Am Coll Rheumatol; San Antonio, TX. 2004.

233. Apprich S, Welsch GH, Mamisch TC, et al. Detection of degenerative cartilage disease: comparison of high-resolution morphological MR and quantitative T2 mapping at 3.0 Tesla. Osteoarthritis Cartilage. 201010.1016/j.joca.2010.06.002

234. Shiomi T, Nishii T, Myoui A, et al. Influence of knee positions on T2, T2*, and DGEMRIC mapping in porcine knee cartilage. Magn Reson Med. 201010.1002/mrm.22469

235. Friedrich KM, Shepard T, Chang G, et al. Does joint alignment affect the T2 values of cartilage in patients with knee osteoarthritis? Eur Radiol. 2010; 20:1532–1538. [PubMed: 20013272]

236. Grunder W, Kanowski M, Wagner M, et al. Visualization of pressure distribution within loaded joint cartilage by application of angle-sensitive NMR microscopy. Magn Reson Med. 2000; 43:884–891. [PubMed: 10861884]

237. Alhadlaq HA, Xia Y. Modifications of orientational dependence of microscopic magnetic resonance imaging T(2) anisotropy in compressed articular cartilage. J Magn Reson Imaging. 2005; 22:665–673. [PubMed: 16220547]

238. Nag D, Liney GP, Gillespie P, et al. Quantification of T(2) relaxation changes in articular cartilage with in situ mechanical loading of the knee. J Magn Reson Imaging. 2004; 19:317–322. [PubMed: 14994300]

239. Stehling C, Liebl H, Krug R, et al. Patellar cartilage: T2 values and morphologic abnormalities at 3.0-T MR imaging in relation to physical activity in asymptomatic subjects from the Osteoarthritis Initiative. Radiology. 2010; 254(2):509–520. [PubMed: 20019141]

240. Mosher TJ, Liu Y, Torok CM. Functional cartilage MRI T2 mapping: evaluating the effect of age and training on knee cartilage response to running. Osteoarthritis Cartilage. 2010; 18:358–364. [PubMed: 19948266]

241. Mosher TJ, Smith HE, Collins C, et al. Change in knee cartilage T2 at MR imaging after running: a feasibility study. Radiology. 2005; 234:245–249. [PubMed: 15550376]

242. Welsch GH, Mamisch TC, Domayer SE, et al. Cartilage T2 assessment at 3-T MR imaging: in vivo differentiation of normal hyaline cartilage from reparative tissue after two cartilage repair procedures---initial experience. Radiology. 2008; 247:154–161. [PubMed: 18372466]

243. Domayer SE, Kutscha-Lissberg F, Welsch G, et al. T2 mapping in the knee after microfracture at 3.0T: correlation of global T2 values and clinical outcome---preliminary results. Osteoarthritis Cartilage. 2008; 16:903–908. [PubMed: 18203632]

244. Trattnig S, Mamisch TC, Welsch GH, et al. Quantitative T2 mapping of matrix-associated autologous chondrocyte transplantation at 3 Tesla: an in vivo cross-sectional study. Invest Radiol. 2007; 42:442–448. [PubMed: 17507817]

245. Trattnig S, Millington SA, Szomolanyi P, et al. MR imaging of osteochondral grafts and autologous chondrocyte implantation. Eur Radiol. 2007; 17:103–118. [PubMed: 16802126]

246. White LM, Sussman MS, Hurtig M, et al. Cartilage T2 assessment: differentiation of normal hyaline cartilage and reparative tissue after arthroscopic cartilage repair in equine subjects. Radiology. 2006; 241:407–414. [PubMed: 17057068]

247. Kangarlu A, Gahunia HK. Magnetic resonance imaging characterization of osteochondral defect repair in a goat model at 8T. Osteoarthritis Cartilage. 2006; 14:52–62. [PubMed: 16242360]

248. Welsch GH, Trattnig S, Hughes T, et al. T2 and T2* mapping in patients after matrix-associated autologous chondrocyte transplantation: initial results on clinical use with 3.0-Tesla MRI. Eur Radiol. 2010; 20:1515–1523. [PubMed: 19937329]

249. Mamisch TC, Trattnig S, Quirbach S, et al. Quantitative T2 mapping of knee cartilage: differentiation of healthy control cartilage and cartilage repair tissue in the knee with unloading —intial results. Radiology. 2010; 254(3):818–826. [PubMed: 20123898]

250. Quirbach S, Trattnig S, Marlovits S, et al. Initial results of in vivo high-resolution morphological and biochemical cartilage imaging of patients after matrix-associated autologous chondrocyte transplantation (MACT) of the ankle. Skeletal Radiol. 2009; 38(3):751–760. [PubMed: 19296100]

251. Welsch GH, Trattnig S, Domayer S, et al. Multimodal approach in the use of clinical scoring, morphological MRI and biochemical T2-mapping and diffusion-weighted imaging in their ability

NIH-PA Author Manuscript

NIH-PA Author Manuscript

NIH-PA Author Manuscript

to assess differences between cartilage repair tissue after microfracture therapy and matrix-associated autologous chondrocyte transplantation: a pilot study. Osteoarthritis Cartilage. 2009; 17(9):1219–1227. [PubMed: 19409295]

252. Robson MD, Gatehouse PD, Bydder M, et al. Magnetic resonance: an introduction to ultrashort TE (UTE) imaging. J Comput Assist Tomogr. 2003; 27:825–846. [PubMed: 14600447]
253. Bae WC, Dwek JR, Znamirowski R, et al. Ultrashort echo time MR imaging of osteochondral junction of the knee at 3T: identification of anatomic structures contributing to signal intensity. Radiology. 2010; 254(3):837–845. [PubMed: 20177096]
254. Bydder, M.; Du, J.; Takahashi, AM., et al. Chemical shift artifact in center-out radial sampling: a potential pitfall in clinical diagnosis [abst]. Proceedings of the Fifteenth Meeting of the International Society for Magnetic Resonance in Medicine; Berkeley, Calif: International Society for Magnetic Resonance in Medicine; 2007. p. 1811
255. Gatehouse PD, Thomas RW, Robson MD, et al. Magnetic resonance imaging of the knee with ultrashort TE pulse sequences. Magn Reson Imaging. 2004; 22:1061–1067. [PubMed: 15527992]
256. Gatehouse PD, Bydder GM. Magnetic resonance imaging of short T2 components in tissue. Clin Radiol. 2003; 58(1):1–19. [PubMed: 12565203]
257. Gatehouse PD, He T, Puri BK, et al. Contrast-enhanced MRI of the menisci of the knee using ultrashort echo time (UTE) pulse sequences: imaging of the red and white zones. Br J Radiol. 2004; 77:641–647. [PubMed: 15326040]
258. Gold GE, Thedens DR, Pauly JM, et al. MR imaging of articular cartilage of the knee: new methods using ultrashort TEs. AJR Am J Roentgenol. 1998; 170:1223–1226. [PubMed: 9574589]
259. Filho GH, Du J, Pak BC, et al. Quantitative characterization of the Achilles tendon in cadaveric specimens: T1 and T2* measurements using ultrashort-TE MRI at 3T. AJR Am J Roentgenol. 2009; 192:W117–W124. [PubMed: 19234239]
260. Lyons TJ, Stoddart RW, McClure SF, et al. The tidemark of the chondroosseous junction of the normal human knee joint. J Mol Histol. 2005; 36(3):207–215. [PubMed: 15900412]
261. Ferguson VL, Bushby AJ, Boyde A. Nanomechanical properties and mineral concentration in articular calcified cartilage and subchondral bone. J Anat. 2003; 203:191–199. [PubMed: 12924819]
262. Li BH, Marshall D, Roe M, et al. The electron microscope appearance of the subchondral bone plate in the human femoral head in osteoarthritis and osteoporosis. J Anat. 1999; 195:101–110. [PubMed: 10473297]
263. Burr DB. Anatomy and physiology of the mineralized tissues: role in the pathogenesis of osteoarthritis. Osteoarthritis Cartilage. 2004; 12:S20–30. [PubMed: 14698637]
264. Martel-Pelletier J. Pathophysiology of osteoarthritis. Osteoarthritis Cartilage. 2004; 12:S31–33. [PubMed: 14698638]
265. Muir P, McCarthy J, Radtke CL, et al. Role of enchondral ossification of articular cartilage and functional adaptation of the subchondral plate in the development of fatigue microcracking of joints. Bone. 2006; 38:342–349. [PubMed: 16275175]
266. Squires GR, Okouneff S, Ionescu M, et al. The pathobiology of focal lesion development in aging human articular cartilage and molecular matrix changes characteristic of osteoarthritis. Arthritis Rheum. 2003; 48:1261–1270. [PubMed: 12746899]
267. Donohue JM, Buss D, Oegema TR, et al. The effects of indirect blunt trauma on adult canine articular cartilage. J Bone Joint Surg Am. 1983; 65:948–957. [PubMed: 6885875]
268. Wansapura JP, Daniel BL, Pauly J, et al. Temperature mapping of frozen tissue using eddy current compensated half excitation RF pulses. Magn Reson Med. 2001; 46(5):985–992. [PubMed: 11675651]
269. Noll DC, Pauly JM, Meyer CH, et al. Deblurring for non-2D Fourier transform magnetic resonance imaging. Magn Reson Med. 1992; 25(2):319–333. [PubMed: 1614315]
270. Lu, A.; Daniel, BL.; Pauly, KB. Improved slice excitation for ultrashort TE imaging with B0 and linear eddy current correction [abstr]. Proceedings of the Fourteenth Meeting of the International Society for Magnetic Resonance in Medicine; Berkeley, Calif: International Society for Magnetic Resonance in Medicine; 2006. p. 2381

NIH-PA Author Manuscript

NIH-PA Author Manuscript

NIH-PA Author Manuscript

271. Hwang J, Bae WC, Shieu W, et al. Increased hydraulic conductance of human articular cartilage and subchondral bone plate with progression of osteoarthritis. Arthritis Rheum. 2008; 58(12): 3831–3842. [PubMed: 19035476]

272. Frisbie DD, Morisset S, Ho CP, et al. Effects of calcified cartilage on healing of chondral defects treated with microfracture in horses. Am J Sports Med. 2006; 34(11):1824–1831. [PubMed: 16832126]

273. Koskinen SK, Komu ME. Low-field strength magnetization transfer contrast imaging of the patellar cartilage. Acta Radiol. 1993; 34:124–126. [PubMed: 8452715]

274. Regatte RR, Akella SV, Reddy R. Depth-dependent proton magnetization transfer in articular cartilage. J Magn Reson Imaging. 2005; 22:318–323. [PubMed: 16028240]

275. Yao L, Gentili A, Thomas A. Incidental magnetization transfer contrast in fast spin-echo imaging of cartilage. J Magn Reson Imaging. 1996; 6:180–184. [PubMed: 8851425]

276. Dixon WT, Engels H, Castillo M, et al. Incidental magnetization transfer contrast in standard multislice imaging. Magn Reson Imaging. 1990; 8:417–422. [PubMed: 2392030]

277. Maier CF, Tan SG, Hariharan H, et al. T2 quantitation of articular cartilage at 1.5T. J Magn Reson Imaging. 2003; 17:358–364. [PubMed: 12594727]

278. Watanabe A, Boesch C, Obata T, et al. Effect of multislice acquisition on T1 and T2 measurements of articular cartilage at 3T. J Magn Reson Imaging. 2007; 26:109–117. [PubMed: 17659569]

279. Martirosian P, Boss A, Deimling M, et al. Systematic variation of off-resonance prepulses for clinical magnetization transfer contrast imaging at 0.2, 1.5, and 3.0 Tesla. Invest Radiol. 2008; 43:16–26. [PubMed: 18097273]

280. Vahlensieck M, Traber F, Giesecke J, et al. Magnetization transfer contrast (MTC): optimizing off-resonance and on-resonance frequency MTC methods at 0.5 and 1.5T. Biomed Tech (Berl). 2001; 46:10–17. [PubMed: 11258135]

281. Peterfy CG, van Dijke CF, Janzen DL, et al. Quantification of articular cartilage in the knee with pulsed saturation transfer subtraction and fat-suppressed MR imaging: optimization and validation. Radiology. 1994; 192:485–491. [PubMed: 8029420]

282. Hohe J, Faber S, Stammberger T, et al. A technique for 3D in vivo quantification of proton density and magnetization transfer coefficients of knee joint cartilage. Osteoarthritis Cartilage. 2000; 8:426–433. [PubMed: 11069727]

283. Vahlensieck M, Dombrowski F, Leutner C, et al. Magnetization transfer contrast (MTC) and MTC-subtraction: enhancement of cartilage lesions and intracartilaginous degeneration in vitro. Skeletal Radiol. 1994; 23:535–539. [PubMed: 7824982]

284. Palmieri F, De Keyzer F, Maes F, et al. Magnetization transfer analysis of cartilage repair tissue: a preliminary study. Skeletal Radiol. 2006; 35:903–908. [PubMed: 16738915]

285. Kim DK, Ceckler TL, Hascall VC, et al. Analysis of water-macromolecule proton magnetization transfer in articular cartilage. Magn Reson Med. 1993; 29:211–215. [PubMed: 8429785]

286. Lattanzio PJ, Marshall KW, Damyanovich AZ, et al. Macromolecule and water magnetization transfer in articular cartilage. Magn Reson Med. 2000; 44:840–851. [PubMed: 11108620]

287. Seo GS, Aoki J, Moriya H, et al. Hyaline cartilage: in vivo and in vitro assessment with magnetization transfer imaging. Radiology. 1996; 201:525–530. [PubMed: 8888253]

288. Toffanin R, Mlynarik V, Russo S, et al. Proteoglycan depletion and magnetic resonance parameters of articular cartilage. Arch Biochem Biophys. 2001; 390:235–242. [PubMed: 11396926]

289. Potter K, Butler JJ, Horton WE, et al. Response of engineered cartilage tissue to biochemical agents as studied by proton magnetic resonance microscopy. Arthritis Rheum. 2000; 43:1580–1590. [PubMed: 10902763]

290. Li W, Hong L, Hu L, et al. Magnetization transfer imaging provides a quantitative measure of chondrogenic differentiation and tissue development. Tissue Eng Part C: Methods. 201010.1089/ten.tec.2009.0777

291. Laurent D, O'Byrne E, Wasvary J, et al. In vivo MRI of cartilage pathogenesis in surgical models of osteoarthritis. Skeletal Radiol. 2006; 35:555–564. [PubMed: 16639625]

NIH-PA Author Manuscript

NIH-PA Author Manuscript

NIH-PA Author Manuscript

292. Laurent D, Wasvary J, O'Byrne E, et al. In vivo qualitative assessments of articular cartilage in the rabbit knee with high-resolution MRI at 3T. Magn Reson Med. 2003; 50:541–549. [PubMed: 12939762]

293. Laurent D, Wasvary J, Yin J, et al. Quantitative and qualitative assessment of articular cartilage in the goat knee with magnetization transfer imaging. Magn Reson Imaging. 2001; 19:1279–1286. [PubMed: 11804755]

294. Wolff SD, Chesnick S, Frank JA, et al. Magnetization transfer contrast: MR imaging of the knee. Radiology. 1991; 179:623–628. [PubMed: 2027963]

295. Niitsu M, Hirohata H, Yoshioka H, et al. Magnetization transfer contrast on gradient echo MR imaging of the temporomandibular joint. Acta Radiol. 1995; 36:295–299. [PubMed: 7742126]

296. Peterfy CG, Majumdar S, Lang P, et al. MR imaging of the arthritic knee: improved discrimination of cartilage, synovium, and effusion with pulsed saturation transfer and fat-suppressed T1-weighted sequences. Radiology. 1994; 191:413–419. [PubMed: 8153315]

297. Mori R, Ochi M, Sakai Y, et al. Clinical significance of magnetic resonance imaging (MRI) for focal chondral lesions. Magn Reson Imaging. 1999; 17:1135–1140. [PubMed: 10499675]

298. Welsch GH, Trattnig S, Scheffler K, et al. Magnetization transfer contrast and T2 mapping in the evaluation of cartilage repair tissue with 3T MRI. J Magn Reson Imaging. 2008; 28(4):979–986. [PubMed: 18821633]

299. Kneeland JB. MRI probes biophysical structure of cartilage. Diagn Imaging (San Franc). 1996; 18:36–40. [PubMed: 10159856]

300. Butts K, Pauly J, de Crespigny A, et al. Isotropic diffusion-weighted and spiral-navigated interleaved EPI for routine imaging of acute stroke. Magn Reson Med. 1997; 38:741–749. [PubMed: 9358448]

301. Xia Y, Farquhar T, Burton-Wurster N, et al. Self-diffusion monitors degraded cartilage. Arch Biochem Biophys. 1995; 323:323–328. [PubMed: 7487094]

302. Mamisch TC, Menzel MI, Welsch GH, et al. Steady-state diffusion imaging for MR in-vivo evaluation of reparative cartilage after matrix-associated autologous chondrocyte transplantation at 3 tesla—preliminary results. Eur J Radiol. 2008; 65(1):72–79. [PubMed: 17977685]

303. Friedrich KM, Mamisch TC, Plank C, et al. Diffusion-weighted imaging for the follow-up of patients after matrix-associated autologous chondrocyte transplantation. Eur J Radiol. 2010; 73(3):622–628. [PubMed: 19181469]

NIH-PA Author Manuscript

NIH-PA Author Manuscript

NIH-PA Author Manuscript

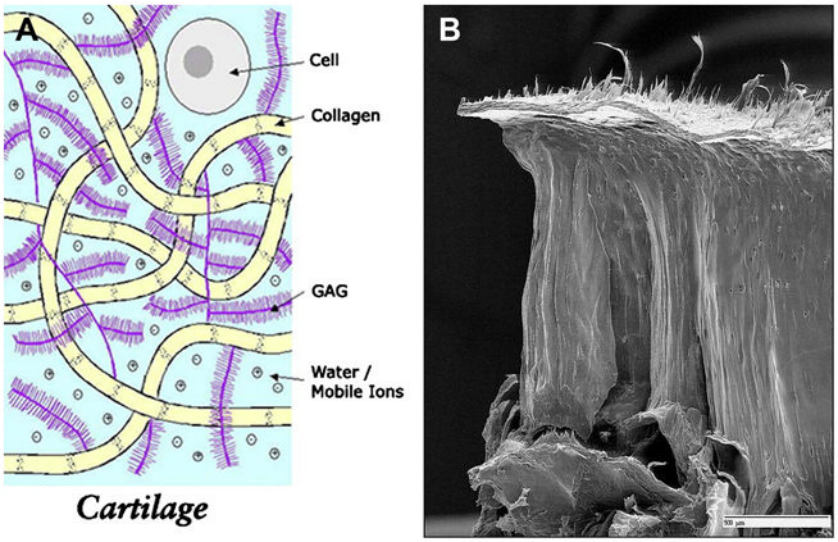


Figure 1.

Figure 1A. Cartilage is mostly acellular and avascular, and has a limited ability to heal. The extracellular matrix consists of water, collagen, and glycosaminoglycan. Several aggrecan molecules are attached to a central core fiber filament of hyaluronic acid, to which the aggrecan monomers are bound through a linking protein. A large number of carboxyl and sulfate residues on the GAG side chains are ionized under physiologic conditions and impart a negative charge density (Courtesy of Deb Burstein, BIDMC).

1B. The collagen fibers have a unique zonal architecture as shown here on this freeze fracture image, with superficial, tangential, radial, and calcified zones (courtesy of Doug Goodwin MD).

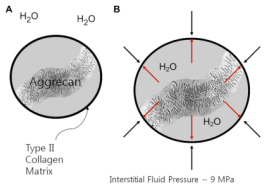


Figure 2.

Figure 2A, B. Negative ions attract positive counter-ions and water molecules and provide a strong electrostatic repulsive force between the proteoglycans, which act together to the swelling pressure of cartilage; this swelling of the proteoglycans is constrained by the surrounding collagen meshwork, which produces an interstitial fluid pressure of about 9MPa (courtesy of Timothy Mosher, MD)..

NIH-PA Author Manuscript
NIH-PA Author Manuscript
NIH-PA Author Manuscript

NIH-PA Author Manuscript

NIH-PA Author Manuscript

NIH-PA Author Manuscript

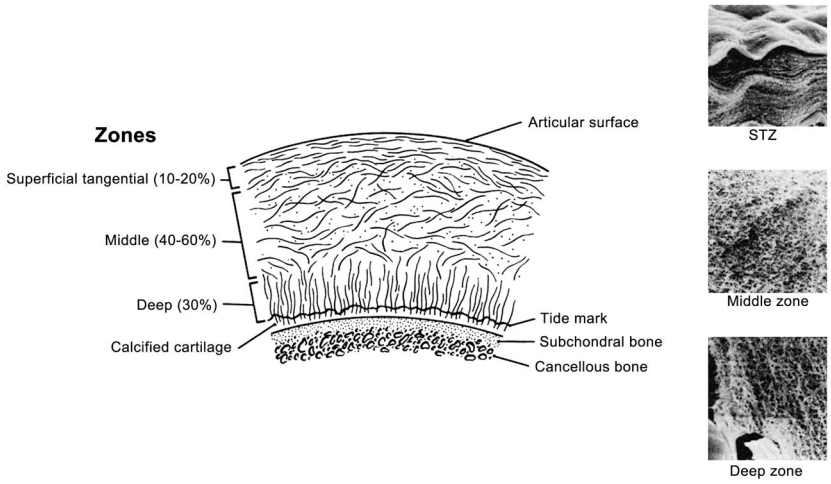


Figure 3.

Type II collagen fibrils pass through the tidemark zone, ending in the zone of calcified cartilage and there is a potential cleavage plane between the zone of calcified cartilage and subchondral cortical bone in response to shear stress (from Basic Orthopedic Biomechanics VC Mow, WC Hayes (1997), Lippincott Williams & Wilkins Publishers; 2nd edition, p. 171)

NIH-PA Author Manuscript

NIH-PA Author Manuscript

NIH-PA Author Manuscript

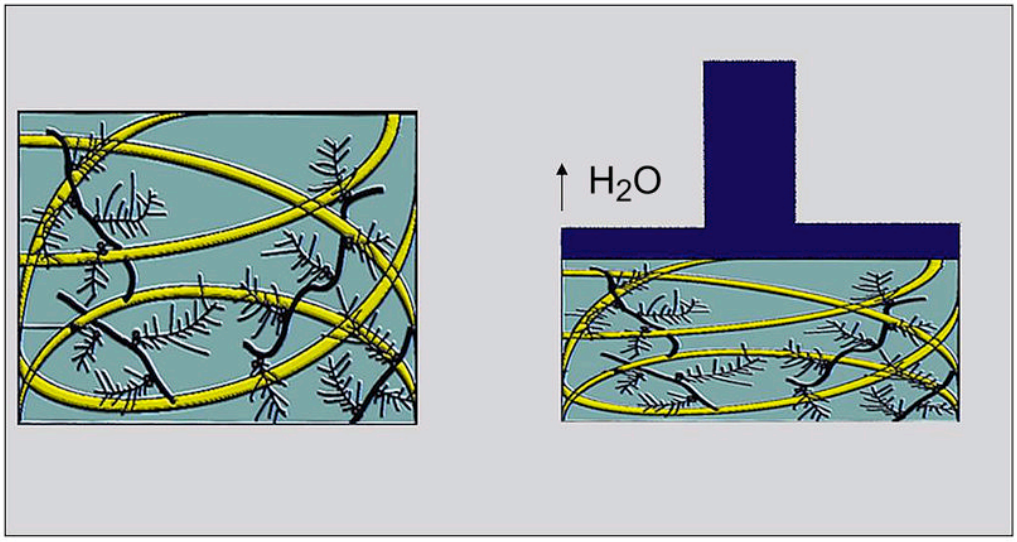


Figure 4.
Forces from compressive loading are dissipated by frictional drag forces as water moves through the extra-cellular matrix (modified by Mosher TJ, from Basic Orthopedic Biomechanics VC Mow, WC Hayes (1997) Lippincott Williams & Wilkins Publishers; 2nd edition, p. 171)

NIH-PA Author Manuscript

NIH-PA Author Manuscript

NIH-PA Author Manuscript

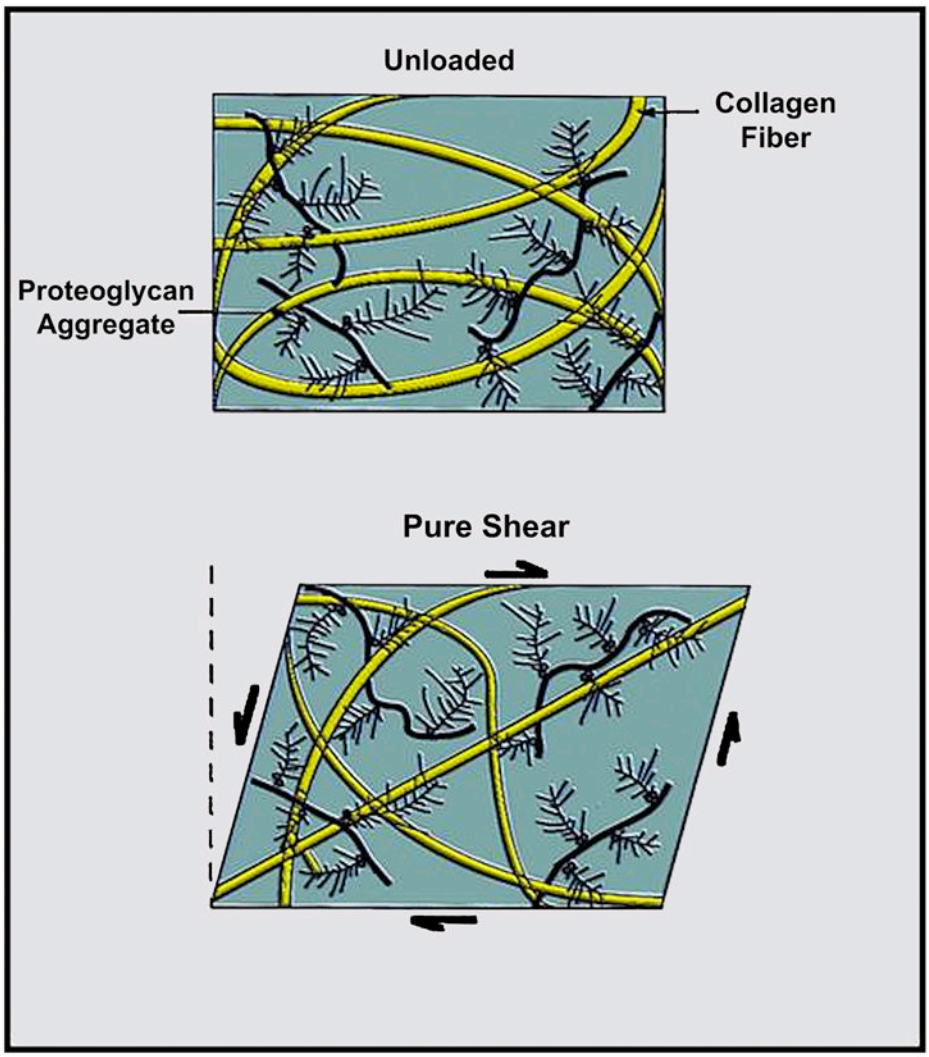


Figure 5.
Shear stress is produced when one articular surface passes over the other and at the bone/cartilage interface, where differences in compressive stiffness of tissues result in shear strain during high compressive loading (modified by Mosher TJ, from Basic Orthopedic Biomechanics VC Mow, WC Hayes (1997) Lippincott Williams & Wilkins Publishers; 2nd edition, p. 171)

NIH-PA Author Manuscript

NIH-PA Author Manuscript

NIH-PA Author Manuscript

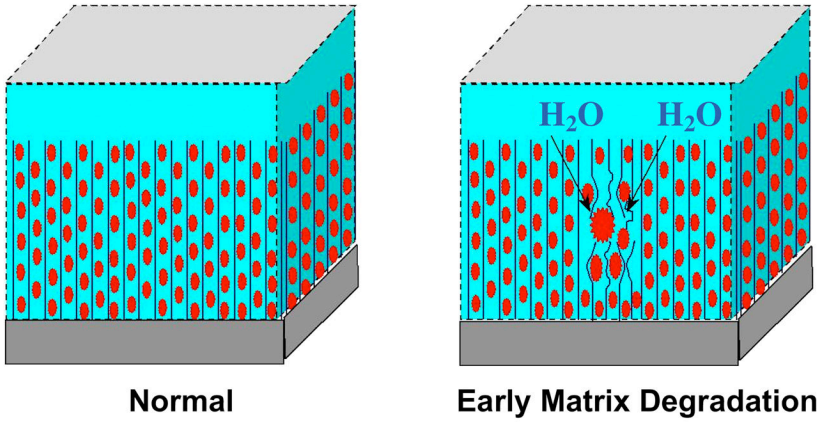


Figure 6.
Maroudas Model of Early Cartilage Damage shows earliest changes including reduced PG concentration, possible changes in the size of collagen fibril, and increased water content (courtesy of Timothy Mosher, MD).

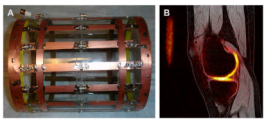


Figure 7.
Figure 7A, B. Sodium MRI requires high field strength and dedicated hardware, such as a dual-tuned $^{23}Na^{+}/^{1}H$ coil (A) allows direct measurement of GAG content (B) (Courtesy of Starosweicki, et al. JMRI 2010, 32(2):446–451).

NIH-PA Author Manuscript
NIH-PA Author Manuscript
NIH-PA Author Manuscript

NIH-PA Author Manuscript

NIH-PA Author Manuscript

NIH-PA Author Manuscript

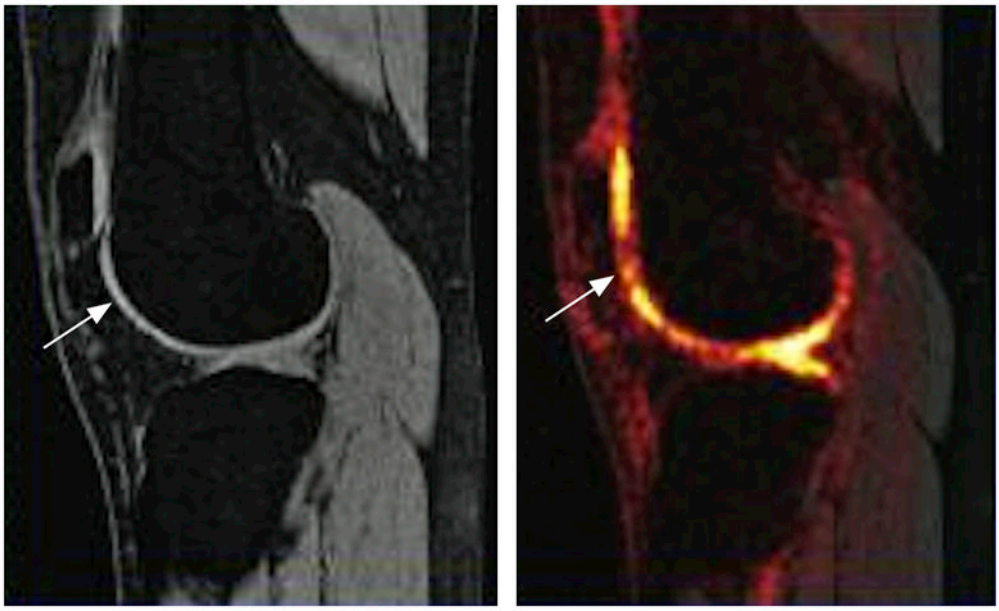


Figure 8.
Sodium MRI is sensitive to cartilage glycosaminoglycan. Advances in coil design and high field have made this a potential clinical tool. Here a patient with a prior anterior cruciate ligament tear shows areas of focal cartilage glycosaminoglycan loss (left) despite a normal proton MRI (right).

NIH-PA Author Manuscript

NIH-PA Author Manuscript

NIH-PA Author Manuscript

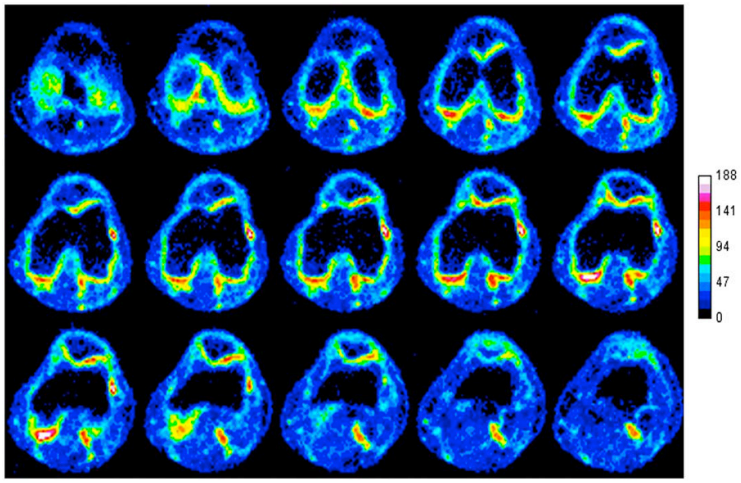


Figure 9.
Sodium MRI at 7T shows direct measurement of cartilage glycosaminoglycan in healthy volunteer knee (Courtesy of Ravinder Reddy, U. Penn).

NIH-PA Author Manuscript

NIH-PA Author Manuscript

NIH-PA Author Manuscript

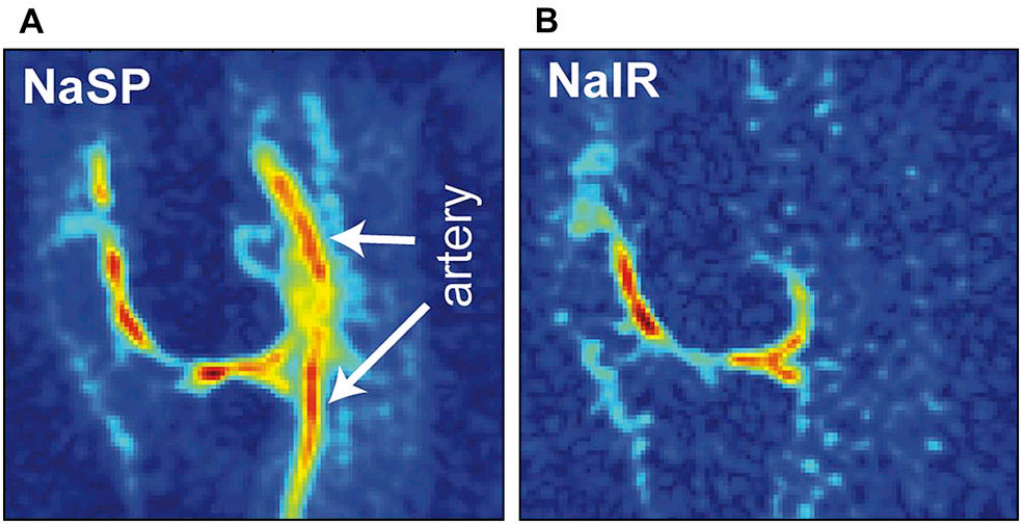


Figure 10.
Figure 10A, B. Use of 7T MRI improves sodium MRI resolution and SNR. Here an inversion recovery technique (B) is used to suppress signal from the popliteal artery (A) (Reproduced with permission from Madelin G, et al. J Magn Reson 207: 42–52 (2010)).

NIH-PA Author Manuscript

NIH-PA Author Manuscript

NIH-PA Author Manuscript

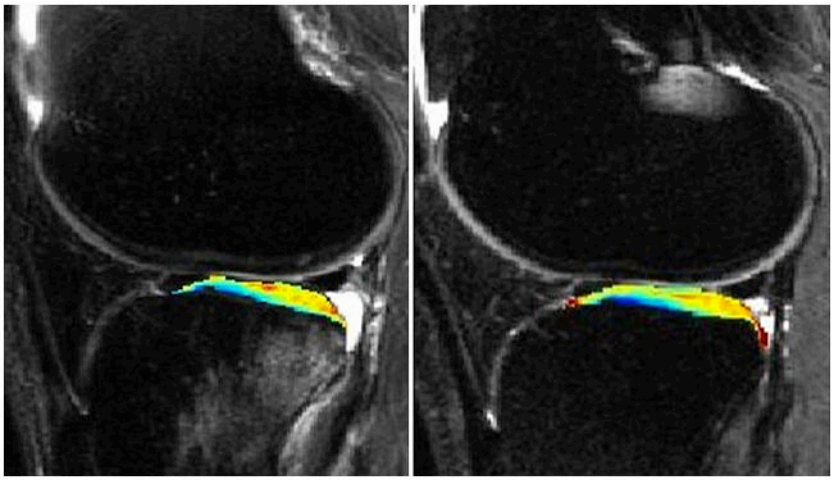


Figure 11.
T1p: One year follow up after ACL tear. Baseline measurements (left) and measurements at one year post ACL-reconstruction (right) show persistent cartilage damage despite resolution of bone marrow edema-like lesions (Li et al, ISMRM 2007).

NIH-PA Author Manuscript

NIH-PA Author Manuscript

NIH-PA Author Manuscript

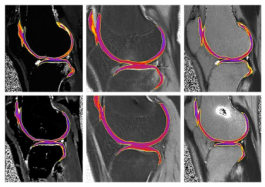


Figure 12.
Measurements of T1 rho (upper left, middle), DGEMRIC (upper right, lower left), and T2(lower middle, right) before (upper left, right, lower middle) and 4 months after surgery (upper middle, lower left, right) show T1 rho and DGEMRIC to be more sensitive than T2 (Courtesy of Dan Thedens, University of Iowa).

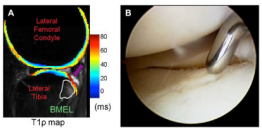


Figure 13.

Figure 13A, B. Elevated T1ρ (A) is seen adjacent to bone marrow edema-like lesions in ACL-injured knee (B) (Reproduced with permission from Theologis AA et al. Arthroscopy 2010 Oct 28 [epub ahead of print], Lozano JJ et al. Bone Joint Surg Am 88(6):1349-52 (2006)).

NIH-PA Author Manuscript
NIH-PA Author Manuscript
NIH-PA Author Manuscript

NIH-PA Author Manuscript

NIH-PA Author Manuscript

NIH-PA Author Manuscript

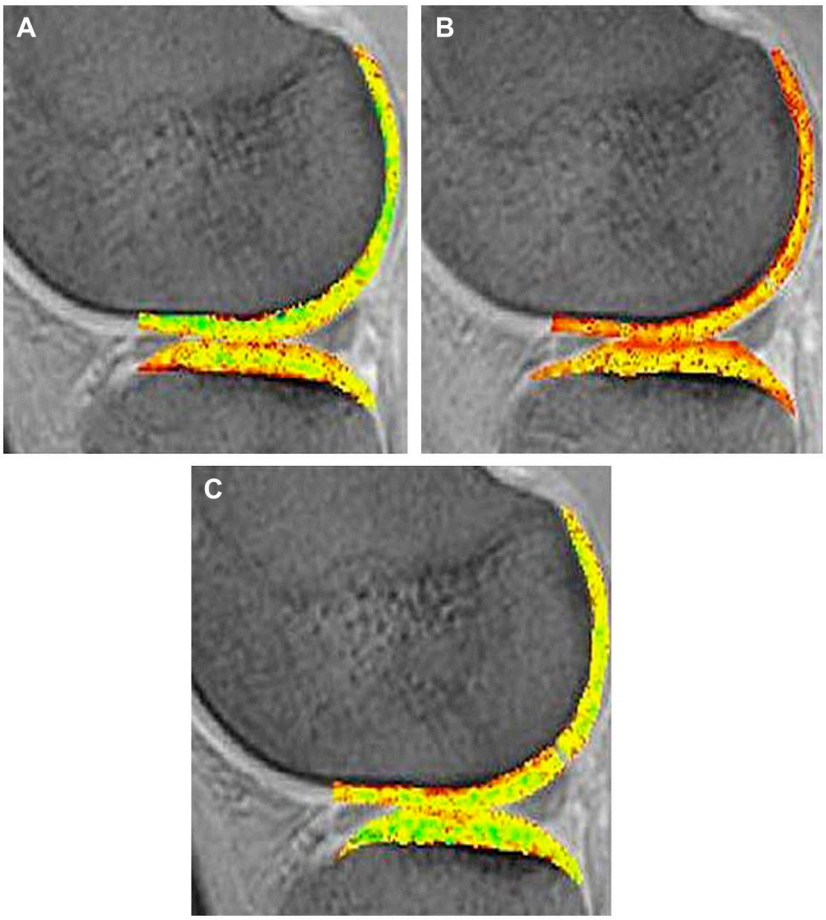


Figure 14.
Figure 14A, B, C. Temporal changes in the dGEMRIC Index have been shown with physiologic events such as seen in the images of an individual (A) before running a marathon, (B) 1 day postmarathon, and (C) 1 week postmarathon (Burstein et al, Radiol Clin N Am 47 (2009) 675–686).

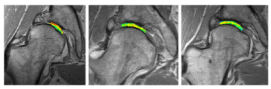


Figure 15.
Cartilage can potentially heal and result in increase in dGEMRIC Index with intervention of osteotomy for hip dysplasia as depicted in pre-operative (left), 20 month-postoperative (middle), and 58 month-postoperative (right) studies (*Courtesy of Deborah Burstein, BIDMC and Harvard University).*

NIH-PA Author Manuscript
NIH-PA Author Manuscript
NIH-PA Author Manuscript

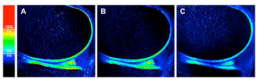


Figure 16.
Physiologic effects of mechanical loading. Sagittal dGEMRIC images of the knee joint, obtained at baseline (A), unloading (B) and compression (C) at identical window levels. While there is no significant difference, with regard to T1-Gd relaxation times, between baseline and unloading, there is a significant T1-Gd decrease between baseline and compression, and between unloading and compression (Mayerhoefer et al, Eur Radiol. 2010 Feb;20(2):443-9).

NIH-PA Author Manuscript
NIH-PA Author Manuscript
NIH-PA Author Manuscript

NIH-PA Author Manuscript

NIH-PA Author Manuscript

NIH-PA Author Manuscript

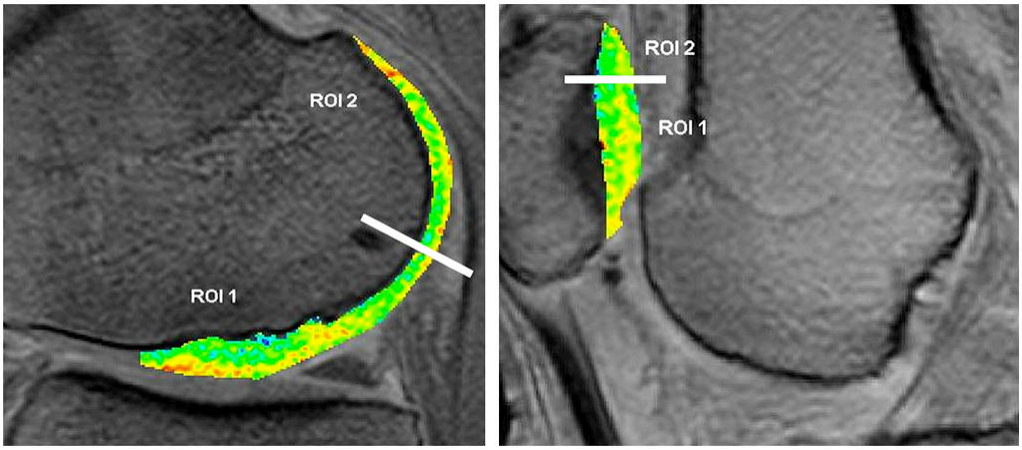


Figure 17.
dGEMRIC measurements in the knee after cartilage implants show Dgemric comparable to surrounding native cartilage 12 years post-implant (ROI1 = implant, ROI2=native) (from Program # 815 ISMRM 2010, publication: Vasiliadis et al, Am J Sports Med. 2010 Feb 25).

NIH-PA Author Manuscript

NIH-PA Author Manuscript

NIH-PA Author Manuscript

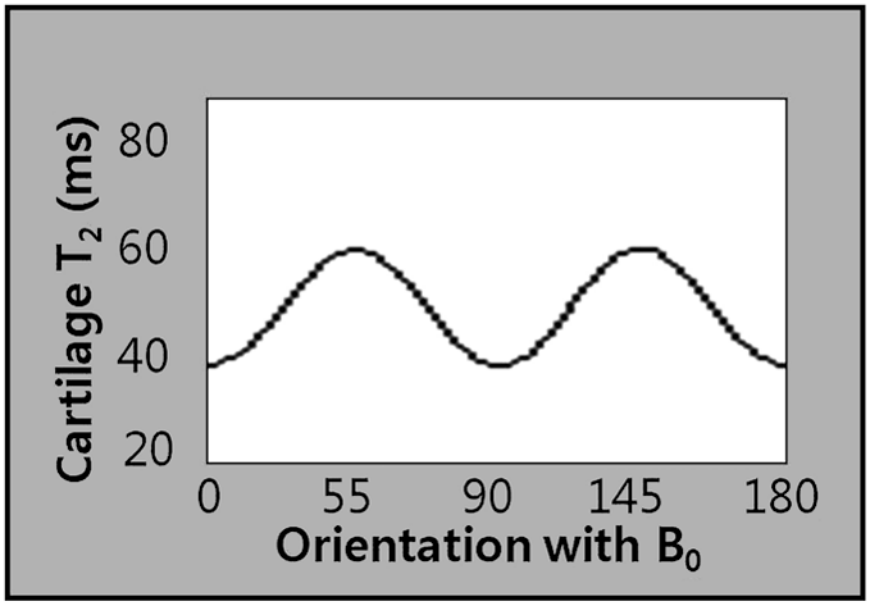


Figure 18.
The magic angle effect in cartilage (Reproduced with permission from Xia Y, et al. Magn Reson Med 48:460–469 (2002)).

NIH-PA Author Manuscript

NIH-PA Author Manuscript

NIH-PA Author Manuscript

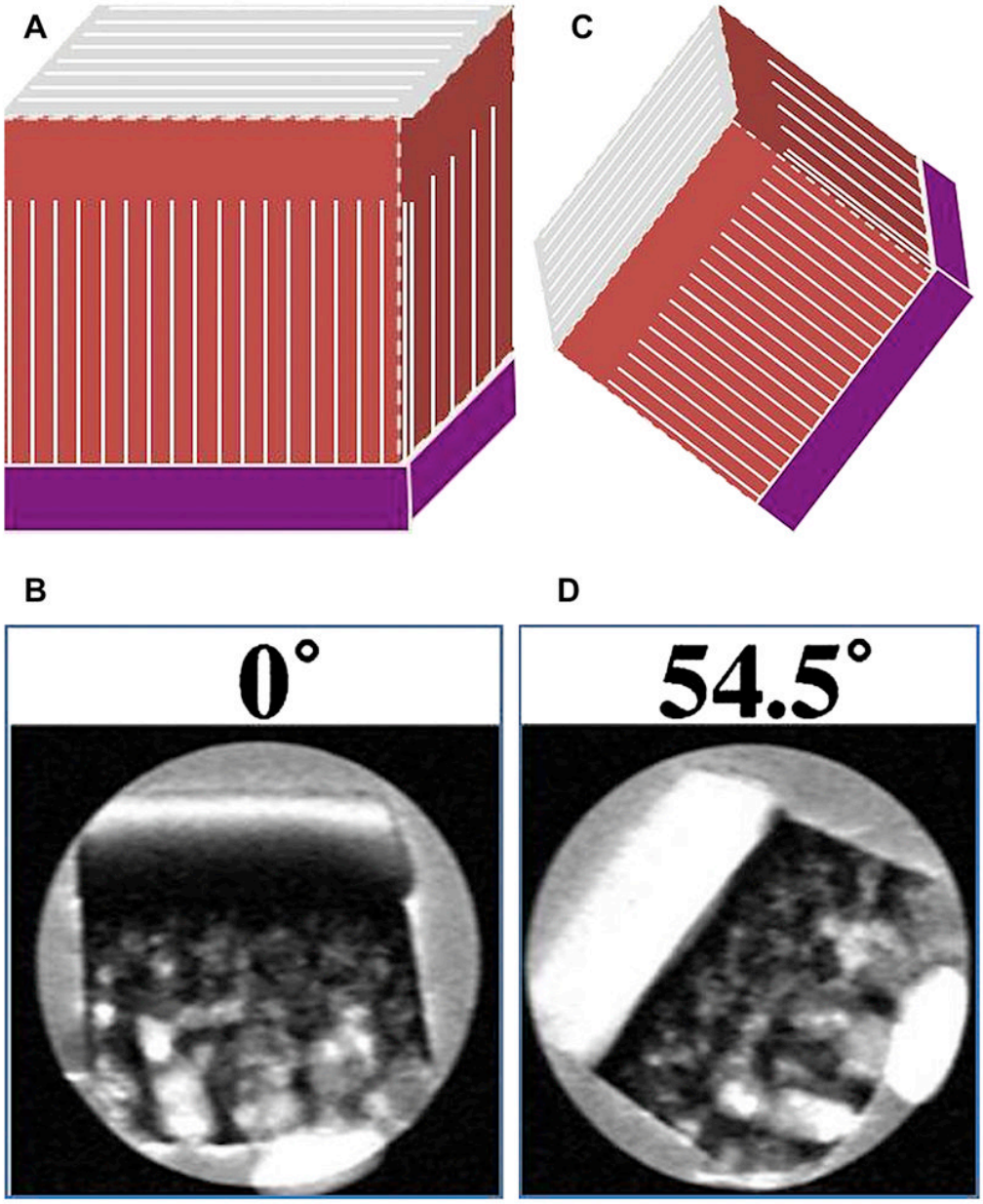


Figure 19.

Figure 19A, B, C, D. Dependence of cartilage T2 on collagen fibril orientation is shown on T2-weighted images (A,B) and the magic angle effects (C, D) as B0 increases approaching 54.5′ (B, D: Reproduced with permission from Xia Y, et al. Magn Reson Med 48:460–469 (2002), A, C:Courtesy of Tim Mosher, M.D., Penn State).

NIH-PA Author Manuscript

NIH-PA Author Manuscript

NIH-PA Author Manuscript

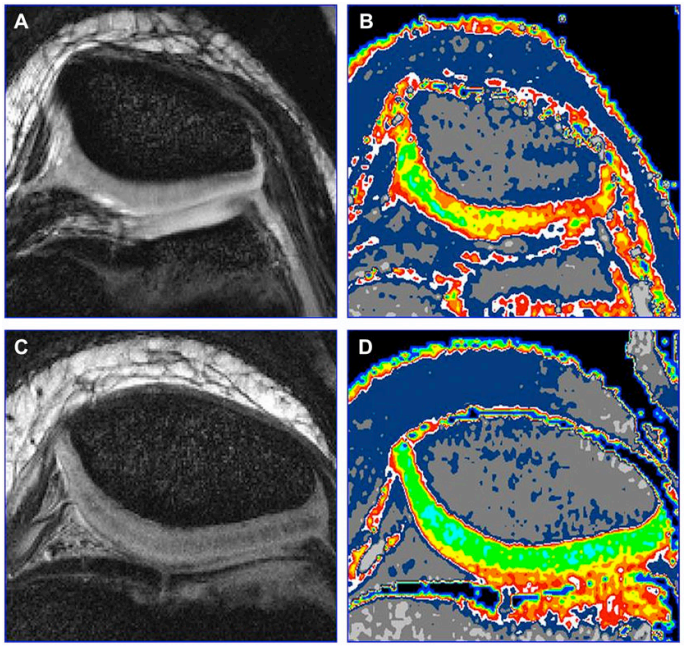


Figure 20.

Figure 20A, B, C, D. Here is an example of the use of T2 mapping to show matrix changes. The morphologic images of 10-year old girl with Juvenile Rheumatoid Arthritis (A) and a healthy 10-year old boy (C) and are both normal. The T2 maps (B, D) show large areas of collagen matrix disruption in the patient with JRA (B) (Courtesy of Bernard Dardzinski, Merck).

NIH-PA Author Manuscript

NIH-PA Author Manuscript

NIH-PA Author Manuscript

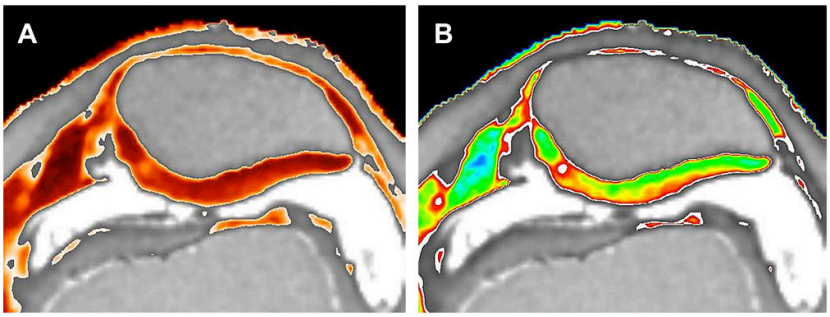


Figure 21.

Figure 21A, B. Heat scale and color scale T2 maps of a 26 year-old female patient who had arthroscopic surgery for meniscal tear (Courtesy of Tim Mosher, M.D., Penn State University).

NIH-PA Author Manuscript

NIH-PA Author Manuscript

NIH-PA Author Manuscript

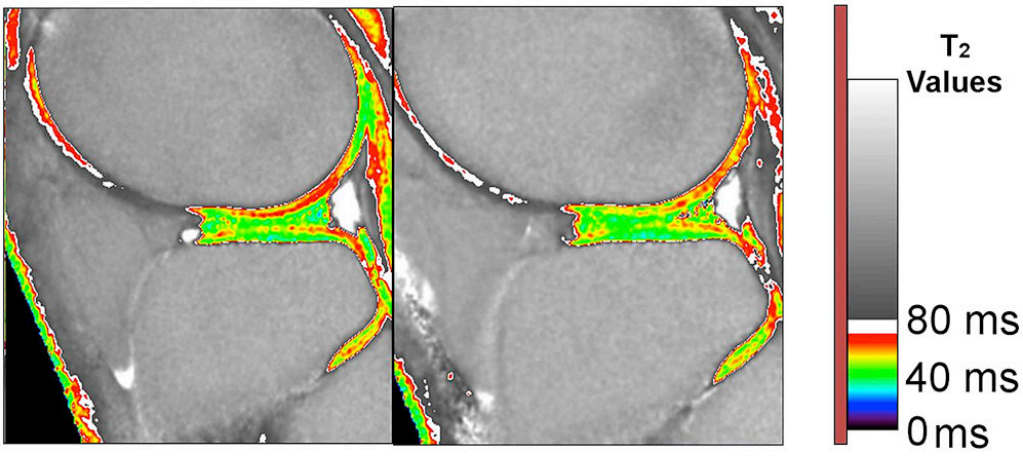


Figure 22.

Functional Cartilage T_2 Mapping: Change in T_2 values after running.

In a 47-year old marathon runner, a T2 map after running show areas of T2 decrease, which may correspond to loss of cartilage water due to compression.

NIH-PA Author Manuscript

NIH-PA Author Manuscript

NIH-PA Author Manuscript

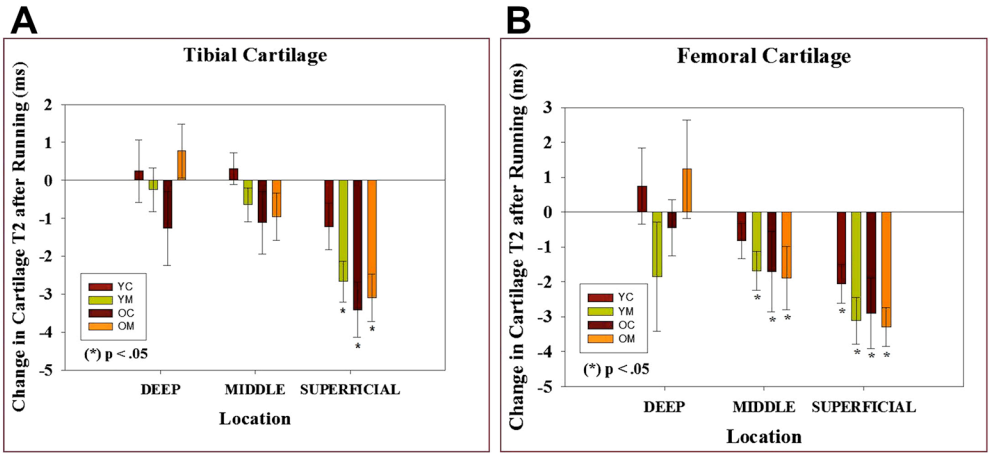


Figure 23.

Figure 23A, B. Functional Cartilage T2 mapping: Evaluating local tissue response to running.

YC: Young (18 – 30) control, YM young marathoner, OC: old (45 – 55 years) sedentary control, OM: old marathoner: Change in cartilage T2 values after 30 minutes of running demonstrate statistically significant decrease in T2 values of superficial femoral and tibial cartilage, but no change in T2 near the bone cartilage interface (reproduced with permission from Mosher TJ et al. Osteoarthritis Cartilage;18(3):358–364).

NIH-PA Author Manuscript

NIH-PA Author Manuscript

NIH-PA Author Manuscript

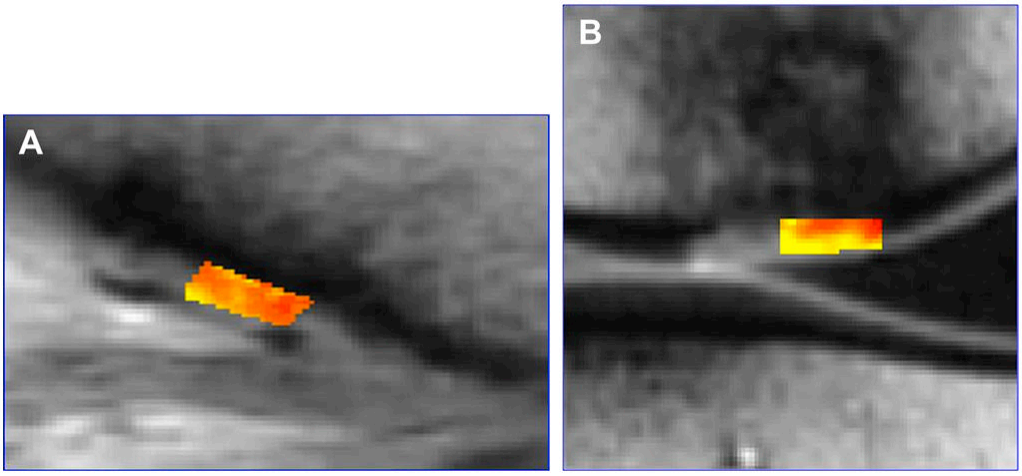


Figure 24.
Figure 24A, B. T2 mapping can be used to follow cartilage repair clinically and shows a microfracture or fibrocartilage repair has lower T2 values than an osteochondral repair with hyaline cartilage (Courtesy of Lawrence White, University of Toronto).

NIH-PA Author Manuscript

NIH-PA Author Manuscript

NIH-PA Author Manuscript

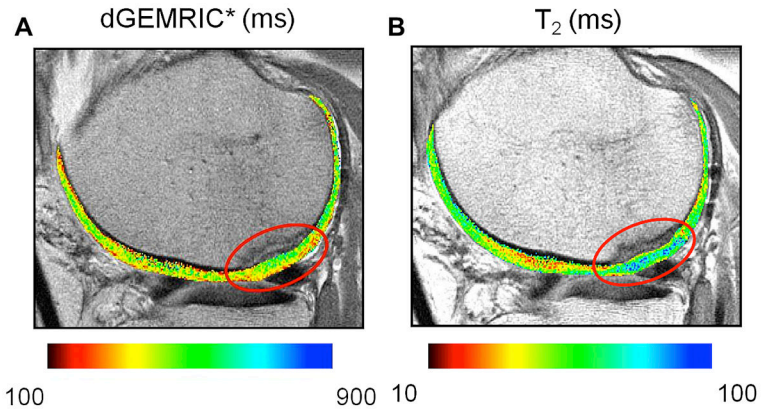


Figure 25.

Figure 25A, B. An example of autologous chondrocyte implantation followed with dGEMRIC and T2 mapping. The dGEMRIC study showed increasing GAG in the repair site (A), indicating formation of hyaline cartilage (*Courtesy of Miika Nieminen, University of Oulu and Oulu University Hospital, Oulu, Finland).*

NIH-PA Author Manuscript

NIH-PA Author Manuscript

NIH-PA Author Manuscript

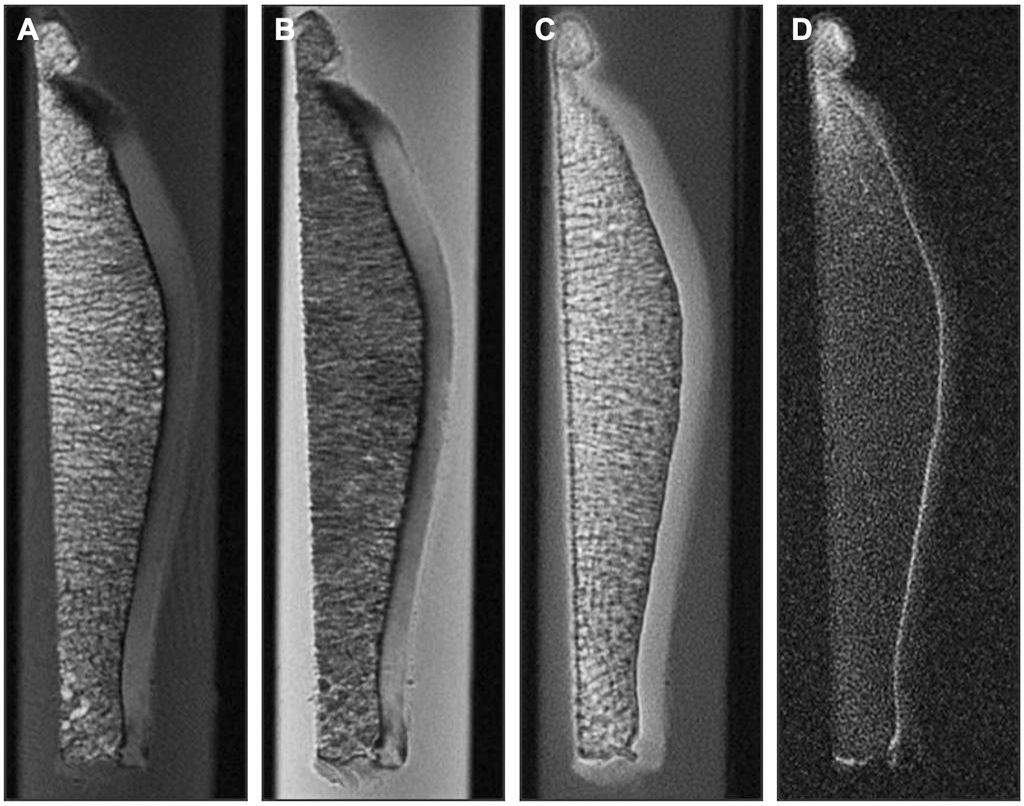


Figure 26.

Figure 26A, B, C, D. Ultra-short Echo TIme MRI can be used to probe the deepest layer of cartilage, the calcified zone. Conventional MRI shows a signal void from this zone on T1- (A) and PD-weighted images (B), but uTE MRI (C) and UTE MRI with long T2 suppression (D) show signal from the calcified zone. This zone may be important in the development of OA (*Courtesy of Christine Chung and Graeme Bydder, UCSD).*

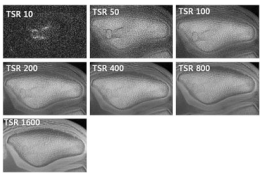


Figure 27.
Images acquired at 7 points with a TSR ranging from 10 to 1600 msecs, where ROI placed in region of normal appearing calcified cartilage (arrow). In these volunteer images, Excellent tissue signal saturation at TSR 10 and best visualization of the calcified layer at TSR 200 – 800 are noted (Courtesy of Christine Chung, UCSD)..

NIH-PA Author Manuscript
NIH-PA Author Manuscript
NIH-PA Author Manuscript

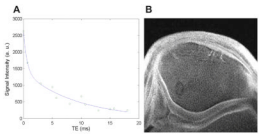


Figure 28.
Figure 28A, B. T2* Measurement in a volunteer by constant TR-variable TE method (Courtesy of Christine Chung, UCSD).

NIH-PA Author Manuscript
NIH-PA Author Manuscript
NIH-PA Author Manuscript

NIH-PA Author Manuscript

NIH-PA Author Manuscript

NIH-PA Author Manuscript



Figure 29.
High resolution (300mm) UTE MRI at 3T depicts the calcified zone well (Courtesy of Christine Boada).

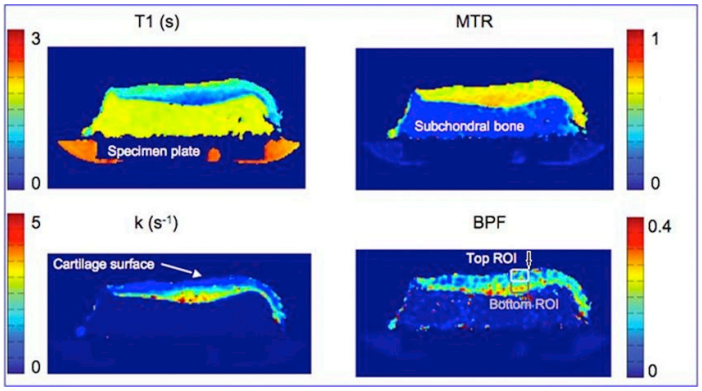


Figure 30.
Quantitative magnetization transfer MRI can be used to detect changes in macromolecules. Here, the bound pool fraction (arrow) correlates with cartilage glycosaminoglycan in its top layer (Courtesy of *Stikov, Keenan, Pauly et al. ISMRM 2010 #827)*..

NIH-PA Author Manuscript
NIH-PA Author Manuscript
NIH-PA Author Manuscript

NIH-PA Author Manuscript

NIH-PA Author Manuscript

NIH-PA Author Manuscript

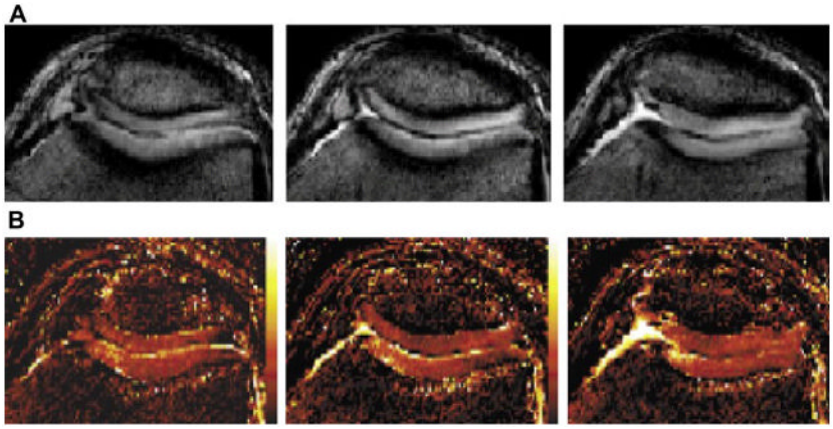


Figure 31.

Figure 31A, B. 3D-SSFP cartilage diffusion Imaging (Reproduced with permission from Miller, et al. Magn Reson Med 51:394–398 (2004) p. 396, Figure 5).

NIH-PA Author Manuscript

NIH-PA Author Manuscript

NIH-PA Author Manuscript

Table 1

Pros and Cons of Various MR Imaging Methods for Evaluating Cartilage Physiology

	Pros	Cons
Sodium imaging	High specificity for PG content. High contrast image without exogenous contrast agent	Requires special coils, high field scanners, and long imaging times.
T1 rho imaging	Sensitive to early PG depletion	Requires high RF power- SAR limits
dGEMRIC	High resolution and sensitivity	Delay prior to imaging. Need for contrast agent. Possibility of nephrogenic systemic fibrosis in patients with kidney problems
T2 mapping	Sensitive to collagen matrix, water content, and motion	May be less sensitive in detection of early degeneration
Ultrashort echo time imaging	Only technique to examine osteochondral junction	Technical challenges. Disadvantage of scan time. Difficulty in slice selection
Magnetization transfer	Improved contrast between cartilage and fluid - detection of localized cartilage lesions	Difficult quantification. SAR limits
Diffusion weighted imaging	Postoperative evaluation	Low SNR and spatial resolution

Review: MR Physics for Clinicians

Hyperpolarized ^{13}C Metabolic Imaging Using Dissolution Dynamic Nuclear Polarization

CME

Ralph E. Hurd, PhD,[1]* Yi-Fen Yen, PhD,[1] Albert Chen, PhD,[2] and Jan Henrik Ardenkjaer-Larsen, PhD[3]

This article is accredited as a journal-based CME activity. If you wish to receive credit for this activity, please refer to the website: www.wileyhealthlearning.com

ACCREDITATION AND DESIGNATION STATEMENT

Blackwell Futura Media Services designates this journal-based CME activity for a maximum of 1 *AMA PRA Category 1 Credit*™. Physicians should only claim credit commensurate with the extent of their participation in the activity.

Blackwell Futura Media Services is accredited by the Accreditation Council for Continuing Medical Education to provide continuing medical education for physicians.

EDUCATIONAL OBJECTIVES

Upon completion of this educational activity, participants will be better able to describe the basic physics of dissolution dynamic nuclear polarization (dissolution-DNP), and the impact of the resulting highly nonequilibrium spin states, on the physics of magnetic resonance imaging (MRI) detection.

ACTIVITY DISCLOSURES

No commercial support has been accepted related to the development or publication of this activity.

Faculty Disclosures:

The following contributors have no conflicts of interest to disclose:

Editor-in-Chief: C. Leon Partain, MD, PhD

CME Editor: Scott B. Reeder, MD, PhD

CME Committee: Scott Nagle, MD, PhD, Pratik Mukherjee, MD, PhD, Shreyas Vasanawala, MD, PhD, Bonnie Joe, MD, PhD, Tim Leiner, MD, PhD, Sabine Weckbach, MD, Frank Korosec, PhD

Authors: Ralph E. Hurd, PhD, Yi-Fen Yen, PhD, Albert Chen, PhD, Jan-Henrik Ardenkjaer-Larsen, PhD

This manuscript underwent peer review in line with the standards of editorial integrity and publication ethics maintained by *Journal of Magnetic Resonance Imaging*. The peer reviewers have no relevant financial relationships. The peer review process for *Journal of Magnetic Resonance Imaging* is double-blinded. As such, the identities of the reviewers are not disclosed in line with the standard accepted practices of medical journal peer review.

Conflicts of interest have been identified and resolved in accordance with Blackwell Futura Media Services's Policy on Activity Disclosure and Conflict of Interest. No relevant financial relationships exist for any individual in control of the content and therefore there were no conflicts to resolve.

INSTRUCTIONS ON RECEIVING CREDIT

For information on applicability and acceptance of CME credit for this activity, please consult your professional licensing board.

This activity is designed to be completed within an hour; physicians should claim only those credits that reflect the time actually spent in the activity. To successfully earn credit, participants must complete the activity during the valid credit period.

Follow these steps to earn credit:

- Log on to www.wileyhealthylearning.com
- Read the target audience, educational objectives, and activity disclosures.
- Read the article in print or online format.
- Reflect on the article.
- Access the CME Exam, and choose the best answer to each question.
- Complete the required evaluation component of the activity.

This activity will be available for CME credit for twelve months following its publication date. At that time, it will be reviewed and potentially updated and extended for an additional period.

[1]GE Healthcare, Menlo Park, California, USA.
[2]GE Healthcare, Toronto, Canada.
[3]GE Healthcare, Denmark.
*Address reprint requests to: R.E.H., GE Healthcare, 333 Ravenswood Ave., Menlo Park, CA 94025. E-mail: ralph.hurd@ge.com
Received November 15, 2011; Accepted June 10, 2012.
DOI 10.1002/jmri.23753
View this article online at wileyonlinelibrary.com.

© 2012 Wiley Periodicals, Inc.

This article describes the basic physics of dissolution dynamic nuclear polarization (dissolution-DNP), and the impact of the resulting highly nonequilibrium spin states, on the physics of magnetic resonance imaging (MRI) detection. The hardware requirements for clinical translation of this technology are also presented. For studies that allow the use of externally administered agents, hyperpolarization offers a way to overcome normal magnetic resonance sensitivity limitations, at least for a brief T_1-dependent observation window. A 10,000–100,000-fold signal-to-noise advantage provides an avenue for real-time measurement of perfusion, metabolite transport, exchange, and metabolism. The principles behind these measurements, as well as the choice of agent, and progress toward the application of hyperpolarized ^{13}C metabolic imaging in oncology, cardiology, and neurology are reviewed.

Key Words: hyperpolarized ^{13}C; DNP; metabolic imaging; pyruvate
J. Magn. Reson. Imaging 2012;36:1314–1328.
© 2012 Wiley Periodicals, Inc.

HYPERPOLARIZED ^{13}C magnetic resonance spectroscopic imaging (MRSI) has recently progressed beyond a substantial number of very exciting preclinical studies, into man (1). The goal of this article is to introduce the basic principles and progress that have been made toward the clinical application of hyperpolarized ^{13}C using dissolution dynamic nuclear polarization (DNP). Topics include the significant contributions to the science of dissolution-DNP, rapid multinuclear spectroscopic imaging methods, and animal model work targeted at a wide variety of potential indications.

In MR, hyperpolarization indicates that the polarization is no longer determined by the static magnetic field of the scanner. The enhanced polarization of the agent is created outside the imaging system by means of a polarizer. Hyperpolarization can be based on several principles (2–4). One such is the dissolution-DNP method that has been very successful over the past 5–10 years in terms of making solutions of biologically interesting molecules with highly polarized nuclear spins. The method takes advantage of DNP in the solid state followed by rapid dissolution in a suitable solvent (2–4). The polarization is retained almost completely in the dissolution step, creating a solution with a nonthermal nuclear polarization approaching unity.

To take advantage of a hyperpolarized liquid state solution requires rapid transfer into the subject, as illustrated in Fig. 1, followed by efficient and rapid ^{13}C spectroscopic imaging sequences.

Hyperpolarization by the Dissolution-DNP Method

DNP was first described theoretically by Overhauser in 1953 (5), and a few months later demonstrated by Carver and Slichter (6) in metallic lithium. Overhauser predicted that saturating the conduction electrons of a metal would lead to a dynamic polarization of the nuclear spins. This was a fundamental discovery causing disbelief at the time: that heating of one spin system could lead to the cooling of another. The prediction by Overhauser for metals was extended to electron spins in solution by Abragam (7), and most nuclear magnetic resonance (NMR) spectroscopists are today familiar with the nuclear and electronic Overhauser effect. However, this effect is limited to solutions where relaxation processes couple the spin systems via molecular motions. Soon after, the Solid Effect was described for spins in the solid state coupled by dipolar interactions (8). Later, DNP in the solid state was extended mechanistically to processes involving several electron spins (thermal mixing) (9). The theory of DNP in the solid state, however, has failed to provide a quantitative description of the general case. In the solid state, the high electron spin polarization is in part transferred to the nuclear spins by microwave irradiation close to the resonance frequency of the electron spin. The efficiency of this process depends on several parameters characterizing the various spin systems, but also on technical factors such as microwave frequency and power.

DNP has mainly been applied to the generation of polarized targets for neutron scattering experiments, and it has been demonstrated that the nuclear polarizations of ^{1}H and ^{13}C could be increased to almost 100% and to ~50%, respectively, in the solid state by means of DNP at low temperature (10,11). The mechanism requires the presence of unpaired electrons (electron paramagnetic agent; EPA), which are added to the sample as, for example, an organic radical. The magnetic moment of the electron is 658 times higher than that of the proton. This means that the electron spin will reach unity polarization at a moderate magnetic field strength and liquid helium temperature. At, eg, 3.35 T and 1 K the electron spin polarization is 98%.

DNP Sample Preparation

The first step of hyperpolarizing a new molecule by the dissolution-DNP method is to add unpaired electron spins to the sample. Unpaired electron spins with well-defined properties are most conveniently provided by chemical doping. In order for the DNP process to be effective, the EPA agent must be homogeneously distributed within the sample. Many molecules will be crystalline, or have a tendency to crystallize as saturated aqueous solutions. This will cause the EPA to concentrate in domains and lead to a poor DNP effect. To prevent this, the sample should stay amorphous when frozen to ensure homogenous distribution of the EPA. Three examples of molecules that are liquids at room temperature and stay amorphous when frozen without additives are [1-^{13}C]pyruvic acid (or any other isotopic labeling), 2-keto-[1-^{13}C]isocaproic acid, and *bis*-1,1-(hydroxymethyl)-[1-^{13}C]cyclopropane-d_8(HP001). All three molecules are liquids at room temperature and dissolve well a hydrophilic EPA. For other compounds it is necessary to prevent crystallization by mixing or dissolving the compound

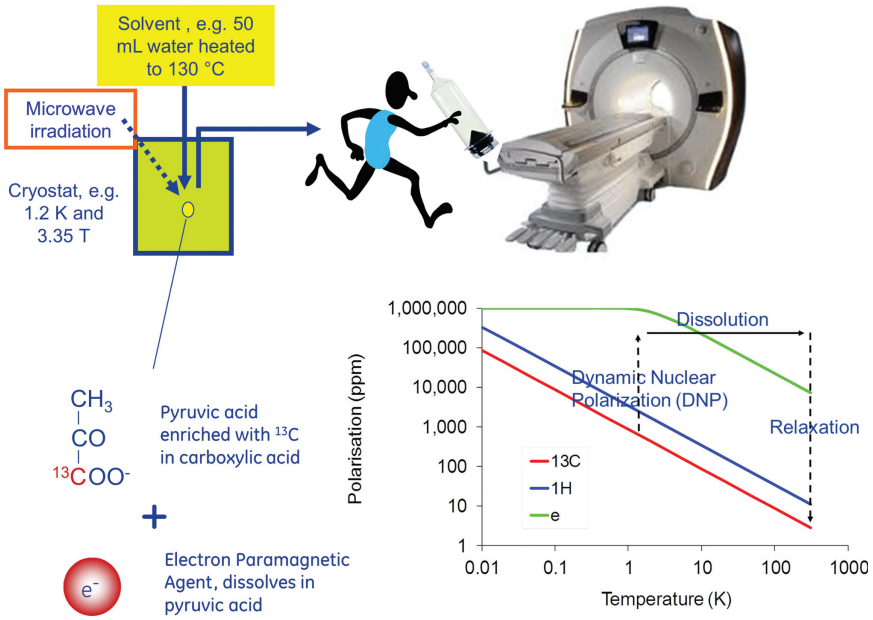


Figure 1. The principle of dissolution-DNP. At room temperature and, eg, 3 T the ^{13}C nuclear spins are only weakly polarized to about 0.00025%, lower right graph. However, an electron spin has a 2700 times stronger magnetic moment and these spins are easily polarized. When the sample is cooled the electron spin polarization of the EPA can reach almost 100%. By irradiation with microwaves close to the resonance frequency of the electron spins, electron-nuclear transitions are induced, and the nuclear spin polarization will be enhanced hundred-fold by DNP, raising the ^{13}C spins to a robust polarization of over 40%. This process is slow and takes typically 15–60 minutes. When the sample is polarized it can be dissolved in, eg, heated water or a buffer, and within seconds a room temperature solution of the hyperpolarized molecule is obtained. The hyperpolarized nuclear spins relax to thermal equilibrium (0.00025%) with a time constant (T_1) of typically 40–80 seconds for carboxylic acids. Therefore the hyperpolarized sample has to be quickly carried to the scanner, injected, and imaged.

in a suitable solvent such as glycerol, or dimethylsulfoxide (DMSO) can be used as solvent for the molecule and the EPA. For in vivo studies it is necessary to be able to formulate the molecule in a concentrated form in order to achieve a high concentration of the molecule after dissolution. To give an estimate of the requirements, a patient dose of 0.1 mmol/kg body weight can be assumed, requiring ~10 mmol of compound, or 1 g with a molecular weight of 100 g/mol. The consequence is that 30%–50% solubility is needed in order to keep the sample size reasonable (see clinical polarizer description). A solvent mixture with high solubility for the molecule and EPA, preventing sample crystallization and with good in vivo tolerance therefore has to be chosen. A good example of a biologically compatible formulation is fumaric acid (eg, [1,4-$^{13}C_2$, 2,3-D_2]fumaric acid) in DMSO. DMSO is a widely used solvent for pharmaceuticals and has a good safety profile (12). It will, however, crystallize when frozen (dry DMSO; melting point 16°C). However, this does not prevent the use of DMSO as solvent for fumaric acid. As saturated solution with a molarity of 3.6 mol/L or 1:1.8 by weight, the solution forms an amorphous solid when frozen. When using DMSO as a glassing agent, care should be taken to ensure the DMSO stays dry (hygroscopic), as small amounts of water will decrease solubility and increase supersaturation.

Another means of improving the solubility involves changing the counterion of salts. Solubility typically increases with increasing size of the counterion, and two examples of this can be mentioned: The cesium salt of bicarbonate ($CsH^{13}CO_3$ (13)), and the TRIS salt of acetate (14). Both of these salts have higher solubility than their sodium counterpart. Finally, for amino acids (zwitter ions at neutral pH) it has shown that either high or low pH preparations increase the aqueous solubility by reducing the charge of the molecule to a point (15) that no or little glycerol is needed to form an amorphous sample.

Electron Paramagnetic Agent (EPA)

The source of the unpaired electron is typically an organic radical, but a few metal ions have been employed successfully for DNP, Cr(V) in particular (16). The choice of EPA will depend on a number of factors. First, the EPA needs to be chemically stable and dissolve readily in the matrix of interest. Second, the electron paramagnetic resonance (EPR) spectrum of the radical should have a width that allows DNP to be effective for the nucleus of interest, ie, a line width that exceeds the Larmor frequency of the nuclear spin. In practice the above criteria mean that two classes of EPA are available, namely nitroxides (17,18) and trityls (19–21). The nitroxides belong to a class of molecules that have been studied extensively by EPR, and which have been used for DNP for many samples. Nitroxides are characterized by having a broad EPR spectrum. The EPR line width is 4.0 per mil (‰) of the EPR frequency, compared to the ^1H resonance frequency, which is 1.5‰ of the EPR frequency. Some of

them have reasonable chemical stability and come with different degrees of hydrophilicity. Another class of EPA with superior properties for direct polarization of low gamma nuclei such as ^{13}C, ^{15}N, and ^{2}H is the trityl. These radicals have a line width that is only 0.80‰ (22,23) of the resonance frequency, much less than the proton resonance frequency, but perfectly matched for ^{13}C, which has a resonance frequency which is 0.37‰ of the EPR frequency. The trityls also exist with a range of hydrophilicities and some of them are chemically very stable.

It has been shown that gadolinium (Gd) can positively affect the solid state DNP enhancement (24). Other paramagnetic ions and molecules (Mn^{2+} and O_2) can in part have the same effect. The physics is not yet understood, but Ardenkjaer-Larsen et al (24) showed that the longitudinal relaxation time of the EPA is shortened by the presence of the Gd ions. The effect of adding 1–2 mmol/L Gd^{3+} is a 50%–100% improvement of the DNP enhancement factor. The effect seems to be general to most samples, but has to be optimized for each sample similarly to the concentration of the EPA. There is no direct DNP effect of the Gd^{3+} by itself under the conditions typically used. Finally, Gd^{3+} may enhance the solid state polarization by DNP, but care should be taken in avoiding accelerated relaxation in the liquid state. Free Gd ions would cause detrimental liquid state relaxation and pose an in vivo safety risk. After dissolution the low concentration of radical and chelated Gd will have a negligible effect on T_1 in most cases.

DNP Instrumentation

Most solid-state DNP has been performed at magnetic fields between 0.35 T (25) and 16.5 T (26,27), and at temperatures from a few hundred mK to room temperature. At temperatures below a few Kelvin and magnetic field strengths above a few Tesla, electron spins are almost fully polarized, and large nuclear polarizations can be obtained. Unlike solid-state NMR spectroscopy applications where nonequilibrium polarizations can be regenerated by repeating the microwave irradiation and NMR acquisition, the polarization generated for in vivo applications will decay irreversibly after dissolution. Hence, the goal is to generate polarizations close to unity. It is therefore important to choose initial operating conditions that have been proven to provide high nuclear polarization, but are at the same time easily achievable using standard instrumentation. Temperatures of ~1 K can be achieved by pumping on liquid helium. In the original dissolution-DNP polarizer design the liquid helium was supplied to the sample space through a needle valve from the magnet cryostat, but in a recent publication an alternative arrangement that used a separate helium dewar was described (28). A magnetic field strength of 3.35 T was chosen since microwave sources are readily available at 94 GHz for irradiation of the electron spin. However, recently it has been demonstrated that for both nitroxides and trityls a significant improvement in polarization can be obtained by increasing the magnetic field strength (29,30) or lowering the temperature (31). For the compound [1-^{13}C]pyruvic acid, the ^{13}C polarization improved from 27% at 3.35 T to 60% at 4.64 T in the solid state. The literature has been limited and disagrees on the magnetic field dependence of DNP (32). On the other hand, it has been well established that lowering the temperature is beneficial for DNP.

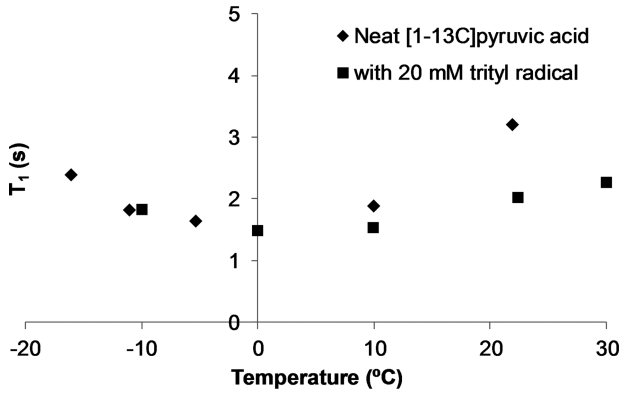


Figure 2. Longitudinal relaxation time, T_1, as a function of temperature for neat [1-^{13}C]pyruvic acid with ■ and without ◆ 20 mmol/L trityl.

Dissolution and Relaxation in the Liquid State

To make the polarized solid sample useful for in vivo imaging, it needs to be dissolved in a suitable buffer. Depending on the solid sample preparation the dissolution may involve neutralization of the agent with acid or base. Buffering of the solution may be required to maintain control of pH within the physiologic range of 6.8 to 8.1. Physiological buffers such as Tris(hydroxymethyl)aminomethane (TRIS) or 4-(2-hydroxyethyl)piperazine-1-ethanesulfonate (HEPES) are commonly used. Attention to the tonicity of the formulation should be paid and close to isotonic is desired. This may mean lowering the concentration of solutes after dissolution by dilution or adding sodium chloride to the dissolution medium. The dissolution has to be efficient and fast compared to the nuclear T_1 in order to preserve the nuclear polarization in this process. Formulating the solid sample as beads or powder may improve the dissolution (in terms of polarization and recovery of the solid sample), but understanding and optimizing the fluid dynamics (33) as well as providing the necessary heat is essential for optimal performance of more difficult agents. Relaxation during the dissolution process can depend on several factors. To minimize relaxation, dissolution is performed inside the cryostat in the high field of the polarizer (eg, ~3 T in the case of a 3.35 T polarizer), but above the liquid helium surface. Any paramagnetic ions that could increase the relaxation rate are chelated by adding, for example, ethylenedinitrotetraacetic acid (EDTA) to the dissolution medium, or to the sample. To illustrate the severity of relaxation during dissolution [1-^{13}C]pyruvic acid (pyruvic acid enriched with ^{13}C to 99% in the C-1, ie, carboxylic acid, position) is chosen as an example. This molecule has been well studied with DNP and has high biological relevance. In Fig. 2 the

Table 1
Dissolution-DNP Compounds (97–106)

Agent	Products	Ref.
[1-^{13}C]pyruvate	[1-^{13}C]lactate, [1-^{13}C]alanine, [^{13}C] bicarbonate, $^{13}CO_2$	41
[2-^{13}C]pyruvate	[2-^{13}C]lactate, [2-^{13}C]alanine, [1-^{13}C]acetyl-carnitine, [1-^{13}C]citrate, [5-^{13}C]glutamate	92,95
[1,2-$^{13}C_2$]pyruvate	[1,2-$^{13}C_2$]lactate, [1,2-$^{13}C_2$]alanine, [1-^{13}C]acetyl-carnitine, [1-^{13}C]citrate, [5-^{13}C]glutamate, [^{13}C]bicarbonate, $^{13}CO_2$	100
[1-^{13}C]lactate	[1-^{13}C]pyruvate, [1-^{13}C]alanine, [^{13}C] bicarbonate, $^{13}CO_2$	101
13C-bicarbonate	$^{13}CO_2$	13
[1,4-$^{13}C_2$]fumarate	[1,4-$^{13}C_2$]malate	85
[1-^{13}C]acetyl-methionine	[1-^{13}C]methionine	102
[2-^{13}C]fructose	[1-^{13}C]fructose-6-phosphate	103
[5-^{13}C]glutamine	[5-^{13}C]glutamate	107
[1-^{13}C]ethylpyruvate	[1-^{13}C]pyruvate, [1-^{13}C]lactate, [1-^{13}C]alanine, [^{13}C] bicarbonate, $^{13}CO_2$	93
[1,1'-$^{13}C_2$]acetic anhydride	Multiple depending on reactant	104
[1-^{13}C]acetate	[1-^{13}C]acetylcarnitine	109
13C Urea	None	105
bis-1,1-(hydroxymethyl)-[1-13C]cyclopropane-d8 HP001	None	108
α-keto-[1-^{13}C]isocaproate	[1-^{13}C]leucine	83
[1-^{13}C]dehydro ascorbic acid	[1-^{13}C]ascorbic acid	97,98
[1-^{13}C]alanine	[1-^{13}C]lactate, [1-^{13}C]pyruvate, [^{13}C]bicarbonate	106

T_1 of the C-1 of [1-^{13}C]pyruvic acid at 9.4 T is given as a function of temperature (unpubl. data). It can be seen that the shortest T_1 is ~1.6 seconds at 0°C. With the trityl radical present (20 mmol/L) there will be an additional (dipolar) relaxation contribution from the electron spin. It can be seen that the contribution from the trityl is marginal, but shifts the minimum to a different temperature (correlation time). According to relaxation theory the minimum T_1 scales with B_0, which means that a minimum T_1 of 0.7 seconds should be expected during the dissolution in the 3 T polarizer field. The data illustrate that the nuclear spin during the dissolution should pass through this T_1 minimum on a much faster time scale to avoid a loss of polarization. The example illustrates that it is not unreasonable to expect that the loss of polarization during dissolution can be overcome, but that a fast and efficient dissolution process is needed. The severity of the problem will depend on the target spin and sample properties, but several parameters can be controlled, eg, the distance to other spins (labeling position), the abundance of other spins (full or partial deuteration), and the concentration of the EPA.

In most cases the EPA or Gd chelate do not cause significant relaxation after dissolution, and may also be safe to inject into animals. For preclinical imaging it is not required to remove the EPA. The same applies to the Gd chelate in case it is used in the formulation. However, the solution may undergo a filtration or chromatography step to remove the EPA involved in the DNP process. In case a Gd chelate has been added, this agent may be removed as well. The filtration can either be in-line with the dissolution process or a subsequent step. In either case the filtration is completed in a matter of a few seconds with insignificant loss of polarization or target molecule (unpubl. work).

Clinical Polarizer Requirements

Recently a DNP polarizer designed with sterile use intent was published (31). The key design criteria of this concept are:

1. To provide a sterile barrier to the product through a single use fluid path.
2. To eliminate consumption of liquid cryogens.
3. To increase throughput by having four independent parallel samples.
4. To increase the size of the individual DNP samples up to 2.0 mL.
5. To automate the operation and remove operator variability and interventions.
6. To add noncontact quality control (QC).

The above criteria are required for successful clinical translation of hyperpolarization. The future will reveal if these are adequate and can fulfill regulatory requirements as well as gain user acceptance. Most important, it should be emphasized that a sealed sterile fluid path for all components in the polarization and dissolution process (compounding) provides a concept that allows filling and sealing at a manufacturing site without the need to break this barrier at any point in the process until the point of product release by the QC system. Second, it has been demonstrated that a closed-cycle, sorption pump based cryogenic system served by a cryo-cooler was able to achieve a base temperature of less than 0.8 K. The lower temperature translated directly into a higher solid state polarization. Thus, the authors reached a solid state polarization of 35%–40% at 0.8 K and 3.35 T.

Dissolution-DNP Agents

Of the growing list of agents investigated in vivo using this method (Table 1), the most studied is

[1-^{13}C]pyruvate. This agent has shown great utility in oncology, as exemplified by studies showing correlations with disease progression (34) and early response to therapy (35). Research in cardiology (36) and brain (37) have also shown promise. [1-^{13}]pyruvate was also the first agent to be used in a human study of hyperpolarized metabolic imaging (1). This molecule illustrates a number of important features of an ideal agent for hyperpolarized metabolic imaging. First, as pyruvic acid, it is a liquid at room temperature and can directly solubilize enough EPA (15 mM trityl) for relatively fast polarization build-up (time constant of ~15 min at 1.4 K and 3.35 T), and relatively high polarization (>20%). The high concentration inherent in the choice of a neat liquid (~14 M for pyruvic acid) also yields a relatively high concentration after dissolution. As a result, this agent can be injected safely at 250 mM, in doses up to 0.43 mL/kg.

MNS Hardware

Standard clinical MR systems and coils are designed to transmit and receive radiofrequency (RF) signals at ^{1}H resonance frequency only. However, multinuclear spectroscopy (MNS) packages are available from most manufacturers of whole-body MR scanners. This option allows the system to perform MR experiments on nonproton nuclei of interest such as ^{13}C and ^{15}N (for simplicity, the remainder of this section focuses on hardware required for ^{13}C studies). An MNS package typically includes a broadband RF power amplifier, in addition to the standard ^{1}H narrowband amplifier, that amplifies the RF pulse waveforms to give them enough power through a transmit RF coil to create the necessary B_1 field at the resonance frequency of the nucleus of interest. This transmit RF coil could be a dedicated coil tuned to the resonance frequency for ^{13}C. The ^{13}C coil can be designed to perform both RF transmission and reception for ^{13}C, or designed to perform RF transmission only with a separate coil(s) for RF reception, also tuned to the ^{13}C resonance frequency. Whether the reception of the MR signal is performed by a dedicated RF receive coil(s) or by a transmit/receive coil, the signal is amplified by a preamplifier prior to digitization, processing, and image reconstruction. The preamplifiers typically work at a narrow range of frequencies and can be built into the MR scanner or into the RF coil, with one preamplifier generally required for each receive channel. Thus, to perform ^{13}C experiments, dedicated preamplifiers that operate at the ^{13}C frequency need to be either added to the system or built into the ^{13}C coils.

Since it is desirable to perform both ^{1}H anatomical imaging and hyperpolarized ^{13}C metabolic imaging during the same exam without repositioning the subject, the ^{13}C RF coil design and setup need to preserve the ability to perform ^{1}H imaging with a minimal compromise of image quality. Volume coils that can operate at both ^{1}H and ^{13}C frequencies (dual-tuned) have been demonstrated for preclinical hyperpolarized ^{13}C imaging (34,38). The coil configuration and design can be further optimized for imaging a particular organ/anatomy. For example, in the first proof-of-concept clinical trial of hyperpolarized ^{13}C metabolic imaging in prostate cancer patients, a ^{13}C transmit-only volume coil built into a custom patient table was used in conjunction with a receive-only endorectal coil that contained both a ^{13}C and a ^{1}H element for signal reception and the system body coil was used for ^{1}H RF transmission during ^{1}H imaging (39). A multichannel ^{13}C receive-only array coil suited for other human applications has also been demonstrated recently (40). Regardless of the coil design and combination, the MR system needs to be configured so that the correct coils/channels are active or disabled during specific periods of the scans to avoid signal degradation due to coupling. The gradient coils existing on all MR scanners to provide spatially varying magnetic fields to allow localization of RF signals can be used for ^{13}C imaging without any hardware modification. However, it is important to note that for a given magnetic field gradient the spatial variation in resonance frequency experienced by the nucleus is proportional to its gyromagnetic ratio. Thus, the highest spatial resolution achievable for ^{13}C imaging is approximately one-fourth that of ^{1}H under the same imaging conditions; the designs and implementations of RF pulse sequences for ^{13}C imaging need to take this limitation into consideration. It is possible to circumvent the low gyromagnetic ratio limitation by transferring the ^{13}C or ^{15}N magnetization to neighboring ^{1}H nuclei for detection (41,42). But simultaneous RF transmission at both ^{1}H and the low γ nucleus frequencies is required for the polarization transfer pulse sequence, and this capability may not be available on some clinical MR systems even with MNS package installed.

Nonrecoverable Magnetization

The magnetization of hyperpolarized ^{13}C substrate is largely enhanced in the DNP polarizer. After dissolution, the liquid state polarization currently achievable is ~20% (or 200,000 ppm). Once dissolved, the hyperpolarized ^{13}C magnetization undergoes T_1 relaxation toward thermal equilibrium in a similar physical mechanism as water protons in the human body after an RF excitation or inversion in a typical MRI scan. But body protons *recover* to thermal equilibrium via T_1 relaxation, whereas the hyperpolarized ^{13}C substrate irreversibly *decays* into thermal equilibrium via T_1 relaxation. Once decayed, the 200,000 ppm hyperpolarized magnetization is not recoverable and the magnetization of the ^{13}C substrate remains at the thermal equilibrium level, about 2.6 ppm at 3 T. In addition to the loss of polarization due to T_1 relaxation, RF pulses deplete polarization in a nonrecoverable way. Hyperpolarized gas imaging using ^{3}He or ^{129}Xe also utilizes nonrecoverable magnetization, subject to T_1 relaxation and RF depletion. Thus, sample delivery and data acquisition in hyperpolarized imaging need to be sufficiently fast in order to utilize this decaying and nonrecoverable magnetization (for [1-^{13}C]pyruvate, most of the nonequilibrium polarization is lost within 2–3 minutes postdissolution). However, different from hyperpolarized gases, some

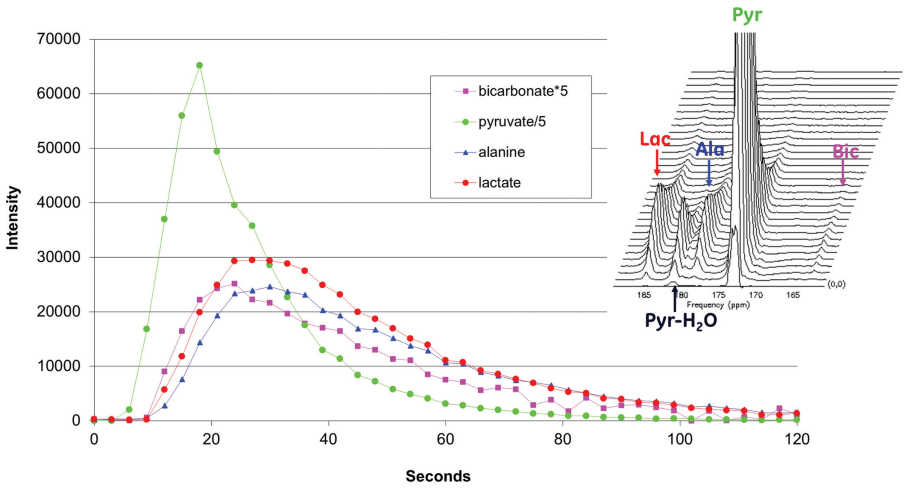


Figure 3. Dynamic curves of ^{13}C-pyruvate, and its metabolic products: ^{13}C-alanine, ^{13}C-lactate, and ^{13}C-bicarbonate (as labeled), following an injection of hyperpolarized [1-^{13}C]pyruvate into a rat. The dynamic signals were obtained from the individual peak height of a stack of spectra (right insert) acquired every 3 seconds from a 90-mm thick section of the rat torso.

hyperpolarized ^{13}C substrates such as [1-^{13}C]pyruvate also undergo metabolic conversions to downstream metabolites. Therefore, the signal-to-noise ratio (SNR) of hyperpolarized ^{13}C in vivo depends on the T_1 relaxation time, metabolic conversion rates, liquid state polarization, concentration, agent delivery time, acquisition timing, and pulse sequence strategies of utilizing the nonrecoverable magnetization. The following section describes the most popular data acquisition strategies for hyperpolarized ^{13}C imaging.

Pulse Sequences

Hyperpolarized ^{13}C MRI typically requires acquisition of ^{13}C signals from the injected metabolite and its metabolic products. These ^{13}C-labeled metabolites can be observed as a spectrum of peaks at different resonance frequencies. Both the spatial distribution and temporal evolution of the metabolite signals are of a strong interest for understanding the dynamic metabolic process in vivo. Pulse sequence design progressed rapidly from single-slice, single-timepoint acquisition to five-dimensional MRSI: temporal, spectral, and three spatial dimensions. Optimizing sampling efficiency of nonrecoverable magnetization has been the primary focus of pulse sequence development for hyperpolarized ^{13}C MRSI. Methods such as compressed sensing and iterative decomposition of water and fat with echo asymmetry and least square estimation (IDEAL) have been applied to accelerate acquisitions in this context, and various RF pulse designs have been used to optimize SNR and/or contrast-to-noise ratio (CNR). In addition, there are specialty sequences for quantitation of T_2 and metabolic kinetics.

Single Timepoint MRSI

Early work in hyperpolarized ^{13}C MRSI employed concentric phase encoding and variable flip angle (38,43–45) techniques to acquire chemical shift images (CSI) in two dimensions within a short time window that coincides with the maximum ^{13}C signals of metabolic products. For these single timepoint images, the optimum acquisition depends on the bolus injection, the organ of interest, and perfusion. Therefore, a nonspatially resolved dynamic scan of the same region (Fig. 3) was often performed (in a separate bolus injection) prior to the imaging study to gain timing information from the metabolic signal–time curves (38). For a typical protocol of a 16 × 16 matrix and 5 × 5 mm in-plane resolution, it requires 15–20 seconds to acquire CSI of a single slice because of the long readout duration (to obtain adequate spectral resolution) and one TR is needed for each spatial encoding point in X and Y. Higher spatial resolution is possible in the same scan time, but requires a smaller field of view (FOV), which may result in spatial aliasing in clinical settings unless the ^{13}C coil receptivity profile limits the FOV, such as is the case for surface coils or endorectal coils.

Rapid CSI techniques have been developed to improve sampling efficiency within the available time window. Echo-planar spectroscopic imaging (EPSI) with flyback (46) or symmetric gradient waveform (47) traverses time and one spatial frequency domain in a single readout period, shortening the acquisition and allowing either single-timepoint 3D MRSI or time-resolved multislice 2D MRSI (34,45) on a standard clinical 3 T system (with a maximum gradient strength of 4 G/cm and slew rate of 150 mT/m/ms). There is a trade-off between spectral bandwidth and spatial resolution in the design of these gradient trajectories. Typically, a 5-mm resolution is achievable with 500 Hz spectral bandwidth without spectral aliasing of [1-^{13}C]pyruvate and its metabolic products (except ^{13}C bicarbonate). A similar trade-off also exists for spiral CSI (48), which employs spiral readout gradients to sample X and Y simultaneously, and concatenates the spiral gradients multiple times for chemical shift encoding. However, even with multiple interleaves to minimize the impact of gradient slew-rate, the 2D spiral readout time can result in a spectral bandwidth that is insufficient to fully cover the metabolite chemical shift range. This causes spectral aliasing, which needs to be corrected in the image reconstruction (48,49) or otherwise, results in image blurring. On a clinical system, spiral CSI completes a 2D MRSI of a single slice in 375 msec, a 50-fold reduction in scan time (50) compared to the

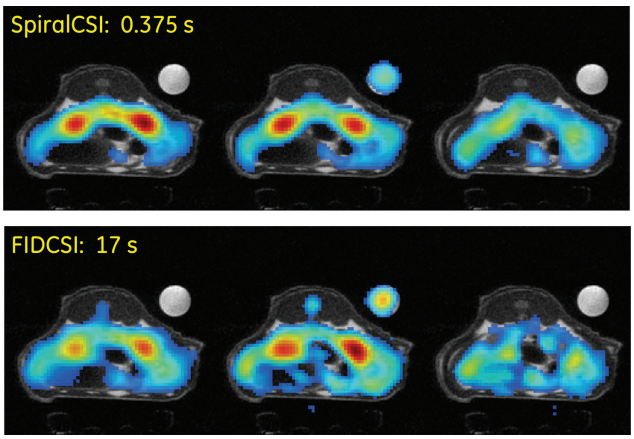


Figure 4. Comparison of spiral CSI and conventional FIDCSI. Images were obtained from a single slice rat kidney for [1-^{13}C]pyruvate (left), [1-^{13}C]lactate (middle), and [1-^{13}C]alanine (right). Spiral CSI (0.375 sec per slice) than FIDCSI (17 sec per slice) with similar image quality. Courtesy of Dr. Dirk Mayer of SRI, International and Stanford University.

conventional CSI method (Fig. 4). However, for clinical applications that require a large FOV, spiral CSI acquisition time may increase drastically due to the increase of interleaves required to maintain the same spatial resolution and spectral bandwidth. In addition, spiral CSI encodes a circular FOV and can become inefficient for a region of interest (ROI) with an asymmetric FOV. On the other hand, EPSI allows asymmetric FOV and the FOV in the one direction encoded by the EPSI readout is virtually unlimited due to the very high sampling rate available on all clinical systems.

Acceleration to 5D MRSI

When the information of temporal dynamics and spatial distribution are both needed, time-resolved MRSI with multislice 2D or 3D volumetric coverage is a good strategy. Time-resolved metabolic data can be used to determine rate constants (51), and signal averaging over the time course for each voxel can regain most of the SNR observed in optimized non-time-resolved methods. In preclinical studies, 5D MRSI has been demonstrated by using spiral CSI (51,52) and compressed sensing (53,54), both yielding high-quality images and dynamic curves. Taking advantage of the considerable sparsity in hyperpolarized ^{13}C spectra, compressed sensing pseudorandomly undersampled spectral and X-Y spatial domains during EPSI flyback readout, yields up to a factor of 7.53 in acceleration (55) relative to the conventional 3D EPSI sequence (46) (Fig. 5). The acceleration can be used to improve spatial resolution and decrease acquisition time, or to cover a larger FOV, which will be useful for clinical applications. The trade-off of this technique is the loss of metabolite peaks with low SNR (appears to break down for SNR less than ~7). This could potentially limit its applications depending on the achievable clinical SNR, which is yet to be determined by clinical trials.

Another approach under development is IDEAL spiral CSI (56), using the iterative least-squares chemical shift-based (LSCS) method. This technique has been used clinically for decompositions of water from fat (57), but is also capable of decomposing multiple ^{13}C-labeled chemical species (58). Spectral sampling is accomplished by shifting the echo time (TE) from excitation to excitation and 2D images at each TE are acquired by using spiral gradient trajectories. IDEAL requires a priori information of chemical shift frequencies of ^{13}C metabolite peaks and, with such, IDEAL allows minimum numbers of excitations for spectral decomposition, an efficient sampling strategy for a sparse spectrum over a wide bandwidth. There is no trade-off between spatial resolution and spectral bandwidth and, therefore, the spatial resolution can be as high as SNR permits. This technique has been demonstrated in time-resolved 2D imaging, with a potential of combining with a pulse-and-acquire FID acquisition to obtain a pseudo spectrum (59). The integrity of the pseudo spectrum obtained by using this technique for quantitation purposes is under investigation in preclinical studies.

RF Designs to Optimize SNR

The signal of the injected, relatively concentrated, hyperpolarized ^{13}C substrate is often 5 to 10 times larger than the signals of its metabolic products

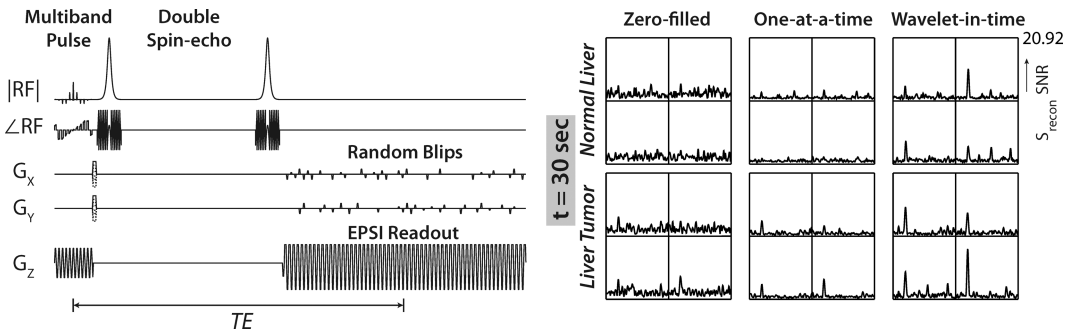


Figure 5. Pulse diagram of multiband and compressed sensing sequence (left), and reconstructed spectra (right) of time-resolved 3D MRSI data. Improved peak detection of the wavelet-in-time method is most evident at 30 seconds after hyperpolarized [1-^{13}C]pyruvate injection. Courtesy of Dr. Peder Larson, Dr. Simon Hu, and Dr. Dan Vigneron, University of California at San Francisco.

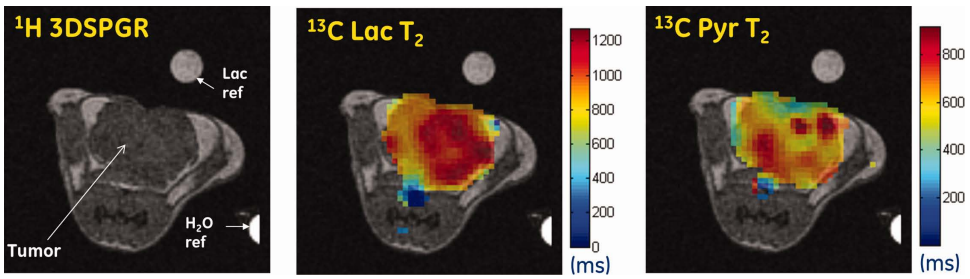


Figure 6. Quantitative ^{13}C-lactate (middle) and ^{13}C-pyruvate (right) T_2 maps of a single 2 mm slice on TRAMP tumor. Tumor appears homogeneous on proton 3D-SPGR image (left) but has heterogeneous T_2 values for [1-^{13}C]lactate and [1-^{13}C]pyruvate. The estimated T_2 errors range from 100 to 200 msec (not shown). [Color figure can be viewed in the online issue, which is available at wileyonlinelibrary.com.]

initially, whereas the product signals are replenished during the acquisition via recirculation of the surplus ^{13}C substrate. Multiband spectral-spatial RF excitation pulses (60) use spectral selectivity to minimally excite the injected hyperpolarized ^{13}C substrate while exciting the metabolic products with a larger flip angle to obtain higher SNR of the metabolites without saturating the substrate magnetization prematurely. The metabolic products are observable for a longer window and with better SNR than a uniformly constant flip angle (60) strategy. A recent development combining multiband RF pulse design and compressed sensing random sampling created a sequence for time-resolved 3D MRSI acquisition (55,61) with good SNR. The flip-angle of the injected ^{13}C substrate and that of the products can be optimized for optimal CNR ratio for a particular organ or for disease characterization (62).

An alternative to spectroscopically resolving multiple metabolites is direct imaging of each metabolite after selective excitation by a spectral-spatial pulse (63). Recently, a multislice cardiac-gated sequence consisting of a large flip-angle spectral-spatial excitation RF pulse with a single-shot spiral trajectory was developed for ^{13}C imaging of cardiac metabolism (64). The sequence alternates among the chemical shift frequencies corresponding to each metabolite and allows for rapid imaging of each individual metabolite.

T_2-Based Sequences

Long T_2 relaxation time of ^{13}C metabolites was first observed using a TRAMP (transgenic adenocarcinoma of the mouse prostate) tumor model (65). The T_2 difference between tumor and normal tissue was explored in a rat hepatocellular carcinoma (HCC) study (66) using a single-voxel preparation pulse followed by a train of spin-echoes to measure the T_2 decay of the signal within the voxel. T_2's of [1-^{13}C]alanine and [1-^{13}C]lactate were found to be longer in HCC tumors (1.2 sec and 0.9 sec, respectively) than in normal liver (0.4 sec and 0.5 sec, respectively). Recently, a T_2 mapping sequence was developed to measure T_2 of ^{13}C-labeled metabolites pixel-by-pixel with high resolution (67). T_2 values were extracted from regions of interest on the T_2 maps with better precision. Figure 6 shows the T_2 map of a single-slice acquired through a TRAMP tumor and the tumor has a T_2 of 1.4 seconds. The large T_2 difference between tumor and normal tissues presents an opportunity for greater imaging contrast when using a T_2-based sequence. A large SNR gain is also expected by using T_2-based sequences as compared to T_2^*-based sequences. For example, most of the sequences mentioned before are limited by signal loss caused by T_2^* decay. T_2^* can be as long as 100–200 msec for [1-^{13}C]pyruvate, but is reduced to about 25 msec for [1-^{13}C]lactate and [1-^{13}C]alanine due to stronger J_{CH} coupling (38), and all these T_2^* values are shorter than the T_2 values. T_2-based sequences, such as multiecho balanced-steady-state free precession (SSFP) (68,69) and stabilized fast spin echo (FSE)-EPSI (70), have significant signal gain and are excellent for single-timepoint MRSI. The challenge to utilize this strategy for time-resolved MRSI lies in the strong RF depletion during the echo train. Multiecho balanced-SSFP has been demonstrated in 3D acquisition for time-resolved hyperpolarized chemical shift imaging (71), but the temporal resolution of 16 seconds may not be sufficient for characterizing the metabolic dynamics.

Kinetic Modeling

Hyperpolarized pyruvate-to-lactate signal-time curves have been described by two-site exchange (35,72) models. Under saturating conditions, the apparent rate constant *Kpl* increases as the pyruvate dose decreases (72). The small tip-angle, pulse-and-acquire dynamic curves are biased by the substrate dose, bolus shape, and accumulated in flow of [1-^{13}C]lactate. These factors can be eliminated by using a saturation recovery method (67,68), resulting in dynamic curves that describe the instantaneous metabolic conversion at the local tissue level during the passage of hyperpolarized [1-^{13}C]pyruvate. This method typically consists of multiple 90°-excitations to acquire dynamic spectroscopic images and spectrally selective saturation pulses applied in between acquisition of time frames to spoil the inflow of [1-^{13}C]lactate while preserving inflow of fresh [1-^{13}C]pyruvate. The resulting kinetic data were fully sampled at each timepoint and were unbiased by the substrate dose, bolus shape, and product decay. Apparent maximal reaction velocity V_{max} and asymptotic conversion rate at saturated condition K_M can be derived by kinetic modeling of the saturation recovery dynamic curves (67).

Exchange vs. Flux

The conversion of [1-^{13}C]pyruvate to [1-^{13}C]lactate, as observed in hyperpolarized metabolic imaging, is a combination of flux (net creation of lactate) and exchange (^{13}C enrichment of the lactate pool with no net change in concentration). In whole blood, pyruvate-lactate exchange occurs at a rate 3–5 times the rate of flux (73). The impact of lactate pool size and exchange was demonstrated for hyperpolarized [1-^{13}C]pyruvate metabolic spectroscopy using cells preconditioned with unlabeled lactate (35). Under conditions of elevated steady-state lactate (unlabeled), a large increase in hyperpolarized [1-^{13}C]lactate was observed. Recently, the importance of exchange has been demonstrated in a lymphoma model, under the high bolus concentration hyperpolarized [1-^{13}C]pyruvate and magnetization transfer technique (74). The authors of this study further concluded that steady-state lactate pool size is the likely limit of detection for [1-^{13}C]lactate in regions-of-interest such as blood and muscle.

The availability of the reduced form of nicotinamide adenine dinucleotide NADH, from sources beyond lactate dehydrogenase (LDH) catalyzed exchange, also impacts the conversion of hyperpolarized [1-^{13}C]pyruvate to [1-^{13}C]lactate. For example, added NADH from aldolase processing of ethanol in liver (75), or from mitochondria via a reverse of the malate-aspartate shuttle (76), have been shown to increase the flux of hyperpolarized [1-^{13}C]pyruvate to [1-^{13}C]lactate. However, the balance of flux and exchange has not yet been quantitatively established, and remains to be determined, even for normal tissues and conditions.

APPLICATIONS

Oncology

Prostate Cancer

Initial experience in hyperpolarized ^{13}C metabolic imaging of prostate cancer was reported by Chen et al (45) by injecting hyperpolarized [1-^{13}C]pyruvate into transgenic adenocarcinoma of mouse prostate (TRAMP) model. The study showed highly elevated lactate signal in late-stage prostate tumors. Albers et al (34) compared hyperpolarized ^{13}C metabolic imaging of prostate cancer with histology. Normal mice and TRAMP of various histologic grades were studied. Images of ^{13}C-pyruvate, ^{13}C-lactate, and ^{13}C-alanine were obtained by using 3D EPSI sequence in 14 seconds. The lactate signal level increases with tumor progression and correlates strongly with histologic grade.

Clinical Trial

The first clinical trial of hyperpolarized ^{13}C-pyruvate metabolic imaging of prostate cancer patients was successfully conducted at the University of California in San Francisco (1). This study was a proof-of-concept trial entitled "A Phase 1/2a Ascending-Dose Study to Assess the Safety and Tolerability and Imaging Potential of Hyperpolarized Pyruvate (^{13}C) Injection in Subjects with Prostate Cancer." This 33-patient study was conducted with the primary objective to assess the safety of hyperpolarized pyruvate (^{13}C) injection in men with prostate cancer and intact prostates. The secondary objectives were to determine: 1) The kinetics of hyperpolarized pyruvate injection delivery and metabolism throughout the prostate, and 2) to determine the SNR for ^{13}C pyruvate metabolites and total hyperpolarized carbon (THC) in regions of cancer and in surrounding benign prostate as a function of the dose of the hyperpolarized pyruvate (^{13}C) injection. All doses were well tolerated without exception, and excellent CNR for [1-^{13}C]lactate was observed even at the lowest dose (private commun.).

Liver Metabolism and Hepatocellular Carcinoma

Using hyperpolarized [1-^{13}C]pyruvate, Hu et al (77) studied liver metabolism in fasted rats and found higher lactate-to-alanine signal ratios and lower alanine signal level in the fasted rats than in free-fed rats. The low alanine signal is most likely due to a reduction of alanine aminotransferase (ALT) activity in fasted rat liver during gluconeogenesis. Alanine is also a good biomarker for HCC detection. Using hyperpolarized [1-^{13}C]pyruvate, Darpolor et al (78) found elevated alanine and lactate levels, consistent with enzyme expression analysis on rat HCC tissue extract. Interestingly, ^{13}C MRSI showed high alanine signals specifically in HCC tumors, whereas it showed high lactate signals in the HCC tumors and in blood vessels. Low ^{13}C-alanine signals in vessels may be due to the much slower transport of alanine than lactate from cells to blood. Therefore, within the 1 minute of ^{13}C acquisition time window, not much ^{13}C-alanine signal was observed in vessels but only in HCC tumors. This is a promising technique for liver cancer diagnosis and treatment monitoring.

Glioma

Park et al (79) assessed the potential use of hyperpolarized ^{13}C-pyruvate for glioma prognosis in rat models. The signal levels of ^{13}C-pyruvate and its metabolic product, ^{13}C-lactate, as well as their relative signal ratios were significantly higher in tumors than in normal brain. The ^{13}C-lactate signal correlated with proliferation. The different ^{13}C metabolic profile between two different models in the study was consistent with their immunohistochemical data. Time-resolved 2D MRSI was reported recently in a rat glioma model, comparing metabolic conversion rates between glioma and normal brain (80). In both studies, large ^{13}C-pyruvate uptake was observed due to the disruption of the blood–brain barrier (BBB) in gliomas. For studies of ^{13}C-pyruvate metabolism in normal rat brain, where the BBB is intact, see the Neurology section below.

Lymphoma

Extracellular pH is known as a biomarker of interstitial lactic acid production (81). Although intracellular pH has been measured by ^{31}P MRS (82), the lower sensitivity of ^{31}P MRS limits its application for human studies with appropriate spatial resolution and

reasonable imaging time window. With the 5 orders of magnitude signal enhancement afforded by the DNP technique, Gallagher et al (13) mapped the pH of murine lymphoma tumor by applying ^{13}C MRSI following an injection of hyperpolarized ^{13}C-bicarbonate. The pH value in each voxel was calculated using the relative signal of ^{13}C-bicarbonate and its metabolic product $^{13}CO_2$ using the Henderson-Hasselbalch equation. The tumor showed lower pH than the surrounding healthy tissues.

Another hyperpolarized ^{13}C substrate that has been tested on lymphoma is 2-keto-[1-^{13}C]isocaproate (KIC). KIC is metabolized to leucine by branched chain amino acid transferase (BCAT), a biomarker for metastasis in some tumors and a target of proto-oncogene c-myc. Following injection of hyperpolarized KIC, Karlsson et al (83) found more than a 7-fold higher signal of ^{13}C-leucine in murine lymphoma than in healthy tissue. In the same study, no ^{13}C-leucine was observed in rat mammary adenocarcinoma. Ex vivo BCAT expression analysis yielded a high BCAT level in murine lymphoma and a very low BCAT level in rat mammary tumor, consistent with the hyperpolarized ^{13}C metabolic imaging findings.

Therapeutic Response

Day et al (35) reported decreased flux between pyruvate and lactate in lymphoma tumors when treated with etoposide and interrogated with hyperpolarized [1-^{13}C]pyruvate. The etoposide induces apoptosis and loss of NADH due to activation of poly (ADP-ribose) polymerase (PARP) leading to reduced LDH activity. This study is the benchmark to demonstrate the feasibility of using hyperpolarized ^{13}C metabolic MR to monitor early treatment effects.

A similar finding was also reported by Chen et al (84) in a study of treatment response on TRAMP tumors by using hyperpolarized [1-^{13}C]pyruvate. Reduced ^{13}C lactate to pyruvate ratio was found in the TRAMP mice that responded to androgen deprivation therapy and no change was found in the ratio in nonresponding mice.

In a study of treatment monitoring of lymphoma tumors using hyperpolarized [1,4-$^{13}C_2$]fumarate, Gallagher et al (85) found that production of [1,4-$^{13}C_2$]malate from the labeled fumarate is a sensitive marker of cellular necrosis. The conversion was 2.4-fold higher in etoposide-treated lymphoma tumors, where significant levels of tumor cell necrosis formed than in the untreated tumors. This technique has clinical potential for monitoring early therapeutic response.

Cardiology

Generation and utilization of adenosine triphosphate (ATP) in the heart are tightly controlled events regulated by physiological conditions and energetic needs. Normally, the heart uses fatty acids, carbohydrates, and ketones as the substrates for energy production. Altered myocardial substrate utilization is associated with diseases such as cardiomyopathy, hypertension, and diabetes; it also occurs during ischemia and reperfusion. Since all substrates are converted to acetyl-CoA prior to entering the Krebs cycle, measurement of the metabolic fluxes of acetyl-CoA production from various substrates can be used to monitor the changes in substrate selection and utilization. Pyruvate dehydrogenase (PDH) is the enzyme that decarboxylates the carbohydrate derived pyruvate to acetyl-CoA and CO_2, and the control of this enzyme's expression and activity is closely tied to myocardial substrate selection, thus the ability of using hyperpolarized ^{13}C pyruvate to noninvasively probe PDH flux is potentially a powerful diagnostic tool in cardiology.

Indeed, a number of recent reports in small and large animal models have demonstrated the ability of hyperpolarized ^{13}C MR imaging and spectroscopy to characterize the PDH flux noninvasively in normal hearts and hearts during ischemia-reperfusion and cardiac diseases (86–90). In normal hearts, the $^{13}CO_2$ derived from [1-^{13}C]pyruvate due to cardiac PDH flux is observed mostly as ^{13}C-bicarbonate (in equilibrium with $^{13}CO_2$) signal (Fig. 7) in MR spectroscopy data (64,87,88), and some [1-^{13}C]lactate and [1-^{13}C]alanine signals can also be observed. In spatially resolved ^{13}C MRI data obtained from large animal models, the substrate signal was found to be localized mostly in the cardiac chambers, while ^{13}C-bicarbonate was localized in the myocardium (Fig. 8); [1-^{13}C]lactate signal was more diffuse and observed in both the blood and cardiac muscle (64,86).

In models of ischemia and reperfusion, impaired PDH flux can be observed as decreased ^{13}C-bicarbonate signal shortly following reperfusion (86,89). Potentially, the viability of the affected tissue may be probed by following the recovery of the PDH flux (or the lack of it) post reperfusion and assessment of interventions targeting this metabolic pathway may also benefit from this technique. Changes in PDH flux due to diabetes have been investigated in a small animal model (88). Very recently it has also been reported that in a porcine pacing model of dilated cardiomyopathy (DCM) the disease progression can be followed noninvasively with ^{13}C metabolic imaging using hyperpolarized [1-^{13}C]pyruvate, and altered cardiac PDH flux was found to be strongly associated with onset of decompensated DCM (90). Monitoring cardiac substrate utilization in patients may provide valuable information regarding progression of these diseases and aid clinical management.

Although most of the efforts so far in utilizing hyperpolarized ^{13}C MR metabolic imaging in cardiology have been focused on probing substrate utilization using [1-^{13}C]pyruvate, the cardiac pH may also be assessed noninvasively by the $H^{13}CO_3^-/^{13}CO_2$ ratio and the Henderson-Hasselbalch equation (87,91), if sufficient SNR is obtained for the $^{13}CO_2$ signal. Monitoring of cardiac Krebs cycle flux in real time using hyperpolarized [2-^{13}C]pyruvate is also feasible since the C2 position on pyruvate is carried into the cycle through acetyl-CoA (instead of being released as $^{13}CO_2$), and changes of Krebs cycle flux can be assessed by measuring changes in the [5-^{13}C]glutamate signal (92). Along with PDH flux, these additional parameters obtainable by hyperpolarized ^{13}C

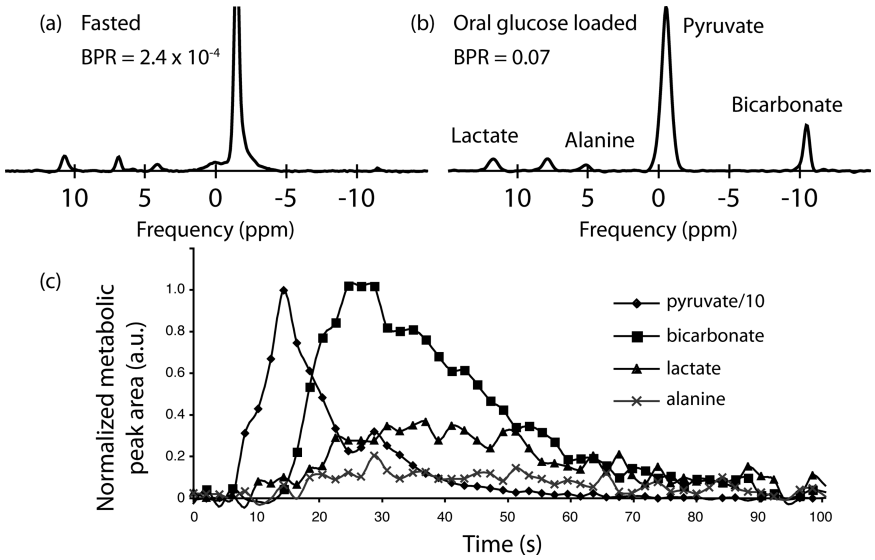


Figure 7. Cardiac-gated dynamic MRS data from pig hearts. **a**: Representative spectrum from the maximum bicarbonate frame in a fasted pig. **b**: Representative spectrum from the maximum bicarbonate frame in an oral glucose loaded pig. **c**: Time course of peak areas of pyruvate, bicarbonate, lactate, and alanine resonances acquired every 4 R-R intervals in the oral glucose loaded pig. The maximum bicarbonate to maximum pyruvate ratio (BPR) altered dramatically based on fed condition of the animal, due to changes in myocardial substrate utilization. Used with permission from Lau AZ, et al., Rapid multislice imaging of hyperpolarized (13)C pyruvate and bicarbonate in the heart. Magn Reson Med 2010;64:1323–1331, John Wiley & Sons.

MR provide insights into cardiac energetics and cellular environment that were not previously accessible noninvasively by other imaging modalities and may become valuable clinical tools in cardiology.

Neurology

The direct quantitative measures of BBB transport, inflammation, and oxidative load with hyperpolarized metabolic imaging has the potential to address unmet clinical needs in neurodegenerative disease, traumatic brain injury, and stroke. Unfortunately, this area of research trails the exciting progress that has been made in oncology and cardiology. Part of the lag in neurology may be due to the concern about the transport rate of T_1-limited hyperpolarized metabolic imaging agents through the BBB. One strategy to overcome the BBB transport limit explored the use of the

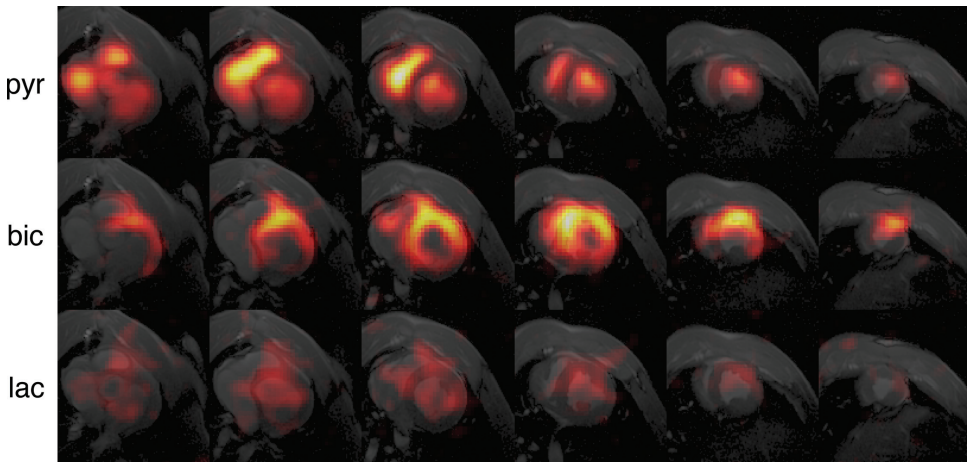


Figure 8. In vivo dynamic ^{13}C MRI data acquired using a multislice respiratory-gated spiral sequence showing spatial distribution of metabolites in a short-axis view of the heart. Pyruvate volume (six slices) were acquired starting from 10 seconds after the start of [1-^{13}C]pyruvate injection to capture the bolus through the heart (one volume of pyruvate images acquired during one respiratory cycle, 10 respiratory cycles of pyruvate data acquired, pyruvate images from peak of the bolus shown). Bicarbonate and lactate image volumes were acquired after the pyruvate bolus and were each repeated three times. The resolution of the overlaid reconstructed ^{13}C images is 10.7 mm in-plane for bicarbonate and pyruvate and 12 mm for lactate with a 1-cm slice thickness (pyruvate images are shown with a difference scale from bicarbonate and lactate images). The scan was completed in ~1 minute. Almost all the [1-^{13}C]pyruvate signal observed was localized in the blood while ^{13}C-bicarbonate was confined mostly in the heart muscle. Figure courtesy of Angus Z. Lau and Charles H. Cunningham of Sunnybrook Health Sciences Centre.

nonpolar precursor molecule, ethyl-pyruvate (93). This molecule is readily taken up by the brain and metabolized, but injection rate is limited, and interpretation is complicated by the rate of hydrolysis. However, as part of this study it was discovered that a substantial amount of [1-^{13}C]pyruvate does make it through normal BBB during the first passage of a bolus, and is converted to [1-^{13}C]lactate. Both ^{13}C-bicarbonate and [1-^{13}C]lactate appear to be formed in brain tissue (51,94,95). In a subsequent dynamic metabolic imaging study, the [1-^{13}C]lactate observed in a brain ROI was found to arise from brain metabolism, while the bulk of the [1-^{13}C]pyruvate observed in that same ROI appeared to arise from the cerebral blood volume (51). Since a substantial amount of [1-^{13}C]pyruvate makes it across the normal BBB and is converted to [1-^{13}C]lactate, it should be possible to quantitatively measure the full range of BBB transport abnormalities. The quantitative nature of the measure of total ^{13}C taken up, as well as the metabolic activity, could make [1-^{13}C]pyruvate metabolic imaging an ideal tool to study the full range of disease-induced disruptions in the BBB, even the subtle ones that have been reported for some nonenhancing MS lesions (96).

Beyond [1-^{13}C]pyruvate, one of the most interesting agents for the study of neurodegenerative disease may be [1-^{13}C]dehydroascorbic acid (DHA) (97,98). This molecule has been shown to rapidly cross the BBB (99), and the conversion rate of DHA to vitamin C is expected to be a direct marker for oxidative stress (97,98). A number of other dissolution DNP agents have also been studied in the brain including KIC and [1-^{13}C]acetate (see Table 1).

CONCLUSION

Dissolution-DNP-enabled metabolic imaging is still a relatively young field, with active preclinical research. This includes rapid discovery of new indications for the lead compound, hyperpolarized [1-^{13}C]pyruvate, as well as a robust exploration of new agents. The success of the first clinical proof-of-concept trial and the development of a clinical polarizer should enable the next steps toward clinical translation of this technology.

REFERENCES

1. Nelson SJ, Kurhanewicz J, Vigneron DB, et al. Proof of Concept Clinical Trial of Hyperpolarized C-13 in Patients with Prostate Cancer. In: Proc 20th Annual Meeting ISMRM, Melbourne; 2012 (abstract 274).
2. Ardenkjaer-Larsen JH, Fridlund B, Gram A, et al. Increase in signal-to-noise ratio of > 10,000 times in liquid-state NMR. Proc Natl Acad Sci U S A 2003;100:10158–10163.
3. Ardenkjaer-Larsen JH, Axelsson O, Golman K, Wistrand L-G, Leunbach I, Petersson S. PCT patent application number WO99/35508, priority date 5 January 1998.
4. Wolber J, Ellner F, Fridlund B, et al. Generating highly polarized nuclear spins in solution using dynamic nuclear polarization. Nucl Meth Phys Res 2004;526:173–181.
5. Overhauser AW. Polarization of nuclei in metals. Phys Rev 1953; 92:411–415.
6. Carver TR, Slichter CP. Polarization of nuclear spins in metals. Phys Rev 1953;92:212–213.
7. Abragam A. Overhauser effect in nonmetals. Phys Rev 1955;98: 1729–1735.
8. Jeffries CD. Polarization of nuclei by resonance saturation in paramagnetic crystals. Phys Rev 1957;108:164–165.
9. Abragam A, Goldman M. Order and disorder. Oxford, UK: Clarendon Press; 1982.
10. de Boer W, Borghini M, Morimoto K, Niinikoski TO, Udo F. Dynamic polarization of protons, deuterons, and carbon-13 nuclei: thermal contact between nuclear spins and an electron spin-spin interaction reservoir. J Low Temp Phys 1974;15:249–266.
11. de Boer WD, Niinikoski TO. Dynamic proton polarization in propanediol below 0.5K. Nucl Instr Meth 1974;114:495–498.
12. Lewis RJ S. Sax's dangerous properties of industrial materials. New York: John Wiley & Sons; 2000.
13. Gallagher FA, Kettunen MI, Day SE, et al. Magnetic resonance imaging of pH in vivo using hyperpolarized 13C-labelled bicarbonate. Nature 2008;453:940–943.
14. Jensen PR, in't Zandt R, Karlsson M, et al. In: Proc 16th Annual Meeting ISMRM, Toronto; 2008 (abstract 892).
15. Jensen PR, Karlsson M, Meier S, Duus JØ, Lerche MH. Hyperpolarized amino acids for in vivo assays of transaminase activity. Chem Eur J 2009;15:10010–10012.
16. Heckmann J, Meyer W, Radtke E, Reicherz G. Electron spin resonance and its implication of the maximum nuclear polarization of deuterated solid target materials. Phys Rev 2006;74:Art. No. 134418.
17. Benjamin PS, Fuminori H, Matsumoto K-I, et al. The chemistry and biology of nitroxide compounds. Free Radic Biol Med 2007; 42:1632–1650.
18. Eaton SS, Eaton GR, Berliner L. Part A: free radicals, metals, medicine, and physiology. Part B: methodology, instrumentation, and dynamics. Series: Biological Magnetic Resonance. J Biomed EPR 2005;23/24.
19. Thaning M. PCT patent application number WO 2006/011811 A2, priority date 30 July 2004.
20. Andersson S, Radner F, Rydbeck A, Servin R, Wisrand L-G. United States patent number US5728370, priority date 5 January 1998.
21. Reddy T, Iwama T, Halpern HJ, Rawal VH. General synthesis of persistent trityl radicals for EPR imaging of biological systems. J Org Chem 1998;67:4635–4639.
22. Bowman MK, Mailer C, Halpern HJ. The solution conformation of triarylmethyl radicals. J Magn Reson 2005;172:254–267.
23. Hu K-N, Bajaj VS, Rosay M, Griffin RG. High-frequency dynamic nuclear polarization using mixtures of TEMPO and trityl radicals. J Chem Phys 2007;126:044512.
24. Ardenkjaer-Larsen JH, Macholl S, Johannesson H. Dynamic Nuclear polarization with trityls at 1.2K. Appl Magn Reson 2008;34:509–522.
25. Duijvestijn MJ, Wind RA, Smidt J. Quantitative investigation of the dynamic nuclear polarization effect by fixed paramagnetic centra of abundant and rare spins in solids at room temperature. Physica B, C 1986;138:147–170.
26. Bajaj VS, Hornstein MK, Kreischer KE, et al. 250 GHz CW gyrotron oscillator for dynamic nuclear polarization in biological solid state NMR. J Magn Reson 2007;189:251–279.
27. Hornstein MK, Bajaj VS, Kreischer KE, Griffin RG, Temkin RJ. CW second harmonic results at 460 GHz of a gyrotron oscillator — for sensitivity enhanced NMR. The Joint 30th International Conference of Infrared and Millimeter Waves and 13th International Conference on Terahertz Electronics 2005;2:437–438.
28. Comment A, van der Brandt B, Uffmann K, et al. Design and performance of a DNP prepolarizer coupled to a rodent MRI scanner. Conc Magn Reson 2007;31:255–269.
29. Jannin S, Comment A, Kurdzesau F, et al. A 140 Ghz prepolarizer for dissolution dynamic nuclear polarization. J Chem Phys 2008;128:241102.
30. Johannesson H, Macholl S, Ardenkjaer-Larsen JH. Dynamic Nuclear Polarization of [1–13C]pyruvic acid at 4.6 Tesla. J Magn Reson 2008;197:167–175.
31. Ardenkjaer-Larsen JH, Leach AM, Clarke N, Urbahn J, Anderson D Skloss TW. Dynamic nuclear polarization polarizer for sterile use intent. NMR Biomed 2011;24:927–932.
32. Goertz, S. Spintemperatur und magnetische Resonanz verdünnter elektronischer Systeme — ein Weg zur Optimierung

polarisierter Festkörper-Targetmaterialien, Ruhr-Universität Bochum, Habilitationsschrift, April 15, 2002.
33. Jain J, Dey S, Muralidharan L, Leach AM, Ardenkjaer-Larsen JH. Jet impingment melting with vaporization: A numerical study. Proceedings of the ASME Summer Heat Transfer Conference, HT 2008, 559–567.
34. Albers MJ, Bok R, Chen AP, et al. Hyperpolarized 13C lactate, pyruvate, and alanine: noninvasive biomarkers for prostate cancer detection and grading. Cancer Res 2008;68:8607–8615.
35. Day SE, Kettunen MI, Gallagher FA, et al. Detecting tumor response to treatment using hyperpolarized 13C magnetic resonance imaging and spectroscopy. Nat Med 2007;13:1382–1387.
36. Schroeder MA, Clarke K, Neubauer S, Tyler DJ. Hyperpolarized magnetic resonance: a novel technique for the in vivo assessment of cardiovascular disease. Circulation 2011;124:1580–1594.
37. Hurd RE, Yen YF, Mayer D, et al. Metabolic imaging in the anesthetized rat brain using hyperpolarized [1–13C] pyruvate and [1–13C] ethyl pyruvate. Magn Reson Med 2010;63:1137–1143.
38. Kohler SJ, Yen Y, Wolber J, et al. In vivo 13 carbon metabolic imaging at 3T with hyperpolarized 13C-1-pyruvate. Magn Reson Med 2007;58:65–69.
39. Tropp J, Calderon P, Carvajal L, et al. An endorectal dual frequency 13C-1H receive only probe for operation at 3.0 Tesla. In: Proc 14th Annual Meeting ISMRM, Seattle; 2006 (abstract 2594).
40. Tropp J, Lupo JM, Chen A, et al. Multi-channel metabolic imaging, with SENSE reconstruction, of hyperpolarized [1-(13)C] pyruvate in a live rat at 3.0 Tesla on a clinical MR scanner. J Magn Reson 2011;208:171–177.
41. Barb AW, Hekmatyar SK, Glushka JN, Prestegard JH. Exchange facilitated indirect detection of hyperpolarized 15ND2-amidoglutamine. J Magn Reson 2011;212:304–310.
42. Harris T, Giraudeau P, Frydman L. Kinetics from indirectly detected hyperpolarized NMR spectroscopy by using spatially selective coherence transfers. Chemistry 2010;17:697–703.
43. Golman K, in't Zandt R, Thaning M. Real-time metabolic imaging. Proc Natl Acad Sci U S A 2006;103:11270–11275.
44. Golman K, in't Zandt R, Lerche M, Pehrson R, Ardenkjaer-Larsen JH. Metabolic imaging by hyperpolarized 13C magnetic resonance imaging for in vivo tumor diagnosis. Cancer Res 2006;66:10855–10860.
45. Chen AP, Albers MJ, Cunningham CH, et al. Hyperpolarized C-13 spectroscopic imaging of the TRAMP mouse at 3T-initial experience. Magn Reson Med 2007;58:1099–1106.
46. Cunningham CH, Chen AP, Albers MJ, et al. Double spin-echo sequence for rapid spectroscopic imaging of hyperpolarized 13C. J Magn Reson 2007;187:357–362.
47. Yen YF, Kohler SJ, Chen AP, et al. Imaging considerations for in vivo 13C metabolic mapping using hyperpolarized 13C-pyruvate. Magn Reson Med 2009;62:1–10.
48. Mayer D, Levin YS, Hurd RE, Glover GH, Spielman DM. Fast metabolic imaging of systems with sparse spectra: application for hyperpolarized 13C imaging. Magn Reson Med 2006;56: 932–937.
49. Levin YS, Mayer D, Yen YF, Hurd RE, Spielman DM. Optimization of fast spiral chemical shift imaging using least squares reconstruction: application for hyperpolarized (13)C metabolic imaging. Magn Reson Med 2007;58:245–252.
50. Mayer D, Yen YF, Levin YS, et al. In vivo application of sub-second spiral chemical shift imaging (CSI) to hyperpolarized 13C metabolic imaging: comparison with phase-encoded CSI. J Magn Reson 2010;204:340–345.
51. Hurd RE, Yen YF, Tropp J, Pfefferbaum A, Spielman DM, Mayer D. Cerebral dynamics and metabolism of hyperpolarized [1-(13)C]pyruvate using time-resolved MR spectroscopic imaging. J Cereb Blood Flow Metab 2010;30:1734–1741.
52. Mayer D, Yen YF, Tropp J, Pfefferbaum A, Hurd RE, Spielman DM. Application of subsecond spiral chemical shift imaging to real-time multislice metabolic imaging of the rat in vivo after injection of hyperpolarized 13C1-pyruvate. Magn Reson Med 2009;62:557–564.
53. Lustig M, Donoho D, Pauly JM. Sparse MRI: the application of compressed sensing for rapid MR imaging. Magn Reson Med 2007;58:1182–1195.
54. Hu S, Lustig M, Chen AP, et al. Compressed sensing for resolution enhancement of hyperpolarized 13C flyback 3D-MRSI. J Magn Reson 2008;192:258–264.
55. Larson PE, Hu S, Lustig M, et al. Fast dynamic 3D MR spectroscopic imaging with compressed sensing and multiband excitation pulses for hyperpolarized (13)C studies. Magn Reson Med 2010;65:610–619.
56. Wiesinger F, Menzel MI, Weidl E, Janich M, Schwaiger M, Schulte RF. Minimum-norm IDEAL spiral CSI for efficient hyperpolarized 13C metabolic imaging. In: Proc 18th Annual Meeting ISMRM, Stockholm; 2010 (abstract 3290).
57. Reeder SB, Pineda AR, Wen Z, et al. Iterative decomposition of water and fat with echo asymmetry and least-squares estimation (IDEAL): application with fast spin-echo imaging. Magn Reson Med 2005;54:636–644.
58. Reeder SB, Brittain JH, Grist TM, Yen YF. Least-squares chemical shift separation for (13)C metabolic imaging. J Magn Reson Imaging 2007;26:1145–1152.
59. Wiesinger F, Weidl E, Menzel MI, et al. IDEAL spiral CSI for dynamic metabolic MR imaging of hyperpolarized [1–13C]pyruvate. Magn Reson Med 2011;25:142–151.
60. Larson PE, Kerr AB, Chen AP, et al. Multiband excitation pulses for hyperpolarized 13C dynamic chemical-shift imaging. J Magn Reson 2008;194:121–127.
61. Larson PE, Bok R, Kerr AB, et al. Investigation of tumor hyperpolarized [1–13C]-pyruvate dynamics using time-resolved multiband RF excitation echo-planar MRSI. Magn Reson Med 2010; 63:582–591.
62. Josan S, Hurd RE, Kerr AB, et al. Effects of RF excitation scheme on signal-to-noise-ratio and apparent rate constant estimation in dynamic volumetric imaging of hyperpolarized [1–13C]-pyruvate. In: Proc 19th Annual Meeting ISMRM, Montreal; 2011 (abstract 3528).
63. Cunningham CH, Chen AP, Lustig M, et al. Pulse sequence for dynamic volumetric imaging of hyperpolarized metabolic products. J Magn Reson 2008;193:139–146.
64. Lau AZ, Chen AP, Ghugre NR, et al. Rapid multislice imaging of hyperpolarized 13C pyruvate and bicarbonate in the heart. Magn Reson Med 2010;64:1323–1331.
65. Yen YF, Le Roux P, Bok R, et al. Apparent T2 of 13C-labeled metabolites in vivo. In: Proc 16th Annual Meeting ISMRM, Toronto; 2008 (abstract 1747).
66. Yen YF, Le Roux P, Mayer D, et al. T(2) relaxation times of (13)C metabolites in a rat hepatocellular carcinoma model measured in vivo using (13)C-MRS of hyperpolarized [1-(13)C]pyruvate. NMR Biomed 2010;23:414–423.
67. Yen YF, Josan S, Senadheera L, et al. Hyperpolarized 13C T2 Mapping. Experimental NMR Conference. Pacific Grove, CA; 2011 (abstract 138).
68. Leupold J, Mansson S, Petersson JS, Hennig J, Wieben O. Fast multiecho balanced SSFP metabolite mapping of (1)H and hyperpolarized (13)C compounds. MAGMA 2009;22:251–256.
69. Leupold J, Wieben O, Mansson S, et al. Fast chemical shift mapping with multiecho balanced SSFP. MAGMA 2006;19:267–273.
70. Yen Y-F, Le Roux P, Bok R, et al. Signal enhancement in low-dose hyperpolarized 13C imaging using multi-slice FSEPSI sequence. In: Proc 16th Annual Meeting ISMRM, Toronto; 2008 (abstract 890).
71. Perman WH, Bhattacharya P, Leupold J, et al. Fast volumetric spatial-spectral MR imaging of hyperpolarized ^{13}C-labeled compounds using multiple echo 3D bSSFP. Magn Reson Imaging 2010;28:459–465.
72. Zierhut ML, Yen YF, Chen AP, et al. Kinetic modeling of hyperpolarized 13C1-pyruvate metabolism in normal rats and TRAMP mice. J Magn Reson 2010;202:85–92.
73. Romijn JA, Chinkes DL, Schwarz JM, Wolfe RR. Lactate-pyruvate interconversion in blood: implications for in vivo tracer studies. Am J Physiol 1994;266(3 Pt 1):E334–340.
74. Kettunen MI, Hu DE, Witney TH, et al. Magnetization transfer measurements of exchange between hyperpolarized [1–13C]pyruvate and [1–13C]lactate in a murine lymphoma. Magn Reson Med 2010;63:872–880.
75. Spielman DM, Mayer D, Yen YF, Tropp J, Hurd RE, Pfefferbaum A. In vivo measurement of ethanol metabolism in the rat liver using magnetic resonance spectroscopy of hyperpolarized [1–13C]pyruvate. Magn Reson Med 2009;62:307–313.
76. Moreno KX, Sabelhaus S, Merritt ME, Sherry D, Malloy CR. Malate-aspartate shuttle reversal allows for lactate concentration increases upon rapid changes in 13C pyruvate

concentration. In: Proc 18th Annual Meeting ISMRM, Stockholm; 2010 (abstract 1329).
77. Hu S, Chen AP, Zierhut ML, et al. In vivo carbon-13 dynamic MRS and MRSI of normal and fasted rat liver with hyperpolarized 13C-pyruvate. Mol Imaging Biol 2009;11:399–407.
78. Darpolor MM, Yen YF, Chua MS, et al. In vivo MRSI of hyperpolarized [1-(13) C]pyruvate metabolism in rat hepatocellular carcinoma. NMR Biomed 2011;24:506–513.
79. Park I, Larson PE, Zierhut ML, et al. Hyperpolarized 13C magnetic resonance metabolic imaging: application to brain tumors. Neuro Oncol 2010;12:133–144.
80. Park J, Josan S, Jang D, et al. Metabolic kinetics of a glioma model using hyperpolarized 13C magnetic resonance spectroscopic imaging. In: Proc 19th Annual Meeting ISMRM, Montreal; 2011 (abstract 3517).
81. Gillies RJ, Barry JA, Ross BD. In vitro and in vivo 13C and 31P NMR analyses of phosphocholine metabolism in rat glioma cells. Magn Reson Med 1994;32:310–318.
82. Stubbs M, Bhujwalla Z, Tozer G, et al. An assessment of 31P MRS as a method of measuring pH in rat tumours. NMR Biomed 1992;5:351–359.
83. Karlsson M, Jensen PR, in 't Zandt R, et al. Imaging of branched chain amino acid metabolism in tumors with hyperpolarized 13C ketoisocaproate. Int J Cancer 2010;127:729–736.
84. Chen AP, Bok R, Zhang V, et al. Serial hyperpolarized 13C 3D-MRSI following therapy in a mouse model of prostate cancer. In: Proc 16th Annual Meeting ISMRM, Toronto; 2008 (abstract 888).
85. Gallagher FA, Kettunen MI, Hu DE, et al. Production of hyperpolarized [1,4–13C2]malate from [1,4–13C2]fumarate is a marker of cell necrosis and treatment response in tumors. Proc Natl Acad Sci U S A 2009;106:19801–19806.
86. Golman K, Petersson JS, Magnusson P, et al. Cardiac metabolism measured noninvasively by hyperpolarized 13C MRI. Magn Reson Med 2008;59:1005–1013.
87. Merritt ME, Harrison C, Storey C, Jeffrey FM, Sherry AD, Malloy CR. Hyperpolarized 13C allows a direct measure of flux through a single enzyme-catalyzed step by NMR. Proc Natl Acad Sci U S A 2007;104:19773–19777.
88. Schroeder MA, Cochlin LE, Heather LC, Clark K, Radda GK, Tyler DJ. In vivo assessment of pyruvate dehydrogenase flux in the heart using hyperpolarized carbon-13 magnetic resonance. Proc Natl Acad Sci U S A 2008;105:12051–12056.
89. Merritt ME, Harrison C, Storey C, Sherry AD, Malloy CR. Inhibition of carbohydrate oxidation during the first minute of reperfusion after brief ischemia: NMR detection of hyperpolarized 13CO2 and H13CO3. Magn Reson Med 2008;60:1029–1036.
90. Schroeder MA, Lau AZ, Chen AP, et al. Hyperpolarized 13C magnetic resonance imaging and spectroscopy uniquely reveal early and late onset metabolic changes in the failing heart. In: Proc 19th Annual Meeting ISMRM, Montreal; 2011 (abstract 21).
91. Schroeder MA, Swietach P, Atherton HJ, et al. Measuring intracellular pH in the heart using hyperpolarized carbon dioxide and bicarbonate: a 13C and 31P magnetic resonance spectroscopy study. Cardiovasc Res 2010;86:82–91.
92. Schroeder MA, Atherton HJ, Ball DR, et al. Real-time assessment of Krebs cycle metabolism using hyperpolarized 13C magnetic resonance spectroscopy. FASEB J 2009;23:2529–2538.
93. Hurd RE, Yen YF, Mayer D, et al. Metabolic imaging in the anesthetized rat brain using hyperpolarized [1–13C] pyruvate and [1–13C] ethyl pyruvate. Magn Reson Med 2010;63:1137–1143.
94. Mayer D, Yen YF, Takahashi A, et al. Dynamic and high-resolution metabolic imaging of hyperpolarized [1-(13) C]-pyruvate in the rat brain using a high-performance gradient insert. Magn Reson Med 2011;65:1228–1233.
95. Marjanska M, Iltis I, Shestov AA, et al. In vivo 13C spectroscopy in the rat brain using hyperpolarized [1-(13)C]pyruvate and [2-(13)C]pyruvate. J Magn Reson 2010;206:210–218.
96. Soon D, Tozer D, Altmann D, Tofts P. Quantification of subtle blood-brain barrier disruption in non-enhancing lesions in multiple sclerosis: a study of disease and lesion subtypes. Multiple Sclerosis 2007;13:884–894.
97. Bohndiek SE, Kettunen MI, Hu DE, et al. Hyperpolarized [1-(13)c]-ascorbic and dehydroascorbic Acid: vitamin C as a probe for imaging redox status in vivo. J Am Chem Soc 2011;133:11795–11801.
98. Keshari KR, Kurhanewicz J, Bok R, Larson PEZ, Vigneron DB, Wilson DM. Hyperpolarized 13C dehydroascorbate as an endogenous redox sensor for in vivo metabolic imaging. Proc Natl Acad Sci U S A 2011;29:1035–1040.
99. Huang J, Agus DB, Winfree CJ, et al. Dehydroascorbic acid, a blood-brain barrier transportable form of vitamin C, mediates potent cerebroprotection in experimental stroke. Proc Natl Acad Sci U S A 2001;98:11720–11724.
100. Chen A, Hurd R, Schroeder MA, et al. Simultaneous investigation of cardiac pyruvate dehydrogenase flux, Krebs cycle metabolism and intracellular pH using hyperpolarized [1,2–13C2] pyruvate. NMR Biomed 2012;25:305–311.
101. Chen AP, Kurhanewicz J, Bok R, et al. Feasibility of using hyperpolarized [1–13C]lactate as a substrate for in vivo metabolic 13C MRSI studies. Magn Reson Imaging 2008;26:721–726.
102. Chen AP, Hurd RE, Gu YP, Wilson DM, Cunningham CH. (13)C MR reporter probe system using dynamic nuclear polarization. NMR Biomed 2011;24:514–520.
103. Keshari KR, Wilson DM, Chen AP, et al. Hyperpolarized [2–13C]-fructose: a hemiketal DNP substrate for in vivo metabolic imaging. J Am Chem Soc 2009;131:17591–17596.
104. Wilson DM, Hurd RE, Keshari K, et al. Generation of hyperpolarized substrates by secondary labeling with [1,1–13C] acetic anhydride. Proc Natl Acad Sci USA 2009;106:5503–5507.
105. Golman K, Ardenkjaer-Larsen JH, Petersson JS, Mansson S, Leunbach I. Molecular imaging with endogenous substances. Proc Natl Acad Sci U S A 2003;100:10435–10439.
106. Jensen PR, Karlsson M, Meier S, Duus JO, Lerche MH. Hyperpolarized amino acids for in vivo assays of transaminase activity. Chemistry 2009;15:10010–10012.
107. Gallagher FA, Kettunen MI, Day SE, et al. Detection of tumor glutamate metabolism in vivo using (13)C magnetic resonance spectroscopy and hyperpolarized [1-(13)C]glutamate. Magn Reson Med 2011;66:18–23.
108. Johansson E, Mansson S, Wirestam R, et al. Cerebral perfusion assessment by bolus tracking using hyperpolarized 13C. Magn Reson Med 2004;51:464–472.
109. Comment A, Uffmann K, Jannin A, et al. In vivo DNP-enhanced 13C labeled acetate brain studies in a 9.4T animal scanner. In: Proc 15th Annual Meeting ISMRM, Berlin; 2007 (abstract 369).